



PROCEEDINGS BOOK OF THE 4TH INTERCONTINENTAL GEOINFORMATION DAYS 20-21 JUNE 2022 TABRIZ, IRAN

MERSIN UNIVERSITY-ENGINEERING FACULTY
DEPARTMENT OF GEOMATICS ENGINEERING



4th Intercontinental Geoinformation Days (IGD) 2022

20-21 June 2022

09:00 – 18:00 (GMT+ 4:30)

University of Tabriz, Iran

ISBN: 978-605-73805-7-9


<https://igd.mersin.edu.tr/>


The proceedings of the 4th Intercontinental Geoinformation Days



4th Intercontinental Geoinformation Days (IGD) 2022

 20-21 June 2022

 09:00 – 18:00 (GMT+ 4:30)

 University of Tabriz, Iran

Editor-in-Chief

Prof. Dr. Murat Yakar

Prof. Dr. Khalil Valizadeh Kamran

Editors

Assoc. Prof. Dr. Abolfazl Ghanbari

Asst. Prof. Dr. Sadra Karimzadeh

Dr. Behnam Khorrami

Asst. Prof. Dr. Ali Ulvi

Asst. Prof. Dr. Lütfiye Kuşak

Asst. Prof. Dr. Fatma BÜNYAN Ünel

Res. Asst. Aydın Alptekin

Res. Asst. Abdurahman Yasin Yiğit

Res. Asst. Mehmet Özgür Çelik

Eng. Engin Kanun

ISBN: 978-605-73805-7-9

Tabriz, 2022

4th Intercontinental Geoinformation Days

I would like to thank all of the contributing authors and reviewers to the 4th Intercontinental Geoinformation (IGD) Symposium, 20-21 June 2022. In this international symposium there are 79 presentations. 32 of the papers are from Türkiye and the rest came from various countries of the world.

Best regards

Prof. Dr. Murat YAKAR



HONOR BOARD

Ali Hamza PEHLİVAN – Governor of Mersin Province
Prof. Dr. Ahmet ÇAMSARI – Rector of Mersin University
Prof. Dr. Safar Nasrollahzadeh – Rector of University of Tabriz
Prof. Dr. Orhan AYDIN – Rector of Tarsus University
Prof. Dr. Ömer ARIÖZ – Rector of Toros University
Mehmet Zeki ADLI – Director of Turkish Land Registry and Cadastre
Prof. Dr. Rudolf STAIGER – FIG President
Prof. Dr. Christian HEIPKE – ISPRS President
Prof. Dr. Chryssy POTSIOU – FIG Honorary President
Prof. Dr. Haluk ÖZENER – Boğaziçi University Director of Kandilli Observatory
Dr. Orhan ERCAN – FIG Vice President

EXECUTIVE COMMITTEE

Prof. Dr. Khalil Valizadeh KAMRAN – University of Tabriz, IRAN
Prof. Dr. Abdurrahman EYMEN – Erciyes University, TURKEY
Prof. Dr. Alexander SAGAYDAK – State University of Land Use Planning, RUSSIA
Prof. Dr. Alias Abdul RAHMAN – Universiti Teknologi Malaysia (UTM), MALAYSIA
Prof. Dr. Andreas GEORGOPOULOS – National Technical University of Athens, GREECE
Prof. Dr. Ariel BLANCO – University of Philippines at Daliman, PHILIPPINES
Prof. em. Dr.-Ing. Dr.h.c. Armin GRÜN – ETH Zürich, SWITZERLAND
Prof. Dr. Ashutosh MOHANTY – Shoolini University, INDIA
Prof. Dr. Edmönd Höxha (Albania University, Titana Albania)
Prof. Dr. Aydın ÜSTÜN – Kocaeli University, TURKEY
Prof. Dr. Bashkim IDRIZI – University of Prishtina, KOSOVO
Prof. Dr. Bülent BAYRAM – Yıldız Technical University, TURKEY
Prof. Dr. Charles TOTH – Ohio State University, USA
Prof. Dr. Chryssy POTSIOU – National Technical University of Athens, GREECE
Prof. Dr. Çetin CÖMERT – Karadeniz Technical University, TURKEY
Prof. Dr. Dursun Zafer ŞEKER – Istanbul Technical University, TURKEY
Prof. Dr. Erkan BEŞDOK – Erciyes University, TURKEY
Prof. Dr. Ferruh YILDIZ – Konya Technical University, TURKEY
Prof. Dr. Fevzi KARSLI – Karadeniz Technical University, TURKEY
Prof. Dr. Füsün BALIK ŞANLI – Yıldız Technical University, TURKEY
Prof. Dr. Hacı Murat YILMAZ – Aksaray University, TURKEY
Prof. Dr. Hediye ERDOĞAN – Aksaray University, TURKEY
Prof. Dr. Haluk ÖZENER – Boğaziçi University, TURKEY
Prof. Dr. Hande DEMİREL – Istanbul Technical University, TURKEY
Prof. Dr. Jiyeon KIM – University of Seoul, REPUBLIC OF KOREA
Prof. Dr. Maria Antonia BROVELLI – Politecnico di Milano, ITALY
Prof. Dr. Mevlüt YETKİN – İzmir Katip Çelebi University, TURKEY
Prof. Dr. Muhammad Bilal – Nanjing University of Information Science and Technology, CHINA
Prof. Dr. Mustafa YANALAK – Istanbul Technical University, TURKEY
Prof. Dr. Naser EL-SHEIMY – University of Calgary, CANADA
Prof. Dr. Nebiye MUSAOĞLU – Istanbul Technical University, TURKEY
Prof. Dr. Nilanchal PATEL – Birla Institute of Technology Mesra, INDIA
Prof. Dr. Niyazi ARSLAN – Çukurova University, TURKEY
Prof. Dr. Pal NIKOLLI – University of Tirana, ALBANIA
Prof. Dr. Reha Metin ALKAN – Istanbul Technical University, TURKEY
Prof. Dr. Sebahattin BEKTAŞ – Ondokuz Mayıs University, TURKEY
Prof. Dr. Sujit MANDAL – Diamond Harbour Womens' University, INDIA
Prof. Dr. Tahsin YOMRALIOĞLU – Beykent University, TURKEY
Prof. Dr. Tayfun ÇAY – Konya Technical University, TURKEY
Prof. Dr. Tamer BAYBURA – Afyon Kocatepe University, TURKEY
Prof. Dr. Tarık TÜRK – Cumhuriyet University, TURKEY
Prof. Dr. Taşkın KAVZOĞLU – Gebze Technical University, TURKEY
Prof. Dr. Uğur DOĞAN – Yıldız Technical University, TURKEY
Prof. Dr. Yasemin ŞİŞMAN – Ondokuz Mayıs University, TURKEY
Prof. Dr. Youkyung HAN – Kyungpook National University, REPUBLIC OF KOREA

Prof. Dr. Fetullah ARIK – Konya Technical University, TURKEY
Prof. Dr. S. Kazem Alavipanah – University of Tehran
Prof. Dr. Manouchehr Farajzadeh – Tarbiat Modares University
Prof. Dr. Seyed Ali Almodaresi – Islamic Azad University, Yazd
Prof. Dr. Orhan Gündüz – İzmir Institute of Technology, Turkey
Assoc. Prof. Dr. Bakhtyar Feizizadeh – University of Tabriz, IRAN
Assoc. Prof. Dr. Anargha DHORDE – Nowrosjee Wadia College, INDIA
Assoc. Prof. Dr. Aziz ŞİŞMAN – Ondokuz Mayıs University, TURKEY
Assoc. Prof. Dr. Bihter EROL – Istanbul Technical University, TURKEY
Assoc. Prof. Dr. Cevdet Coşkun AYDIN – Hacettepe University, TURKEY
Assoc. Prof. Dr. Erol YAVUZ – Uşak University, TURKEY
Assoc. Prof. Dr. Fatih DÖNER – Gümüşhane University, TURKEY
Assoc. Prof. Dr. Fatih POYRAZ – Cumhuriyet University, TURKEY
Assoc. Prof. Dr. Halil AKINCI – Artvin Çoruh University, TURKEY
Assoc. Prof. Dr. Lyubka PASHOVA – Bulgarian Academy of Sciences, BULGARIA
Assoc. Prof. Dr. Murat UYSAL – Afyon Kocatepe University, TURKEY
Assoc. Prof. Dr. Özgün AKÇAY – Çanakkale Onsekiz Mart University, TURKEY
Assoc. Prof. Dr. Serdar EROL – Istanbul Technical University, TURKEY
Assoc. Prof. Dr. Şükran YALPIR – Konya Technical University, TURKEY
Assoc. Prof. Dr. Uğur AVDAN – Eskişehir Technical University, TURKEY
Assoc. Prof. Dr. Zaide DURAN – Istanbul Technical University, TURKEY
Assoc. Prof. Dr. Alireza Gharagozlou – Shahid Beheshti University
Assoc. Prof. Dr. Ali Shamsoddini – Tarbiat Modarres University
Assoc. Prof. Dr. Ara Toomanian – University of Tehran
Assoc. Prof. Dr. Gordana Kaplan – Eskişehir Technical University
Assoc. Prof. Dr. Babak Vaheddoust – Bursa Technical University
Assoc. Prof. Dr. Najmeh Neysani Samany – University of Tehran
Asst. Prof. Dr. Sadra Karimzadeh – University of Tabriz, Iran
Asst. Prof. Dr. Mehrdad Jeyhouni – University of Tabriz, Iran
Asst. Prof. Dr. Berk ANBAROĞLU – Hacettepe University, TURKEY
Asst. Prof. Dr. Esra TEKDAL YILMAZ – Nicholls State University, USA
Asst. Prof. Dr. Jorge ROCHA – University of Lisbon, TURKEY
Asst. Prof. Dr. Kemal ÇELİK – Gümüşhane University, TURKEY
Asst. Prof. Dr. Khalid MAHMOOD – University of Punjab, PAKISTAN
Asst. Prof. Dr. Mahmut Oğuz SELBESOĞLU – Istanbul Technical University, TURKEY
Asst. Prof. Dr. Mustafa Utkan DURDAĞ – Artvin Çoruh University, TURKEY
Asst. Prof. Dr. Mustafa ÜSTÜNER – Artvin Çoruh University, TURKEY
Asst. Prof. Dr. Nizar POLAT – Harran University, TURKEY
Asst. Prof. Dr. Osman Sami KIRTILOĞLU – İzmir Katip Çelebi University, TURKEY
Asst. Prof. Dr. Sadra KARIMZADEH – University of Tabriz, IRAN
Asst. Prof. Dr. Serdar BİLGİ – Istanbul Technical University, TURKEY
Asst. Prof. Dr. Subija IZEIROSKI – Geo-SEE Institute, NORTH MACEDONIA
Asst. Prof. Dr. Surendra Pal SINGH – Wollega University, ETHIOPIA
Asst. Prof. Dr. Süleyman Sefa BİLGİLİOĞLU – Aksaray University, TURKEY
Asst. Prof. Dr. Serdar BİLGİ – Istanbul Technical University, TURKEY
Asst. Prof. Dr. Tae-Suk BAE – Sejong University, REPUBLIC OF KOREA
Asst. Prof. Dr. Tirthankar BANERJEE – Banaras Hindu University, INDIA
Asst. Prof. Dr. Volkan YILMAZ – Artvin Çoruh University, TURKEY
Asst. Prof. Dr. Shirin Mohammadkhan – University of Tehran
Asst. Prof. Dr. Hossein Aghighi – Shahid Beheshti University
Asst. Prof. Dr. Hamid Reza Ghafarian Malamiri – Yazd University
Asst. Prof. Dr. Samira Abushova – Azerbaijan National Academy of Science
Dr. Behnam Khorrami – 9 Eylül University, Turkey
Dr. Abdel Aziz ELFADALY – Nat. Auth. for Remote Sensing and Space Science, EGYPT
Dr. Abdul-Lateef BALOGUN – Universiti Teknologi PETRONAS (UTP), MALAYSIA
Dr. Artur GIL – University of the Azores, PORTUGAL
Dr. Ajoy DAS – Gujarat University, INDIA
Dr. Bayartungalag BATSAIKHAN – Chairwoman of Mongolian Geo-spatial Association, MONGOLIA
Dr. Cesar CAPINHA – University of Lisbon, PORTUGAL
Dr. Erman ŞENTÜRK – Kocaeli University, TURKEY
Dr. Gojko NIKOLIC – University of Montenegro, MONTENEGRO
Dr. Ismail KABASHI – Angst, AUSTRIA

Dr. Narendra KUMAR – HNB Garhwal University, INDIA
Dr. Krishna Prasad BHANDARI– Tribhuvan University, NEPAL
Dr. Olalekan Adekunle ISIOYE – Ahmadu Bello University, NIGERIA
Dr. MD Firoz KHAN – University of Malaya, MALAYSIA
Dr. Muhammad IMZAN BIN HASSAN – Universiti Teknologi Malaysia, MALAYSIA
Dr. Eng. Colonel Altan YILMAZ – Turkish Gen. Directorate of Mapping, TURKEY
M.Sc. R.S. AJIN – Dpt. Of Disaster Management, Govt. Of Kerala, INDIA
M.Sc. Ochirkhuyag LKHAMJAV – Mongolian Geo-spatial Association, MONGOLIA
M.Sc. Mohamed Ahmed Badawi ATTALLAH – Higher Institute of Literary Studies, EGYPT
M.Sc. Abubakar BELLO – Islamic Learning Centre, NIGERIA
Dereje SUFA – Wollega University, ETHIOPIA
Byeong-Hyeok YU – Korean Soc. of Environment & Ecology, REPUBLIC OF KOREA

International Association of Turkish Literature Culture Education (TEKE Derneği)

Prof. Dr. Cengiz ALYILMAZ –Bursa Uludağ University
Assoc. Prof. Dr. Onur ER – Düzce University
Assoc. Prof. Dr. Faruk POLATCAN – Sinop University
Assoc. Prof. Dr. Beyhan KOCADAĞIŞTAN – Atatürk University
Dr. İsmail ÇOBAN – Artvin Çoruh University

ORGANIZING COMMITTEE

Prof. Dr. Murat Yakar – Conference Chairman – Head of Department
Assoc. Prof. Dr. Erdinç Avaroğlu
Assoc. Prof. Dr. Jalal Shiri – Vice Chancellorship for Research and Technology
Prof. Dr. Behrouz Sari Sarraf – Head of Planning and Environmental sciences Faculty.
Prof. Dr. Khalil Valizadeh Kamran– Head of Organizing Committee
Assoc. Prof. Dr. Bakhtiar Feizizadeh – Head of Scientific committee
Prof. Dr. Maryam Bayati Khatibi
Assoc. Prof. Dr. Aboulfazl Ghanbari
Asst. Dr. Sadra Karimzadeh
Asst. Dr. Iraj Teymouri
Asst. Dr. Husain Karimzadeh
Prof. Dr.Saeid Jahabakhsh
Prof. Dr. Shahram Rostaei
Assoc. Prof. Dr. Shahrivar Rostaei
Asst. Dr. Mohsen Aghayari
Dr. Behnam Khorrami
Asst. Prof. Dr. Ali Ulvi
Asst. Prof. Dr. Fatma Bünyan Ünel
Asst. Prof. Dr. Lütfiye Kuşak
Dr. Hakan Doğan
Lect. Atilla Karabacak
Lect. Şafak Fidan
Res. Asst. Abdurahman Yasin Yiğit
Res. Asst. Aydın Alptekin
Eng. Engin Kanun
Eng. Mücahit Emre Oruç
Eng. Seda Nur Gamze Hamal



4th Intercontinental Geoinformation Days (IGD) 2022



20-21 June 2022



09:00 – 18:00 (GMT+ 4:30)



University of Tabriz, Iran

20 June 2022		
09.00-09.30	Opening Speeches Prof. Dr. Safar Nasrollahzadeh Assoc. Prof. Dr. Jalal Shiri Prof. Dr. Murat Yakar Prof. Dr. Behrouz Sarisarraf Prof. Dr. Khalil Valizadeh Kamran Assoc. Prof. Dr. Bakhtiyar Feizizadeh	
Keynote Lectures		
09.35-09.55	Prof. Dr. Jozef Strobel	Spatial Data Infrastructures to Geospatial Ecosystems
09.55-10.15	Prof. Dr. Ayyoob Sharifi	Integrated approaches for climate change adaptation and mitigation in cities
10.15-10.35	Prof. Dr. Chryssy Potsiou	Building Back Better Self-made Cities in the Post Covid 19 Era
10.35-10.55	Prof. Dr. Abbas Rajabifard	Digital Transformation-the role of Land Information and Location Intelligence in Sustainability and Resilience
10.55-11.15	Prof. Dr. Saied Homani	Paradigm Shift in Satellite Earth Observation Analytics; from Desktop to Cloud
11.15-11.35	Prof. Dr. Aliakbar Rasuly Pirouzian	Smart Environment Monitoring Systems: Operating Real-Time Sensors
11.35-12.00	Break	



4th Intercontinental Geoinformation Days (IGD) 2022



20-21 June 2022



09:00 – 18:00 (GMT+ 4:30)



University of Tabriz, Iran

20 June 2022

Session 1 (Photogrammetry & Remote Sensing)

Moderator: Prof. Dr. Seyed Ali Almodaresi

Time	Presentations
12.00-13.30	Spatiotemporal assessment of suspended sediment concentration and salinity in Lake Urmia using satellite imagery and remote sensing Mehran Dadashzadeh, Alireza Mojtahedi, Javad Parsa
	Evaluation of structural elements in the collision zone by remote sensing method Cihan Yalçın
	Introducing a new approach to temperature validation of remote sensing thermal images Hassan Emami, Arash Rahmanizadeh
	Usage of Unmanned Aerial Vehicles in Open Mine Sites Gulsum Yuksel, Ali Ulvi, Murat Yakar
	An assessment of support vector machines for crown delineation of pine single trees on unmanned aerial vehicle imagery Ali Hosseingholizade, Yousef Erfanifard, Seyed Kazem Alavipanah, Hooman Latifi, Yaser Jouybari-Moghaddam
	Investigation The Effect of UAV Flight Altitude in Map Production Mustafa Demirel, Yunus Kaya, Nizar Polat
	Comparison Between Multicopter Uav and Total Station for Volume Calculation Mustafa Ozkan, Nizar Polat
	Comparison Of the Effect of Different Vegetation Indices on Land Surface Temperature Values Gulshan Mammadli, Filiz Bektas Balcık
	Evaluation of urban heat island based on the land surface temperature and spatial variables in Tabriz Iraj Teymouri, Mohammad Nematı
	Exploring the Spatial distribution and intensity of Urban Heat Islands (UHI) in Ardabil city Iraj Teymouri
	Determination of burned areas using Sentinel-2A imagery and machine learning classification algorithms Ceydanur Arıkan, İlay Nur Tümer, Samet Aksoy, Elif Sertel
	Determination of first take-off points for UAVs in case of a disaster Rıdvan Ertuğrul Yildirim, Aziz Şişman
13.30-14.30	Lunch Break



4th Intercontinental Geoinformation Days (IGD) 2022



20-21 June 2022



09:00 – 18:00 (GMT+ 4:30)



University of Tabriz, Iran

20 June 2022

Session 2 (Geographic Information Systems) Moderator: Assoc. Prof. Dr. Ali Shamsoddini

Time	Presentations
14.30-16.00	Modeling of groundwater quality based on Water Quality Index using M5P decision tree method Shokouh Mohsenzadeh, Sahar Javidan, Mohammad Taghi Sattari
	Developing a participatory WebGIS for monitoring the physical problems of rural settlements Fatemeh Sadate Hosseini, Mohammadreza Jelokhani-Niaraki, Hasanali Faraji-Sabokbar
	Estimation of Mordagh Chay River water quality using gaussian process regression method Kambiz Falsafian
	Modeling of access and spatial mobility changes associated with floods in the field of transportation and movement of vehicles in areas 3, 6 and 7 of Tehran Abolfazl Ghanbari, Vahid Isazade, Esmail Isazade, Keyvan Seraj
	Geostatistical-based mapping of topsoil texture in Fluvisols and Vertisols around Lake of Manyas Fuat Kaya, Onur Meşe, Levent Başayığit
	Predicting the monthly flow of the Kaleybar Chay River based on M5 model tree Kambiz Falsafian
	Classification of surface water quality using data-driven methods Sahar Javidan, Shokouh Mohsenzadeh, Mohammad Taghi Sattari
	Exploring maps from childhood to adulthood: a journey to basic map knowledge with field experts Nuri Erdem
	The Analysis of 3D Geometric Features on Point Clouds by using Open-Source Software Ramazan Alper Kuçak
	Second Order Control Extension in Millennium City, Chikun Local Government Area, Kaduna State, Nigeria Adamu Bala, Shola Daniels Oyekunle, Nasiru Danlami
16.00-16.30	Break



4th Intercontinental Geoinformation Days (IGD) 2022



20-21 June 2022



09:00 – 18:00 (GMT+ 4:30)



University of Tabriz, Iran

20 June 2022

Session 3 (Photogrammetry & Remote Sensing)

Moderator: Assoc. Prof. Dr. Ara Toomanian

Time	Presentations
16.30-18.00	Analysis of a strong thunderstorm process observed in the eastern part of the Republic of Azerbaijan on June 1, 2017 Said Safarov, Elnur Safarov, Yegana Bayramova
	Determining Infestation of Pine Processionary Moth using Remote Sensing Gonca Ece Özcan, Fatih Sivrikaya
	Crop mapping using Sentinel-1 and Sentinel-2 images and random forest algorithm Ali Shamsoddini, Bahar Asadi
	View Angle Importance of SAR Satellite Imageries for Mapping Areas Susceptible to Floods: A Case Study of Kumamoto Prefecture, Japan Ayub Mohammadi, Himan Shahabi
	A review of Mud volcanoes situation in Caspian seaboard and new methods of their identification by remote sensing techniques Babak Kheradmand
	Analysis of heat island formation in land use of Ardabil city using thermal remote sensing imagers Hossein Fekrat, Sayyad Asghari Saraskanrood, Seyed Kazem Alavipanah
	Modeling of Land Subsidence in Shabestar Plain and its Relation to Groundwater by Radar Interferometry Naghme Mousakhani, Khalil Valizadeh Kamran
	Geometric shape fitting on simulated and TLS-based learning tree-trunk point cloud for precision forestry measurements Mustafa Zeybek
	Automated building extraction from very high-resolution remote sensing data with deep learning approaches Volkan Dağdelen, Ugur Alganci, Elif Sertel
	Comparison of open-source and commercial software for 3 modeling with terrestrial photogrammetry Muhammed Enes Atik, Zaide Duran
	Air Pollution Analysis in Istanbul Between January 2019 and April 2022 through Remote Sensing Technology HamedReza Vafa, Ahmet Ozgur Dogru , Dursun Zafer Seker



4th Intercontinental Geoinformation Days (IGD) 2022



20-21 June 2022



09:00 – 18:00 (GMT+ 4:30)



University of Tabriz, Iran

21 June 2022

Session 1 (Land Administration, Cadaster and Land Use) Moderator: Dr. Behnam Khorrami

Time	Presentations
09.00-10.30	Land Use Change Forest Scenarios on the Horizon 2025 Maryam Sadeghi, Khalil Valizadeh Kamran, Sayed Asadollah Hejazi
	Impact of Climatic Change on the Irrigated Agriculture – Case Study: Seyhan River Basin Bulent Ozekici, Burcak Kapur
	Evaluation of land consolidation impact criteria for rural development Halil Burak Akdeniz, Tayfun Çay, Şaban İnam
	Challenges of Integrating Cadastral Map and Urban Data Infrastructure in Iran Alireza Hajiheidari, Mahmoud Reza Delavar, Abbas Rajabifard
	Mapping Urban Land Use and Land Cover Variations Based on Support Vector Machine Algorithm: A Case Study of Sowme'eh Sara County Khalil Valizadeh Kamran, Behnam Khorrami, Hadi Beygi Heidarlou, Asma Karamat Mirshekarlou
	Optimal weighting approach for real-time positioning with Android smartphones Berkay Bahadur
	Land-use change on Peri-Urban: The Role of Rural-Urban Centralized and segregated Planning strategy Naser Shafieisabet, Sogand Khaksar
	Ecological-geomorphological analysis of surface processes in the Kura-Araz lowland and adjacent territories on the base of remote sensing data Gasimov Jeyhun Yashar
	Land cover classification in an arid landscape of Iran using Landsat 8 OLI science products: Performance assessment of machine learning algorithms Ali Keshavarzi, Fuat Kaya, Gordana Kaplan, Levent Başayığit
	Estimation of land use and land cover changes in Konya Closed Basin Hüseyin Emre Kaya, Vahdettin Demir
	Effects of Urban Vegetation in Mitigating Land Surface Temperature (LST) in Kaduna Metropolis, Nigeria Bello Abubakar Abubakar, Sani Abubakar Abubakar
	Assessing the importance of variable selection in Land Subsidence Susceptibility Mapping Sepideh Tavakkoli Piralilou, Golzar Einali, Shokrolah Kiani, Khalil Gholamnia
10.30-11.00	Break



4th Intercontinental Geoinformation Days (IGD) 2022



20-21 June 2022



09:00 – 18:00 (GMT+ 4:30)



University of Tabriz, Iran

21 June 2022

Session 2 (Photogrammetry & Remote Sensing) Moderator: Assoc. Prof. Dr. Masoud Minaei

Time	Presentations
11.00-12.30	Comparison of Photogrammetric Software Using the Terrestrial Photogrammetric Method: The Case of Hüseyin Paşa Mosque Fatih Pulat, Murat Yakar, Ali Ulvi
	Modelling a landslide site using UAV photogrammetry in Değirmençay village, Mersin Aydın Alptekin, Murat Yakar
	Comparison of shoreline extraction indexes performance using Landsat 9 satellite images in the heterogeneous coastal area Çiğdem Esendağlı, Serdar Selim, Nusret Demir
	Detection of surface algae blooms using the Sentinel 2A: An algorithm of the best strip ratio for a freshwater lake Pathmalal Manage, Charith Madushanka
	Global Scale-Biomass Estimation Based on a Deep Learning Method Somayeh Talebiesfandarani, Ali Shamsoddini
	Relationship between Net Primary Production (NPP) and Dust Storms in Different Land Cover Classes Shamsoddini Ali, Sadeghnezhad Ali
	Study of land subsidence by INSAR time series of ALOS-2, Sentinel-1 and GNSS CORS stations in Chaopraya basin, samutprakan, Thailand Adisorn Sittiwong
	Determination of the conversion of the stone fields into potential agricultural lands using Sentinel-2 satellite Hasan Lafçı, Halil İbrahim Şenol, Nizar Polat
	Preliminary results of surface displacement of the Elazığ Sivrice region by comparing D-InSAR and SBAS methods Dilara Solmaz, Furkan Veziro, Nusret Demir
	Evaluation of U-Th enrichments in QGIS platform; Example of Arıklı (Çanakkale, Turkey) district Cihan Yalçın, Sercan Öztürk, Mustafa Kumral
	Applications of Machine Learning and Deep Learning Techniques in Smart Agriculture: A Review Mehran Dadashzadeh, Kosar Sakhaeian
12.30-13.30	Lunch Break



4th Intercontinental Geoinformation Days (IGD) 2022



20-21 June 2022



09:00 – 18:00 (GMT+ 4:30)



University of Tabriz, Iran

21 June 2022

Session 3 (Photogrammetry & Remote Sensing)

Moderator: Assoc. Prof. Dr. Sadra Karimzadeh

Time	Presentations
13.30-15.00	Monitoring of growth of wheat's height using time series analysis of synthetic aperture radar (SAR) images and the corresponding parameters: A case study of a field in Hamedan province Ahya Rezaei, Sadra Karimzadeh, Khalil Valizadeh Kamran
	Identification of dust source and its modeling using HYSPLIT algorithm in West of Iran Behnaz Ghaderi, Zahra Azizi
	The effect of Covid-19 epidemic on the Land surface temperature of Asaluyeh Industrial City with an approach to image processing in Google Earth Engine Platform Mostafa MahdaviFard , Shahin Jafari , Khalil Valizadeh Kamran , Seyed Kazem Alavipanah
	Vis-NIR spectroscopy coupled with machine learning algorithms to predict soil gypsum in calcareous soils, southern Iran Monire Mina, Mahrooz Rezaei, Leila Hossein Abadi, Abdolmajid Sameni
	Heavy vehicle detection using optical remote sensing images and deep learning Roya Talebi, Sadra Karimzadeh, Gordana Kaplan
	Remote sensing of Nighttime Light Samaneh Bagheri, Hooman Moradpour, Khalil Valizadeh Kamran, Sadra Karimzadeh
	Applying Object-Oriented Processing Techniques for Investigating Land Use/Land Cover Changes and Predicting Future Changes (Case Study: Miandoab, IRAN) Abolfazl Ghanbari, Khalil Valizadeh Kamran, Arezoo Rahimi
	GNSS-R of Soil Moisture Content in Khuzestan for Optimal Crop Distribution Andres Calabia, Iñigo Molina, Catherine Jones
	Due to the drop in the level of the Caspian Sea evaluation of the geomorphological properties of the coastal region based on the processing of satellite images Turkan Mamishova
	Aircraft Detection in Very High-Resolution Satellite Images using YOLO-based Deep Learning Methods Berkay Yaban, Ugur Alganci, Elif Sertel
15.00-15.30	A review of the various advances in smart cities: Application of artificial intelligence and machine learning Mehran Dadashzadeh, Farhad Jedari Zarezadeh
15.00-15.30	Break



4th Intercontinental Geoinformation Days (IGD) 2022



20-21 June 2022



09:00 – 18:00 (GMT+ 4:30)



University of Tabriz, Iran

21 June 2022

Session 4 (Geographic Information Systems) Moderator: Assoc. Prof. Dr Alireza Gharagozlou

Time	Presentations
15.30-17.30	Calculate wastage and optimize building energy consumption using GEO BIM Saeed Rasti, Majid Kiyavarz, Abbas Rajabifard
	Investigation of land cover change with GIS using CORINE data Aslan Cihat Basara, Mehmet Emin Tabar, Sumeyra Gulsun, Yasemin Sisman
	Fire vulnerability of Hyrcanian forests (FVHF): A conceptual framework for an enhanced forest fire risk management in northern Iran Elnaz Nejatianpour, Omid Ghorbanzadeh, Josef Strobl, Mahmoud Daneshvar Kakhki, Hamid Amirnezhad, Mahmoud Sabouhi Sabouni
	A correlation study for determination risk area of dengue fever and dengue hemorrhagic fever: a case study of Sisaket province, Thailand Nutchanon Chantapoh
	Chi-square automatic interaction detection (CHAID) algorithm for flood susceptibility assessment in Sardabroud watershed, Iran Alireza Habibi, Mahmoud Reza Delavar, Mohammad Sadegh Sadeghian, Borzo Nazari
	Wind farm suitability analysis using Geographic Information System with Best-Worst Method in Amhara region of Ethiopia Zelalem Ayalke, Aziz Şişman
	Low latitude ionosphere responses to solar wind forcing from GNSS data in March 2001 Chukwuma Moses Anoruo, Francisca Nneke Okeke, Kingsley Chukwudi Okpala, Andres Calabia
	Using the Firefly algorithm for geoid determination Ulku Kirici Yildirim, Yasemin Sisman
	Combining GIS and AHP models for Landfill site selection in Niğde, Turkey Cemil Gezin
	Exploring the effect of Steiner points on the simplification algorithms Amir Gholami, Abolfazl Ghanbari, Neda Kaffash Charandabi
	Evaluation of geochemical analyzes in complex geological structures in GIS environment: Maden (Elazığ) district Mehmet Ali Ertürk, Cihan Yalçın
	Landslide susceptibility assessment of the high range areas in Thiruvananthapuram district (Southwest India) using the MCDA-AHP model and geospatial techniques Suchithra Jayakumar Anchima, Ajayakumar Gokul, Nelson Harshith, Romulus Costache, Rajendran Sobha Ajin

CONTENTS	Page
Spatiotemporal assessment of suspended sediment concentration and salinity in Lake Urmia using satellite imagery and remote sensing Mehran Dadashzadeh, Alireza Mojtahedi, Javad Parsa	1
Evaluation of structural elements in the collision zone by remote sensing method Cihan Yalçın	5
Introducing a new approach to temperature validation of remote sensing thermal images Hassan Emami, Arash Rahmanizadeh	9
Usage of Unmanned Aerial Vehicles in Open Mine Sites Gulsum Yuksel, Ali Ulvi, Murat Yakar	13
An assessment of support vector machines for crown delineation of pine single trees on unmanned aerial vehicle imagery Ali Hosingholizade, Yousef Erfanifard, Seyed Kazem Alavipanah, Hooman Latifi, Yaser Jouybari-Moghaddam	17
Investigation The Effect of UAV Flight Altitude in Map Production Mustafa Demirel, Yunus Kaya, Nizar Polat	21
Comparison Between Multicopter Uav and Total Station for Volume Calculation Mustafa Ozkan, Nizar Polat	25
Comparison Of the Effect of Different Vegetation Indices on Land Surface Temperture Values Gulshan Mammadli, Filiz Bektas Balcık	28
Evaluation of urban heat island based on the land surface temperature and spatial variables in Tabriz Iraj Teymouri, Mohammad Nemati	32
Exploring the Spatial distribution and intensity of Urban Heat Islands (UHI) in Ardabil city Iraj Teymouri	37
Determination of burned areas using Sentinel-2A imagery and machine learning classification algorithms Ceydanur Arıkan, İlay Nur Tümer, Samet Aksoy, Elif Sertel	43
Determination of first take-off points for UAVs in case of a disaster Rıdvan Ertuğrul Yildirim, Aziz Şişman	47
Modeling of groundwater quality based on Water Quality Index using M5P decision tree method Shokouh Mohsenzadeh, Sahar Javidan, Mohammad Taghi Sattari	51
Developing a participatory WebGIS for monitoring the physical problems of rural settlements Fatemeh Sadate Hosseini, Mohammadreza Jelokhani-Niaraki , Hasanali Faraji-Sabokbar	55
Estimation of Mordagh Chay River water quality using gaussian process regression method Kambiz Falsafian	58
Modeling of access and spatial mobility changes associated with floods in the field of transportation and movement of vehicles in areas 3, 6 and 7 of Tehran Abolfazl Ghanbari, Vahid Isazade, Esmail Isazade, Keyvan Seraj	62
Geostatistical-based mapping of topsoil texture in Fluvisols and Vertisols around Lake of Manyas Fuat Kaya, Onur Meşe, Levent Başayığit	68

Predicting the monthly flow of the Kaleybar Chay River based on M5 model tree Kambiz Falsafian	74
Classification of surface water quality using data-driven methods Sahar Javidan, Shokouh Mohsenzadeh, Mohammad Taghi Sattari	78
Exploring maps from childhood to adulthood: a journey to basic map knowledge with field experts Nuri Erdem	82
The Analysis of 3D Geometric Features on Point Clouds by using Open-Source Software Ramazan Alper Kuçak	87
Second Order Control Extension in Millennium City, Chikun Local Government Area, Kaduna State, Nigeria Adamu Bala, Shola Daniels Oyekunle, Nasiru Danlami	91
Analysis of a strong thunderstorm process observed in the eastern part of the Republic of Azerbaijan on June 1, 2017 Said Safarov, Elnur Safarov, Yegana Bayramova	95
Determining Infestation of Pine Processionary Moth using Remote Sensing Gonca Ece Özcan, Fatih Sivrikaya	99
Crop mapping using Sentinel-1 and Sentinel-2 images and random forest algorithm Ali Shamsoddini, Bahar Asadi	103
View Angle Importance of SAR Satellite Imageries for Mapping Areas Susceptible to Floods: A Case Study of Kumamoto Prefecture, Japan Ayub Mohammadi, Himan Shahabi	108
A review of Mud volcanoes situation in Caspian seaboard and new methods of their identification by remote sensing techniques Babak Kheradmand	111
Analysis of heat island formation in land use of Ardabil city using thermal remote sensing imagers Hossein Fekrat, Sayyad Asghari Saraskanrood, Seyed Kazem Alavipanah	114
Modeling of Land Subsidence in Shabestar Plain and its Relation to Groundwater by Radar Interferometry Naghme Mousakhani, Khalil Valizadeh Kamran	118
Geometric shape fitting on simulated and TLS-based learning tree-trunk point cloud for precision forestry measurements Mustafa Zeybek	122
Automated building extraction from very high-resolution remote sensing data with deep learning approaches Volkan Dağdelen, Ugur Alganci, Elif Sertel	127
Comparison of open-source and commercial software for 3 modeling with terrestrial photogrammetry Muhammed Enes Atik, Zaide Duran	131
Air Pollution Analysis in Istanbul Between January 2019 and April 2022 through Remote Sensing Technology HamedReza Vafa, Ahmet Ozgur Dogru , Dursun Zafer Seker	135
Land Use Change Forest Scenarios on the Horizon 2025 Maryam Sadegih, Khalil Valizadeh Kamran, Sayed Asadollah Hejazi	139

Impact of Climatic Change on the Irrigated Agriculture – Case Study: Seyhan River Basin Bulent Ozekici, Burcak Kapur	147
Evaluation of land consolidation impact criteria for rural development Halil Burak Akdeniz, Tayfun Çay, Şaban İnam	151
Challenges of Integrating Cadastral Map and Urban Data Infrastructure in Iran Alireza Hajiheidari, Mahmoud Reza Delavar, Abbas Rajabifard	155
Mapping Urban Land Use and Land Cover Variations Based on Support Vector Machine Algorithm: A Case Study of Sowme'eh Sara County Khalil Valizadeh Kamran, Behnam Khorrami, Hadi Beygi Heidarlou , Asma Karamat Mirshekarlou	159
Optimal weighting approach for real-time positioning with Android smartphones Berkay Bahadur	163
Land-use change on Peri-Urban: The Role of Rural-Urban Centralized and segregated Planning strategy Naser Shafieisabet, Sogand Khaksar	167
Ecological-geomorphological analysis of surface processes in the Kura-Araz lowland and adjacent territories on the base of remote sensing data Gasimov Jeyhun Yashar	171
Land cover classification in an arid landscape of Iran using Landsat 8 OLI science products: Performance assessment of machine learning algorithms Ali Keshavarzi, Fuat Kaya, Gordana Kaplan, Levent Başayığit	175
Estimation of land use and land cover changes in Konya Closed Basin Hüseyin Emre Kaya, Vahdettin Demir	180
Effects of Urban Vegetation in Mitigating Land Surface Temperature (LST) in Kaduna Metropolis, Nigeria Bello Abubakar Abubakar, Sani Abubakar Abubakar	184
Assessing the importance of variable selection in Land Subsidence Susceptibility Mapping Sepideh Tavakkoli Piralilou , Golzar Einali, Shokrolah Kiani, Khalil Gholamnia	188
Comparison of Photogrammetric Software Using the Terrestrial Photogrammetric Method: The Case of Hüsrev Paşa Mosque Fatih Pulat, Murat Yakar, Ali Ulvi	192
Modelling a landslide site using UAV photogrammetry in Değirmençay village, Mersin Aydın Alptekin, Murat Yakar	196
Comparison of shoreline extraction indexes performance using Landsat 9 satellite images in the heterogeneous coastal area Çiğdem Esendağlı, Serdar Selim, Nusret Demir	199
Detection of surface algae blooms using the Sentinel 2A: An algorithm of the best strip ratio for a freshwater lake Pathmalal Manage, Charith Madushanka	203
Global Scale-Biomass Estimation Based on a Deep Learning Method Somayeh Talebiesfandarani, Ali Shamsoddini	207
Relationship between Net Primary Production (NPP) and Dust Storms in Different Land Cover Classes Shamsoddini Ali, Sadeghnezhad Ali	211

Study of land subsidence by INSAR time series of ALOS-2, Sentinel-1 and GNSS CORS stations in Chaopraya basin, samutprakan, Thailand Adisorn Sittiwong	215
Determination of the conversion of the stone fields into potential agricultural lands using Sentinel-2 satellite Hasan Lafçı, Halil İbrahim Şenol, Nizar Polat	218
Preliminary results of surface displacement of the Elazig Sivrice region by comparing D-InSAR and SBAS methods Dilara Solmaz , Furkan Veziro , Nusret Demir	221
Evaluation of U-Th enrichments in QGIS platform; Example of Arıklı (Çanakkale, Turkey) district Cihan Yalçın, Sercan Öztürk, Mustafa Kumral	225
Applications of Machine Learning and Deep Learning Techniques in Smart Agriculture: A Review Mehran Dadashzadeh, Kosar Sakhaeian	229
Monitoring of growth of wheat's height using time series analysis of synthetic aperture radar (SAR) images and the corresponding parameters: A case study of a field in Hamedan province Ahya Rezaei, Sadra Karimzadeh, Khalil Valizadeh Kamran	233
Identification of dust source and its modeling using HYSPLIT algorithm in West of Iran Behnaz Ghaderi, Zahra Azizi	239
The effect of Covid-19 epidemic on the Land surface temperature of Asaluyeh Industrial City with an approach to image processing in Google Earth Engine Platform Mostafa MahdaviFard , Shahin Jafari , Khalil Valizadeh Kamran , Seyed Kazem Alavipanah	242
Vis-NIR spectroscopy coupled with machine learning algorithms to predict soil gypsum in calcareous soils, southern Iran Monire Mina, Mahrooz Rezaei, Leila Hossein Abadi, Abdolmajid Sameni	246
Heavy vehicle detection using optical remote sensing images and deep learning Roya Talebi, Sadra Karimzadeh, Gordana Kaplan	250
Remote sensing of Nighttime Light Samaneh Bagheri, Hooman Moradpour, Khalil Valizadeh Kamran, Sadra Karimzadeh	254
Applying Object-Oriented Processing Techniques for Investigating Land Use/Land Cover Changes and Predicting Future Changes (Case Study: Miandoab, IRAN) Abolfazl Ghanbari, Khalil Valizadeh Kamran, Arezoo Rahimi	258
GNSS-R of Soil Moisture Content in Khuzestan for Optimal Crop Distribution Andres Calabia, Iñigo Molina, Catherine Jones	262
Due to the drop in the level of the Caspian Sea evaluation of the geomorphological properties of the coastal region based on the processing of satellite images Turkan Mamishova	266
Aircraft Detection in Very High-Resolution Satellite Images using YOLO-based Deep Learning Methods Berkay Yaban, Ugur Alganci, Elif Sertel	270
A review of the various advances in smart cities: Application of artificial intelligence and machine learning Mehran Dadashzadeh, Farhad Jedari Zarezadeh	274
Calculate wastage and optimize building energy consumption using GEO BIM Saeed Rasti, Majid Kiyavarz, Abbas Rajabifard	278

Investigation of land cover change with GIS using CORINE data Aslan Cihat Basara, Mehmet Emin Tabar, Sumeyra Gulsun, Yasemin Sisman	282
Fire vulnerability of Hyrcanian forests (FVHF): A conceptual framework for an enhanced forest fire risk management in northern Iran Elnaz Nejatiyanpour, Omid Ghorbanzadeh, Josef Strobl, Mahmoud Daneshvar Kakhki, Hamid Amirnezhad, Mahmoud Sabouhi Sabouni	286
A correlation study for determination risk area of dengue fever and dengue hemorrhagic fever: a case study of Sisaket province, Thailand Nutchanon Chantapoh	290
Chi-square automatic interaction detection (CHAID) algorithm for flood susceptibility assessment in Sardabroud watershed, Iran Alireza Habibi, Mahmoud Reza Delavar, Mohammad Sadegh Sadeghian, Borzo Nazari	294
Wind farm suitability analysis using Geographic Information System with Best-Worst Method in Amhara region of Ethiopia Zelalem Ayalke, Aziz Şişman	298
Low latitude ionosphere responses to solar wind forcing from GNSS data in March 2001 Chukwuma Moses Anoruo, Francisca Nneke Okeke, Kingsley Chukwudi Okpala, Andres Calabia	303
Using the Firefly algorithm for geoid determination Ulku Kirici Yildirim, Yasemin Sisman	306
Combining GIS and AHP models for Landfill site selection in Niğde, Turkey Cemil Gezin	310
Exploring the effect of Steiner points on the simplification algorithms Amir Gholami, Abolfazl Ghanbari, Neda Kaffash Charandabi	314
Evaluation of geochemical analyzes in complex geological structures in GIS environment: Maden (Elazığ) district Mehmet Ali Ertürk, Cihan Yalçın	319
Landslide susceptibility assessment of the high range areas in Thiruvananthapuram district (Southwest India) using the MCDA-AHP model and geospatial techniques Suchithra Jayakumar Anchima, Ajayakumar Gokul, Nelson Harshith, Romulus Costache, Rajendran Sobha Ajin	323

4th Intercontinental Geoinformation Days

igd.mersin.edu.tr



Spatiotemporal assessment of suspended sediment concentration and salinity in Lake Urmia using satellite imagery and remote sensing

Mehran Dadashzadeh ¹, Alireza Mojtahedi¹, Javad Parsa ²

¹University of Tabriz, Faculty of Civil Engineering, Tabriz, Iran

²University of Tabriz, Faculty of Agriculture, Tabriz, Iran

Keywords

Spatio-temporal analysis
Causeway
Salinity
SSC
Urmia Lake

Abstract

Lake Urmia is considered as the largest salt water lake in Iran. Due to climate change and human activities in the lake's basin, the salinity of the lake has risen to more than 300 g/L during recent years, and large areas of the lake bed have been desiccated. Consequently, awareness of the hydro-ecological factors during the last few decades is crucial for identifying the problems. In the present study, the impacts of changes in suspended sediment concentration and saline features are explored using satellite imagery and remote sensing. The main purpose of this study is to conduct supervised monitoring in order to evaluate the Urmia Lake crisis with regard to human-involved factors such as the construction of the causeway. The results highlight an alarming increase of saline features around the lake during the studied period, from 287.718 km² in 2000 to 3006.5 km² in 2015. Also, it is concluded that the SSC has increased in the lake during recent years. The results of this study confirm that anthropogenic factors can be considered as the main cause of the crisis.

1. Introduction

Urmia Lake is one of the largest hyper-saline lakes in the world, with considerable ecological, environmental, and cultural value. Its watershed is an important agricultural region with a population of around 5 million people. Over the past few years, the lake's surface area and water level have been declining. The decline is generally attributed to a combination of climate change, increased water diversion for irrigated agriculture within the lake's watershed, and mismanagement (AghaKouchak et al. 2015; Hassanzadeh et al. 2011; Khatami 2013; Okhravi et al. 2017; Mojtahedi et al. 2022). Also, a causeway has been built across the lake with a gap of less than 2000 m, which may decrease the water circulation between the northern and southern halves of the lake.

Satellite imagery during the recent 17-year period illustrates the water retrogradation and the expansion of saline features around the lake. As the surface water continues to shrink in size, more of the lakebed and salt will be exposed (Garousi et al. 2013). Of the serious salinization effects, one can mention the ecological threats caused by the lake bed turning into a salt-covered

wasteland and the consequent soil erosion (Pitman and L  uchli 2002). Considering the importance of the problem, a comprehensive analysis of the changes in dominant parameters is essential for the control and management of the lake, and the evaluation and implementation of effective restoration methods require appropriate spatial information. Thus, remote sensing methods are able to provide valuable information to conduct a comprehensive monitoring strategy, which is crucial for ecological management. In recent years, several studies have been carried out using satellite imagery and remote sensing technologies to develop monitoring procedures for the lake.

Mitchell (2013) used remote sensing technology and Landsat 5 and Landsat 8 satellite imagery to study changes in the water area and saline features of Urmia Lake and concluded that the saline features had increased by 898 km² from 1998 to 2013. Khademi et al. (2015) studied the saline features around the lake using Landsat satellite imagery, remote sensing, and spatial analysis. The study of Landsat satellite images over a 13-year period illustrated a very rapid increase in saline features, and that the area of salt marsh in 2011 was approximately 26 times that of 1998. Chaudhari et al.

* Corresponding Author

(mehrandadashzadeh@tabrizu.ac.ir) ORCID ID 0000-0001-9521-7330
*(a.mojtahedi@tabrizu.ac.ir) ORCID ID 0000-0002-7917-434X
(jparsa@tabrizu.ac.ir) ORCID ID 0000-0002-4993-4475

Cite this study

Dadashzadeh, M., Mojtahedi, A., & Parsa, J. (2022). Spatiotemporal assessment of suspended sediment concentration and salinity in Lake Urmia using satellite imagery and remote sensing. 4th Intercontinental Geoinformation Days (IGD), 1-4, Tabriz, Iran

(2018) studied the natural and human-induced changes in the hydrology of the Urmia Lake basin based on remote sensing data, ground observations, and a hydrological model. The results indicated that the reduction in lake volume is primarily due to direct anthropogenic alterations.

Various factors have been mentioned which affect the crisis. In general, scientists believe that a combination of drought, climate change, increased water diversion for irrigated agriculture within the lake's watershed, mismanagement, and the constructed causeway are the most important causes of the lake's decline (Abbaspour et al. 2012; Shadkam et al. 2016). This study attempts to monitor the crisis by exploring the impact of key features such as the salinity and suspended sediment concentration (SSC) via satellite imagery, remote sensing, and fieldwork.

2. Method

In the present study, a spatio-temporal analysis is performed for the last decade of data (2000-2015) obtained from Landsat and MODIS satellite images integrated into Geographical Information System (GIS) software. The ArcGIS 10.3 package is used for calibrating, analyzing, and characterizing the recorded images to be used for decision-making and problem management.

2.1. Detection of causeway impacts on suspended sediment concentration and salinity

A 1.25 km-long dike-type causeway has been built across the lake to provide road access between the western and eastern provinces and divides the lake into northern and southern basins. Some scientists and environmental experts have suggested that this has decreased circulation within the lake and subsequently flow and salinity regimes are affected (Karbassi et al. 2010; Dadashzadeh et al. 2020). In this study, the effects of the construction of the causeway are investigated by evaluating the changes in two parameters, which include the saline features (around the causeway and shoreline of the lake) and the suspended sediment concentration, as described in the following sections.

2.1.1. Analyzing changes in suspended sediment concentration

The research uses Landsat 5, 7 and 8 satellite imagery to study changes in the SSC of Urmia Lake from 2000 to 2015. The images are calibrated using the expressed equations and the lake boundary is determined from the 1999 image. Due to the large size of the Landsat imagery in the full scene and to reduce computational volume, all images are masked and cropped using this boundary and areas outside the border are removed. Also, to quantify the SSC, the water boundary of each year should be determined and salts should be removed. In this regard, the supervised classification is applied to the images using the Linear Mode SVM algorithm. The method of research uses three types of spectral transformation for suspended sediment that is Normalized Suspended Material Index (NSMI), Normalized Differences

Suspended Sediment Index (NDSSI), and Band Ratio (BR).

2.1.2. Change detection of saline features

In this study, Iso-cluster unsupervised classification and then supervised classification are implemented by conducting field visits. When setting a land cover map, it is necessary to take many GPS points of different features. To cover a study area with a representative set of sampled points, a schedule plan must be made before going out to the field. In this work, points such as samples of saline fields around the lake are located and marked by a Garmin 62 GPS. In addition, GPS points are taken at locations like road crossings, etc. to help create a coordinate system and for geo-referencing. Cloud-free images captured during the period of the fieldwork are ordered. After classifying the images, they are used to determine the ranges of salinity around the causeway and lake.

On the other hand, Landsat 5, 7 and 8 satellite imagery are used to study changes in saline features as the process worked in the SSC estimation. Radiometric correction of satellite imagery is carried out and the lake boundary is determined from the 1999 image. Then, all images are masked and cropped using this boundary. Therefore, the images are in the same size and number of pixels. ArcGIS and ENVI software programs are used to determine the lake boundary and to crop and mask images, respectively. To quantify the saline features in the lake, Brightness Index (BI) and Salinity Index (SI) are applied to images. After applying the indices, saline feature areas and the number of pixels are calculated for each image. MATLAB coding is performed to calculate area, number of pixels and total saline features from masked index results.

3. Results and discussion

3.1. Estimation of suspended sediment concentration

This section presents the results of applying the algorithm to determine the SSC in Urmia Lake. In this study, 3 typical indices are used to determine sediment content. The average results of each index are calculated to investigate the changes in SSC over the considered period (2000-2015) and the results are presented in Figure 1. The lower the NSMI and BR values, the cleaner the water, and the larger these values indicate the increase in SSC in the study area. The values of these indices have increased per year, indicating the increment in sedimentation rate, as shown in Fig. 1. Also, both BR and NSMI indices have provided better results compared to NDSSI.

3.2. Evaluation of saline features

In this study, satellite imagery is used to investigate the changes in areas of saline soils and the range of salinity around the causeway from 1999 to 2016. Development of the salinization area is visualized in Figure 2 for the years 1999 and 2016. The observed

changes in the area were compared with consideration of the lake shapefile for 1995 (when the lake reached its maximum expansion during the studied period), as the base area.

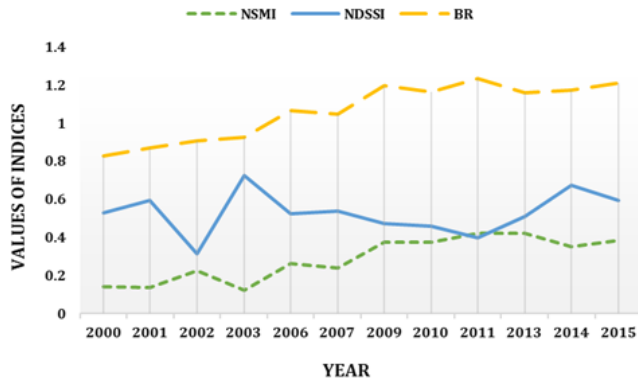


Figure 1. Average of sediment indices results for the years 2000 to 2015

Furthermore, the saline features around the lake are quantified using two types of spectral transformation for the period 2000-2015. After applying the proposed algorithm, the number of salt pixels, salt area, and the number of fresh salt pixels are calculated to evaluate the salinity increase and drought spread in Urmia Lake. The total number of pixels detected as saline features has increased during the studied period. That is, the drought has developed and more parts of the lake have been turned into a salt pan. The results indicate a significant increase in saline features around the lake during the studied period, from 287.718 km² to 3006.5 km² and consequently a decrease in lake water.

As previously mentioned, Lake Urmia salt is classified into two categories of fresh and old salt. Figure 3 indicates the number of pixels of fresh salt obtained by the algorithm. The number of pixels related to fresh salt has been added each year, reflecting the expansion of saline features in the lake.

As is clear from the results presented in Figure 3, the values of SI and BI indices have increased in the boundary during the studied period. The incremental trend of indices values demonstrates a considerable increase in saline features around the lake. Also, Figure 3 illustrates a reasonable agreement between the results of the two indices. For visual comparison, maps of the salinization areas are provided according to the results of the indices. The maps obtained from the SI index are illustrated in Figure 4 for the years 2000 and 2015.

4. Conclusion

There are many studies showing that human activities can be considered one of the main factors responsible for the ecological crises of lakes and wetlands in arid or semi-arid regions around the world. During recent decades, Urmia Lake has also experienced dramatic changes in its watershed. These factors include climate change, land-use changes, increased water diversion for irrigated agriculture within the watershed, construction of a causeway across the lake, several dams on the rivers around the lake, etc. The relationship

between the lake's crisis and hydrological drought and anthropogenic factors is a challenging problem for the local population and governmental organizations, noting the hierarchy in planning and making final decisions. However, there are not yet enough detailed studies on temporal and spatial change detection to conclude with certainty which of the anthropogenic and climate factors is the main cause of the crisis. This study has tried to investigate the problem, and the following results can be concluded based on the observations.

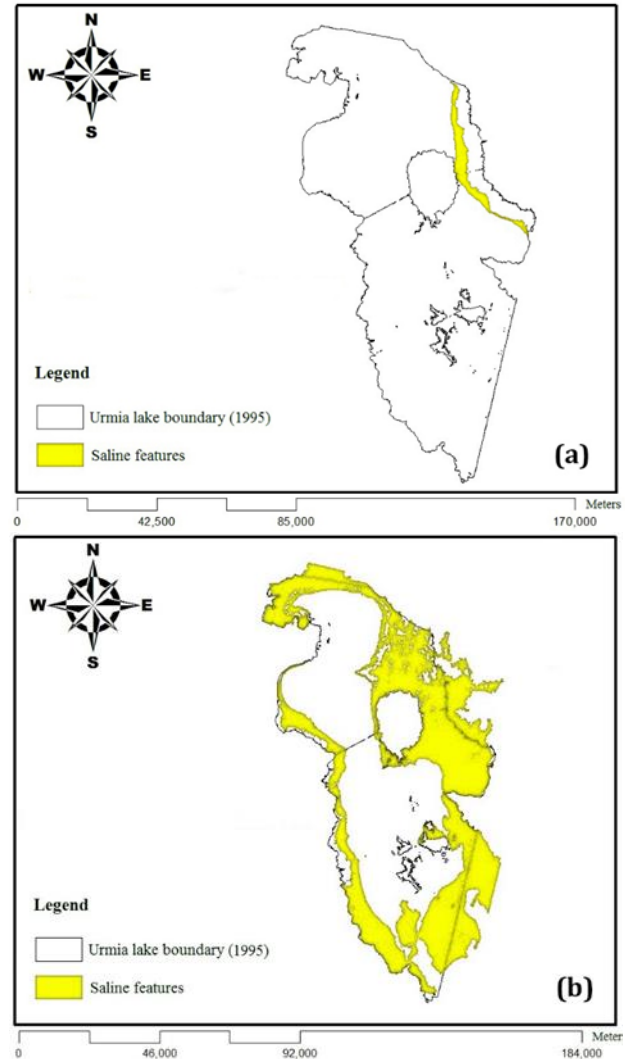


Figure 2. Maps of the salinization areas for the years, a) 1999 and b) 2016

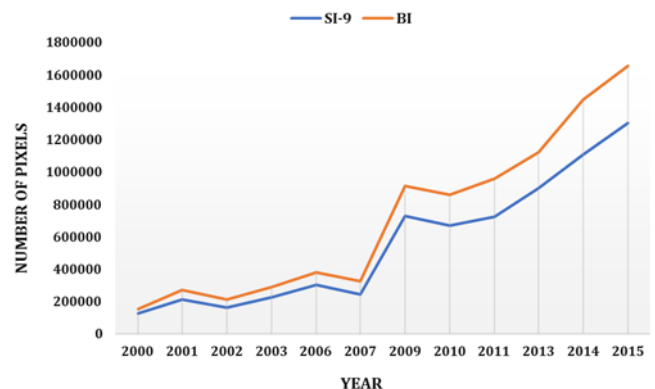


Figure 3. The number of pixels related to fresh salt

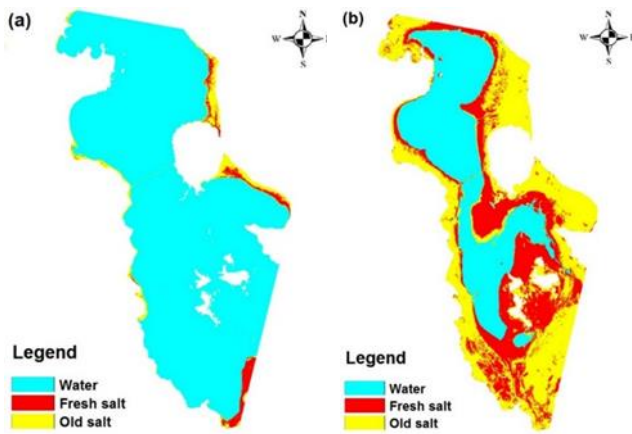


Figure 4. Maps of the salinization areas obtained from SI index for the years, a) 2000 and b) 2015

The results show that there is a notable increase in saline feature areas around the lake during the studied period, from 287.718 km² in 2000 to 3006.5 km² in 2015. The results warn that the continuation of the crisis of reduced water volume will lead to collapse of the lake's ecosystem as well as salt storms which could have serious negative impacts on the regional environment and public health. Considering the importance of the problem, maps of potential high-salinity areas are essential for the control and management of the environmental risks in the lake region.

Furthermore, the SSC and saline features have been investigated using satellite imagery over the past 15 years, from 2000 to 2015. In this regard, the algorithms have been implemented on the images and the results are analyzed. The results demonstrate that the SSC has increased in the lake during recent years. By analyzing the images and the amount of SSC around the causeway, it had no significant impact on the SSC pattern.

References

- Abbaspour, M., Javod, A. H., Mirbagheri, S. A., Ahmadi, Givi F., & Moghimi, P. (2012). Investigation of Lake Drying Attributed to Climate Change. *Int J Environ Sci Technol*, 9 (2), 257-266.
- AghaKouchak, A., Norouzi, H., Madani, K., Mirchi, A., Azarderakhsh, M., Nazemi, A., Nasrollahi, N., Farahmand, A., Mehran, A., & Hasanzadeh, E. (2015). Aral Sea syndrome desiccates Lake Urmia: Call for action. *J Great Lakes Res*, 41(1), 307-311.
- Chaudhari, S., Felfelani, F., Shin, S., & Pokhrel, Y. (2018). Climate and anthropogenic contributions to the desiccation of the second largest saline lake in the twentieth century. *J Hydrol*, 560, 342-353.
- Dadashzadeh, M., Parsa, J., & Mojtahedi, A. (2020). Investigation over the Interaction of Lake Urmia Wave Pattern and Causeway Using Meteorological Models and Computational Fluid Dynamics. *J. Oceanogr*, 11(41), 49-61.
- Garousi, V., Najafi, A., Samadi, A., Rasouli, K., & Khanaliloo, B. (2013). Environmental Crisis in Lake Urmia, Iran: A Systematic Review of Causes, Negative Consequences and Possible Solutions. *Lake Urmia Conservation Institute*.
- Hassanzadeh, E., Zarghami, M., & Hassanzadeh, Y. (2011). Determining the main factors in declining the Urmia Lake level by using System Dynamics Modeling. *Water Res. Manage*, 26 (1), 129-145.
- Karbassi, A., Bidhendi, G. N., Pejman, A., & Bidhendi, M. E. (2010). Environmental impacts of desalination on the ecology of Lake Urmia. *J. Great Lakes Res*, 36(3), 419-424.
- Khademi, F., Pirkharrati, H., & Shahkarami, S. (2015). Investigation of Increasing Trend of Saline Soils around Urmia Lake and its Environmental Impact, Using RS and GIS. *J. Geosci*, 24(94), 93-99.
- Khatami, S. (2013). Nonlinear Chaotic and Trend Analyses of Water Level at Urmia Lake, Iran. Master's thesis, Lund University, Sweden.
- Mitchell, D. E. (2013). Identifying Salinization through Multispectral Band Analysis. Master of Spatial Analysis (MSA). Toronto, Ontario, Canada.
- Mojtahedi, A., Dadashzadeh, M., Azizkhani, M., Mohammadian, A., & Almasi, R. (2022). Assessing climate and human activity effects on lake characteristics using spatio-temporal satellite data and an emotional neural network. *Environ Earth Sci*, 81(61).
- Okhravi, S., Eslamian, S., Tarkesh Esfahany, S., & Fb, A. (2017). Drought in Lake Urmia, in: Eslamian S, Eslamian F (Eds.), *Drought and Water Scarcity: Environmental Impacts and Analysis of Drought and Water Scarcity*. Boca Raton: CRC Press, 605-617.
- Pitman, M. G., & Lächli, A. (2002). Global Impact of Salinity and Agricultural Ecosystems, in: Lächli A, Lüttge U (Eds.), *Salinity: Environment - Plants - Molecules*. Springer, Dordrecht, pp. 3-20.
- Shadkam, S., Ludwig, F., van Oel, P., Kirmitt, Ç., & Kabat, P. (2016). Impacts of climate change and water resources development on the declining inflow into Iran's Urmia Lake. *J. Great Lakes Res*, 42(5), 942-952.



4th Intercontinental Geoinformation Days

igd.mersin.edu.tr



Evaluation of structural elements in the collision zone by remote sensing method

Cihan Yalçın *¹

¹Ministry of Industry and Technology, World Bank Project Implementation Unit, Ankara, Türkiye

Keywords

Suture zone
Satellite image
Fault
DEM
QGIS

Abstract

Topographic and linear data are precisely linked to the tectonic structure of the region. This relation can be identified both in the field and in satellite images. As it is recognized, high topographic areas are formed with the effect of the compression regime in the zones where different continents are sutured. There are traces of the suture zone in the northeast of Kahramanmaraş. Because of the closure of the Neotethys Ocean, a collision zone developed in and around Çağlayancerit, located in the northeast of Kahramanmaraş. Units in the Arabian Autochthonous and Taurus Orogenic belts came together in this district. Thrust belts and faults have been observed in this vicinity. This structural event has developed linearity and topographic elevations, respectively. When the data obtained in the field and the digital elevation method (DEM) data of the region are checked out together in the QGIS environment, the topographic elevations in the collision belt are approximately higher than the areas in the south. As a result of the north-south compression, the thrust lines formed definite linearity. Each different characterized fault in the region controlled the morphology immediately.

1. Introduction

Many geological studies utilise lineament and topographic components as ancillary indicators (Guild, 1974; Masoud et al., 2007). Depending on the geological development of a region, basins and orogenic belts are observed. In this situation, regional lineaments and morphological data have their ultimate form under tectonic and sedimentation control (Oakey, 1994; Fichler et al., 1999; Austin and Blenkinsop, 2008).

Remote sensing (RS) and geographic information systems (GIS) are platforms for map-based evaluation of geological structures. With technological advances and recent developments in spatial analysis techniques, large-scale linearity and morphological analyses have become relatively practicable (Masoud and Koike, 2011). These studies use numerical data such as satellite images and Digital Elevation Model (DEM). Such studies interpret morphological and linear structures (Morris, 1991; Süzen and Toprak, 1998; Tripathi et al., 2000).

In terms of its geological structure, Kahramanmaraş is a complex region where different tectonic units are observed together. Many thrust and fault zones associated with the closure of the southern branch of the Neotethys Ocean are observed in this region (Şengör and

Yılmaz 1981). Suture belts were formed by the closure of this ocean and the convergence of the Tauride and Arabian plates as a result (Robertson and Dixon 1984; Robertson et al., 2012). With the depletion of the ocean floor, allochthonous units were thrust onto the Arabian platform in the south, and a suture belt was formed between these two continents (Yılmaz, 1984; Yılmaz et al., 1987). Gül (1987) explained that the collision of the Anatolian and Arabian plates occurred in the Late Cretaceous and that a compressional regime was active in the region during the Paleocene-Early Eocene period. Yılmaz and Yiğitbaş (1990) stated that as a result of the movement of the Arabian continent towards the Anatolian plate between the Late Cretaceous-Miocene, the region gained a nappe character.

Rigo De Righi and Cortesini (1964) divided the tectonostratigraphic units in the Southeast Anatolian Region into four primary tectonic belts: the Taurus Orogenic Belt, the Margin Fold Belt, the Folded Belt, and the Foreland, respectively. On the other hand, Gül (2000) described Kahramanmaraş and its vicinity as Orogenic Belts. Yalçın (2012) mapped the rocks of different origins in Çağlayancerit and its west and revealed the deformation structures of the region. This region still has an active fault, such as the East Anatolian Fault (EAF). It

* Corresponding Author

*(cihan.yalcin@sanayi.gov.tr) ORCID ID 0000-0002-0510-2992

Cite this study

Yalçın, C. (2022). Evaluation of structural elements in the collision zone by remote sensing method. 4th Intercontinental Geoinformation Days (IGD), 5-8, Tabriz, Iran

is recognised that this main fault affects many morphological formations. In this region, distinctive morphological structures have cropped up due to the coexistence of rocks belonging to two different plates and the presence of different tectonic sequences on the thrust zones.

2. Method

The study area is located in the Çağlayancerit region, approximately 60 km northeast of Kahramanmaraş province (Figure 1a), in the Eastern Taurus Orogenic Belt. This region and its vicinity were named Engizek Askuşağı by Gül (2000) (Figure 1b). Just south of this belt is the marginal fold belt of the Arabian plate.

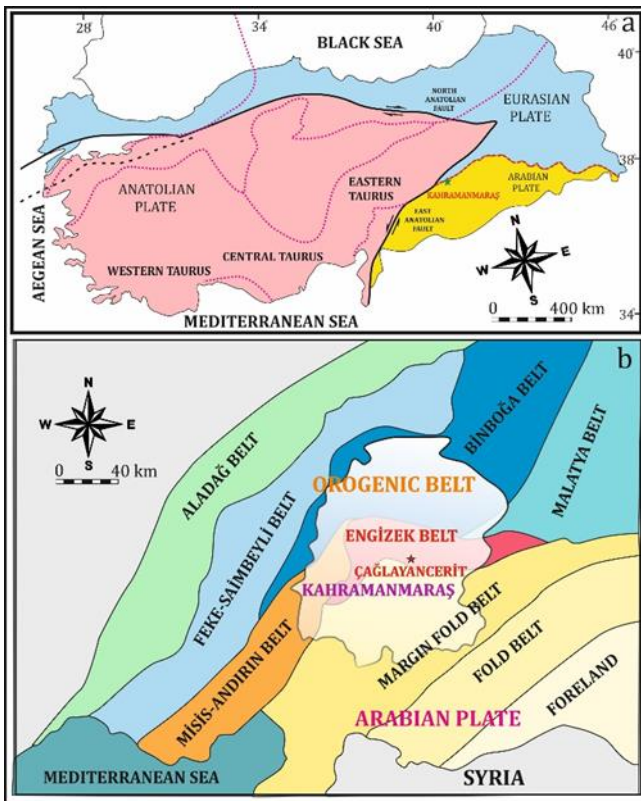


Figure 1. a) Tectonic location of the study area (Modified from Işık, 2016) b) Location of the study area according to tectonic belts. (Modified from Gül, 2000).

The DEM image of this geologically significant region has been downloaded from the United States Geological Survey (USGS) website. Aspect and slope maps of the region were created by evaluating the downloaded images in the QGIS environment. In addition, active faults in the region are placed on these images.

2.1. Geological background

Different stratigraphic sequences have emerged due to the coexistence of rock groups of different origins in the study area and allochthonous rocks overlying nappes and younger rocks in large areas. Allochthonous rocks, Suture Belt and Autochthonous units were defined from north to south (Yalçın, 2012). In the study area, the tectonic slices present an imbricated structure and the units belonging to different plates come together,

indicating a very complex structural position in the region (Figure 2). According to the structural elements examined, it can be said that the region has been under the influence of an N-S oriented compression for a long time.

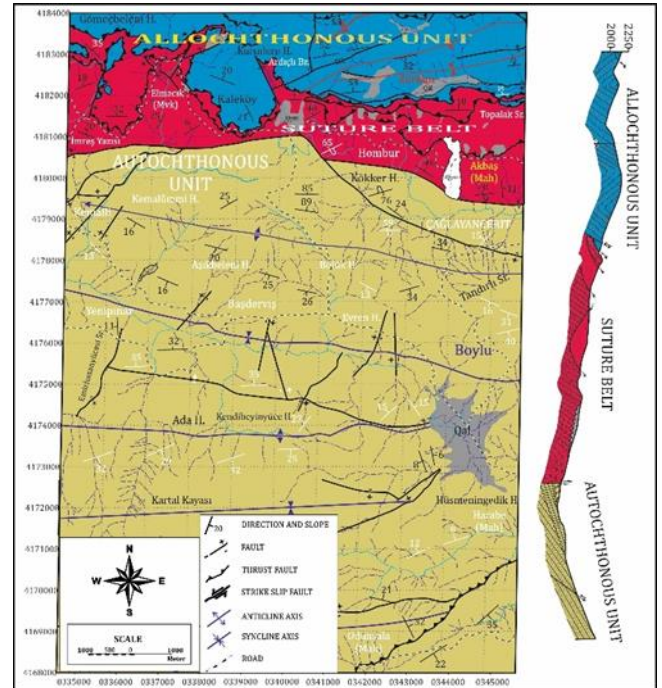


Figure 2. Structural map of the study area (Modified from Yalçın, 2012).

2.2. Remote sensing

Topographical approaches were obtained with the DEM image of Çağlayancerit and its vicinity, a tectonically active region and an important belt where two different continents collide. The downloaded DEM images were evaluated in the QGIS environment, an open-source Geographical Information System.

The DEM data downloaded on the Google Earth image and the active faults in the region were overlapped (Figure 3). Considering that there are different active and inactive faults in and around Çağlayancerit, the region's morphology is quite rugged, and the topographic elevations are relatively lower in the southern areas. According to these images, some important lineaments have been determined, which are structures generally affected by faults.

The images of the region generally obtained by remote sensing were evaluated in the QGIS environment, respectively, as follows.

1. DEM data was classified and coloured in the QGIS environment with a single band pseudocolour application (Figure 4a).
2. The relief image for the slope map of the region and the slope image on it were overlaid, revealing the slope map (Figure 4b). The red coloured areas represent the areas with the highest topographic elevation.
3. A view map of the region was created. According to the field studies, it has also been revealed with satellite images that the slopes generally face

south because there are thrusts from north to south (Figure 4c).

4. A 3D map of the region was created to obtain a more understandable image. The most important linearity obtained according to this image belongs to EAF. Other important linearities are thrust zones and dip-slip faults that form the boundary of the thrust front and autochthonous units (Figure 4d).



Figure 3. Satellite and DEM image of the study area.

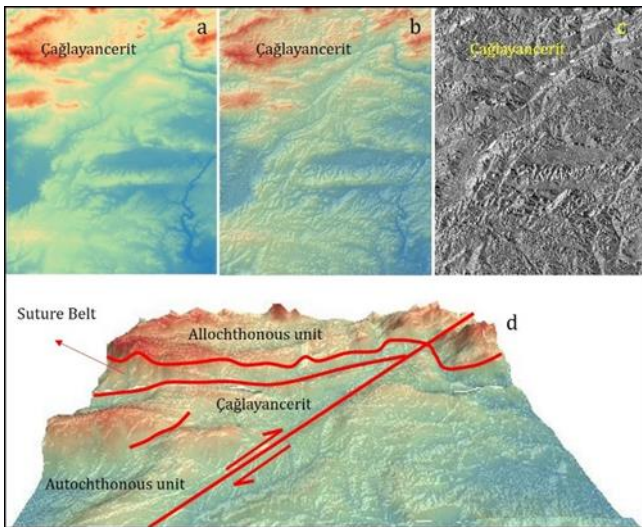


Figure 4. a. DEM b. slope, c. aspect and d. 3D image of the study area.

3. Results

In the research prepared by Yalçın (2012), it was stated that the units belonging to the collision belt in Çaglayancerit and its west came together, and deformation structures belonging to different periods developed in the region. The region's structural elements and surroundings were re-evaluated in this study with remote sensing methods. Topographic data and linear structures reveal that tectonic forces in the region are effective in geomorphology. In supplement, the faults in the structural map obtained in the field study are in harmony with the satellite images.

4. Conclusion

The maps prepared for tectonic and structural purposes can still be verified with remote sensing methods in today's technology. Morphological changes are the most common, especially in tectonically active areas where different continents come together. Very high topographic data is obtained in the thrust belts. In this study, the units of the Arabian Autochthonous and Taurus Orogenic belts collided, and then the position of the EAF was evaluated together. DEM and field data can be compared by evaluating them in the GIS environment. In such studies, other remote sensing methods such as hydrological factors, lithology and shading should be applied and detailed.

References

- Austin, J. R., & Blenkinsop, T. G., (2008). The Cloncurry Lineament: Geophysical and geological evidence for a deep crustal structure in the Eastern Succession of the Mount Isa Inlier. *Precambrian Research* 163 (1-2), 50–68.
- Fichler, C., Rundhovde, E., Olesen, O., Saether, B. M., Ruelatten, H., Lundin, E., & Dore, A. G., (1999). Regional tectonic interpretation of image enhanced gravity and magnetic data covering the mid-Norwegian shelf and adjacent mainland. *Tectonophysics* 306 (2), 183–197.
- Guild, P. W., (1974). Distribution of metallogenic provinces in relation to major earth features: *Schriftenreihe der erdwissenschaftlichen Kommission der Österreichischen Akademie der Wissenschaften Band 1*, pp. 10–24.
- Gül, M. A., (1987). Kahramanmaraş Yöresinin Jeolojisi ve Petrol Olanakları. T.P.A.O. Rap. No: 2359, (Yayınlanmamış), Ankara.
- Gül, M. A., (2000). Kahramanmaraş Yöresinin Jeolojisi. Hacettepe Üniversitesi, Fen Bilimleri Enstitüsü, Doktora Tezi, 304 s.
- Işık, V., (2016). Torosların Jeolojisi; Türkiye Jeolojisi Ders Notu. Ankara Üniversitesi, Jeoloji Mühendisliği Bölümü, Ankara.
- Masoud, A., Koike, K., & Teng, Y., (2007). Geothermal Reservoir Characterization Integrating Spatial GIS Models of Temperature, Geology, and Fractures. *Proc. 12th Conference of International Association for Mathematical Geology*, Beijing, China, August 26-31, (on CD-ROM).
- Masoud, A. A., & Koike, K., (2011). Auto-detection and integration of tectonically significant lineaments from SRTM DEM and remotely-sensed geophysical data, *ISPRS Journal of Photogrammetry and Remote Sensing*, Volume 66, Issue 6, 2011, Pages 818-832, ISSN 0924-2716, <https://doi.org/10.1016/j.isprsjprs.2011.08.003>.
- Morris, K., (1991). Using knowledge-base rules to map the three-dimensional nature of geologic features. *Photogrammetric Engineering & Remote Sensing* 57 (9), 1209–1216.
- Oakey, G., (1994). A structural fabric defined by topographic lineaments: Correlation with Tertiary

- deformation of Ellesmere and Axel Heiberg Islands, Canadian Arctic. *Journal of Geophysical Research* 99 (B10), 0148–0227.
- Rigo De Righi, M. & Cortesini, A., (1964). Gravity tectonics in Foothills structure belt of southeast Turkey, *A.A.P.G. Bull.*, 48-12, 1911-1938.
- Robertson, A. H. F. & Dixon, J. E., (1984). Introduction: aspects of the geological evolution of the Eastern Mediterranean. In: Dixon JE, Robertson AHF (eds) *The Geological Evolution of the Eastern Mediterranean*, *Geol Soc London, Spec Publ* 17:1–74.
- Robertson, A. H. F., Parlak, O. & Ustaömer, T., (2012). Overview of the Paleozoic-Neogene evolution of Neotethys in the Eastern Mediterranean region (southern Turkey, Cyprus, Syria). *Petrol Geosci*, 18(381):404.
- Süzen, M. L., & Toprak, V., (1998). Filtering of satellite images in geological lineament analyses: an application to a fault zone in Central Turkey. *International Journal of Remote Sensing* 19 (6), 1101–1114.
- Şengör, A. M. C., & Yılmaz, Y., (1981). Tethyan evolution of Turkey, A plate tectonic approach. *Tectonophysics*, 75, 181-241.
- Tripathi, N., Gokhale, K., & Siddiqu, M., (2000). Directional morphological image transforms for lineament extraction from remotely sensed images. *International Journal of Remote Sensing* 21 (17), 3281–3292.
- Yalçın, C., (2012). Çağlayancerit (Kahramanmaraş) Batısının Tektono-Stratigrafisi ve Yapısal Evrimi. Kahramanmaraş Sütçü İmam Üniversitesi Fen Bilimleri Enstitüsü, Yüksek Lisans Tezi, 129s.
- Yılmaz, Y., (1984). Amanos dağlarının jeolojisi: İ. Ü. Müh. Fak. (TPAO Arş. No. 1920, İstanbul).
- Yılmaz, Y., Gürpınar, O., Kozlu, H., Gül, M. A., Yiğitbaş, E., Yıldırım, M., Genç, C. & Keskin, M., (1987). Maraş kuzeyinin jeolojisi (Andırın- Berit-Engizek-Nurhak-Binboğa Dağları) yapı ve jeolojik evrimi. İstanbul Üniversitesi, Mühendislik Fakültesi.
- Yılmaz, Y. & Yiğitbaş, E., (1990). SE Anadolu'nun Farklı Ofiyolitik Metamorfik Birlikleri ve Bunların Jeolojik Evrimdeki Rolü Türkiye 8. Petrol Kong. Bild. s. 128-140, Ankara.



4th Intercontinental Geoinformation Days

igd.mersin.edu.tr



Introducing a new approach to temperature validation of remote sensing thermal images

Hassan Emami ^{*1}, Arash Rahmanizadeh ¹

¹University of Tabriz, Marand Faculty of Engineering, Geomatics Engineering Department, Iran

Keywords

Remote sensing
Land surface temperature
Landsat
MODIS
LST validation

Abstract

Assessing the accuracy of the Land surface temperature (LST) has been and remains a challenging task. Rapid LST fluctuations in time and space, and a spatial scale mismatch between satellite and terrestrial sensors, have made validation using terrestrial data challenging. In addition to using ground data, there are three techniques for evaluating this parameter: radiance-based validation, indirect assessment, and cross-validation between two sensors. One of the most prevalent approaches for measuring LST accuracy is cross-validation. The main requirements of the cross-validation approach are temporal, spectral, spatial, and sensor angle of view adaptation. A technique for cross-validating LST from Landsat 8 using MODIS sensors is provided in this research. MODIS ' temperature product was chosen as the reference since it was collected twice per day by each of their sensors. The suggested method's results revealed that the accuracy evaluation in regions with high homogeneity, using the parameters of mean differences and root mean square error, has an accuracy of 0.6 and 1.63 degrees Kelvin in the first study's image, respectively. These values, 0.94 and 1.27 kelvin, were likewise achieved in the image of the second research. The suggested approach is applicable to any thermal sensor at any time and place.

1. Introduction

Surface temperature is one of the variables required in a wide range of earth science and environmental studies and research, as well as in numerous applications such as evapotranspiration modeling, soil moisture estimation, urban climate, hydrology, vegetation monitoring, and environmental studies. Remote sensing technology allows for large-scale geographical and temporal monitoring of this quantity. However, evaluating the accuracy and validation of this quantity has been and continues to be a difficult issue because, on the one hand, its rapid changes in the range of space and time, such as changing more than ten degrees Kelvin in a very short distance or more than one degree Kelvin in a very long time, have been and continue to be a challenge. It is brief (less than a minute)) Li et al., 2013; Prata, Caselles, Coll, Sobrino, & Otle, 1995(but due to the incompatibility of the spatial scale between satellite and terrestrial sensors, its confirmation using terrestrial data is complex and challenging.

Although various methods for retrieving surface temperature from thermal data have been established in

recent decades, validation of the temperature acquired from this data has not been developed due to the following issues, which need the creation of new algorithms))Coll et al., 2005; Guillevic et al., 2012; Pinker, Sun, Hung, Li, & Basara, 2009; Wan, 2008(. The primary issue with surface temperature validation is that ground-based temperature observations at the local scale have coupled impacts with ambient and atmospheric factors. Measuring the environment, which takes time and is tough to monitor. The second issue is measuring the surface temperature on a pixel scale using the terrestrial method, because each pixel image covers an area of a few hundred meters or kilometers due to spatial variation in surface characteristics and large spatiotemporal variations in the surface temperature itself. It's tough to think of a method for acquiring a reference temperature on a pixel scale. The third issue is temporal sampling of the surface temperature, which must be done at a very high frequency since the surface temperature might vary by several degrees owing to wind, shadow, and other environmental conditions. A three-step strategy for cross-validating ground surface temperature collected from Landsat 8 sensors with MODIS temperature sensor

* Corresponding Author

^{*}(h_emami@ut.ac.ir) ORCID ID 0000-0002-0171-6487
(arahmanizadeh@tabrizu.ac.ir) ORCID ID xxxxx – xxxxx – xxxxx – xxxxx

Cite this study

Emami, H., & Rahmanizadeh, A. (2022). Introducing a new approach to temperature validation of remote sensing thermal images. 4th Intercontinental Geoinformation Days (IGD), 9-12, Tabriz, Iran

products in Fars provincial areas is provided in this research. MODIS' temperature product was chosen as a reference in cloud-free weather circumstances due to its vast coverage and collection twice per day by each of its sensors. Because our nation lacks a temperature validation database, our suggested technique relied on MODIS data only in homogenous thermal zones as a reference. As a result, the suggested approach may be used for any time-place and any thermal sensor.

2. Method

The steps in the proposed method are as follows: The study datasets were preprocessed and topographic and atmospheric correction were applied in the first step. In the second stage, the emission coefficients of different classes were calculated using the method of calculating surface emissivity, using the ASTER spectral library, Kirchhoff law, and the spectral response functions of Landsat 8 thermal bands. After producing the product temperature of the MODIS, Terra, and Aqua sensors, the appropriate processing was conducted on them, and the data was prepared to apply the suggested approach in the third step. The suggested approach is executed in three phases for temporal-spectral and spatial adaptation of the product of Landsat 8 and MODIS sensors in the fourth stage, and the results are studied and reviewed.

2.1. Study area and datasets

The research area is an arid and semi-arid region with a diversified land cover that includes heterogeneous pixels covered by various flora, soil, and rocky kinds. It is located between the latitudes of 26° 25'–32° 44'N and the longitudes of 50° 32'–55° 54'E. Figure 1 depicts the land use/land cover data recorded in June 2018, which included seventeen classes and two scenes of LDCM data.

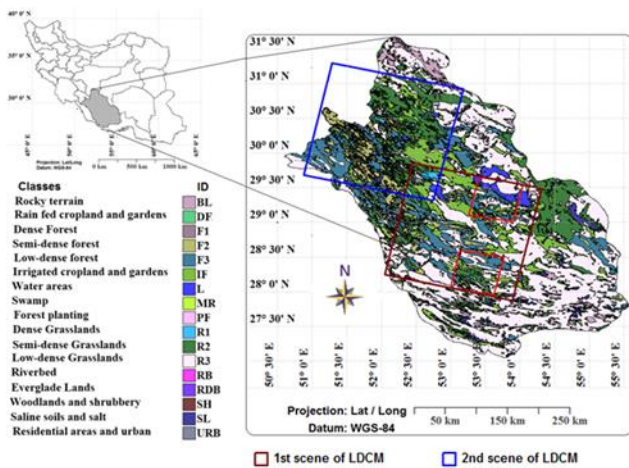


Figure 1. The study area with the seventeen-class land cover map

Besides the LDCM data, the LST products of MOD/MYD 11 L2 and MOD/MYD11A1 MODIS are employed in the current work for LST cross-comparison in the suggested scaling approach that is obtained from a generalized split-window algorithm.

2.2. The LST Retrieval

Having LSEs, to evaluate the impact of the LSE improvement on LST, based on the USGS recommendation on the LDCM data, the single channel (SC) algorithm of (Jiménez-Muñoz & Sobrino, 2003) is used. SC algorithm is utilized for sensitivity analysis using only band 10. Therefore, the σ_{alg} is below 1 K since the VW contents of the study area are 0.8 and 1.2 for examined datasets (Table 1). The $SC^{JM\&S}$ algorithm retrieves LST (T_s) using the general (1).

$$T_s = \left(\left(\frac{k_2 L_{sen}}{T_{sen}^2} \left[\frac{\lambda_e^4}{k_1} + \lambda_e^{-1} \right] \right)^{-1} \right) * \left[\frac{1}{\epsilon} (\psi_1 L_{sen} + \psi_2) + \psi_3 \right] + T_{sen} - \gamma L_{sen} \quad (1)$$

where L_{sen} is the at-sensor radiance in $W m^{-2} sr^{-1} \mu m^{-1}$, T_{sen} is the at-sensor brightness temperature in K, λ_e is the effective wavelength in μm , k_1 and k_2 are constant of thermal bands in $W m^{-2} sr^{-1} \mu m^{-1}$ and K, respectively. ϵ is the surface emissivity and unitless, ψ_1 , ψ_2 , and ψ_3 are referred to as atmospheric functions (AFs) which computed by (2) (Jimenez-Munoz, Sobrino, Skokovic, Mattar, & Cristobal, 2014).

$$\psi_1 = \frac{1}{\tau}, \quad \psi_2 = -L^\downarrow - \frac{L^\uparrow}{\tau}, \quad \psi_3 = L^\downarrow \quad (2)$$

Where L^\uparrow is the upwelling radiation and L^\downarrow is the downwelling radiation in $W m^{-2} sr^{-1} \mu m^{-1}$ and τ is unitless and atmospheric transmittance.

Table 1. Atmospheric parameters for band 10 LDCM

Scene ID	τ	L^\uparrow	L^\downarrow	$wv[gcm]^{-2}$
162-40	0.85	1.19	1.98	1.20
163-39	0.92	0.64	1.09	0.80

For each image, τ , L^\uparrow and L^\downarrow were obtained using online radiative transfer codes (<http://www.atmcorr.gsfc.nasa.gov/>) from Atmospheric Correction Parameter Calculator (ACPC) developed by NASA for Landsat satellites (J. Barsi, Barker, & Schott, 2003; J. A. Barsi, Schott, Palluconi, & Hook, 2005).

2.3. The LST Validation

Because there is no available database of *in situ* LST measurements that coincides with the LDCM satellite overpasses, is one of the major problems in LST validation in our case study. Generally, the LST changes rapidly in space and time, and it changes more than 10 K in a very short distance or more than 1 K in a very short time (less than one minute) (Li et al., 2013; Prata et al., 1995). Hence, the strong spatial heterogeneity and temporal variation of LST limit ground-based validation only to several relatively homogeneous surfaces (Tang & Li, 2014). Furthermore, the selection of homogeneous surface is scarce and a risky question. For this purpose, (Liu, Hiyama, & Yamaguchi, 2006) suggested that scaling methods must be developed to assist for the validation retrieved of LSTs. Since the acquisition date of the ASTER

LST product is asynchronous with the LDCM data, it is not possible to use it for LST cross-comparison. Therefore, due to the limited accessibility to the actual LSTs measured in situ, the daily LST products of MODIS (MOD/MYD 11_L2 and MOD/MYD11A1 (V5)) were selected as the reference data. These products include 1 km pixels, using the SW algorithm. Because of the wide coverage and taken LST product twice per day by each of Terra and Aqua satellites, these products were selected as the reference temperature. The LST products of MODIS sensors have been validated with in situ measurements and by various methods in more than 50 clear-sky cases taking into account the higher accuracies less than 1°K for both Terra and Aqua (Qian, Li, & Nerry, 2013). In this regard, geographic coordinate matching, time matching and view zenith angle matching between LST of the LDCM data and the MODIS product arises for cross-comparison. To deal with these problems, we proposed an alternative scaling method of cross-comparison based on LST products of MODIS to yield a compatible dataset for accuracy assessment as in the following three steps.

In the first step, to consider the spatial resolution differences between the LDCM and MODIS LST products, the obtained LST of LDCM data by the proposed and compared methods should be scaled up to the MODIS LST product with 1km spatial resolution. Hence, similar to (Qian et al., 2013) which provided the aggregation algorithm area-weighted pixel, the LST of LDCM data aggregated to the same spatial resolution of the MODIS product using an 11 x 11 processing window size. After scale up between the two sensors, it certainly cannot be said that the pixels in terms of spectral range are the same. Because spectral data received by the sensor depends on several factors such as the surface emissivity, surface topography, zenith angle of sensor, misregistration error between the sensors data and so on. Therefore, in the second step, for spectral and view zenith angle matching, the thermal homogeneity area was determined. The select thermal homogeneous regions not only confirm time-invariant assumption of LSE (Tang & Li, 2014) but also the impact of misregistration on LSE and LST between different sensor data, makes little and negligible (Wan, 1999). That is, co-occurrence matrix (CM) which contains a large amount of local spatial information about an image is used. A set of texture features derived from the CM matrix was suggested by (Haralick, Shanmugam, & Dinstein, 1973). In particular, two texture features of the inverse difference moment (IDM) and angular second moment (ASM) describe the homogeneity in an image.

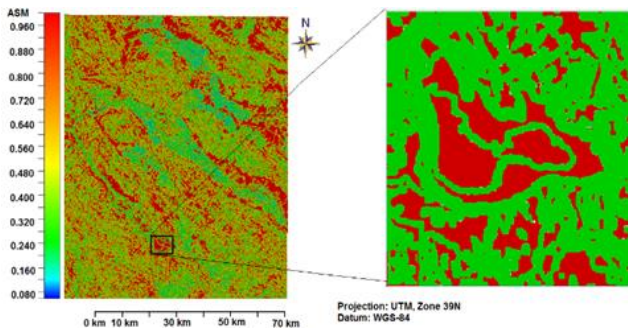


Figure 2. Example of extracted homogeneous regions

An 11 x 11 processing window size was selected and homogeneity measures were obtained. The processing window size is selected as spatial resolution of MODIS is about ten times of LDCM thermal bands. Fig.2 shows an example of extracted homogeneity regions on ASM feature. In this research, the areas with homogeneity content between 0.9 and 1 were selected as testing and validation sites in both homogeneity features.

The third step is time matching between LST of the LDCM data and MODIS products. In this regard, the approximate overpass times of the Terra and Aqua satellites in study area (scan start times from 01:30 to 24:00 UTC for MOD/ MYD 11_L2 and MOD/MYD 11 A1products) were considered during a day. Then coordinates matching between LST MODIS products are performed. Afterward, for each selected validation point at least five overpass times of LST MODIS products are selected. In weather condition that is sunny and cloud free, the main factor controlling the surface temperature is radiation and energy of sun. Usually, solar radiation changes during a day is almost a sine function. It is worthy to note that the situation in study area is same as aforementioned weather condition. Accordingly, we modeled the pattern of surface temperature changes during the day, as a sinusoidal function at a given point as (3).

$$LST_{ij}^{Modis} = a_i + b_i \times \cos(c_i T_{ij}^{Modis} + d_i) \quad (3)$$

Where LST_{ij}^{MODIS} is the LST of the i th point at the j th overpass time, T_{ij}^{MODIS} is the j th overpass time of Terra or Aqua over the i th point and a_i , b_i , c_i , and d_i are constant coefficients of the i th point. For the i th point, these coefficients were obtained by five available LSTs of MODIS. Accuracy of (13) that obtained for each validation point is less than one degree Kelvin that is the range of accuracy of MODIS LST product. Fig.16 shows a sample of the sinusoidal function obtained for a desired point. Finally, the LST of MODIS is yielded at the overpass time of LDCM for the i th point by (3) as reference values for LST validation. It is worth noting that the proposed sinusoidal function in (3) can only describe the LST variation for entire clear days with at least five LST values in during a day.

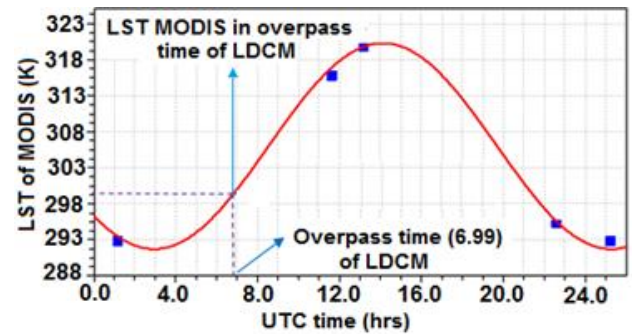


Figure. 3. The model of daily temperature change obtained by LST of MODIS products.

3. Results

To validate the suggested approach, two Landsat 8 images were selected at separate times, and 38 and 62

validation points in high homogeneity regions (0.90 to 1.0) were recovered from the first and second images, respectively. In the first and second Landsat 8 images, homogeneity (0.80 to 0.90) was calculated using 30 and 49 points, respectively. The outcomes evaluation is described below.

Table 2. Surface temperature comparison between Landsat 8 and MODIS products during Landsat 8 transit duration at validation locations.

$LST_{LDCM} - LST_{MODIS}^{opt.LdcM}$				
SD _{ST} (K)	RMSE(K)	N	homogeneity	Image ID
1.79	1.72	38	0.90-1.00	162-40
1.73	1.95	62	0.90-1.00	163-39
4.96	4.82	30	0.80-0.90	162-40
3.79	4.58	49	0.80-0.90	163-39

4. Conclusion

In this paper, an alternative scaling method based on LST products of MODIS was proposed for LST cross-comparison. According to the findings of this study, validation points should come from regions with high homogeneity for many applications at the local scale, such as evapotranspiration modeling, soil moisture estimation, urban climate, hydrology, vegetation monitoring, and environmental studies. In the illustration, (0.90 to 1.00) is chosen. Such environments include heavily vegetated areas, aquatic areas such as dams or lakes, salt marshes, and similar thermally homogeneous places where vegetation and aquatic areas may be seen in most photos. In this proposed technique, thermal homogenous regions were employed to assess and validate the surface temperature. Areas with homogeneity in the range (0.80 to 1.00) can also be selected and utilized for global-scale applications that need less precision in computing the surface temperature of validation sites. In general, the benefit of employing the suggested approach is that no ground temperature observations are required. Furthermore, this approach, in addition to being a robust method for measuring the accuracy of surface temperature, is applicable for any time and location, as well as any thermal sensor, due to the lack of a temperature validation database in our nation.

References

- Barsi, J., Barker, J. L., & Schott, J. R. (2003). *An atmospheric correction parameter calculator for a single thermal band earth-sensing instrument*. Paper presented at the IEEE International Geoscience and Remote Sensing Symposium, 2003. IGARSS'03. Proceedings.
- Barsi, J. A., Schott, J. R., Palluconi, F. D., & Hook, S. J. (2005). *Validation of a web-based atmospheric correction tool for single thermal band instruments*. Paper presented at the Optics & Photonics 2005.
- Coll, C., Caselles, V., Galve, J. M., Valor, E., Niclos, R., Sánchez, J. M., & Rivas, R. (2005). Ground measurements for the validation of land surface temperatures derived from AATSR and MODIS data. *Remote Sensing of Environment*, 97(3), 288-300.
- Guillevic, P. C., Privette, J. L., Coudert, B., Palecki, M. A., Demarty, J., Ottlé, C., & Augustine, J. A. (2012). Land Surface Temperature product validation using NOAA's surface climate observation networks—Scaling methodology for the Visible Infrared Imager Radiometer Suite (VIIRS). *Remote Sensing of Environment*, 124, 282-298.
- Haralick, R. M., Shanmugam, K., & Dinstein, I. H. (1973). Textural features for image classification. *IEEE Transactions on Systems, Man and Cybernetics*, 3(6), 610-621.
- Jimenez-Munoz, J. C., Sobrino, J., Skokovic, D., Mattar, C., & Cristobal, J. (2014). Land surface temperature retrieval methods from Landsat-8 thermal infrared sensor data. *Geoscience and Remote Sensing Letters, IEEE*, 11(10), 1840-1843.
- Jiménez-Muñoz, J. C., & Sobrino, J. A. (2003). A generalized single-channel method for retrieving land surface temperature from remote sensing data. *Journal of Geophysical Research: Atmospheres (1984–2012)*, 108(D22).
- Li, Z.-L., Tang, B.-H., Wu, H., Ren, H., Yan, G., Wan, Z., . . . Sobrino, J. A. (2013). Satellite-derived land surface temperature: Current status and perspectives. *Remote Sensing of Environment*, 131, 14-37.
- Liu, Y., Hiyama, T., & Yamaguchi, Y. (2006). Scaling of land surface temperature using satellite data: A case examination on ASTER and MODIS products over a heterogeneous terrain area. *Remote Sensing of Environment*, 105(2), 115-128.
- Pinker, R. T., Sun, D., Hung, M.-P., Li, C., & Basara, J. B. (2009). Evaluation of satellite estimates of land surface temperature from GOES over the United States. *Journal of Applied Meteorology and Climatology*, 48(1), 167-180.
- Prata, A., Caselles, V., Coll, C., Sobrino, J., & Ottle, C. (1995). Thermal remote sensing of land surface temperature from satellites: Current status and future prospects. *Remote Sensing Reviews*, 12(3-4), 175-224.
- Qian, Y.-G., Li, Z.-L., & Nerry, F. (2013). Evaluation of land surface temperature and emissivities retrieved from MSG/SEVIRI data with MODIS land surface temperature and emissivity products. *International Journal of Remote Sensing*, 34(9-10), 3140-3152.
- Tang, H., & Li, Z.-L. (2014). *Quantitative Remote Sensing in Thermal Infrared: Theory and Applications* (pp. 257-279): Springer Berlin Heidelberg.
- Wan, Z. (1999). MODIS land-surface temperature algorithm theoretical basis document (LST ATBD). *Institute for Computational Earth System Science, Santa Barbara*, 75.
- Wan, Z. (2008). New refinements and validation of the MODIS land-surface temperature/emissivity products. *Remote Sensing of Environment*, 112(1), 59-74.



4th Intercontinental Geoinformation Days

igd.mersin.edu.tr



Usage of unmanned aerial vehicles in open mine sites

Gülsüm Yüksel^{*1}, Ali Ulvi ^{*2}, Murat Yakar³

¹Mersin University, Institute of Sciences, Department of Remote Sensing and Geographic Information Systems, Mersin, Türkiye

²Mersin University, Faculty of Engineering, Department of Survey Engineering, Mersin, Türkiye

³Mersin University, Geomatics Engineering Department, Mersin, Türkiye

Keywords

UAV
Open Mine Sites
Advantages of UAV Usage

Abstract

Today, technological developments show themselves in the fields dealing with earth sciences as in every field. Unmanned aerial vehicles (UAV), one of these technological developments, have offered an innovative approach to many sectors. In addition to being used in various fields such as geodesy, disaster management, meteorology, agriculture and security, its use in mining has also become widespread. Topographic surveying problem in open pit mining sites is one of the important challenges to be overcome. Topographic measurements require expensive surveying equipment and professional technical personnel. UAV technology provides cost control to the difficulties encountered in the fields and can easily produce solutions with time saving and measurement accuracy. In recent years, in mining activities in the world; It is used in areas such as production planning, blasting, ore production and stock tracking and volumetric calculations, monitoring of slope sensitivities and changes, calculating the amount of waste, dust emission, security. In this article, the structure of UAVs, their advantages and areas of use in open mining areas, the availability of reasonable results and the benefits that affect the studies are explained by adding case studies in open mining areas.

1. Introduction

Open pit mine sites are often complex terrains and areas with varied geological conditions, limiting accessibility in mining, but sometimes causing inaccessibility in extreme cases, so the use of conventional methods causes difficulties for ground surveys.

The rapid development of unmanned aerial vehicles (UAV) technology, which is one of today's technological developments, has benefited not only the military but also the mining industry as well as in various civilian areas. Mining companies use UAV technologies to monitor and plan mining operations and increase their efficiency, speed and safety. With UAVs, which is a remote sensing technology, comprehensive analyzes can be made by obtaining high resolution data in a short time with less labor.

Recently, a photogrammetry system using UAV has been used for topographic surveys to complement the strengths and weaknesses of ground/air measurement equipment. The UAV photogrammetry system has a relatively large working area compared to existing

ground crew equipment and a relatively small measurement error compared to air measurement technologies. Because of these features, the UAV photogrammetry system is considered as a technology that can replace or complement existing measuring equipment (Siebert & Teizer, 2014) and civil construction (Park et al., 2013).

In this study, the usability of UAVs in open pit mines and the advantages of UAV systems are emphasized in line with the studies and analyzes of these studies.

2. Definition, classification and usage areas of unmanned aerial vehicle

There are different definitions of unmanned aerial vehicles in various sources. The common denominator to be derived from these definitions is; UAV is a kind of aircraft that does not have a pilot or passenger, carries only the equipment suitable for its intended use (camera, GNSS, laser scanning device, etc.), can be controlled in the air by a pilot on the ground, or can perform a pre-planned flight plan autonomously. It can be defined as in this context, UAVs basically consist of three components; The

* Corresponding Author

^{*}(gulsummertyuksel@gmail.com) ORCID ID 0000 – 0002 – 4650– 2255
(aliulvi@mersin.edu.tr) ORCID ID 0000 – 0003 – 3005 – 8011
(myakar@mersin.edu.tr) ORCID ID 0000 – 0002 – 2664 – 6251

Cite this study

Yüksel, G., Ulvi, A., & Yakar, M. (2022). Usage of unmanned aerial vehicles in open mine sites. 4th Intercontinental Geoinformation Days (IGD), 13-16, Tabriz, Iran

aircraft itself is the payload on the aircraft and the ground control station.

UAVs, also called drones, are classified as fixed-wing, rotary-wing and Vertical Take of Landing (VTOL) according to their flight capabilities "Fig. 1".



Figure 1. Fixed-wing UAV (a), Rotary-wing UAVs (b), VTOL UAV (c)

Today, UAVs are used in agriculture, meteorology, archaeology, forestry, communications, security, wildlife surveys, habitat studies, landscape planning, environmental surveillance, natural disasters, traffic management, transportation, energy, geology, hydrology, civil engineering, mapping and mining. used in a variety of disciplines, including Some examples of usage area are shown below "Fig. 2".



Figure 2. UAV use in military field (a), UAV use in disaster management (b), UAV use in agricultural applications (c)

2.1. Use of Unmanned Aerial Vehicles in Mine Sites

Mineral resources have an important place in economic development due to their importance in terms of both raw materials and energy (Hu et al., 2014; Xioa et al., 2018a). The demand for mineral resources has increased significantly with the growth of industry and urbanization, and this has led to a greater need for mining. In general, two types of mining are widely used, namely above-ground and underground.

UAVs play an important role in various challenging aspects of the mining industry, inspecting belt conveyors and electrical overhead lines, up-to-date mining databases, blast optimization, mine tailings pond surveillance and tracking of trucks and equipment, geological hazards, pollution monitoring, land reclamation, ecological restoration assessment. is playing. In addition, UAVs provide punctual and regular images to obtain photogrammetric three-dimensional (3D) models of mines in order to monitor the stability of steps and slopes and production amounts.

From UAV photogrammetry, current map production in open mines, determination of production and pickling amount, stock and dump site cubage calculations, land damage assessment, rock detection, geological mapping, excavation planning and installation of hyperspectral cameras, alteration and mineral detection,

determination of steep and inaccessible points. used in studies such as mapping.

3. Applications in Open Mine Fields with Unmanned Aerial Vehicles

In open mining areas, sensitive data can be collected in a short time in all kinds of terrain conditions, thanks to UAVs and aerial imaging and measurement systems. Depending on the UAV used, comprehensive and easy-to-analyze quality data can be obtained within a few hours.

With the advancement of drones, the development of high-resolution cameras, and the development of image-based mapping techniques, drone imagery has been a topic of considerable interest among researchers and industries. These images have the potential to provide data with unprecedented spatial and temporal resolution for 3D modelling.

3.1. Use of UAVs in Stock Volume Calculation Studies

Obtaining up-to-date information about an open pit is an understanding of the ever-changing shape of the pit and its embankments, row heights, slopes, etc. It consists of the continuous investigation of elements such as Mining companies tend to monitor their quarries frequently, depending on the material they dig. Monitoring can be done weekly, monthly or quarterly (Mazhdakov, 2007). No matter how frequent the need to investigate stocks, mining companies should be offered the fastest, most effective and reliable measurement and calculation methods.

Filipova et al., (2016) selected a quarry in Lukovit town of Sofia, the capital of Bulgaria, for the evaluation of volumetric measurements in their study. In this study, it is aimed to test and evaluate the accuracy of UAV data according to GNSS techniques. Two sets of measurements were made. First, stock measurement with GNSS technologies, and secondly, the entire quarry area was mapped by a UAV flight. The selected UAV is eBee SenseFly and the GNSS receiver is Leica viva GS08 Plus. Aerial photographs taken by UAV were processed with PIX4D Mapper software and volumetric calculations were made with this program. AutoCAD Civil 3D was used for volume calculation obtained from GNSS measurements.

With this study, a confirmation of the promising application of UAV in stock volume calculation was sought. Since the data were obtained by two different methods and processed in different ways, two values of the volume of the same stock were created. The volume obtained from the UAV data is 12,749 m³ and the volume obtained from the GNSS points is 12,606 m³. As a result, it was revealed that the volume of the UAV was 143.99 m³ more. In some countries legislation specifies that the volume must be calculated with an accuracy of $\pm 3\%$ of all material. The accuracy achieved is within the 3% legitimate error, which is the main target of the working condition.

Filipova et al., (2016) presented the efficiency and reliability of the data obtained with high resolution by UAV when it comes to volumetric measurements.

3.2. UAV use in production and waste determination studies

Continuous control is required in order to direct production in mines, to produce limited resources efficiently and to maintain economic balances. Because; Continuous monitoring of parameters such as quarry operating efficiency, annual production amount, annual waste amount is required. Inspection of the entire field and amount of waste is both time consuming and very laborious with traditional methods.

Kun & Guler (2019) used a DJI Phantom4 Pro drone in a natural stone open pit mining operation in the district of Korkuteli in Antalya province, and studied the availability of UAVs to determine the production and waste amount in the quarry over a 15-month period. Flights were made in an area of 300,000 m². The first data set is the data set obtained with the flight made on April 22, 2017, and the second data set is the data set obtained with the flight on July 01, 2018. During this period, the changes in the natural stone quarry were clearly observed and reflected in the results. The data were processed in the Pix4D Mapper program and the total error of the digital surface model (DEM) optimized with ground control points (GCP) in three axes was found to be less than 5 cm.

Two separate DEMs were created from the two data sets. In the 3D mining software, DEMs were superimposed, cross-sectional images were obtained, and excavation and fill volumes were calculated. At the end of the calculations, the annual excavation amount of the enterprise was determined as 1,20148.37 m³. When the amount offered for sale is subtracted from the annual excavation amount value, the remaining amount constitutes the total amount of waste. According to this; According to the information obtained from the records of the enterprise, as a result of all excavation and on-site dismantling operations, the amount obtained as smooth, dimensional and salable is around 10,500 m³. When this value is compared to the annual excavation amount in the quarry, the yield of the quarry is 8.74%.

Kun & Guler (2019) stated that the datasets obtained by processing the images collected by UAV are processed with photogrammetric software and additionally supported with 3D mining software, operating parameters such as annual excavation and/or production, waste amount, quarry yield of open mining enterprises can be determined quickly and precisely. have reported.

3.3. UAV Use in Topographic Research Studies

Since the unmanned aerial photogrammetry system has a relatively small measurement error compared to the current aerial measurement methods and has a relatively large working area compared to ground survey methods, it is actively used in topographic research applications in open pit mine sites in the country and abroad.

Lee & Choi (2015) conducted a study in an open limestone mine located in Samcheok-si Gangwon-do, Korea to prove that topographic survey can be done with UAV in the mine. 4 YKNs were placed in the study area

with the Novatel Smart-V1 GPS device. eBee SenseFly was used as the UAV and Postflight Terra 3D software was used to process the aerial photographs taken. Point cloud data with 3D coordinates was created and finally DEM was produced.

GCPs measured using GPS and the results produced from UAV data were compared and it was seen that the mean square error (RMSE) for 4 GCPs was 15 cm in the X direction, 2 cm in the Y direction, and 14 cm in the Z direction. In other words, it has been analyzed that there is an error of about 15 cm according to the results of the ground survey using high-precision GPS. This result satisfies the maximum vertical error of 30 cm (1:1200, at map scale) and the maximum vertical error of 25 cm (1:1000, at map scale) recommended by ASPRS (1988) for topographic maps. Some studies (Turner et al., 2012; Jung et al., 2009; Uysal et al., 2015) using UAVs show similar error levels. Considering the studies carried out in open pits, it has been concluded that the results of the surveys made with an error level of 15 cm can be sufficiently utilized in the creation of topographic maps.

Lee & Choi (2015) stated that topographic surveys with fixed-wing UAVs are very effective in terms of working time, compared to the one week or longer operating time required for ground survey with light waves, which was done approximately once a year in the research area.

3.4. UAV use in air quality monitoring studies

Both shallow coal seam and large-scale mine blasting produce large amounts of pollutants such as NO_x, SO_x, CO_x and heat radiation. Air quality monitoring relies on several stationary samplers to model and verify or predict gas emissions based on indicators such as coal consumption. In recent years, UAVs equipped with gas sensors have been used for remote monitoring and control of pollutants, with good results (Dunnington & Nakagawa 2017; Martin et al., 2015).

In the study by Bui et al., (2019) at the Coc Sau coal mine in Vietnam, various data, primarily images and airborne pollutant concentrations, were collected with the RGB Zenmuse X4S camera mounted on a low-cost rotary-wing DJI Inspire2 UAV, several dust sensors. Field tests were conducted to evaluate the performance of the system. Sensors mounted on the UAV were able to monitor the levels of environmental variables associated with air quality in the pit such as temperature, dust, CO, CO₂ and NO_x. Taken aerial photographs were processed using Agisoft Photoscan software and 3D topographic maps were modeled. As a result of the evaluation of the accuracy with GCPs, it was seen that the X,Y,Z root mean square error (RMSE) was 6.6 cm, 6.1 cm, 13.8 cm and 16.4 cm, respectively. These values show that it meets the accuracy requirement for mineral exploration tasks.

The distribution of pollutants in a deep pit is dependent on surface wind and air density differences inside and outside the pit. The space inside the pit is divided into 2 sections and named as H1 at -140 m and H2 at 120 m. The UAV systematically passed through these regions. In order to measure the vertical temperature profiles in the pit, it started from the center of the pit floor and flew 250 m above sea level along the

vertical line. The collected data was used to create 3D environmental maps. Environment maps in terms of Co, Dust (PM10), NO and temperature were created with ArcGIS software.

According to the field test results in this study, Bui et al., (2019) the availability of low-cost UAV for 3D mapping, demonstrates with relatively high accuracy the air quality monitoring in large and deep coal mines, pollutant control measures can be taken by the system as air pollution profiles can be seen on 3D maps and the main causes of pollution can be easily verified based on 3D maps.

4. Results

The use of UAVs has become widespread in the mining field, as in many other fields, in recent years, as it offers advantages in terms of measurement accuracy, equipment and the variety and quality of data obtained, time saving and cost compared to many measurement methods.

In mining, new measurement technologies, which are practical and cost-effective, have begun to be preferred in order to control, maintain and map the production and the operations performed at this stage. Developing UAV technology has provided solutions to these, not only measuring, but also enabling new areas of use in mining with its aerial imaging system and the variety of equipment that can be used. Sensitive and comprehensive results can be obtained by processing the data taken by the UAV in necessary software suitable for the purpose. The resulting products can be analyzed in many ways in the digital environment. In addition, UAVs can easily make measurements in topography or conditions that are difficult to measure with traditional methods, and can provide precise results in a short time with healthy data, regardless of large or small area according to the UAV capability used

References

- Bui, X. N., Lee, C., Nguyen, Q. L., Adeel, A. (2019). Use of Unmanned Aerial Vehicles for 3D topographic Mapping and Monitoring the Air Quality of Open-pit Mines. *Journal of the Polish Mineral Engineering Society*, 01-07.06.2019, 222-238.
- Dunnington, L., & Nakagawa, M. (2017). Fast and safe gas detection from underground coal fire by drone fly over. *Environ Pollut* 229, 139–145
- Filipova, S. L., Filipov, D. G., & Raeva, P. L. (2016). Volume Computation of A Stockpile – A Study Case Comparing Gps And Uav Measurements In An Open Pit Quarry. *The International Archives of the Photogrammetry, Remote Sensing and Spatial Information Sciences*, Volume XLI-B1, 2016 XXIII ISPRS Congress, 12–19 July 2016, Prague, Czech Republic
- Hu, Z., Yang, G., Xiao, W. (2014). Farmland damage and its impact on the overlapped areas of cropland and coal resources in the eastern plains of China. *Res Con Rec* 86 (3), 1-8
- Jung, S. H., Lim, H. M., & Lee, J. K. (2009). Analysis of the Accuracy of the UAV Photogrammetric Method using Digital Camera, *J. of the Korean Society of Surveying, Geodesy, Photogrammetry and Cartography*, 27(6), 741-747.
- Kun, M., & Guler, O. (2019). İnsansız Görüntüleme Sistemleri ile Elde Edilen Sayısal Yüzey Modellerinin Mermer Madencilğinde Kullanımı. *DEUFMD*, 21(63), 1005-1013.
- Lee, S., & Choi, Y. (2015). Topographic survey at small-scale open-pit mines using a popular rotary-wing unmanned aerial vehicle (Drone). *Tunn Undergr Sp Tech* 25(5), 462–469
- Martin, P. G., Payton, O. D., Fardoulis, J. S. (2015). The use of unmanned aerial systems for the mapping of legacy uranium mines. *J Environ Radioact* 143, 135–140
- Mazhrakov, M. (2007). *Mine Engineering*. Sofia: Sofia University, 2007.
- Park, M., Kim, S. G., & Choi, S. Y. (2013). The study about building method of geospatial informations at construction sites by unmanned aircraft system (UAS), *Journal of the Korean Cadastre Information*, 15(1), 145-156
- Siebert, S., & Teizer, J. (2014). Mobile 3D mapping surveying earthwork projects using an Unmanned Aerial Vehicle (UAV) system, *Automation in Construction*, 41, 1-14.
- Turner, D., Lucieer, A., & Watson, C. (2012). An automated technique for generating georectified mosaics from ultra-high resolution unmanned aerial vehicle (UAV) imagery based on structure from motion (SfM) point clouds, *Remote Sensing*, 4(5), 1392-1410.
- Uysal, M., Toprak, A. S., & Polat, N. (2015). DEM generation with UAV Photogrammetry and accuracy analysis in Sahitler hill, *Measurement*, 73, 539-543.
- Xiao, W., Chen, J., Da, H. (2018). Inversion and analysis of maize biomass in coal mining subsidence area based on UAV images. *Trans Chin Soc Agric Eng*, 49(8), 169–180



4th Intercontinental Geoinformation Days

igd.mersin.edu.tr



An assessment of support vector machines for crown delineation of pine single trees on unmanned aerial vehicle imagery

Ali Hosingholizade¹, Yousef Erfanifard¹, Seyed Kazem Alavipanah¹, Hooman Latifi², Yaser Jouybari-Moghaddam³

¹University of Tehran, College of Geography, Dept. of Remote Sensing and GIS, Tehran, Iran

²K. N. Toosi University of Technology, College of Geodesy and Geomatics Engineering, Department of Photogrammetry and Remote Sensing, Tehran, Iran

³University of Bojnord, College of Engineering, Department of Surveying Engineering, Bojnord, Iran

Keywords

UAV
Segmentation
classification
Crown Area
Bojnord

Abstract

The aim of this study was to compare the performance of the Support Vector Machine (SVM) algorithm with pixel and basic object-oriented approaches for identifying the crown of single pine trees in a man-made forest. For this purpose, the SVM algorithm was evaluated based on four different kernels: Linear, Polynomial, RBF and Sigmoid. In pixel base approach, the ROI obtained from the user's choice, and in the object-oriented approach, the ROI obtained from segmentation for part of the image. Then, the results of crown area estimation in both approaches were compared with each other and in-situ data. The results showed that using ROI from the object-oriented provides accurate result with less run time consuming. The SVM classification algorithm with RBF and ROI obtained from segmentation were showed the best performance in comparison to other approaches.

1. Introduction

The area of tree crown is constantly changing for various reasons such as growth process, age, amount of sunlight, as well as the surface microclimate of each region (Miraki et al. 2021). In fact, crown area has a different growth rate due to the conditions of the region, season, and type of each tree unequally in different directions. Also, the crown of trees, even if they are of the same type, has a variable area, making it difficult to measure (Wu et al. 2021). On the other hand, accurate calculation of crown area is an essential parameter in physiological models (Ding et al. 2022). Ecologically, the size of the crown directly affects many plant and animal components by regulating the penetration of sunlight and precipitation into the lower layers, while maintaining forest moisture. Traditionally, the characteristics of a crown are determined by its length and width (maximum dimensions on perpendicular axes), the area and generalities of the crown shape (Shovon et al. 2022). Previous research has also highlighted the importance of measuring tree crown area

(Ahongshangbam et al. 2019; Ouattara et al. 2022). Since accurate measurement of the physical characteristics of a crown depends on direct measurement of its size in all directions. Therefore, crown measurements based on data, sample diagrams and tables and their generalization to the whole region, while providing far-fetched results, also violate the assumption of error independence between observations. Therefore, the use of UAVs (Unmanned aerial vehicle) has been welcomed by providing very high spatial resolution information, the need for less infrastructure, more accurate postal harvesting of land elevations in forests, and the possibility of indirectly measuring tree characteristics (Chianucci et al. 2016; Tang and Shoa 2015).

UAVs have been used in many man-made forest research over the past few years to significantly save time, workforce, funding for various projects, and reduce the cost of maintaining and continuously Monitoring man-made forests (Matese 2020 ;Paneque-Gálvez et al. 2014) which require sufficient and continuous knowledge and application of effective methods in the

* Corresponding Author

(a.hosingholizade@ut.ac.ir) ORCID ID 0000 – 0001 – 5286 – 1361

(erfanifard@ut.ac.ir) ORCID ID 0000-0002-1996-4526

(salavipa@ut.ac.ir) ORCID ID 0000-0002-3554-111X

(hooman.latifi@kntu.ac.ir) ORCID ID 0000-0003-1054-889X

(jouybari@ub.ac.ir) ORCID ID 0000 – 0001 – 5455 – 6352

Cite this study

Hosingholizade, A., Erfanifard, Y., Alavipanah, S. K., Latifi, H., & Jouybari-Moghaddam, Y. (2022). An assessment of support vector machines for crown delineation of pine single trees on unmanned aerial vehicle imagery. 4th Intercontinental Geoinformation Days (IGD), 17-20, Tabriz, Iran

correct diagnosis and extraction of the crown, which can be referred to as two methods of classification of pixel base and object-oriented (Region Of Interest from segmentation). SVM classification methods work based on spectral information. As the power of spatial resolution increases, classification based solely on spectral data creates many problems. One of these problems is the variability of spectral information at the level of the crown of trees due to the shadow of one part of the crown and the location of the other part facing the sun. This effect is especially pronounced in the morning or afternoon. Therefore, samples in supervised methods cannot be very effective and practical in increasing the accuracy of classification in such conditions. Also, in the forest environment, surface features such as grasslands with tree crown are very similar in terms of spectral characteristics and the amount of gray value, and practically their proper separation from each other only on the basis of spectral information with only three RGB bands (blue, green and red) is not well possible (Li et al. 2017). Choosing an ROI (Region of Interest) is also very time consuming and fraught with error. On the other hand, the implementation of segmentation algorithm with all its advantages is a big problem and it takes a very long time (multiple times of classification), especially for images with very high spatial accuracy (such as UAV images) compared to classification, which is the use of segmentation algorithms. It faces limitations, especially if the area has a large area and spatial resolution. These limitations become even more severe, requiring a powerful processor and more time. To solve this problem and simultaneously use the advantages of segmentation and classification and eliminate the limitations (for example, lack of spectral bands and long processing time), a combination of both methods was used. In this study, we will specifically compare the estimation of the crown area with the basic and object-oriented pixel methods and compare it with the ground data in the eldarica pine man-made forest (known as Tehran pine).

2. Method

2.1. Study area

Pardisan Park of North Khorasan is located at the eighth kilometer of Bojnord-Mashhad Road (37° 28 ' 57 N "-57° 25 ' 49 " E, Zone 40 N), at an average altitude of 1080 meters above sea level. This complex is purely covered with Tehran pine (*Pinus eldarica*). The region is cold semi-arid according to the coupon criteria and has a relatively high slope in terms of topography (altitude range 1112 to 1037 meters). The average rainfall and its temperature according to the statistics of Bojnurd Airport Meteorological Synoptic Station (the closest station to the study area) for a period of 10 years (2011-2021) are 260 mm and 15 ° C, respectively.

2.2. Data

In this study 324 trees were selected and determined their location using GNSS. Two diameters perpendicular to each other were also used to determine the field area of the crown using a standard metal meter.

Then, using the Phantom 4 Pro UAV with forward and side overlap coverage of 80% and 40% Respectively and a height of 40 meters, 952 ortho images were obtained from the study area at 14:30 local time on March 4, 2021.

2.2.1. Tree crown area estimation

Two basic and object-oriented pixel approaches were used to estimate the crown area of pine trees. In the pixel base approach, due to the knowledge of the site and having an image with high spatial resolution after selecting the ROI by the user with the appropriate scatter and number, SVM classification algorithm with RBF, Sigmoid, Polynomial and Linear functions to extract Estimation of the crown area of pine trees was performed (Lou et al. 2021).

In the object-oriented method, due to the reduction of processing time and introduction of parts, using segmentation of part of the image (not the whole image), the parts were presented as ROI to the SVM classification algorithm. In the segmentation process, according to the shape of the crown of pine trees as well as previous studies (Gu et al. 2020; Iqbal et al. 2021; Mesner and Ostir 2014) and the conditions of the study area, appropriate coefficients for segmentation parameters (Scale Parameter = 25 Pixel, Shape = 0.1, Compactness = 0.5 per pixel) was determined to accurately detect the crown of trees. Then, in the smaller fragmented image, the crown pieces were extracted as a training sample in separate layers with pixel format to distinguish them from other existing features (shadow and soil). Then, by comparing the area of tree canopies, the execution time of the algorithm and comparing it with direct field perceptions for both SVM approaches with Linear, Sigmoid, Polynomial and RBF functions were discussed. Finally, by introducing the crown layer as the ROI of the image, the SVM classification algorithm was implemented and finally in both approaches, the error matrix was calculated.

3. Results

Pine trees with different crown areas were directly measured in the field and photographed by UAV. summarizes the field measurements in the study area shown in "Table 2". According to the results, in general, the use of ROI from segmentation and its use for classification has given better results in the extraction of crown pixels and also has the closest crown area to the area obtained from field data "Fig. 1" and "Table 3".

4. Discussion

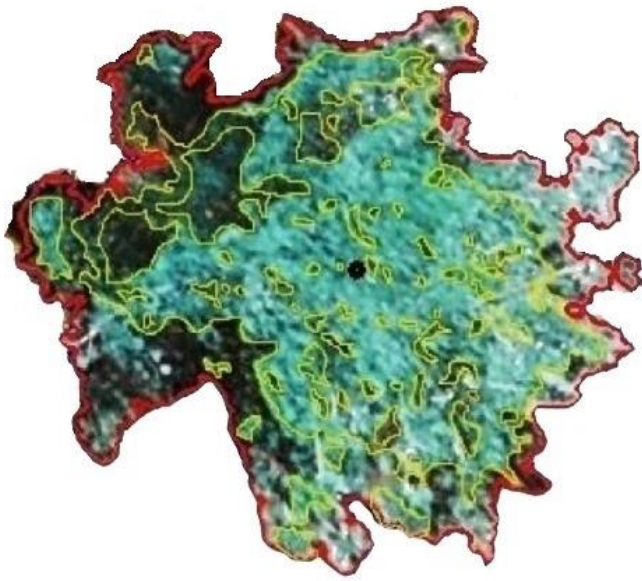
Based on the data in "Table 3", the identification of the general shape of the crown, followed by the estimation of the area in the segmentation, has been done with better accuracy. Unlike the classification methods used in this study (SVM), in segmentation, three parameters, scale, compactness and shape, are simultaneously involved in selecting a set of pixels to be placed in a single segment.

Table 2. Summary of statistical characteristics of the crown area of 324 Tehran pine trees Estimated UAV events

Characteristic	MIN	Max	Mean	STD	CV
Height (meters)	0.5	13.1	6.6	2.6	38.9
Small diameter of the crown	1.0	7.8	4.3	1.1	25.4
Large crown diameter (meters)	2.3	11.6	5.8	1.4	23.4
Crown area (square meters)	0.8	49.9	15.9	7.9	49.7

Table 3. Classification results with ROI resulting from user selection and ROI derived from object-oriented method

		Kappa coefficient (%)	Overall accuracy (%)	User accuracy (%)	Product accuracy (%)	Omission	Commission (%)	Crown Area(m ²)	Time of classification and selection ROI (min)	Field crown area (m ²)	Number of training data	Number of testing data
ROI from User	RBF	75	82	79	81	21	19	4297	83			
	Sigmoid	73	80	78	72	22	28	4272	86	5106	11731	1523
	Polynomial	67	73	69	74	31	26	3978	93			
	linear	61	68	66	70	34	30	3681	72			
ROI from Segmentation	RBF	93	98	92	96	8	4	5021	27			
	Sigmoid	91	92	89	93	11	7	4942	33	5106	10419	894
	Polynomial	88	91	86	89	14	11	4847	39			
	linear	79	86	83	84	17	16	4673	21			

**Figure 1.** Extraction of pine tree crown with object-oriented approach (red border), pixel base (yellow border), and center of tree (black point)

Each of these parameters can weaken the use of each other in solve single parameter mode, which leads to higher efficiency. The effect of segmentation capabilities in this study, in which pixels with close gray levels (crown and grass on the ground) and similar spectra in a phenomenon is more obvious.

The use of segmentation, despite the effect of shadow on the crown and the angle of sunlight on the surface of the tree crown (facing the sun or behind it) has separated

the crown well and has been more stable in recognizing the main shape of the tree and its shadow effect. The existence of empty space between the branches of a tree, which is originally part of the crown, is not considered part of the crown in the classification, but is correctly part of the crown area in the segmentation “Fig. 1”. The results of this study also showed that the use of segmentation method works well even with a small number of bands (RGB), while the use of segmentation, especially in features with varying gray value (such as crown and shadow) requires more bands that cost, time And will result in heavier processing. In addition, the time-consuming selection of ROIs and the selection of a sufficient number of pixels for which there is no specific rule are among the reasons for the lower accuracy of classification in the pixel basic approach compared to the object-oriented approach “Table 3”. According to the information in “Table 3”, the classification accuracy with the ROI resulting from segmentation, with a smaller number of pixels, has increased the “overall accuracy” and “kappa coefficient”. Also, processing time was measured in completely similar system modes in both approaches, which results in a significant reduction in time (even up to 60%) when using segmentation ROIs for classification. Examining the accuracy of Omission and Commission in “Table 3”, it can be seen that the use of SVM method with RBF function in ROI mode resulting from segmentation has the least difference with the area obtained from field data collection compared to other methods used in “Table 3”. Only 8% of the pixels are not in the crown category (Omission). While 4% of the pixels belong to another class in the crown class (Commission).

5. Conclusion

Although having a point cloud can easily distinguish the crown of trees, but sometimes due to high cost, technical limitations and the impossibility of providing a three-dimensional model in inappropriate forward and side overlap coverage, the point cloud is not available to everyone. Therefore, it is suggested to use the ROI obtained from segmentation to classify the crown in RGB images. However, the purpose of the work in choosing the final method can make a difference.

Acknowledgement

The authors of the study are grateful to the General Directorate of Environmental Protection of North Khorasan province. Also, part of the costs of this research has been provided through the plan number 4003393 approved by the Fund for Support of Researchers and Technologists of the country.

References

- Ahongshangbam, J., Khokthong, W., Ellsaesser, F., Hendrayanto, H., Hoelscher, D., & Roell, A. (2019). Drone-based photogrammetry-derived crown metrics for predicting tree and oil palm water use. *Ecohydrology*, 12(6), e2115. <https://doi.org/10.1002/eco.2115>
- Chianucci, F., Disperati, L., Guzzi, D., Bianchini, D., Nardino, V., Lastri, C., & Corona, P. (2016). Estimation of canopy attributes in beech forests using true colour digital images from a small fixed-wing UAV. *International journal of applied earth observation and geoinformation*, 47, 60-68. <https://doi.org/10.1016/j.jag.2015.12.005>
- Ding, J., Li, Z., Zhang, H., Zhang, P., Cao, X., & Feng, Y. (2022). Quantifying the Aboveground Biomass (AGB) of Gobi Desert Shrub Communities in Northwestern China Based on Unmanned Aerial Vehicle (UAV) RGB Images. *Land*, 11(4), 543. <https://doi.org/10.3390/land11040543>
- Gu, J., Grybas, H., & Congalton, R. G. (2020). Individual tree crown delineation from UAS imagery based on region growing and growth space considerations. *Remote Sensing*, 12(15), 2363. <https://doi.org/10.3390/rs12152363>
- Iqbal, I. A., Osborn, J., Stone, C., & Lucieer, A. (2021). A Comparison of ALS and Dense Photogrammetric Point Clouds for Individual Tree Detection in Radiata Pine Plantations. *Remote Sensing*, 13(17), 3536. <https://doi.org/10.3390/rs13173536>
- Li, Q. S., Wong, F. K. K., & Fung, T. (2017). Assessing the utility of UAV-borne hyperspectral image and photogrammetry derived 3D data for wetland species distribution quick mapping. *The International Archives of Photogrammetry, Remote Sensing and Spatial Information Sciences*, 42, 209. <https://doi.org/10.5194/isprs-archives-XLII-2-W6209-2017>
- Lou, X., Huang, Y., Fang, L., Huang, S., Gao, H., Yang, L., & Hung, I. K. (2021). Measuring loblolly pine crowns with drone imagery through deep learning. *Journal of Forestry Research*, 1-12. <https://doi.org/10.1007/s11676-021-01328-6>
- Mateo, A. (2020). Editorial for the Special Issue "Forestry Applications of Unmanned Aerial Vehicles (UAVs)". *Forests*, 11(4), 406. <https://doi.org/10.3390/f11040406>
- Mesner, N., & Ostir, K. (2014). Investigating the impact of spatial and spectral resolution of satellite images on segmentation quality. *Journal of Applied Remote Sensing*, 8(1), 083696. <https://doi.org/10.1117/1.JRS.8.083696>
- Miraki, M., Sohrabi, H., Fatehi, P., & Kneubuehler, M. (2021). Individual tree crown delineation from high-resolution UAV images in broadleaf forest. *Ecological Informatics*, 61, 101207. <https://doi.org/10.1016/j.ecoinf.2020.101207>
- Ouattara, T. A., Sokeng, V. C. J., Zo-Bi, I. C., Kouamé, K. F., Grinand, C., & Vaudry, R. (2022). Detection of Forest Tree Losses in Côte d'Ivoire Using Drone Aerial Images. *Drones*, 6(4), 83. <https://doi.org/10.3390/drones6040083>
- Panagiotidis, D., Abdollahnejad, A., Surový, P., & Chiteculo, V. (2017). Determining tree height and crown diameter from high-resolution UAV imagery. *International journal of remote sensing*, 38(8-10), 2392-2410. <https://doi.org/10.1080/01431161.2016.1264028>
- Shovon, T. A., Sprott, A., Gagnon, D., & Vanderwel, M. C. (2022). Using imagery from unmanned aerial vehicles to investigate variation in snag frequency among forest stands. *Forest Ecology and Management*, 511, 120138. <https://doi.org/10.1016/j.foreco.2022.120138>
- Tang, L., & Shao, G. (2015). Drone remote sensing for forestry research and practices. *Journal of Forestry Research*, 26(4), 791-797. <https://doi.org/10.1007/s11676-015-0088-y>
- Wu, S., Wang, J., Yan, Z., Song, G., Chen, Y., Ma, Q., & Wu, J. (2021). Monitoring tree-crown scale autumn leaf phenology in a temperate forest with an integration of PlanetScope and drone remote sensing observations. *ISPRS Journal of Photogrammetry and Remote Sensing*, 171, 36-48. <https://doi.org/10.1016/j.isprsjprs.2020.10.017>



4th Intercontinental Geoinformation Days

igd.mersin.edu.tr



Investigation of the effect of UAV flight altitude in map production

Mustafa Demirel ¹, Yunus Kaya ^{*1}, Nizar Polat ¹

¹Harran University, Faculty of Engineering, Department of Geomatics Engineering, Şanlıurfa, Türkiye

Keywords

UAV
Flight Altitude
Level of detail
Position accuracy

Abstract

Unmanned Aerial Vehicles (UAVs) are used in many areas because of their low cost and high resolution. Although the existing maps obtained from classical measurements meet sufficient accuracy, they are no longer preferred because they require a lot of time. On the other hand, UAVs are effectively used in base map production thanks to their high spatial resolution and location accuracy. In this study, orthophotos were produced using UAV images obtained from different flight altitudes (50, 80 and 120 meters). The level of detail was determined by comparing the produced orthophotos with the observations made on the land. In addition, position accuracies at different heights were determined. In order to increase location accuracy, Ground Control Points (GCP) have been established homogeneously distributed over the land. As a result of the study, it was seen that low-altitude flights show higher levels of detail and provide greater location accuracy. However, less area was visualized in low-altitude flights. In high-altitude flights, it has been observed that large buildings can be easily viewed, but small objects cannot be detected. At the end of the study, it was seen that a more sensitive base map is produced when the vector drawings obtained from high-altitude and low-altitude flights are combined.

1. Introduction

Unmanned Aerial Vehicles (UAVs), which are increasingly used in recent years, are physically non-pilot and passengers, can only carry measurement equipment such as camera, laser scanner, GNSS (Global Navigation Satellite System) and can be operated remotely or automatically (Ulvi et al., 2020). Thanks to the cameras placed on the UAVs, measurements can be made in places where people's access is dangerous. Although UAVs find a field of use in almost every sector, they are also widely used in the land surveying sector (Kaya et al., 2021; Şenol et al., 2020). It is widely used in the production of the base map, digital terrain model (DTM), digital elevation model (DEM), and area and volume calculations in projects where excavation-filling works are carried out. The use of UAVs in land surveying processes is more advantageous than other remote sensing platforms due to their low cost and higher spatial and temporal resolution, so they are more advantageous to be used in small-scale projects (Özcan, 2017). The most important issue in the base map production with

UAV is the level of detail on the map. Accordingly, as the flight altitude increases, the level of detail decreases, and as the flight altitude decreases, the level of detail increases. On the other hand, the increase in flight altitude allows less battery usage and more area to be viewed in a single flight.

Özcan (2017) compared position accuracies in DTM and DEM production using UAV images taken from different heights. Ozturk et al. (2017), the effect of images obtained with different heights and camera angles on the position accuracy of the images; Hastaoğlu et al. (2021), on the other hand, investigated the effects of different focal lengths on position accuracy.

In this study, the detail levels obtained from UAV images obtained from different flight altitudes were compared.

2. Method

As the study area, Şanlıurfa province, Harran University Osmanbey campus, Engineering Faculty area was chosen (Fig. 1).

* Corresponding Author

(16musti@gmail.com) ORCID ID 0000-0002-3407-5866
(yunuskaya@harran.edu.tr) ORCID ID 0000-0003-2319-4998
(nizarpolat@harran.edu.tr) ORCID ID 0000-0002-6061-7796

Cite this study

Demirel, M., Kaya, Y. & Polat, N. (2022). Investigation of the effect of UAV flight altitude in map production. 4th Intercontinental Geoinformation Days (IGD), 21-24, Tabriz, Iran

DJI Mavic 2 Pro Unmanned Aerial Vehicle was used in the study area. The UAV equipment used and their features are given in Table 1. In order to increase the location accuracy of the produced orthophoto, a Ground Control Points (GCPs) was established to be homogeneously distributed over the area. GCP coordinates were measured with Stonex GPS.

Within the scope of land studies, flights were carried out from three different heights as 50, 80 and 120 m (Fig. 2). Orthophotos were produced in Agisoft Photoscan software by using GCPs homogeneously distributed over the area and UAV images. The situation in the land was compared with the obtained orthophoto data. Detail points that are important in the base map production are determined in NETCAD software over orthophoto. The rules of the Large-Scale Map and Map Information Production Regulation (BÖHHBÜY) were taken as basis in the determination of the detail points and the production of the base map.

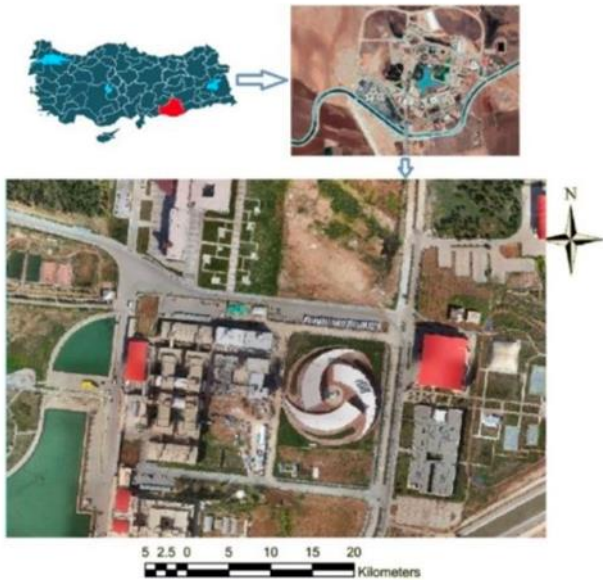


Figure 1. Study area

3. Results

In order to determine the level of detail in the land, analyzes were made on images obtained from three different heights. Detail points determined on the produced orthophotos were digitized in NETCAD software and compared with the observations in the land. It was determined which details were lost as the height level increased. While the roof of the building can be determined in the orthophoto image obtained from 50 meters and 80 meters height, it appears flat over 120 meters (Fig. 3). Stairs can also be identified at 50 and 80 meters but cannot be distinguished at 120 meters (Fig. 4). Small objects such as signage, manhole cover and small stair steps can only be seen on flights with a height of 50 meters (Fig. 5).

Considering the flight altitude and overlap ratios, some buildings can only be seen in flights from 120 meters altitude (Fig. 6).

As seen in Fig. 3-6, flight altitude is an important factor in perceiving details. Flights from a height of 50

meters gave better detail but could not detect some building corners. In flights made from a height of 120 meters, all the buildings were easily viewed, but small objects could not be distinguished. Base maps to be done by combining details obtained from different flight altitudes of an area give more accurate results. In Figure 7, the vectoral details obtained from three different heights are overlapped to see all the details.

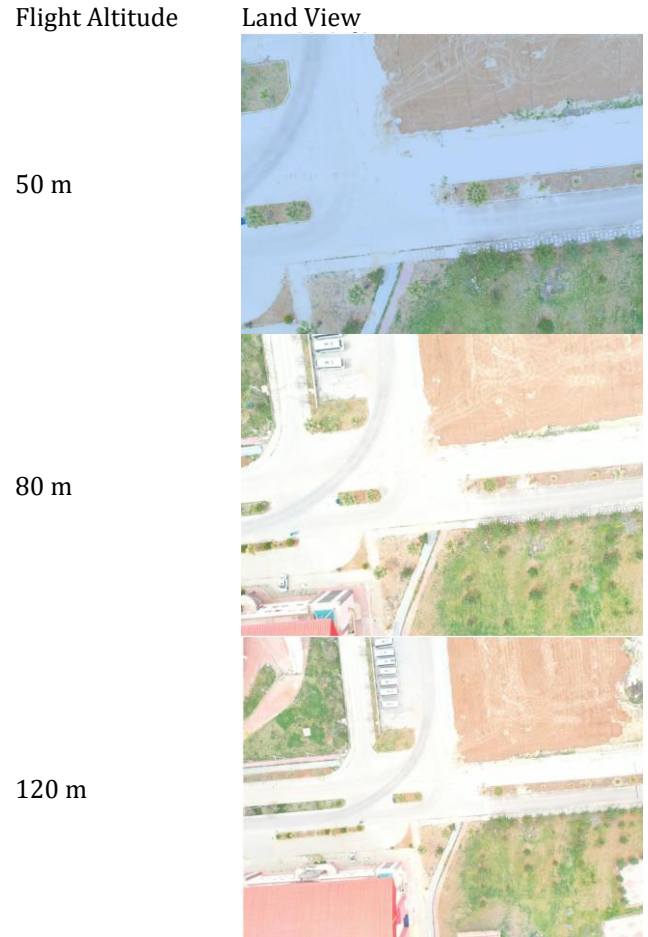


Figure 2. View of the study area from different heights

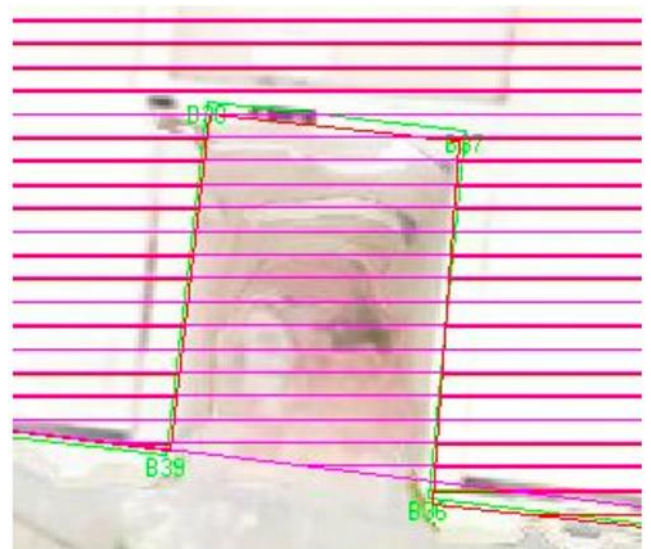


Figure 3. Building roof distinguishable from 50 and 80 meters

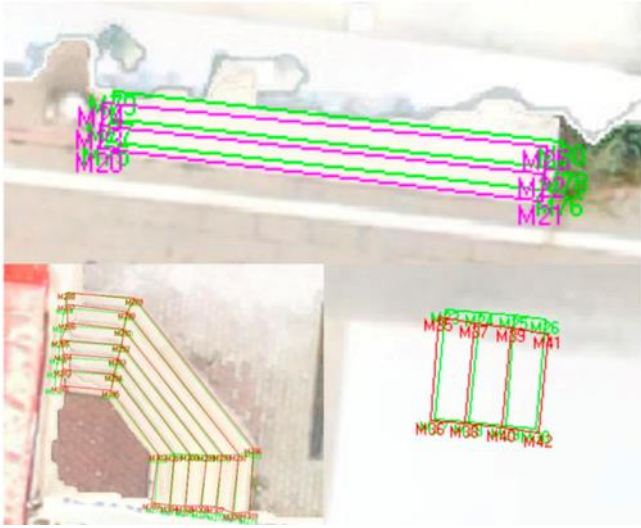


Figure 4. Stairs indistinguishable from 120 meters altitude



Figure 5. Stair steps that can only be distinguished from 50 meters altitude



Figure 6. (a) missing building corners at 50 meters height, (b) building visible from 120 meters



Figure 7. Combination of different details

The measurements taken from different parts of the land were compared with the measurements obtained from three different heights. The smallest amount of slip between points is 2.2 cm and the largest amount of slip is 19.4 cm. The amount of slip at all points is 6.9 cm on average.

4. Conclusion

UAV images are unquestionably advantageous for create base map. It is used in many studies because its temporal and spatial resolution is very high compared to other remote sensing platforms and its cost is low. In this study, orthophoto production was performed on UAV images obtained from different heights. Depending on the flight altitude, detectable detail levels were determined and position errors at different altitudes were determined. If the flight altitude was 120 meters, more area was displayed, but small details could not be detected. Details from different heights were combined to obtain more detail. Position accuracies vary between 2.2 cm and 19.4 cm depending on height. The average position accuracy is 6.9 cm.

References

- Hastaoğlu A, Hastaoğlu K Ö, Poyraz F & Gül Y (2021). İHA fotogrametrisi konum doğruluğuna kamera odak uzaklığı etkisinin incelenmesi. Türkiye Fotogrametri Dergisi, 3(1), 22-28.
- Kaya Y, Yiğit A Y, Ulvi A & Yakar M (2021). Arkeolojik Alanların Dokümantasyonunda Fotogrametrik Tekniklerinin Doğruluklarının Karşılaştırmalı Analizi: Konya Yunuslar Örneği. Harita Dergisi, 87(165), 57-72.
- Özcan O (2017). İnsansız hava aracı (İHA) ile farklı yüksekliklerden üretilen sayısal yüzey modellerinin (SYM) doğruluk analizi. Mühendislik ve Yer Bilimleri Dergisi, 2(1), 1-7.
- Öztürk O, Bilgilioglu B B, Çelik M F, Bilgilioglu S S & Uluğ R (2017). İnsanız Hava Aracı (İHA) Görüntüleri İle Ortofoto Üretiminde Yükseklik Ve Kamera Açısının Doğruluğa Etkisinin Araştırılması. Geomatik, 2(3), 135-142.

Şenol, H. İ., Memduhoglu, A., & Ulukavak, M. (2020). Multi instrumental documentation and 3D modelling of an archaeological site: a case study in Kizilkoyun Necropolis Area. Dicle Üniversitesi Mühendislik Fakültesi Mühendislik Dergisi, 11(3), 1241-1250.

Ulvi A, Yakar M, Yiğit A Y & Kaya Y (2020). İHA ve yersel fotogrametrik teknikler kullanarak Aksaray Kızıl Kilise'nin 3 Boyutlu nokta bulutu ve modelinin üretilmesi. Geomatik Dergisi, 5(1), 22-30.



4th Intercontinental Geoinformation Days

igd.mersin.edu.tr



Comparison between multicopter UAV and total station for volume calculation

Mustafa Ozkan ^{*1} , Nizar Polat ²

¹Harran University, Engineering Faculty, Geomatics Engineering Department, Şanlıurfa, Türkiye

Keywords

Volume Calculation
UAV
Photogrammetry
Geodesy
Total Station

Abstract

Currently, the UAV (Unmanned Aerial Vehicle) has become an alternative for different engineering applications, especially in surveying; one of these applications is the calculation of volumes of stockpiled material, but there are questions about its accuracy and efficiency; the purpose of this article is to compare traditional surveying methods for estimating total volumes through data obtained by total stations and data obtained by a multicopter UAV. In order to answer these questions, we obtain data from the exact location. This study is located in Şanlıurfa/Haliliye in a Hospital construction excavation. The data from the same location, which are gotten different methods, were compared.

1. Introduction

In these days, volume calculation is becoming harder with traditional methods. Companies demand monthly or twice in a month volume calculation. That's why terrestrial systems are becoming unuseful, and it's hard to get more details with human power.

The good news is that new digital technologies now make it possible to collect and process huge amounts of critical data at minimal costs—thus making a field operation more insight-driven, and potentially more productive and efficient.

This saves time, human resources, and also transportation costs because it is possible to map a large object in one day using a UAV, whereas mapping the same object using traditional methods could take up to a week. Furthermore, it is possible to map areas that are dangerous or difficult to access using an UAV, whereas it would be necessary to use some form of special equipment for mapping it otherwise. Using an UAV is also contactless, so it is possible to map 2088 sensitive areas, without driving or walking on the endangered area. In endangered areas, where getting a flight permit is difficult, terrestrial photogrammetry or laser scanning could be used as an alternative (Dlouhy et al., 2016; Burdziakowski, 2017).

Therefore, we aimed to compare old methods with photogrammetry. Firstly, excavating areas got with a total station and has been created a surface before then

excavation. At the same time, this process was made with the UAV. All area gotten with Multicopter and DTM, DSM, and Point cloud has been created. All GCP (Ground Control Points) giving from the same polygon points.

2. Method

This study map is made with the Structure from Motion (SfM) photogrammetry technic. SfM runs under the same basic conditions as stereoscopic Photogrammetry. It uses overlapping images in order to get a 3D structure of an interested object. Existing software can generate a 3D point cloud such as Pix4d mapper (commercial software) that has been used in this study.

The software advances in UAV applications and allows generating orthophoto in a willed coordinate system. For full performance of software, it is recommended to use a powerful computer due to the huge amount of data.

2.1. Preperation and Flight

The flight plan was prepared with Pix4d-Capture mobile application. The drone was set up in the field. All calibration settings were checked. Calibration settings must work properly. Big metal masses must be avoided throughout the calibration process since such masses

* Corresponding Author

(surveyozkan0@gmail.com) ORCID ID 0000-0002-1476-9756
(nizarpolat@harran.edu.tr) ORCID ID 0000-0002-6061-7796

Cite this study

Ozkan, M., & Polat, N. (2022). Comparison between multicopter UAV and total station for volume calculation. 4th Intercontinental Geoinformation Days (IGD), 25-27, Tabriz, Iran

locally affect Earth's magnetic field and satellite signals which is used for calibration by UAV.

The flight had two separate missions. All missions have 100 meters altitude and %80-%80 overlap. The drone was set up according to the pre-flight preparations in the field. The flight was performed with multiple batteries which is DJI Phantom 4 Pro V2. In this study 9 GCP's has been used and they have been determined with total station."Table.1".

Table 1. GCP's Coordinates Table

YKN1	484.693.429	4.115.742.488	520.655
YKN2	484.772.010	4.115.750.681	520.047
YKN3	484.812.369	4.115.689.421	520.578
YKN4	484.907.310	4.115.749.711	530.27
YKN5	484.933.462	4.115.814.434	535.623
YKN6	484.901.557	4.115.879.010	538.635
YKN7	484.861.587	4.115.825.045	533.447
YKN8	484.784.872	4.115.840.921	529.81
YKN9	484.848.105	4.115.910.520	536.768

2.2. Creating Surface with Total Station

All excavation area is 31 ha. And all area has been taken with total station. The study took 15 days with 3 persons. With UAV study took 45 min. There is a big difference between of two methods. But in this study, we only aimed in a 1.9 ha. Stockpile area." Fig.1". After the excavation process, 1.9 ha area was taken with Total Station (Leica Ts09). This process took half a day with 3 people.

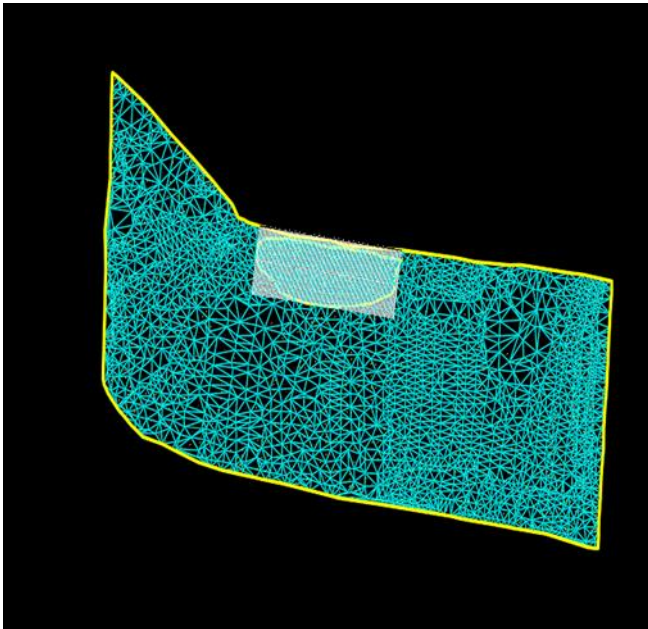


Figure 1. 1.9 ha. Surface Model in Autocad Civil3D

3. Creating point cloud with UAV

This work has been done with Phantom 4 pro V2 drone. After the excavation process, the second flight was done for 2.5 ha. area. It took 15 min. with same altitude (100 m) and same overlapping (%80-%80). The point

cloud was created in Pix4d software. The other works for volume calculation have been done in Virtual **Surveyor** software. Virtual Surveyor more useful for CAD processes than Pix4d. That's why we decided to use Virtual Surveyor for volume calculations."Figure.2".

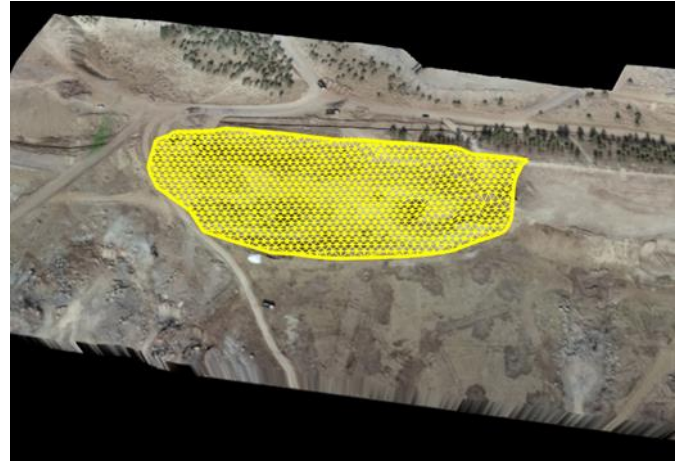


Figure 2. Surface Model in Virtual Surveyor

4. Results

All processes are made in Pix4d software. The ground sample distance (GSD) was calculated as 2.74 cm. The point cloud, DSM, DTM, and orthomosaic map were created in the study. And all volume calculation has been done in Virtual Surveyor"Fig3". The result of Virtual Surveyor is 102265.40 m³.

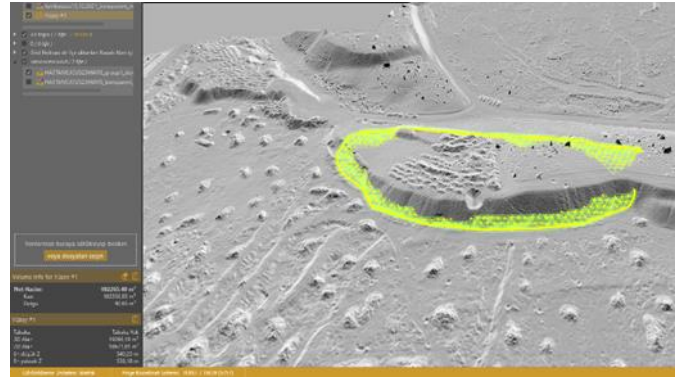


Figure 3. Volume calculation in Virtual Surveyor

On the other hand, all CAD process has been done in CIVIL3D "Fig.4", The result is 101958.20 m³.

KÜBAJ CETVELİ							
KILOMETRE	ARAMESAFE	YARMA ALANI	DOLGU ALANI	YARMA HACMI	DOLGU HACMI	KUM YARMA HACMI	KUM DOLGU HACMI
0-200.00	2.00	0.00	0.00	136.00	0.00	101958.20	0.00
0-202.00	2.00	0.00	0.00	0.00	0.00	101958.20	0.00
0-204.00	2.00	0.00	0.00	0.00	0.00	101958.20	0.00
0-206.00	2.00	0.00	0.00	0.00	0.00	101958.20	0.00
0-208.00	2.00	0.00	0.00	0.00	0.00	101958.20	0.00
0-210.00	2.00	0.00	0.00	0.00	0.00	101958.20	0.00
0-212.00	2.00	0.00	0.00	0.00	0.00	101958.20	0.00
0-214.00	2.00	0.00	0.00	0.00	0.00	101958.20	0.00
0-216.00	2.00	0.00	0.00	0.00	0.00	101958.20	0.00
0-218.00	2.00	0.00	0.00	0.00	0.00	101958.20	0.00
0-220.00	2.00	0.00	0.00	0.00	0.00	101958.20	0.00
0-222.00	2.00	0.00	0.00	0.00	0.00	101958.20	0.00
0-224.00	2.00	0.00	0.00	0.00	0.00	101958.20	0.00
0-226.00	2.00	0.00	0.00	0.00	0.00	101958.20	0.00
0-228.00	2.00	0.00	0.00	0.00	0.00	101958.20	0.00
0-230.00	2.00	0.00	0.00	0.00	0.00	101958.20	0.00
0-232.00	2.00	0.00	0.00	0.00	0.00	101958.20	0.00
0-234.00	2.00	0.00	0.00	0.00	0.00	101958.20	0.00
0-236.00	2.00	0.00	0.00	0.00	0.00	101958.20	0.00
0-238.00	2.00	0.00	0.00	0.00	0.00	101958.20	0.00
0-240.00	2.00	0.00	0.00	0.00	0.00	101958.20	0.00
0-242.00	2.00	0.00	0.00	0.00	0.00	101958.20	0.00
0-244.00	2.00	0.00	0.00	0.00	0.00	101958.20	0.00
0-246.00	2.00	0.00	0.00	0.00	0.00	101958.20	0.00
0-248.00	2.00	0.00	0.00	0.00	0.00	101958.20	0.00
0-250.00	2.00	0.00	0.00	0.00	0.00	101958.20	0.00
0-252.00	2.00	0.00	0.00	0.00	0.00	101958.20	0.00
0-254.00	2.00	0.00	0.00	0.00	0.00	101958.20	0.00
0-256.00	2.00	0.00	0.00	0.00	0.00	101958.20	0.00
0-258.00	2.00	0.00	0.00	0.00	0.00	101958.20	0.00
0-260.00	2.00	0.00	0.00	0.00	0.00	101958.20	0.00
0-262.00	2.00	0.00	0.00	0.00	0.00	101958.20	0.00
0-264.00	2.00	0.00	0.00	0.00	0.00	101958.20	0.00
0-266.00	2.00	0.00	0.00	0.00	0.00	101958.20	0.00
0-268.00	2.00	0.00	0.00	0.00	0.00	101958.20	0.00
0-270.00	2.00	0.00	0.00	0.00	0.00	101958.20	0.00
0-272.00	2.00	0.00	0.00	0.00	0.00	101958.20	0.00
0-274.00	2.00	0.00	0.00	0.00	0.00	101958.20	0.00
0-276.00	2.00	0.00	0.00	0.00	0.00	101958.20	0.00
0-278.00	2.00	0.00	0.00	0.00	0.00	101958.20	0.00
0-280.00	2.00	0.00	0.00	0.00	0.00	101958.20	0.00
0-282.00	2.00	0.00	0.00	0.00	0.00	101958.20	0.00
0-284.00	2.00	0.00	0.00	0.00	0.00	101958.20	0.00
0-286.00	2.00	0.00	0.00	0.00	0.00	101958.20	0.00
0-288.00	2.00	0.00	0.00	0.00	0.00	101958.20	0.00
0-290.00	2.00	0.00	0.00	0.00	0.00	101958.20	0.00
0-292.00	2.00	0.00	0.00	0.00	0.00	101958.20	0.00
0-294.00	2.00	0.00	0.00	0.00	0.00	101958.20	0.00
0-296.00	2.00	0.00	0.00	0.00	0.00	101958.20	0.00
0-298.00	2.00	0.00	0.00	0.00	0.00	101958.20	0.00
0-300.00	2.00	0.00	0.00	0.00	0.00	101958.20	0.00
0-300.31	0.31	0.00	0.00	0.00	0.00	101958.20	0.00

Figure 4. Volume calculation in Civil3D

5. Conclusion

In this study, the traditional method with TST to estimate volumes of stockpile were compared with UAVs, data from the same site were taken and the post processing was done in Virtual Surveyor with a TIN model from the point cloud data obtained with TST and in Pix4D from data obtained by the UAV. The results were compared with the actual volume of material, which was obtained from one of the engineers of the site where the data collection was performed.

At the end of all processes, we can see two results. There is a too small difference of the % 0.3. It's a pretty good result for the volume calculation. The volume calculation with photogrammetry is quite adequate and reliable, as we can see.

References

- Kavanagh, B. F., & Glenn Bird, S. J., (1996). Surveying principles and applications (4 Ed.). Prentice Hall. pp. 257–264. ISBN 0- 13-438300-1. Pix4D, website <https://support.pix4d.com> (accessed, April 15, 2015)
- Burdziakowski, P. (2017). Towards Precise Visual Navigation and Direct Georeferencing for MAV Using ORB-SLAM2. In: 2017 Baltic Geodetic Congress (BGC Geomatics). Gdansk, Poland, 394–398. doi: 10.1109/BGC.Geomatics.2017.21.
- DJI 2020. <https://www.dji.com/ee/phantom-4-pro-v2> Accessed 05.05.2020
- Yakar, M., & Yilmaz, H. M. (2008). Using in volume computing of digital close range photogrammetry. *The International Archives of the Photogrammetry, Remote Sensing and Spatial Information Sciences. Vol. XXXVII. Part B3b*.
- Leica Geosystems, website http://www.leicageosystems.com/en/Leica-FlexLine-TS02plus_99086.htm (accessed, June 20, 2015)

4th Intercontinental Geoinformation Days

igd.mersin.edu.tr



Comparison of the effect of different vegetation indices on land surface temperature values

Gulshan Mammadli^{*1}, Filiz Bektas Balcik²¹Istanbul Technical University, Informatics Institute, Applied Informatics Department, Istanbul, Türkiye²Istanbul Technical University, Civil Engineering Faculty, Geomatics Engineering Department, Istanbul, Türkiye

Keywords

Remote sensing
Vegetation indices
Mono-window algorithm
NDVI threshold
Land cover map

Abstract

Land surface temperature (LST), which is a very important parameter in many fields such as ecology, hydrology and climate studies, can be monitored on a regional and global scale with satellite images. This study aimed to investigate the effects of different Vegetation indices (VI) on LST. The study focused on to generate LST maps over North-Rhine-Westphalia and Rhineland-Palatinate states of German using 23 August 2016 dated Landsat 8 OLI&TIRS data. Additionally, Sentinel-FCOVER data was used to examine the effect of VI on LST. The LST values were retrieved with Mono-window method, and Land Surface Emissivity (LSE) maps were calculated with NDVI_{THM} method. Normalized Difference Vegetation Index (NDVI), Renormalized Difference Vegetation Index (RDVI), Soil Adjusted Vegetation Index (SAVI), Enhanced Vegetation Index (EVI) were selected for the study. Additionally, soil emissivity values were calculated from LUCAS (Land Use and Coverage Area frame Survey) and ASTER Spectral Libraries datasets. Finally, the accuracy of FVC (Fractional vegetation cover) and LST maps were evaluated. Although the best FVC result was achieved with RDVI, LST maps showed similar results for all selected vegetation indices. Thus, transects were extracted from the LST maps for different land cover categories and the results were compared to determine the differences.

1. Introduction

The Land Surface Temperature (LST) parameter, which refer to the temperature of the Earth's surface is one of the important factors in hydrology, ecology and global change studies. Thermal remote sensing technologies provide unique methods for collecting LST information on both a regional and global scale (Yu et al. 2014).

Land Surface Emissivity (LSE) parameter is very important to calculate LST from thermal band. Many different methods have been developed to calculate LSE from remotely sensed data. The NDVI threshold (NDVI_{THM}) method is one of the most widely used approaches to determine LSE (Sobrino et al. 2008; Sobrino and Raissouni 2000). This method is based on the NDVI index. There are many studies in the literature evaluating the effects of LSE on LST (Sekertekin and Bonafoni 2020a; Sekertekin and Bonafoni 2020b;). However, there are very few studies investigating the effect of the VI factor on LST. One of these studies was carried out by Neinavaz et al. (2020). In their study, the

VARIGreen, WDRVI, TGDVI VIs in addition to NDVI index were evaluated using NDVI_{THM} method. The result of the study showed that LSE is not the only factor to effect LST values. Therefore, LST_{WDRVI} and LST_{TGDVI} maps were had higher accuracy than LST_{NDVI} and LST_{VARIGreen} maps.

The aim of our study was to investigate and compare the performance of selected VIs as NDVI, RDVI, SAVI and EVI on LST calculation according to land cover classes (Mammadli 2022).

2. Method

In this study, Germany's North Rhine Westphalia and Rhineland Palatinate states were chosen as the test area.

Within the scope of the study, the LST maps were retrieved from August 23, 2016 dated Landsat 8 OLI & TIRS data using the Mono-window (MW) method. To implement the MW algorithm, atmospheric parameters and emissivity values are required. To calculate atmospheric parameters, water vapor (ω) and near-surface temperature (T_0) data were gathered from DWD

* Corresponding Author

^{*}(mammadlig19@itu.edu.tr) ORCID ID 0000-0003-2063-9971
(bektasfi@itu.edu.tr) ORCID ID 0000-0003-3039-6846

Cite this study

Mammadli, G., & Balcik, F. B. (2022). Comparison of the effect of different vegetation indices on land surface temperature values. 4th Intercontinental Geoinformation Days (IGD), 28-31, Tabriz, Iran

(Germany weather station) meteorological stations. Additionally, two different Sentinel-2A products were used to evaluate the accuracy of the FVC and Land Cover (LC) maps.

Sentinel-FCOVER data were used to examine the FVC results were produced by using selected VIs. ASTER spectral library and LUCAS soil samples were used to calculate soil emissivity values in the NDVI threshold method.

2.1. Vegetation index calculation

NDVI, RDVI, SAVI and EVI vegetation indices were used to investigate the effects of spectral indices on LST. These VIs were integrated to the emissivity equation as input parameters. The original NDVI threshold method uses the NDVI index. The main reasons for choosing other indices were summarized below;

i) The SAVI index, unlike the NDVI index, helps to minimize the effects caused by soil reflection and provides a contribution to this index.

ii) The RDVI index provides improvement in background effects caused by geometry and ground.

iii) The EVI vegetation index optimizes vegetation signals by eliminating background reflection and saturation problems, as well as atmospheric pollution caused by dust and clouds.

Equations developed for VIs are given in Table 1.

Table 1. Vegetation indices equations

Index	Equation	Reference
NDVI	$(B5-B4)/(B5+B4)$	Rouse et al. (1973)
EVI	$2.5*((B5-B4)/B5+B4-7.5*B2+1))$	Jiang et al. (2008)
RDVI	$(B5-B4)/(B5+B4)^{1/2}$	Roujean and Breon (1995)
SAVI	$1.5*((B5-B4)/B5+B4+0.5))$	Huete (1988)

2.2. LST calculation

The MW algorithm was proposed by Qin et al. (2001) to calculate LST from Landsat TM data. The improved MW algorithm was used in this study to calculate LST values (Wang et al. 2015).

2.2.1. Land surface emissivity calculation

The LSE values integrated into the LST maps were calculated with the NDVI threshold method.

2.2.2. NDVI_{THM} method

This method assumes that the satellite image pixels are composed of vegetation, soil or mixed pixels. An equation is proposed for each of these approaches. Soil, vegetation emissivity values and FVC map are required to use the equations. FVC maps were calculated from vegetation indices (Sobrino and Raissouni 2000). Vegetation emissivity value (0.99) was selected from the literature. The emissivity values of mixed pixels were estimated from FVC. Contrary to vegetation, soil emissivity values were calculated from the ASTER spectral library and LUCAS soil sample since soil have a

high emissivity variation. LUCAS soil samples were used to determine the soil classes of the test area, and the ASTER spectral library were used to extract the soil reflectance. Multiple regression analysis was applied to the soil reflectance values to estimate the average soil emissivity and band coefficients (Li & Jiang 2018).

2.2.3. Mono-window method

In order to calculate the LST with the MW algorithm, first atmospheric transmission (τ) and effective mean atmospheric temperature (T_a) values were estimated from ω and T_0 . This data was collected by DWD Germany Weather Station. After τ and T_a values were calculated, Landsat 8 thermal band 10 first was converted to TOA radiance and then BT was calculated. The required data for this process were extracted from the metadata file of Landsat 8 OLI & TIRS.

2.3. Accuracy assessment

The accuracy assessment of the FVC and LST maps were performed by means of statistical parameters such as R^2 (Coefficient of determination), RMSE (Root Mean Square Error), MSE (Mean Squared Error), MAE (Mean Absolute Error) and Correlation.

2.4. Land cover map

In this study, in order to examine the spatial distribution of LST, five LC classes were determined and classified using the Maximum Likelihood method. The accuracy assessment of this map was performed using error matrix.

3. Results

The VI maps created from the Landsat 8 OLI & TIRS satellite image are shown in Fig 1.

3.1. Results of FVC maps

In the study, FVC maps were calculated by means of vegetation indices, soil and vegetation emissivity values, and accuracy was evaluated based on Sentinel-FCOVER data. FVC values ranged from 0 to 1. For case FVC=0; the soil emissivity value was calculated as 0.9695 in the study. According to the results of the FVC maps, RDVI has the highest accuracy (Table 2).

Table 2. FVC results for each index

Index	R2	RMSE	MSE
NDVI	0.60	0.285	0.081
EVI	0.68	0.248	0.062
RDVI	0.73	0.207	0.043
SAVI	0.70	0.215	0.046

3.2. Results of LC map

In the study, five main classes were determined and classified from the Landsat 8 OLI & TIRS image to evaluate the relationship of LST with LC classes (Fig. 2).

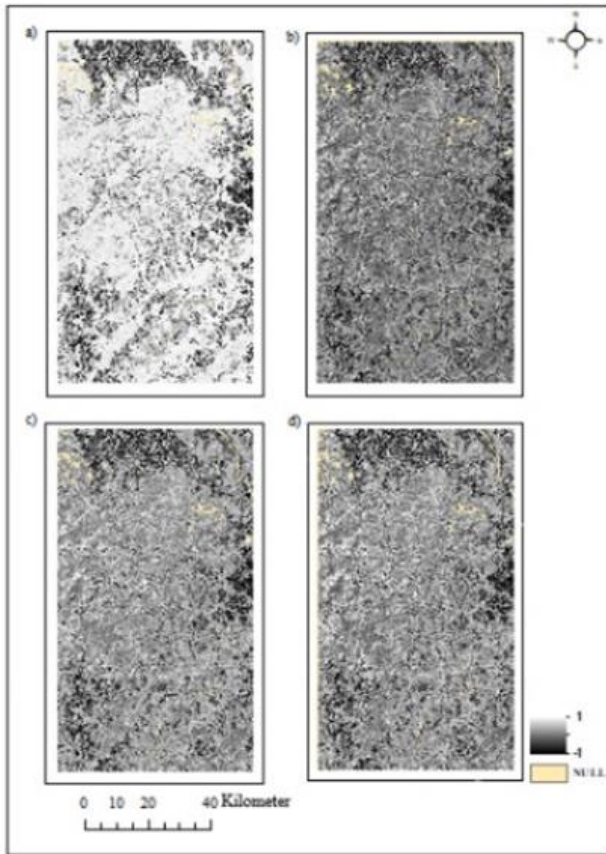


Figure 1. Vegetation index maps; a) forest & green areas b) agricultural areas, c) bareland d) artificial surfaces

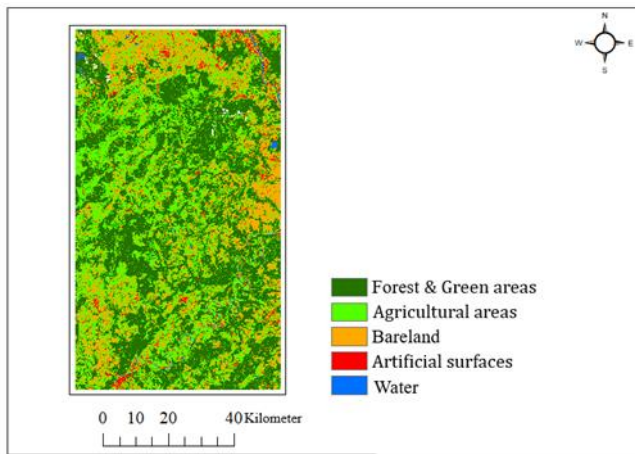


Figure 2. Land Cover map

According to the results of the LC map, the LST decreased with the increase of vegetation cover. The overall accuracy of the LC map is 0.89 based on error matrix and Kappa statistics is 0.85.

3.3. Result of LST

The accuracy assessment of the LST maps were carried out using 13 meteorological stations. R^2 , RMSE, MAE, Correlation statistical parameters were calculated for each LST map. According to the statistical analysis results of the LST maps that were produced using selected vegetation indices, the LST values were relatively similar (Table 3).

Table 3. LST results for each selected index

Index	R^2	RMSE	MAE	Correlation
NDVI	0.588	1.882	1.331	0.767
EVI	0.585	1.931	1.379	0.765
RDVI	0.581	1.904	1.348	0.762
SAVI	0.581	1.904	1.348	0.762

Then transects were obtained and analysed from the images to reveal the existing differences between the LST values. These transects were extracted according to LC classes. First transects were created for forest & green areas, and agricultural areas (Fig 3.).



Figure 3. LST transects a) forest & green b) agricultural areas

The color scale in the graphs shows the temperature curves of the indices. Also transects for artificial surfaces and bareland were extracted from LST that calculated using selected VI (Fig. 4).

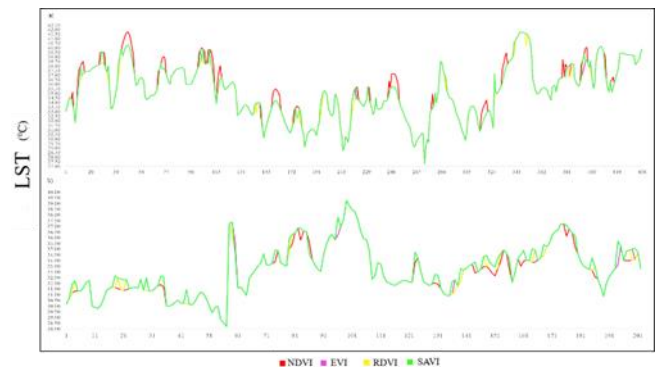


Figure 4. LST transects a) artificial surfaces b) bareland

According to these graphs, some pixel samples of LST_{NDVI} values were showed different results than the other three indices. The RDVI index and SAVI indices were showed very similar curves. The EVI index has relatively different values only in forest & green area classes.

4. Discussion

The results of the study showed that the effects of indices on the LST are quite low. In order to find out the reasons of this result, studies investigating the effects of LSE values calculated from VIs on LST were examined.

According to researches; The MW method is sensitive to parameters such as LSE, ω and T_a . Sensitivity analysis

of the MW algorithm performed by Qin et al. (2001) and Wang et al. (2015) found that LST error dT was less sensitive to LSE compared to other parameters (ω , T_a). Additionally, LST error increase with the brightness temperature.

Jiang and Lin (2021), Sekertekin and Bonafoni (2020b), Windahl and Beurs (2016) have determined that the LST values for the winter and nighttime show more accurate results due to the decrease in the brightness temperature.

Neinavaz et al. (2020) suggested that specific factors of the study area, such as elevation or soil moisture, should also be included in the equation.

5. Conclusion

The temperature parameter has a significant effect on living and non-living things. These effects cause both positive and negative implication. Many studies focus on the negative aspects of these effects. Today, the sharp effects of the temperature increase cause environmental problems on a global scale. Continuous data is required to avoid from these effects. Remote sensing technologies is very effective to obtain the high temporal resolution data for large areas to quickly identify and solve the problems.

Within the scope of this study, the effect of different vegetation indices on LST calculation was investigated and evaluated. In the study, it was determined that the LST results were relatively similar and the effect of the indices on LST was quite low. Field studies could be carried out to support the results of this study. In addition, other factors affecting LST calculation should be investigated and evaluated in the study area. The emissivity effects of artificial surfaces are not addressed in this study.

Acknowledgement

We are grateful to the NextGEOSS project team, German Weather Service DWD, the European Soil Data Centre ESDAC and the ECOSTRESS Spectral Library for the data they have provided.

References

- Huete, A. R. (1988), A Soil-adjusted vegetation index (SAVI), *Remote Sensing of Environment*, 25, 295-309.
- Jiang, Z., Huete, A. R., Didan, K., & Miura, T. (2008). Development of a two-band enhanced vegetation index without a blue band. *Remote Sensing of Environment*, 112, 3833-3845.
- Li, S., & Jiang, G. M. (2018). Land surface temperature retrieval from Landsat-8 data with the generalized split-window algorithm. *IEEE Access*, 6, 18149–18162, <https://doi.org/10.1109/ACCESS.2018.2818741>.
- Mammadli, G. (2022). Farklı uzaktan algılama bitki indekslerinin Yer Yüzey Sıcaklığı hesabına etkisinin araştırılması. MS Thesis, Istanbul Technical University, Istanbul.
- Neinavaz, E., Skidmore, A. K., & Darvishzadeh, R. (2020). Effects of prediction accuracy of the proportion of vegetation cover on land surface emissivity and temperature using the NDVI threshold method. *International Journal of Applied Earth Observation and Geoinformation (JAG)*, 85, 1-13. [101984]. <https://doi.org/10.1016/j.jag.2019.101984>.
- Qin, Z., Karnieli, A., & Berliner, P. (2001). A mono-window algorithm for retrieving land surface temperature from Landsat TM data and its application to the Israel-Egypt border region. *International Journal of Remote Sensing*, 22 (18), 3719–3746.
- Rouse, J. W., Haas, R. H., Schell, J. A., Deering, D. W. (1973), Monitoring the vernal advancement and retrogradation of natural vegetation. Type II, Progress Report RSC 1978-1.
- Roujean, J. L., & Breon, F. M. (1995). Estimating PAR absorbed by vegetation from bidirectional reflectance measurements. *Remote Sensing of Environment*, 51, Issue 3, [https://doi.org/10.1016/0034-4257\(94\)00114-3](https://doi.org/10.1016/0034-4257(94)00114-3).
- Jiang, Y., & Lin, W. (2021). A Comparative analysis of retrieval algorithms of Land Surface Temperature from Landsat-8 Data: A case study of Shanghai, China. *International Journal of Environmental Research and Public Health*, 18, 5659. <https://doi.org/10.3390/ijerph18115659>.
- Sobrino, J. A., & Raissouni, N. (2000) Toward remote sensing methods for Land Cover Dynamic Monitoring: application to Morocco. *International Journal of Remote Sensing*, 21, 353-366.
- Sobrino, J. A., Jimenez-Munoz, J. C., Soria, G., Romaguera, M., Guanter, L., Moreno, J., Plaza, A., & Martinez, P. (2008). Land surface emissivity retrieval from different VNIR and TIR sensors. *IEEE Transactions on Geoscience and Remote Sensing*, 46 (2), 316–327.
- Sekertekin, A., & Bonafoni, S. (2020a). Land Surface Temperature retrieval from Landsat 5, 7, and 8 over rural Areas: assessment of different retrieval algorithms and emissivity models and toolbox implementation. *Remote Sensing* 12 (2), 294. <https://doi.org/10.3390/rs12020294>.
- Sekertekin, A., & Bonafoni S. (2020b). Sensitivity analysis and validation of daytime and nighttime Land Surface Temperature retrievals from Landsat 8 using different algorithms and emissivity Models. *Remote Sensing* 12 (17), 2776; <https://doi.org/10.3390/rs12172776>
- Wang, F., Qin, Z., Song, C., Tu, L., Karnieli, A., & Zhao, S. (2015). An Improved Mono-Window Algorithm for Land Surface Temperature Retrieval from Landsat 8 Thermal Infrared Sensor Data. *Remote Sensing* 7, 4268–4289. <https://doi.org/10.3390/rs70404268>.
- Windahl, E., Beurs, K. (2016). An intercomparison of Landsat land surface temperature retrieval methods under variable atmospheric conditions using in situ skin temperature. *International Journal of Applied Earth Observation and Geoinformation*, 51, 11–27, <http://dx.doi.org/10.1016/j.jag.2016.04.003>
- Yu, X., Guo, X., & Wu, Z. (2014). Land Surface Temperature retrieval from Landsat 8 TIRS—comparison between Radiative Transfer Equation-Based method, Split Window Algorithm and Single Channel method. *Remote Sensing*, 6, 9829-9852; <https://doi.org/10.3390/rs6109829>.

4th Intercontinental Geoinformation Days

igd.mersin.edu.tr



Evaluation of urban heat island based on the land surface temperature and spatial variables in Tabriz

Iraj Teymouri¹, Mohammad Nemati¹

¹University of Tabriz, Planning & Environmental Studies, Urban Planning and Geography, Tabriz, Iran

Keywords

Land Surface Temperature
Urban Heat Island
Spatial Variables
One-Way ANOVA
Multiple Linear Regression
Tabriz

Abstract

In this study, the relationship between land surface temperature (LST) and spatial variables in Tabriz Metropolitan city was investigated using Land sat 8 OLI/TIRS images for summer and winter of 2018. For this, LST was calculated in accordance with the algorithm (Jimenez-Munoz & Sobrino, 2003) and proximity variables were prepared based on Distance Function in Arc GIS. According to the LST map obtained, down town area in Tabriz city experienced lower temperature than the suburban areas during day time. Some of the contributing factors such as population density, elevation, proximity to green space, could decrease the surface temperature, but on the other hand, the residential, industrial, religious and bare lands could increase the temperature in the city. Results of multiple linear regression analysis between LST and explanatory variables showed the model could estimate 63.7 % of the dependant variable in summer and 61.7% of it in winter. Based on the Beta, the results showed negative correlation between LST and some of the independent variables as, Population density, Elevation, proximity to green space, military and educational areas. Also, the one-way ANOVA test revealed that the difference between mean average temperature of various land use type were not significant

1. Introduction

One of the more serious impacts of urbanization is its effect on urban climate, especially the rise in urban temperature which called urban heat island (UHI) effect (Hirano & Fujita, 2012). Increasing use of materials with high heat absorption and retention capacity, such as asphalt as well as thermal emissions derived from transport activities and industrial process intensify UHI effect (Jato-Espino, 2019). UHI is a phenomenon whereby urban regions experience warmer temperatures than their rural surroundings (EPA, 2008). UHI influences well-being and welfare (Jato-Espino, 2019), Average energy consumption (Rizwan et al., 2008; Hirano & Fujita, 2012) and consequently, pollution (Li et al., 2018) and social equity of cities (Harlan et al., 2006). Many factors contribute to urban heat island formation, as time (day and season), synoptic weather (wind, cloud), city form (materials, geometry, greenspace), city function (energy use, water use, pollution), city size (linked to form and function), geographic location (climate, topography, rural surrounds) (Voogt & Oke, 2003). Due to its adverse impacts, significant research efforts have

been performed to evaluate the urban heat island phenomenon's impact on the urban environment.

Takebayashi, Moriyama (2009), explored UHI mitigation effect achieved by converting to grass-covered parking, determined the air temperature reduce by the spread of grass-covered parking areas. Rajasekar and Weng (2009) also focused on the UHI monitoring and analysis using a non-parametric model: a case study of Indianapolis, highlighted the areas with maximum heat signatures have a strong correlation with impervious surfaces. Susca, Gaffin and Delloso (2011), investigated the positive effects of vegetation: UHI and green roofs, found an average of 2°C difference of temperature between the most and the least vegetated areas. Zhang, Yiyun, Qing, Jiang, (2012) in the study of UHI effect based on NDVI in the case of Wuhan city, showed that there is obvious negative correlation between NDVI and surface radiation and heating island strength is higher in industrial and commercial areas than others. Hathway and Sharples (2012) found that the urban form on the river bank influenced the levels of cooling felt away from the river bank. Peron, De Maria, Spinazze and Mazzali

* Corresponding Author

(iraj-teymouri@tabrizu.ac.ir) ORCID ID 0000 – 0002 – 3168 – 5583
(mo.nemati@tabrizu.ac.ir) ORCID ID 0000 – 0003 – 2054 – 8535

Cite this study

Teymouri, I., & Nemati, M. (2022). Evaluation of urban heat island based on the land surface temperature and spatial variables in Tabriz. 4th Intercontinental Geoinformation Days (IGD), 32-36, Tabriz, Iran

(2015), confirmed thermal impact of vegetation in the urban environment. Bokaei, kheirkhah Zarkesh, Daneshkar Arasteh and Hosseini (2016) showed negative correlation between land cover and LST. El-Hattab, Amany and Lamia (2018) found industrial buildings released a higher temperature than its surroundings and indicated that urban bare and semi bare land increased the UHI effect. Dwivedi and Krishna Mohan, (2018), recommended vertical walls and also dense urban vertical cover of forests to reduce the effect of UHI effect. Xiao et al., (2018) confirmed the cooling and humidifying effect of large green spaces was more obvious and stable. Jato-Espino (2018) highlighting the role of low reflectance of built- up surfaces in the UHI effect. Shirani-bidabadi et al, (2019) indicated that the areas which influenced by UHI are often in parts of Isfahan's city where vegetation cover is very sparse, the land is arid and industrialization and regional settlements are booming.

UHI literature has focused on explaining the UHI spatial pattern generally in summer based on explanatory variables, generally with 2D and 3D space factors. Among the explanatory variable's vegetation covers, water bodies play a key role in minimizing the UHI effect while urban bare and semi bare land, industrial and commercial zones maximizing the UHI effect.

According to the foregoing, the present study was carried out to follow two objectives: (1) the study of LST in Tabriz City using Landsat 8 OLI/ TIRS satellite image during the summer and winter of the year 2018, and, (2) using the parametric statistical method for analysing the spatial distribution of LST and its relationship with explanatory variables (Table. 8). To calculate LST, one of the widely used remote sensing methods that is based on thermal infrared wavelength was used (Jimenez-Munoz & Sobrino, 2003). The land use map prepared from the municipality land use map, and population distribution was also studied in the form of map prepared from the census in 2016.

2. Method

In this study, to evaluate the UHI and influenced area of the city, the satellite images of land sat 8 OLI/ TIRS (thermal band 10) were used the metadata of images were featured in Table 2.

In order to compute the LST, the thermal band digital number (DN) is numerically converted to radiometric scale using Eq. (1).

Eq. (1) is used for converting DN to radiance in Landsat 7 ETM image:

$$L_{\lambda} = \left(\frac{LMAX_{\lambda} - LMIN_{\lambda}}{QCALMAX - QCALMIN} \right) * (QCAL - QCALMIN) + LMIN_{\lambda} \quad (1)$$

Where,

L_{λ} = the cell value as the radiance

QCAL=digital number

$LMIN_{\lambda}$ = spectral radiance scales to QCALMIN

$LMAX_{\lambda}$ = spectral radiance scales to QCALMAX

QCALMIN=the minimum quantized calibrated pixel value (typically =1)

QCALMAX+ the maximum quantized calibrated pixel value (typically =255)

The value of $LMIN_{\lambda}$ and $LMAX_{\lambda}$ extracted from the header file of landsat images are 0.10033 and 22.00180 respectively (Table.1)

Converting radiance to brightness temperature

After calculating spectral radiance (L_{λ}), the images were computed for their brightness temperature using either Planck's radiance function for temperature (Weng et al.,2004) or the approximation formula shown in Eq. (2).

$$T_c = \frac{k_2}{\ln\left(\frac{k_1}{L} + 1\right)} - 273.15 \quad (2)$$

Where T is the effective at sensor brightness temperature in Celsius, k_1 is calibration constant (in kelvin), k_2 is the calibration constant (Watts/[$m^2 * sr * \mu m$]), and Ln is the natural logarithm. Values of, k_1 and k_2 for images are shown in Table 2

Table 1. Metadata of satellite image

Variable	description	value	Image. DATE_ACQUIRED	Scene center time
K1	Thermal Constants Band 10	774.8853		
K2		1321.0789	2018-08-09	07:31:48
Lmax	Maximum and minimum values of Radiance, Band 10	22.00180	2018-01-13	07:32:29
Lmin		0.10033		
QCALMAX	Maximum and minimum values of Quantize Calibration, Band 10	65535		
QCALMIN		1		
Q1	Correction value, Band 10	0.29		

LST retrieved from each image of the studied period using the Eq. (3): (Weng & Lu, 2008).

$$LST = \frac{BT}{1 + W * \left(\frac{BT}{P}\right) * \ln(\varepsilon)} \quad (3)$$

W is the effective band wave length (11.475 μm), $P = h * \frac{c}{s} (1.438 * 10^2 - mK)$, h = Planck's constant, c = velocity of light, s = Boltzman constant ($1.38 * 10^{23} - j/k$) and ε is land surface emissivity.

Land surface emissivity (ε) was estimated based on NDVI thresholds method as proposed by Sorbrino et al. (2004) as follows:

Normalized Differential Vegetation Index (NDVI) is calculated using the equation 4.

$$NDVI = \frac{(NIR - VIS)}{(NIR + VIS)} \quad (4)$$

Where NIR and VIS are the near-infrared and visible light bands, respectively

If $NDVI < 0.15$, then the pixel is considered as bare soil and the mean emissivity value used in this study was 0.97 if, $NDVI > 0.62$

These kinds of pixels are considered as fully vegetated, and then a constant value for emissivity is assumed typically of 0.99

In the case of $0.15 < NDVI < 0.62$

Is this case emissivity is calculated according to Eq. (5)

$$\varepsilon = \varepsilon_v P_v + \varepsilon_s (1 - P_v) \quad (5)$$

Where ε_v is the vegetation emissivity and ε_s is the soil emissivity. P_v is the proportion of vegetation obtained according to Eq. (6) (Sobrino et al., 2004).

$$P_v = \left(\frac{NDVI - NDVI_{min}}{NDVI_{max} - NDVI_{min}} \right)^2 \quad (6)$$

Where $NDVI_{max}=0.62$ and $NDVI_{min}=0.15$

In this context, the proximity was calculated based on Distance Function in Arc GIS for maximum distance of 150 m, and based on population density, elevation and building height, the urban blocks categorised into 5 different classes as in (Table. 2).

Table 2. Classes

Class	Building height (number of floors)	Elevation	Proximity(meter)	Population density	description
1	1-2	1400	30	100	Very low
2	3-4	1500	60	200	low
3	5-6	1600	90	300	moderate
4	7-8	1700	120	500	high
5	9-13	1800	150	500+	Very high

LST and explanatory variables were combined and because the continues nature of them the result was examined using parametric tests, for this purpose, the one-way analysis of variance (ANOVA) (Fisher, 1919) was used to explore the similarity between the samples belonging to each group.

Further investigation of possible influence of explanatory variables on LST has been explored by carrying out, Linear Regression Model. The linear regression model is estimated with Eq. (8):

$$LST = \alpha + \beta_1 X_1 + \beta_2 X_2 + \dots + \beta_n X_n + \varepsilon \quad (8)$$

3. Results

Fig.1 and Fig.2 demonstrate the LST maps. The surface temperature in winter varied between -5 °c and 27 °c at the time of imaging, the minimum temperature was -5 °c related to urban constructed areas specially, residential, commercial and industrial land use type and the maximum temperature was 27 °c related to urban bare lands in the study area. The maximum mean average of land surface was 18.61 °c related to military sites.

And the surface temperature in summer varied between 10 °c and 45 °c at the time of imaging, the lowest average temperature was 24.5°c related to urban constructed areas specially, settlement, commercial and industrial land use type and the maximum average temperature was 37.5 °c recorded from transportation,

military and urban bare lands in the study area. The mean average temperature of industrial areas was 34.5 °c. for the imaging time in summer.

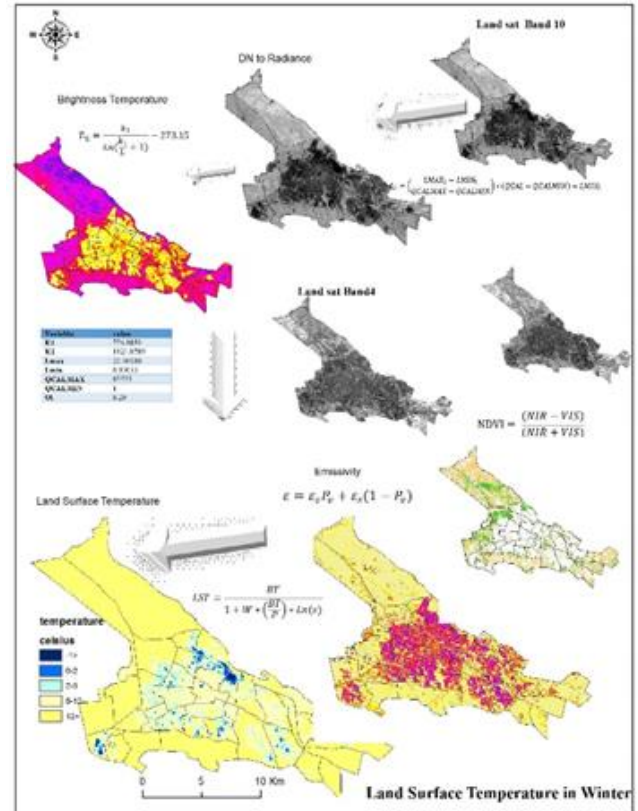


Fig.1. Land Surface Temperature of Tabriz in the 2018/01/13

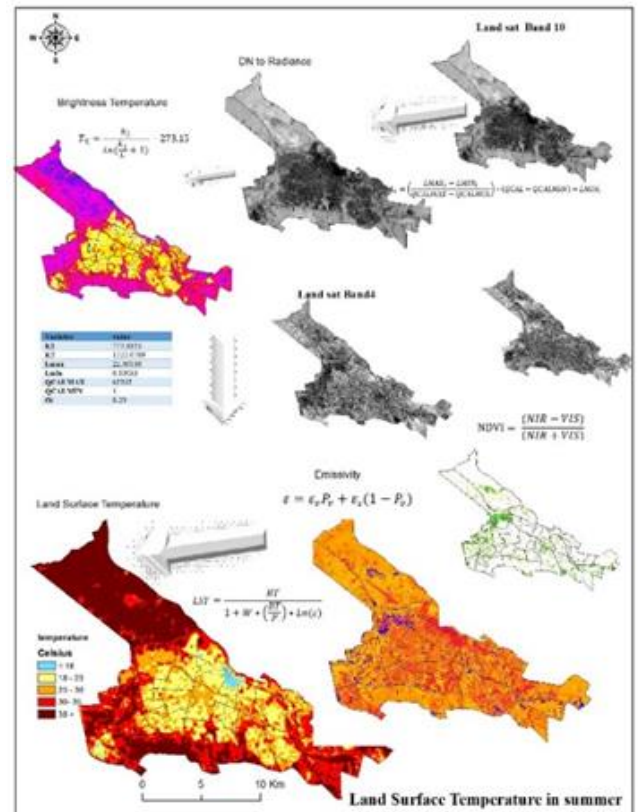


Fig.2. Land Surface Temperature of Tabriz in the 2018/08/09

Table 3. One – way ANOVA analysis

Analysis	Land surface temperature				
	Population density	Proximity to green space	Land use type	Elevation	Building high
Sig. between groups	0.00		0.001	0.00	0.00
F	190.352	7.891	2.288	21.713	14.283
	Reject H0	Reject H0	Reject H1	Reject H0	Reject H0

The out puts of One- Way ANOVA test (Table. 3) revealed that the difference between the groups were significant for all the variables except land use type.

Table 4. and Table 5 present the result of regression model for summer and winter time respectively.

Table 4. Model summery for summer time

Pearson Correlation													
Model Summary													
R	R Square	Adjusted R	B	T	F change	DF1	DF2	Sig. change	F	Durbin Watson			
0.79	0.63	0.63	36.4	0.63	7606	389	17	0.038	4	200	297		
0	0	0	0	0	0	0	0	0	0	0	0		
Coefficients													
	Elevation	Pop. density	Building high	Green space	Military administration	Commercial	Education	Industrial	Religious	River	Bare land	Sport	Facilities and equipment
B	-0.001	-0.001	-0.001	-0.001	-0.001	-0.001	-0.001	-0.001	-0.001	-0.001	-0.001	-0.001	-0.001
T	-0.001	-0.001	-0.001	-0.001	-0.001	-0.001	-0.001	-0.001	-0.001	-0.001	-0.001	-0.001	-0.001
F	0.00	0.00	0.00	0.00	0.00	0.00	0.00	0.00	0.00	0.00	0.00	0.00	0.00

Table 5. Model summery for winter time

Pearson Correlation													
Model Summary													
	R	R Square	Adjusted R	B	T	F change	DF1	DF2	Sig. change	F	Durbin Watson		
	0.705	0.517	0.517	18.130	65.906	6479.19	3	17	0	0.326	0.326		
Coefficients													
	Beta	SE	t	df	SS	MS	F	Sig.	Partial	Zero-order	Part	Coll. Tol.	VIF
(Constant)	-0.001	0.001	-0.001	17	0.000	0.000	0.000	0.999	-0.001	0.000	0.000	1.000	1.000
Elevation	-0.001	0.001	-0.001	17	0.000	0.000	0.000	0.999	-0.001	0.000	0.000	1.000	1.000
Pop. density	-0.001	0.001	-0.001	17	0.000	0.000	0.000	0.999	-0.001	0.000	0.000	1.000	1.000
Building high	0.001	0.001	0.001	17	0.000	0.000	0.000	0.999	0.001	0.000	0.000	1.000	1.000
Green space	-0.001	0.001	-0.001	17	0.000	0.000	0.000	0.999	-0.001	0.000	0.000	1.000	1.000
ARMS/ARMS	-0.001	0.001	-0.001	17	0.000	0.000	0.000	0.999	-0.001	0.000	0.000	1.000	1.000
ARMS/ARMS	-0.001	0.001	-0.001	17	0.000	0.000	0.000	0.999	-0.001	0.000	0.000	1.000	1.000
Commercial	0.001	0.001	0.001	17	0.000	0.000	0.000	0.999	0.001	0.000	0.000	1.000	1.000
Education	-0.001	0.001	-0.001	17	0.000	0.000	0.000	0.999	-0.001	0.000	0.000	1.000	1.000
Industrial	0.001	0.001	0.001	17	0.000	0.000	0.000	0.999	0.001	0.000	0.000	1.000	1.000
Religious	-0.001	0.001	-0.001	17	0.000	0.000	0.000	0.999	-0.001	0.000	0.000	1.000	1.000
River	0.001	0.001	0.001	17	0.000	0.000	0.000	0.999	0.001	0.000	0.000	1.000	1.000
Bare land	0.001	0.001	0.001	17	0.000	0.000	0.000	0.999	0.001	0.000	0.000	1.000	1.000
Sport	0.001	0.001	0.001	17	0.000	0.000	0.000	0.999	0.001	0.000	0.000	1.000	1.000
Facilities and equipment	-0.001	0.001	-0.001	17	0.000	0.000	0.000	0.999	-0.001	0.000	0.000	1.000	1.000
Tourism	-0.001	0.001	-0.001	17	0.000	0.000	0.000	0.999	-0.001	0.000	0.000	1.000	1.000
Transport	-0.001	0.001	-0.001	17	0.000	0.000	0.000	0.999	-0.001	0.000	0.000	1.000	1.000

4. Discussion

The results of this study showed that the high temperature is most widespread in suburban areas especially in north west and south east rather than central parts of the city. Similarly, Shirani-bidabadi et al. (2019) suggested that down town area in Isfahan city experienced lower temperature than the suburban areas during day time. (Shirani-bidabadi et al. 2019; Georgescu et al., 2011; Lazzarini et al., 2015). Also, the same results were obtained by Lazzarini et al. (2015), highlighted that down town area in some other arid and semi-arid cities such as Abu Dhabi, Kuwait City, Riyadh, Las Vegas, Phoenix, and Biskra experienced lower temperature than suburban areas during the day time. According to the results, the down town area of Tabriz in winter time experienced lower temperature than the suburban areas during day time, as well. This can be partly due to the existence of large number of bare lands in suburban areas (in the suburban areas of Tabriz) which mostly absorb sunlight than reflecting it and that leads to a

higher temperature in suburbs than down town (Georgescu et al., 2011; Lazzarini et al., 2015). Because the imaging time is in early morning, so there are not significant differences between the variance of mean average temperatures for different type of land use in the city, but on the other hand the difference among the different categories of population density, elevation, and proximity to green space (Table.3) are significant. According to the regression analysis, due to the status of urban structure mainly in the informal parts of the city with high elevation, the population density has negative effect on LST, which is different to Bokaei, et al, (2016) finding, suggested area with high temperature in the 14, 5,2,15,4 and 20 districts of Tehran face a high density of population. In the case of Tabriz, the relation between temperature and building high was not significant, and according to the one –way ANOVA test the effect of the distance to green space on LST were significant, which is consistent with previous studies (Kolokotroni & Girdharan, 2008; Nastaran et al., 2019; Susca, Gaffin & Dell'Osso, 2011; Takebayashi & Moriyama, 2009),

El-Hattab et al., 2018, state that the high temperature was compatible with the distribution of industrial areas, industrial zones surface temperature is nearly 5 °c higher than the center of Cairo, but the current study shows that differences between the variance of temperatures for different type of land use in the city is not significant. Rajasekar & Weng, 2009; suggested that the areas with maximum heat signatures have a strong correlation with impervious surfaces, similarly the current study highlighted the areas with maximum temperature related to transportation and bare lands.

5. Conclusion

The research concerning influence of multiple variables on LST is set on a Tabriz city for two different time during 2018 in order to determine the general laws of LST in Tabriz regarding to the one- way ANOVA and multiple linear regression analysis. Due to the geographical position of the city and the imaging time, correlation between the selected variables is relatively strong which could estimate only 63.7 and 61.7 percent of the LST. The study is unique by its case study and statistical methodology comparing to the other studies. However, similarity to the previous studies some pattern between LST and proximity to different land use type, population density, building high, have been shown. in general, it could be said that the city has a low temperature than the suburban areas. The one –way ANOVA analysis of the various land use type indicate that the difference between temperature across the land use type not significant.

This study opens an opportunity and necessity for further research about the spatial pattern recognition of UHI and LST in Tabriz. There is need for more in-depth analysis of a selected city.

References

- A.Mirzaei. Parham & Haghighat. Fariborz. (2010). Approaches to study Urban Heat Island- Abilities and Limitations, *Building and Environment*, 45, 2191-2201
- Bokaei. Mehdi, Kheirkhah Zarkesh. Mirmasoud, Daneshkar Arasteh. Peyman, Hosseini. Ali. (2016). Assessment of urban heat island based on the relationship between land surface temperature and land use/ land cover Tehran, 23, 94-104
- Deosthali. Vrishali. (2000). Impact of rapid urban growth on heat and moisture islands in Pune City, India, *Atmospheric Environment*, 34, 2745-2754
- Dwivedi. Aparna, Krishna. Mohan. Buddhiraju (2018). Impact of green roof on micro climate to reduce urban heat island, *Remote Sensing Applications: Society and Environment*, 10, 56-69
- EPA (US Environmental Protection Agency). (2008) Reducing Urban Heat Islands: Compendium of Strategies. US Environmental Protection Agency, Washington, D.C.
- Estoque. Ronald C, Murayma. Yuji. (2017). Monitoring surface urban heat islands formation in a tropical mountain city using Landsat data (1987-2015), *ISPRS Journal of Photogrammetry and Remote sensing*, 133, 18-29
- Harlan. Sharon L et al., (2006). Neighborhood microclimates and vulnerability to heat stress, *Social Science & medicine*, 63, 2847-2863
- Hathway. E.A, Sharples. S, (2012). The interaction of rivers and urban form in mitigating the urban Heat Island effect: A UK study, *Building and Environment*, 58, 14-22
- Hirano. Y and Fujita. T. (2012). Evaluation of the impact of the urban heat island on residential and commercial energy consumption in Tokyo, *Energy*, 37, 371-383
- Howard. Luke. (1818). The climate of London, deduced from Meteorological Observations Made in the Metropolis and at Various Places around It (Electronic Resource); Harvey and Darton, London. Uk
- Jato-Espino. Daniel. (2019). Spatiotemporal Statistical analysis of Urban Heat island effect in a Mediterranean region, *Sustainable Cities and Society*, 46,
- Lazzarini, M. Molini, A. Marpu, P. R, Quarda, T. B. M. J & Ghedira, H. (2015). Urban climate modifications in hot desert cities: the role of land cover, local climate, and seasonality. *Geophysical research Letters*, 42 (22)
- Li, Huidong et al. (2018). Interaction between urban heat island and urban pollution island during summer in Berlin, *Science of Total Environment*, 636, 818-828
- Peron. F, De Maria. M.M, Spinazze. F and Mazzali. U. (2015). An analysis of the urban heat island of Venice mainland, *Sustainable cities and society*, 19, 300-309
- Rajasekar. Umamaheshwaran, Weng. Qihao. (2009). Urban heat island monitoring and analysis using a non-parametric model: a case study of Indianapolis, *ISPRS Journal of Photogrammetry and remote sensing*, 64, 86-96
- Rizwan, A. M, Dennis, L. Y., & Chunho, L. I. U. (2008). A review on the generation, determination and mitigation of Urban Heat Island, *Journal of Environmental Science*, 20, 120-128
- Shirani-bidabadi, Niloufar, Nasrabadi. Touraj, Faryadi. Shahrzad, Larijani. Adnan and Shadman Roodposhti. Majid. (2019). Evaluating the spatial distribution and the intensity of urban heat island using remote sensing, case study of Isfahan city in Iran, 45, 686-692
- Statistical Center of Iran. (2016). Selected Finding of the 2016 National Population and Housing Census, Statistical Center of Iran.
- Susca. T, Gaffin. S.R, Dell'Oso. (2011). Positive effects of vegetation: Urban heat island and green roofs, *Environmental Pollution*, 159, 2119-2126
- Takebayashi. Hideki, Moriyama. Masakazu. (2009). Study on the urban heat island mitigation effect achieved by converting to grass-covered parking, *Solar Energy*, 83, 1211-1223
- United Nations. (2014). World Urbanization Prospects: the 2014 Revision, Highlights. Department of Economic and Social Affairs. Population Division, United Nations.
- Voogt. J. & Oke. T.R. (2003). Thermal remote sensing of urban climates, *remote sensing of environments*, 86, 370-384
- Weng. Q, Lu. D, Schubring. J. (2004). Estimation of land surface temperature- vegetation abundance relationship for urban heat island studies, *Remote Sens. Environ.* 89, 467-483
- Xiao. Xiang Dong, Dong. Li, Yan. Hainan, Yang. Nan, Xiong. Yimei. (2018). The influence of the spatial characteristics of urban green space on the urban heat island effect in Suzhou Industrial Park, *Sustainable Cities and Society*, 40, 428-439
- Z.Xian. George. (2016). Remote Sensing Applications for the Urban Environment, CRC Press, Taylor & Francis Group.
- Zhang. Yang, Yiyun Chen, Qing. Ding, Jiang. Ping. (2012). Study on urban heat island effect based on normalized difference vegetated index: a case study of Wuhan city, *Procedia Environmental Sciences*, 13, 574-581



4th Intercontinental Geoinformation Days

igd.mersin.edu.tr



Exploring the spatial distribution and intensity of Urban Heat Islands (UHI) in Ardabil city

Iraj Teymouri *¹

¹University of Tabriz, Planning & Environmental Studies, Urban Planning and Geography, Tabriz, Iran

Keywords

Land surface temperature
Urban Heat Island
Water Bodies
Thermal effect

Abstract

The first purpose of this paper was, calculating land surface temperature (LST) and exploring the spatial distribution of UHI in Ardabil city which was investigated using Land sat 8 OLI/TIRS images for summer and winter of 2019. The second purpose was exploring the thermal effects of Shourabil Lake on surrounding area. The results showed, high temperature is most widespread in suburban areas especially in south, south west, west and north west rather than central parts of the city. Also, the results showed the maximum average temperature in imaging time of winter was 18 °C, recorded from industrial areas and the maximum average temperature in imaging time of summer was 27 °C recorded from military and Festival site. The average temperature of water body in summer and winter were 17 °C and 16 °C respectively. According to the results thermal effects of the Shourabil lake was limited to 200m, the resultant correlation model for LST and distance to lake based on the calculated R (0.896, 0.988, 0.950) demonstrate a strong correlation, notably the regression could estimate the thermal variation around the lake in this distance.

1. Introduction

Urban Heat Island (UHI) is one of the more serious impacts of urbanization on urban climate (Hirano & Fujita, 2012). Thermal properties of different materials, evaporation of surfaces and reduced ability of the released infrared (IR) radiation to escape from urban structures into the atmosphere have also evolved significant causes of UHI (R. P. Gupta, n.d.; Mathew, Sreekumar, Khandelwal, & Kumar, 2019). The UHI effect can be reduced by making changes in built form, material selection, and land use proportion in cities in order to raise the albedo and cool the surrounding (Nastran, Kobal, & Eler, 2019). Land surface temperature (LST) varies significantly across different land cover classes (Ren et al., 2016; Susca et al., 2018). LST is usually higher in built-up areas, such as those for residential and industrial land use, and bare surfaces (Shaker, Altman, Deng, Vaz, & Forsythe, 2019). It is lower in water bodies like ponds, lakes and river which have a significant role in reducing the UHI (Hathway & Sharples, 2012). Also vegetation, as a key instrument of mitigating urban heat island, influences the cooling process due to evaporative cooling and shading surfaces which absorb short-wave radiation (Kolokotroni & Giridharan, 2008). During last

years' significant research efforts have been performed to evaluate the urban heat island phenomenon and the mitigating effects of water bodies and green space. (Cai, Han, & Chen, 2018), indicate that the cooling effect of water bodies can reach one kilometer (horizontal distance). (Nakayama & Hashimoto, 2011), highlighted that effective management of water resources would be powerful for ameliorating the heat island. (Amani-Beni, Zhang, Xie, & Xu, 2018), found that for every 1000 m increase in distance from the river, the UHI decreased by 0.6 °C to 3 °C depending on season. Also (Xiao, Dong, Yan, Yang, & Xiong, 2018), found that the cooling and humidifying effect of large green spaces was more obvious and stable, and the cooling effect of small green spaces was more variable. (Hathway & Sharples, 2012) showed that the urban form on the river bank influenced the levels of cooling felt away from the river bank. Also (Giridharan & Kolokotroni, 2009), showed that the winter climate control modes have the same correlation, indicating that most change in outdoor temperature are caused by climate factors and not the on-site variables.

The review of previous studies pointed out mitigation effect of water bodies and green space in urban heat

* Corresponding Author

^{*}(iraj-teymouri@tabrizu.ac.ir) ORCID ID 0000 – 0002 – 3168 – 5583

Cite this study

Teymouri, I. (2022). Exploring the spatial distribution and intensity of Urban Heat Islands (UHI) in Ardabil city. 4th Intercontinental Geoinformation Days (IGD), 37-42, Tabriz, Iran

island. The purpose of this study is to investigate the urban heat island and the mitigation effect achieved by water body during February and June. According to foregoing the present study was carried out to follow 3 objectives: (1) the study of LST in Ardabil city using Land Sat 8 OLI/TIRS satellite image during the summer and winter of the year 2019, (2) Calculating of UHI in the city, (3) analysing the effect of Shourabil lake on the surrounding achieved temperature.

2. Method

In this study, to evaluate the UHI and influenced area of the city, the satellite images of land sat 8 OLI/ TIRS (thermal band 10) were used. The metadata of images were featured in Table 1.

In order to compute the LST, the thermal band digital number (DN) is numerically converted to radiometric scale using Eq. (1).

Eq. (1) is used for converting DN to radiance in Landsat 7 ETM image:

$$L_{\lambda} = \left(\frac{LMAX_{\lambda} - LMIN_{\lambda}}{QCALMAX - QCALMIN} \right) * (QCAL - QCALMIN) + LMIN_{\lambda}$$

Where

L_{λ} = the cell value as the radiance

QCAL = digital number

$LMIN_{\lambda}$ = spectral radiance scales to QCALMIN

$LMAX_{\lambda}$ = spectral radiance scales to QCALMAX

QCALMIN = the minimum quantized calibrated pixel value (typically = 1)

QCALMAX = the maximum quantized calibrated pixel value (typically = 255)

The value of $LMIN_{\lambda}$ and $LMAX_{\lambda}$ extracted from the header file of landsat images are 0.10033 and 22.00180 respectively (Table.1)

Table 1. Metadata of satellite image

Variable	description	value	Image, DATE_ACQUIRED	Scene center time
K1	Thermal Constants Band 10	774.8853		
K2		1321.0789	2019-02-26	07:25:32
Lmax	Maximum and minimum values of Radiance, Band 10	22.00180	2019-06-18	07:25:41
Lmin		0.10033		
QCALMAX	Maximum and minimum values of Quantize Calibration, Band 10	65535		
QCALMIN		1		
Q1	Correction value, Band 10	0.29		

Converting radiance to brightness temperature

After calculating spectral radiance (L_{λ}), the images were computed for their brightness temperature using either Planck's radiance function for temperature (Weng et al., 2004) or the approximation formula shown in Eq (3).

Where T is the effective at sensor brightness temperature in Celsius, k_1 is calibration constant (in kelvin), k_2 is the calibration constant (Watts/[$m^2 * sr * \mu m$]), and Ln is the natural logarithm. Values of k_1 and k_2 for images are shown in Table 2.

$$T_c = \frac{k_2}{\ln\left(\frac{k_1}{L} + 1\right)} - 273.15$$

Table 2. UHI Category

0-0.2	0.2-0.4	0.4-0.6	0.6-0.8	0.8-1
Very Low	Low	Moderate	High	Very High

LST retrieved from each image of the studied period using the Eq. (4): (Weng & Lu, 2008).

$$LST = \frac{BT}{1 + W * \left(\frac{BT}{P}\right) * \ln(\varepsilon)}$$

W is the effective band wave length (11.475 μm), $P = h * \frac{c}{s} (1.438 * 10^{-2} mK)$, h= Planck's constant, c= velocity of light, s= Boltzman constant ($1.38 * 10^{-23} j/k$) and ε is land surface emissivity.

Land surface emissivity (ε) was estimated based on NDVI thresholds method as proposed by Sorbrino et al. (2004) as follows:

Normalized Differential Vegetation Index (NDVI) is calculated using the equation

$$NDVI = \frac{(NIR - VIS)}{(NIR + VIS)}$$

Where NIR and VIS are the near-infrared and visible light bands, respectively

If $NDVI < 0.15$, then the pixel is considered as bare soil and the mean emissivity value used in this study was 0.97 if, $NDVI > 0.62$

These kinds of pixels are considered as fully vegetated, and then a constant value for emissivity is assumed typically of 0.99

In the case of $0.15 < NDVI < 0.62$

In this case emissivity is calculated according to Eq. (6).

$$\varepsilon = \varepsilon_v P_v + \varepsilon_s (1 - P_v)$$

Where ε_v is the vegetation emissivity and ε_s is the soil emissivity. P_v is the proportion of vegetation obtained according to Eq. (7) (Sobrino et al., 2004).

$$P_v = \left(\frac{NDVI - NDVI_{min}}{NDVI_{max} - NDVI_{min}} \right)^2$$

Where $NDVI_{max} = 0.62$ and $NDVI_{min} = 0.15$

based on the Eq. (8) we construct the UHI intensity index;

$$UHI_{ii} = \frac{LST_{max} - LST}{LST_{max} - LST_{min}}$$

Then, achieved data were classified based on defined interval method with intervals of 0.2. in this method we obtained 5 classes, which categorized as Table 2.

2.2. Statistical modeling methodology

The approach behind this study bass on assumption that water body has mitigation effect on LST, thus the relation ship between LST and distance to Shourabil-Lake were correlated using with Pearson Correlation test in SPSS 25. Further investigation of possible influence of Shourabil - Lake on LST has been explored by profile tools in ArcGIS10.2 3D analyst and Linear Regression Model in SPSS. The linear regression model is estimated with Eq. (9):

$$LST = \alpha + \beta x$$

2.3. Spatial analysis

This study used Land use map as a Zone data feature in ArcGIS. 10.2 for calculation of descriptive statistic such as, Mean, Maximum, Minimum of obtained LST for every land use type.

Finally, the temperature of the city was calculated based on Eq. (10)

$$total = \sum_{i=1}^n LST_{LU_i} * W_{LU_i}$$

Where; W_{LU_i} is;

$$W_{LU_i} = \frac{Area_{LU_i}}{\sum Area_{LU}}$$

3. Results

To find the relationship between LST and land use, the thermal values of each land use class was obtained by overlaying a LST map with Land-use map in ArcGIS 10.2-Zonal Analysis Tool. The same was used for obtaining UHI. The LST (mean, minimum and maximum) values for various land use type for each of the images is summarized in Table 3. According to the LST map, surface temperature varied between 11°C and 36 °C at the imaging time in June. As Table 3. shows, the lowest average temperature was 15 °C related to parking area and the maximum average temperature was 27 °C recorded from military and Festival site, also average temperature of water body and residential areas were low, the calculated temperature for these areas were, 17 °C. The calculated temperature for industrial site was high, 26 °C. based on calculation the average temperature of the city in the imaging time of June was 20.6 °C. according to the table. 2. the UHII in the industrial, police station and festival site were high and the lowest UHII related to parking, water bodies, residential, cultural, sanitation and treatment areas. The UHII in the other type of land uses were moderate, specially in bare lands. Finally, the UHII of the city was low, 0.39, which refer to a cool weather in the imaging time.

In this paper for exploring the Shourabil Lake's effect on surrounding area, we used correlation test and regression analysis, the explanatory variable was distance to lake which extracted by line profile in ArcGIS

10.2- 3d Analyst tools, Fig 2. demonstrate the position of line profiles.

Table 3. Model summery

Area	June 2019				February 2019				Area																
	Mean	Min	Max	Mean UHI	Mean	Min	Max	Mean UHI																	
M ² × 10 ⁴	53100	11502	99630	M	27594	13860	24000	M	25600	91403	32580	26010	70200	39150	69570	67500	12483	24390	21400	15500	17843	27198	5400	43703	
Female Site	42	98	62	H	16	16	16	H	16	16	16	16	15	14	14	14	M	11	12	10	9	16	10	8	12
Military Site	42	15	33	H	18	18	18	M	9	9	9	9	5	5	5	5	M	11	13	10	10	25	17	10	21
Industrial	42	15	33	H	18	18	18	M	9	9	9	9	5	5	5	5	M	11	13	10	10	25	17	10	21
Green	42	15	33	H	18	18	18	M	9	9	9	9	5	5	5	5	M	11	13	10	10	25	17	10	21
Agriculture	42	17	31	M	54	54	54	M	17	17	17	17	13	13	13	13	M	11	13	10	10	25	17	10	21
Facilities	42	19	33	M	52	52	52	M	15	15	15	15	11	11	11	11	M	11	13	10	10	25	17	10	21
Blackland	42	19	33	M	52	52	52	M	15	15	15	15	11	11	11	11	M	11	13	10	10	25	17	10	21
Grass	42	16	32	M	50	50	50	M	13	13	13	13	9	9	9	9	M	11	13	10	10	25	17	10	21
Barbican	42	19	33	M	52	52	52	M	15	15	15	15	11	11	11	11	M	11	13	10	10	25	17	10	21
Transport	42	15	32	M	47	47	47	M	14	14	14	14	10	10	10	10	M	11	13	10	10	25	17	10	21
Sport	42	15	32	M	47	47	47	M	14	14	14	14	10	10	10	10	M	11	13	10	10	25	17	10	21
Tourism	42	15	32	M	47	47	47	M	14	14	14	14	10	10	10	10	M	11	13	10	10	25	17	10	21
Recreation	42	15	32	M	47	47	47	M	14	14	14	14	10	10	10	10	M	11	13	10	10	25	17	10	21
Administrative	42	15	32	M	47	47	47	M	14	14	14	14	10	10	10	10	M	11	13	10	10	25	17	10	21
Commercial	42	15	32	M	47	47	47	M	14	14	14	14	10	10	10	10	M	11	13	10	10	25	17	10	21
University	42	15	32	M	47	47	47	M	14	14	14	14	10	10	10	10	M	11	13	10	10	25	17	10	21
Cultural	42	15	32	M	47	47	47	M	14	14	14	14	10	10	10	10	M	11	13	10	10	25	17	10	21
Other	42	15	32	M	47	47	47	M	14	14	14	14	10	10	10	10	M	11	13	10	10	25	17	10	21
Residents	42	15	32	M	47	47	47	M	14	14	14	14	10	10	10	10	M	11	13	10	10	25	17	10	21
Water	42	15	32	M	47	47	47	M	14	14	14	14	10	10	10	10	M	11	13	10	10	25	17	10	21
Police	42	15	32	M	47	47	47	M	14	14	14	14	10	10	10	10	M	11	13	10	10	25	17	10	21
Total	9.02	1.83	1.50	0.39	1.24	1.24	1.24	0.39	1.24	1.24	1.24	1.24	0.90	0.89	0.89	0.89	0.39	1.24	1.24	1.24	1.24	2.14	2.14	2.14	2.14

Fig.2. Position of the profiles, profile 1,2,3-left to right
a. February, 2019

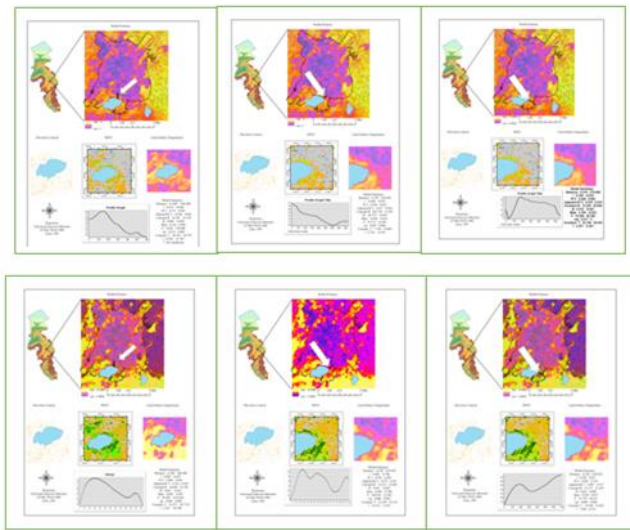


Table 4. The model summary for Summer, June 2019

		Distance	R	R ²	AdjR ²	Constant B	B	Beta	F	Constant T	T	Sig
Profile 1	Class 1	0-180	0.896	0.803	0.764	18.689	0.025	0.896	20.389	31.073	4.515	0.006
	Class2	180-400	-0.997	0.994	0.993	24.702	-0.013	0.997	1332.820	197.724	-36.508	0.000
Profile 2	Class 1	0-210	0.988	0.976	0.972	14.133	0.034	0.988	240.916	52.250	15.521	0.000
	Class2	210-650	-0.700	0.490	0.451	21.028	-0.005	0.700	12.482	32.142	-3.533	0.004
Profile 3	Class 1	0-210	0.950	0.903	0.887	21.127	0.025	0.950	55.739	52.940	7.466	0.000
	Class2	210-650	-0.857	0.734	0.715	21.350	0.008	0.857	38.615	34.262	6.214	0.000

4. Discussion

Different type of urbans can cause the formation of different forms of heat islands. this study highlighted that the residential areas of the Ardabil city were cooler than the surrounding areas. In other words, Lower LST values tended to be distributed in the center of study area while the highest LST values were scattered around the city. On the whole, only 5% of Ardabil area suffer from High values of UHI, on the other hand the UHI values for 46% of the city area were low. Similarly, (Shirani-bidabadi, Nasrabadi, Faryadi, Larijani, & Shadman Roodposhti, 2019) suggested that down town area in Isfahan city experienced lower temperature than the suburban areas during day time. In the case of Ardabil this can be partly due to existence of bare lands in suburban areas, especially in the south and south west, which mostly absorb sunlight than reflecting it and that leads to a higher temperature in suburban than downtown. Also the same results were obtained by (Lazzarini, Marpu, & Ghedira, 2013), highlighted that down town area in some other aired and semi-arid cities such as Abu Dhabi, Kuwait City, Riyadh, Las Vegas, Phoenix, and Biskra experienced lower temperature than suburban areas during the day time. (Bokaie et al., 2016), state that industrial area in Tehran suffer from high level of LST during day time. Our results show a similar finding which the average temperature of industrial areas was high, especially in the imaging time of winter, the calculated temperature for industrial areas were about 18 °C, which is 6 °C higher than the mean temperature of the city. Also

similar results highlighted by (El-Hattab, Amany, & Lamia, 2018), According to the results, because of surrounding topography and Land use type, the thermal effects of Shourabil lake was limited to a short distance. Different to (Moyer & Hawkins, 2017) this study showed that after certain distance from the lake temperature tends to reduce; case profile 1, profile 3 in February 26th 2019, and all cases of summer. According to the analysis, due to the achieved r (0.896, 0.988, 950) and Beta, the lake's impact on temperature is positive, which means in class1 the lake warms up the surrounding area. The reduction of temperature after 200 m was variable based on the nature of topography and land cover. Similarly (N. Gupta, Mathew, & Khandelwal, 2019), highlighted that the temperature in the river bank of Sabarmati was low within 200 m of the river and shows a sharp ascent there onwards. Also, the results which were obtained by (Wu & Zhang, 2019), it can be said that various factors affect the thermal impacts of water bodies, in the case of Shourabil lake, the rising temperature in the surrounding areas especially in the north, west and south of the lake may be due to the presence of bare lands. In the east of the lake-built area alongside the green space cause a decrease in temperature

5. Conclusion

The research concerning distribution of LST in Ardabil city for two different time during 2019. In order to determine the general distribution of UHI in Ardabil regarding to land use type the land sat 8 images were used. Due to the geographical position of the city and the imaging time, residential areas of the Ardabil city were cooler than the surrounding areas. As the results showed, Lower LST values tended to be distributed in the center of city while the highest LST values were scattered around the study area. The results highlighted that the average temperature of industrial areas in the imaging time of winter were high. Also, we explored the thermal effect of Shourabil Lake on surrounding area, our study indicated that the thermal effect of the lake is limited to a short distance from lake, the study showed during imaging time because of surrounding land use type the temperature after 200 m onward tends to reduce. This study opens an opportunity and necessity for further research about the spatial pattern recognition of UHI and LST in Ardabil. There is need for more in-depth analysis of a selected city and thermal effect of water bodies.

References

- Amani-Beni, M., Zhang, B., Xie, G. di, & Xu, J. (2018). Impact of urban park's tree, grass and waterbody on microclimate in hot summer days: A case study of Olympic Park in Beijing, China. *Urban Forestry and Urban Greening*, 32(January), 1–6. <https://doi.org/10.1016/j.ufug.2018.03.016>
- Bokaie, M., Zarkesh, M. K., Arasteh, P. D., & Hosseini, A. (2016). Assessment of Urban Heat Island based on the relationship between land surface temperature and Land Use/ Land Cover in Tehran. *Sustainable Cities and Society*, 23, 94–104. <https://doi.org/10.1016/j.scs.2016.03.009>

- Cai, Z., Han, G., & Chen, M. (2018). SC. *Sustainable Cities and Society*.
<https://doi.org/10.1016/j.scs.2018.02.033>
- Centre, S. (n.d.). *Population based on the National Population and Housing Census, 2016*.
- Dwivedi, A., & Mohan, B. K. (2018). Impact of green roof on micro climate to reduce Urban Heat Island. *Remote Sensing Applications: Society and Environment*, 10(February), 56–69.
<https://doi.org/10.1016/j.rsase.2018.01.003>
- El-Hattab, M., Amany, S. M., & Lamia, G. E. (2018). Monitoring and assessment of urban heat islands over the Southern region of Cairo Governorate, Egypt. *Egyptian Journal of Remote Sensing and Space Science*, 21(3), 311–323.
<https://doi.org/10.1016/j.ejrs.2017.08.008>
- Giridharan, R., & Kolokotroni, M. (2009). Urban heat island characteristics in London during winter. *Solar Energy*, 83(9), 1668–1682.
<https://doi.org/10.1016/j.solener.2009.06.007>
- Gupta, N., Mathew, A., & Khandelwal, S. (2019). The Egyptian Journal of Remote Sensing and Space Sciences Analysis of cooling effect of water bodies on land surface temperature in nearby region: A case study of Ahmedabad and Chandigarh cities in. *The Egyptian Journal of Remote Sensing and Space Sciences*, 22(1), 81–93.
<https://doi.org/10.1016/j.ejrs.2018.03.007>
- Gupta, R. P. (n.d.). *Remote Sensing Geology*.
- Hathway, E. A., & Sharples, S. (2012). The interaction of rivers and urban form in mitigating the Urban Heat Island effect: A UK case study. *Building and Environment*, 58, 14–22.
<https://doi.org/10.1016/j.buildenv.2012.06.013>
- Hirano, Y., & Fujita, T. (2012). Evaluation of the impact of the urban heat island on residential and commercial energy consumption in Tokyo. *Energy*, 37(1), 371–383. <https://doi.org/10.1016/j.energy.2011.11.018>
- Jato-Espino, D. (2019). Spatiotemporal statistical analysis of the Urban Heat Island effect in a Mediterranean region. *Sustainable Cities and Society*, 46(October 2018), 101427.
<https://doi.org/10.1016/j.scs.2019.101427>
- Kolokotroni, M., & Giridharan, R. (2008). Urban heat island intensity in London: An investigation of the impact of physical characteristics on changes in outdoor air temperature during summer. *Solar Energy*, 82(11), 986–998.
<https://doi.org/10.1016/j.solener.2008.05.004>
- Lazzarini, M., Marpu, P. R., & Ghedira, H. (2013). Temperature-land cover interactions: The inversion of urban heat island phenomenon in desert city areas. *Remote Sensing of Environment*, 130, 136–152.
<https://doi.org/10.1016/j.rse.2012.11.007>
- Levermore, G., Parkinson, J., Lee, K., Laycock, P., & Lindley, S. (2018). The increasing trend of the urban heat island intensity. *Urban Climate*, 24, 360–368.
<https://doi.org/10.1016/j.uclim.2017.02.004>
- Mathew, A., Sreekumar, S., Khandelwal, S., & Kumar, R. (2019). Prediction of land surface temperatures for surface urban heat island assessment over Chandigarh city using support vector regression model. *Solar Energy*, 186(March), 404–415.
<https://doi.org/10.1016/j.solener.2019.04.001>
- Mirzaei, P. A., Haghighat, F., Nakhaie, A. A., Yagouti, A., Giguère, M., Keusseyan, R., & Coman, A. (2012). Indoor thermal condition in urban heat Island - Development of a predictive tool. *Building and Environment*, 57, 7–17. <https://doi.org/10.1016/j.buildenv.2012.03.018>
- Moyer, A. N., & Hawkins, T. W. (2017). River effects on the heat island of a small urban area. *Urban Climate*, 21, 262–277.
<https://doi.org/10.1016/j.uclim.2017.07.004>
- Nakayama, T., & Hashimoto, S. (2011). Analysis of the ability of water resources to reduce the urban heat island in the Tokyo megalopolis. *Environmental Pollution*, 159(8–9), 2164–2173.
<https://doi.org/10.1016/j.envpol.2010.11.016>
- Nastran, M., Kobal, M., & Eler, K. (2019). Urban heat islands in relation to green land use in European cities. *Urban Forestry and Urban Greening*, 37(January 2018), 33–41.
<https://doi.org/10.1016/j.ufug.2018.01.008>
- Oltra-Carrió, R., Sobrino, J. A., Franch, B., & Nerry, F. (2012). Land surface emissivity retrieval from airborne sensor over urban areas. *Remote Sensing of Environment*, 123, 298–305.
<https://doi.org/10.1016/j.rse.2012.03.007>
- Rajasekar, U., & Weng, Q. (2009). Urban heat island monitoring and analysis using a non-parametric model: A case study of Indianapolis. *ISPRS Journal of Photogrammetry and Remote Sensing*, 64(1), 86–96.
<https://doi.org/10.1016/j.isprsjprs.2008.05.002>
- Ren, Y., Deng, L. Y., Zuo, S. Di, Song, X. D., Liao, Y. L., Xu, C. D., ... Li, Z. W. (2016). Quantifying the influences of various ecological factors on land surface temperature of urban forests. *Environmental Pollution*, 216, 519–529.
<https://doi.org/10.1016/j.envpol.2016.06.004>
- Shaker, R. R., Altman, Y., Deng, C., Vaz, E., & Forsythe, K. W. (2019). Investigating urban heat island through spatial analysis of New York City streetscapes. *Journal of Cleaner Production*, 233, 972–992.
<https://doi.org/10.1016/j.jclepro.2019.05.389>
- Shirani-bidabadi, N., Nasrabadi, T., Faryadi, S., Larijani, A., & Shadman Roodposhti, M. (2019). Evaluating the spatial distribution and the intensity of urban heat island using remote sensing, case study of Isfahan city in Iran. *Sustainable Cities and Society*, 45(December 2018), 686–692.
<https://doi.org/10.1016/j.scs.2018.12.005>
- Sobrino, J. A., Oltra-Carrió, R., Jiménez-Muñoz, J. C., Julien, Y., Soria, G., Franch, B., & Mattar, C. (2012). Emissivity mapping over urban areas using a classification-based approach: Application to the Dual-use European Security IR Experiment (DESIREX). *International Journal of Applied Earth Observation and Geoinformation*, 18(1), 141–147.
<https://doi.org/10.1016/j.jag.2012.01.022>
- Susca, T., Gaffin, S. R., Dell'Osso, G. R., Nakayama, T., Hashimoto, S., Tayyebi, A. A. H., ... Stewart, I. D. (2018). Reducing Urban Heat Islands: Compendium of Strategies. *Sustainable Cities and Society*, 24(1), 39p.
<https://doi.org/10.1016/j.uclim.2017.02.004>

- Weng, Q., Lu, D., & Schubring, J. (2004). Estimation of land surface temperature-vegetation abundance relationship for urban heat island studies. *Remote Sensing of Environment*, 89(4), 467–483. <https://doi.org/10.1016/j.rse.2003.11.005>
- Wu, Z., & Zhang, Y. (2019). *Water Bodies ' Cooling Effects on Urban Land Daytime Surface Temperature : Ecosystem Service Reducing Heat Island Effect*. 1–11. <https://doi.org/10.3390/su11030787>
- Xiao, X. D., Dong, L., Yan, H., Yang, N., & Xiong, Y. (2018). The influence of the spatial characteristics of urban green space on the urban heat island effect in Suzhou Industrial Park. *Sustainable Cities and Society*, 40(April 2017), 428–439. <https://doi.org/10.1016/j.scs.2018.04.002>

4th Intercontinental Geoinformation Days

igd.mersin.edu.tr



Determination of burned areas using Sentinel-2A imagery and machine learning classification algorithms

Ceydanur Arıkan^{*1}, İlay Nur Tümer¹, Samet Aksoy¹, Elif Sertel¹

¹Istanbul Technical University, Faculty of Civil Engineering, Department of Geomatics Engineering, Istanbul, Türkiye

Keywords

Remote sensing
Google Earth Engine
Machine Learning
Sentinel 2
Burnt Severity Indexes

Abstract

We aimed to determine the spatial extent of burned areas using remote sensing (RS) data and machine learning methods. It is often difficult, time-consuming and costly to collect in-situ data after fires; therefore, RS is used in determining burnt regions. We selected the Manavgat district of Antalya province as the study area due to the major forest fires occurred in 2021. We used pre-post Sentinel 2A images due to the ability of Sentinel in burned area mapping, fire density and damage determination, and being openly available. Then we implemented indices to determine the changes caused by fires. The indices are Normalized Burned Ratio (NBR), Normalized Vegetation Index (NDVI), Relative differenced Normalized Burn Ratio (RdNBR), Relativized Burn Ratio (RBR), Burned Area Index (BAI), and Modified Soil Adjusted Vegetation Index (MSAVI), Soil Adjusted Vegetation Index (SAVI). Afterwards, we utilized Random Forest (RF) Algorithm, Support Vector Machine (SVM), and Classification Regression Tree (CART) for the Machine Learning (ML) classification. We used the Google Earth Engine (GEE) platform to obtain satellite images and apply indices and ML based classification. Results illustrated that, RF was the most accurate algorithm with 98.57% overall accuracy and SVM has the lowest overall accuracy with 86.19% for the region.

1. Introduction

Forests are essential for natural balance in terms of the sustainability of ecosystem services, and human survival. However, wildfires, occurring as the result of accidents, intentional, or global warming, has been threatening forest areas and nearby regions. Wildfire frequencies have been increasing in recent years throughout the world, and aside from that Turkey faced a critical year in 2021. Because "major fires," which are exceptionally fast-moving, high-intensity, and catastrophic, occurred between the end of July to mid-August both in Turkey and nearby countries such as Greece, when meteorological conditions were beyond the normal (Bilgili et al., 2021). According to information from the European Forest Fire Information System, 227 forest fire incidents occurred in Turkey in 2021, affecting a total area of 192 hectares, with the fires that began on July 28 in the Manavgat district of Antalya and continued in the Mediterranean, Aegean, Marmara, and the Black Sea regions during August, causing loss of life and property in large areas (Kavzaoglu et al., 2021). Accurate,

fast and timely detection of fire damages in is a challenging task. Satellite images have a vital role to provide support during the fire and to understand its effects immediately after the fire event (Sertel & Alganci, 2016).

Since the land surface changes after a fire, many indices could use to determine these changes and estimate the extent of the burnt regions. Even though there are various methods to detect damaged areas, the most widely used and functional approaches are based on the spectral differences of burnt forest areas after and before fires (Alganci et al., 2010). The Differenced Normalized Burn Ratio (dNBR) measures a decrease in the near infrared (NIR) region and an increase in the shortwave infrared (SWIR), which are the most widely utilized bands (Masshadi & Alganci, 2021). Furthermore, for the Normalized Difference Vegetation Index (NDVI), the difference between NIR and red spectral bands is used to estimate different vegetation conditions and then it can be used to detect vegetation loss. To sum up, indices integrate different spectral bands to deduce

* Corresponding Author

(arikan17@itu.edu.tr) ORCID ID 0000-0002-5174-9471
(tumer17@itu.edu.tr) ORCID ID 0000-0002-1102-4505
(aksoysa@itu.edu.tr) ORCID ID 0000-0001-6420-7316
(sertele@itu.edu.tr) ORCID ID 0000-0003-4854-494X

Cite this study

Arıkan, C., Tümer, İ. N., Aksoy, S., & Sertel, E. (2022). Determination of burned areas using Sentinel-2A imagery and machine learning classification algorithms. 4th Intercontinental Geoinformation Days (IGD), 43-46, Tabriz, Iran

information about different features and surface characteristics.

Sentinel-2 satellites provide various spectral bands, spatial and temporal resolution capabilities and Sentinel-2 images have been used to monitor natural resources and burned scar mapping (Bar et al., 2020).

Machine Learning (ML) classification methods such as Random Forest (RF) and Support Vector Machines (SVM) have been used by different researchers to determine the extent of forest fires and identify the burned areas (Masshadi & Alganci, 2021). The Classification Regression Tree (CART) is an alternative machine learning algorithm for predictive mapping (Bar et al., 2020).

Google Earth Engine (GEE) is a cloud-based service that may instantly connect for encoding large geospatial data without dealing with the computer processing challenges (Aksoy et al., 2022). It includes extensive geospatial data and various functions that can be used collaboratively.

We investigated the Antalya Forest fires for this research using Sentinel-2 images and GEE platform. Firstly, we applied the indices RBR, RdNBR and differences in the pre-and post-fire indexes MSAVI, SAVI, NBR, NDVI, BAI, and SWIR (Short Wave Infrared) The second phase of the project involves the creation of classification images using several ML approaches such as RF, SVM, and CART. Lastly, we compared different methods to propose the most appropriate one for our selected case study.

2. Method

2.1. Study area

We focused on the research area which is the Mediterranean region and time intervals selected according to forest fires that occurred due to high temperatures in the summer of 2021 in Turkey. So, forest fires occurred in many of the provinces on this coast, and one of them is the province of Antalya.

2.2. Data

Sentinel-2 satellite images for the post- and pre-fire dates were chosen in GEE based on cloud cover rate. We tried to find clear images which are closely collected before and after the fire to accurately deal with the changes caused only by the result of the fires but no other conditions. As a result, Sentinel-2 satellite image obtained on 20 July 2021 just before the fire and another image obtained on 14 August 2021 just after the fire were used in this study. It is also important to consider whether the fire was entirely extinguished or not to find out the exact distribution of burned areas.

2.3. Burn Severity Indices and Mapping

RS platforms are providing spectral information of burned objects which can be easily to related spatial burn severity field measurements. In addition to spectral information, RS indices can also be applied to improve this relationship. Therefore, RS indices combined with

the field measurements are the foundation for producing burn severity maps (Zheng et al., 2016). In this research, we applied 8 different indices to determine the burned areas and classify the severity. These indexes are dNDVI, dNBR, RdNBR, RBR, dSAVI, dMSAVI, dSWIR, and dBAI. Over time, NDVI potential uses and data sources have changed significantly. From the 1990s to the 2010s, forest estimation is done in at least one third of the total number of publications. The ultimate goal of NDVI implementation is to improve the evaluation of RS data for vegetation information (Huang et al., 2021). Variations in vegetation, humidity levels, and specific ground conditions in the NIR and SWIR bands which might happen after the fire are acutely susceptible to the NBR (Nasery & Kalkan, 2020). By dividing dNBR by the pre-fire NBR value, RdNBR was a form of the dNBR that took into account the approximate amount of before and after fire variations (Miller et al., 2009). Fire-affected regions can be especially targeted by BAI. The reverse spectral range to an intersection, specified by the lowest reflection of burnt vegetation in the NIR and the highest in the red band is used to create BAI (Chuvieco et al., 2008).

2.4. Burned Area Detection and Classification

We carried on the ML classification by using the Red, Green, and Blue (RGB) bands of the Sentinel 2A post-fire image and a composite image that consists of the indices that were created before. Then we added the indices to the Sentinel post-fire image as a band to create the composite image. Using SVM, RF, and CART algorithms pixel-based classification is applied to images. The SVM classifier which is an effective analytical algorithm provides defining the hyperplane which helps to separate the different groups (Masshadi & Alganci, 2021). In order to get the accurate result, gamma and cost parameters are significant in the SVM algorithm. For this reason, while the RGB image is classified, the gamma value is taken as 1e-2 and the cost value as 1e7, while the gamma value for the composite image is taken as 1e-6 and the cost value as 1e14. The CART classifier relies on Decision Tree approaches, which are widely used in Land use/land cover classification (Bar et al., 2020). Through a robust accumulated sample of the training set, the RF classifier builds associated classification and regression trees (Masshadi & Alganci, 2021). For each algorithm, we used the same training samples for comparability. While the number of training polygons is 28, the number of validating polygons is 12 according to the %70 and %30 ratio of training and testing respectively. By using the GEE, we obtained three classified images from composite of indices and RGB bands and three classified images from only RGB bands.

3. Results

We investigated the performance of ML derived burnt areas severity maps. The first algorithm was the SVM algorithm, and it has the lowest overall accuracy for our study area, providing 86.19% overall accuracy. On the other hand, the CART algorithm is providing 86.64% overall accuracy and the RF algorithm with the highest

overall accuracy is 87.54%. Instead, when the burned area indices and post-fire image's RGB bands become a composite image and are used to classify burning areas severity, the SVM algorithm provides 95.3% overall accuracy, and it has the lowest overall accuracy for this study. The CART algorithm is 97.9%, and the RF algorithm has the highest overall accuracy which is

98.57%. The results are shown in Figure 2. When we compare burned areas statistics across ML algorithms in the burn severity classification maps which are made with the composite image, the total burned area in the CART algorithm produced maps is 450 km², while the unburned area is 1156 km².

Table 2. Burnt severity indices classification intervals

INDEX	Regrowth after fire	Unburned	Low Severity	Moderate Severity	High Severity
dNBR	<-0.1	-0.1<x<0.1	0.1<x<0.27	0.27<x<0.66	0.66<
dNDVI	<-0.23	-0.23<x<0.1	0.1<x<0.35	0.35<x<0.50	0.50<
RdNBR	<-9	-9<x<0.30	0.30<x<1.0	1.0<x<1.6	1.6<
RBR	<-0.15	-0.15<x<0.10	0.10<x<0.30	0.30<x<0.50	0.50<
dSAVI	<-0.1	-0.1<x<0.1	0.1<x<0.23	0.23<x<0.32	0.32<
dMSAVI	<-0.1	-0.1<x<0.1	0.1<x<0.22	0.22<x<0.32	0.32<
dbAI	25<	-20<x<25	-150<x<-20	-340<x<-150	<-340
dSWIR	0.1<	-0.01<x<0.1	-0.13<x<-0.01	-0.13<x<-0.06	<-0.13

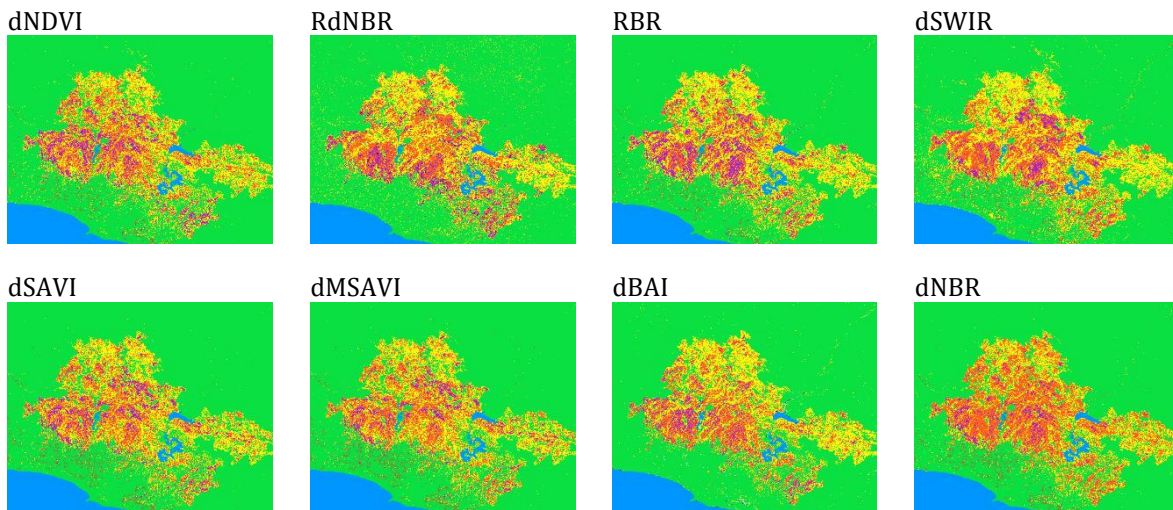


Figure 1. Burn severity indices classified images

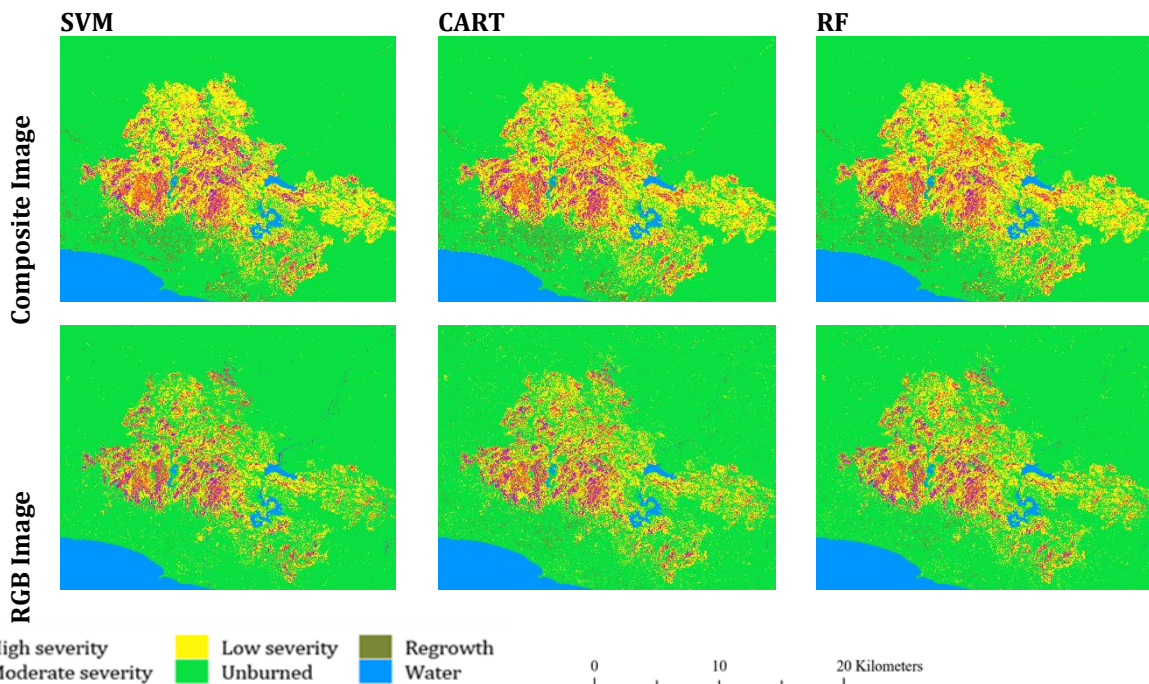


Figure 2. Machine Learning burn severity classifications

Whereas the total burned area in the SVM algorithm produced maps is 439 km², the unburned area was 1167 km². Furthermore, in the burn severity classification maps which are made with RGB images, the CART algorithm has a total burned area of 341 km², and the unburned area is 1265 km². For the RF algorithm, the total burned area is 329 km², and the unburned area is 1277 km².

SVM algorithm found the total burned area is 300 km², and the unburned area is 1306 km². In the calculation of the burned area, we considered high severity, moderate severity, and low severity regions, and for the unburned areas, the sum of the areas of the unburned and regrowth classes.

4. Discussion

In this research, we intended to evaluate and compare the results from images obtained from the medium-resolution Sentinel-2A satellite in the Antalya Province, in terms of fire severity, by using various ML methods. Firstly, it is clear that CART and RF are slightly better than the SVM algorithm in terms of overall accuracy. Bar et al. (2020) mentioned in their article, that they applied ML algorithms to identify forest fires using Sentinel-2 images, and CART and RF algorithms outperformed the SVM algorithms in terms of kappa values. As seen in Figure 2, there is no significant difference between fire severity classes in classification using composite images. When burn severity maps which are produced using RGB and composite images are compared, the amount of burned and unaffected areas have similar bias. For both of them, CART estimated the highest amount of burned area, and SVM estimated the lowest amount of burned area. As a result of the classification of CART, RF and SVM algorithms using RGB bands, less burning and regrowth area was obtained compared to the composite image.

5. Conclusion

In the scope of the project there are six classified images which are composite and RGB. While for the composite and RGB image the SVM algorithm has the lowest overall accuracy, RF has the highest overall accuracy. Although there are no significant differences between algorithms, there is a difference approximately 120 km² between the burned and unburned area amounts for the RGB and composite classified images. In conclusion, this study shows that by using different types of indices and ML algorithms the burnt areas and their severities can be determined effectively using Sentinel 2A imagery in the Google Earth Engine platform. Determining the burnt forest fire areas is important for understanding its impact on the environmental life cycle.

References

- Aksoy, S., Yildirim, A., Gorji, T., Hamzehpour, N., Tanik, A., & Sertel, E. (2022). Assessing the performance of machine learning algorithms for soil salinity mapping in Google Earth engine platform using sentinel-2a and landsat-8 oli data. *Advances in Space Research*, 69(2), 1072–1086. <https://doi.org/10.1016/j.asr.2021.10.024>
- Alganci, U., Sertel, E., & Ormeci, C. (2010). Forest fire damage estimation using remote sensing and GIS. In *Proceedings of EARSeL Symposium* (pp. 423-430).
- Bar S., Parida B. R. & Pandey A. C., (2020). Landsat-8 and Sentinel-2 based Forest fire burn area mapping using machine learning algorithms on GEE cloud platform over Uttarakhand, Western Himalaya, *Remote Sensing Application: Society and Environment*, 18, <https://doi.org/10.1016/j.rsase.2020.100324>
- Bilgili, E., Küçük Ö., Sağlam B. & Coşkun K. A. (2021). Mega Forest Fires: Causes, Organization and Management. In Kavzaoğlu T., Orman Yangınları:Sebepleri, Etkileri, İzlenmesi, Alınması Gereken Önlemler ve Rehabilitasyon Faaliyetleri (pp. 1-24). *Turkish Academy of Sciences*. <https://doi.org/10.53478/TUBA.2021.039>
- Chuvieco, E., Englefield, P., Trishchenko, A. P., & Luo, Y. (2008). Generation of long time series of burn area maps of the boreal forest from NOAA-AVHRR composite data. *Remote Sensing of Environment*, 112(5), 2381–2396. <https://doi.org/10.1016/j.rse.2007.11.007>
- Huang, S., Tang, L., Hupy, J. P., Wang, Y., & Shao, G. (2021, February 1). A commentary review on the use of normalized difference vegetation index (NDVI) in the era of popular remote sensing. *Journal of Forestry Research*. Northeast Forestry University. <https://doi.org/10.1007/s11676-020-01155-1>
- Kavzaoğlu, T., Çölkesen İ., Tonbul, H. & Öztürk, M. Y., (2021). Temporal Analysis Of Forest Fires With Remote Sensing Technologies:Mediterranean And Aegean Fires In 2021. In Kavzaoğlu T., Orman Yangınları:Sebepleri, Etkileri, İzlenmesi, Alınması Gereken Önlemler ve Rehabilitasyon Faaliyetleri (pp. 219-252). *Turkish Academy of Sciences*. <https://doi.org/10.53478/TUBA.2021.048>
- Masshadi, N. & Alganci, U., (2021). Determination of forest burn scar and burn severity from free satellite images: a comparative evaluation of spectral indices and machine learning classifiers, *International Journal of Environment and Geoinformatics (IJEGEO)*, 8(4):488-497. <https://doi.org/10.30897/ijegeo.87966>
- Miller, J. D., Thode, A. E. (2007). Quantifying burn severity in a heterogeneous landscape with a relative version of the delta Normalized Burn Ratio (dNBR). *Remote Sens Environment*, 109(1), 66–80.
- Nasery S., & Kalkan, K. (2020). Burn area detection and burn severity assessment using Sentinel 2 MSI data: The case of Karabağlar district, İzmir/Turkey. *Turkish Journal of Geosciences*, 1(2), 72–77.
- Sertel, E., & Alganci, U. (2016). Comparison of pixel and object-based classification for burned area mapping using SPOT-6 images. *Geomatics, Natural Hazards and Risk*, 7(4), 1198-1206. <https://doi.org/10.1080/19475705.2015.1050608>
- Zheng, Z., Zeng, Y., Li, S., & Huang, W. (2016). A new burn severity index based on land surface temperature and enhanced vegetation index. *International Journal of Applied Earth Observation and Geoinformation*, 45, 84–94. <https://doi.org/10.1016/j.jag.2015.11.002>

4th Intercontinental Geoinformation Days

igd.mersin.edu.tr



Determination of first take-off points for UAVs in case of a disaster

Rıdvan Ertuğrul Yıldırım^{*1} , Aziz Şişman¹ ¹Ondokuz Mayıs University, Engineering Faculty, Department of Geomatics, Samsun, Türkiye

Keywords

GIS
UAV
Disaster
Emergency Management

Abstract

The increase in the frequency of occurrence of natural disasters in the world in recent years leads to an increase in the loss and damage that occurs and negatively affects the lives of millions of people every year. Likewise, the incidence and severity of disasters are increasing in Turkey. There is a need for effective emergency management in order to minimize the loss of lives and properties in large quantities. Emergency management is the management process that starts before the realization of predictable or sudden emergencies and includes the work done to restore the situation and the organization of these works. With the developing technology, unmanned aerial vehicles (UAVs) have started to be used frequently in studies such as pre-disaster risk estimation and post-disaster situation determination. The advantages of UAVs such as being fast, safe, flexible and providing easy access to inaccessible areas are some of the reasons why they play an important role in disaster management. In this study, the first take-off points of the UAVs were determined for post-disaster process.

1. Introduction

In disasters and emergencies that cause great damage to the daily life of humans and other living things, quick planning, decision-making, and being able to apply the most correct one at a time are of vital importance. In such cases, when all processes are considered, a complex and dynamic structure is encountered. In order for the management processes to progress rapidly, it is necessary to obtain data at every stage and analyze the incoming data, to alleviate the effects of disasters and to facilitate the response processes (Caglayan et al. 2018).



Figure 1. Disaster management phases (Bosher et al. 2021)

Modern disaster management consists of risk and mitigation, preparedness, response and recovery phases.

These stages are called risk management, the steps to be done before the disaster, and the work to be done during and after the disaster are called crisis management (Figure 1)(Uysal et al. 2018).

The most important advantage of using an UAV is that it provides data collection from places that are difficult to reach. Engineering studies using UAVs have been increasing rapidly in recent years (Aykut 2022). Determination of coastline, evaluation of rockfall potential, modeling of river topography, modeling of cities and historical structures, etc. The use of UAVs has increased with the developing technology in many engineering fields such as (Alptekin and Yakar 2022).

Common application areas of UAVs in disaster operations management are; mapping the affected areas after the disaster, analyzing the collected images, coordinating the UAV networks, detecting the disasters through some chemical sensors, integrating the UAVs with other communication tools and providing fast and high quality information transmission (Değirmen et al. 2018). Technological developments provide great convenience in modeling regions exposed to disasters. By using the photographs taken with the UAV, the current situation of an area can be learned in 3D as soon as possible and at the most affordable cost (Alptekin et al. 2019).

* Corresponding Author

^{*}(ridvan.yildirim@omu.edu.tr) ORCID ID 0000-0002-2226-773X
(asisman@omu.edu.tr) ORCID ID 0000-0001-6936-5209

Cite this study

Yıldırım, R. E., & Şişman, A. (2022). Determination of first take-off points for UAVs in case of a disaster. 4th Intercontinental Geoinformation Days (IGD), 47-50, Tabriz, Iran

2. Method

Samsun Atakum province was chosen as the study area. In this study, 11 neighborhoods with the highest human and building population were selected (Figure 2), considering that the devastating effect of the disaster affected urban areas and damage assessment studies would be located in areas with dense urban construction.

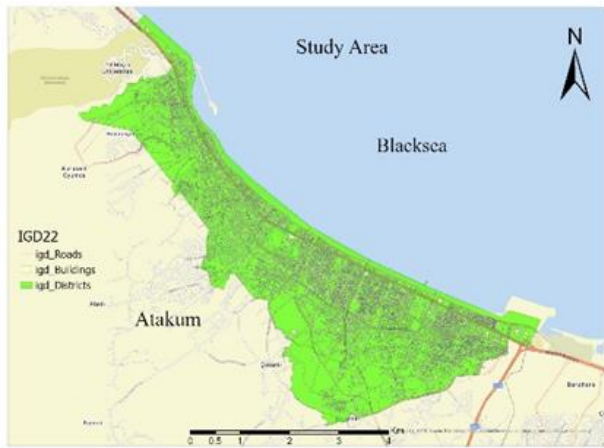


Figure 2. Study Area

In this study to determine red zones for the flight DEM, buildings footprints, roads, waterways, gas stations locations used as a data. DEM is created using SRTM satellite images. Buildings footprints collect from Atakum zoning plan, Open Street Map was used as road data and waterways data (Farr and Kobrick 2000), gas stations locations obtained from addresses.

2.1. Buffer Analysis

Buffer analysis is a GIS querying for desired information within a certain geographic distance. This analysis is done for point, line or polygon features in vector data. Buffer analysis is performed around a point with respect to a certain diameter, to the right or left of a line for a certain distance, or both, and inside or outside a polygon with respect to a certain distance. 2D buffer analysis, which is one of the classical GIS operations, is a spatial analysis based on the examination of the distances of any geographical feature from other features around it (Karaş 2011). In this study, Buffer Analysis was used to determine the distance to restricted objects.

2.2. Directorate General of Civil Aviation - Unmanned Aerial Vehicle Systems Instructions (SHT-UAV)

Directorate General of Civil Aviation (DGCA) has published an SHT-UAV instruction containing all the rules about flight rules. This Instruction has been prepared in order to determine the procedures and principles regarding the import, sale, registration and registration of civil UAV systems to be operated or to be used in Turkish Airspace, ensuring airworthiness, qualifications required of people who will use the systems, air traffic services and UAV operations (DGCA, 2019).

Flight zones subject to special permission and no-fly zones are clearly stated in the 18th and 19th articles of the instruction (Figure 3).

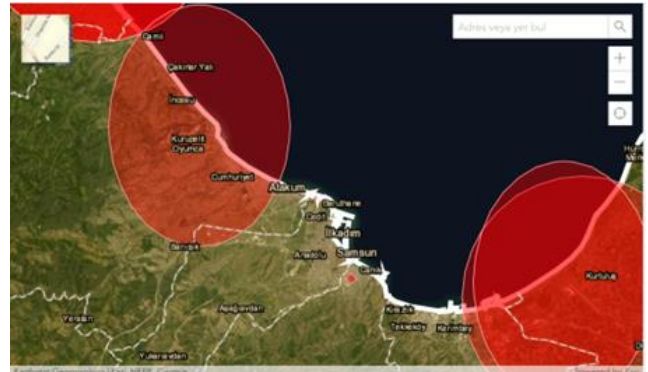


Figure 3. DGCA SHT-UAV Instructions red zones for the flight (DGCA 2019)

The contents of these articles are given below.

- for flights over 400ft
- at a distance of 5NM (9km) to any airport, heliport, etc.
- to fly in "Forbidden, Restricted and Dangerous Areas" in ENR 5.1 section of Turkish AIP
- around critical structures and facilities such as military facilities, prisons and fuel stations and warehouses
- In the fields declared with NOTAM

While the above points are about the situations subject to special permission, the points that attract attention as flight conditions are;

- The UAV must be in the pilot's field of view, not exceeding 500 meters horizontally,
- Do not exceed 400 feet (120 meters) above the ground,
- Flight must be carried out at a distance of at least 50 meters from people and structures.

2.3. Defining red zones for the study

"In unforeseen emergencies such as search, rescue and disaster, Flight Permit may be granted exceptionally, provided that the necessary coordination is ensured with the General Directorate" is clearly stated in Article 18 (DGCA 2019).

In case of a disaster, immediate flights will be required to detect damaged structures as a first response after the disaster. In this case, the effects of the disaster as the risk of flooding, the possible collapse of structures, and the inability to take off on road networks should also be taken into account when choosing the location as the flight departure area. While performing the disaster analysis, the first take-off area should be determined at a distance of 50 meters from structures, 50 meters from rivers, 20 meters from road structures, and 250 meters from gas stations. Areas with a slope of more than 5% were selected as unsuitable for take-off. Considering the post-disaster tsunami effect, areas up to 10 m above sea level were determined as unsuitable areas (Figure 4-9).



Figure 4. Roads buffer 20m



Figure 5. Buildings buffer 50m



Figure 6. Over 5% slope



Figure 7. 10m from sea level



Figure 8. Waterways buffer 50m

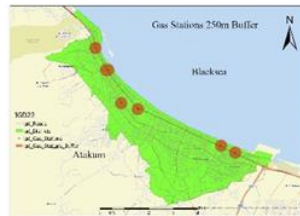


Figure 9. Gas stations buffer 250m

3. Results

All areas that hindered the take-off were combined and areas that were not suitable for the first take-off in case of post-disaster were created.

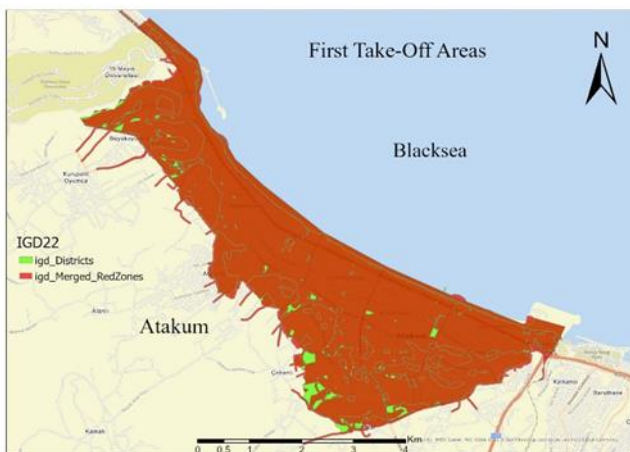


Figure 10. Green zones for the first take-off

When Figure 10. is examined, it is seen that the small green areas in the study area are suitable for take-off in the post-disaster situation when all the areas that prevent take-off are combined. 75 points detect as a take-off points.

When these areas are selected as the take-off point, 2 km buffer areas have been created since it is known that they can fly at an average distance of 2 km, considering the flight capabilities of UAVs (Figure 11).

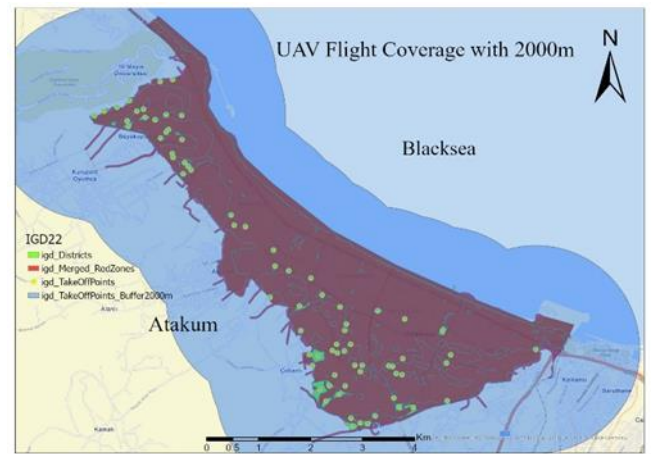


Figure 10 2000m flight coverage

Considering the Modeling Capacity and DGCA flight directives, the 500 m buffer analysis result created when it is thought that a healthy flight can be made at a distance of 500 meters within the pilot's vision is seen in the Figure 12.

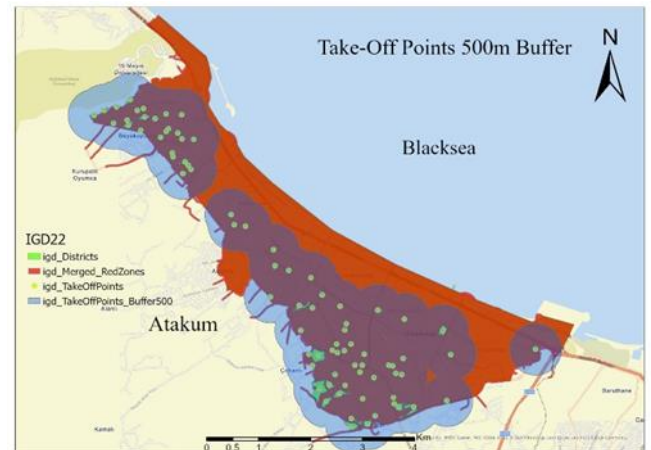


Figure 11. 500m flight coverage

4. Conclusion

It is critical for disaster management to immediately collect ground data, damage assessment and modeling in post-disaster studies. As a result of the analyzes made, the first departure points were determined by considering the disaster effects. The coverage areas that can be reached with the flights to be made using these points have been determined.

75 points suitable for take-off have been identified. It is seen that there is sufficient coverage for the flights that can be carried out at 75 points and the studies to be carried out at a distance of up to 2000 meters. However, it has been determined that there is not enough coverage in the densely populated areas of the coast during the flights to be made at a distance of 500 meters and within the pilot's field of view.

Acknowledgement

"Map data copyrighted OpenStreetMap contributors and available from <https://www.openstreetmap.org>".

References

- Alptekin, A., & Yakar, M. (2020). Heyelan bölgesinin İHA kullanarak modellenmesi. *Türkiye İnsansız Hava Araçları Dergisi*, 2(1), 17-21.
- Alptekin, A., Çelik, M. Ö., Kuşak, L., Ünel, F. B., & Yakar, M. (2019). Anafi Parrot'un heyelan bölgesi haritalandırılmasında kullanımı. *Türkiye İnsansız Hava Araçları Dergisi*, 1(1), 33-37.
- Aykut, N. O. (2022). "İnsansız Hava Araçlarının Kıyı Çizgisinin Belirlenmesinde Kullanılabilirliğinin Araştırılması." 4.
- Bosher, L., Chmutina, K., & van Niekerk, D. (2021). Stop going around in circles: towards a reconceptualisation of disaster risk management phases. *Disaster Prevention and Management: An International Journal*, 30(4/5), 525-537.
- Çağlayan, N., Satoğlu, Ş. I., & Kapukaya, E. N. (2018). Afet Yönetiminde Büyük Veri Ve Veri Analitiği Uygulamaları: Literatür Araştırması, 7. *Ulusal Lojistik ve Tedarik Zinciri Kongresi, ULTZK*, 3-5.
- Değirmen, S., Çavdur, F., & Sebatlı, A. (2018). Afet operasyonları yönetiminde insansız hava araçlarının kullanımı: Gözetleme operasyonları için rota planlama. *Uludağ Üniversitesi Mühendislik Fakültesi Dergisi*, 23(4), 11-26.
- DGCA (2019), Directorate General of Civil Aviation - Unmanned Aerial Vehicle Systems Instructions (SHT-UAV) 2019.
- Farr, T. K., M. (2000). Shuttle Radar Topography Mission produces a wealth of data. E. T. AGU.
- Karaş, İ. R., & Yeşil, E. (2011). 3B CBS Kapsamında Çok katlı ve Büyük Yapılar İçin 3B Tampon Analizi Uygulaması. Akademik Bilişim 2011 Kongresi. Malatya, Türkiye.
- Uysal, M., Yılmaz, M., Tiryakioğlu, İ., & Polat, N. (2018). İnsansız hava araçlarının afet yönetiminde kullanımı. *Anadolu University Journal of Science and Technology B-Theoretical Sciences*, 6, 219-224.

4th Intercontinental Geoinformation Days

igd.mersin.edu.tr



Modeling of groundwater quality based on water quality index using M5P decision tree method

Shokouh Mohsenzadeh¹, Sahar Javidan¹, Mohammad Taghi Sattari^{*1}

¹University of Tabriz, Faculty of Agriculture, Water Engineering Department, Tabriz, Iran

Keywords

Average Water Quality Index
Data Mining
GIS
Groundwater

Abstract

Groundwater is recognized as one of the most important sources of fresh water for agricultural and drinking purposes in the world. About one-third of the world's population needs groundwater to supply drinking water. Therefore, groundwater plays an important role in providing water for consumption in various sectors such as industry, agriculture and drinking. In the present study, first the WQI index was calculated using data related to water quality parameters of 23 wells in Qazvin plain from 2015 to 2018. Then the performance of M5P tree model in estimating groundwater quality in Qazvin plain was evaluated based on WQI index. The results of the model were compared with the indices of Correlation Coefficient (R), Root Mean Square Error (RMSE) and Mean Absolute Error (MAE). The results showed that the third scenario including TDS, EC, TH with RMSE= 5.2198, MAE= 3.7747 and R= 0.9817 was selected as the best scenario. The mean values of WQI index showed that most of the area of Qazvin plain is allocated to poor quality class.

1. Introduction

In today's world, despite the reduction of surface water resources, attention to groundwater resources has increased, so the groundwater level and their quality has changed (Asghari Moghaddam and Vadiati 2016). In Iran, due to its special location in the arid and semi-arid region, it is important to pay attention to this source and its conditions (Emami et al. 2021). The physical and chemical properties of the aquifer and its composition determine the quality of groundwater. In agricultural issues, knowing the quality of groundwater for agricultural use can help researchers and soil and water managers to make appropriate plans to preserve soil and increase water productivity.

Mokaram et al. (2017) used the Adaptive Network-based Fuzzy Inference System (ANFIS) to predict groundwater quality in the west of Fars province. Based on the results, they found that among the various forecasting models, the hybrid model in the FCM method with the highest R and the lowest error, has the highest accuracy in predicting the groundwater quality of the study area.

Hasani et al. (2018) predicted the groundwater quality class of Khan Mirza plain based on the USSL

diagram using the tree decision method. The results of their study showed that only using 4 hydrochemical parameters can determine the water quality class with high accuracy.

Asadi et al. (2020) evaluated and zoned the quality of groundwater in Tabriz aquifer for drinking and agricultural uses. The results showed that about 37% (296 km²) of groundwater in the study area has high adaptability and the remaining 63% (495 km²) has moderate adaptation for agricultural use. The trend of WQI and IWQ indices indicates that the groundwater of the region becomes more unfavorable over time.

Trabelsi et al. (2022) used the machine learning index to evaluate the effectiveness of machine learning models to predict the suitability of groundwater in the downstream basin of the Sidi Salem Dam for irrigation purposes. The results showed that Ada Boost model is the most suitable model and ML model is the most cost-effective model. Launching a DSS based on machine learning models enhances the efficient use of water and rationalizes its use by all water stakeholders at the basin level.

The aim of this study was to evaluate the performance of the M5P tree model in estimating groundwater quality in the Qazvin plain based on the WQI index.

* Corresponding Author

(Shkmsn2000@gmail.com) ORCID ID 0000 – 0003 – 3982 – 3082
(javidansahar77115@gmail.com) ORCID ID 0000 – 0001 – 6739 – 8242
(mtsattar@gmail.com) ORCID ID 0000 – 0002 – 5139 – 2118

Cite this study

Mohsenzadeh, S., Javidan, S., & Sattari, M. T. (2022). Modeling of groundwater quality based on water quality index using M5P decision tree method. 4th Intercontinental Geoinformation Days (IGD), 51-54, Tabriz, Iran

2. Method

The study area of Qazvin plain aquifer in Iran with an area of 3733.68 square kilometers. In Qazvin province, the average annual rainfall in the last 10 years is 306.3 mm and the average annual temperature is 14.9 °C, which according to De Martonne classification has a semi-arid climate. About 72% of the necessary expenditures in the agricultural sector are provided from the province's groundwater resources. Alluvial soils of Qazvin region have good permeability and any type of waste produced on the ground penetrates into the ground due to rainfall or proximity to water sources and contaminates groundwater reservoirs that are continuously and widely spread in the area.

In the present study, the quality parameters of 23 wells including Total Hardness (TH), alkalinity (pH), Electrical Conductivity (EC), Total Dissolved Solid (TDS), Calcium (Ca), Sodium (Na), Magnesium (Mg), Potassium (K), Chlorine (Cl), Bicarbonate (HCO₃) and Sulfate (SO₄) have been used in the aquifer of Qazvin plain in the statistical period of 4 years (2018-2015). The spatial location of the studied wells is shown in Figure 1.

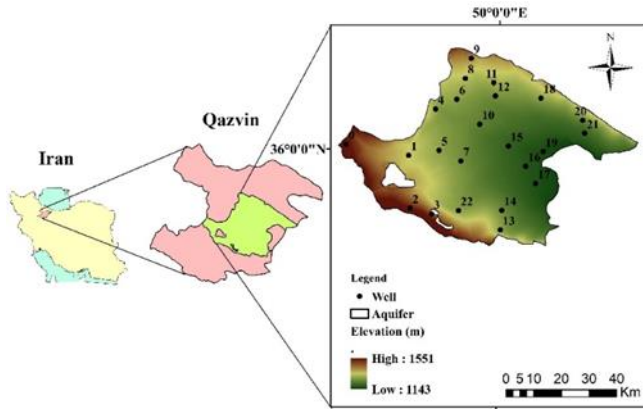


Figure 1. Location of the study area and distribution of sampling wells

The statistical characteristics of the variables used are presented in Table 1.

Table 1. Statistical characteristics of implemented parameters

Statistic	Minimum	Maximum	Mean	Skewness	Kurtosis
pH	5.60	8.70	7.63	-0.94	5.00
TDS	219.00	6296.00	1049.31	2.82	10.29
TH	120.00	1404.50	410.39	1.86	3.88
EC	351.00	9837.00	1645.50	2.80	10.17
K	0.02	0.87	0.08	7.84	82.27
Na	0.55	63.20	8.23	3.06	12.34
Mg	0.63	18.97	3.66	3.04	12.27
Ca	1.23	21.99	4.55	2.61	10.22
SO ₄	0.21	26.66	5.30	1.72	3.94
Cl	0.44	58.07	7.56	2.81	9.58
HCO ₃	0.50	6.45	3.78	-0.25	1.28

WQI index values were considered as target outputs. Using the correlation method, the types of input compounds (including parameters with a correlation above 0.8) were identified (Table 2). The M5P tree model was used to estimate WQI values. Of the available data, 70% were considered for calibration and 30% for validation.

Table 2. Parameters involved in each scenario

Scenario Number	Input Parameters
1	TDS
2	TDS, EC
3	TDS, EC, TH
4	TDS, EC, TH, Ca
5	TDS, EC, TH, Ca, SO ₄
6	TDS, EC, TH, Ca, SO ₄ , Cl
7	TDS, EC, TH, Ca, SO ₄ , Cl, Na

2.1. Water Quality Index

Drinking water quality index was calculated using formulas 1 to 3. In these formulas, w is the weight of each parameter due to its importance in drinking and W is the relative weight of each parameter, C is the concentration of each parameter, S is the standard concentration of each parameter, q is the quality rank of each parameter and WQI is the drinking water quality index (Singh 1992).

$$W_i = \frac{w_i}{\sum_{i=1}^n w_i} \quad (1)$$

$$q_i = \left(\frac{C_i}{S_i} \right) \times 100 \quad (2)$$

$$WQI = \sum_{i=1}^n W_i q_i \quad (3)$$

Calculated WQI values are usually divided into five categories (Table 3).

Table 3. Water quality classification based on WQI value

Classification of Drinking Water Quality		
WQI Range	Class	Type of Water
below 50	I	Excellent water
50-100	II	Good water
100-200	III	Poor water
200-300	IV	Very poor water
above 300	V	Water unsuitable for drinking

Finally, by plotting the average WQI values with the help of GIS software, it is possible to achieve changes in groundwater quality at the aquifer level. Kriging interpolation method was used to draw this map and estimate the WQI index in non-sampled points. Kriging is a statistical method that uses statistics in addition to mathematical functions to predict unknown points.

Equation 4 shows the general kriging relationship:

$$Z^* = \sum_{i=1}^N \lambda_i Z(x_i) \quad (4)$$

Where n is the number of data, Z^* is the estimated spatial data value, $Z(x_i)$ is the spatial data value observed at point i , and λ_i is the sample weight x_i , indicating the importance of point i in kriging calculations, and the sum of the coefficients λ_i is 1. Will be (Meng 2020).

A semi-variable is used to determine the spatial relationship of a random variable in the statistics field. Equation 5 is the relation to the criterion of the experimental γ semivariogram (Metron 1963):

$$\gamma(h) = \frac{1}{2n(h)} \sum_{i=1}^{n(h)} [Z(x_i) - Z(x_i + h)]^2 \quad (5)$$

$n(h)$ The number of pairs of points in a certain class of distance and direction, $Z(x_i)$ and $Z(x_i + h)$ represent the location of Z and (h) γ the values of the semi-experimental exponential change at distances h .

2.2. M5P Tree Model

The M5P algorithm is a logical reconstruction of the M5 introduced by Wang and Witten in 1997. The M5P tree model has the ability to predict numerically continuous variables from numerical traits, and the predicted results appear as multivariate linear regression models on tree leaves. The criterion of division in a node is based on the selection of the standard deviation of the output values that reach that node as a measure of error. By testing each attribute (parameter) in the node, the expected reduction in error is calculated. The reduction in standard deviation is calculated by Equation (6) (Wang and Witten 1997).

$$SDR = \frac{m}{|T|} \times \beta(i) \times \left[sd(T) - \sum_{j \in (L,R)} \frac{|T_j|}{|T|} \times sd(T_j) \right] \quad (6)$$

In the above relation, SDR decreases the standard deviation, T represents the series of samples that are bound, m is the number of samples that do not have missing values for this attribute, $\beta(i)$ is a correction factor, TL and TR are sets that are divided by this attribute into There are.

To compare the values obtained from the M5P tree model with the values calculated from the WQI index, the criteria of evaluation of Correlation Coefficient (R), Root Mean Square Error (RMSE), Mean Absolute Error (MAE) were used. The formulas of the above statistics are presented in Equations (7) to (9), respectively:

$$R = \frac{\sum_{i=1}^N (x_i - \bar{x})(y_i - \bar{y})}{\sqrt{\sum_{i=1}^N (x_i - \bar{x})^2 \cdot \sum_{i=1}^N (y_i - \bar{y})^2}} \quad (7)$$

$$RMSE = \sqrt{\frac{\sum_{i=1}^N (x_i - y_i)^2}{N}} \quad (8)$$

$$MAE = \frac{1}{N} \sum_{i=1}^N |x_i - y_i| \quad (9)$$

In the above relations, y_i represents the estimated value of the model, x_i represents the value calculated from the qualitative index, and N represents the amount of data.

3. Results

The results obtained from the 7 input scenarios used in the M5P tree model are presented in Table 4.

Table 4. Evaluation criteria for estimating quantitative WQI values

Scenario	M5P		
	R	RMSE	MAE
1	0.9901	7.419	6.7142
2	0.9895	7.3441	6.6159
3	0.9817	5.2198	3.7747
4	0.9598	7.3118	5.2855
5	0.9694	6.9329	4.6595
6	0.9694	6.9329	4.6595
7	0.9694	6.9329	4.6595

According to Table 4, Scenario 3 including TDS, EC, TH with the lowest error rate was selected as the best scenario for estimating WQI values.

A map of the average WQI values is shown in Figure 2.

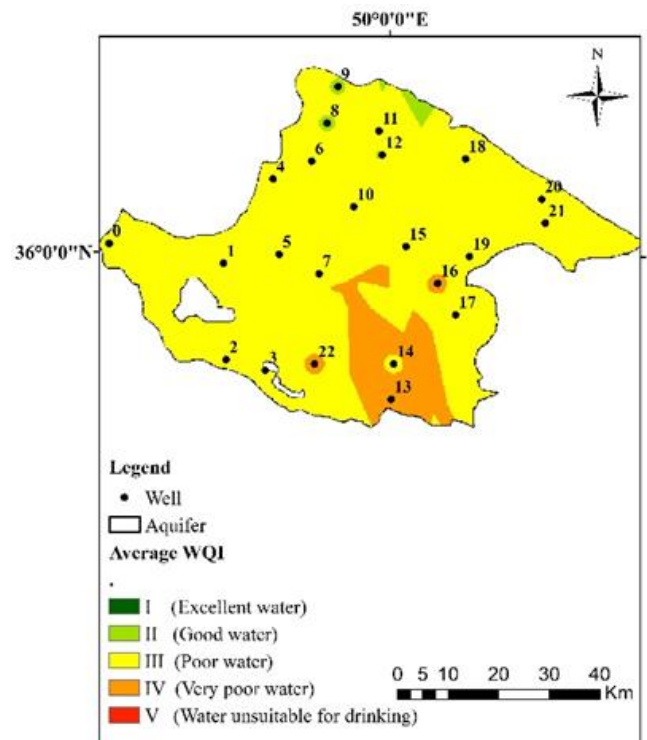


Figure 2. Map of average WQI values in Qazvin plain

According to Figure 2, it can be concluded that most of the area of Qazvin plain has water with poor quality class, also a part of the south of the plain has a very poor-

quality class and only a very small part of the north of the plain has good quality water.

4. Discussion

Calculating Water Quality Index with a large number of parameters is time consuming and difficult. However, data-based methods with a very small number of parameters provide more acceptable results, and this increases the popularity of data-based methods. The results of the present study showed that the M5P tree model using the parameters TH, TDS, EC had considerable accuracy in estimating WQI values. In general, the results showed that most of the Qazvin plain has water with poor quality class.

5. Conclusion

In the present study, Water Quality Index using the parameters of Total Hardness (TH), alkalinity (pH), Electrical Conductivity (EC), Total Dissolved Solid (TDS), Calcium (Ca), Sodium (Na), Magnesium (Mg), Potassium (K), Chlorine (Cl), Bicarbonate (HCO_3) and Sulfate (SO_4) were calculated. Then, the M5P tree model was used to estimate the WQI values, considering different scenarios. The results showed that TH, TDS and EC parameters were the most effective parameters in determining the groundwater quality of Qazvin plain. Most of the plain also had a WQI index between 100 and 200, which indicates a poor-quality class.

References

- Asadi, E., Isazadeh, M., Samadianfard, S., Ramli, M., Mosavi, A., Nabipour, N., Shamshirband, Sh., Hajnal, E., & Chau, K. (2020). Groundwater Quality Assessment for Sustainable Drinking and Irrigation. *Sustainability*, 12, 177. doi:10.3390/su12010177.
- Asghari Moghaddam, A., & Vadiati, M. (2016). Sarab plain groundwater quality rating for drinking water using entropy method. *Water and Soil Knowledge*, 26(32), 1–13.
- Emami, S., Norouzi sarkarabad, R., & Chopan, Y. (2021). Use of artificial neural network (ANN) and colonial competition algorithm to evaluate the groundwater quality of Jolfa plain for different uses. *Journal of Civil Engineering Amirkabir*, 53(1), 313–330.
- Hasani, Z., Mirabasi najafabadi, R., & Ghasemi, A. (2018). Predicting the groundwater quality of Khanmirza plain for agricultural use using tree decision method. *Hydrogeology*, 3(1), 99–110.
- Meng, J. (2020). Raster data projection transformation based on kriging interpolation approximate grid algorithm. *Alexandria Engineering Journal*. <https://doi.org/10.1016/j.aej.2020.12.006>.
- Mokaram, M., Mokaram, M., Zarei, A., & Nejadian, B. (2017). Use of Adaptive Neural-Fuzzy Network (ANFIS) to Predict Groundwater Quality in the West of Fars Province from 2004 to 2014. *Ecohydrology*, 4 (2), 547-559.
- Singh, D. F. (1992). Studies on the water quality index of some major rivers of Pune, Maharashtra. *Proceedings of the Academy of Environmental Biology*, 1, 61–66.
- Trabelsi, F., & Bel Hadj Ali, S. (2022). Exploring Machine Learning Models in Predicting Irrigation Groundwater Quality Indices for Effective Decision Making in Medjerda River Basin, Tunisia. *Sustainability*, 14(4), 2341. <https://doi.org/10.3390/su14042341>.
- Wang, Y., & Witten, I. H. (1997). Inducing model trees for continuous classes, in *Proceedings of the Ninth European Conference on Machine Learning*. Prague, Czech Republic: Springer, 128-137.



4th Intercontinental Geoinformation Days

igd.mersin.edu.tr



Developing a participatory WebGIS for monitoring the physical problems of rural settlements

Fatemeh Sadate Hosseini ¹, Mohammadreza Jelokhani-Niaraki ^{*1}, Hasanali Faraji-Sabokbar ²

¹ Department of Remote Sensing and GIS, Faculty of Geography, University of Tehran, Tehran, Iran

² Department of Human Geography, Faculty of Geography, University of Tehran, Tehran, Iran

Keywords

Rural settlements
Physical problems
Participatory GIS

Abstract

Nowadays, with the growth of population in rural settlements and the complexity of the relations governing these settlements, the physical problems have become wider and more complex. The physical problems of the rural areas are related to water resource, waste water, roads, healthcare centers, electricity, as well as other infrastructures. There are various ways to monitor these problems, many of which are traditionally implemented in rural areas. The present study seeks to develop a web-based participatory Geographic Information System (GIS) to monitor the physical problems of rurals. For this purpose, a web GIS was first designed and developed. This system was implemented for participatory monitoring of the problems of Eskaman, Dehshad Bala, Razi Abad and Asilabad villages. The people of these villages were invited to report their problems locally through the web GIS and complete a questionnaire related to the usability of the system. The results show that the highest number of problems reported by villagers (24%) is related to water and sewage problems. Assessing the usability of the system shows that despite the desire of villagers to use the system, the need to teach the use of GIS tools and simplification of the user interfaces is of critical importance.

1. Introduction

Given that the majority of the country's population lives in rural areas, addressing issues and problems in this area is of great importance. In examining the problems of rural settlements, addressing the physical dimensions is of particular importance. The natural environment of a settlement and the changes made to it, such as buildings, streets, facilities and major facilities, are considered as physical elements occupying space (Bahraïni, 1370).

There are various methods for monitoring the physical problems of the villages, many of which are traditionally utilized in the villages. Due to the increasing number of rural problems, the need for prompt and optimal treatment of physical problems in rural areas is felt more than ever. One of the appropriate methods to identify, monitor and solve physical problems is to use participatory web Geographic Information System (GIS) tools. On the one hand, the use of GIS as a platform that manages, visualizes and analyzes spatial data, and on the other hand, web technology that can provide a platform

accessible to the public, enables the location-based participation in monitoring the rural physical problems. Easy access to the required GIS data and tools, anywhere, anytime and through any device, has led to the increasing use of web-based GIS systems for people to participate in solving spatial problem or spatial planning/decision making processes (Jelokhani et al. 2016). This technology provides the ground for the participation of the villagers in identifying the physical problems of the village by providing more interaction and participation, connection to wider networks and multiple communication channels. Using this technology, villagers become active observers and act as active, analytical, intelligent, responsible, conscious, mobile, distributed and interactive sensors to monitor and report on their surroundings (Jelokhani et al. 2017). This type of monitoring is based on the notion that villagers can use their five senses, like artificial sensors or even better (Goodchild 2007), to provide information about rural physical problems in more detail and accurate manner.

The present study seeks to develop and evaluate a web-based participatory GIS for monitoring and

* Corresponding Author

(fa.s.hosseini@gmail.com) ORCID ID 0000-0001-8433-0290
*(mrjelokhani@ut.ac.ir) ORCID ID 0000-0001-7448-7833
(hfaraji@ut.ac.ir) ORCID ID 0000-0002-5470-4287

Cite this study

Hosseini, F. S., Jelokhani-Niaraki, M., & Faraji-Sabokbar, H. (2022). Developing a participatory WebGIS for monitoring the physical problems of rural settlements. 4th Intercontinental Geoinformation Days (IGD), 55-57, Tabriz, Iran

reporting rural problems. For this purpose, in the first step, the need assessment of the web-based GIS was performed, and in the next step, the system was used experimentally to report the problems of Shahriar villages. Finally, the system was evaluated through a questionnaire in the system.

2. Method

To explain the objectives of the present study, a web-based GIS was designed. The designed system was developed based on the views of the residents of Shahriar villages. After the implementation of the system, the results of the participation of villagers including the number and type of problems reported, the type of spatial data (point, line and polygon) and views on the usability of the system were examined.

2.1. Research objectives

The main purpose of this study is to develop a participatory GIS in order to solve the physical problems of rural settlements. In order to achieve this goal, the present study pursues the following sub-objectives: (1) Needs assessment and design of a participatory GIS for rural areas in order to solve physical problems of rural settlements and (2) Evaluation of the participatory GIS from the perspective of villagers in order to assess the usability of the system in rural areas.

To start working with the system, first the villagers register on the site and then the tools in the site become available to each user. Villagers can report the problems and location of the problems using the tools available on the map, and for each problem, upload text, photos and videos, and complete a questionnaire related to the usability of the system. These inputs are stored in the database and then categorized and analyzed by the admin (Figure 1).

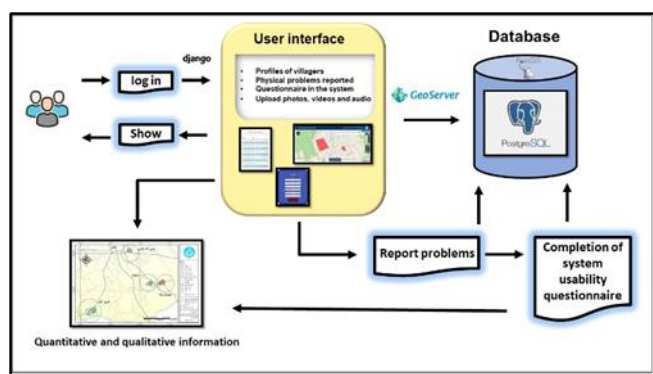


Figure 1. System process

One of the important tools of the system is the ability to draw shapes in the form of points, lines and polygons, so that the user can specify the location of the physical problems to be shown for officials on the map. The possibility of deleting and editing drawings is also considered in this section (Figure 2). Immediately after drawing the desired location on the map, a window opens for the user, which has features such as the problem submission box, the suggestion box, and the comment box and follow-up of the person in charge

about the problem. The user can also talk about the place and the problems with other villagers and officials, and it is possible for other villagers to talk about the problem in the same box.



Figure 2. Drawings in the system

2.2. Study area

Shahriar city with an area of 320 square kilometers is one of the 12 cities of Tehran province. This city is located in the west of Tehran province, which is bordered by Mallard city from the west, Quds city from the north, Robat Karim city and Baharestan city from the south, and Islamshahr city from the east (Figure 3).

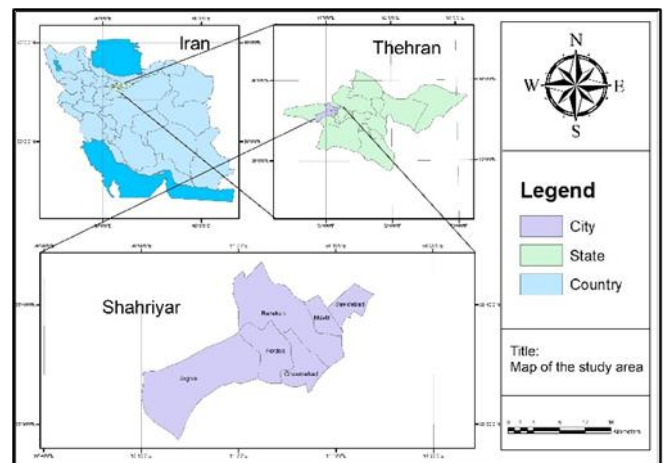


Figure 3. Study area

3. Discussion and Results

In terms of using the capabilities of the system, 92% of the participants used the data type of point to record problems, 100% of the recorded problems were accompanied by text, and 95%, in addition to the text of the report, presented their suggestions to solve the problem. Furthermore, 20% and 2% of the participants uploaded reports along with photos and short videos, respectively.

The results of the system usability assessment show that 31% want to use the system. Analysis of statistics related to the usability of the system shows that although statistically the majority were willing to use the system and participate in reporting problems or considered the use of the system simple, but close to the pros and cons and the relatively high statistical people who were hesitant about responding indicate that the villagers, despite their desire to participate in this field, need to be

trained and have the cultural background to use the system. The need to use the system is still not clear to many villagers and they prefer to use the traditional methods of the past to convey their problems to the authorities. Also, the user interface of the site needs to be strengthened and reviewed in order to be able to attract the audience in the first place and encourage them to use the system. Villagers also need to learn to interact with systems and map-based tools. One of the problems they faced when working with the system was finding the village where they lived on the map, and this made them think first that working with the map could be difficult and complicated.

4. Conclusion

The study has presented a participatory Web GIS tool for monitoring and reporting rural problems. The proposed system involves using the map-based visual tools to report physical and spatial problems of rural areas. In general, the findings show that villagers are willing to participate in monitoring and reporting rural problems in a location-based way and through the web-based system, but considering a number of prerequisites and trainings, as well as eliminating system flaws and correcting the wrong mentality of the past, can alleviate the matter.

5. Recommendations

In general, it seems that considering the existing capacities, using a participatory GIS to report the physical problems of the villages can be helpful, but it requires that the public awareness be increased in relation to the benefits of the system among the rural people and officials. As the future work, the system user interface should be strengthened and look simpler and freer of any complexity according to the usability assessment results. Infrastructure issues such as antenna problems and the Internet should also be addressed with the help of officials to enable the use of system capabilities. Once the problems are solved, people gradually trust the authorities and gradually learn to use

the system and can report problems in much more detail and accuracy.

It is also suggested that the future studies adopt data logging approach to better monitor the behavior of users while interacting with the system. Moreover, production of mobile applications for the system can also make the capabilities of the system better, faster and more accessible to the villagers.

As another suggestion, future study might investigate and evaluate the relationship between villagers' motivation and system use. Obviously, the more motivated villagers are to report problems (for example, problems related to where they live), the more time and effort they will spend reporting the problems. This would lead to increased participation and use of the system in reporting rural physical problems. The results of a study conducted by Amini Rad (2021) show that there is a direct relationship between the motivation of participants and the quality of participatory geographic data.

References

- Amini, Rad, M. (2021). Assessing the relationship between participants' motivation and the quality of citizen-centered geographic data. Thesis, University of Tehran, Faculty of Geography
- Bahraini, H. (1991). Concept and characteristics of physical planning, Proceedings of the First International Conference on Physical Planning (national and regional).
- Goodchild, M. F. (2007). Citizens as sensors: The world of volunteered geography, *GeoJournal*, Vol. 69, No. 4, pp, 211–221.
- Mir-Mohammadi, F., Jelokhani-Niaraki, M., Alavi-Panah, K. & Neysani-Samany (2016). Development of Support System Participatory spatial decision-making under the web based on user-assigned spatial options (Case study: Location of permanent health services in Region 1 of Mashhad), *Journal of Surveying Science and Technology*, Volume 6, Number 1.



4th Intercontinental Geoinformation Days

igd.mersin.edu.tr



Estimation of Mordagh Chay River water quality using gaussian process regression method

Kambiz Falsafian *¹

¹University of Tabriz, Marand Technical College, Tabriz, Iran

Keywords

Gaussian process regression
Mordagh Chay River
Water quality

Abstract

Accurate modeling of river quality parameters is essential for environmental planning, optimal operation of reservoirs, designing of hydraulic structures and irrigation planning. Considering that direct measurement of quality parameters is time consuming and costly, it is possible to predict these parameters with less time and cost and with high accuracy using artificial intelligence methods. In this regard and in the present study, the electrical conductivity parameter of Mordagh Chay River has been estimated using the gaussian process regression method. Based on this, the amounts of calcium, magnesium, sodium, chlorine and sulfate of this river on a monthly scale over a period of 47 years (1971-2018) were used as input parameters of the models. Statistical parameters of correlation coefficient, scattering index and Wilmott's index were also used to compare the obtained results with the observed values. Finally, the obtained results showed that the GPR5 model with SI of 0.093 and WI of 0.995 had the best performance. It was also generally concluded that using the models used in this study, the EC value in the Mordagh Chay River can be estimated with appropriate accuracy.

1. Introduction

Rivers are the main and most important source of fresh water for various industrial, drinking and agricultural usages, and all over the world, the high quality of river water is very important and vital. Various environmental factors such as the construction of industrial factories, population growth and the use of pesticides in agricultural lands have affected the quality of river water. Therefore, the study of variability of water quality criteria along a river has been researched and considered by researchers as modeling and predicting water quality to provide appropriate solutions to control and reduce river pollution. Also, one of the key factors in water resources management and fresh water processing in accordance with urban, industrial and agricultural needs is modeling and estimating water quality. Various criteria are used to indicate water quality. Water salinity is one of the most important criteria that is measured by the parameter of electrical conductivity (EC). In this regard, classical statistical methods have been used to develop water resources management and investigate changes in river water quality. In recent years, machine learning methods have

been used significantly in predicting various parameters of water resources due to their accuracy and the need for low cost and time. Studies of Yesilnacar et al. (2008), Rankovic et al. (2010), Emamgholizadeh et al. (2013) and Shokoohi et al. (2017) are examples of research conducted in the field of modeling water quality parameters.

Haghiabi et al. (2018) examined the methods of artificial neural network (ANN), group method of data handling (GMDH) and support vector machine (SVM) in predicting the water quality of the Tireh River located in southwestern Iran. Comparison of the results by error indices showed the superiority of the SVM model over other models. Najah Ahmad et al. (2020) utilized techniques of Adaptive Neuro-Fuzzy Inference System (ANFIS), Radial Basis Function Neural Networks (RBF-ANN) and Multi-Layer Perceptron Neural Networks (MLP-ANN) for estimating water quality parameters in the Johor River Basin in Malaysia. They also used a hybrid method of Neuro-Fuzzy Inference System based augmented wavelet de-noising technique (WDT-ANFIS) to increase the accuracy and showed that in the validation section, the proposed model had a satisfactory

* Corresponding Author

^{*}(kfalsafian@tabrizu.ac.ir) ORCID ID 0000 – 0002 – 1567 – 7976

Cite this study

Falsafian, K. (2022). Estimation of Mordagh Chay River water quality using gaussian process regression method. 4th Intercontinental Geoinformation Days (IGD), 58-61, Tabriz, Iran

performance in estimating all water quality parameters. Melesse et al. (2020) predicted salinity in the Babol River in northern Iran using random forest and M5P methods and eight new hybrid algorithms. In this research, the parameters PH, TDS, flow rate and some cations and anions were used as input of the models. Using the results, it was shown that hybrid models increase accuracy of the single models.

According to studies on water quality parameters, machine learning methods in most researches have had accurate and desirable results. Therefore, in this study, with the aim of modeling water quality in Mordagh Chay River located in Maragheh city, Gaussian process regression technique has been used and the amount of electrical conductivity in the study area has been estimated to manage and protect the water quality of this river using the obtained results.

2. Method

2.1. Study area

Mordagh Chay is a river located in northwestern Iran in the province of East Azerbaijan. This river originates from Sahand mountains and after passing through the lands of Maragheh and Malekan cities, it reaches a branch of Zarrineh river. In this study, water quality data Mordagh Chay at Gheshlagh Amir station, which is located at 46° 17' longitude and 37° 18' latitude, has been used. The data used in this study include the parameters of calcium (Ca), magnesium (Mg), sodium (Na), chlorine (Cl), sulfate (SO₄) and electrical conductivity (EC) on a monthly scale and over a period of 47 years, from 1971 to 2018, so that the mentioned parameters in different combinations have been used as input of models to estimate EC. Table 1 shows the different combinations of input parameters of the studied models.

Table 1. Different combinations of input parameters of the studied models

Combination Number	Input Parameters	Output Parameter
1	Ca, Mg	EC
2	Ca, Na	EC
3	Mg, Na	EC
4	Ca, Mg, Cl	EC
5	Ca, Mg, Na	EC
6	Ca, Mg, Na, SO ₄	EC
7	Ca, Mg, Na, Cl	EC
8	Ca, Mg, Na, Cl, SO ₄	EC

2.2. Gaussian process regression (GPR)

Gaussian process regression models are based on the assumption that adjustment observations should carry information about each other. Gaussian processes are a way to specify a priority directly on the function space. This is a natural generalization of the Gaussian distribution which mean and covariance are vectors and matrices, respectively (Yang et al. 2018). The Gaussian

distribution is on vectors while the Gaussian process is on functions. As a result, Gaussian process models do not need any validation process to generalize due to prior knowledge of functional dependencies and data, and Gaussian process regression models are able to understand the prediction distribution corresponding to the test input (Pal and Deswal, 2010).

Consider the set S with n observations $S = \{(x_i, y_i) | i = 1, \dots, n\}$, in which x_i is the input vector with D dimension and y_i is the output with scalar or target. This set consists of two components, input and output, as sample or experimental points. For ease of operation, the inputs of the set are aggregated in $X = [x_1, x_2, x_3, \dots, x_n]$ matrix and the outputs are also collected in $Y = [y_1, y_2, y_3, \dots, y_n]$ matrix. The regression task is to create a new x^* input in order to achieve the predicted distribution for y^* corresponding values of the observational data and based on the S data set. The Gaussian process is a set of random variables, a limited number of which are integrated with Gaussian distributions. The Gaussian process is a generalization of the Gaussian distribution. The Gaussian distribution is actually the distribution between random variables, while the Gaussian process represents the distribution between functions. The Gaussian process is defined by the functions of mean and covariance in the form of Equations 1 and 2:

$$m(x) = E(f(x)) \quad (1)$$

$$k(x, x') = E(f(x) - m(x))(f(x') - m(x')) \quad (2)$$

which $k(x, x')$ is a function of covariance (or kernel) that is calculated in x and x' points. The Gaussian process can be expressed as Equation 3:

$$f(x) \sim GP(m(x), k(x, x')) \quad (3)$$

Which is usually considered to be zero to simplify the value of the average function.

2.3. Performance evaluation criteria of models

Error values between the studied models and observational data were estimated and evaluated by correlation coefficient (R), scatter index (SI) and Wilmott's index (WI) using Equations 4 to 6.

$$R = \frac{\left(\sum_{i=1}^n x_i y_i - \frac{1}{n} \sum_{i=1}^n x_i \sum_{i=1}^n y_i \right)}{\left(\sum_{i=1}^n x_i^2 - \frac{1}{n} \left(\sum_{i=1}^n x_i \right)^2 \right) \left(\sum_{i=1}^n y_i^2 - \frac{1}{n} \left(\sum_{i=1}^n y_i \right)^2 \right)} \quad (4)$$

$$SI = \frac{RMSE}{\bar{y}} = \frac{\sqrt{\frac{1}{n} \sum_{i=1}^n (x_i - y_i)^2}}{\bar{y}} \quad (5)$$

$$WI = 1 - \left[\frac{\sum_{i=1}^n (y_i - x_i)^2}{\sum_{i=1}^n (|x_i - \bar{y}| - |y_i - \bar{y}|)^2} \right] \quad (6)$$

In Equations 4 to 6, x_i and y_i are the predicted and observed monthly electrical conductivity values, respectively and n is the number of observations.

3. Results

In this study, in order to model the electrical conductivity in the Mordagh Chay River, the parameters of calcium (Ca), magnesium (Mg), sodium (Na), chlorine (Cl) and sulfate (SO₄) were used as input data and the EC parameter was estimated as the output of the models. Therefore, based on the correlation of input parameters with EC, eight different scenarios were defined by combining different input data for the studied models and the obtained results were compared using the statistical parameters of correlation coefficient, scatter index and Wilmott's index with observational data and superior models were introduced. Table 2 shows the statistical indicators of the studied models.

Table 2. Statistical indicators of studied models

Model	R	SI	WI
GPR1	0.992	0.105	0.995
GPR2	0.984	0.184	0.985
GPR3	0.913	0.396	0.881
GPR4	0.992	0.109	0.994
GPR5	0.991	0.093	0.995
GPR6	0.989	0.107	0.994
GPR7	0.989	0.103	0.994
GPR8	0.986	0.124	0.992

According to Table 2, the obtained results show that the GPR5 model with correlation coefficient of 0.991, scatter index of 0.093 and Wilmott's index of 0.995 had the best results. The second place was taken by GPR1 model with correlation coefficient of 0.992, scatter index of 0.55 and Wilmott's index of 0.995 with only two input parameters (Ca and Mg). Also, GPR7 model with correlation coefficient of 0.989, scatter index of 0.103 and Wilmott's index of 0.994 had good accuracy and was ranked third. In general, the results show that the developed models have appropriate and acceptable accuracy in modeling the EC values of the Mordagh Chay River.

4. Discussion

In order to better understand the performance of the superior models, the diagram of monthly changes of EC using the best models (Figure 1) and the graph of the distribution of computational EC values with the superior studied models in comparison with the observational EC (Figure 2) are given.

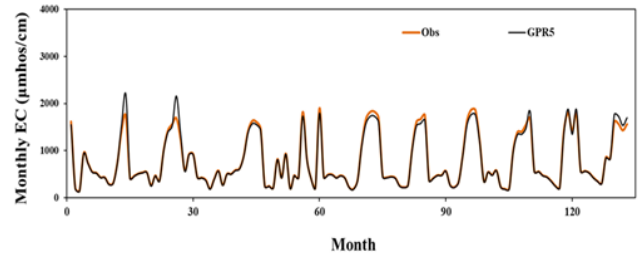


Figure 1. Diagram of monthly changes of EC using the best implemented model

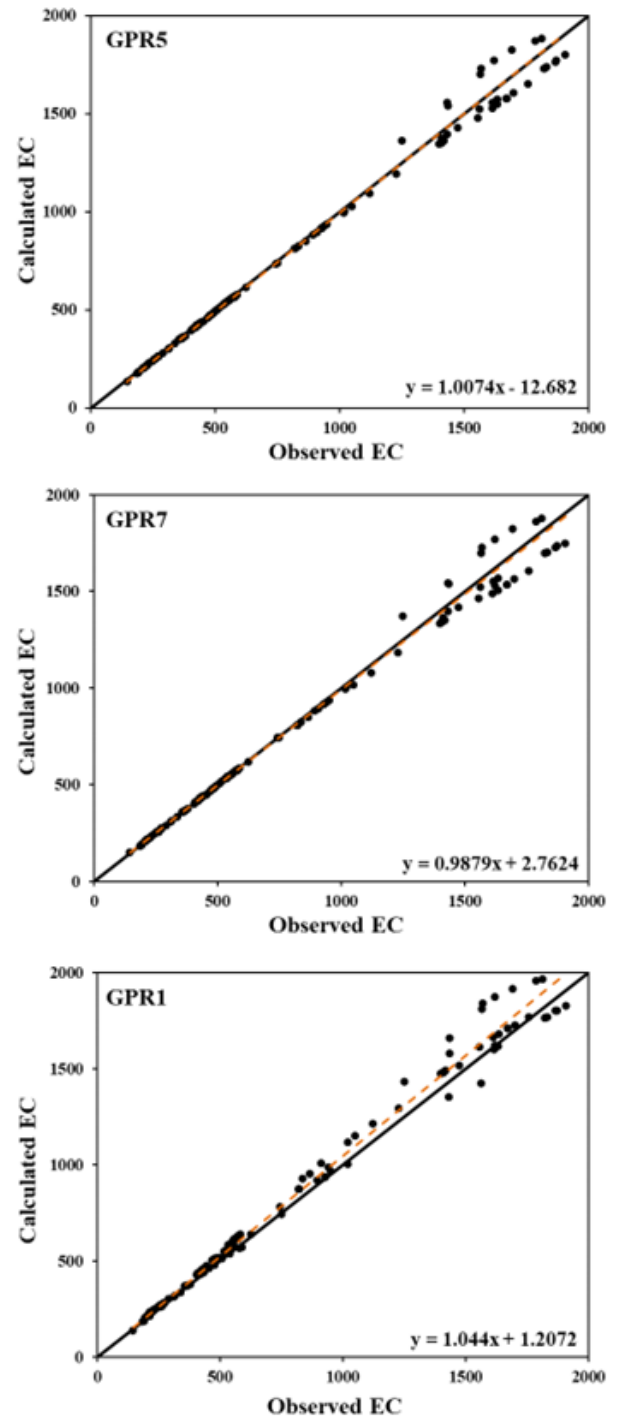


Figure 2. Distribution diagram of computational EC values with the superior studied models in comparison with observational EC

According to Figure 1, the high agreement of the GPR5 model with the observational data can be deduced. In Figure 2, the distribution of points around the bisector axis is lower in superior models which have less error and are closer to the observational values of EC.

5. Conclusion

Pollution and low water quality of rivers directly affect the environment and human life and estimation and determination of quality parameters of river water has a significant role in the management of water resources. Therefore, in the present study, machine learning method, Gaussian process regression was used to model and predict the electrical conductivity of the Mordagh Chay River. Hence, the anions and cations (calcium, magnesium, sodium, chlorine, sulfate) of this river were used as input data over a period of 47 years. The obtained results showed that GPR5 model with scatter index of 0.093 and Wilmott's index of 0.995 had the best results. It was also shown that all implemented models used were successful in estimating the EC value. In general, it is concluded that using GPR method, the EC parameter and water quality in the Mordagh Chay River can be modeled and estimated with low error and desirable accuracy.

References

- Ahmed, A. N., Othman, F. B., Afan, H. A., Ibrahim, R. K., Fai, C. M., Hossain, M. S., Ehteram, M., & Elshafie, A. (2019). Machine learning methods for better water quality prediction. *Journal of Hydrology*, 578, 124084, 1-18.
- Emamgholizadeh, S., Kashi, H., Marofpoor, I., & Zalaghi, E. (2013). Prediction of water quality parameters of Karoon River (Iran) by artificial intelligence-based models. *International Journal of Environmental Science and Technology*, 11 (3), 645-656.
- Haghiabi, A. H., Nasrolahi, A. H., & Parsaie, A. (2018). Water quality prediction using machine learning methods. *Water quality research journal of Canada*, 53(1), 3-13.
- Melesse, A. M., Khosravi, K., Tiefenbacher, J. P., Heddam, S., Kim, S., Mosavi, A., & Thai Pham, B. (2020). River water salinity prediction using hybrid machine learning models. *Water*, 12, 2951, 1-21.
- Pal, M., & Deswal, S. (2010). Modelling pile capacity using Gaussian process regression. *Computer. Geotechnical*, 37, 942-947.
- Ranković, V., Radulović, J., Radojević, I., Ostojić, A., & Čomić, L. (2010). Neural network modeling of dissolved oxygen in the Gruža reservoir, Serbia. *Ecological Modelling*, 221 (8), 1239-1244.
- Shokoohi, M., Tabesh, M., Nazif, S., & Dini, M. (2017). Water quality based multi-objective optimal design of water distribution systems. *Water Resources Management*, 31 (1), 93-108.
- Yang, D., Zhang, X., Pan, R., Wang, Y., & Chen, Z. (2018). A novel Gaussian process regression model for state-of-health estimation of lithium-ion battery using charging curve. *Journal of Power Sources*, 384, 387-395.
- Yesilnacar, M. I., Sahinkaya, E., Naz, M., & Ozkaya, B. (2008). Neural network prediction of nitrate in groundwater of Harran Plain, Turkey. *Environmental Earth Sciences*, 56(1), 19- 25.

4th Intercontinental Geoinformation Days

igd.mersin.edu.tr



Modeling of access and spatial mobility changes associated with floods in the field of transportation and movement of vehicles in areas 3, 6 and 7 of Tehran

Abolfazl Ghanbari¹, Vahid Isazade², Esmail Isazade³, Keyvan Seraj⁴

¹University of Tabriz, Faculty of Planning and Environmental Sciences, Department of Remote Sensing and GIS, Tabriz, Iran

²University of Tehran, Faculty of Geography, Department of Remote Sensing and GIS, Tehran, Iran

³University of Kharazmi, Faculty of Geographical Sciences, Department of Urban planning, Tehran, Iran

⁴University of Kharazmi, Faculty of Engineering, Department of Civil Engineering, Tehran, Iran

Keywords

Flood
AHP
PSO
GIS
Areas 3, 6 and 7 of Tehran

Abstract

The expansion of urbanization and the changing natural conditions of waterways increase the likelihood of flooding in cities. In this paper, we model the flood-sensitive areas for vehicle movement in areas 3, 6 and 7 of Tehran and determine the critical area of the critical tissue against floods using the AHP method, GIS and PSO algorithm. For this purpose, land use, rivers, roads, subways, population density, traffic density, altitude and slope are selected as effective flood parameters in areas 3, 6 and 7 of Tehran and weighting of these parameters in the Expert software environment. Choice done. Then the results were transferred to GIS software environment and a map of flood-sensitive areas in three areas 3, 6 and 7 was prepared for vehicle movement. The results of flood risk in areas 3, 6, and 7 in Tehran show that areas with very low risk are 0.5%, areas with low risk are 6.8% and areas with medium to high risk are 25.7%. This indicates the movement of the vehicle in case of flood risk in the 7th district of Tehran, which is due to population density, building (land use), proximity to the central area to the canal, and the lack of proper drainage. While using the PSO algorithm, districts 6 and 7 of Tehran are flood-prone areas.

1. Introduction

Floods occur when the water level in a place exceeds the allowable limit, and according to researchers and experts, floods are a destructive phenomenon in which water flows from various sources and can be sudden or intentional (Fernandes et al., 2018; Desai et al., 2015; Santos and Reis, 2018; Prăvălie and Costache, 2013; Mishra and Sinha, 2020; Sarkar and Mondal, 2020).

In various parts of the world, natural factors like height, soil tissue, drainage compression, interval, vegetation, and others operate as flood triggers (Azareh et al., 2019; Hosseini et al., 2020). Floods frequently cause a catastrophic hazard to human life as well as a socioeconomic ruin (Hirabayashi et al., 2013; Costache, 2019). Also floods trigger human life and economic loss, as well as the demolition of agricultural products, harm to the ecosystem, and the extension of infectious illnesses (Shafapour et al., 2019; Isazade and Aliégig, 2021).

With the occurrence of floods, many users downstream of the river are exposed to threats and

dangers, and also floods occur due to heavy rainfall in the city due to the impenetrability of urban surfaces these floods often appear as flooding of roads and streets, houses, especially in low-lying areas of the city (Grimaldi et al., 2016; Grimaldi et al., 2018; Khorrami et al., 2019; Li et al., 2018; Li et al., 2016; Wright et al., 2018).

But no one knows when and how floods will occur, the hydraulic properties of urban drainage systems are affected by daily activities (for example, the discharge of solid waste into drainage systems), and the characteristics of surface runoff affect transportation and Urban relocation affects different areas of the city. Therefore, it is very difficult to determine the areas for moving the vehicle when the streets in the city are flooded (Bozorgy, 2007).

Based on the literature, research has been done on this subject, for example, Karahan et al. (2012) Estimated the parameters of the nonlinear masking method using the Hybrid Harmony Search (HHS) algorithm. The proposal was able to more accurately estimate the parameters of the Muskingham nonlinear model.

* Corresponding Author

(a_ghanbari@tabrizu.ac.ir) ORCID ID 0000 – 0001 – 6225 – 0433
(vahidisazade75@gmail.com) ORCID ID 0000 – 0002 – 6348 – 4028
(ismailisazadeh75@gmail.com) ORCID ID 0000 – 0002 – 3825 – 7739
(Keyvanseraj825@gmail.com) ORCID ID 0000 – 0001 – 5629 – 9003

Cite this study

Ghanbari, A., Isazade, V., Isazade, E., & Seraj, K. (2022). Modeling of access and spatial mobility changes associated with floods in the field of transportation and movement of vehicles in areas 3, 6 and 7 of Tehran. 4th Intercontinental Geoinformation Days (IGD), 62-67, Tabriz, Iran

Xu et al. (2017) used the Differential Evolution (DE) algorithm to estimate the parameters of the Musking model nonlinearly, comparing their results with those of HS, PSO, and GA, which were compared by other researchers. The results obtained from DE are not much different from other meta-exploration algorithms and can.

As mentioned previously, storm surges of sufficient strength can flood roadways and render them impassable for several hours to multiple days or weeks (Karim and Mimura, 2008; Kleinosky et al., 2006). The roads are not only interdicted by standing water, they are blocked by deposited debris, or may be destroyed by the force of the storm surge via hydrostatic uplift (Kelman and Spence, 2004). Aside from directly impacting the overall connectivity of the network, in the worst cases, local and regional damage to the streets may accelerate the balkanization process, where large portions of the road network are disconnected from the system at large, creating distinct sub-networks.

Assessing the impact of river floods on the transportation system with emphasis on travel demand is of great importance in Tehran to reduce the risk of floods in the future. In the field of climate change and urbanization, there is already a risk of increasing river floods. However, managing mass evacuations is so complex that it requires the coordination of government agencies, local authorities, and civil society members to ensure clear guidelines. Followed by the population to achieve effective and safe evacuation. When other emergency response processes are not sufficient to protect people's lives, widespread organized evacuation is the ultimate choice. It is a very serious and risky action that often affects many people. In terms of time, money and credit can be costly. In this paper, to process and interpret human and qualitative information along with quantitative information, we used AHP methods and the PSO algorithm to drain floods in areas 3, 6 and 7 of Tehran to move the vehicle. In addition, the AHP method can be consistent with human reasoning and is therefore able to integrate expert experience, which can be important for flood evacuation decisions in different urban areas.

2. Study area

Tehran, the capital of Iran and the center of Tehran province, is geographically situated at 51° 17' to 51° 33' East and 35° 36' to 35° 45' North Figure 1. Tehran is composed of 22 regions, of which regions 3, 6 and 7 are very vulnerable to urban floods due to being mountainous and were selected as the study area in this paper.

3. Method and materials

In this paper, we weighted ground data including land use, rivers, roads, subways, population density, traffic density, altitude and slope using the AHP model from 1 to 9 and gave the most weight to river data. We allocated population, and passages considered the lowest weight for subway data. AHP method was used to make the

weighting of the criteria compatible with the human mind and nature.

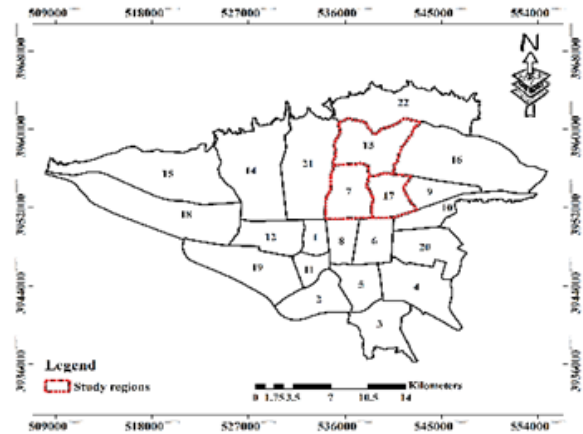


Figure 1. Study area

Because each of the variables had a different effect on the distribution of floods in the streets of districts 3, 6 and 7 of Tehran. To make the weighting of the criteria compatible with the human mind and nature, the AHP method was used in Expert Choice software.

Because each of the variables had a different effect on the distribution of floods in the streets of districts 3, 6 and 7 of Tehran. In the PSO algorithm, we used the values obtained from the AHP model, and our parameters in this algorithm were a distance from the river, a distance from the road, population density, slope and altitude.

In implementing the PSO algorithm, we made a comparison between the PSO method and local search.

3.1. Analytical Hierarchy process (AHP model)

The process of hierarchical analysis is one of the most popular multi-criteria decision-making methods, first invented by Thomas L. Saati in the 1970s. This method is used in a variety of decision-making situations from simple personal decisions to complex economic decisions. The process is based on three basic principles: model structure and judgment judging.

Criteria, inference from priorities Two important issues in this approach are consistency and consistency, and the length of time it takes to make judgments on a complex decision issue, especially as the number of options increases (Dagdeviren et al., 2009).

3.2. Particle swarm optimization (PSO)

The second level headings should be written with left aligned, 10 font size, first character capital, bold. Each paragraph should separate with one line from former paragraph. You can delete this section and write the article text without disturbing the formatting.

For an N-dimensional problem with solution P, the velocity of the i-th particle is calculated from Equation (1) (Kim et al., 2001).

$$x_{id}^{n+1} = x_{id}^n + v_{id}^{n+1} \quad (1)$$

According to experience, if the value of w is large at first and decreases during the optimization process, it gives better results, so equation (2) is used for w (McCarthy, 1983).

$$w_n = w_{max} - \frac{(w_{max} - w_{min}) \times n}{iter_{max}} \quad (2)$$

Where is w_{max} the initial inertia, w_{min} the final inertia $iter_{max}$ is the maximum number of iterations of the algorithm.

4. Discussion and results

4.1. Investigating the effect of effective parameters on the occurrence of floods

Lithology: Lithology is an important variable in the field of potential for urban floods because it affects hydrological and hydrogeological conditions such as soil permeability and surface runoff (Miller et al., 1990; Siahkamari et al., 2018). Lithological map of regions 3, 6 and 7 using 1: 100000 and 1: 250,000 geological maps taken from the Geological Survey of Iran and prepared in the ArcGIS software environment. Most human activities such as urban planning and agricultural land are concentrated in areas 3, 6 and 7.

Soil: This parameter indicates soil quality based on the minimum amount of water infiltration (USDA, 1986). Soils are classified into four groups A, B, C and D in terms of hydrological characteristics. Group A soils have little potential for runoff production and Group D soils have more potential for urban runoff (Gittleman et al., 2017) to prepare a hydrological map of areas 3, 6 and 7 of Tehran from geological maps, land use as well as global data. Soil Hydrology Group from the NASA website was used in the Arc SWAT model.

Land use: According to Garcia Ruiz et al. (2008), land use in each region is very important for hydrological responses in different periods (García-Ruiz et al., 2008). Bakers et al. (2013) in their research showed that changes in land use can increase the likelihood of flooding in the region (Becker et al., 2013). In this article, to prepare the land use map of the region, the Landsat 8 OLI sensor product related to April 2022 was used.

Elevation classes: In general, there is an inverse relationship between flood risk and altitude. The frequency of floods decreases with increasing altitude, so lower altitudes are more sensitive to flooding (Khosravi et al., 2016). The map of the elevation classes of the region was prepared using the digital elevation model (DEM) with a spatial resolution of 12.5 meters on 4 floors.

Slope: A strong positive correlation can be found between the slope of the area and the surface flow velocity (Das et al., 2018). Areas experiencing a sudden drop in slope are likely to encounter large volumes of water, causing severe flooding in these areas (Pradhan et al., 2009). Slope maps of areas 3, 6 and 7 of Tehran were

prepared using digital elevation model data with a spatial resolution of 12.5 meters in the Arc GIS software environment and four floors.

Distance from the river: This parameter is an important geomorphic factor that must be considered to prepare an accurate flood risk map. As the distance increases, the slope. The height increases. Areas far from the river channel are less vulnerable to floods (Das et al., 2018). In this paper, the distance map of waterways was prepared using Euclidean tools in the Arc GIS software and the distance values ranged from 0 to 3145 meters.

4.2. Flood modeling in areas 3, 6 and 7 of Tehran using the AHP method and PSO

Examination of the results obtained from Expert Choice software showed that among the effective factors in flood risk in areas 3, 6 and 7 of Tehran, distance from the river with a weight of 0.185, passages, height of 0.107, land use with a weight of 0.103, slope with a weight of 0.102, respectively. It has the highest weight and impact on the risk of urban floods in areas 3, 6 and 7 of Tehran for vehicle movement. Also, population density with a weight of 0.101, traffic density with a weight of 0.100 and metro with a weight of 0.99 have the least impact on the occurrence of flood damage in areas 3, 6 and 7 of Tehran in the movement of vehicles.

The results of this study with the results of Ahmadi et al. (2011) concluded that among the effective factors in urban floods, the distance from the river has the highest weight and impact, and also the study of Elsheikh et al. (2015) in Malaysia that Soils have the least impact on the occurrence of floods, respectively. Then, the final map of flood risk zoning in areas 3, 6 and 7 of Tehran in the movement of vehicles was prepared by combining different layers and applying the weight of each, which is shown in Figure 2. Figure 2. shows that the route of all canals and canals in areas 3, 6 and 7 are in the range of flood risk with high and very high intensity that Bahminafar et al. (2016) in the city of Shandiz, Mashhad, which was destroyed.

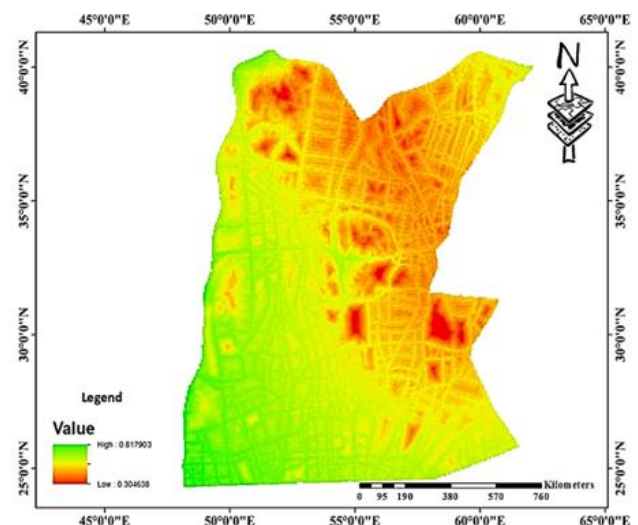


Figure 2. modeling changes in accessibility accompanying occurrence of flood.

Natural routes with urban development as well as the expansion of the city along the riverbed and non-compliance with engineering principles and improper design of structures such as bridges are exacerbating floods in the region. In the PSO algorithm, we made a comparison between the PSO method and local search, which is shown in Figure 3. Identification of flood sensitivity points in areas 3, 6 and 7 of Tehran for moving the device has almost the same performance as the PSO algorithm when flooding roads due to flooding for vehicle movement in areas 3, 6 and 7 of Tehran, while the local PSO search algorithm for areas 3, 6 and 7 has the best high-cost function. It was 0.68%, but the PSO algorithm obtained close to 0.6% using this function Figure 4.

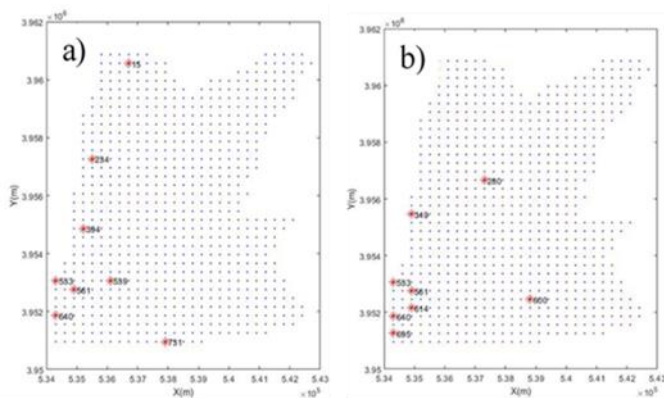


Figure 3. a) Identification of flood sensitive points in areas 3, 6 and 7 of Tehran for vehicle movement with PSO algorithm, b) Identification of flood sensitivity points in areas 3, 6 and 7 of Tehran for vehicle movement by local search of PSO algorithm

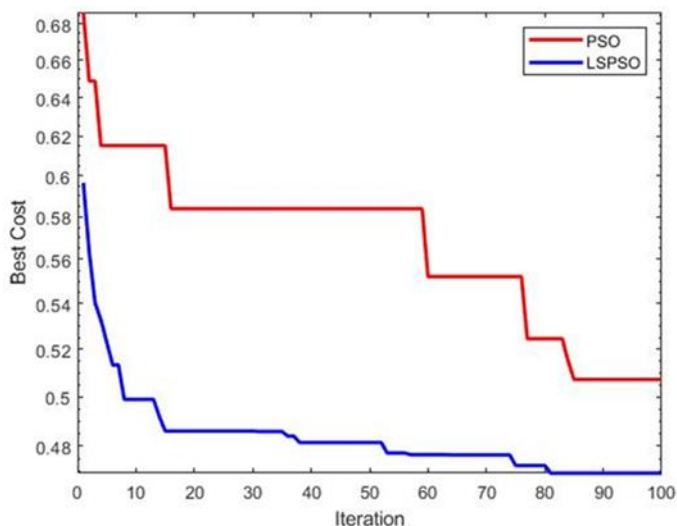


Figure 4. Comparison of PSO algorithm and local search of PSO algorithm

5. Conclusion

In this paper, modeling to identify flood-prone and flood-prone areas for vehicle movement in areas 3, 6 and 7 of Tehran and they are better and more efficient management during floods, flood risk zoning using the AHP model, GIS and PSO algorithm to be examined. By examining the results of Expert Choice software and PSO algorithm, the most effective factors in case of flood risk

for the vehicle can be identified and by prioritizing them, effective solutions can be adopted during urban floods.

The results of flood risk in areas 3, 6 and 7 in Tehran show that areas with very low risk are 0.5%, areas with low risk are 6.8% and areas with medium to high risk are 25.7%. This indicates the movement of the vehicle in case of flood risk in the 7th district of Tehran, which is due to population density, building (land use), proximity to the central area to the canal and the lack of proper drainage. Is. While using the PSO algorithm, districts 6 and 7 of Tehran are flood-prone areas.

References

- Azareh, A., Rafiei Sardooi, E., Choubin, B., Barkhori, S., Shahdadi, A., Adamowski, J., & Shamsirband, S. (2021). Incorporating multi-criteria decision-making and fuzzy-value functions for flood susceptibility assessment. *Geocarto International*, 36(20), 2345-2365. <https://doi.org/10.1080/10106049.2019.1695958>.
- Amirahmadi, A., Behnamifar, A., & Ebrahimi, M. (2012). Microzonation of flood risk in Sabzevar suburb with the aim of sustainable urban development, 5 (16), 17.
- Bahminafar, A., Hadi, G., Sakineh, P., & Mojtaba, A. (2016). Zoning of flood risk sensitive areas using AHP hierarchical analysis model with emphasis on urban geomorphology Case study of Shandiz watershed. Fourth National Conference on Sustainable Development in Geography and Planning, Architecture and Urban Planning.
- Costache, R. (2019). Flash-flood Potential Index mapping using weights of evidence, decision trees models and their novel hybrid integration. *Stochastic Environmental Research and Risk Assessment*, 33 (7), 1375-1402. <https://doi.org/10.1007/s00477-019-01689-9>.
- Desai, B., Maskrey, A., Peduzzi, P., De Bono, A., & Herold, C. (2015). Making Development Sustainable: The Future of Disaster Risk Management, Global Assessment Report on Disaster Risk Reduction. United Nations Office for Disaster Risk Reduction (UNISDR), Geneva, Suisse. <https://archiveouverte.unige.ch/unige:78299>
- Das, S. (2018). Geomorphic characteristics of a bedrock river inferred from drainage quantification, longitudinal profile, knickzone identification and concavity analysis: a DEM-based study. *Arab J. Geosci*, 11 (21), 680. <https://doi.org/10.1007/s12517-018-4039-8>.
- Dağdeviren, M., Yavuz, S., & Kılınc, N. (2009). Weapon selection using the AHP and TOPSIS methods under fuzzy environment. *Expert systems with applications*, 36(4), 8143-8151. <https://doi.org/10.1016/j.eswa.2008.10.016>.
- Elsheikh, R., Ouerghi, S., & Elhag, A. (2015). Flood Risk Map Based on GIS, and Multi Criteria Techniques (Case Study Terengganu Malaysia). *Journal of Geographic Information System*, 7: 348-357. <https://doi.org/10.4236/jgis.2015.74027>.

- Fernandes, O., Murphy, R., Adams, J., & Merrick, D. (2018). Quantitative Data Analysis: CRASAR Small Unmanned Aerial Systems at Hurricane Harvey. In Proceedings of the 2018 IEEE International Symposium on Safety, Security, and Rescue Robotics (SSRR), Philadelphia, PA, USA, 6–8. <https://doi.org/10.1371/journal.pone.0227808>.
- Grimaldi, S., Li, Y., Walker, J. P., & Pauwels, V. R. N. (2018). Effective representation of river geometry in hydraulic flood forecast models. *Water Resour. Res.*, 54 (2), 1031–1057. <https://doi.org/10.1002/2017WR021765>.
- García-Ruiz, J. M., Regüés, D., Alvera, B., Lana-Renault, N., Serrano-Muela, P., Nadal-Romero, E., ... & Arnáez, J. (2008). Plant cover, flood generation and sediment transport at catchment scale: a gradient of experimental catchments in the central Pyrenees. *Journal of Hydrology*, 356(1-2), 245-260. <https://doi.org/10.1016/j.jhydrol.2008.04.013>.
- Gittleman, M., Farmer, C. J., Kremer, P., & McPhearson, T. (2017). Estimating stormwater runoff for community gardens in New York City. *Urban ecosystems*, 20(1), 129-139. <https://doi.org/10.1007/s11252-016-0575-8>.
- Grimaldi, S., Li, Y., Pauwels, V. R., & Walker, J. P. (2016). Remote sensing-derived water extent and level to constrain hydraulic flood forecasting models: opportunities and challenges. *Surv. Geophys.* 37 (5), 977–1034. <https://doi.org/10.1007/s10712-016-9378-y>.
- Hirabayashi, Y., Mahendran, R., Koirala, S., Konoshima, L., Yamazaki, D., Watanabe & Kanae, S. (2013). Global flood risk under climate change. *Nat. Clim. Chang*, 3 (9), 816–821. <https://doi.org/10.1038/nclimate1911>.
- Hosseini, F. S., Choubin, B., Mosavi, A., Nabipour, N., Shamshirband, S., Darabi, H., & Haghighi, A. T. (2020). Flash-flood hazard assessment using ensembles and Bayesian-based machine learning models: application of the simulated annealing feature selection method. *Sci Total Environ*, 711:135161. <https://doi.org/10.1016/j.scitotenv.2019.135161>.
- Isazade, V., & Aliégigy, Z. (2021). Simulation of Flood Prone Areas using Perceptron Neural Network and GIS (Study Area: Zolachai watershed, Salmas City. *Journal watershed management research*, 12 (24) :97-108. <https://doi.org/20.1001.1.22516174.1400.12.24.21.8>.
- Becker's A, Dewals B, Erpicum S, Dujardin S, Detrembleur S, Teller J, ... & Archambeau P (2013). Contribution of land use changes to future flood damage along the river Meuse in the Walloon region. *Natural Hazards and Earth System Sciences*, 13(9), 2301-2318. <https://doi.org/10.5194/nhess-13-2301-2013>.
- Kleinosky, L. R., Yarnal, B., & Fisher, A. (2006). Vulnerability of Hampton Roads, Virginia to storm-surge flooding and sea-level rise. *Nat. Hazards*, 40 (1), 43–70. <https://doi.org/10.1007/s11069-006-0004-z>.
- Khosravi, K., Nohani, E., Maroufinia, E., & Pourghasemi, H. R. (2016). A GIS-based flood susceptibility assessment and its mapping in Iran, a comparison between frequency ratio and weights-of-evidence bivariate statistical models with multi-criteria decision-making technique. *Natural Hazards*, 83(2), 947-987. <https://doi.org/10.1007/s11069-016-2357-2>.
- Karim, M. F., & Mimura, N. (2008). Impacts of climate change and sea-level rise on cyclonic storm surge floods in Bangladesh. *Global Environ. Change*, 18 (3), 490–500. <https://doi.org/10.1016/j.gloenvcha.2008.05.002>.
- Kelman, I., & Spence, R. (2004). An overview of flood actions on buildings. *Eng. Geol.* 73 (3), 297–309. <https://doi.org/10.1016/j.enggeo.2004.01.010>.
- Kim, J. H., Geem, Z. W., & Kim, E. S. (2001). Parameter estimation of the nonlinear muskingum model using harmony search 1. *JAWRA Journal of the American Water Resources Association*, 37(5), 1131-1138. <https://doi.org/10.1111/j.17521688.2001.tb03627.x>.
- Khorrami M, et al (2019). How groundwater level fluctuations and geotechnical properties lead to asymmetric subsidence: a PSInSAR analysis of land deformation over a transit corridor in the Los Angeles Metropolitan Area. *Remote Sens*, 11 (4), 377. <https://doi.org/10.1148/ryai.2019180012>.
- Karahan, H., Gurarslan, G., & Geem, Z. W. (2013). Parameter estimation of the nonlinear Muskingum flood-routing model using a hybrid harmony search algorithm. *Journal of Hydrologic Engineering*, 18(3), 352-360. [https://doi.org/10.1061/\(ASCE\)HE.1943-5584.0000608](https://doi.org/10.1061/(ASCE)HE.1943-5584.0000608).
- Li, Y., Grimaldi, S., Walker, J. P., & Pauwels, V. (2016). Application of remote sensing data to constrain operational rainfall-driven flood forecasting: A review. *Remote Sensing*, 8(6), 456. <https://doi.org/10.3390/rs8060456>.
- Li, Y., Grimaldi, S., Pauwels, V. R. N., & Walker, J. P. (2018). Hydrologic model calibration using remotely sensed soil moisture and discharge measurements: the impact on predictions at gauged and ungauged locations. *J. Hydrol.* 557, 897–909. <https://doi.org/10.1016/j.jhydrol.2018.01.013>.
- Mishra, K., & Sinha, R. (2020). Flood risk assessment in the Kosi megafan using multi-criteria decision analysis: A hydro-geomorphic approach. *Geomorphology* 350, 106861. <https://doi.org/10.1016/j.geomorph.2019.106861>.
- Miller, J. R. (1990). morphometric assessment of lithologic controls on drainage basin evolution in the Crawford upland, South-Central Indiana Jerry R. Miller, Dale F. Ritter, & R. Craig Kochel. *Craig Kochel. Am. J. Sci*, 290, 569-599.
- McCarthy, G. T. (1938). The unit hydrograph and flood routing. In proceedings of Conference of North Atlantic Division, US Army Corps of Engineers, 1938 (pp. 608-609).
- Prăvălie, R., & Costache, R. (2013). The vulnerability of the territorial-administrative units to the hydrological phenomena of risk (flash-floods). Case study, the sub Carpathian sector of Buzau catchment. *Analele Universității din Oradea-Seria Geografie*, 23 (1), 91–

- 98.<http://istgeorelint.uoradea.ro/Reviste/Anale/ale>.
- Pradhan, B. (2010). Flood susceptible mapping and risk area delineation using logistic regression, GIS and remote sensing. *Journal of Spatial Hydrology*, 9(2).
- Santos, P. D., & Reis, E. (2018). Assessment of stream flood susceptibility: a cross-analysis between model results and flood losses. *J. Flood Risk Manage.* 11, S1038–S1050. <https://doi.org/10.1111/jfr3.12290>.
- Sarkar, D., & Mondal, P. (2020). Flood vulnerability mapping using frequency ratio (FR) model: a case study on Kulik river basin, Indo-Bangladesh Barind region. *Appl Water Sci* 10 (1), 17. <https://doi.org/10.1007/s13201-019-1102-x>.
- Shafapour, T. M., Kumar, L., Neamah, J. M., & Shabani, F. (2019). Evaluating the application of the statistical index method in flood susceptibility mapping and its comparison with frequency ratio and logistic regression methods. *Geomatics, Natural Hazards and Risk*, 10(1), 79–101. <https://doi.org/10.1080/19475705.2018.1506509>.
- Size, B. (2007). Sustainable flood management with risk management. Doctoral dissertation, Khajeh Nasir al-Din Tusi University of Technology.
- Siahkamari, S., Haghizadeh, A., Zeinivand, H., Tahmasebipour, N., & Rahmati, O. (2018). Spatial prediction of flood-susceptible areas using frequency ratio and maximum entropy models. *Geocarto international*, 33(9), 927-941.
- USDA, S. C. S. (1986). Urban hydrology for small watersheds, Technical Release, 55, pp. 2–6.
- Wright, A. J., Walker, J. P., & Pauwels, V. R. N. (2018). Identification of hydrologic models, optimized parameters, and rainfall inputs consistent with in situ streamflow and rainfall and remotely sensed soil moisture. *J. Hydrometeorology*, 19 (8), 1305–1320. <https://doi.org/10.1175/jhm-d-17-0240.1>.
- Xu, D. M., Qiu, L., & Chen, S. Y. (2012). Estimation of nonlinear Muskingum model parameter using differential evolution. *Journal of Hydrologic Engineering*, 17(2), 348-353.

4th Intercontinental Geoinformation Days

igd.mersin.edu.tr



Geostatistical-based mapping of topsoil texture in Fluvisols and Vertisols around Lake of Manyas

Fuat Kaya^{*1}, Onur Meşe¹, Levent Başayığit¹¹Isparta University of Applied Sciences, Department of Soil Science and Plant Nutrition, Isparta, Türkiye

Keywords

Geostatistics
Soil particle fractions
Manyas
Kriging
IDW

Abstract

It is critical to understand the spatial distribution of soil particle fractions to create sustainable soil management methods. The spatial distribution of particle fractions has long been studied using geostatistics. Soil particle fractions can be assessed and mapped using a variety of approaches, but selecting the best appropriate method for anywhere has always been a controversial topic in all soil mapping applications. In this study, there is an evaluation of the estimation performance of ordinary kriging (OK) and IDW (Inverse distance weighting) methods for digital mapping of soil particle fractions. It was determined that the clay content of the soil samples was between 24% and 76%, the sand content was between 2% and 69%, and the silt content was between 3% and 44%. The performance of the models was evaluated by the results of the root mean square error (RMSE) and the sum of the fractions. The best results were found using the OK method for Silt (RMSE: 5.36%), while IDW produced more high predictions for Clay (RMSE: 13.80%) and Sand (RMSE: 19.90%). In the control of composition structure, IDW is the method that most closely predicted the relative sum of the three fractions defined as 100%. Creating texture classes in a GIS environment and comparing the efficiency of the produced soil fraction maps is advised.

1. Introduction

The relative proportions of sand, silt, and clay are key soil properties that affect many important physical, chemical, and biological properties of soils (Saurette et al., 2022). Each particle fraction's geographic variation patterns are critical for the creation of sustainable management techniques.

Besides the inverse distance weighting (IDW) method, which is based on Tobler's first law of geography and has no additional requirements regarding spatial distribution and sample size (Zhu et al., 2018), ordinary kriging (OK), a linear geostatistical interpolation technique based on weighting the sums of values at adjacent sampled points are the most widely used spatial modeling applications for the estimation of soil particle fractions (Mousavi et al., 2017).

From fluvial (river terraces) and colluvial sediments to marine and lacustrine deposits containing marl, shale, claystone, and flysch as well as limestone and basalts,

Türkiye's vertisols have a wide range of parent materials. Moreover, these soils are also in spatial proximity to Fluvisols, which are predominantly formed in aquatic sediments associated with rivers and flood plains, and lake (Özsoy and Aksoy, 2007). The delta of the Kocaçay River and the lacustrine deposits of Lake Manyas form the Fluvisol-Vertisol landscape in our study area.

Any particular area's soil particle fractions are controlled by geological and pedological factors, which affect their spatial variability. However, in locations where alluvial processes are in play, this variability can be extremely large.

Soil texture is one of the most well-known types of compositional data. Soil particle fractions that are relevant to our investigation total 100%. In the process of modeling the soil fractions that we are interested in, this has been a topic that has been overlooked.

The accuracy of this compositional structure can be checked by collecting the raster maps of the obtained clay, silt, and sand fractions in the geographic

* Corresponding Author

(fuatkaya@isparta.edu.tr) ORCID ID 0000-0003-0011-9020
(onur_mese@outlook.com) ORCID ID 0000-0002-8300-8328
(leventbasayigit@isparta.edu.tr) ORCID ID 0000-0003-2431-5763

Cite this study

Kaya, F., Meşe, O., & Başayığit, L. (2022). Geostatistical-based mapping of topsoil texture in Fluvisols and Vertisols around Lake of Manyas. 4th Intercontinental Geoinformation Days (IGD), 68-73, Tabriz, Iran

information systems environment. Soil scientists can analyze the maps created using this approach in addition to testing the correctness of the model.

This study aims to compare two different geostatistical methods, which have found widespread application in the literature, in an area dominated by fluvisols and vertisols soil types, in terms of surface soil particle fraction.

2. Method

2.1. Study area

Lake of Manyas is in Northwest Türkiye. The research land was located around of lake and covers an undulating area of approximately 600 km² (N35 Zone UTM, 570000-595000 East, 4440000-4460000 North). The climatic conditions are characterized by an average annual temperature of 15°C and annual precipitation of about 700 mm (TSMS, 2022). From the Precambrian through the Quaternary, the region's geology is divided into distinct strata. It was alluvium transported by rivers that blanketed the area following the Miocene deposition of Neogene limestones and marls (Mater et al., 2003). There are dry agricultural areas in the north of the study area, and extensively irrigated agricultural areas like rice in the south and west, according to CORINE (CLC, 2018). The northern, eastern, and western parts of Lake Manyas are dominated by vertisols, whereas the southern parts are dominated by fluvisols (Aksoy et al., 2010).

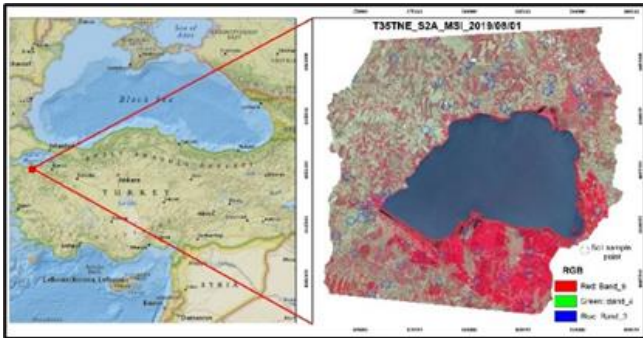


Figure 1. Location of the study area, and the spatial distribution of the soil sampling points overlaid on the Sentinel 2A satellite false-color image

2.2. Soil data

50 soil samples at a depth of 30 cm were taken from the research area between June and August of 2019. The GPS Magellan eXplorist XL was used to record the positions of all sampling points. Fig. 1 depicts the locations of the sampling points. The hydrometer method (Bouyoucos, 1962) was used to determine the distribution of the soil particles fractions were defined based on the international soil particle size classification of sand (0.05 to 2 mm), silt (0.002 to 0.05 mm), and clay (<0.002 mm).

2.3. Geostatistical analysis

Geostatistical analyzes were carried out with the features measured at 50 points of the studied region. Maximum and minimum statistics, mean, standard

deviation, skewness, and kurtosis were determined to examine the frequency distribution and determine the descriptive statistics for each fraction (Table 1). Two different geostatistical approaches are presented under separate headings.

2.3.1. Inverse distance weighting (IDW)

The IDW model uses the inverse distance relationship with the following equation to calculate the weights of the values. The IDW interpolation of a value a_j for a given location j is computed as (Emmendorfer and Dimuro 2020):

$$\hat{a}_j^{IDW} = \sum_{i=1}^n w_{i,j} \hat{a}_i \quad (1)$$

where each \hat{a}_i , $i = 1, \dots, n$ is a data point available at a location i . The weights of $w_{i,j}$, for each data point are given as:

$$w_{i,j} = \frac{d_{i,j}^{-\alpha}}{\sum_{k=1}^n d_{i,k}^{-\alpha}} \quad (2)$$

where $d_{i,j}$ is the Euclidean distance between a data point available at location i and the unknown data at location j ; n is the number of data points available; α means the power, is a control parameter. The ArcGIS 10.8-Geostatistical Wizard-IDW tool was used to generate distribution maps and model results for geographic coordinated soil particle fractions (ESRI, 2021).

2.3.2. Ordinary Kriging (OK)

To examine the spatial variations of the soil particle fractions, the experimental semivariogram was calculated and the spatial structure of the data was investigated in the studied region. Theoretical models were fitted to these.

The spatial variation structure, the Semivariogram, is determined using the following equation;

$$\gamma(h) = \frac{1}{2n(h)} \sum_{i=1}^n [Z(X_i) - Z(X_i + h)]^2 \quad (3)$$

where n is the number of pairs of the sample separated by the distance h and $Z(X_i)$ the value of sampled point in i th point ($i = 1, 2, 3, \dots, n$). Each of the three fractions studied had a different best model (in terms of RMSE) (Fig. 2, Table 3).

To estimate soil particle fraction at unsampled points

$$Z(\mu) = \sum_{i=1}^n \lambda_i Z(\mu_i) \quad (4)$$

where $Z(\mu)$ is the predicted value of unsampled point; $Z(\mu_i)$ is the i th point by measured value; λ_i is the i th point by undefined weight for the estimated value; n is the number of sampled values.

The ArcGIS 10.8-Geostatistical Wizard-Ordinary Kriging tool was used to generate distribution maps and model results for geographic coordinated soil particle fractions (ESRI, 2021).

2.4. Summation of the predicted soil particle size fractions

Clay, silt, and sand all make up 100% of the soil texture composition. Using such data, the predicted components must amount to 100% over the entire model (Amirian-Chakan et al., 2019). Raster maps of the soil particle fraction produced by two different approaches were collected with the ArcGIS 10.8-Arctoolbox-Spatial Analyst-Map Algebra-Raster calculator tool (ESRI, 2021).

3. Results

3.1. Descriptive statistics of soil particle fractions

Table 1 was listed the descriptive statistics results of the analyzed datasets. In the study area, the highest average was determined in Clay with 48.2%, while the lowest was in Silt with 19.8%.

Table 1. Descriptive statistics of soil particle fractions. Abbreviations: SD: Standard deviation, CV: Coefficient of Variation (%). Min.: Minimum, Max.: Maximum, Ske.: Skewness, Kur.: Kurtosis

	Mean	SD	CV	Min.	Max.	Ske.	Kur.
Clay	48.2	13.2	27.4	24.1	75.6	0.0	-0.9
Silt	19.8	6.7	33.8	3.00	44.2	1.5	5.0
Sand	31.9	13.5	42.4	2.60	68.6	0.3	0.0

The highest coefficient of variation (CV) in the study area was found in the sand with 42.4%. The skewness coefficients were quite close to 0 for clay and sand, while positive skewness values were present for Silt. Meanwhile, the kurtosis coefficient for silt was quite high compared to the other two fractions (Table 1).

3.2. Variogram analysis and spatial autocorrelation

Figure 2 depicts the experimental variograms of clay, silt, and sand content, together with the fitted different models.

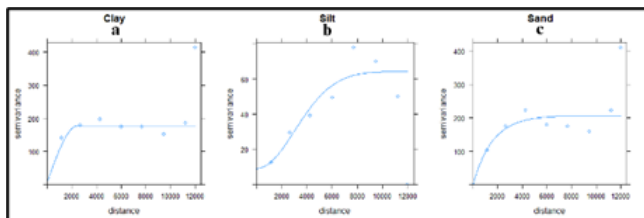


Figure 2. Variograms and fitted models.

The tested models (Spherical, Gaussian, Exponential) were modeled with an experimental variogram of soil

fractions. The nugget: sill ratio (NSR) represents a contribution of the nugget to the overall spatial structure of the variogram and it can be calculated as $NSR = C_0/(C_0+C)$. The NSR indicates how geographically dependent or autocorrelated the measured attribute is. Ratios below 0.25 indicate a strong spatial correlation, while ratios above 0.75 indicate a weak spatial correlation, with a median value between 0.25 and 0.75 suggesting moderate spatial dependency (Adhikari et al. 2013). The NSR ranged from 0.0 to 0.12 within the three fractions, showing strong spatial dependence (Table 2).

Table 2. Semivariogram model properties for soil particle fractions.

Soil particle fractions	Model	Nugget (c ₀)	Sill (c ₀ +c)	Nugget /Sill Ratio	Range (m)
Clay	Sph.	8.74	177.2	0.04	2425
Silt	Gau.	6.48	51.9	0.12	5450
Sand	Exp.	0.0	188.9	0.0	3358

3.3. Model performance and predicted maps

Table 3 displays the results of modeling soil particle fractions with IDW and OK geostatistical methods. The fitted variograms for the soil particle fractions were spherical for Clay, gaussian for silt, and exponential for sand (Fig. 2 and Tablo 3). Zeraatpisheh et al. (2022) found predominantly spherical and exponential mathematical models in the modeling process of soil fractions. While for Silt the lowest root mean square error values were obtained from the OK-Gaussian model, Clay and Sand, it was obtained from the model produced as a result of setting the power parameter of IDW to 1 (Table 3).

Table 3. Comparisons of the accuracy of IDW and OK models for cross-validation results of soil particle fractions (Root mean square value)

Fractions Model /Parameter	OK			IDW	
	Sph.	Exp.	Gau.	1	2
Clay	14.47	14.54	14.63	13.80	14.68
Silt	5.54	5.71	5.36	6.16	6.06
Sand	14.54	14.31	14.37	13.94	14.54

Continuous maps for each soil fraction in the study area were shown in Fig. 3. Both different methods produced similar distributions for clay and silt. The southeast of the study area was characterized by higher silt and lower sand contents than the overall area (Fig. 3-a-d). This was a considerable difference in the distribution of the sand fraction between the two models. Considering the minimum and maximum values in the data set for Sand (Table 1), it is seen that the OK method cannot exemplify the minimum values of Sand (Fig.4-f).

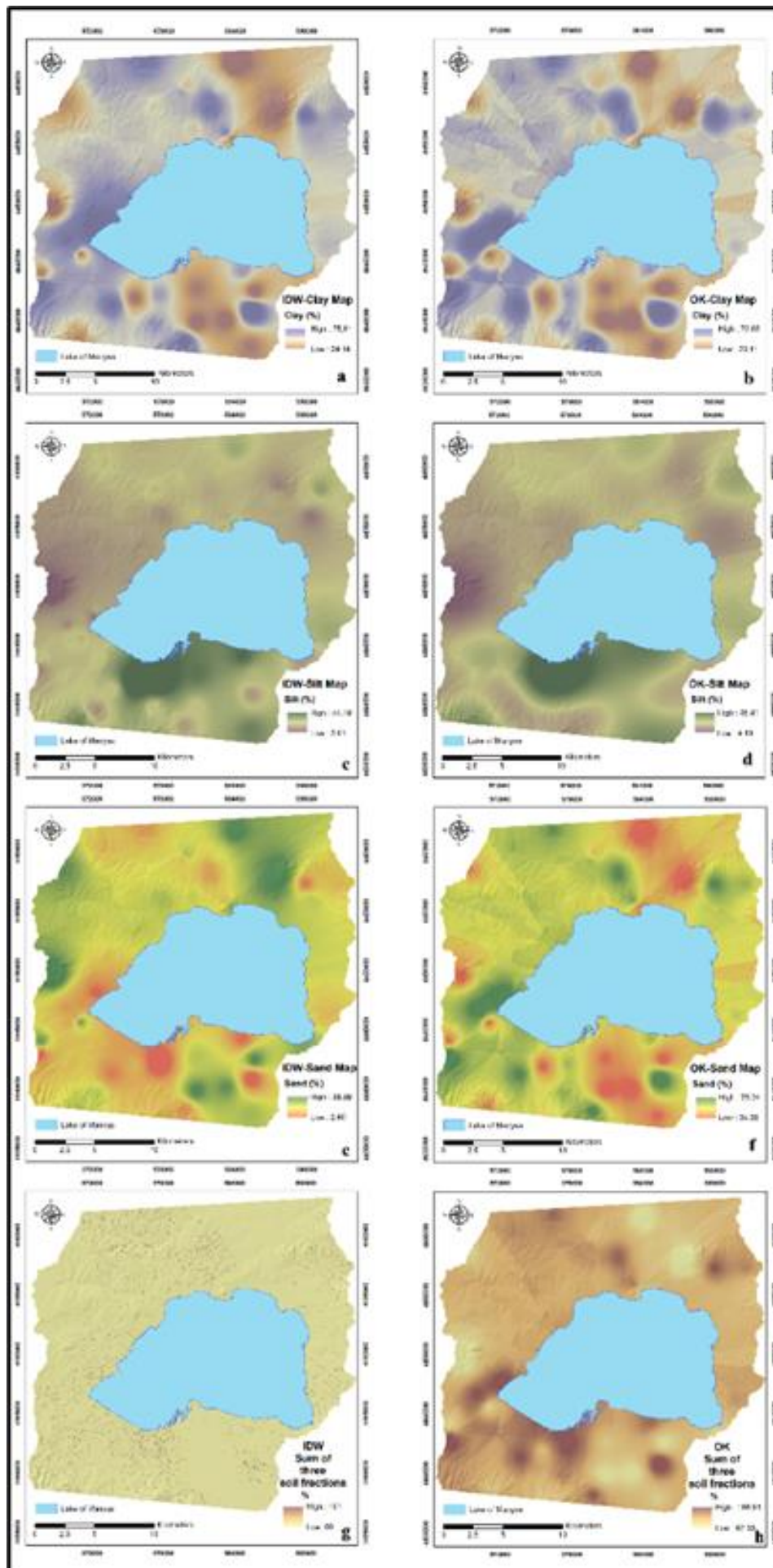


Figure 3. Map of predicted soil particle fractions

4. Discussion

Spatial modeling of each of the soil particle fractions is a popular approach because of the particular importance of each of the fractions (Saurette et al., 2022). Geostatistical models based on distinct mathematical foundations shows to have similar model accuracy (Table 3). Significant differences were determined for Sand in particular for the produced spatial maps. Here, it should be well known for IDW that the maximum and minimum of estimated values from IDW are limited to the extreme data points in the data set (Emmendorfer and Dimuro, 2020). When compared to OK, this IDW made no significant change in forecast maps for Silt and Clay, while it made a substantial difference for Sand. IDW was found to be more successful in reflecting the minimum and maximum values of the sand fraction better in the fluvisols areas concentrated in the southeast of the study area. OK and IDW produced similar distribution maps and minimum and maximum values for silt. Again for Clay, OK and IDW produced similar minimum and maximum values, while OK produced sharp map boundaries. (Fig. 3-b,f). The sharp boundaries that OK produces based on mathematical calculations may not have a counterpart in the field. The fact that OK produces such maps, especially for Sand and Clay, may be related to the decrease in model accuracy values (Table 3). Sharply demarcated maps may not represent the mapping unit boundary approach in soil maps. Soil texture, which is well-known for its compositional structure, must be evaluated to see if these three functions are all equal to 100% totally. Considering the maps produced as a result of collecting the estimated 3 fractions in a raster environment, those regions that have a total of more than 100 and less than 100 are concentrated in the research area's southern and southeasterly sections (Fig. 3-h). These regions are characterized by alluvial deposits. In this regard, it is recommended to carry out spatial mapping applications by making precise and more sampling in these regions, specific to the study area. High changes in soil fraction at short distances are characteristic of alluvial deposition zones (Basayigit and Senol, 2008). Similarly, in a study area that developed mainly on Quaternary aged alluvial deposits, the totals of the spatially estimated soil fraction maps with different approaches appeared in the range of 96% to 104 (Amirian-Chakan et al., 2019). The summing values for IDW range from 99 to 101%, whereas the summing values for OK range from 62.39 to 166.91% based on our findings (Fig. 3 g-h). The mathematical basis of the OK method for each fraction may have caused this difference. Using GIS tools, it is possible to create texture classes and compare the resulting soil particle fractions (Saurette et al., 2022).

3. Conclusion

The results of our study demonstrate the effectiveness of 2 different well-known geostatistics (OK and IDW) applications to study and analyze the spatial behavior of soil texture content in an area with high variability over short distances. To evaluate the uncertainty of the maps obtained, the collection of the

fractions we suggest and the control due to the compositional structure should be expressed as a significant issue. For soil surveyors, the geostatistical-based model must resemble natural classes that will form the distribution map of soil texture, as well as statistical success. Using other data layers such as digital data to represent the formation of soils (topographic parameters, parent material, organism) and other information that may affect the spatial distribution of soil texture in fluvisols and vertisols, and using advanced statistical learning algorithms suggest that studies be carried out by making more analysis in a way that can reveal non-linear relationships.

References

- Adhikari, K., Kheir, R. B., Greve, M. B., Greve, M. H. (2013). Comparing kriging and regression approaches for mapping soil clay content in a diverse Danish landscape. *Soil science*, 178(9), 505-517. <https://doi.org/10.1097/SS.0000000000000013>
- Aksoy, E., Panagos, P., Montanarella, L., Jones, A. (2010). Integration of the soil database of Turkey into European soil database 1: 1.000. 000. European Commission JRC Research Report, EUR 24295EN. Italy.
- Amirian-Chakan, A., Minasny, B., Taghizadeh-Mehrjardi, R., Akbarifazli, R., Darvishpasand, Z., Khordehbin, S. (2019). Some practical aspects of predicting texture data in digital soil mapping. *Soil and Tillage Research*, 194, 104289. <https://doi.org/10.1016/j.still.2019.06.006>
- Basayigit, L., Senol, S. (2008): Comparison of soil maps with different scales and details belonging to the same area. *Soil and Water Research*, 3, 31-39.
- Bouyoucos, G. J. (1962). Hydrometer method improved for making particle size analyses of soils. *Agronomy Journal*, 54, 464-465. <https://doi.org/10.2134/agronj1962.00021962005400050028x>
- CLC (2018). Corine land cover class 2018 V 2.0 data. (Accessed 04 October 2021).
- Emmendorfer, L. R., & Dimuro, G. P. (2020). A Novel Formulation for Inverse Distance Weighting from Weighted Linear Regression. *Lecture Notes in Computer Science*. Springer, Cham. https://doi.org/10.1007/978-3-030-50417-5_43
- ESRI, (2021). ArcGIS user's guide, <http://www.esri.com>.
- Mater, B., Turoğlu, H., Uludağ, M., Cürebal, İ., Yıldırım, C. (2003). Uluabat-Manyas Gölleri ve Yakın Çevresinin Jeomorfolojik Gelişim Modellemesi. *Türkiye Kuvaterneri Çalıştayı IV*, 180-186, Türkiye.
- Mousavi, S. R., Sarmadian, F., Dehghani, S., Sadikhani, M. R., Taati, A. (2017). Evaluating inverse distance weighting and kriging methods in estimation of some physical and chemical properties of soil in Qazvin Plain. *Eurasian Journal of Soil Science*, 6(4), 327-336. <https://doi.org/10.18393/ejss.311210>
- Özsoy, G., Aksoy, E. (2007). Characterization, classification and agricultural usage of vertisols developed on neogen aged calcareous marl parent materials. *Journal of Biological & Environmental Sciences*, 1(1), 5-10.

- Saurette, D. D. (2022). Comparing direct and indirect approaches to predicting soil texture class. *Canadian Journal of Soil Science*, <https://doi.org/10.1139/CJSS-2022-0040>
- TSMS (2022). Turkish State Meteorological Service.
- Zeraatpisheh, M., Bottega, E. L., Bakhshandeh, E., Owliaie, H. R., Taghizadeh-Mehrjardi, R., Kerry, R., & Xu, M. (2022). Spatial variability of soil quality within management zones: Homogeneity and purity of delineated zones. *CATENA*, 209, 105835. <https://doi.org/10.1016/j.catena.2021.105835>
- Zhu, A., Lu, G., Liu, J., Qin, C., & Zhou, C. (2018). Spatial prediction based on Third Law of Geography. *Annals of GIS*, 24(4), 225–240. <https://doi.org/10.1080/19475683.2018.1534890>



4th Intercontinental Geoinformation Days

igd.mersin.edu.tr



Predicting the monthly flow of the Kaleybar Chay River based on M5 model tree

Kambiz Falsafian ^{*1}

¹University of Tabriz, Marand Technical College, Tabriz, Iran

Keywords

River flow
Statistical indicators
M5 model tree

Abstract

Due to its importance in the designing of water projects, flood investigation and estimation has always been one of the key issues in the field of hydrology and researchers have tried to estimate the river flow more accurately by using different methods. In this regard and in the present study, the monthly discharge values of Kaleybar Chay River were predicted using machine learning method of M5 model tree. Based on this, time series data of discharge and precipitation in monthly delays are used as input parameters of the models and the results are evaluated using the statistical indicators of correlation coefficient, root mean square error and mean absolute error. Finally, the values obtained from the M5 models showed that among the studied models, M5(6) model with the root mean square error of 0.968 and the mean absolute error of 0.625, had the highest correlation with the observed values and recorded the most accurate results in this study. It was also found that most of the M5 models had a successful performance in estimating the monthly flow in the study area.

1. Introduction

Control and use of surface water have great important especially in areas with water shortage problems and seasonal rivers. Accurate estimation of river flow is necessary for planning and managing water resources and organizing the river. It is also important to predict the flow rates of the river from various aspects such as the optimal operation of dam reservoirs. In addition, river flow is one of the influential factors in the phenomena of drought, floods, sources of drinking water supply and in general issues related to water systems. In recent years, researchers have used various methods to estimate river discharge values, among which, machine learning models have shown better performance due to high accuracy and the need for less cost and time. Among the studies conducted in this field, the following can be mentioned:

Cannas et al. (2005) estimated the monthly flow of the Tirso Basin River in Sardinia, Italy, using a combined neural network model and wavelet analysis, and investigated the effect of data preprocessing on the neural network using discrete and continuous wavelet transforms. The results showed that the integrated model is more accurate than the neural network model.

Huang et al. (2014) predicted monthly discharge values in Wei River Basin using a specific hybrid model of empirical mode decomposition-support vector machine (EMD-SVM). Comparison of the results showed that in all studied stations, the model performed better than the ANN and SVM methods. In another study, Nouri and Kalin (2016) simulated daily river flow rates in Atlanta, USA. They first used the SWAT model to simulate daily flow and used the results obtained from this model as input to the artificial neural network method. Finally, it was shown that the combination of semi-distributed models with artificial neural network method improves the accuracy of river flow prediction in the study area.

The M5 model tree is also one of the machine learning methods that has been used in recent years to predict many hydrological phenomena. One of them is the study of Sattari et al. (2013). They evaluated the ability of the M5 model tree to predict the daily discharge of the Sohu Stream in Ankara, Turkey. Sattari et al. (2013) compared the results using statistical indicators with the support vector machine method and showed that in general the M5 model had a better performance. Also, using M5 model tree, Zahiri and Azamathulla (2014) estimated river flow, Singh et al. (2010) estimated the average annual flood, Shaghaghi et al. (2019) predicted the

* Corresponding Author

^{*}(kfalsafian@tabrizu.ac.ir) ORCID ID 0000-0002-1567-7976

Cite this study

Falsafian, K. (2022). Predicting the monthly flow of the Kaleybar Chay River based on M5 model tree. 4th Intercontinental Geoinformation Days (IGD), 74-77, Tabriz, Iran

dimensions of the river regime and Unes et al. (2020) modeled river flow.

According to the studies conducted in the field of using machine learning methods in modeling hydrological phenomena, the high importance of estimating river discharge values by applying the mentioned techniques can be inferred. Therefore, the purpose of this study is to predict the monthly discharge values of Kaleybar Chay River in Kaleybar station applying M5 model tree and using discharge (in two-time delays of one and two months) and precipitation (without time delay and time delay of one Month) data.

2. Method

2.1. Study area

Kaleybar Chay Basin with an area of 144960 hectares is located in northwestern Iran and north of East Azerbaijan province. This basin is considered as a subset of Aras basin and is located between the geographical coordinates of 46° 40' to 47° 13' east longitude and 38° 39' to 39° 09' north latitude. Kaleybar Chay River is the most important river of Kaleybar Chay Basin and one of the permanent rivers of East Azerbaijan province. This river originates from the heights of Qara Dag and the main branch of this river passes through Kaleybar and finally flows into Aras River. In the present study, the flow and precipitation data of Kaleybar Chay River in Kaleybar station from 2002 to 2015 have been used on a monthly scale, so that the flow data with two-time delays of one and two months and the precipitation data has been applied with a delay of one month and without a time delay.

In this study, using different combinations of time series of discharge and precipitation data as input of M5 model tree, river discharge values were estimated. Table 1 shows the different combinations of input parameters of the models.

Table 1. Different combinations of input parameters of the studied models

Combination Number	Input Parameters	Output Parameter
1	P _t	Q _t
2	Q _{t-1}	Q _t
3	P _t , Q _{t-1}	Q _t
4	P _{t-1} , Q _{t-1}	Q _t
5	P _{t-1} , P _t , Q _{t-1}	Q _t
6	P _{t-1} , P _t , Q _{t-1} , Q _{t-2}	Q _t

2.1. M5 model tree

The M5 model tree (Quinlan 1992) is a subset of machine learning and data mining methods. Data mining refers to the process of searching for and discovering various models, summarizing, and obtaining values from a set of known values. Data mining methods are designed for large data sets with many variables, so they are different from older statistical methods designed for small data sets with small variables. Decision tree-based methods as one of the most well-known data mining

techniques, predict or classify the objective property as output in the form of a model with a tree structure using input data. M5 model is a tree model for predicting continuous numerical traits in which linear regression functions are displayed on the leaves of this tree (Sattari et al. 2013), which in recent years has made a significant change in classification and predictions issues. Decision trees are a useful solution to many classification problems that use complex databases and complex or erroneous information. Decision trees, which have predictive and descriptive properties, are the most widely used classification models because of their easy installation, interpretation, and integration into database systems, and better reliability. The division criterion is based on the standard deviation of the subset values. The mathematical formula for calculating the standard deviation reduction (SDR) is as follows:

$$SDR = SD(T) - \sum \frac{T_i}{T} \times SD(T_i) \quad (1)$$

In Equation (1), T represents a group of samples that are bound, T_i represents a subset of samples that is the product of a potential group, and SD represents a standard deviation. After examining all possible structures, a structure is selected that has the maximum expected error reduction. This division process often produces an excellent tree-like structure that leads to an over-appropriate structure (Unes et al. 2020).

2.2. Criteria for evaluating the accuracy of models

The error values between the applied models and the observational data were evaluated by correlation coefficient (R), root mean square error (RMSE) and mean absolute error (MAE) using the Equations 2 to 4.

$$R = \frac{(\sum_{i=1}^n x_i y_i - \frac{1}{n} \sum_{i=1}^n x_i \sum_{i=1}^n y_i)}{(\sum_{i=1}^n x_i^2 - \frac{1}{n} (\sum_{i=1}^n x_i)^2)(\sum_{i=1}^n y_i^2 - \frac{1}{n} (\sum_{i=1}^n y_i)^2)} \quad (2)$$

$$RMSE = \sqrt{\frac{1}{n} \sum_{i=1}^n (x_i - y_i)^2} \quad (3)$$

$$MAE = \frac{1}{n} \sum_{i=1}^n |x_i - y_i| \quad (4)$$

In Equations 2 to 4, x_i and y_i are the observed and predicted monthly flow rates, respectively, and n is the number of observations.

3. Results

In this study, using time series of discharge and precipitation data and using M5 model tree, the monthly discharge values of Kaleybar Chay River in Kaleybar station were estimated. Then the results of the mentioned methods were compared by statistical indices

of correlation coefficient, root mean square error and mean absolute error and the most appropriate and best model for predicting river discharge in the study area was determined and introduced. Table 2 shows the values of statistical indicators for different models with different combinations of input parameters.

Table 2. Statistical indicators of different flow estimation models

Model	R	RMSE	MAE
M5(1)	0.437	1.38	0.815
M5(2)	0.678	1.1	0.693
M5(3)	0.708	1.06	0.675
M5(4)	0.678	1.1	0.693
M5(5)	0.708	1.06	0.675
M5(6)	0.77	0.968	0.625

Figure 1 shows the bar graph of statistical indicators of all studied models. Figure 2 demonstrates the temporal changes of river flow using the best studied models. Also figure 3 shows the distribution diagram of discharge values calculated by the superior models compared to the observed discharge.

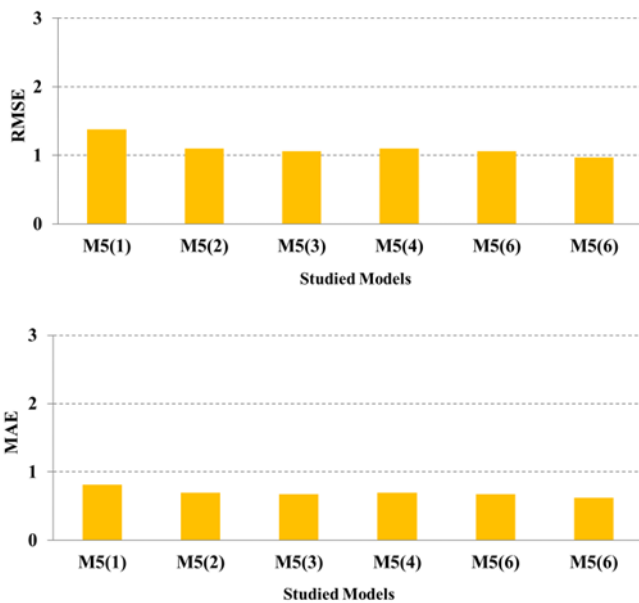


Figure 1. Bar graph of statistical indicators for all studied models

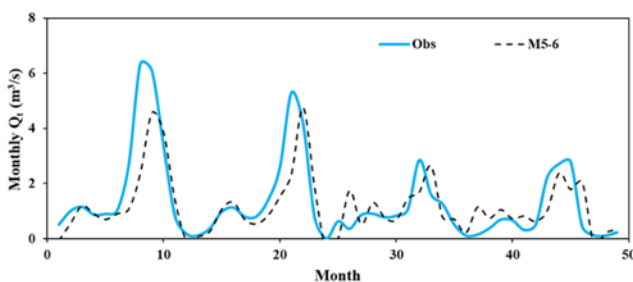


Figure 2. Diagram of temporal changes in river flow using the best studied models

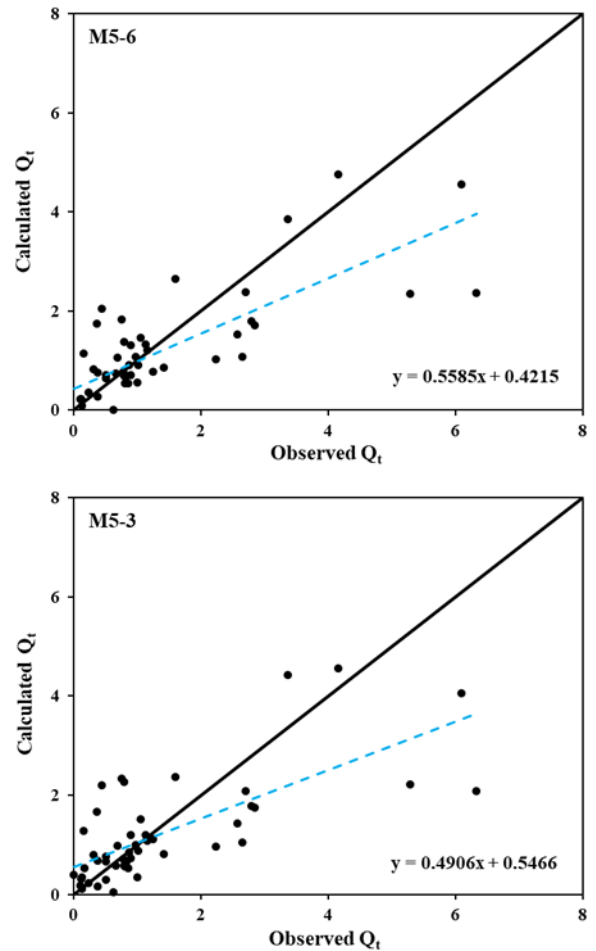


Figure 3. Distribution diagram of discharge values calculated by the superior models in comparison with the observed discharge

4. Discussion

According to the obtained results (Table 2), M5(6) model with correlation coefficient of 0.77, root mean square error of 0.968 and mean of absolute error of 0.625 had the best performance. M5(3) and M5(5) models were in the next position with the same performance and correlation coefficient of 0.708, root mean square error of 1.06 and mean absolute error of 0.675 with input parameters of P_t , Q_{t-1} and P_{t-1} , P_t , Q_{t-1} , respectively. In general, all implemented models provided acceptable and good performance. However, by comparing the results, it was found that except for the first model, other models can be used to estimate the flow rate with the desired accuracy in the Kaleybar Chay River.

According to Figure 1, the mentioned trend about the high accuracy of M5 models can also be concluded from this figure. Figure 2 also shows the high agreement of the superior models with the observational data. Similarly, Figure 3 displays the lower distribution of points of the superior models around the axis of the half-instrument.

5. Conclusion

Estimating the flow rate of rivers in each region is one of the most important and fundamental issues in planning and managing water resources. Therefore, in this study, the discharge values of Kaleybar Chay River

were modeled on a monthly scale. Accordingly, the M5 model tree technique was used and the time series of precipitation and discharge data were utilized as input data of this model in different combinations. The results showed that most of the studied models had acceptable and good performance so that M5(6) model with the root mean square error of 0.968 and the mean of absolute error of 0.625 estimated the most accurate values. In general, it can be concluded that using the superior models of this research, the flow rate of Kaleybar Chay River can be estimated with good accuracy.

References

- Cannas, B. & Fanni, A. & Sias, G. & Tronci, S. and Zedda, M.K. (2005), River flow forecasting using neural networks and wavelet analysis. *Geophysical Research Abstracts*, 7, 08651, 1-11.
- Huang, S., Chang, J., Huang, Q., & Chen, Y. (2014). Monthly streamflow prediction using modified EMD-based support vector machine. *Journal of Hydrology*, 511, 764-775.
- Noori, N., & Kalin, L. (2016). Coupling SWAT and ANN models for enhanced daily streamflow prediction. *Journal of Hydrology*, 533, 141-151.
- Quinlan, J. R. (1992). *Learning with continuous classes*. Fifth Australian Joint Conference on Artificial Intelligence, 343-348, World Scientific. Singapore.
- Sattari, M. T., Pal, M., Apaydin, H., & Ozturk, F. (2013). M5 model tree application in daily river flow forecasting in Sohu Stream, Turkey. *Water Resources*, 40, 233-242.
- Shaghaghi, S., Bonakdari, H., Gholami, A., Kisi, O., Binns, A., & Gharabaghi, B. (2019). Predicting the geometry of regime rivers using M5 model tree, multivariate adaptive regression splines and least square support vector regression methods. *International Journal of River Basin Management*, 17, 333-352.
- Singh, K. K., Pal, M., & Singh, V. P. (2010). Estimation of mean annual flood in Indian catchments using backpropagation neural network and M5 model tree. *Water Resources Management*, 24, 2007-2019.
- Unes, F., Demirci, M., Zelenakova, M., Calisici, M., Tasar, B., Vranay, F., & Ziya Kaya, Y. (2020). River Flow Estimation Using Artificial Intelligence and Fuzzy Techniques. *Water*, 12(2427), 1-21.
- Zahiri, A., & Azamathulla, H. M. (2014). Comparison between linear genetic programming and M5 tree models to predict flow discharge in compound channels. *Neural Computing and Applications*, 24, 413-420.



4th Intercontinental Geoinformation Days

igd.mersin.edu.tr



Classification of surface water quality using data-driven methods

Sahar Javidan ¹, Shokouh Mohsenzadeh ¹, Mohammad Taghi Sattari ^{*1}

¹University of Tabriz, Faculty of Agriculture, Water Engineering Department, Tabriz, Iran

Keywords

Bagging Method
Total Dissolved Solid
Water Quality Index

Abstract

Access to clean and quality water resources has been one of the main concerns of human beings for a long time. Therefore, determining the quality of water for various uses, including irrigation is very important. River pollution is one of the most important problems in the world today, especially in developing countries. In the present study, using data related to water quality parameters of Bagh Kalayeh hydrometric station in the 23-year statistical period, first the WQI index was calculated, then using data mining technique, factors affecting water quality were determined. Finally, the results of data mining methods were compared with the results obtained from the qualitative index. Quantitative results of the models were evaluated by Correlation Coefficient (R), Root Mean Square Error (RMSE), Mean Absolute Error (MAE) and qualitative results of the models were evaluated by Kappa, RMSE and MAE statistics. The results showed that in quantitative modeling, scenario 5 including TH, K, SO₄, TDS and EC and in qualitative modeling, scenario 3 including TH, K and SO₄ were selected as the superior scenario.

1. Introduction

Surface and groundwater pollution is one of the most important problems in the world and environmental concerns. In recent decades, due to rapid population growth, water needs and consequently pollution load to water sources have increased. There are several methods for classifying groundwater and surface water quality according to the type of consumption, one of the most widely used methods is the use of quality indicators. Due to the lack of facilities in all water quality monitoring stations and the need to save time and money, the use of alternative methods such as modern data mining methods can be a good way to predict and classify water quality.

Sattari et al. (2017) used data mining methods to predict surface water quality. They concluded that the tree decision model using the four parameters of Electrical Conductivity (EC), pH, Sodium Adsorption Ratio (SAR) and Sodium (Na) is able to classify water quality very accurately.

Babbar and Babbar (2017) predicted the river Water Quality Index using data mining techniques. They found that decision tree classifiers and Support Vector

Machines were the best predictive models in determining water quality.

Gakii and Jepkoech (2019) used the decision tree model to classify and analyze water quality in Kenya. They introduced the J48 and Decision Stump decision trees as the most accurate and least accurate models, respectively. They found that analysis of water alkalinity, pH level and Electrical Conductivity could play an important role in assessing water quality.

Othman et al. (2020) predicted the river Water Quality Index by considering the minimum number of input variables. The results showed the exceptional ability of the artificial neural network model to calculate WQI. They also introduced Dissolved Oxygen (DO) as the most effective parameter in determining water quality.

The aim of this study is to calculate the WQI index using data related to water quality parameters of Bagh Kalayeh station in Qazvin province and then to use data mining techniques to determine the factors affecting water quality.

2. Method

Qazvin province is located in the northwestern part of Iran and its area is about 15820 km². Bagh Kalayeh is

* Corresponding Author

(javidansahar77115@gmail.com) ORCID ID 0000 – 0001 – 6739 – 8242
(Shkmsn2000@gmail.com) ORCID ID 0000 – 0003 – 3982 – 3082
(*mtsattar@gmail.com) ORCID ID 0000 – 0002 – 5139 – 2118

Cite this study

Javidan S., Mohsenzadeh, S., & Sattari, M. T. (2022). Classification of surface water quality using data-driven methods. 4th Intercontinental Geoinformation Days (IGD), 78-81, Tabriz, Iran

a village in the Rudbar Alamut section of Qazvin city in Qazvin province. Bagh Kalayeh hydrometric station is located at latitude 36°23' 38", longitude 50° 29' 51" and altitude 1287m above sea level. The average rainfall for 20 years at this station is 423.06mm. The location of the station under study is shown in Figure 1.

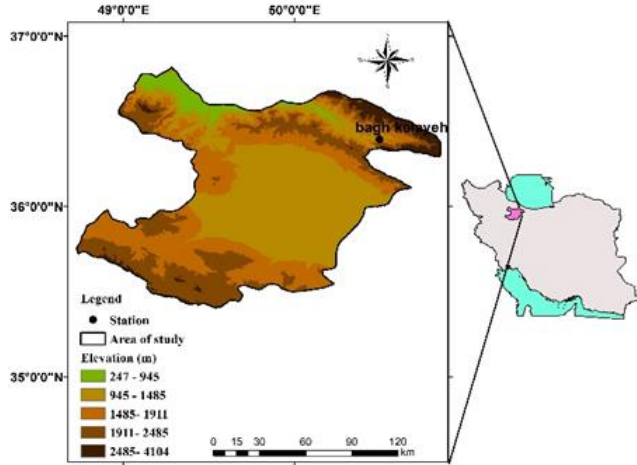


Figure 1. Location of the studied station

In the present study, to calculate the WQI index from the qualitative parameters of Bagh Kalayeh hydrometric station, including Total Hardness (TH), alkalinity (pH), Electrical Conductivity (EC), Total Dissolved Solid (TDS), Calcium (Ca), Sodium (Na), Magnesium (Mg), Potassium (K), Chlorine (Cl), Carbonate (CO₃), Bicarbonate (HCO₃) and Sulfate (SO₄) were used over a 23-year statistical period (1998-2020). The statistical characteristics of the variables used are presented in Table 1.

Table 1. Statistical characteristics of implemented parameters

Statistic	Minimum	Maximum	Mean
TH	95.00	481.50	278.15
PH	4.50	8.40	7.83
EC	279.00	1048.00	627.94
TDS	186.00	663.00	388.05
Ca	0.00	159.80	73.94
Na	0.46	60.49	17.26
Mg	2.76	58.20	22.18
K	0.39	19.50	1.99
Cl	0.00	89.60	27.36
CO ₃	0.00	33.00	0.21
SO ₄	22.08	374.88	140.21
HCO ₃	50.02	391.62	163.60

Quantitative and qualitative values calculated with WQI index were considered as target outputs. Using the relief method, the types of input compounds (including the most effective parameters) were identified (Table 2). To estimate the quantitative values of WQI, the Bagging method was used with the Support Vector Regression algorithm (B-SVR) and for qualitative values, the Random Forest (RF) method was used. Of the available data, 70% were considered for calibration and 30% for validation. Both methods were performed in Weka software.

Table 2. Parameters involved in each scenario

Scenario Number	Input Parameters
1	TH
2	TH, K
3	TH, K, SO ₄
4	TH, K, SO ₄ , TDS
5	TH, K, SO ₄ , TDS, EC

2.1. Water Quality Index (WQI)

Drinking Water Quality Index was calculated using formulas 1 to 3. In these formulas, w is the weight of each parameter due to its importance in drinking and W is the relative weight of each parameter, C is the concentration of each parameter, S is the standard concentration of each parameter, q is the quality rank of each parameter and WQI is the drinking Water Quality Index (Singh 1992).

$$W_i = \frac{w_i}{\sum_{i=1}^n w_i} \quad (1)$$

$$q_i = \left(\frac{C_i}{S_i} \right) \times 100 \quad (2)$$

$$WQI = \sum_{i=1}^n W_i q_i \quad (3)$$

Calculated WQI values are usually divided into five categories (Table 3).

Table 3. Water quality classification based on WQI value

Classification of Drinking Water Quality		
WQI Range	Class	Type of Water
below 50	I	Excellent water
50-100	II	Good water
100-200	III	Poor water
200-300	IV	Very poor water
above 300	V	Water unsuitable for drinking

2.2. Bagging Method

The Bagging method, first proposed by Breiman in 1996, connects several basic learners in parallel to reduce set variance. Each basic learner is trained on the same Bootstrap version using the same learning algorithm, then the output of these basic learners is aggregated by majority vote (for classification) or averaging (for regression) to obtain the final output. To achieve better and stronger performance, basic learners in a group must be precise and diverse (Breiman, 1996).

2.3 Support Vector Regression

Support Vector Machine (SVM) is a machine learning approach in data-driven research. This method is based on statistical learning theory and is used primarily for the best distinction between two data classes. Support Vector Machine models are divided into two main parts: (1) backup vector machine Bagging models, (2) backup vector regression model (SVR). The SVM model is used to

solve the classification of data into different classes and the SVR model is used for forecasting (Demirci 2019).

2.4. Random Forest

The RF algorithm is a supervised classification algorithm. There is a direct relationship between the number of algorithm trees and the results that can be obtained. As the number of trees increases, a definite result is obtained. The difference between the RF algorithm and the decision tree algorithm is that root node detection and node splitting in RF are performed randomly. This is why the RF algorithm can be used in classification and regression tasks (Sachetana et al. 2017).

To compare the values obtained from data mining methods with the values calculated from the WQI index, the criteria of Correlation Coefficient (R), Root Mean Square Error (RMSE), Mean Absolute Error (MAE) and Kappa statistics were used. The formulas of the above statistics are presented in Equations (4) to (7), respectively:

$$R = \frac{\sum_{i=1}^N (x_i - \bar{x})(y_i - \bar{y})}{\sqrt{\sum_{i=1}^N (x_i - \bar{x})^2 \cdot \sum_{i=1}^N (y_i - \bar{y})^2}} \quad (4)$$

$$RMSE = \sqrt{\frac{\sum_{i=1}^N (x_i - y_i)^2}{N}} \quad (5)$$

$$MAE = \frac{1}{N} \sum_{i=1}^N |x_i - y_i| \quad (6)$$

$$Kappa = p_i = (PA_0 - PA_E) / (1 - PA_E) \quad (7)$$

In the above relations, y_i is the estimated value of the model, x_i is the value calculated from the qualitative index, N is the number of data, M is the number of samples found in the wrong class, T is the total number of samples, PA_0 is the agreement of the two evaluators and PA_E is the expected agreement.

3. Results

First, the results obtained from the 5 input scenarios used in the Bagging method with the backup vector regression algorithm for estimating quantitative values and the Random Forest method for estimating qualitative values were presented in Tables 4 and 5, respectively:

Table 4. Evaluation criteria for estimating quantitative WQI values

Scenario	B-SVR		
	R	RMSE	MAE
1	0.96	3.01	2.28
2	0.96	2.82	2.08
3	0.97	2.70	2.08
4	0.98	2.06	1.39
5	0.98	1.92	1.23

Table 5. Evaluation criteria for estimating WQI quality values

Scenario	RF		
	Kappa	RMSE	MAE
1	1	0.0089	0.0008
2	1	0.0089	0.0018
3	1	0.0055	0.0007
4	1	0.0156	0.0026
5	1	0.0222	0.0046

According to Tables 4 and 5, however, the method has provided acceptable results in all scenarios. To select the best scenario, bar graphs of RMSE and MAE values for both methods are shown in Figures 2 and 3.

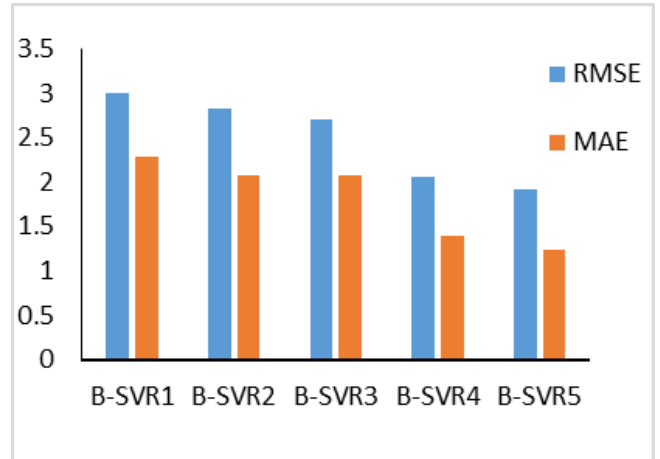


Figure 2. Bar chart of quantitative modeling errors

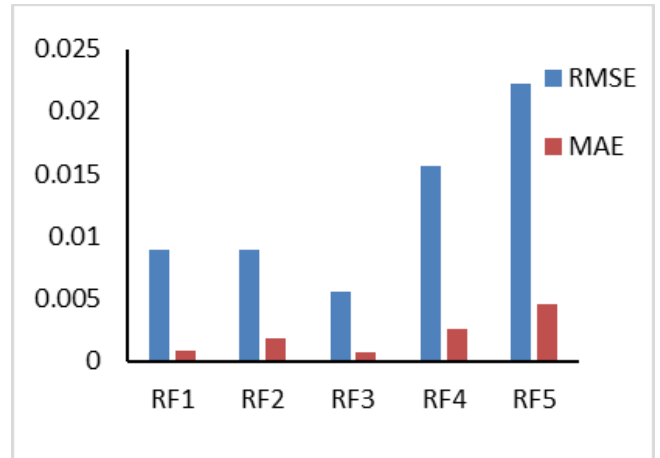


Figure 3. Bar chart of qualitative modeling errors

According to Figure 2 and 3, Scenario 5 (including TH, K, SO₄, TDS, EC) with the lowest error rate as the superior scenario for estimating quantities of WQI and Scenario 3 (including TH, K, SO₄) as Scenario Superior was selected to estimate WQI quality values.

4. Discussion

Calculating Water Quality Index with a large number of parameters is time consuming and difficult. However, data-based methods with a very small number of parameters provide more acceptable results, and this increases the popularity of data-based methods. The results of the present study showed that the data mining methods using the parameters TH, K, So₄, TDS, EC instead

of the 12 parameters used in calculating the Water Quality Index, had considerable accuracy in estimating the quantitative and qualitative values of WQI.

5. Conclusion

In the present study, first Water Quality Index using parameters of Total Hardness (TH), alkalinity (pH), Electrical Conductivity (EC), Total Dissolved Solid (TDS), Calcium (Ca), Sodium (Na), Magnesium (Mg), Potassium (K), Chlorine (Cl), Carbonate (CO₃), Bicarbonate (HCO₃) and Sulfate (SO₄) were calculated. Then, to estimate the quantitative values of WQI, the Bagging method was used with the basic vector regression algorithm, and to estimate the qualitative values, the Random Forest method was used, taking into account different scenarios. The results showed that B-SVR5 and RF3 methods had good accuracy for quantitative and qualitative estimation of WQI index in Bagh Kalayeh hydrometric station, respectively.

References

- Babbar, R., & Babbar, S. (2017). Predicting river water quality index using data mining techniques. *Environmental Earth Sciences*, DOI 10.1007/s12665-017-6845-9.
- Breiman, L. (1996). Bagging predictors. *Machine Learning*, 24, 123–140.
- Demirci, M. (2019). Estimation of rainfall-runoff relationship using support vector machines and M5 decision tree methods. *DÜMF Mühendislik Dergisi*, 10 (3), 1113–1124.
- Gakii, C., & Jepkoech, J. (2019). A classification model for water quality analysis using desicion tree. *European Journal of Computer Science and Information Technology*, 7 (3).
- Othman, F., Alaaeldin, M., Seyam, M., Ahmed, A., Teo, F., Ming Fai, Ch., Afan, H., Sherif, M., Sefelnasr, A., & Shafie, A. (2020). Efficient river water quality index prediction considering minimal number of inputs variables. *Engineering Applications of Computational Fluid Mechanics*, 14 (1), 751-763. <https://doi.org/10.1080/19942060.2020.1760942>.
- Sattari, M. T., Mir Abbasi, R., & Nayebyzadeh, M. (2017). Use of Mining in Predicting Surface Water Quality (Case Study: North Sahand Rivers). *Echo Hydrology*, 4 (2), 419-407.
- Suchetana, B., Rajagopalan, B., & Silverstein, J. (2017). Assessment of wastewater treatment facility compliance with decreasing ammonia discharge limits using a regression tree model. *Science of The Total Environment*, 598, 249–257.



4th Intercontinental Geoinformation Days

igd.mersin.edu.tr



Exploring maps from childhood to adulthood: a journey to basic map knowledge with field experts

Nuri Erdem *¹

¹Osmaniye Korkut Ata University, Department of Geomatics Engineering, Osmaniye, Türkiye

Keywords

Map Reading
Sketch
Compass
Map Making
Orienteering

Abstract

The need for maps and map information is increasing every day. This need is felt not only for the preparation of zoning plans, the implementation of technical infrastructure projects, but also for the ability to read the map, find directions in nature, use the compass together with a map, detect the shapes, positions and movements of the moon, earth and other planets. In this context, within the scope of the project titled “Journey to Basic Map Information with Field Experts” supported by TÜBİTAK-4004, it is aimed to provide basic map information to participants covering a wide range of segments from kindergarten to university students with practical training, to eliminate deficiencies experienced in this field, to introduce and implement orienteering based on map use. The target audience of the project was formed by 7 groups of 30 students and teachers at the university level from kindergarten located in Osmaniye. The participants were asked to be able to produce a map using cartography measurement tools, to be able to use and interpret it easily, and to have basic map knowledge. A suitable program has been prepared for this. At the end of the project, “map information” was removed from being just an educational tool and the map was ensured to be a constantly used auxiliary material. The findings revealed that the participants’ desire to learn basic cartography knowledge and to use maps increased at the end of practical project activities.

1. Introduction

Improving the quality of education, training qualified individuals in all areas can only be possible with teamwork. It is of great importance that specialists in various fields work together to improve the quality of education. At this stage, a number of tasks also fall on the Map Engineers (Buğdaycı and Bildirici, 2009). The project called “Journey to Basic Map Information with Field Experts” was also planned in order to transfer the developments in this field to students in the educational community with modern methods and techniques.

With easily learned information, orienteering sports can be done by everyone from a 3-year-old child to a 100-year-old (Güler, 2003). Orientation is the finding of the current location and the way to go with the help of a map and compass. Orienteering sports can be performed in everyday life, business life, recreation and entertainment activities, outdoors, in the rain, in the city / village

environment. This sport can be done on foot, as well as use transportation vehicles such as horses, cars, bicycles, boats and kayaks (Sevim, 1997).

Osmaniye kindergarten, elementary school, middle school, high school, undergraduate and graduate level students at the contributor group of 30 people for a total of 6 experts in the field, accompanied by practical training in an office environment aims to give basic information and land map with this project, which with;

- Learning basic map information, which is becoming increasingly important, learning how to make a map using tools and computer CAD programs used in land measurement, calculation and drawing stages,
- Types of navigation in nature, using a compass, using a map and compass together,
- Orienteering sports applications, Sketches and characteristics, the concept of the northern direction used in cartography, its importance and types,

* Corresponding Author

^{*}(nurierdem@osmaniye.edu.tr) ORCID ID 0000-0002-1850-4616

Cite this study

Erdem, N. (2022). Exploring maps from childhood to adulthood: a journey to basic map knowledge with field experts. 4th Intercontinental Geoinformation Days (IGD), 82-86, Tabriz, Iran

- Reading the map and learning the meaning of special signs on it, the concept of projection (Projection) used in map making, its importance and types, Types of maps, explaining where and for what purpose they are used,
- Concept of scale, importance, types and representation of scale-map relationship, types of plans, stages of urban planning,
- Map making from ground laser and lidar scanner, aircraft, UAV and satellite images,
- Introduction of developments in satellite-based geolocation (GNSS), its types and artificial satellite technology,
- Providing information on visual materials and moving models about the importance, shape and movements of the Moon, which is the natural satellite of our world, introducing the measuring instruments necessary for the production of maps and conducting land applications,
- Making 2D and 3D drawings with the basic menus of the programs used in map drawing,
- Visualization using cartographic techniques, Visualization of the created maps by transferring them to a paper medium with the help of a plotter, organizing competitions by providing information about the sport of orienteering,
- Raising awareness in the community about basic map information in groups of participants that will be created from different segments of society, especially starting with children in kindergarten,
- Teaching the shape, position, movements, obliquity of our world, the number of meridians and parallels, their use and what they do on a moving and illuminated globe model by enabling participants to make a globe model using various stationery materials,
- On the other hand, young participants have discovered the fun side of science by making their own science toys about the moon, earth and other planets in the solar system,
- Simultaneously with the new educational methods developing in the world, to introduce our children to the basic concepts of the future on the subject of maps, it is intended to.

2. Material and Method

During the study, the “Regulation on the Production of Large-Scale Maps and Map Information-(BÖHHBÜY)”, which was put into effect by the Council of Ministers on 23/06/2005 on the basis of the Article No. 684 dated 29.04.2005 of the Ministry of National Defense, was taken as the basis. In accordance with the articles of the regulation, maps were produced and named according to their scale (URL_1). Maps of various purposes, forms and scales are produced for all kinds of construction, planning and infrastructure projects around the world. Regardless of what needs it is for, the creation of a map is generally divided into land and clerical work. It is possible to divide land studies into fixed point facility and measurement parts, office studies into calculation works, map drawing, printout and archiving studies (Yıldız, 1999). In this context, some of the simple application

examples that are planned to be made at the office stages of the project have been planned by using the Map Drawing (Linear-Numeric) book. For example; in order to create the substrate necessary for map drawing, the source book was used for the issues of information about the edge of the sheet, framing, scale selection, placement of special signs and inscriptions in the appropriate place.

Many of the problems in today's cities are caused by the fact that the relevant zoning plans are not made correctly, forward-looking and long-term. In this context, Zoning Information Planning-Implementation-Legislation was used for issues such as reading zoning plans that constitute an important part of the maps produced about the city, their importance, planning stages, existing maps used as underlays, special signs on zoning and cadastral sheets, and their meaning.

First, the basic map information was given theoretically in the classroom environment, and then land and laboratory applications were made. The measurements obtained were uploaded to map drawing programs and color drawings were made. The created maps were visualized by transferring them to paper media with the help of a printer. Information about the sport of orienteering was given and competitions were organized. Drawing, painting, direction finding and orienteering sports applications have been made especially for kindergarten and elementary school student groups accompanied by special games that develop the concept of maps.

One of the important events considered in the project is that a map of a small region with participants is made in different scales and sizes. The aim of this application is to see and understand the stages of obtaining the shape of a map belonging to a region on paper media, which is the result of the first measurement stage, in practice (Figure 1). During the project, practical activities such as obtaining 2D and 3D color drawings, making digital maps were also planned to be carried out. During these applications, studies were carried out such as finding out what signs such as settlements, lakes, streams, roads, hills are located on the topographic map that will be used as an example (URL_2).



Figure 1. Land measurement study of high school students with a GPS device

3. Findings

All groups of participants participating in this study were given preliminary tests to measure their scientific infrastructure about basic map information in accordance with their age and educational status (Table

1). In these tests, for basic map information according to age groups; map, sketch, scale, etc. questions were prepared in the fields and the knowledge levels of the participants were determined. The results obtained have been evaluated and the deficiencies seen during the applications have been corrected.

Table 1. Pre/final test questions applied to the participants

Class	Pre/Post Test Questions
KINDERGARTEN	<p>A country map is shown and asked to point to the mountains.</p> <p>A map of the area is shown and asked to point out roads.</p> <p>A country map is shown and asked to point to the lakes.</p> <p>An island and country map is shown. Ask the candidate to point.</p> <p>He is asked to describe the geographical features of the island on the map.</p> <p>Students are asked to describe what the mountains on the map look like in the real world.</p> <p>Students are asked to comment on what the roads they see on the map do.</p> <p>Ask them to describe how the lakes on the map look like in the real world.</p>
PRIMARY SCHOOL 4th GRADE	<p>Is it true that weather maps can show values such as average temperature, coldness and precipitation?</p> <p>Which of the following statements describes a roadmap?</p> <p>Which of the following maps shows elevation, slope, or other physical characteristics of the terrain?</p> <p>What maps show where people live?</p> <p>Which of the following can help you read or understand a map?</p> <p>In which of the following can we see the round view of the earth?</p> <p>How can map scale help with map reading?</p> <p>Some maps show us what types of crops are grown in a particular area. What are these maps called?</p> <p>Which of the following maps is used to show the past boundaries of an area?</p>
MIDDLE SCHOOL	<p>How many continents are there in the world?</p> <p>Which of the following is not a continent?</p> <p>Which is the biggest mountain in Turkey?</p> <p>What is not included in the neighborhood map?</p> <p>What is the function of the map scale?</p> <p>Which is the largest continent?</p> <p>Which is the smallest continent?</p> <p>Which of the following is the largest lake in Turkey?</p> <p>What does island mean in cartography?</p>
HIGH SCHOOL	<p>On which map can we see the districts of Istanbul? Why is that?</p> <p>On which map can we not see the Golden Horn? Why is that?</p> <p>Streets and roads are more prominent on which map? Why is that?</p> <p>On which map can we see larger areas? Why is that?</p> <p>Rank the maps according to their scale from largest to smallest.</p> <p>Which map has the smallest scale? Can you rank the maps according to their scale from largest to smallest?</p> <p>In which of maps B and C are streets and alleys more prominent? What is the reason of this?</p> <p>Which of the maps A and B is smaller in scale? Why is that?</p> <p>Which of the B and C maps is larger in scale? Why is that?</p> <p>We cannot see Kule Site AVM on map A. What could be the reason for this?</p>
ASSOCIATE AND LICENSE AND TEACHERS	<p>What is the reduction ratio of maps called?</p> <p>What is a space-conserving projection?</p> <p>What is the name of the part that shows the meaning of the special signs used on the map?</p> <p>What is a drawing that shows a bird's eye view of a place called?</p> <p>Which type of map shows the shape and elevation of the earth?</p> <p>Which type of projection preserves the shape of the earth?</p> <p>What is the distance from a point on earth to the equator called?</p> <p>What are imaginary curves connecting points of the same height called?</p> <p>What is the imaginary line assumed to lie between two poles called?</p> <p>What is the name of the map that shows the borders of the countries in the world?</p> <p>What is it called when the bird's-eye view of the earth is transferred to the plane within a certain ratio?</p>

According to the results of the pre-test; The deficiencies in the basic map information of the participants were determined, the theoretical explanations in the classroom environment and practical field / laboratory applications were shaped accordingly. Care was taken to ensure that the expressions of the professional literature used in the theoretical lectures in the classroom were as appropriate for the level of the participants as possible and that they included the information that students should use in their classes.

However, since the experts and trainers in the project are academicians, this desired level could not be achieved in kindergarten and primary school students.

As another result of the pre-tests, it was decided which of the map making stages, land measuring instruments and measurement methods should be explained in more detail. Field applications were also shaped according to this test result. For example, more time was allocated to electronic total stations and GNSS

receivers from measuring instruments and participants were enabled to use them actively.

In addition, a great interest in advanced cartography was aroused, especially among the participants of associate, undergraduate and teachers' groups, and many questions were received from the participants on special topics such as cadastre and zoning practices during breaks and other free times. Since the trainers in the project team are experts and experienced in their fields, they gave satisfactory answers to these and similar questions. This has been pleasing in terms of solving the problems experienced by the participants in this area and making the project more efficient.

According to the pre-test results; The infrastructure of the participants on orienteering was measured, and the theoretical explanations and practical field applications in the classroom were shaped accordingly (Picture 2). According to the results of this test, it has emerged that the basic map information subjects should be explained in more detail. Although a few of the participants were at an advanced level in these subjects, it caused them to get a little bored, but the applications in the field measurement applications and Netcad map drawing program environment attracted the attention of everyone. While choosing Netcad program applications, it was determined which subjects should be applied according to the results of these pre-tests.



Figure 2. Orienteering sport activity

At the end of the activity studies of the relevant groups in the project, post-tests were also applied (Table 1). The post-test questions were kept the same as the first-test questions to observe the improvement in the group members. As a result of the 2-day theory and practical training given to each participant group in accordance with their age group, it was observed that the participants' knowledge of basic map information and orienteering increased and an awareness could be created on this subject. The final test results were at a much better level than the first test results.

One of the important activities implemented in the project is the mapping of a small region in different scales and sizes in a place where no measurement and mapping work has been done before by the participants. With this application, the stages of obtaining the shape of the map of a region in the paper environment, which is the result from the first measurement stage, is to be seen and

understood in practice. During the applied field studies, activities such as the introduction of the compass and its use in the field, and the finding of direction in the field were carried out, improving the social and technical skills of the participants and increasing their self-confidence.

During the project, practical activities such as obtaining 2D and 3D-colored drawings, digital map making, and creating a smart interrogative map in Netcad were also carried out. Especially in the studies carried out with Netcad program, applications such as map coordinating, map digitization, digital elevation model creation were emphasized.

During the activities, map-land comparison studies were carried out through observation, enabling the participants to learn basic map information permanently, and their knowledge and skills in this field increased.

Basic cartography information consists of measurements, calculations and observations in the field. The values obtained do not mean much unless they are written on paper by drawing. Therefore, it has been one of the most important studies to transform the data we have into map format by drawing. The accuracy of the map depends on the precision, attention and care to be shown in the measurements made in the field and the drawings to be made in the computer environment afterwards. Within the scope of the project, map drawings were made in computer environment in accordance with the Large-Scale Map and Map Information Production Regulation.

4. Conclusion

In the researches, it has been seen that there are deficiencies in reaching and using this information correctly in every part of the society about basic map information, and that teachers cannot provide sufficient number and quality of tools and materials that they can use in their lessons.

The measuring instruments, map drawing programs and other materials used in the project process were used to support applied teaching. Materials chosen in accordance with the subject and purpose make the taught subject alive, enrich the teaching process and increase learning. With this idea, applications made in the field and office environment will accelerate learning and ensure that the information becomes permanent.

As a result of the project, the participants, who permanently learn their basic map knowledge by practicing and doing sports competitions, will be able to follow the current developments in this field, learn the necessary skills for everyone, such as reading the map, finding direction in nature, using a compass, and raise awareness in the society with their knowledge of space, earth and other planets. In addition, students will be able to do their own map-based studies more easily.

Acknowledgement

This study was supported by TUBITAK 4004-Nature Education and Science Schools program in 2019 within the scope of TUBITAK Project (Project No: 218B149)

titled “Journey to Basic Map Information with Field Experts”.

References

- Buğdaycı, İ. & Bildirici, İ. Ö. (2009). Harita Kullanımının Coğrafya Eğitimindeki Önemi, TMMOB Harita ve Kadastro Mühendisleri Odası, 12. Türkiye Harita Bilimsel ve Teknik Kurultayı, Mayıs, Ankara.
- Demir Alp, N. (2007). Coğrafya Eğitiminde Materyaller ve 2005 Coğrafya Dersi Öğretim Programı, Kastamonu Eğitim Dergisi, 373-384, Cilt:15 No:1.
- Güler, V. (2003). Orienteering ve Çocuklar İçin Orienteering Eğitimi, Lisans Bitirme Tezi, Gazi Üniversitesi, Beden Eğitimi ve Spor Yüksekokulu, Antrenörlük Eğitimi Bölümü, Ankara.
- Sevim, Y. (1997). Antrenman Bilgisi, Geliştirilmiş Baskı, Tutibay Ltd. Şti., Ankara
- URL_1:
https://www.tkgm.gov.tr/sites/default/files/icerik/ekleri/aciklamali_orneklemeli_bohhbuy_0.pdf, Date of access: 12.11.2021
- URL_2:
http://www.kantitatifekoloji.net/cbsproje/belgeler/etkinlik_programi.pdf, Date of access: 02.10.2021
- Yıldız, F. (1999). Harita Çizimi (Çizgisel-Sayısal), 2. Baskı, Nobel Yayın Dağıtım, ISBN: 9755910050.
- Yıldız, F., İnal, C. & Erdi, A. (2016). Topografya-Ölçme Bilgisi, 10. Baskı, Nobel Yayın Dağıtım, ISBN: 6051330112.



4th Intercontinental Geoinformation Days

igd.mersin.edu.tr



The analysis of 3D geometric features on point clouds by using open-source software

Ramazan Alper Kuçak*¹

¹Niğde Ömer Halisdemir University, Faculty of Engineering, Department of Geomatics, Türkiye

Keywords

LiDAR
TLS
Point Cloud
Geometric Features
3D Model

Abstract

The modeling of point clouds is significant for geomatics engineering and others (such as machinery and construction) engineering and architectural applications. Furthermore, 3D models, which are currently used for various engineering fields, have been increasingly crucial with the introduction of digital twins, virtual reality, 3D city modeling, reverse engineering, and metaverse recently. For this reason, the importance of 3D models is increasing more and more. Range-based modeling (e.g., laser scanning) is one of the most common approaches for generating 3D models. Also, 3D model acquisition (terrestrial and airborne Light Detection and Ranging (LiDAR) or structure-from-motion (SfM)) and 2D imaging techniques are usually transformed into models such as 3D mesh and parameter surface before they are visualized or analyzed for 3D surfaces. This study analyzed 3D point cloud models obtained with terrestrial laser scanners with open source software (Cloud Compare). Also, many approaches to model extraction have been tried to obtain corner points and lines using various 3D geometric analyses.

1. Introduction

3D models, which are currently used for cultural heritage or various engineering fields, have been increasing in importance with the introduction of technologies such as digital twins, virtual reality, 3D city modelling, reverse engineering and metaverse into human life recently. Also, Historical artifacts are exposed to many natural or unnatural destructions from the past to the present. Because; the studies carried out to protect the cultural heritage for informing the next generations about the history are accelerating day by day all over the world, and their (3D Models) importance is increasing to a great extent. (Kuçak, R. A., 2013; Kuçak, R. A., et al., 2016)

Nowadays, the generation of a 3D model for cultural heritage or archaeological sites is mainly achieved using non-contact systems based on light waves, particularly using active or passive sensors. There are currently four alternative methods for object and scene modeling:

1. Image-based rendering, which does not generate the geometry of a 3D model but might be preferred as a promising technique for the generation of virtual aspects

2. Image-based modeling (e.g., photogrammetry), the widely preferred method for geometric surfaces of architectural objects and Cultural Heritage documentation

3. Range-based modeling (e.g., laser scanning) is becoming a widespread approach for the scientific community and non-expert users such as Cultural Heritage professionals.

4. The combination of an image and range-based modeling, as they both have advantages and disadvantages, and their integration can allow the generation of detailed 3D models efficiently and quickly (Almagro A. and Almagro Vidal A., 2007, Kuçak, R. A., et al., 2016).

From the air or the ground, laser scanning is one of those technological developments that enable many 3D measurements to be collected in a short time. It generates a 3D point cloud in a local coordinate system with intensity values; internal or external digital cameras usually provide additional information such as RGB values. Laser scanners can operate from the ground or be integrated into an airplane. However, Laser scanning from any platform generates a point cloud: a collection of XYZ coordinates in a coordinate system that portrays to the viewer an understanding of the spatial distribution of

* Corresponding Author

^{*}(akucak@ohu.edu.tr) ORCID ID 0000-0002-1128-1552

Cite this study

Kuçak, R. A. (2022). The analysis of 3D geometric features on point clouds by using open-source software. 4th Intercontinental Geoinformation Days (IGD), 87-90, Tabriz, Iran

a subject. It may also include pulse, amplitude, intensity, or RGB values. Generally, a 3D point cloud contains a relatively large number of coordinates compared to the volume the cloud occupies, rather than a few widely distributed points. (Kuçak, Kiliç, & Kisa, 2016)

Terrestrial laser scanning data can be used by editing in various CAD programs for architectural projects. This study aims to carry out a 3D analysis of the building scanned with 3D terrestrial laser scanning technology. After analyzing object details by scanning with the terrestrial laser scanner, the 3D geometric features of the 3D point clouds were generated. Also, the advantages and disadvantages of open source code software are evaluated for obtaining 3D surfaces and performing various surface analyses using an Open Source program (Cloud Compare).

In this study, the TLS point clouds are selected to gain the 3D Geometric Features. Thus, it is intended a contribution to the geometric accuracy of cultural heritage and 3D city models to be produced with point clouds. The faculty of Civil Engineering in the Ayazaga Campus of ITU in Turkey was selected as the study area. The study area was scanned with Leica C10, which can get 50,000 points per second with 6 mm accuracy. Furthermore, the 3D geometric features of the 3D point cloud were carried out.

2. Data and Method

The faculty of Civil Engineering located in Ayazaga Campus of ITU in Turkey was selected as study area (Figure 1). The study area scanned with Leica C10, which can get 50,000 points per second with 6 mm accuracy. The 3D surface analysis of 3D point cloud were carried out.

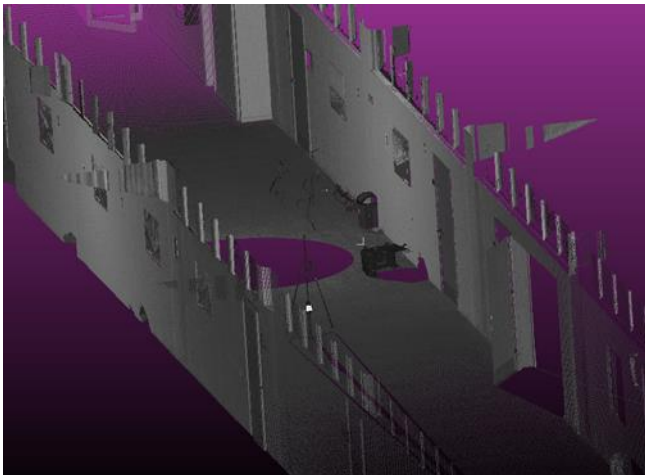


Figure 1. TLS Point Cloud (Leica C10)

2.1. TLS

LiDAR (Light Detection and Ranging), from the airborne or terrestrial, is one of technical systems that enables to collect a large quantity of 3D data in a short space of time. It creates a point cloud with density values in the local coordinate system; additional information such as RGB values are usually provided by internal or external digital cameras. (Kuçak, Kiliç, & Kisa, 2016; Kuçak, Özdemir, & Erol, 2017)

TLS is a powerful technology for collecting 3D data spread over a large area in a short time. (Kuçak et al., 2013, Kuçak et al., 2016, Kuçak et al., 2020). TLSs consist of lasers, precisely calibrated receivers, precision timing, high-speed micro-controlled motors, and precise mirrors (Fowler & Kadatskiy, 2011). The basic information obtained from each scan is the virtual point cloud formed by all of the 3D points of the surfaces measured in harmony with each other (Scaioni, 2005). The precision and accuracy of TLS make the TLS system a powerful technology for creating a 3D dense point cloud according to the conventional measuring methods (Çelik et al., 2020). However, the registration of TLS scans must be done carefully because the registration errors affect the 3D model quality.

2.2. 3D Geometric Features

Surface parameters help explain the local geometry of the surface. These surface features are nowadays widely applied in point cloud analyses. They are aimed to extract these geometric features (surfaces, lines, corners and key points). Surface parameters (Table 1) can be calculated by the eigenvalues ($\lambda_1, \lambda_2, \lambda_3$) of the eigenvectors (v_1, v_2, v_3) derived from the covariance matrix of any point p of the point cloud (Atik, M. E., Duran, Z., & Seker, D. Z. 2021).

Table 1. Geometric Features derived from eigenvalues

Sum of eigenvalues	$\lambda_1 + \lambda_2 + \lambda_3$
Omnivariance	$(\lambda_1 \lambda_2 \lambda_3)^{1/3}$
Anisotropy	$(\lambda_1 - \lambda_3)/\lambda_1$
Planarity	$(\lambda_2 - \lambda_3)/\lambda_1$
Linearity	$(\lambda_1 - \lambda_2)/\lambda_1$
Surface variation	$\lambda_3/(\lambda_1 + \lambda_2 + \lambda_3)$
Sphericity	λ_3/λ_1
Verticality	$\lambda_1 \ln \lambda_1 + \lambda_2 \ln \lambda_2 + \lambda_3 \ln \lambda_3$

Many values are calculated using eigenvalues (Table 1). (Sum of eigenvalues, omnivariance, roughness, anisotropy, planarity, linearity, surface variation, sphericity and curvatures etc.) these parameters derived from only 3D coordinates.

2.2.1. Gauss and Mean curvatures

Curvatures are a surface's geometrical features that are invariant according to rotation, translation, and scaling. There are many methods to calculate the Curvature of a surface. The Curvature can be calculated easily when the analytical formula is available for a surface, but these methods are not usually applicable to point clouds' surfaces. So, the surface fitting method depending on a point and its neighbors is a good way. (Foorginejad & Khalili, 2014)

$$Z = r(x, y) = a_0x^2 + a_1y^2 + a_2xy + a_3x + a_4y \quad (1)$$

This quadratic surface's (1) parameters (a_0, a_1, a_2, a_3, a_4) is estimated by the least square method, and the Gaussian (K)(2) and Mean Curvature (H) (3) can be calculated by the differential geometry (He, Lin, & Li, 2013):

$$K = \frac{LN - M^2}{2(EG - F^2)} \quad (2)$$

$$H = \frac{EN - 2FM^2 + GL}{2(EG - F^2)} \quad (3)$$

where $E=r_x.r_x$, $F=r_x.r_y$, $G=r_y.r_y$, $L=r_{xx}.n$, $M=r_{xy}.n$, $N=r_{yy}.n$, and r_x , r_y , r_{xx} , r_{yy} , r_{xy} are the partial derivatives of the quadratic surface. (He, Lin, & Li, 2013)

For the curvature estimation, another method is the covariance analysis method (Hoppe, DeRose, Duchamp, McDonald, & Stuetzle, 1992), which uses the ratio between the minimum eigenvalue and the sum of the eigenvalues. This method is known as the surface variance (Pauly, Gross, & Kobbelt, 2002). The surface variance is appropriate for point clouds because it uses the coordinate of a point and its neighbors, and it is not expensive to process. (Foorginejad & Khalili, 2014).

3. Results

In this study, we calculated the curvatures of a surface by using TLS point clouds. Also, the TLS base distances were compared with the total station base distance using statistical methods to determine the TLS data accuracy. Then, the coarse errors had removed from both data. Thus, the standard deviation of the difference of the base distances was calculated. As a result, the standard deviation for TLS data was obtained as 0.005 m. Then, we filtered and segmented the data according to optimum curvatures. In this way, we could quickly obtain vertices and boundary lines from 3D point clouds.

Many values are calculated using eigenvalues (Table 1). (Sum of eigenvalues, omnivariance, roughness, anisotropy, planarity, linearity, verticality (Figure 2) surface variation, sphericity and curvatures (Figure 3) etc.) Since the datasets used contained only geometric information (3D coordinates).

By using 3D geometric features, corner lines of 3D point clouds and various curved surfaces are obtained as in figure 4. These lines can serve many purposes by automatically converting them into lines and key points in various engineering works.

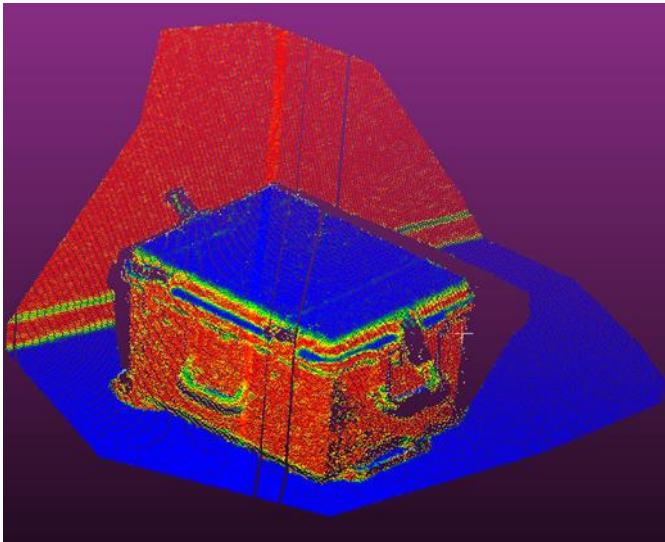


Figure 2. TLS Data According to verticality (Leica C10)

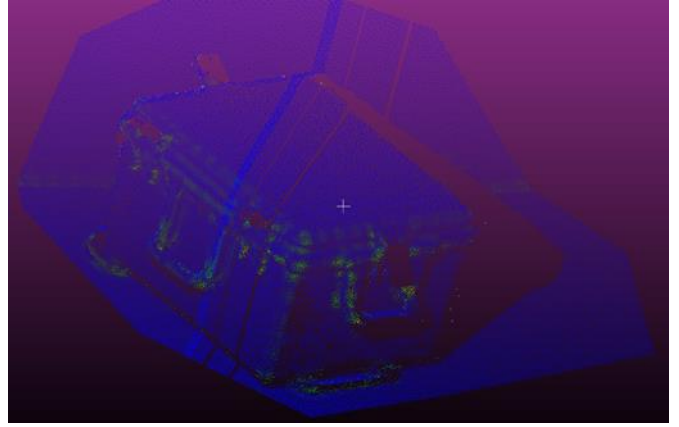


Figure 3. TLS Data According to Gauss Curvature (Leica C10)

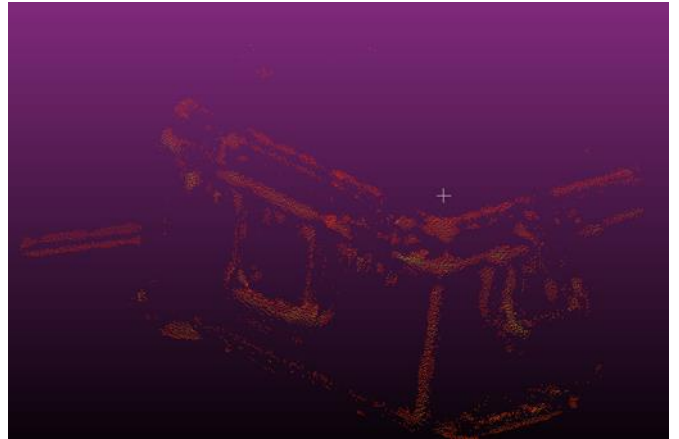


Figure 4. Vertices and boundary points from 3D point clouds.

4. Discussion

In this study, the TLS point clouds are selected to gain the 3D Geometric Features. Thus, it is intended a contribution to the geometric accuracy of cultural heritage and 3D city models to be produced with point clouds. The faculty of Civil Engineering in the Ayazaga Campus of ITU in Turkey was selected as the study area.

Then, the curvatures of a surface were calculated. the data was filtered and segmented according to optimum curvatures. In this way, we could quickly obtain vertices and boundary lines from 3D point clouds.

The resolution and accuracy of point clouds are very important to generate 3D accurate models and surface parameters. For this reason, to work with high resolution and accuracy point clouds is the basis of studies to be done in the point clouds rather than more point clouds in the 3D modeling. So, the use of high-precision point and sufficient point clouds for data modeling is very important. Various filtering methods can be applied for modeling and interpolation and surface pass-through operations; however, if the data were missing or incorrectly measured, modeling or interpolating the data is always a challenge. There are a few methods to correct this deficiency; either the resolution of data should be increased, or the accuracy analysis of point clouds should be done. According to the obtained results, combining the point clouds and performing the interpolations will pave the way for more correct models.

5. Conclusion

To work with high-accuracy points to model point clouds and enough data is very important issue for point cloud studies. Also, in point cloud studies which accuracy or resolution is enough for modelling important. If the point clouds are sufficient for the desired works, the registration or modeling steps can be realized. However; if the desired surface data in the existing point cloud is missing and not in sufficient accuracy and resolution, it will be a more accurate approach to produce a more accurate point cloud from the existing point cloud and integrate it into the reference data for interpolation or modeling.

The experiments performed in this study show that one unique technique or geometric feature cannot be recommendable for the 3D Surface parameters or models of a 3D point cloud. However, geometric features of point clouds produced at multi scales can be used for vertices, boundary lines, and 3D surfaces from 3D point clouds.

Acknowledgement

Thanks to everyone who contributed to using the Leica C10 laser scanner, which belongs to the ITU Geomatics Engineering Department, and bringing it to the department.

References

- Almagro, A., Almagro Vidal, A. (2007). Traditional Drawings Versus New Representation Techniques. The ISPRS International Archives of the Photogrammetry, Remote Sensing and Spatial Information Sciences, Athens, Greece, Vol. XXXVI5/C53, pp. 52-57
- Atik, M. E., Duran, Z., & Seker, D. Z. (2021). Machine learning-based supervised classification of point clouds using multiscale geometric features. *ISPRS International Journal of Geo-Information*, 10(3), 187.
- Çelik, M. Ö., Hamal, S. N. G., & Yakar, İ. (2020). Yersel Lazer Tarama (YLT) Yönteminin Kültürel Mirasın Dokümantasyonunda Kullanımı: Alman Çeşmesi Örneği. *Türkiye LiDAR Dergisi*, 2 (1), 15-22.
- Foorginejad, A., & Khalili, K. (2014). Umbrella curvature: a new curvature estimation method for point clouds. *Procedia Technology*, 12, 347-352.
- Fowler, A., & Kadatskiy, V. (2011). Accuracy and error assessment of terrestrial, mobile and airborne LiDAR. Paper presented at the Proceedings of American Society of Photogrammetry and Remote Sensing Conference (ASPRP 2011), 1–5 May 2011, Milwaukee, Wisconsin.
- He, B., Lin, Z., & Li, Y. F. (2013). An automatic registration algorithm for the scattered point clouds based on the curvature feature. *Optics & Laser Technology*, 46, 53-60.
- Hoppe, H., DeRose, T., Duchamp, T., McDonald, J., & Stuetzle, W. (1992). *Surface reconstruction from unorganized points* (Vol. 26): ACM.
- Kuçak, R., Kılıç, F., & Kısa, A. (2016). Analysis of terrestrial laser scanning and photogrammetry data for documentation of historical artifacts. The International Archives of Photogrammetry, Remote Sensing and Spatial Information Sciences, 42, 155.
- Kuçak, R., Özdemir, E., & Erol, S. (2017). The segmentation of point clouds with k-means and ANN (artificial neural network). The International Archives of Photogrammetry, Remote Sensing and Spatial Information Sciences, 42, 595.
- Kuçak, R. A., Kılıç, F., & Kısa, A. (2014). Analysis Of Various Data Collection Methods For Documentation Of historical Artifacts. Paper presented at the 5. Remote Sensing-GIS Conference , İstanbul.
- Kuçak, R., Erol, S., & İşiler, M. (2020). The Accuracy Assessment of Terrestrial and Mobile LiDAR Systems for 3D Modelling. Proceedings book of the 1st Intercontinental Geoinformation Days (IGD) Symposium, Mersin, Mersin, Turkey.
- Pauly, M., Gross, M., & Kobbelt, L. P. (2002). *Efficient simplification of point-sampled surfaces*. Paper presented at the Proceedings of the conference on Visualization'02.



4th Intercontinental Geoinformation Days

igd.mersin.edu.tr



Second order control extension in Millennium City, Chikun Local Government Area, Kaduna State, Nigeria

Adamu Bala ^{*1}, Shola Daniels Oyekunle ^{1,2}, Nasiru Danlami ³

¹Ahmadu Bello University, Faculty of Environmental Design, Department of Geomatics, Zaria, Nigeria

²Kaduna Geographic Information Service (KADGIS), Kaduna, Nigeria

³Bayero University Kano, Faculty of Engineering, Department of Civil Engineering, Kano, Nigeria

Keywords

Control Extension
Network adjustment
PDOP
Hi-Target GNSS
Static mode

Abstract

GNSS control establishment is a continuous exercise in the field of Geomatics. This forms the basis upon which other surveys and engineering works geared toward development are referenced. This study employed the use of Hi-Target GNSS to extend and establish control stations within the study area in static mode. The control points were situated in such a way that they are free from disturbances, multipath and open for satellite acquisition. Observations were made between 90 to 120 minutes depending on the baseline length. To extrapolate this, three existing primary controls were selected for connection, checked for in-situ, and found to be in good condition for use. A minimum of fifteen (15) satellites were acquired by the GNSS receivers during observation with a dilution of precision (PDOP) value range of 1.2 to 2.8. The recorded data were downloaded and processed with the Hi-target Geomatics Office software. Network adjustment, for the newly established control stations, was carried out while the master station was held fixed. The final coordinates from the post-processing were plotted using QGIS 2.18.23. In conclusion, further research should be carried out in the study area to break the network of the control points established into shorter distances.

1. Introduction

Control survey provides consistent and accurate horizontal and vertical control for all subsequent project surveys, it covers an extensive area where long distances are involved and provides the standard of accuracy for subsequent and subordinate surveys to be attained (Olayanju, 2017). All projects, including route surveys, photogrammetric mapping, topographical mapping, planning, design, construction, and right of way, are made up of a series of vertical and horizontal field surveys. These secondary surveys are dependent on the control for position and relative accuracy (Basak, 2002).

For surveying to operate effectively, there is a need to have a reference framework that will be used for orientation. A control station is a small mark set immovably into the ground, such that an instrument (e.g., a total station or GNSS receiver) or optical target can be set up above it, to an accuracy of about 1 mm in the horizontal plane (Johnson, 2004).

Control extension is important in surveying because every survey practiced either in a large or small area

requires a set of control frameworks to fit into, i.e. vertical and horizontal controls. The vertical controls deal with the determination of the height of points, the process employed is known as leveling. In achieving the elevation of a point above a given datum, classical methods employed are Bathymetric, trigonometric, reciprocal, and spirit leveling. However, in the recent past, the total station and Global Navigation Satellite System (GNSS), have been used for height determination (Johnson, 2004).

In the determination of the horizontal control framework, controls can be established using various conventional methods like triangulation, trilateration, and traversing. These methods are used to determine the coordinates of a point, that is, the position of the point. However, due to the time spent in the production of a network of control and the huge amount expended on the course of creating this framework using the conventional method, this led to the rise of modern surveying instruments and techniques, so we have the advent of GNSS in surveying which is a satellite-based radio

* Corresponding Author

(adamubala09@gmail.com) ORCID ID 0000-0002-9666-5722
(sholaoyekunle4real@yahoo.com) ORCID ID 0000-0001-5233-2566
(nassdan@gmail.com) ORCID ID 0000-0003-3796-9387

Cite this study

Bala, A., Oyekunle, S. D., & Danlami, N. (2022). Second order control extension in Millennium City, Chikun Local Government Area, Kaduna State, Nigeria. 4th Intercontinental Geoinformation Days (IGD), 91-94, Tabriz, Iran

navigation system, or we call it satellite surveying (Johnson, 2004).

Satellite surveying relies on a lot of systems such as the Global Positioning System (GPS), GLONASS, GALILEO, and more. By using differential GPS (DGPS), in which data recorded by a receiver at a 'known' station are combined with data recorded simultaneously by a second receiver at a new station which might be 30 km away, it is possible to find the position of the second receiver to within about 5 mm. The advantage of GNSS compared to all earlier methods of surveying is that the two stations do not need to have a line of sight between them.

Studies on control establishment and extension have been carried out in the recent past. Jolaoso (2016) used the traditional method of traversing to obtain planimetric coordinates of the points using south digital theodolite for angular observation on four Zeroes, while the south distance measurer was used for the distance measurement. The coordinates obtained were analyzed, represented, and structured in a database after the application of necessary correction.

Similarly, Ahmadu (2016) carried out a second order control densification from Sambam-Kwoi junction, Jaba Local Government Area of Kaduna State. The researcher covered a length of 7.637km and established 24 control points that were inter-visible. The instrument used for observations was three numbers of Promark 3 differential GNSS receivers. The researcher concluded that Azimuth observation to control the bearing was not needed because GNSS observation uses satellites of which each position is independent of the other.

Furthermore, Oluwaseun (2017) implemented a Second order control extension from Mobolaje junction via Oba Adeyemi Grammar School to Folatyre, Oyo East Local Government Area Oyo, Oyo State. The researcher covered a length of 6.5km and established 20 control points. Two numbers of South H66/68 DGPS receivers were used to carry out observations. The researcher explained that control surveys establish a common, consistent network of physical points that are the basis for controlling the horizontal and vertical positions of transportation improvement projects and facilities.

Additionally, Emeka (2017) executed a project, the establishment of second order horizontal controls along the Umaru Musa Yar'dua expressway, Abuja. The researcher covered a linear length of 7.8km. In his choice of instrument, a lot were at his disposal. The Wild T1, Wild T2, Kern DKM3 and Ashtech Promark 3 DGPS. He opted for the Ashtech Promark3 DGPS because of the terrain and traffic. Although he spent an average of 90mins on each point. The plan for the control points was plotted using AutoCAD 2009 software.

Adamu (2019) performed a project, third order control extension from ABU Main Campus Samaru to College of Aviation Technology, along Zaria-Sokoto Road, Kaduna State. The methodology adopted was the application of the DTM (SET 624R) total station and its accessories for data collection. The researcher used AutoCAD Civil 3D and ArcGIS 10.4.1 for the plotting.

The rapid spring up of infrastructural development within Kaduna State with the Millennium city as a case study, resulted in a shortage of control networks, hence the need for second order controls to be extended to

enable Engineers and Land Surveyors to tie their third order jobs to survey control. There had been controls established before, however, these are mostly situated along Umaru Yar'dua Expressway and were not enough. It was difficult for survey activities in the interior because of the distance of the controls. It is against this problem that the researcher decided to come up with a second order control extension network and used modern survey equipment to extend controls to the interiors of the area.

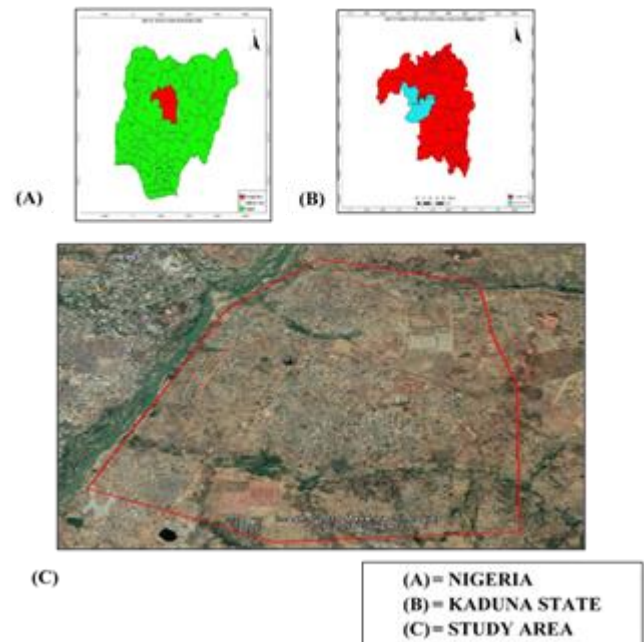


Figure 1. Study Area location

The project is located at Millennium City, Chikun Local Government Area of Kaduna State. The study area lies within Latitude $10^{\circ} 30' 33''$ N to $10^{\circ} 32' 38''$ N and Longitude $7^{\circ} 28' 18''$ to $7^{\circ} 30' 06''$ E. The total perimeter length to be covered is approximately 12.8km. Figure 1 shows the map of Nigeria, Kaduna state, and the study area of the project which is a millennium city.

2. Method

The equipment used are arranged in Table 1.

The software used include Hi-Target Geomatics Office; AutoCAD 2010; QGIS; MAPS.ME Navigation on Mobile Phone; Microsoft Office 2016, & Google Earth Pro.

Existing control points that were closer to the site area were accomplished by collecting the coordinates from Kaduna State Geographic Information Service (KADGIS) for easy connection.

A search was made at Kaduna Geographic Information Service (KADGIS) to determine the existing control points that are closer to the project area that had a better accuracy estimate of First Order to serve as a control for the project. Control station FGPKDY139 was closest to the project area.

The coordinates listed in Table 1, were collected from Kaduna Geographic Information Service (KADGIS), Kaduna state which were used as base stations for the work as well as in situ checks.

Hi-Target V30 dual-frequency GNSS receivers were used for data acquisition. Also, three GNSS receivers were used for simultaneous observation by the baseline solution method. Three datum controls FGPKDY139, KADGISC101, and KADGISC102 were used for the project network. During observation, a minimum of 90 minutes and a maximum of 120 minutes were made (to ensure that enough ephemeris data had been gathered) while the cut-off angle during the observation was 15 degrees.

The observed data were transferred and processed using Hi-Target Geomatics Office (HGO) processing software. Finally, a constraint adjustment was carried out to generate the final coordinates. The final coordinates were checked for discrepancies. The result suggested that the control stations are in situ and could be used for the research project.

Table 1. Equipment and materials used

S/ No.	Name	Quantity	Purpose
1	Hi-Target (V30) & its accessories	3	Used to collect static raw data
2	Handheld GPS	1	Used for navigation to proposed points
3	Shovel	2	Used for mixing sand and cement
4	Cutlass	2	Used for Clearing line of sight
5	Pocket Tape	1	Used for measuring Instrument Height
6	Mold	1	Used for Casting of Beacons
7	Head pan	2	Used to carry mixed concrete material
8	12mm Iron Rod	20	Used as station marker
9	Hammer	1	Used in driving the iron rod into the ground

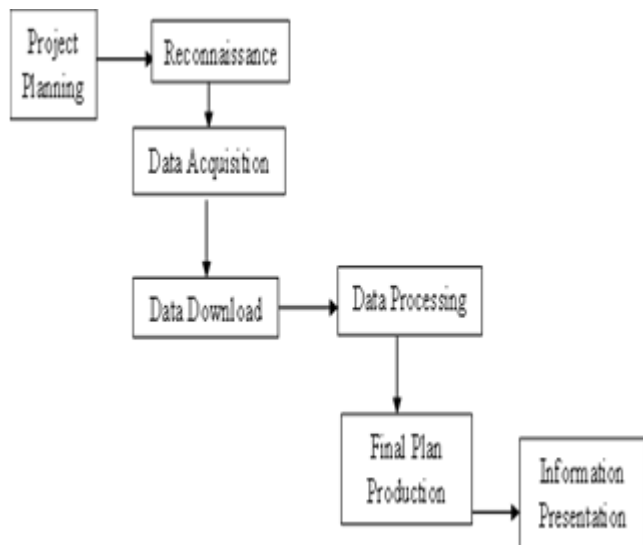


Figure 2. Study workflow diagram

The selected points were noted with safety as a consideration. The suitable location for the new control points position was accomplished effectively by plotting the data with the aid of Ortho-photo, and all the points were connected into a triangular network.

Table 1. Co-ordinate of controls (WGS84 Z32)

Beacon Number	Easting (m)	Northing (m)	Ellipsoidal Height
FGPKDY139	332813.950	1165452.920	613.278
KADGISC P101	332381.890	1165351.120	619.408
KADGISC P102	332402.310	1165316.060	619.996



Figure 3. GNSS Static Mode Observation in Progress

This research project was restricted to part of the millennium city, Kaduna, and a control network was made to cover the project area of 1,128.340 Ha, with a total number of twenty (20) control points established. The control points were limited to static GNSS observation procedures and the accuracy limited second order control survey accuracy in Nigeria. Also, the processing of the raw GNSS data was limited to manual post-processing using the Hi-Target Geomatics Office (HGO) and the final analysis and presentation of results to the scope of the research project.

3. Results and discussion

The result of data in Table 2 obtained from the adjusted data was analyzed and the result proved reliable as the unit variance and standard error values fell within the allowable limit.

Figure 3 shows the access road network to the controls, starting from Umaru Musa Yar'dua Expressway to the first control point (MCCP 106). There were 10 loops of triangles networks that made up the entire project area. The twenty (20) established controls station were plotted, taking into consideration the intervisibility between them. Similarly, a minimum of six (6) controls were established within a community, this was to enable other users with no access to GNSS equipment to have the minimum number of three controls required for in-situ check before embarking on any survey work.

The qualities obtained after adjustment in a GNSS network shows the adjusted baseline vector

components, their covariance, and the final coordinates. The baseline adjustment was performed using FGPKDY139 as the master or base control point which was held fixed. Adjustment of the data made it possible for further use in a GIS software environment.

Table 2. Established GNSS coordinate (UTM Minna Z32)

Station Name	Easting (m)	Northing (m)	Ellp_H (m)
FGPKDY139	332890.866	1165333.654	613.278
KADGISC101	332458.783	1165231.876	619.400
KADGISC102	332479.211	1165196.806	618.996
MCXT101	333144.364	1165231.854	619.414
MCXT102	332885.189	1163109.782	609.907
MCXT103	333206.120	1162964.613	613.143
MCXT104	333473.500	1163097.548	621.550
MCXT105	333868.285	1163274.886	627.389
MCXT106	333772.199	1162894.176	618.864
MCCP101	336259.490	1164043.913	649.816
MCCP106	333983.893	1164931.016	618.878
MCCP107	335724.455	1165315.584	626.182
MCCP108	334521.403	1165468.996	620.231
MCCP112	334338.943	1163783.478	629.963
MCCP114	333338.655	1163866.929	615.645
MCCP111	334643.066	1163135.566	622.775
MCCP116	335649.891	1162290.101	612.915
MCCP115	334589.411	1162202.006	609.778
MCCP117	333670.778	1162454.478	606.296
MCCP105	335191.044	1164865.017	640.931
MCCP109	335254.304	1164078.384	637.639
MCCP110	335472.478	1163336.933	634.268
MCCP113	334463.632	1164396.381	626.768

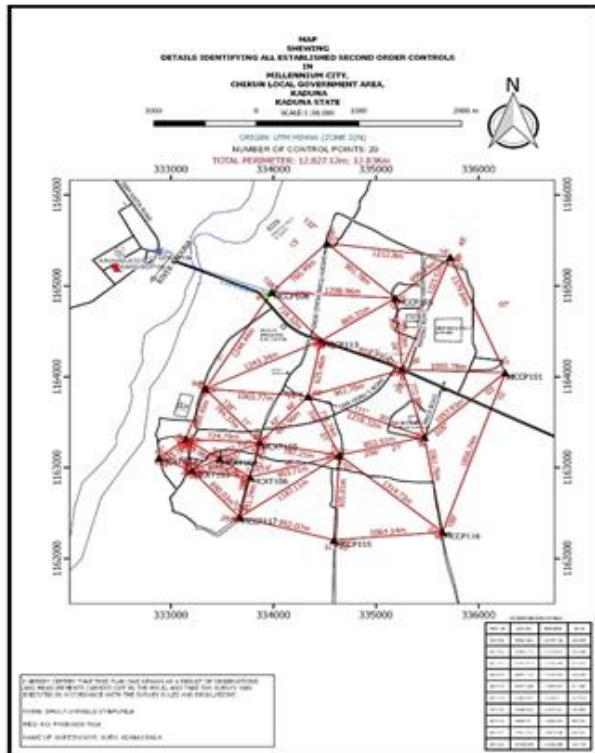


Figure 4. Composite Plan of the established controls

4. Conclusion

GNSS controls were successfully established at Millennium city in Chikun L.G.A. of Kaduna State. These controls can serve as bases for further surveying and mapping exercises around the area. GNSS method of

control extension is a versatile, accurate, quick, time saving, and economical way of establishing control points. The data collected was in WGS84 and transformed to UTM Minna Local datum. The data was found to be of very high accuracy. The benefits of the control stations established are numerous to government agencies and the private sector interested in cadastral and engineering surveys along with the project site. It is recommended that existing controls on the ground must be checked, and maintained more frequently to know their conditions; controls should be located where they are not liable to destruction, and awareness campaigns to educate people on the importance of government control pillars and property survey beacon to avoid them being tampered with or destroyed.

References

- Adamu, M. (2019). Third Order Control Extension from ABU Zaria Main Campus Samaru to College of Aviation Technology Along Zaria Sokoto Road. A Final Year Project at ABU Zaria, Kaduna State.
- Ahmadu, F.B. (2016). Second Order Control Densification from Sambam-Kwoi Junction, Jaba L.G.A of Kaduna State. A Final Year Project (PDS) at Kaduna Polytechnic, Kaduna.
- Baarda, W. (1968). *A Testing Procedure for Use in Geodetic Network*. Netherlands: Netherland Geodetic Commission.
- Basak, N. (2002). *Surveying and Levelling*. New Delhi: Tata McGraw Hill Education Private Limited.
- Caspary, W. F. (1987). *Concepts of Network and Deformation Analysis*. Volume 11 of Monograph (J. M. Rueger, Ed.) New South Wales, Wale: School of Surveying, University of New South Wales.
- Ehigior, O.M., Oladosu, S.O. and Ehigior, I. (2017). Densification of GNSS control points for Cadastral and Mapping Purpose. Article in Nigerian Journal of Environmental Sciences and Technology.
- Emeka, I. (2017). Establishment of Second Order Horizontal Control along Umaru Musa Yar'Adua Expressway, F.C.T, Abuja. A Final Year Project (PDS) at Kaduna Polytechnic, Kaduna.
- Johnson, A. (2004). *Plane and Geodetic Surveying*. Son Press, Talor and Francis group.
- Jolaoso, Y. A. (2016). Application of Classical Method for Third Order Survey Control Densification. *International Journal of Emerging Technologies in Computation*, pp. 93-96.
- Olayanju, O. (2017). Horizontal and vertical control survey along Osogbo – Ogbomosho Road, running from Oke – Awesin in Ifon up to Illajue in Oyo State.
- Oluwaseun, A. (2017). Second Order control Extension from Mobolaji Junction via Oba Adeyemi Grammar School to Folatyre, Oyo east L.G.A of Oyo State. A Final Year Project (PDS) at Kaduna Polytechnic, Kaduna.
- SURCON. (2008). Specification for Second Order Geodetic Control Establishment. Surveyors Council of Nigeria
- Uzodinma, N.V. & Ezenwere, O. C. (1993). Map Projections. Practical Computations on the Traverse Mercator Projection. EL' Demark Company, Enugu, Nigeria.



4th Intercontinental Geoinformation Days

igd.mersin.edu.tr



Analysis of a strong thunderstorm process observed in the eastern part of the Republic of Azerbaijan on June 1, 2017

Said Safarov^{*1} , Elnur Safarov¹ , Yegana Bayramova²

¹*Institute of Geography of National Academy of Sciences (Azerbaijan)*

²*National Hydrometeorological Department (Azerbaijan)*

Keywords

Cumulonimbus clouds
Anomalous multicellular processes
Rainfall
Thunderstorm
Hail
Floods
Mudflow

Abstract

The article is devoted to a comprehensive analysis of severe flood events that took place on the southern slope of the Greater Caucasus, including in the Gobustan region, on June 1, 2017. As a result of heavy rain and hail, farms and other facilities were seriously damaged in this area, and mudflows led to traffic stop on the section of the main Baku-Shamakhi Road, called the Jeyrankechmez valley. The influence of the dynamics of the development of thunderstorm clouds, as well as other factors on the formation of a strong flood, is analyzed. Based on the data of radar and satellite observations, as well as the analysis of aero synoptic material, considering the physical and geographical conditions of the given region, appropriate proposals were made for more reliable forecasting of such processes using radar data.

1. Introduction

As it is known, on the territory of Azerbaijan, thunderstorm processes and related mudflow phenomena are associated with high contrasts of surface temperatures and the influence of invading air currents (Climate of Azerbaijan). In recent years, due to global warming in various regions of the world, including in the territory of Azerbaijan, the intensity and frequency of such phenomena has increased. In some cases, these phenomena reach the level of a natural disaster by the intensity and scale of the damage. In most cases, heavy rainfall, hail, mudflows, and floods cause serious damage to certain sectors of the economy, including agriculture. From this point of view, a comprehensive study of such phenomena is of the greatest scientific and practical interest.

Ground-based radar and meteorological observations conducted on the territory of the Republic show that in recent years there has been an activation of the above-mentioned dangerous phenomena (Safarov et al. 2017).

From this point of view, the spring-summer period of 2017 was not an exception. Hazardous hail and storm events observed during this period, as well as mudflows and floods associated with them, are distinguished by great intensity and the scale of the damage caused.

Hazardous hail and storm events observed during this period, as well as mudflows and floods related with them, are distinguished by great intensity and the scale of the damage caused. The most powerful processes were noted on April 30, on May 16, 21, 27, 28, 31, on June 1, 10, 12, 13, 15, 20, 30 and on September 7, 16, 25, because of which serious damage was caused to crops and livestock, transport infrastructure, power lines and communications, residential and social facilities, as well as flora and fauna. The hailstorm process observed on June 1, 2017 in some places of the southeastern slope of the Greater Caucasus, by features of the dynamics of development, intensity, and amount of precipitation, as well as the scale and extent of damage, is of interest. The purpose of this article is a radar analysis of this process.

2. Material and Method

Radar data of automated MRL-5 of Shamakhi and Geygel radar stations and satellite data of the platform GPM were used in the work. The heights of the terrain, where both radar stations are standing, are about 1000 m. Automated MRL-5 was created based on meteorological incoherent radar MRL-5 with the introduction of the corresponding software and hardware complex. This system allows within a radius of

* Corresponding Author

^{*}(safarov53@mail.ru) ORCID ID 0000-0002-8447-2843
(elnur.safarov854@gmail.com) ORCID ID xxxx – xxxx – xxxx – xxxx
(bayramova.y@inbox.ru) ORCID ID xxxx – xxxx – xxxx – xxxx

Cite this study

Safarov, S., Safarov, E., & Bayramova, Y. (2022). Analysis of a strong thunderstorm process observed in the eastern part of the Republic of Azerbaijan on June 1, 2017. 4th Intercontinental Geoinformation Days (IGD), 95-98, Tabriz, Iran

250 km at any time and at any point in space to quickly assess the intensity, quantity, and other characteristics of precipitation. MRL data on the presence, location, direction, and speed of displacement of the centers of showers are the most operational and complete. Automated MRL-5 allows to monitor the dynamics of development and the cellular structure of the thunderstorm processes and determine the type of such processes. Other features of this system are described in detail in (Safarov, 2012). We also used synoptic maps and ground observation data.

3. Results and Discussion

According to synoptic maps, by 00 o'clock (GMT) on this day, the meteorological situation in Azerbaijan was determined by a local cyclone that formed over the Black Sea and deep baric hollows at different altitudes. This situation created a condition for the invasion of moist air masses from the Black Sea and cold air from the north,

which allowed the development of intensive convective processes.

According to synoptic maps, by 00 o'clock (GMT) on this day, the meteorological situation in Azerbaijan was determined by a local cyclone that formed over the Black Sea and deep baric trough at different altitudes. This situation created a condition for the invasion of moist air masses from the Black Sea and cold air from the north, which allowed the development of intensive convective processes.

According to the radar data of the Shamakhi and Geygel radiometeorological stations, on this day, beginning from noon, the formation of a cumulonimbus clouds was observed on the territory of Gabala, Ismayilli, Guba, Shamakhi and Gobustan regions. At the initial stage, the process of precipitation were a disordered nature, and in some places local showers were noted. Starting from 15 o'clock, precipitation intensified on the territory of Gusar, Zagatala, Gakh, Oguz, Gabala, Ismayilli, Shamakhi, Shabran and Khyzi districts in some places led to a descent of mudflow and floods (Fig. 1).

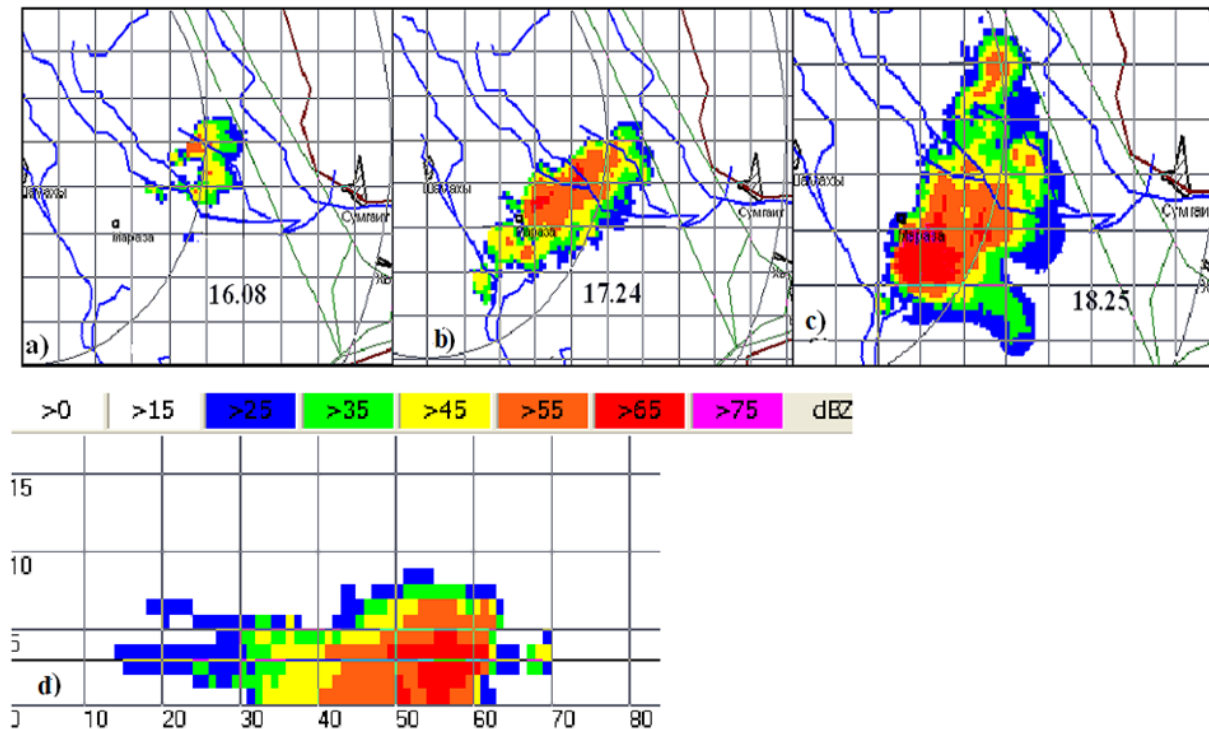


Figure 1. Evolution of the horizontal section of the radio-echo of the thunderstorm process at the level of 5000 m from the sea level observed in the Gobustan region (a, b, c) and the vertical section of the radio-echo to 18.25 (d).

According to radar observations, starting at 4 pm, a more powerful thunderstorm process was observed on the territory of Gobustan region (Fig. 1a).

Cumulonimbus (Cb) cloud rapidly developing by 18.30 turned into a powerful multi-cell thunderstorm process (Fig. 1a, b, c). According to its radar characteristics, (radar reflectivity Z_{10} , dBZ; height of the upper boundary of the radio echo cloud H_u , km; hail area S_h , km²; duration of the process and hail precipitation; intensity and amount of precipitation) this process turned out to be much more powerful than previous processes (Table 1).

Heavy hail fell in some places and precipitation intensity has reached a catastrophic level. As can be seen

from Fig. 2, from 16.00 to 20.00 more than 80 mm of precipitation fell, which is 45 mm more than the monthly norm of the area.

At times, precipitation intensity exceeded 60 mm/hour, which is confirmed by radar and satellite data. The temporal course of precipitation intensity built according to the GPM platform (Global Precipitation Measurement) of the Giovanni portal with a time resolution of 0.5 hours and a spatial resolution of 8 km is shown in Fig. 3. As can be seen from Fig. 3, by about 18:00 (14:00 GMT), the intensity of precipitation increased sharply and exceeded 60 mm/h.

Analyzing the character of the evolution of this hailstorm process using the patterns of distribution of the radar reflectivity and their animation, it is possible to explain the reason for the precipitation that is too abundant. As in most of the highly hazardous regions of

the world, the thunderstorms processes observed on the territory of Azerbaijan, according to their cell structure and development dynamics, are mainly divided into single-cell, multi-cell, and supercell.

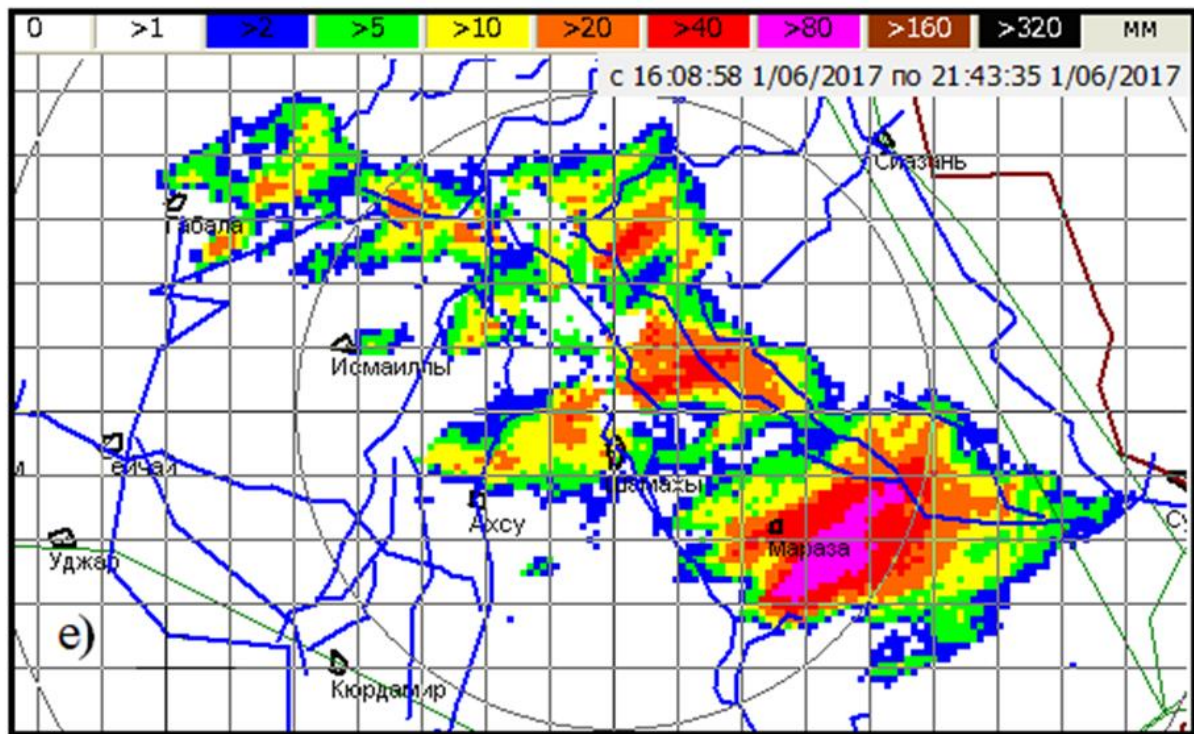


Figure 2. Distribution of precipitation over the territory in the thunderstorm process on June 1, 2017 from 16:08 to 21:43

Time Series, Area-Averaged of Multi-satellite precipitation estimate with gauge calibration - Final Run (recommended for general use) half-hourly 0.1 deg. [GPM GPM_3IMERGHH v06] mm/hr over 2017-06-01 00:00Z - 2017-06-02 00:00:00Z, Region 49.0986E, 40.5993N, 49.2002E, 40.7009N

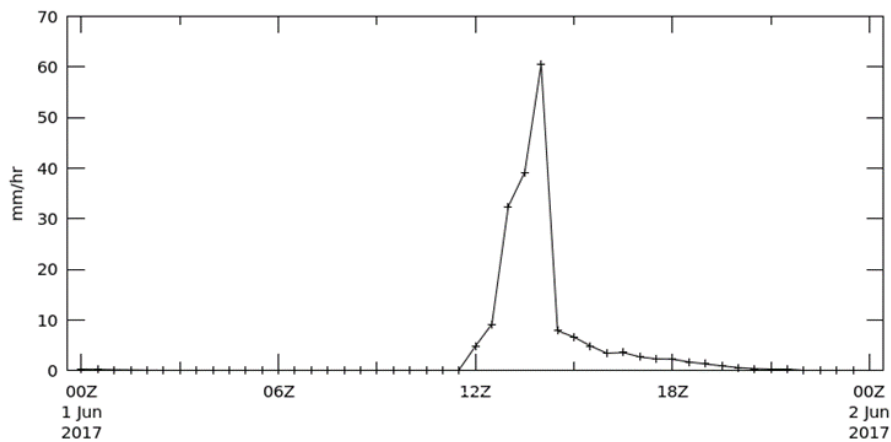


Figure 3. Time course of the precipitation intensity in the thunderstorm process on June 1, 2017, built by the data of GPM

Table 1. The maximum radar characteristics of the multi-cell hailstorm process 01.06.2017

Area	Horizontal sizes of hail area, km major axis	Horizontal sizes of hail area, km minor axis	Duration of the process, min	Length of hail strip, km	Amount of precipitation, n, mm	Z _{10,d} bz	Horizontal section area, km ²	H _u km	H _h km
Gobustan district	11	8	340	42	> 80	73	107	10	6
Nearby areas	7	4	125	23	45	68	65	9,2	5,8

Notes: 1. Z₁₀-radar reflectivity at a wavelength of 10 cm;

2. H_u - the height of the upper boundary of the radio echo of the cloud from sea level;

3. H_h - the height of the upper boundary of the hail cloud from sea level.

The characteristic features of these types of processes are described in more detail in (Safarov, 2012). Ordered multi-cell processes, in turn, are divided into normal and anomalous subtypes. In normal processes, due to the fact that new convective cells are formed on the right flank of the cloud system, to the right and slightly ahead of the previous cell, the stripes of precipitation of individual cells are almost parallel to each other.

In normal processes, due to the fact that new convective cells are formed on the right flank of the cloud system, to the right and slightly ahead of the previous cell, the stripes of precipitation of individual cells are almost parallel to each other. And with abnormal subtypes, new cells form at the back of the previous cell, relative to their direction of movement (Safarov, 2012; Safarov, 2018; Safarov 2019)

A detailed analysis of the radar material of the considered thunderstorm process has shown that it can be classified as anomalously ordered. Thus, new powerful convective cells periodically appearing behind the previous one (relative to the direction of their movement), moving along practically identical paths on the territory of the Gobustan district, led to long and intense rainfall, sometimes accompanied by dropping of large hail.

Despite the fact that individual convective cells moved from the south-west to the northeast at a speed of 15-20 km/h, the thunderstorm process as a whole and the corresponding cloud system stood still and did not move. All this led to heavy precipitation in the local territory, the amount of which exceeded 80 mm.

The disaster caused serious damage to the infrastructure of the territory, power lines and communications, bridges, and to a greater extent agriculture. In rivers, especially in the course of the Pirsaat River, water sharply increased, and the water level rose. In some places, intense precipitation led to the collapse of mudflows, as a result of which part of the Baku-Shamakhi main road in the area of the Dzheyranchekmez valley was flooded. Due to accumulated mud and flooding, more than 500 cars were stuck in transit and traffic in this part of the road was temporarily stopped.

It should be noted that in the territory of Azerbaijan, such anomalously ordered multi-cell processes are often observed, and in most cases, they lead to the loss of dangerous and sometimes catastrophic rainfall, sometimes accompanied by intense hail. For example, on

June 20, 1985, on the territory of Shamkir district, in one and the same places, strong precipitation was observed three times in one evening [4]. On May 21, 2014, an abnormally orderly process led to dangerous flooding in the Tovuz region. In some places of the region, the amount of precipitation was more than 100 mm [5].

4. Conclusion

Thus, radar detection of abnormally ordered multi-cell lightning-hail processes in any part of the territory of the Azerbaijan Republic, taking into account the relief and other terrain features, can be a reliable predictor of long-lasting heavy rainfall and associated mudflows and floods

References

- Climate of Azerbaijan / ed. A.A. Madatzade, EM Shyhlinsky. Baku, 1968, 343 p. (in Russian)
- Safarov, S. H., Nasibli, A. A., Huseynov, J. S., & İbrahimova, İ. V. Influence of Climate Warming on Hail Events in the Western Part of Azerbaijan / Proceedings of International Scientific Conference on Sustainable Development Goals 24-25 November 2017, Baku, Azerbaijan, pp. 83-89.
- Safarov, S. H. Thunderstorm and mudflow phenomena on the territory of Azerbaijan and radar methods for their forecasting / Baku: Elm, 2012, 292 p. (in Russian)
- Safarov, S. H. Radar study of various mechanisms for the formation of mudflows of storm genesis on the territory of Azerbaijan / II All-Russian Scientific Conference / "Modern problems of remote sensing, radar, propagation and diffraction of waves." Murom (Russia). 2018, s. 562-566 (in Russian)
- Safarov, S. H., Safarov, E. S. Mechanisms for the formation of mudflows of storm genesis in the territory of Azerbaijan / Materials of the International Scientific and Practical Conference "Global Climate Change: Regional Effects, Models, Forecasts" (Voronezh, Russia, October 3 - 5, 2019). 2019. p. 501-505 (in Russian)

4th Intercontinental Geoinformation Days

igd.mersin.edu.tr



Determining infestation of Pine Processionary Moth using remote sensing

Gonca Ece Özcan¹, Fatih Sivrikaya^{1*}¹Kastamonu University, Faculty of Forestry, Department of Forest Engineering, Kastamonu, Türkiye

Keywords

Landsat 8 OLI
 Thaumetopoea pityocampa
 Calabrian pine
 NDVI
 The paired sample t-test

Abstract

Insects are one of the most important elements of the natural balance in forest ecosystems. *Thaumetopoea pityocampa*, which is one of the important pests of Turkey's forests, causes increment loss, tree dead and economic losses in the forest stands. Therefore, there is a need for alternative methods of detecting and monitoring beetle damage with low cost and acceptable accuracy. Remote sensing data is widely used in beetle damage detection. In this study, the infestation of *Thaumetopoea pityocampa* in Calabrian pine forests in Kahramanmaraş Regional Directorate of Forestry, Elmalar Planning unit was determined with Remote Sensing data. 70 forest stands (sub-compartments) belonging to the infested (2016) and non-infested (2022) periods were determined in the study area. The minimum, average, maximum and total values of NDVI values were calculated using Landsat 8 OLI satellite images. The Kolmogorov-Smirnov normality test was used to determine whether the NDVI values were normal. Using SPSS software, the difference in NDVI values in infested and non-infested forest stands were statistically analyzed using a paired sample t-test. According to results, there was a statistically significant difference between all NDVI values in the years 2016 and 2022.

1. Introduction

Insects are the most important factors that threaten the existence, productivity and sustainability of Turkey's forests (Onaran and Kat 2010; Özcan, 2017). The Pine Processionary Moth (PPM) (*Thaumetopoea pityocampa* Schiff (Denis & Schiffermüller, 1775) (Lepidoptera: Notodontidae), which can cause significant damage to the forests in the Mediterranean region (Salvato et al. 2002) and has been known for many years in Turkey, spreads along the whole coastline (İpekdağ and Çağlar 2011). PPM larvae feed on pine needles (Kanat et al. 2002; Kerdellu et al. 2009), and in the advanced stage, they can cause the death of the trees. Due to the defoliation, they cause a great deal of needle loss and reduced tree growth. Generally, young trees suffer more damage than older trees (Jacquet et al. 2013).

PPM causes economic losses as it negatively affects diameter and height growth in trees, health problems due to its allergen and aesthetic problems due to defoliation of trees (Mendel 1990). While trees rarely die in old forest stands, significant decrease in increment can

occur. It was determined that trees with significant defoliation decreased by 24% in diameter, 36% in height and 52% in growing stock (Carus 2004). It was reported that, increment in Calabrian pine forests was decreased as 38.2% (Kanat et al. 2002) and 22.3% (Kanat and Sivrikaya 2005). In the afforestation areas of Crimean pine, the annual increment decreased by 34.6%-39.7% compared to the general average, and decreased by 58.3%-43.1% the following year (Altunışık and Avcı 2016). General Directorate of Forestry uses biological, chemical, mechanical, biotechnical and integrated control methods against this harmful species.

In the control against pests, the spatial determination of the damage is important in terms of the precautions to be taken. However, detection of the PPM in field survey is a time and cost-consuming activity. Therefore, there is a need for alternative methods with lower cost and acceptable accuracy. In this context, remote sensing (RS) techniques are used effectively in the detection and monitoring of PPM. Detection of beetle infestation using RS data depends on leaf discoloration and degree of leaf damage (Wulder et al. 2006). Each satellite image reveals

* Corresponding Author

(goncaece@kastamonu.edu.tr) ORCID ID 0000-0003-0141-1031
 (fsivrikaya@kastamonu.edu.tr) ORCID ID 0000-0003-0860-6747

Cite this study

Özcan, G. E., & Sivrikaya, F. (2022). Determining infestation of Pine Processionary Moth using remote sensing. 4th Intercontinental Geoinformation Days (IGD), 99-102, Tabriz, Iran

a different degree of beetle infestation in terms of its characteristics (White et al. 2006). Medium resolution satellite images such as Landsat satellite images are used effectively in beetle infestation detection studies due to their multispectral bands, covering large areas, 30 m spatial resolution and 16-day temporal resolution (Collins and Woodcock 1996; Franklin et al. 2003; Skakun et al. 2003).

The aim of this study is to determine the PPM infestation in the Calabrian pine forests with RS data in Kahramanmaraş Regional Directorate of Forestry, Kahramanmaraş Forest Enterprise, Elmalar Forest Planning Unit at 37°35'26" N, 36°53'04" E (WGS 84 datum, 37 zone) (Figure 1). The Mediterranean climate is in the south of Kahramanmaraş, and the continental climate is not harsh in the north. Winters are warm and rainy, and summers are hot and dry. The annual average temperature is 17.2 C°, the monthly average precipitation is 750.9 mm, the lowest temperature is -9.6 C° and the highest temperature is 45.2 C°. The total forest area in the planning unit is 13.575 ha, of which 11.223 ha (83% of the total study area) is productive forest and 2.352 ha (17% of the total study area) is degraded forest. The main tree species in the study area are Calabrian pine (*Pinus brutia* Ten.), Oak (*Quercus* spp.), and Stone pine (*Pinus pinea* L.).

2. Method

The study area is located Kahramanmaraş Regional Directorate of Forestry, Kahramanmaraş Forest Enterprise, Elmalar Forest Planning Unit at 37°35'26" N, 36°53'04" E (WGS 84 datum, 37 zone) (Figure 1). The Mediterranean climate is in the south of Kahramanmaraş, and the continental climate is not harsh in the north. Winters are warm and rainy, and summers are hot and dry. The annual average temperature is 17.2 C°, the monthly average precipitation is 750.9 mm, the lowest temperature is -9.6 C° and the highest temperature is 45.2 C°. The total forest area in the planning unit is 13.575 ha, of which 11.223 ha (83% of the total study area) is productive forest and 2.352 ha (17% of the total study area) is degraded forest. The main tree species in the study area are Calabrian pine (*Pinus brutia* Ten.), Oak (*Quercus* spp.), and Stone pine (*Pinus pinea* L.).

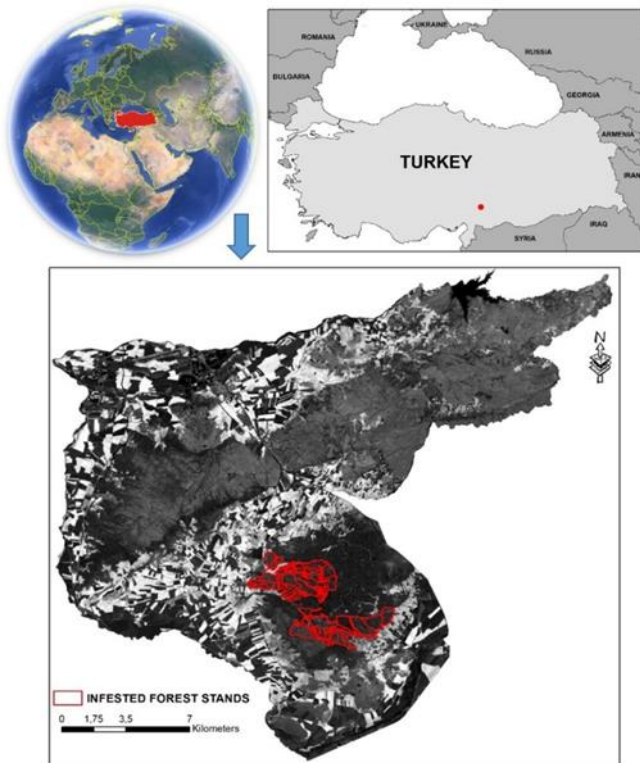


Figure 1. Study area location in Kahramanmaraş, Türkiye

In the study area, the natural outbreak was observed in 2015, followed by 2016, and 2017. Landsat images from *T. pityocampa* infested (2016) and non-infested (2022) periods were compared in Calabrian forests in Kahramanmaraş Regional Directorate of Forestry. Landsat 8 Operational Land Imager (OLI) images of two different time periods (2016 and 2022) were used to compare the (Normalized Vegetation Index) NDVI values in 2016 and 2022. These data with cloud cover less than 5% were downloaded from <https://earthexplorer.usgs.gov> (USGS, 2022) (Table 1). Some pre-processes were applied to make the Landsat 8 OLI satellite images to be used in the study ready for analysis. Atmospheric correction was made on Landsat 8 OLI satellite images and the digital number values of the bands (Red and NIR) to be used for NDVI were converted to reflectance values.

Table 1. The properties of Landsat 8 OLI images used in the study

Acquisition Date	Cloud cover (%)	Band Name	Central wavelength (µm)	Spatial resolution (m)
2016/04/23	0.52	Blue	0.45-0.51	30
		Green	0.53-0.59	
		Red	0.64-0.67	
		NIR	0.85-0.88	
2022/04/16	3.29	SWIR 1	1.57-1.65	
		SWIR 2	2.11-2.29	

In the study area, 70 forest stands (sub-compartments) were overlaid to satellite images of 2016 and 2022. NDVI values were estimated according to the obtained reflectance values. NDVI values for 70 selected forest stands were calculated according to the Eq. 1

$$NDVI = (NIR - RED) / (NIR + RED) \quad (1)$$

Where NIR is the near infrared wavelength of the spectrum (0.851 – 0.879 µm), RED is the red region wavelength (0.636 – 0.673 µm), and NDVI is the vegetation index value.

Since the area of each forest stand and the number of pixels falling into these forest stands will be different, the minimum, average, maximum and total values of NDVI in each forest stands were calculated using ArcGIS 10.6. The normality of the NDVI values was performed using the Kolmogorov-Smirnov normality test. Paired sample t-test was used to statistically analyze the differences between NDVI values in infested and non-infested forest stands using SPSS software.

3. Results and Discussion

In recent studies, NDVI is a frequently used method for monitoring beetle infestation (Rullan-Silva et al. 2013). Figure 2 shows NDVI images of the study area for infested (2016) and non-infested (2022) periods that were generated to investigate the infestation by PPM in the Elmalar planning unit using Landsat 8 OLI images.

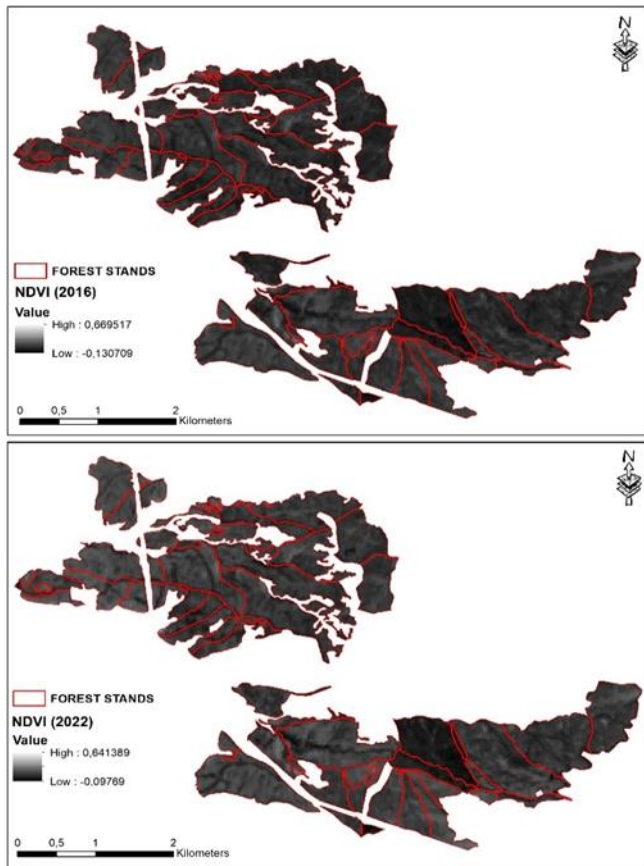


Figure 2. NDVI images in infested (2016) and non-infested (2022) periods (lighter pixels = high NDVI values, darker pixels = low NDVI values)

The minimum, average, maximum and total values of NDVI obtained from PPM infested (2016) and non-infested (2022) periods were statistically compared. All NDVI values were normally distributed according to the Kolmogorov-Smirnov test of normality. The paired sample t-test of the minimum, average, maximum and total values of NDVI results figure out that there was a statistically significant difference between all NDVI values in the years 2016 and 2022 (Table 2). Severe beetle infestation was in the study area in 2016. For this reason, the Regional Directorate of Forestry carried out successful efforts to control against beetle damage. The results also support this situation. In 2016, NDVI values are lower than in 2022 due to beetle damage.

Table 2. The result of the paired sample t-test for the minimum, average, maximum and total values of NDVI

Years	Mean	N	Std. Dev.	t	P
2016 Min.	0.071	70	0.019	-	0.000
2022 Min.	0.086	70	0.025	11.370	0.000
2016 Ave.	0.112	70	0.019	-	0.000
2022 Ave.	0.139	70	0.024	25.154	0.000
2016 Max	0.173	70	0.050	-8.417	0.000
2022 Max	0.210	70	0.055		
2016 Total	21.380	70	23.658	-7.761	0.000
2022 Total	26.612	70	29.054		

NDVI values were significantly reduced in the year of infestation due to the reduction in NIR band value (Junttila et al. 2015; Rock et al. 1988). De Beurs and Townsend (2008) used the NDVI and EVI indices in MODIS satellite images to determine the damage caused by *Lymantria dispar* (L.) (Lepidoptera: Erebidiae) on deciduous trees in the central Appalachian region of the USA. NDVI decreases at the beginning of epidemic beetle infestation, according to research on oak mortality in California using high-resolution images (Kelly 2002). Townsend et al. (2012) successfully classified and mapped defoliation severity using NDIIb5 together with a logistic regression model in Landsat TM. Spruce et al. (2011) stated that NDVI is better at distinguishing moderate damage from low damage in a deciduous forest. NDVI has a strong positive linear correlation between 25% and 80% vegetation cover in forest ecosystems (Zhang et al. 2010).

4. Conclusion

Landsat satellite images with medium spatial resolution can be used to assess the damage caused by PPM outbreaks, identify and analyze their ecological impact. Our results are consistent with similar studies. Gooshbor et al. 2016 stated that NDVI values for 2002 (before infestation), and 2007 and 2014 (after infestation) showed a statistically significant decrease in oak forest infested by oak leaf roller.

Acknowledgement

We would like to express our gratitude to the Kahramanmaraş Regional Directorate of Forestry personnel for providing the forest stand type map and related beetle information.

References

- Altunışık, A., & Avcı, M. (2016). Isparta çam ormanlarında çam kese böceği (*Thaumetopoea wilkinsoni* Tams, 1926) (Lep.: Notodontidae) zararının artım üzerine etkisi. Türkiye Entomoloji Bülteni, 6(3), 231-244.
- Carus, S. (2004). Impact of defoliation by the pine processionary moth (*Thaumetopoea pityocampa*) on radial, height and volume growth of Calabrian pine (*Pinus brutia*) trees in Turkey. Phytoparasitica, 32(5):459-469.
- Collins, J. B., & Woodcock, C. E. (1996). An assessment of several linear change detection techniques for mapping forest mortality using multitemporal Landsat TM data. Remote Sensing of Environment, 56: 66-77.
- De Beurs, K., & Townsend, P. (2008). Estimating the effect of gypsy moth defoliation using MODIS. Remote Sensing and Environment, 112: 3983-3990.
- Franklin, S. E., Wulder, M. A., Skakun, R. S., & Carroll, AL. (2003). Mountain pine beetle red-attack forest damage classification using stratified Landsat TM data in British Columbia, Canada. Photogrammetric Engineering and Remote Sensing, 69: 283-288.
- Gooshbor, L., Bavaghar, M. P., Amanollahi, J., & Ghobari, H. (2016). Monitoring infestations of oak forests by

- Tortrix viridana* (Lepidoptera: Tortricidae) using remote sensing. *Plant Protection Science*, 52(4), 270-276.
- İpekdağ, K., & Çağlar, S. S. (2011). *Thaumetopoea pityocampa* ve *T. wilkinsoni*'nin Türkiye'deki yayılışının ve melezleşmesinin moleküler yöntemlerle araştırılması. *Türkiye I. Orman Entomolojisi ve Patolojisi Sempozyumu*, 23-25.
- Jacquet, J. S., Bosc, A., O'Grady, A. P., & Jactel, H. (2013). Pine growth response to processionary moth defoliation across a 40-year chronosequence. *Forest Ecology and Management*, 293:29-38.
- Junttila, S., Kaasalainen, S., Vastaranta, M., Hakala, T., Nevalainen, O., & Holopainen, M. (2015). Investigating bi-temporal hyperspectral lidar measurements from declined trees- experiences from laboratory test. *Remote Sensing*, 7:13863-13877.
- Kanat, M., & Sivrikaya, F. (2005). Çam kese böceğinin kızılçam ağaçlarında çap artımı üzerine etkileri. *Kahramanmaraş Sütçü İmam Üniversitesi Fen ve Mühendislik Dergisi*, 8(2), 74-78.
- Kanat, M., Sivrikaya, F., & Serez, M. (2002). A research on damage of pine processionary moth (*Thaumetopoea pityocampa* Schiff.) on *Pinus brutia* Ten. trees, and the effect of tending activities on the diameter increment of Calabrian pine in Kahramanmaraş. Pages 44-51 in *Pine Processionary Moth Symposium*, (Ed. M. Kanat), (Kahramanmaraş, Turkey).
- Kerdelhué, C., Zane, L., Simonato, M., Salvato, P., Rousselet, J., Roques, A., & Battisti, A. (2009). Quaternary history and contemporary patterns in a currently expanding species. *BMC Evolutionary Biology*, 9(1):220.
- Mendel, Z. (1990). On the origin of the pine processionary caterpillar, *Thaumetopoea wilkinsoni* Tams (Lep.: Thaumetopoeidae) in Israel. *Journal-of-Applied-Entomology*, 109: 3, 311-314.
- Onaran, M. A., & Katı, M. (2010). Çam kese böceği (*Thaumetopoea pityocampa* Schiff) ile biyolojik mücadele. *Balıkesir Üniversitesi Fen Bilimleri Enstitüsü Dergisi*, 12(2), 21-27.
- Özcan, G. E. (2017). Assessment of *Ips sexdentatus* population considering the capture in pheromone traps and their damages under non-epidemic conditions. *Şumarski list*, 141(1-2), 47-55.
- Rock, B., Hoshizaki, T., & Miller, J. (1988). Comparison of in situ and airborne spectral measurements of the blue shift associated with forest decline. *Remote Sensing of Environment*, 24: 109-127.
- Rullan-Silva, C. D., Olthoff, A. E., Delgado, de la Mata J. A. & Pajares-Alonso, J. A. (2013). Remote monitoring of forest insect defoliation. A review. *Forest Systems*, 22: 377-391.
- Salvato, P., Battisti, A., Concato, S., Masutti, L., Patarnello, T., & Zane, L. (2002). Genetic differentiation in the winter pine processionary moth (*Thaumetopoea pityocampa* – wilkinsoni complex), inferred by AFLP and mitochondrial DNA markers. *Molecular Ecology*, 11, 2435-2444.
- Skakun, R. S., Wulder, M. A., & Franklin, S. E. (2003). Sensitivity of the thematic mapper enhanced wetness difference index to detect mountain pine beetle red-attack damage. *Remote Sensing of Environment*, 86: 433-443.
- Spruce, J., Sader, S., Ryan, R., Smoot, J., Kuper, P., & Ross, K. (2011). Assessment of MODIS NDVI time series data products for detecting forest defoliation by gypsy moth outbreaks. *Remote Sensing and Environment*, 115: 427-437.
- Townsend, P., Singh, A., Foster, J., Rehberg, N., Kingdon, C. & Eshleman, K. (2012). A general Landsat model to predict canopy defoliation in broadleaf deciduous forests. *Remote Sensing and Environment*, 119: 255-265.
- U.S. Geological Survey (2021). <https://earthexplorer.usgs.gov/>. Accessed 25 March 2022.
- White, J. C., Wulder, M. A., & Grills, D. (2006). Detecting and mapping mountain pine beetle red-attack damage with SPOT-5 10-m multispectral imagery. *BC Journal of Ecosystems and Management*, 7: 105-118.
- Wulder, M. A., Dymond, C. C., White, J. C., Leckie, D. G., & Carroll, AL. (2006). Surveying mountain pine beetle damage of forests: a review of remote sensing opportunities. *Forest Ecology and Management*, 221: 27-41.
- Zhang, T., Zhang, X., Liu, H., & Pei, X. (2010). Application of remote sensing technology in monitoring forest diseases and pests. *Plant Diseases and Pests*, 1(3), 57-62.

4th Intercontinental Geoinformation Days

igd.mersin.edu.tr



Crop mapping using Sentinel-1 and Sentinel-2 images and random forest algorithm

Ali Shamsoddini ^{*1}, Bahar Asadi ¹¹Tarbiat Modares University, faculty of Humanities, Department of Remote Sensing and GIS, Tehran, Iran**Keywords**

Optical and radar image fusion
Crop mapping
Red-Edge Band
Random Forest
Remote Sensing

Abstract

Crop mapping can provide valuable information for agricultural land management and crop estimation. This study investigated the spectral bands of Sentinel-2 time series, their vegetation indices, Sentinel-1 VV and VH time series of the radar backscatter coefficient, and the VV/VH ratio. This study explored the importance of the red-edge wavelengths of Sentinel-2 imagery for crop mapping using the random forest (RF) method. Therefore, the 2019 time series of Sentinel-1 and 2 images for the growing season in northwest Ardabil, Iran, were retrieved from the Google Earth Engine. After pre-processing, these images were segmented using the multi-scale method, and then the spectral features of optical imagery and the radar backscatter coefficient were extracted for each segment. To examine the importance and role of red-edge wavelengths, in addition to the three red-edge bands, visible and infrared wavelengths, and plant indices derived from these bands, red-edge indices were also factored in as input features. Overall, nine scenarios were simulated using different inputs and combinations. In each scenario, key features were identified using RF feature selection and introduced as inputs for the RF algorithm for an object-oriented classification. The research results showed that the addition of red-edge bands and the derived indices increased the accuracy of crop type mapping. The best result was obtained for a combination of optical and radar images with an overall accuracy of 87.59% and a kappa coefficient of 85.40%.

1. Introduction

The area of land used for cultivating different crops in a certain period is called the cropping pattern. Meanwhile, the agricultural production level is a decisive factor that influences the agricultural economy (Aduvukha et al., 2021).

Aside from the significance of temporal information, considering the unique phenological properties of different crops, it is crucial to identify and employ suitable data for specific dates in a time series in order to obtain more accurate results. Therefore, it is worthwhile to assess the relative importance of Sentinel-2 spectral bands for crop classification and particularly the performance of data from red-edge bands, which are missing in conventional sensors such as Landsat and SPOT and are less often studied. Indices used based on red-edge features are influenced by leaf structure, leaf chlorophyll, and leaf canopy cover and can acceptably distinguish crops (Zhong et al., 2014). Although the spectral reflectance of crops is affected by the vegetation cover status (e.g., chlorophyll content, pigmentation,

canopy, and leaf water content) and provides valuable information for crop mapping (Zhang et al., 2017), plant structure information can also prove critical in this regard. When it comes to crops with similar phenological cycles, spectral information alone can hardly be enough for crop classification. Radar images, such as Sentinel-1 data, contain information about the vegetation structure, and so combined optical and radar images can complement each other and help to improve the results (Sun et al., 2020). Some studies confirm the high capability of radar images, especially cross-polarized imagery, in the separation of agricultural products (Ban et al., 2003; Skriver et al., 2011). Meanwhile, considering the differences in plant growth stages and spectral features of different crops during the growth period, various combinations of optical time series images and radar back-scattering coefficients were tested to assess the performance of different indices in crop mapping. Several similar studies have used multi-time Sentinel-2 and Sentinel-1 images, whereas few have investigated the spectral features of the three red-edge bands of this sensor's optical images and their vegetation indices.

* Corresponding Author

^{*}(ali.shamsoddini@modares.ac.ir) ORCID ID 0000-0002-4559-7563
(bahar.66asadi@gmail.com) ORCID ID 0000-0002-6355-7418

Cite this study

Shamsoddini, A., & Asadi, B. (2022). Crop mapping using Sentinel-1 and Sentinel-2 images and random forest algorithm. 4th Intercontinental Geoinformation Days (IGD), 103-107, Tabriz, Iran

Therefore, this study also aimed to assess the performance of Sentinel red-edge bands in crop classification through different approaches and combinations of optical and radar images.

2. Case Study and Research Data

The study area is located at 38.13 to 38.23 N and 48.16 to 48.9 E in northwestern Iran (Figure 1). Monocropping is dominant across the study area due to the region's climatic conditions, yet adequate precipitation makes it suitable for growing a variety of crops, including cereals, legumes, potatoes, and sugar beet.

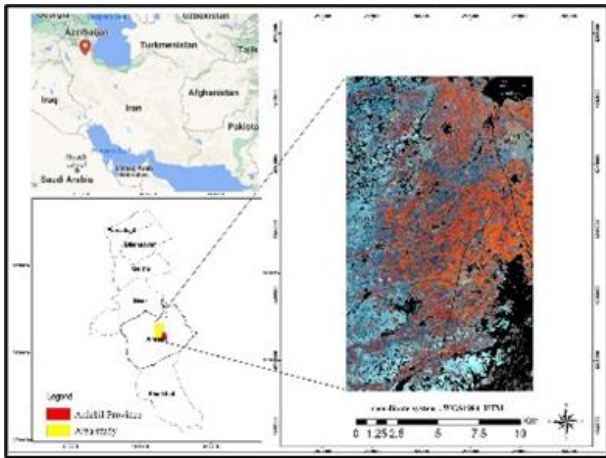


Figure 1. Location of the study area and its false-color image from Sentinel-2

The research data consisted of the region's crop type in 2019 collected through ground monitoring. These included alfalfa/sainfoin, wheat, barley, beans, corn, broad bean, Linaceae (flax), potatoes, and sugar beet, which make up the primary produce of the Ardabil plain. The fields' location and crop type were acquired through land survey and GPS measurements.

3. Methodology

The research flowchart is presented in Figure 3. After image collection and preprocessing (e.g., radiometric corrections and speckle noise reduction in radar images), the necessary features were extracted from the imagery. More detailed descriptions of each step are provided below.

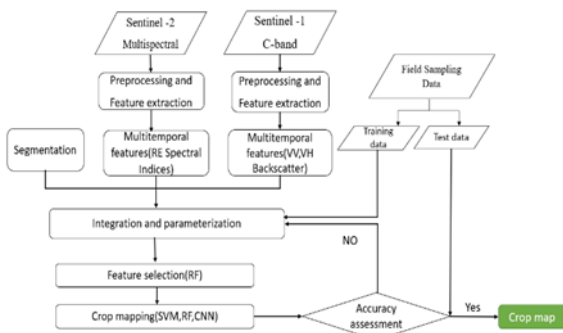


Figure 2. Conceptual diagram and research flowchart

This study used time series images of Sentinel-2 and Sentinel-1. Considering the features of different time series bands, 10 m and 20 m bands (specifically, bands 2–7, 8 and A8, and also 11 and 12) were selected here and the pixel size of the 20 m bands was downscaled from 20 m to 10 m. The crop phenological dates were obtained from the crop calendar and NDVI time-series curves to determine the suitable research period, and accordingly, L2A time series images for a two-month period (from June 18 to September 18) were retrieved for the study area using the Google Earth Engine (i.e., Sen2Cor atmospherically-corrected L2A images in GEE). The Sentinel-1 Ground Range Detected (GRD) time series images were retrieved from May 7 to September 28 using the GEE platform. Then the images were preprocessed, including conversion of images into sigma0 images in the logarithmic scale (dB) and reduction of speckle effects using the Enhanced Lee Filter.

3.1. Image Segmentation

Image segmentation means partitioning a digital image into multiple distinct regions, that is, grouping the image elements using specific homogeneity criteria (Meinel et al., 2001). The first stage in object-based classification is segmenting the image into meaningful parts, which was performed here using the popular multi-scale segmentation method (Salehi et al., 2017). Therefore, segmentation was done using the time series (10, 20 m) images, the first four (PCA1-PCA4) components of the time series of sentinel-2 image bands (showing the regional changes), and NDVI.

3.2. Feature Extraction

In the second stage, vegetation indices, spectral features, and the radar backscattering coefficient ratio were extracted (Table 1). A total of 27 vegetation indices based on visible, infrared, and red bands were calculated and the time series (10, 20 m) of optical images were selected as input features for classification. Features obtained from SAR images include the VV and VH backscattering time series, the VV/VH back-scattering ratio, and the Normalized Ratio Procedure between Bands (NRPB) estimated using the VV and VH backscatter (Filgueiras et al., 2019).

3.3. Random Forest Algorithm

The random forest (RF) algorithm is a collection of decision trees that make output predictions by combining outcomes from all decision trees. To classify an input vector, it is submitted as an input to each of the trees in the forest, and the classification is then determined based on the class label with the majority vote (Rodriguez et al., 2012). The parameters that need to be optimized in this classifier are the number of trees and the number of features used in each tree. The former was obtained through cross-validation and out-of-the-box data analysis and the latter through the square root of the number of features (Belgiu et al., 2018).

Due to the large size of input features, the RF feature selection method was used to reduce the dimensionality of the input data (Shamsoddini et al., 2013).

Table 1. Research features

Sentinel-2 time series features	Spectral band time series (B2, B3, B4, B5, B6, B7, B8, B8A, B11, and B12) Vegetation indices, including, NDVI (Tucker, 1979b), ReNDVI (Fernández et al., 2016), MSRre (Chen et al., 1996), MCARI (Daughtry et al., 2000), IRECI (Frampton et al., 2013), TVI (Khosravi et al., 2018), Ndre1 (Gitelson et al., 1994), NDSAVI (Qi et al., 2002), NDRI (Gelder et al., 2009), NDWI (Sun et al., 2020) (192 features in total)
SAR time series features	1. VV and VH radar backscattering coefficient 2. VV/VH ratio, NRPB (Filgueiras et al., 2019) (48 features in total)

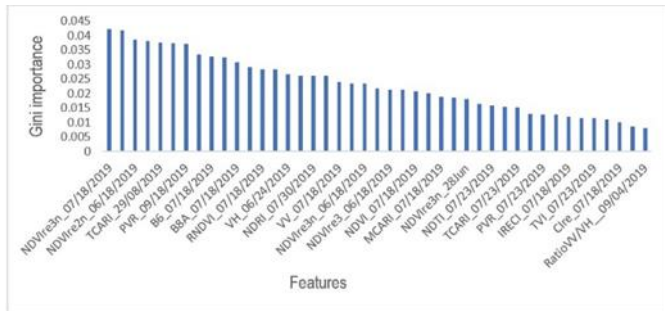
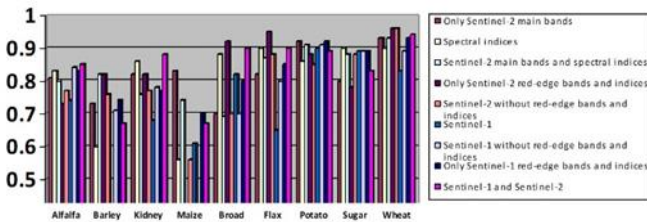


Figure 3. Feature importance results of combined Sentinel 1 and 2 imagery using RF

Table 2. Object-oriented classification results using different input data combination scenarios



3.4. Assessment of classification accuracy

The k-fold cross-validation method was used to prevent feature over-fitting in machine learning methods and optimize the RF algorithm parameters. Aiming to assess the performance of the classifier, the field data was split into training sample (70%) and testing sample (30%) sets, and different indices such as overall kappa accuracy, user accuracy, producer accuracy, and F1-Score were used.

4. Results and Discussion

Based on the Gini index (Figure 3), the most important features in crop classification using a

combination of optical and radar imagery were the red-edge vegetation indices NDVIre3n (July 18), IRECI (Sept. 18), and NDVIre2n (June 18), respectively. These results demonstrate the importance of red-edge bands and the vegetation indices obtained from them in crop mapping, with the most effective bands being red-edge (especially bands B6 and B7), B8 near-infrared, and B8A near-infrared wavelengths. The first red-edge B5 band was more affected by the leave chlorophyll content than the other two red-edge bands. Many crops have a high chlorophyll content in the middle and peak stages of their growth and fruiting. Green and red bands are saturated in areas with high chlorophyll content, which limits their application in crop classification, whereas, Sentinel-2 6B band, with more sensitivity to chlorophyll concentration, can provide the necessary information (Gitelson et al., 1996).

According to Table 2, the best result was obtained for the combination of all the features obtained from optical and radar images through the object-oriented classification with an overall accuracy of 87% and a kappa coefficient of 85%. The results showed that RF-based feature selection in all different combinations of features extracted from Sentinel images increased the accuracy by 2-3% compared to the scenario of using all the features. Random forest is highly effective in reducing the effect of data redundancy in a time series and enhancing the classification accuracy with minimal image input (Nitz et al., 2015). This method enjoys a high training and classification speed and can effectively classify high-dimensional features (Joelsson et al., 2005). The advantages of the RF algorithm in this study included higher training speed, no overfitting, and compatibility with high-dimensional features (Kang et al., 2021). According to Table 2, classification using only the red-edge bands and their vegetation indices can acceptably separate crops; followed by the near-infrared (NIR) and short-wave infrared (SWIR) bands (Zahang et al., 2020). Moreover, using the red-edge bands along with other Sentinel-1 and Sentinel-2 bands improved the classification accuracy. Overall, red-edge bands performed better than visible wavelengths, mainly due to their higher capability to obtain plant biochemical information (Zahang et al., 2020). In Scenario 4, classification using red-edge bands and their vegetation indices was more accurate for crops such as barley, wheat, broad beans, kidney beans, and flax.

The selection of spectral bands and their vegetation indices influences the accuracy of crop classification (Orynbaikyzy et al., 2019). The accuracy of wheat, beet, potato, and broad bean classification was 83%, 89%, 90%, and 82%, respectively. For other classes, product classification based only on Sentinel-1 images was not adequately successful, likely because: (1) the radar backscattering intensity is different for different crops based on their canopy cover, however, the radar incidence angle and soil surface moisture can affect the radar backscattering, which makes it difficult to differentiate between crops with a similar canopy and appearance (Orynbaikyzy et al., 2019). (2) The speckle in radar images increases the inter-class diversity and decreases the separability of different classes, even though speckle is highly dependent on the surface properties and is not

actually noise. On the other hand, speckles can affect the statistics and the distribution of pixel values in the feature space by increasing the variance of each class and the covariance between classes. This increases the separability between classes and possibly the classification error (Tavakoli, 2011). (3) The incidence angle leaves little room for differentiating certain crop types. Therefore, the limited viewing angle and radar data orbits make using only radar data insufficient for crop classification, especially when there are various crop types (Brisco, 1998). The higher the radar viewing angle, the higher the accuracy of crop separation (Brisco, 1998). According to the results, vegetation indices outperformed the main bands in crop classification. Specifically, the NDVI_{re3n}, IRECI, and NDVI_{re2n} indices proved highly effective. The data extracted from Sentinel-1 images alone did not provide enough accuracy, and so the classification accuracy was increased (by 6%) after including three red-edge bands and their vegetation index (NDVI_{re}, CI_{re}, and MSR_{re}). In this scenario, alfalfa, maize, and potato plants were separated more accurately than in other scenarios. The combined use of Sentinel-1 and 2 imageries in this study showed that optical images alone can accurately map crops. Considering that combining optical and radar images increases the data dimensionality, which hinders machine learning, this should be done in specific circumstances and based on the type of crops under study (Orynbaikyzy et al., 2019).

5. Conclusion

This study examined the performance of a random forest classifier with nine different scenarios in crop classification using input features extracted from Sentinel-1 and 2 imageries. The research results can be summarized as follows:

- Separation of crops with only optimal features from the RF classifier provided better results than classification using all features.
- In this study, indices based on red-edge, near-infrared, narrow-band near-infrared, and short-wave infrared (SWIR) wavelengths were more accurate. Overall, the inclusion of red-edge wavelengths increased the crop classification accuracy.
- The combined use of the Sentinel-1 and Sentinel-2 time series data had the best performance in crop separation.
- Red-edge vegetation indices showed optimal performance in identifying crops such as wheat, barley, broad beans, kidney beans, and flax.
- The research findings can inform decisions concerning the selection of spectral bands for achieving higher accuracy in crop classification.

References

- Aduvukha, G. R., Abdel-Rahman, E. M., Sichangi, A. W., Makokha, G. O., Landmann, T., Mudereri, B. T., ... & Dubois, T. (2021). Cropping Pattern Mapping in an Agro-Natural Heterogeneous Landscape Using Sentinel-2 and Sentinel-1 Satellite D atatasets. *Agriculture*, 11(6), 530.
- Breiman, L. (2001). Random forests. *Machine learning*, 45(1), 5-32.
- Bégué, A., Arvor, D., Bellón, B., Betbeder, J., Abelleira, D. D., Ferraz, R. P. D., ... & Verón, S. R. Remote Sensing and Cropping Practices: A Review. *Remote Sens*, 2018, 10 (1), 99.
- Belgiu, M., & Csillik, O. (2018). Sentinel-2 cropland mapping using pixel-based and object-based time-weighted dynamic time warping analysis. *Remote sensing of environment*, 204, 509-523.
- Congalton, R. G. (1991). A review of assessing the accuracy of classifications of remotely sensed data. *Remote sensing of environment*, 37(1), 35-46.
- Chong, L. U. O., LIU, H. J., LU, L. P., LIU, Z. R., KONG, F. C., & ZHANG, X. L. (2021). Monthly composites from Sentinel-1 and Sentinel-2 images for regional major crop mapping with Google Earth Engine. *Journal of Integrative Agriculture*, 20(7), 1944-1957.
- Drăguț, L., Tiede, D., & Levick, S. R. (2010). ESP: a tool to estimate scale parameter for multiresolution image segmentation of remotely sensed data. *International Journal of Geographical Information Science*, 24(6), 859-871.
- Filgueiras, R., Mantovani, E. C., Althoff, D., Fernandes Filho, E. I., & Cunha, F. F. D. (2019). Crop NDVI monitoring based on sentinel 1. *Remote Sensing*, 11(12), 1441.
- Haghshenas, N., Shamsoddini, A., & Aghighi, H. (2021). Urban Tree Canopy Mapping Using Object Oriented Classification and Machine Learning Algorithms. *Iranian Journal of Remote Sensing & GIS*, 13(1), 17-32.
- Gitelson, A. A., Kaufman, Y. J., & Merzlyak, M. N. (1996). Use of a green channel in remote sensing of global vegetation from EOS-MODIS. *Remote sensing of Environment*, 58(3), 289-298.
- James, G., Witten, D., Hastie, T., & Tibshirani, R. (2013). An introduction to statistical learning (Vol. 112, p. 18). New York: Springer
- Joelsson, S. R., Benediktsson, J. A., & Sveinsson, J. R. (2005, July). Random forest classifiers for hyperspectral data. In *Proceedings. 2005 IEEE International Geoscience and Remote Sensing Symposium, 2005. IGARSS'05.* (Vol. 1, pp. 4-pp). IEEE.
- Kang, Y., Meng, Q., Liu, M., Zou, Y., & Wang, X. (2021). Crop Classification Based on Red Edge Features Analysis of GF-6 WFV Data. *Sensors*, 21(13), 4328
- Nitze, I., Barrett, B., & Cawkwell, F. (2015). Temporal optimisation of image acquisition for land cover classification with Random Forest and MODIS time-series. *International Journal of Applied Earth Observation and Geoinformation*, 34, 136-146.
- Meinel, G., Neubert, M., & Reder, J. (2001). The potential use of very high resolution satellite data for urban areas—First experiences with IKONOS data, their classification and application in urban planning and environmental monitoring. *Regensburger Geographische Schriften*, 35, 196-205.
- Orynbaikyzy, A., Gessner, U., & Conrad, C. (2019). Crop type classification using a combination of optical and radar remote sensing data: a review. *international journal of remote sensing*, 40(17), 6553-6595

- Pal, M., & Mather, P. M. (2004). Assessment of the effectiveness of support vector machines for hyperspectral data. *Future generation computer systems*, 20(7), 1215-1225.
- Shamsoddini, A., J. C. Trinder, and R. Turner. 2013. "Non-Linear Methods for Inferring Lidar Metrics Using SPOT-5 Textural Data." *ISPRS Annals of Photogrammetry, Remote Sensing and Spatial Information Sciences II-5/W2*: 259–264. doi:10.5194/isprsannals-II-5-W2-259-2013.
- Salehi, B., Daneshfar, B., & Davidson, A. M. (2017). Accurate crop-type classification using multi-temporal optical and multi-polarization SAR data in an object-based image analysis framework. *International Journal of Remote Sensing*, 38(14), 4130-4155.
- Rodriguez-Galiano, V. F., Ghimire, B., Rogan, J., Chica-Olmo, M., & Rigol-Sanchez, J. P. (2012). An assessment of the effectiveness of a random forest classifier for land-cover classification. *ISPRS Journal of Photogrammetry and Remote Sensing*, 67, 93-104.
- Zhong, L., Gong, P., & Biging, G. S. (2014). Efficient corn and soybean mapping with temporal extendability: A multi-year experiment using Landsat imagery. *Remote Sensing of Environment*, 140, 1-13.
- Zhang, T., Su, J., Liu, C., Chen, W. H., Liu, H., & Liu, G. (2017, September). Band selection in Sentinel-2 satellite for agriculture applications. In *2017 23rd international conference on automation and computing (ICAC)* (pp. 1-6). IEEE.
- Zhang, H., Kang, J., Xu, X., & Zhang, L. (2020). Accessing the temporal and spectral features in crop type mapping using multi-temporal Sentinel-2 imagery: A case study of Yi'an County, Heilongjiang province, China. *Computers and Electronics in Agriculture*, 176, 105618.

4th Intercontinental Geoinformation Days

igd.mersin.edu.tr



View angle importance of SAR satellite imageries for mapping areas susceptible to floods: A case study of Kumamoto Prefecture, Japan

Ayub Mohammadi¹, Himan Shahabi^{*1}

¹University of Kurdistan, Department of Geomorphology, Sanandaj, Iran

Keywords

Remote Sensing
Satellite Imagery
Flood
View Angle
Japan

Abstract

Natural hazards including landslides, flash floods, earthquakes and hurricanes have been constituted a significant problem in many countries. Kumamoto Prefecture in Japan was selected as the study area in the current research. One of the most considerable natural hazards in the study area is flood. Without using any automated classifier, this paper aims to map flooded areas in the region using synthetic aperture Radar (SAR) imagery of ALOS-2 PALSAR-2. A total number of six satellite imageries (before and right after the events) were collected. Using Sentinel application platform (SNAP) software the images were corrected, stacked and combined in order to map flooded areas. Results indicate that this kind of flood mapping is precise, fast and easy to use. This paper can be helpful to policy and decision makers in order to map flooded areas immediately, especially when we need a quick action for settling camps for evacuees during flooding days.

1. Introduction

Natural disasters like flash floods, landslides, earthquakes, and hurricanes result in a considerable threat to human life and loss of property not only in the study area but also in many parts of the Earth (Khan, Shaari, Bahar, Baten, & Nazaruddin, 2014; Lawal, Matori, Hashim, Wan Yusof, & Chandio, 2012; Rahman & Di, 2017). In recent years, Japan has been hit by heavy floods (Yang, Panjaitan, Ujiie, Wann, & Chen, 2020), causing millions of dollars in property damage and loss of life.

Flood is one of the common phenomenon in the study area (Yang et al., 2020). Study area has been faced flooding almost every year, which is seen as common natural disaster in the region. The problems caused by flash floods, can be addressed if effective planning and detailed studies are taken.

Flood is a very common disaster in Japan (Yang et al., 2020). However, identifying the flood prone areas is highly essential for decision and policy makers for sustainable development. Because of the all-weather capability and sensitivity to the structure of flooded surface, SAR remote sensing has made notable contribution in flood studies, (Dronova, Gong, Wang, & Zhong, 2015; Martinez & Le Toan, 2007; Tehrany, Pradhan, & Jebur, 2014). This study is significant in two

ways (1), (1) without using any classification algorithms we distinguished flooded areas precisely, and (2) ALOS-2 PALSAR-2 was used as L-band satellite imagery. Fully control over these kinds of floods is a challenging task to a great extent.

Many studies have been conducted using different methods and models for mapping flood susceptible areas, including analytical neural network (Pradhan & Buchroithner, 2010), analytic hierarchy process (Lawal et al., 2012), support vector machine (Tehrany et al., 2014; Tehrany, Pradhan, Mansor, & Ahmad, 2015), fuzzy logic (Jiang, Deng, Chen, Wu, & Li, 2009; Perera & Lahat, 2015), frequency ratio (Lee, Kang, & Jeon, 2012; Tehrany et al., 2015), random forest classifier (Feng, Liu, & Gong, 2015), logistic regression (Pradhan, 2010) and Neural Network Algorithm (Li, Xu, & Chen, 2016).

The main objective of the current study was to employ L-band SAR imagery to map flooded areas for crisis management using a quick approach.

2. Description of the Study Area

Because of data availability, the Kumamoto Prefecture in Japan was selected as the study area for performing this research. Figure 1, shows the study area.

* Corresponding Author

(ayubmohammadi1990@gmail.com) ORCID ID 0000-0001-8848-8917
(*h.shahabi@uok.ac.ir) ORCID ID 0000-0001-5091-6947

Cite this study

Mohammadi, A., & Shahabi, H. (2022). View angle importance of SAR satellite imageries for mapping areas susceptible to floods: A case study of Kumamoto Prefecture, Japan. 4th Intercontinental Geoinformation Days (IGD), 108-110, Tabriz, Iran

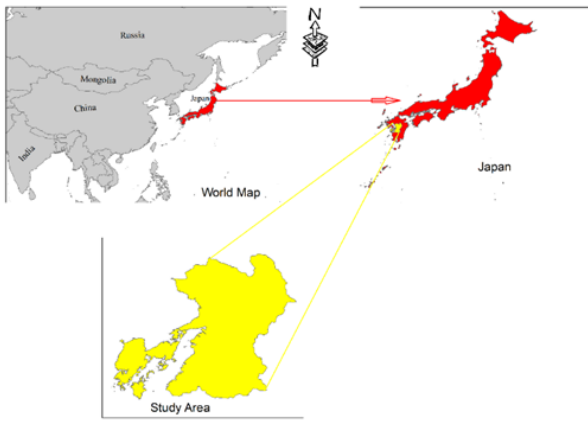


Figure 1. Geographical location of the study area

3. Material and Methods

To acquire information, ALOS-2/PALSAR-2 emits microwave and receives the reflection from the ground. The L-band SAR data is less affected by clouds and rains, which is suitable for monitoring rapid disasters. In addition, L-band microwave can penetrate through vegetation to obtain information. ALOS-2/PALSAR-2 has a spotlight mode of 1m×3m resolution in azimuth/range direction.

The satellite data were acquired from Department of architecture and building engineering, Tokyo Institute of Technology. Table 1, demonstrates technical characteristics of data used in this study. It is worth mentioning that six satellite data of ALOS-2/PALSAR-2 (two descending and four ascending) were used.

Table 1. Technical attributes of ALOS-2 PALSAR-2 satellite imagery

Observation Mode (Sensor)	Processing Level	View Angle	Date
Spotlight	SLC (1.1)	Ascending	2016/04/16
			2020/07/04
			2020/07/04
		Descending	2016/04/30
			2018/02/20
			2020/07/07

In order to extract accurate information, once, satellite imageries have been collected then pre-processing must be applied on them (Jensen & Lulla, 1987). Therefore, using SNAP software, images were radiometrically corrected, multi-looked and filtered. Moreover, before projected to Universal Transverse Mercator (UTM) coordinate system, they were geo-referenced.

After correction process, for saving time it is better to clip imageries as the study area. In order to place the maximum accuracy, we loaded imageries in decibels (dB). Furthermore, for combining bands of satellite images they must be stacked. Therefore, we can separate flooded areas from the other areas by selecting dB or actual band of before event imagery as Red and after event image for both Green and Blue in RGB band combination (Figure 2).

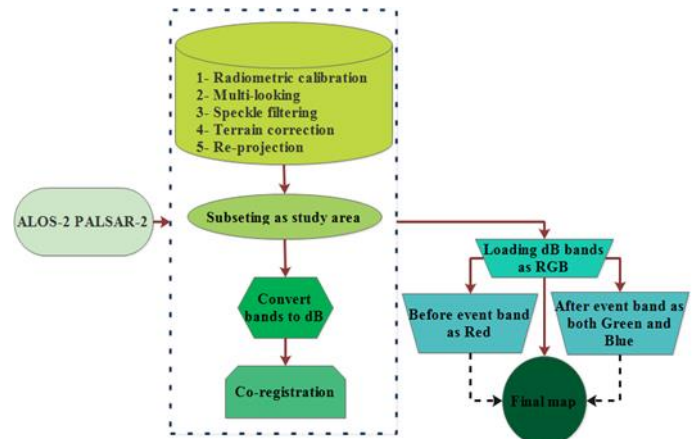


Figure 2. Research methodology of the study.

4. Results and Discussion

In this study using SAR imagery of ALOS-2/PALSAR-2, areas prone to flood were mapped, which can be valuable for authorities to consider it in the preventive actions in the study areas during flooding times.

In order to prevent such disasters, it is needed to develop an accurate technique to map areas prone to flood. In such situations, the first action is to map areas prone to flood so that policy makers can do preventive actions; including settling lifeguards in high susceptible areas, to act against unlicensed housing in high susceptible regions as well as to build shields along the highly sensitive river banks. Despite this fact that flood events are generally unavoidable (Pradhan & Youssef, 2011); however, authorities should not be easy-going on this matter and should try to reduce the fatalities and damages from such events in near and remote future.

Figure 3 clearly shows the flooded regions in the study area. In fact, this method is precise, accurate and easy to apply in SNAP and ArcGIS software environments. Electromagnetic waves of SAR imagery will be reflected from water surfaces specularly; therefore, in the imagery appears in black color (Oliver & Quegan, 2004). Overall, in this model flooded areas in red color are differentiated from the other water resources in black color.

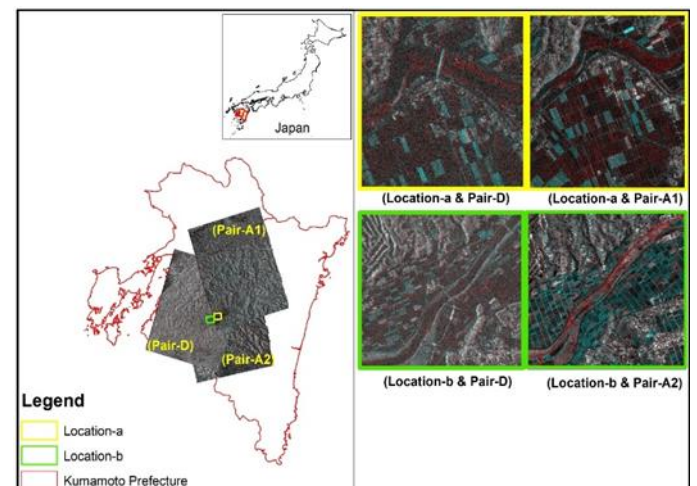


Figure 3. Flooded area of Kumamoto Prefecture, Japan.

As it can be seen from Figure 3, based on the geomorphological condition of the study area, ascending imageries are more suitable for the study area from which the flooded areas are more visible than the descending ones.

5. Conclusion

One of the most common disasters in the study area is flooding, which mostly induced by heavy rainfall. In this manuscript, we have shown how to map flooded areas by using SAR imagery without using any automated classifier. For this model, two SAR satellite imagery of before and right after floods should be acquired. These data through SNAP software were corrected, stacked and combined in order to map flooded areas. For obtaining the maximum accuracy, we loaded both imageries in decibels (dB). Furthermore, for combining the satellite images, they were stacked first and in order to map the flooded areas, the data were loaded in RGB combination. Moreover, this kind of flood mapping is precise, fast and easy to use, especially when we need to map flooded areas immediately to settle evacuees in safer places.

Acknowledgement

Many thanks are given to the Department of architecture and building engineering, Tokyo Institute of Technology for providing us with the satellite imageries.

References

- Dronova, I., Gong, P., Wang, L., & Zhong, L. (2015). Mapping dynamic cover types in a large seasonally flooded wetland using extended principal component analysis and object-based classification. *Remote Sensing of Environment*, 158, 193-206.
- Feng, Q., Liu, J., & Gong, J. (2015). Urban flood mapping based on unmanned aerial vehicle remote sensing and random forest classifier—A case of Yuyao, China. *Water*, 7(4), 1437-1455.
- Jensen, J. R., & Lulla, K. (1987). *Introductory digital image processing: a remote sensing perspective*.
- Jiang, W., Deng, L., Chen, L., Wu, J., & Li, J. (2009). Risk assessment and validation of flood disaster based on fuzzy mathematics. *Progress in Natural Science*, 19(10), 1419-1425.
- Khan, M. M. A., Shaari, N. A. B., Bahar, A. M. A., Baten, M. A., & Nazaruddin, D. A. B. (2014). Flood impact assessment in Kota Bharu, Malaysia: a statistical analysis. *World Applied Sciences Journal*, 32(4), 626-634.
- Lawal, D. U., Matori, A. N., Hashim, A. M., Wan Yusof, K., & Chandio, I. A. (2012). Detecting flood susceptible areas using GIS-based analytic hierarchy process.
- Lee, M.-J., Kang, J.-e., & Jeon, S. (2012). Application of frequency ratio model and validation for predictive flooded area susceptibility mapping using GIS. Paper presented at the Geoscience and Remote Sensing Symposium (IGARSS), 2012 IEEE International.
- Li, L., Xu, T., & Chen, Y. (2016). Improved urban flooding mapping from remote sensing images using generalized regression neural network-based super-resolution algorithm. *Remote Sensing*, 8(8), 625.
- Martinez, J.-M., & Le Toan, T. (2007). Mapping of flood dynamics and spatial distribution of vegetation in the Amazon floodplain using multitemporal SAR data. *Remote Sensing of Environment*, 108(3), 209-223.
- Oliver, C., & Quegan, S. (2004). *Understanding synthetic aperture radar images*: SciTech Publishing.
- Perera, E. D. P., & Lahat, L. (2015). Fuzzy logic-based flood forecasting model for the Kelantan River basin, Malaysia. *Journal of Hydro-environment Research*, 9(4), 542-553.
- Pradhan, B. (2010). Flood susceptible mapping and risk area delineation using logistic regression, GIS and remote sensing. *Journal of Spatial Hydrology*, 9(2).
- Pradhan, B., & Buchroithner, M. F. (2010). Comparison and validation of landslide susceptibility maps using an artificial neural network model for three test areas in Malaysia. *Environmental & Engineering Geoscience*, 16(2), 107-126.
- Pradhan, B., & Youssef, A. (2011). A 100-year maximum flood susceptibility mapping using integrated hydrological and hydrodynamic models: Kelantan River Corridor, Malaysia. *Journal of Flood Risk Management*, 4(3), 189-202.
- Rahman, M. S., & Di, L. (2017). The state of the art of spaceborne remote sensing in flood management. *Natural Hazards*, 85(2), 1223-1248.
- Tehrany, M. S., Pradhan, B., & Jebur, M. N. (2014). Flood susceptibility mapping using a novel ensemble weights-of-evidence and support vector machine models in GIS. *Journal of hydrology*, 512, 332-343.
- Tehrany, M. S., Pradhan, B., Mansor, S., & Ahmad, N. (2015). Flood susceptibility assessment using GIS-based support vector machine model with different kernel types. *Catena*, 125, 91-101.
- Yang, S.-H., Panjaitan, B. P., Ujiie, K., Wann, J.-W., & Chen, D. (2020). Comparison of food values for consumers' preferences on imported fruits and vegetables within Japan, Taiwan, and Indonesia. *Food Quality and Preference*, 87, 104042.

4th Intercontinental Geoinformation Days

igd.mersin.edu.tr



A review of Mud volcanoes situation in Caspian seaboard and new methods of their identification by remote sensing techniques

Babak Kheradmand *¹

¹Senior expert of geology at Iranian Gas Engineering & Development Company (I.G.E.D.C.), Tehran, Iran

Keywords

Mud volcano
Caspian Sea
Remote Sensing

Abstract

The main issues presented in this paper, considering the future plans of the oil and gas industries in the region, include the status of the distribution of Mud volcanoes in the Caspian region as well as the presentation of the total framework of new ways of identifying and analyzing them based on remote sensing techniques using experiences in other neighboring countries of the Caspian Sea. These structures are associated with hydrocarbon deposits, subduction tectonic zones, and orogeny belts, and in very rare cases are associated with mud volcanoes. Fortunately, most mud volcanoes are found on the seabed and their effects are far less.

1. Introduction

Mud volcanoes are important morphological features that are often in the form of clay cones and from a height of 2 meters to a maximum of 500 meters around them and with a base diameter of 20 meters to a maximum of 3500 meters. It is possible that their central part is made of sand and the outer part is made of mud. These mud volcanoes are hilly and circular in shape and have a main opening and several smaller side openings. The main opening is usually located in the middle of the mud volcano and is bowl-shaped or blade-shaped and the side openings are not fixed and permanent. Sometimes mud volcanoes have no eruptions and some are not permanent and are active periodically and pulsating springs and, in this respect, they are similar to volcanoes which are much smaller than them. Mud volcanoes are found both on land and in the oceans (Kheradmand, 2013).

2. Caspian coastal mud volcanoes in Iran

"Gomishan", "Qarniaraq Tappeh" and "Naftlije" mud volcanoes in Golestan province of Iran are among the most beautiful natural phenomena in the form of small volcanic cones made of mud or sand, the dimensions of which vary from a few centimeters to several meters, and it seems that the central parts they are made of sand and

their outer part is made of mud. In these golf courses, mud and sand materials are injected from below into the gap and with water. The rapid release of flowing, watery muds, accompanied by bubbles and noise, causes the formation of cones, and in the center of these cones, there is a crater-like hole for material to exit, which creates a gap in the ground and injects material from below. They are formed with water and gas.

Studies show that these cones occur in earthquake-prone areas and along some faults, and the rapid settling of materials and subsequent outflow of water from the particle bed causes the formation of mud volcanoes on the surface of sediments.

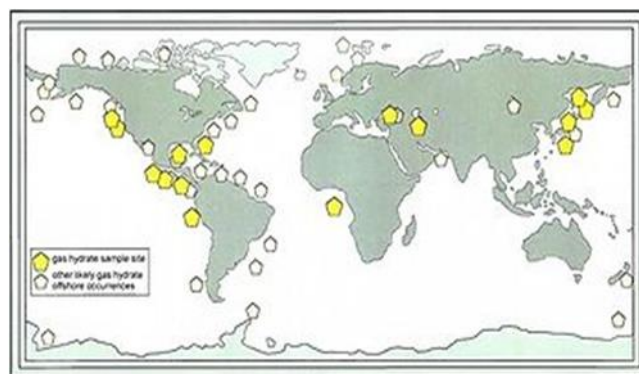


Figure 1. Map showing the distribution of mud volcanoes in the world (Wikipedia).

* Corresponding Author

^{*}(kheradmand_babak@yahoo.com) ORCID ID 0000-0002-7213-6287

Cite this study

Kheradmand, B. (2022). A review of Mud volcanoes situation in Caspian seaboard and new methods of their identification by remote sensing techniques. 4th Intercontinental Geoinformation Days (IGD), 111-113, Tabriz, Iran

Some believe that mud volcanoes have a tectonic origin and the subduction action and pressures caused by tectonic movements are the reason for their occurrence and some believe that mud volcanoes are formed in volcanic areas.

"Qarniaraq Tappeh" mud volcano in the east of Gomishan, "Naftalijeh" in the northeast of Gomishan and "Incheh" next to Incheh Borun wetland are famous mud volcanoes in Golestan province and all of them are active with gas, water containing sodium chloride and aromatic petroleum products.

Naftlijeh mud volcano in the northeast of Gomishan is associated with petroleum products and has created a hill in the middle of a flat plain of mud paste, oil that comes out of its mouth and has a high gas activity.

Qarniaraq in the local language, where the abdomen is split; With a diameter of about 600 meters, it is considered to be the largest mud volcano in Golestan province, from which salt deposits, methane gas and traces of petroleum products are extracted, and the locals believe in its healing properties.

Incheh mud volcano is also located next to Incheh Borun wetland, which in recent years, the issuance of licenses for exploitation wells along the wetland, has disabled this mud volcano (Mirkazemian, 2009).

3. Mud volcanoes of the Republic of Azerbaijan

The mud volcanoes of the Republic of Azerbaijan are spectacular symbols of the hidden oil and gas resources deep in the land in the Caspian Sea. Gas leakage occurs when subsoil is saturated with methane gas and seeks to find a passage to the surface.

A famous example of gas leakage is in Yanardag (Mountain of Fire) on the Absheron Peninsula. People often go there to watch the flames dance and enjoy watching this fascinating phenomenon that never goes out, and it is interesting for them to understand how this fire lasts forever and burns from the ground and is a tool. It is for worship.

The people of Azerbaijan link the emergence of Zoroastrianism in Azerbaijan about 2000 years ago with this geological phenomenon. According to them, the name of the country "Azerbaijan" is also derived from the Persian word "Azar" meaning "fire". This ritual has been the most important pre-Islamic historical ritual in this region.

The final annual volume of gas emitted by all mud volcanoes in the Republic of Azerbaijan is estimated at about 20 million cubic meters per year. In 1964, the Turaghayi mud volcano ignited flames that burned for several years and released 500 million cubic meters of gas (Scholte, 2011).

The mud volcanoes of the Republic of Azerbaijan, usually outside the population centers, occur suddenly and in a short time. For this reason, it is not possible to observe them from the beginning to the end. With the exception of the "Lokbatan" mud volcano, which was studied by the Faculty of Science of the Azerbaijan Institute of Geology and its eruption lasted more than 20 hours. Lokbatan is the name of an area 15 km south of Baku where camels have drowned in the past due to mud.

Mud volcanoes of the Republic of Azerbaijan vary in size and shape, but most of the mud volcanoes of this country have small cones or small mud outlets. These small cones are interesting and even have a beautiful view and cold mud, water and gas are coming out. Therapeutic properties (iodine, bromine, calcium, magnesium, organic acids and aromatic hydrocarbons) have been reported in these muds. This mud solution has no significant toxic substance (Scholte, 2011).

4. New methods of identifying and analyzing mud volcanoes

Geological researchers from the Republic of Azerbaijan have recently succeeded in using new methods to find mud volcanoes, and with these methods, they have identified buried mud volcanoes in the southwest of the Absheron Peninsula.

These mud volcanoes were studied for 40 years at the Geological Survey of this country; but there were some doubts about this part of the science. There was no complete theory of the formation and mechanism of mud volcanoes, and no significant information was provided about buried mud volcanoes.

These researchers use a combination of wavelengths of images taken from the region with ASTER, InSAR, TM7 systems as well as Hyperion method and spectrometric analysis method; they have identified mud volcanoes and have even succeeded in determining the percentage of mineral compounds in each of them.

As it has been determined, more than 90% of the oil and gas deposits of the Republic of Azerbaijan have mud volcanic structures; thus, newly discovered mud volcanoes can testify to the oil and gas content of these areas (Figures 2 to 6) (Scholte, 2003).

Absorption wavelength (um)	Mineral Group
2.165	Low pH / acid environments
2.205	Al-OH bearing minerals
2.260	Jarosite
2.327	Carbonates and Mg-OH bearing minerals

Figure 2. Demonstrates the relationship between the accumulation of minerals in mud volcanoes and the wavelength in the ASTER imaging method (Scholte, 2003).

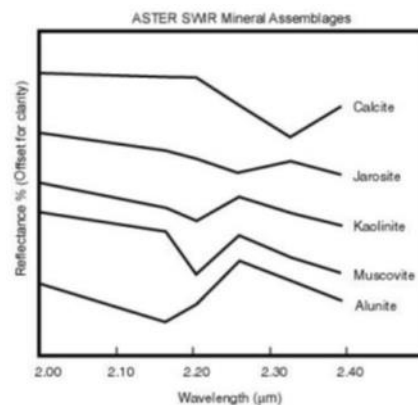


Figure 3. Representation of reflecting wavelength range of different groups of minerals in mud volcanoes in ASTER imaging method (after USGS) (Scholte, 2003).

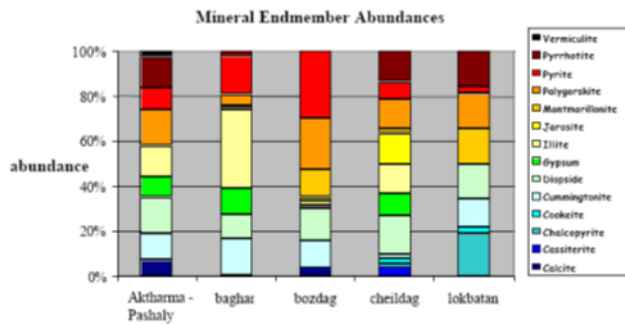


Figure 4. Indicates the percentage of abundance of different minerals in each of the mud volcanoes located in the Republic of Azerbaijan (Scholte, 2003).

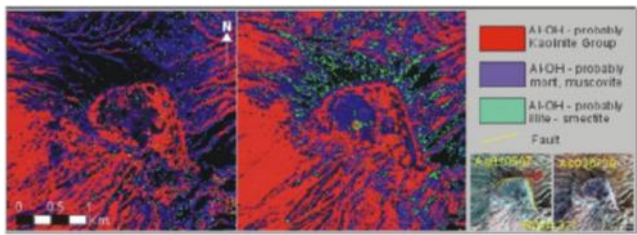


Figure 5. Mineralogy map of Aktharma-Pashaly mud volcano located in the Republic of Azerbaijan (using ASTER images method) (Scholte, 2003).

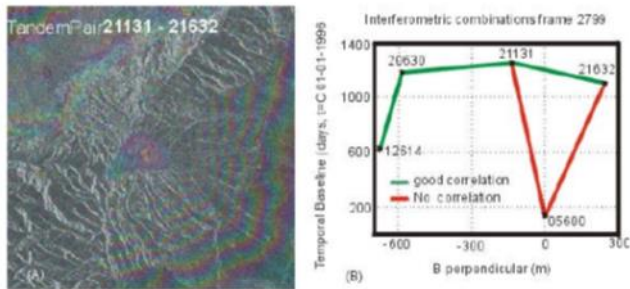


Figure 6. Matching two consecutive images of the Aktharma-Pashaly mud volcano (Figure A) using the InSAR technique (green and red lines in Figure B indicate the degrees of good matching and non-matching, respectively) (Scholte, 2003).

5. Results

- Mud volcanoes are among the natural phenomena that are caused by tectonic activities in the region and are consistent with fault structures and are morpho-

neotectonic signs that indicate the activity of the area containing them from a tectonic point of view.

- These structures (mostly conical) are formed by the pressure of gases from hydrocarbon layers (oil and gas) and their reserves so that the lower clay and marl rocks are saturated and softened by groundwater or in the form of mud in have come; They are ejected, creating sometimes very large craters resembling volcanic craters (quasi-craters or craters).

- Due to the special morphological condition of these structures, construction operations, especially permanent structures (such as power plants, dams and the route of lifelines such as oil and gas pipelines and related facilities) are not recommended at all and should be avoided. From the wastage of expenses and unfortunate events, the location of these complications should be carefully determined and studied using new methods.

- Since mud volcanoes are among the obvious surface signs of the presence of rich hydrocarbon resources in the region (such as oil or sulfur springs or protrusions of bitumen and natural asphalt in the southern and southwestern parts of Iran), planning for studies comprehensive geology and geophysics are recommended to explore for oil and gas resources in such areas.

References

- Eye- Eruption of Shikhzayirli mud volcano in Gobustan, Azerbaijan, (2011).
- Kheradmand, B., (2013). Mud volcanoes, Special issue of deep waters of KEPCO (Zharfa), 40-41.
- Mirkazemian, M., (2009). Mud volcanoes, INGIDIR.
- Rangzan, K. et al, (2010). Investigation of water quality of Karun River, Ahvaz area by timely images of Hyperion, 29th Earth Sciences Conference, Geological Survey of Iran.
- Scholte, K.H, (2011), Imaging Spectroscopy of Oil Mud Volcanoes in Azerbaijan.
- Scholte, K. H, et al., (2003). Preliminary ASTER and InSAR Imagery Combination for Mud Volcano Dynamics, Azerbaijan.
- Wikipedia, the free encyclopedia, Mud volcano.



4th Intercontinental Geoinformation Days

igd.mersin.edu.tr



Analysis of heat island formation in land use of Ardabil city using thermal remote sensing imagers

Hossein Fekrat^{*1}, Sayyad Asghari Saraskanrood¹, Seyed Kazem Alavipanah²

¹ University of Mohaghegh Ardabili, Faculty of Social Sciences, Department of Natural Geography, Ardabil, Iran

² University of Tehran, Faculty of Geography, Department of Remote Sensing and GIS, Tehran, Iran

Keywords

LST
Application
Single channel
GEE
Moran global indices

Abstract

Land surface temperature (LST) is one of the essential parameters of environmental science studies. In this study the land surface temperature of Ardabil city using a LST automatic calculator application was estimated with a single channel algorithm. for this purpose, Landsat 5 and 8 satellite images on 2000/07/31 and 2019/08/21 were used. In order to validate the LST map of the application output in addition to the data of two meteorological stations in the study area, from the surface temperature of two ground stations that were recorded simultaneously with the satellite was also used. Finally using the LST map, hot spots analysis and hot and cold clusters of thermal islands of Ardabil city were extracted. Also, using the GEE web platform, the land use map of the study area with the RF algorithm was prepared. The analysis spatial correlation with Moran global indices showed the land surface temperature of Ardabil city has a spatial structure and are distributed in clusters. The results showed that the lowest surface temperatures to water areas, irrigated agriculture and residential areas are formed and thermal cores are mostly created outside residential areas in barren lands rainfed agriculture and rangeland.

1. Introduction

Land surface temperature is an important indicator for studying environmental changes and the energy balance of the earth Which can be used to monitor the temperature changes of cities (Stephens and L'Ecuyer 2015). Urban areas continue to expand in population and built-up extent, with faster rates in developing countries (Nyamekye et al, 2020). its adverse impacts that include increased air pollution, surface urban heat islands and dust, significantly influence urban micro- and macro-climate and affect urban environmental quality and human health (Heaviside et al, 2016).

Remote sensing technology using satellite imagery can be a great help for managers and urban planners to study temperature conditions and land use changes in the past, evaluate current trends and ultimately predict and manage the future. For instance, missions such as Landsat offer large archival data spanning as far back as

1972 at reasonable and improved radiometric, spectral and spatial resolution, valuable for assessing both large scale and localized temporal and multi-temporal landscape and environmental patterns (Keramitsoglou et al, 2019). Recently, several studies around the world have been conducted on the formation of thermal islands and its effects on the urban environment. like the (Heaviside et al, 2016; Dutta et al, 2020; Zhao et al, 2021; Lee et al, 2021; You et al, 2021).

In this study, an application was designed to automatically calculate the land surface temperature. Due to the large area of the study and the insufficient number of meteorological stations and in order to synchronize the validation data with the satellite transit time, In addition to surface temperature data measured at synoptic stations, land surface temperature was recorded at two ground stations at the same time as the satellite.

* Corresponding Author

(Hossein7181@gmail.com) ORCID ID 0000-0003-4306-1236
(asghari@uma.ac.ir) ORCID ID 0000-0002-5015-904X
(salavipa@ut.ac.ir) ORCID ID 0000-0002-3554-111X

Cite this study

Fekrat, H., Saraskanrood, S. A., & Alavipanah, S. K. (2022). Analysis of heat island formation in land use of Ardabil city using thermal remote sensing imagers. 4th Intercontinental Geoinformation Days (IGD), 114-117, Tabriz, Iran

2. Method

2.1. Study area

Ardabil city is located in the geographical range of 37 degrees and 55 minutes and 60 seconds to 38 degrees and 36 minutes and 27 seconds north latitude and 48 degrees and 39 minutes and 20 seconds to 47 degrees and 48 minutes and 21 seconds east longitude (Figure 1).

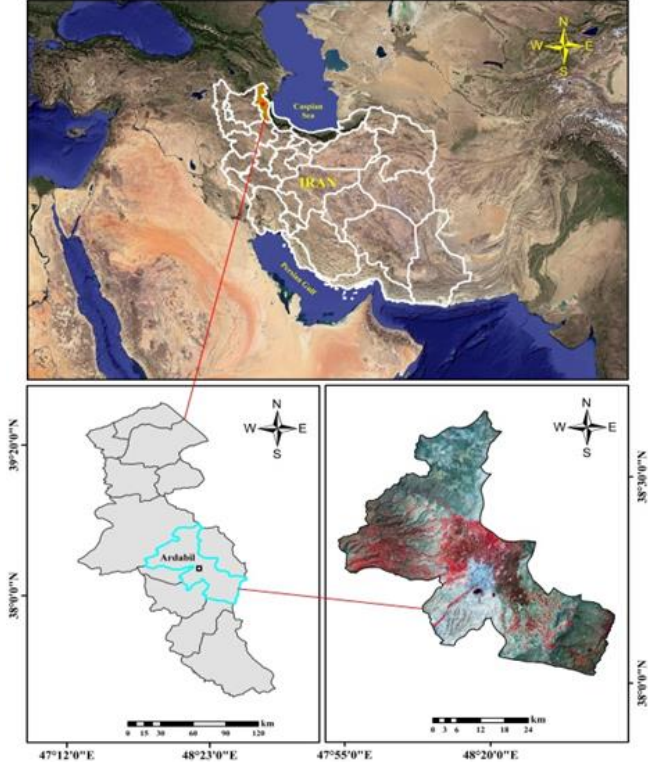


Figure 1. Location of the study area

2.2. Methodology

2.2.1. LST (Single Channel Algorithm)

Only first letter of first word is capital, left aligned, 10 font size, bold. It should be separated from the former paragraph with single line.

The generalized Single Channel Algorithm was developed for the purpose of extracting LST from a single thermal infrared band (Jiménez-Muñoz and Sobrino 2003). According to the algorithm, the LST is expressed as shown in Equations (1–8).

$$LST = \gamma[\varepsilon^{-1}(\psi_1 L_{\text{sensor}} + \psi_2) + \psi_3] \quad (1)$$

$$\gamma = \left\{ \frac{c_2 L_{\text{sensor}, \lambda}}{T_{\text{sensor}}^2} \left[\frac{\lambda^4}{c_1 L_{\text{sensor}, \lambda} + \lambda^{-1}} \right] \right\}^{-1} \quad (2)$$

$$C1 = 1.19104 \times 10^8 (W \cdot \mu m \cdot m^{-2} \cdot sr^{-1}) \quad (3)$$

$$C2 = 1.43877 \times 10^4 (\mu m \cdot K) \quad (4)$$

$$\delta = -\gamma L_{\text{sensor}, \lambda} + T_{\text{sensor}} \quad (5)$$

$$\psi_{1(\omega, T_a)} \equiv \frac{1}{\tau_{(\omega, T_a)}} \quad (6)$$

$$\psi_{2(\omega, T_a)} \equiv -L_{\text{atm}(\omega, T_a)}^{\downarrow} - \frac{L_{\text{atm}(\omega, T_a)}^{\uparrow}}{\tau_{(\omega, T_a)}} \quad (7)$$

$$\psi_{3(\omega, T_a)} \equiv -L_{\text{atm}(\omega, T_a)}^{\downarrow} \quad (8)$$

where ε and L_{senso} represent emissivity and thermal radiance, the γ gamma calculated using Equation 2, $C1$ and $C2$ Planck constant radiation coefficients, is δ equal to the delta obtained from equation 5, $L_{\text{sensor}, \lambda}$ and T_{sensor} are equal to the radius of the thermal sensor, respectively (10 band TIRS sensor and 6 band TM sensor and ψ_1 , ψ_2 and ψ_3 are atmospheric correction parameters.

2.2.2. Spatial Analysis of the LST

The geospatial dependence phenomenon is known as spatial autocorrelation, having a significant effect on the spatial distribution pattern of LST and the inherent driving forces utilizing statistical analysis. The global spatial autocorrelation analysis of this study is mainly based on Moran's I, reveals the aggregation of LST spatial layout as a whole, and indicates whether LST has spatial autocorrelation as follows (equation 9,10 and 11):

$$I = \frac{n \sum_{i=1}^n \sum_{j=1}^n w_{ij} z_i z_j}{S0 \sum_{i=1}^n z_i^2} \quad (9)$$

$$S0 = \sum_{i=1}^n \sum_{j=1}^n w_{ij} \quad (10)$$

$$Z_i = \frac{i - E(I)}{\sqrt{V(I)}} \quad (11)$$

In general, if the value of the Moran index is close to +1 data have spatial autocorrelation and have a cluster pattern and if the value of the Moran index is close to -1, then the data are fragmented (Goodchild 1986).

GetisOrd G_i^* (hot-spot analysis) reveals the significant high-value and low-value clusters in the spatial region and identifies the spatial distribution of LST cold and hot-spots in the region. Its formula is (Getis and Ord, 1992):

$$G_i = \frac{\sum_{j=1}^n W_{ij} X_j - X \sum_{j=1}^n W_{ij}}{S \sqrt{\frac{n \sum_{j=1}^n W_{ij}^2 - (\sum_{j=1}^n W_{ij})^2}{n-1}}} \quad (12)$$

where G_i statistic is a z-score. The higher the z-score, the tighter the clustering of hot-spots (high values). The lower the z-score, the tighter the clustering of cold-spots (low values). Here, X_i and X_j are the LST at the location of grid i and j . $W_{i,j}$ is the spatial weight matrix, and X is the mean of LST.

3. Results and Discussion

Figure 2 shows the land surface temperature output maps using the 6-band TM sensor images and the 10-band TIRS band of Landsat 5 and 8 satellites for 2000/07/31 and 2019/08/21. In order to validate the accuracy of the output LST map of 2000, the surface temperature data of two meteorological stations were used and for the LST map of 2019, the surface temperature data of two meteorological stations and two ground stations were used and the result is shown in Table 1.

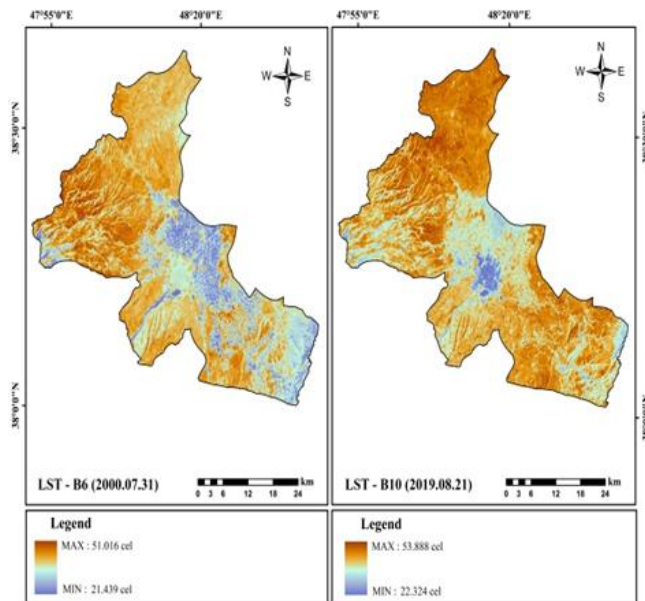


Figure 2. LST maps in 2000 and 2019

Table 1. Estimated LST difference with meteorological and ground station data

LST map	Station-1	Station-2	Station-3	Station-4
2000	+2.5	-2		
2019	+1.3	+0.9	-1	-0.9

To calculate Moran's correlation analysis, first the standard score of Z and P-value were calculated, the results of which are presented in Table 2. In the next step, the significance of Moran global correlation analysis was examined. Moran's global zero hypothesis states that spatial clustering is by no means formed between values. Based on the results of Table 2 and Figure 3, for both years the null hypothesis is rejected and confirms the existence of a relationship and spatial structure in the temperature values of Ardabil city.

Getis-Ord-Gi statistics for 2000 and 2019 were used to determine areas with high and low value clusters and hot and cold spots and the results are presented in Figure 4.

Table 2. Output of Moran index

p-value	Variance	z-score	Expected index	Moran Index	date
0	0.000003	540.443	-0.000005	0.8684	2000
0	0.000003	540.289	-0.000005	0.8682	2019

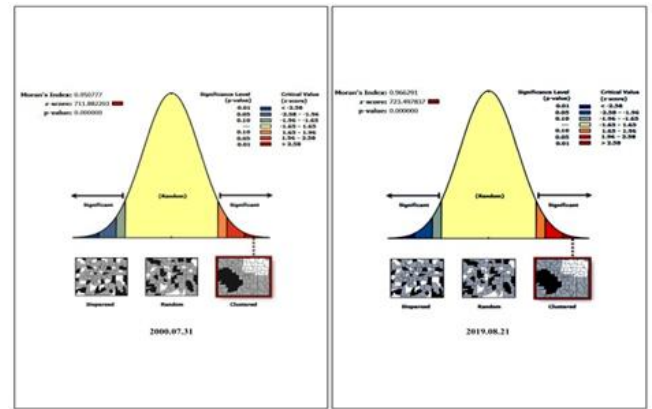


Figure 3. Graphic output of global Moran index for LST in Ardabil city

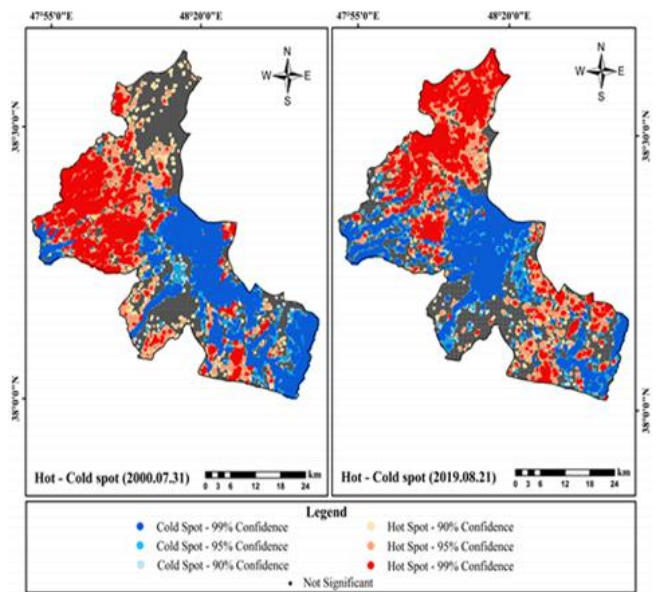


Figure 4. Hot and cold spots of Ardabil city

Figure 5 shows the land use map of Ardabil city, which has been prepared using the Random Forest algorithm in the gee platform with seven classes. to evaluate the trend of land surface temperature change, especially in the residential sector surface temperature profiles with a radius of 10 km are drawn around residential areas, the results of which are shown in Figure 5. The trend of the profiles shows that as the curve approaches the urban sector, the trend of the graphs gradually takes a downward shape. This trend of decreasing temperature in the urban sector reaches its lowest point and after passing this area, again due to rising temperatures, the upward trend.

4. Conclusion

The results of the study showed that the formation of thermal cores in 2000 was mainly in the northwestern parts and with a small amount in the northern and southern parts. while in 2019, the main thermal core of the city has been formed in the northern parts and with a lower percentage in the southeastern part, it seems that the main reason has been the disappearance of pastures in the northern parts in recent years. Also based on the values of Z and P and the value of the global Moran index, the land surface temperature in Ardabil city is

distributed in clusters and high and low temperature values tend to cluster. The results show the high temperature difference between the residential part of the region and other uses (agriculture, pastures and barren lands). Existence of agricultural lands with irrigated cultivation around the residential part is one of the main factors of low temperature in the central part of the region.

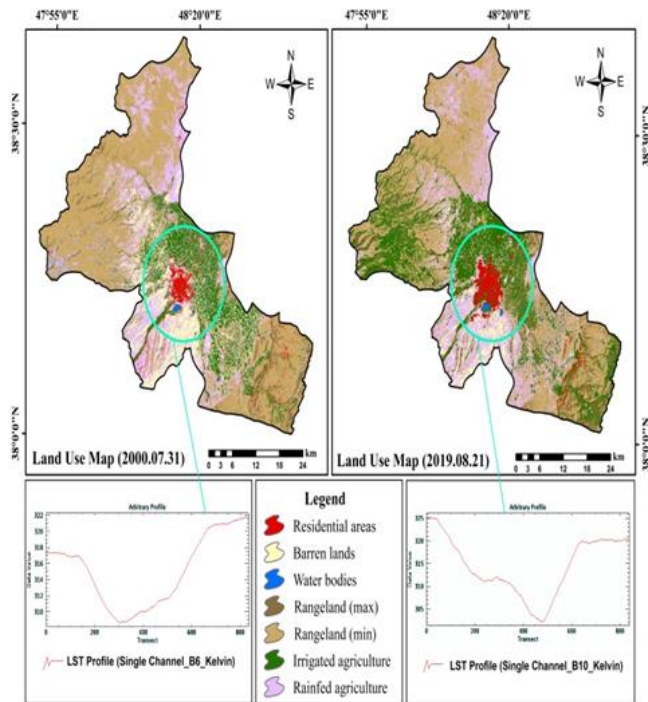


Figure 5. Land use map and surface temperature profile around the residential area with a radius of 10 km

References

- Dutta, K., Basu, D., & Agrawal, S. (2021). Evaluation of seasonal variability in magnitude of urban heat islands using local climate zone classification and surface albedo. *Int. J. Environ. Sci. Technol.* 1–22.
- Getis, A., & Ord, J. K. (1992). The analysis of spatial association by use of distance statistics. *Geogr. Anal.* 24, 189–206.
- Goodchild (1986). spatial autocorrelation (CATMOG47). Geobooks, Norwich, UK.
- Heaviside, C., Vardoulakis, S., & Cai, X. M. (2016). Attribution of mortality to the urban heat island during heatwaves in the West Midlands, UK. *Environ. Health A Glob. Access Sci. Source*, 15, 49–59.
- Jiménez-Muñoz, J. C., & Sobrino, J. A. (2003). A generalized single-channel method for retrieving land surface temperature from remote sensing data. *J. Geophys. Res. Atmos.*, 108.
- Keramitsoglou, I., Kiranoudis, C. T., Ceriola, G., Weng, Q., & Rajasekar, U. (2011). Identification and analysis of urban surface temperature patterns in Greater Athens, Greece, using MODIS imagery. *Remote Sens. Environ.* 115, 3080–3090.
- Lee, Y., Lee, S., Im, J., & Yoo, C. (2021). Analysis of Surface Urban Heat Island and Land Surface Temperature Using Deep Learning Based Local Climate Zone Classification: A Case Study of Suwon and Daegu, Korea. *Korean J. Remote Sens.* 37, 1447–1460.
- Nyamekye, C., Kwofie, S., Ghansah, B., Agyapong, E., & Appiah, L. (2020). Land Use Policy Assessing urban growth in Ghana using machine learning and intensity analysis: A case study of the New Juaben Municipality. *Land Use Policy*, 99, 105057.
- Stephens, G., L'Ecuyer, T. (2015). The Earth's energy balance. *Atmos. Res.* 166, 195–203. <https://doi.org/10.1016/j.atmosres.06.024>.
- You, M., Lai, R., Lin, J., & Zhu, Z. (2021). Quantitative Analysis of a Spatial Distribution and Driving Factors of the Urban Heat Island Effect: A Case Study of Fuzhou Central Area, China. *Int. J. Environ. Res. Public Health*, 18, 13088.
- Zhao, C., Jensen, J. L. R., Weng, Q., & Currit, N. (2020). Use of Local Climate Zones to investigate surface urban heat islands in Texas Use of Local Climate Zones to investigate surface urban heat islands in Texas. *GISci. Remote Sensing.* 57, 1083–1101.

4th Intercontinental Geoinformation Days

igd.mersin.edu.tr



Modeling of land subsidence in Shabestar Plain and its relation to groundwater by radar interferometry

Naghmeh Mousakhani^{*1} Khalil Valizadeh Kamran¹

¹University of Tabriz, Faculty of Planning and Environmental Sciences, Department of Remote Sensing and GIS, Tabriz, Iran

Keywords

Land subsidence
Radar interferometry
Groundwater
Moran index
Shabestar Plain

Abstract

Shabestar plain has been faced the phenomenon of gradual subsidence in recent years and it is one of the most important plains in East Azerbaijan province in terms of agricultural lands. In this research, the radar interferometry interferogram time series analysis was used in order to predict the subsidence centers of the plain and InSAR data of Sentinel 1as satellite was employed for measuring land subsidence in Shabestar plain with high spatial and temporal resolution in the period 2015-2019 and Adaptive filter was used to modify and refine the phase in each of the images. The result of radar interferometry showed a significant subsidence in the center and west of Shabestar plain with a subsidence rate of 24 cm in this interval. The subsidence level of groundwater level was about 16 m³ measured with Kriging tool. The spatial analysis technique and Moran index of 98% and P value of zero depicted a strong relationship between land subsidence and groundwater level. Unauthorized wells with more exploitation and consequent change of land use and geological conditions in this plain have increased the rate of land subsidence and implementation of the plans for reduction of the risks of land subsidence seems essential.

1. Introduction

In recent years, with domination of dry climate in most parts of Iran and concentration of increasing agricultural exploitation of drinking water and industrial groundwater resources have provided the necessary infrastructure for this phenomenon that is a serious crisis in many plains of the country.

Shabestar plain is located in East Azerbaijan province in the north of Tabriz plain and on the southern slopes of Mishu mountain. This plain is located on 60 km from the city of Tabriz and is one of the 25 sub-basins of Lake Urmia "Fig. 1".

According to the USGS database, more than 100 recorded subsidence factors are related to groundwater (USGS 2014). As a result of reaction to the quality and quantity of groundwater in the surface aquifer, two environmental phenomena of subsidence and settlement can be mentioned which are usually associated with the dissolution of bedrock and gradual sinking of the surface (Ford and William 2007).

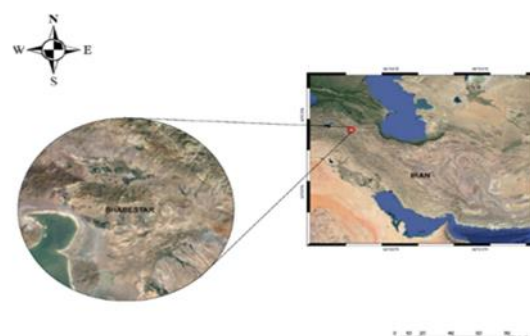


Figure 1. Location map of the studied area in Iran

The use of InSAR technique for detection and monitoring long-term movements has been well proven in the last decade for various types of landslides and subsidence due to its vast spatial coverage, high spatial and temporal resolution, operational capability and

* Corresponding Author

(naghmeh.mousakhani@gmail.com) ORCID ID 0000-0002-8778-5968
(valizadeh@tabrizu.ac.ir) ORCID ID 0000-0003-4648-842X

Cite this study

Mousakhani, N., Kamran, K. V. (2022). Modeling of land subsidence in Shabestar Plain and its relation to groundwater by radar interferometry. 4th Intercontinental Geoinformation Days (IGD), 118-121, Tabriz, Iran

weather conditions (Raucoles et al. 2020) (Vietmeier et al. 1999).

Since InSAR time series perform accurate mapping of land subsidence, the relationships between the geological fault subsidence and the groundwater level in the studied plain have been investigated to consider the evolution parameters of land subsidence. An interferogram is an image that contains a phase difference between two radar images that are geometrically recorded relative to each other (Daniel et al. 2003).

Subsidence phenomenon can cause superficial morphological effects such as morphological irregularities, damage to man-made buildings, highways and streets, agricultural water supply network and subsurface effects such as reduced aquifer volume (Chen et al. 2010; Galloway 1998).

If the site of subsidence is prone to other hazards such as earthquakes and floods, which can have catastrophic destructive effects, then monitoring the rate and extent of subsidence and measuring the changes and morphological effects in these areas can be an effective step in preventing and relative control of the phenomenon.

Severe subsurface subsidence has caused various adverse effects in Shabestar-Sufiyan plain, including reduction of water reservoir and drying of a number of wells, reduction of underground water quality and the occurrence of subsidence or downward movement in some areas.

2. Method

For processing, radar interferometry method with artificial valve and InSAR radar interferometry technique and Sar Map software Envi 5.3 have been used.

Differential radar interferometry calculates phase changes from two pairs of radar images taken at different times to quantitatively and qualitatively reveal these changes in the earth's crust (Ketelaar 2008). It was also used to remove the topographic effect from the USRS site SRTM digital elevation model.

Adaptive filter was used to filter the differential interferometers obtained from the previous step and to improve the quality of the interferometers. Adaptive algorithms have been applied to various problems such as noise cancellation, echo signal prediction, channel equalization and compatible presentations. Also, due to the real-time auto-tuning feature, an adaptive filter can be used to track the behavior of maximum variable slow signals (Haykin et al. 2007).

After phase correction and refinement of the results of interferogram by applying the phase-to-distance conversion factor, displacement rate maps were prepared in the period 2015-2019.

In addition, the groundwater level data belonging to the studied area were compared and evaluated in order to find the causes of subsidence in relation to the groundwater water level obtained in the well.

In this research, the use of SAR data of Sentinel S1a sensor in SLC form, uses polarization data of vv bands, is the slope angle and distance of azimuth meter. In

addition, simulation of DEM topographic signal with coverage of the area has been used.

Although the Sentinel 1A provides bipolar data sources, the vertical transmission / vertical reception VV and its cross-pole receive horizontal reception. VH provides better VV data (Clement et al. 2018) (Twele et al. 2016).

InSAR technology is capable of producing large maps of about 10000 km³ (Sun et al. 2016). The selection of SAR images, one as a master and the other as a slave, has been downloaded from the Sentinel images site, which interferes with the pairing of two SAR images.

Calculation of the interferogram phase is done by the following equation:

An interferogram is calculated by multiplying the amplitude of two images and the phase difference.

Differences are created by distinguishing the phase value of two radar images obtained from different times in the same area (Karimzadeh and Ahmadi 2013). Some of these interactions have been selected to help the stack shift map (Wright et al. 2001) (Motagh et al. 2006) and (Walters et al. 2011).

The resulting images must have approximately the same geometry to be able to use coherent interferometry pairs used to generate digital elevation models, mapping and monitoring the deformation of the earth (Zebker 1992) (Gatelli et al. 1994).

In this regard, a phase change of 2π is equivalent to a displacement of half the wavelength used by the satellite, which represents a complete French in the interferogram.

The interferogram phase is created due to components such as orbital component, topography, displacement, atmosphere and noise that each of the parameters causes the phase change.

Relative position of a number of the terrestrial events changes slightly between the two SAR images, which is independent of the baseline. Therefore, the signals received from the structures and the road surface lead to the loss of coherence and the difference between the two synchronous image pairs is less than the coherent of the pre-event pair images.

The difference between the two images pairs can be calculated for plotting the affected areas (Ishitsuka et al. 2012) (Lu et al. 2018). These changes are resultant from subsidence, landslide and displacement of the faults.

After flattening in the formula, interferometry phase interferogram will be according to following relation

$$\Delta\varphi = -\frac{4\pi}{\lambda} \frac{B_{nq}}{R \sin \Theta} + \frac{4\pi}{\lambda}$$

The obtained interferogram from this step is called differential interferogram and the remained phase is basically the result of the earth crust changes.

SRTM arc secdata topography with a resolution of 30 meters along with GCP points was used to eliminate topographic and atmospheric phases. For selecting GCP points, the coherent areas with smooth topography and away from shifted areas were identified.

In the last stage, the image was converted to the WGS84 global system and for analyzing its classification

in GIS software and its relationship with the groundwater level of the areas were determined.

2.1. Hydrograph Analysis

The time series diagram of the level of piezometer wells in the region from 2015-2019 is also shown as a groundwater interpolation map using the Kriging method to show groundwater changes.

2.2. Geographical Balanced Regression

Moran's index is an instrument in spatial self-correlation analysis that analyzes the pattern of distribution of features in space with simultaneous consideration of location and the value of the desired feature.

3. Results

The results of processing on the images show subsidence of about 24 cm in the studied area "Fig. 2". In order to study subsidence and its impact on the extraction of groundwater reserves in the part of Shabestar plain that has higher subsidence event has been selected as the studied area. The center of Shabestar and Tasuj plain has experienced the most subsidence and other areas have witnessed the occurrence of this phenomenon to a lesser extent.

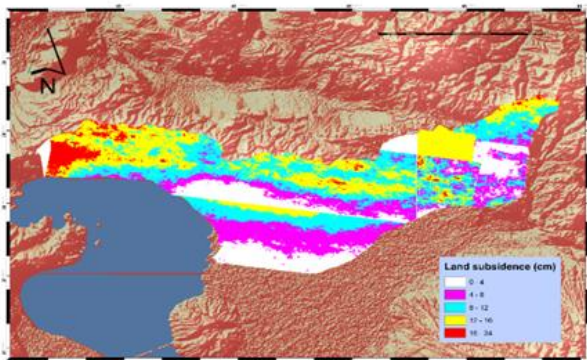


Figure 2. Map of Shabestar plain subsidence

The research tries to find a relationship between exploitation of water from existing wells and the phenomenon of subsidence. "Fig. 3" shows the distribution of water exploitation wells and the level of groundwater. The highest density of exploitation wells is observed in the center of the region located in the western parts of the studied area "Fig. 3".

Spatial analysis of these two parameters was performed by having a subsidence density map and changes in water level. Examination of these changes confirmed the existence of significant clustering in the area. Clusters with high values correspond to changes in water level shifted with the occurrence of subsidence and clusters with low values confirm the slight correlation of changes in level with the occurrence of subsidence "Fig. 4".

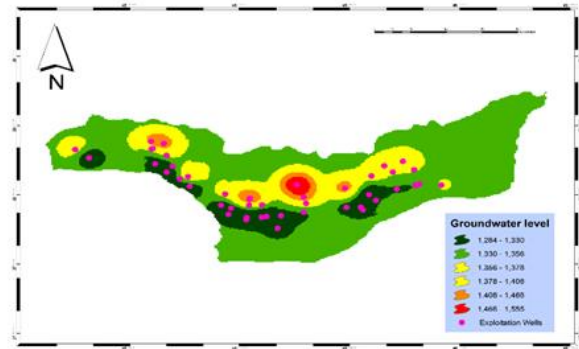


Figure 3. Groundwater water level map

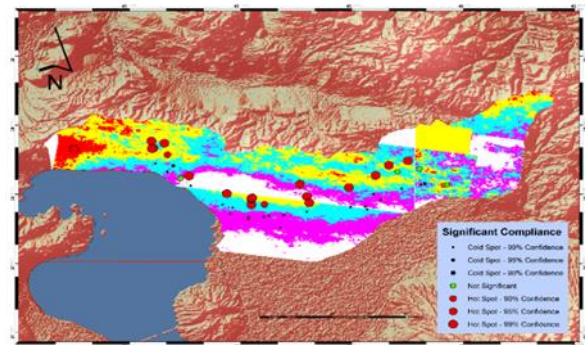


Figure 4. Adaptation map of groundwater level changes and subsidence occurrence density

This analysis confirmed the Moran index of clustering subsidence under the influence of water changes in the studied area. The closer Moran index to one depicts the stronger cluster pattern. The results of the analysis of the present research indicated 0.98 for Moran index. On the other hand, the high standard score of Z and the low value of P-VALUE confirm the strong correlation between the studied elements, which in the present analysis are 477 and 0, respectively "Fig. 5".

Global Moran's I Summary	
Moran's Index:	0.987086
Expected Index:	-0.000044
Variance:	0.000004
z-score:	477.593058
p-value:	0.000000

Figure 5. Moran index Processing

4. Discussion

Interferogram of Sentinel A1 images with coherence values of 0.2 and base line 82 was provided. The results of InSAR analysis showed that the highest amount of subsidence is about 24 cm, which occurred in 2015-2019. Groundwater level in relation to the results of subsidence of Shabestar-Sufiyan plain indicated the plain subsidence in parts where the use of groundwater and the density of exploitation wells in the region and the amount of drought and subsidence in these areas have been reported.

According to the region climate, the groundwater level fluctuations used by farmers in this area with agricultural land covers, irrigated agricultural lands and gardens around the area in the villages of Chelekhaneh Oliya, Ali Akbar Lou, Cheshmeh Kanan, Ghezeljeh, Cheshmeh Kanan Station, Gholmansarai and Sahlan Customs are important factors in land subsidence.

5. Conclusion

In recent decades, it has experienced population growth along with agricultural development and has the highest subsidence of 24 cm, which can be imaged from the Sentinel A1 satellite with v-v bands in summer, which is the best result considered for accurate monitoring of the ground by InSAR radar interferometry. Low precipitation in recent years and successive droughts, resource constraints, improper irrigation methods in the agricultural sector in the studied area along with inappropriate cultivation pattern have led to excessive digging of water wells in the area. This subsidence, which is mostly seen in agricultural lands, has endangered the expansion of sinkholes, lands and villages of Shabestar and Tasuj plains and by destroying agricultural and garden lands, destroying roads and communication and service facilities and trapping livestock have influenced the lives of the residents of this area and have other negative effects that require sustainable and principled management of resources and awareness of managers in this area for solving the problem of crises and basic planning of the area.

References

- Chen, C., Wang, C., Chen Kuo, L. (2010). Correlation between groundwater level and altitude variations in land subsidence area of the Choshuichi Alluvial Fan. *Taiwan Engineering Geology* 115:122–131.
- Clement, M., Kilsby, C., & Moore, P. (2018). Multi-temporal synthetic aperture radar flood mapping using changedetection. *J. Flood Risk Manag*, 11, 152–168.
- Dai, K., Li, Z., Tomás, R., Liu, G., Yu, B., Wang, X., Cheng, H., Chen, J., & Stockamp, J. (2016). Monitoring activity at the Daguanbao mega-landslide (China) using Sentinel-1 TOPS time series interferometry. *Remote Sens. Environ*, 186, 501–513.
- Daniel, R., Maisons, C., Carnec, S., Le Mouelic, C., Kingands, H. (2003). Monitoring of slow ground deformation by ERS radar interferometry on the Vauvert salt mine (France) Comparison with ground-based measurement. *Remote Sensing of Environment*, 88(4): 468-478.
- Galloway, D. L., Hudnut, K. W., Ingebritsen, S. E., Philis, S. P., Peltzer, G., Rogez, F., Rosen, P. A. (1998). Detection of aquifer system compaction and land subsidence using interferometric synthetic aperture radar, Antelope valley, Mojave Desert, California, *Water Resour. Res.*, 34: 2573-2585.
- Gatelli, F., Monti Guarnieri, A., Parizzi, F., Pasquali, P., Prati, C., & Rocca, F. (1994). The wavenumber shift in SARinterferometry. *IEEE Trans. Geosci. Remote Sens.*, 32, 855–865.
- Haykin, S. (2007). *Adaptive Filter Theory*, 4th edition, Pearson Education Inc.
- Ishitsuka, K., Tsuji, T., & Matsuoka, T. (2012). Detection and mapping of soil liquefaction in the 2011 Tohoku earthquake using SAR interferometry. *Earth Planets Space*, 64, 1267–1276.
- Karimzadeh, S., & Ahmadi, F. (2013). Using Advanced Space-borne Radar Technology for Detection and Measurement of Land Subsidence and Interseismic Slip Rates, the Case Study: NW Iran.
- Ketelaar, V. B. H. (2008). *Satellite Radar Interferometry Subsidence Monitoring Techniques*. Vol, 14. Netherlands. Springer Science.
- Lu, C. H., Ni, C. F., Chang, C. P., Yen, J. Y., & Chuang, R. Y. (2018). Coherence difference analysis of Sentinel-1 SARinterferograms to identify earthquake-induced disasters in urban areas. *Remote Sens*, 10, 1318.
- Motagh, M., Djamour, Y., Walter, T. R., Wetzell, H. U., Zschau, J., Arabi, S. (2006). Land subsidence in Mashhad Valley, northeast Iran: results from InSAR, levelling and GPS. *Geophysical Journal International*, 1-9.
- Raucoules, D., de Michele, M., & Aunay, B. (2020). Landslide displacement mapping based on ALOS-2/PALSAR-2 data using image correlation techniques and SAR interferometry: Application to the Hell-Bourg landslide. *Geocarto Int.*, 35, 113–127.
- Sun, H., Zhang, Q., Zhao Yang, Ch., Sun, Q., & Weiran, Ch. (2016). Monitoring Land Subsidence in the southern part of the lower liaohai plain, China with a multitrack PS-InSAR technique.
- Twele, A., Cao, W., Plank, S., & Martinis, S. (2016). Sentinel-1-based flood mapping: A fully automated processing chain. *Int. J. Remote Sens.*, 37, 2990–3004.
- USGS (2014). Land Subsidence, The USGS Water Science School, online.
- Vietmeier, J., Wagner, W., & Dikau, R. (1999). Monitoring moderate slope movements (landslides) in the southern French Alps using differential SAR interferometry. In *Proceedings of the Fringe 1999 Workshop: Advancing ERS SAR Interferometry from Applications Towards Operations*, Liège, Belgium, 10–12 November; Volume 99, pp. 10–12.
- Walters, R. J., Holley, R. J., Parsons, B., & Wright, T. J. (2011). Interseismic strain accumulation across the North Anatolian Fault from Envisat InSAR measurements. *Geophysical Research Letters*, VOL. 38.
- Wright, T., Parsons, B., & Fielding, E. (2001). Measurement of interseismic strain accumulation across the North Anatolian Fault by satellite radar interferometry. *Geophysical Research Letters*, 28, NO. 10, 2117-2120.
- Zebker, H. A. (1992). Decorrelation in interferometric radar echoes. *IEEE Trans. Geosci. Remote Sens.* 30, 950–959.

4th Intercontinental Geoinformation Days

igd.mersin.edu.tr



Geometric shape fitting on simulated and TLS-based leaning tree-trunk point cloud for precision forestry measurements

Mustafa Zeybek*¹

¹Selcuk University, Guneysinir Vocational School of Higher Education, Konya, Türkiye

Keywords

Point cloud
Geometric primitive
Best fitting
Cylinder
Circle
Robust PCA

Abstract

Remote sensing and measurement methods have gained great importance in forest surveys, forest inventory, growth, and planning of assets in the last decade. In particular, it is important to obtain geometric parameters from dense point cloud data and estimate the diameter at breast height (DBH), which is a common parameter in forest inventory. In this way, "precision forestry" measurements come to the fore and leave traditional measurement methods behind. However, these processes are rather tedious and more complex than one might think. The accuracy of geometric estimations depends on the application of convenient methods. In estimating tree trunk diameters, 2D planar calculation of the diameter determinations of leaning trees is an important source of error. In order to eliminate this error, it is planned to prevent it with the robust principal components analysis (PCA) algorithm. For this purpose, the proposed methodology has been tested on simulation and real test datasets. The results show that the application of robust PCA algorithms prevents significant errors.

1. Introduction

The diameter of a tree at breast or breast height is one of the most important measurements made by forest surveyors and experts, and it is also commonly referred to as "DBH". Another important parameter is the tree height, which is important in calculating the wood volume. This way, forest inventory, and forest assets are calculated "precisely" with these correctly obtained parameters. A total evaluation is made with the number of trees in the stand with all these parameters.

DBH measurements are measured from the tree's outer bark at a point close to approximately breast height. Breast height measurement is generally made at 1.30 meters above the tree trunk. Ground extraction is also important in determining breast height, and it is a key parameter in measuring growth, volume, and forest wealth in different periods with DBH data evaluation. This parameter of breast height is a suitable technique for measuring a tree to facilitate field measurements.

In forest management and inventory studies, forest practitioners applied formulations based on DBH to calculate growth, volume, and yield tables based on this parameter. There are traditional and modern techniques that can be used to measure the diameter of a tree (Fan,

Dong, Chen, & Chen, 2020). The most commonly used device is to go near trees and use calipers, tape measure, or rope (Mokros et al., 2018; Reddy, Jha, & Rajan, 2018). Although these techniques have been used as the most accurate techniques from the past to the present, non-contact measurement techniques have also been developed today. Image processing and point cloud methods have emerged as effective alternatives for calculating DBH (Gollob, Ritter, & Nothdurft, 2020a).

On the other hand, this study is research to determine DBH measurements to be obtained from point clouds in leaning trees. The study was presented as a test both on a simulated cylinder and on a real data set.

2. Method

The methodology applied for DBH extraction from point clouds was carried out in 2 stages. The first of these is creating a cylindrical model and bending this model on the X-axis of 10 degrees with five different rotations. In the second stage, a 10 cm section is taken between 1.25 and 1.35 m above the ground height, and the circle fitting process is applied. The same methodology was applied to terrestrial laser scanning data. After the principal component analysis (PCA) (Wold, Esbensen, & Geladi,

* Corresponding Author

^{*}(mzeybek@selcuk.edu.tr) ORCID ID 0000-0001-8640-1443

Cite this study

Zeybek, M. (2022). Geometric shape fitting on simulated and TLS-based leaning tree-trunk point cloud for precision forestry measurements. 4th Intercontinental Geoinformation Days (IGD), 122-126, Tabriz, Iran

1987) application, the rotation of the cylinder, which was converted into a point cloud, was determined, and the effect of this leaning on the fitting of a circle and its elimination was performed with the circle fitting process. PCA is one of the most widely used multivariate statistical methods in practice. It is used to reveal the variation among the data and the subsets of the variables. The major axes of P point clouds are defined with their associated magnitudes v (eigenvalues) and λ (eigenvectors) (Burt, Disney, Calders, & Goslee, 2018). PCA is used to determine the basic axes in point cloud data and detect components in the field of statistics. PCA is highly sensitive to outliers, commonly encountered in point clouds. Outliers are classical measures of variance that increase excessively, and because the principal components follow the directions of maximum variance, they cause increased errors by outliers. A robust version of PCA has been developed. In this way, the principal components are defined in a structure that will not be disturbed by outlier noises. As a result, PCs are computed with reliable data, leaving out unreliable data (Varmuza & Filzmoser, 2016).

All applications were carried out in the *R* program (Team, 2021), 3DReshaper (3DReshaper, 2020), and CloudCompare (Girardeau-Montaut, 2019) software. The proposed methodology is coded in the *R* program.

2.1. Cylinder forming and leaning

In forest measurements, some trees lean with different effects. The trunks of these trees, which should be perpendicular to the surface normal according to the topographical effect, can be leaning to the ground instead of perpendicular to the ground. In this case, the DBH 1.30 circle fitting process from the point clouds is incorrect. After removing the cylindrical trunk, the leaning of this cylindrical trunk should be corrected.

This situation was simulated with the 3DReshaper software program. It was produced as a cylindrical mesh model with a height of 3 m and a radius of 10 cm. The cylinder center is taken as (0,0,0). The mesh model is decomposed into point clouds at 1 cm intervals.

This cylindrical point cloud was produced in 5 copies with 10-degree inclinations around the X-axis (Fig.1).

2.2. Pre-processing point cloud

In order to determine the height of the cylinder point clouds from the ground, the ground plane was produced as a planar mesh model. In this way, the height of the tree trunk points from the ground can be taken. Since the bodies are assumed to be cylindrical, the noisy points must be filtered with the RANSAC algorithm (Schnabel, Wahl, & Klein, 2007), or a different noise removal algorithm can be used. After this stage, the point cloud section between 0.80 m and 1.80 m height values is taken on Z-axis, and the PCA algorithm is applied in this section. After the orientations are determined, the next step is the geometric parameter fitting phase.

2.3. Circle Fitting (Späth)

In order to extract the geometric parameters from the point clouds, the circle fitting process suggested by the Späth algorithm (Späth, 1996) was performed on the PCA de-rotation point clouds. X and Y coordinate information in point clouds are extracted from the *las* file, and a planar 2D circle fitting is performed. The fitting process in the planar and parametric form given below is performed in the given point clouds.

$$\begin{aligned} x &= a + r \cos z \\ y &= b + r \sin z \end{aligned} \quad (1)$$

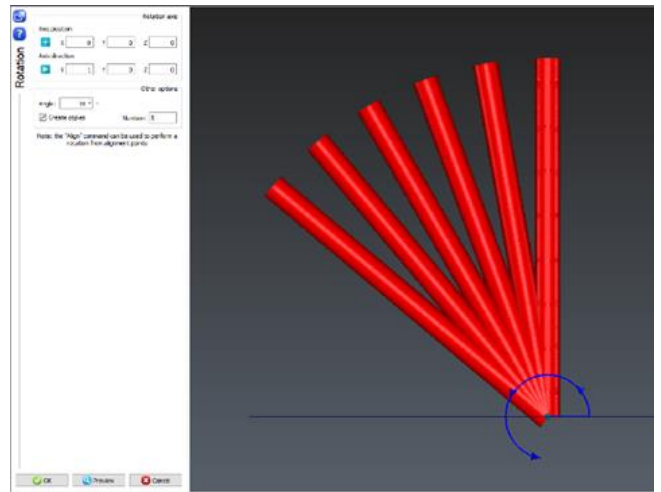


Figure 1. Cylinder forming and leaning

The minimization function of the errors with the sum of the total orthogonal distances is applied. The following function is used for this.

$$S(a, b, r, z_{1-n}) = \sum_{k=1}^n \left[\frac{(y_k - b - r \sin z_k)^2 + (x_k - a - r \cos z_k)^2}{2} \right] \quad (2)$$

where (a, b) represents the center coordinates of the circle, r represents the circle's radius, and z values represent the center angle values. First, z is eliminated in the circle model and put into a non-parametric equation. Moreover, it transforms into the following form.

$$\begin{aligned} (x - a)^2 + (y - b)^2 &= r^2 \\ S(a, b, r) &= \sum_{k=1}^n \left(\sqrt{(x_k - a)^2 + (y_k - b)^2} - r \right)^2 \end{aligned} \quad (3)$$

All the calculations mentioned above have been implemented using the *R conicfit* package (Gama & Chernov, 2015).

3. Results

Radius values were obtained after PCA and Robust PCA application with circle fitting algorithms obtained at five angles and perpendicular to an original ground. The actual cylinder radius value is 10 cm. Fitting leaning cross-section values are named Raw data, PCA, and

Robust PCA. The original cross-section and curvature values of 10 and 50 degrees are called c0-c5. The circle fitting to c0, c3, and c5 data is shown in Fig.2.

Table 1. Descriptive statistics of circle fitting results on the simulated cylinder dataset

Statistics	Raw	PCA	Robust PCA
Mean [m]	0.1799	0.0999	0.1002
Median [m]	0.0871	0.0003	0.0003
Sd [m]	0.1553	0.0999	0.1001

In terms of descriptive statistical values, fitting a circle to the raw data yields very erroneous results (Table 1).

PCA and Robust PCA, on the other hand, provided high accuracy in tenths of a millimeter for both methods on data that has been de-skewed. The deviation values are quite low. However, it should not be forgotten that this is a perfectly cylindrical data produced by simulation, and there are point clouds from every angle to form the circle (Fig. 2). In practice, it is obvious that such data is not very smooth.

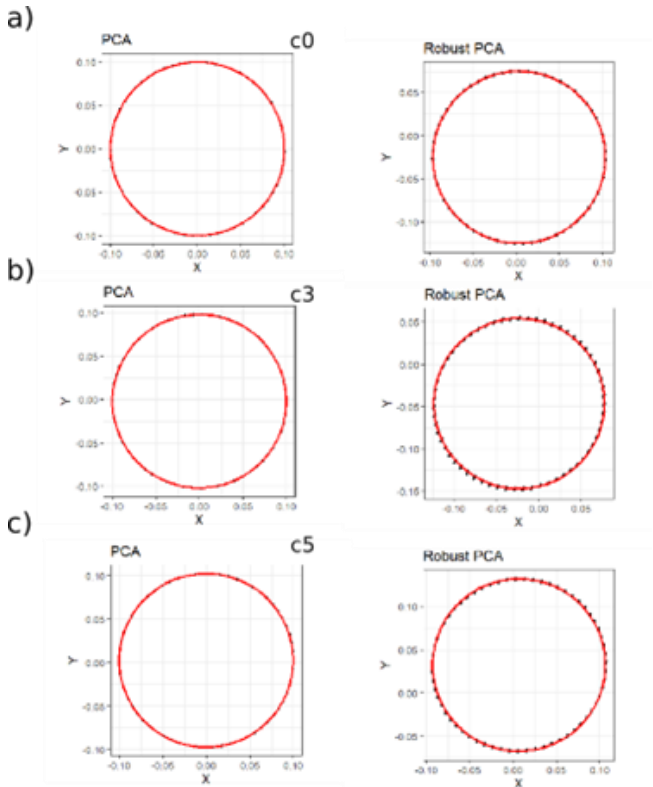


Figure 2. c0, c3, and c5 dataset circle fitting results at 1.25 m and 1.35 m

According to Fig.3, while PCA and Robust PCA methods produce results close to each other for all kinds of data, in the application of the circle fitting algorithm without using any leaning correction, the error rates increase linearly as the angles increase.

In this research, terrestrial laser scanner (TLS)-based point clouds obtained from the real forest were analyzed in addition to the simulation dataset. The laser scanning device used is a static terrestrial laser scanner (TLS) (Focus3D X330, Faro Technologies Inc., Lake Mary, FL, USA) (Gollob, Ritter, & Nothdurft, 2020b).

As shown in Fig. 4, the tree trunk was extracted from the point clouds. This data showed the importance of the Robust PCA application as it does not contain point clouds in every aspect like simulation data.

According to the reference dataset of the test data owners, the DBH value of this tree, which is in the eighth plot region and tree id 80, was obtained as 20 cm in the field. In addition, it has also been investigated to what extent the circle fitting process would be affected if it was a leaning tree.

Table 2. TLS point cloud data single-tree circle fitting and geometric results of radius

DBH	Reference	Raw	PCA	Robust PCA
R [m]	0.1	0.0813	0.0967	0.1019

In TLS-based point cloud sections, the DBH value on a single tree was measured as 0.1 m in diameter and 0.2 m in the field as a reference (Table 2). The proposed methodology used a geometric estimation with a deviation of 1.9 millimeters, which means a relative difference of 1%. It has been shown that the proposed method achieves more relevant results as Robust compared to other raw and normal PCA implementations (Fig. 5).

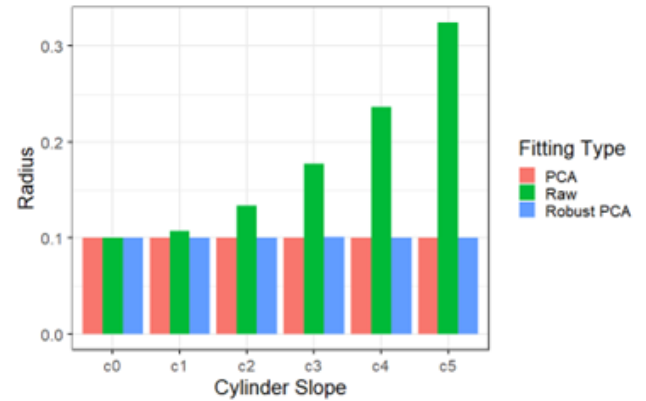


Figure 3. Fitting results of the three different methods on original and five leaned data

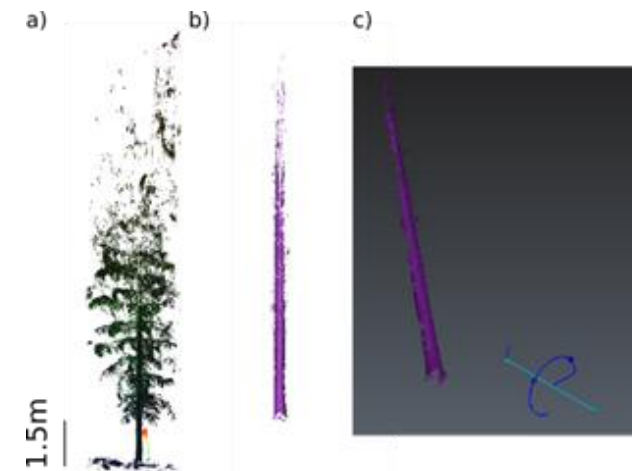


Figure 4. A manually cropped tree from TLS data, a) all point cloud data with surface normals calculated, b) extraction of the cylindrical body structure according to the RANSAC algorithm, c) trunk with 10 degrees inclination in the X-axis

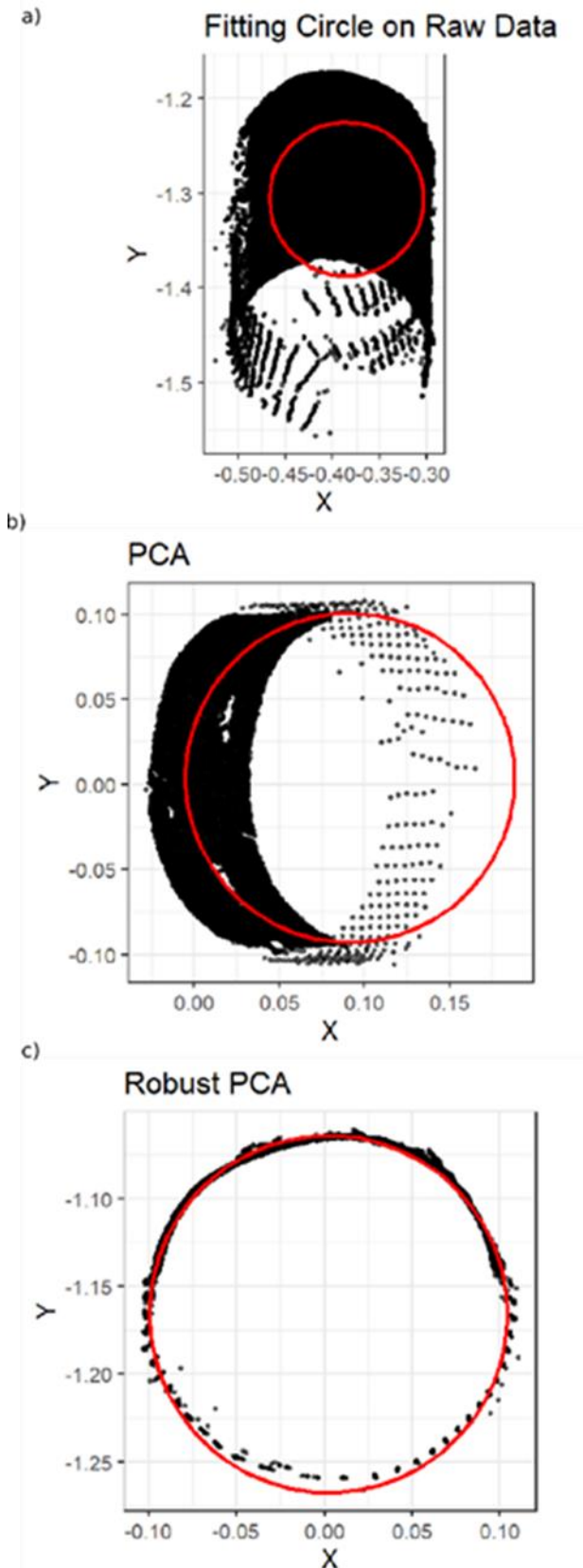


Figure 5. Single station TLS-based trunk point cloud circle fitting results a) raw data fitting, b) PCA rotated point cloud fitting, c) robust PCA based circle fitting

4. Discussion

In this study, circle fitting processes are complete for a single tree, and an important step is mandatory for forestry measurements. However, the study was carried

out on the point cloud, which can be considered clear and very good, and based on a single tree. These methods also have certain limitations in real forest inventory measurements. Using the cylindrical and parametric model and TLS data used in this study, calculations were made on the trunk model with high accuracy on a noiseless stem. However, obtaining such high accuracy in hand-held laser scanners or noisy tree trunks is among the high possibilities, depending on the data structure. In addition, the complexity of forest structures, difficulties that may be encountered in individual tree detection, double trunk trees, etc., can be challenging. In this case, applying the proposed methodology to "easy" measurement point cloud data on a single tree basis and where the trunk points can be separated from the branches and leaves means that there may be limitations when faced with the mentioned situations.

In geometric parameter estimation, the proposed methodology was able to detect with high accuracy by providing flexibility in point cloud data that do not represent full circles, which are frequently encountered in TLS-based point clouds. Especially in single station scanning applications in TLS data, there are deficiencies in the point clouds of trees at certain ratios and directions. Since the proposed methodology uses the Späth algorithm, a geometric circle fitting algorithm, it gives better results than algebraic algorithms. It evaluates all point cloud data of the body in the DBH estimation. In this way, when the pre-processed data is used, it achieves successful results in estimating the DBH parameters of the trees.

5. Conclusion

This study is aimed to extract DBH from point clouds, which is common use in forest parameters. The application of the robust PCA method to evaluate and eliminate errors in the DBH fitting process that occurs in the leaned trees in DBH extraction has ensured that this error is minimized. The proposed methodology has been tried to make DBH measurements caused by tree slant, which can be encountered frequently in forest measurements and be used in a more "precision" forestry measurement. The study has two different test data; It has been tested on the simulated cylinder and TLS-based data, with significant success.

Acknowledgment

In this study, the LAUT - Terrestrial and Personal laser scanner data from Austrian forest inventory plots (1.0) (<https://doi.org/10.5281/zenodo.3698956>) [Data set] was used, which was produced by Gollob, Christoph, Ritter, Tim, & Nothdurft, Arne

References

3DReshaper. (2020). 3DReshaper Retrieved from <https://www.3dreshaper.com/fr/>

- Burt, A., Disney, M., Calders, K., & Goslee, S. (2018). Extracting individual trees from lidar point clouds using treeseg. *Methods in Ecology and Evolution*. doi:10.1111/2041-210x.13121
- Fan, G., Dong, Y., Chen, D., & Chen, F. (2020). New Method for Forest Resource Data Collection Based on Smartphone Fusion with Multiple Sensors. *Mobile Information Systems*, 2020, 1-11. doi:10.1155/2020/5736978
- Gama, J., & Chernov, N. (2015). Conicfit: algorithms for fitting circles, ellipses and conics R package version 1.0.4. In.
- Girardeau-Montaut, D. (2019). Cloudcompare GPL software version 2.10. Retrieved from <https://www.danielgm.net/cc/>
- Gollob, C., Ritter, T., & Nothdurft, A. (2020a). Forest inventory with long range and high-speed personal laser scanning (PLS) and simultaneous localization and mapping (SLAM) technology. *Remote Sensing*, 12(9). doi:10.3390/rs12091509
- Gollob, C., Ritter, T., & Nothdurft, A. (2020b). LAUT - Terrestrial and Personal laser scanner data from Austrian forest Inventory plots. In.
- Mokros, M., Vybost'ok, J., Tomastik, J., Grznarova, A., Valent, P., Slavik, M., & Merganic, J. (2018). High Precision Individual Tree Diameter and Perimeter Estimation from Close-Range Photogrammetry. *Forests*, 9(11). doi:10.3390/f9110696
- Reddy, R. S., Jha, C. S., & Rajan, K. S. (2018). Automatic Tree Identification and Diameter Estimation Using Single Scan Terrestrial Laser Scanner Data in Central Indian Forests. *Journal of the Indian Society of Remote Sensing*, 46(6), 937-943. doi:10.1007/s12524-018-0753-7
- Schnabel, R., Wahl, R., & Klein, R. (2007). Efficient RANSAC for point-cloud shape detection. *Computer Graphics Forum*, 26(2), 214-226. doi:10.1111/j.1467-8659.2007.01016.x
- Späth, H. (1996). Least-squares fitting by circles. *Computing*, 57(2), 179-185. doi:10.1007/bf02276879
- Team, R. C. (2021). R: A Language and Environment for Statistical Computing. Retrieved from <https://cran.r-project.org/>
- Varmuza, K., & Filzmoser, P. (2016). *Introduction to Multivariate Statistical Analysis in Chemometrics* (Vol. 64).
- Wold, S., Esbensen, K., & Geladi, P. (1987). Principal Component Analysis. *Chemometrics and Intelligent Laboratory Systems*, 2(1-3), 37-52. doi:10.1016/0169-7439(87)80084-9



4th Intercontinental Geoinformation Days

igd.mersin.edu.tr



Automated building extraction from very high-resolution remote sensing data with deep learning approaches

Volkan Dağdelen¹, Ugur Alganci^{*1}, Elif Sertel¹

¹Istanbul Technical University, Civil Engineering Faculty, Geomatics Engineering Department, İstanbul, Türkiye

Keywords

Remote sensing
Building extraction
Deep learning
Automated detection
Unet Architecture

Abstract

Building extraction from very high-resolution satellite images is an important task due to the various different usage of the extracted information such as population estimation, city planning, and disaster management. Manual extraction of the buildings is a labor-intensive task that is prone to human-induced errors and mistakes. Index-based and classical machine learning approaches remain insufficient due to diversity in building geometries, changes in reflectance values, and similar properties with other objects. Recently deep learning-based approaches show promising developments and results for this task. Unet architecture is one of the most popular deep learning architectures for building extraction within the scope of semantic segmentation. This study aims to automatically detect buildings by using the Unet architecture. The Unet model was trained twice with the same hyperparameters and Resnet50 backbone on 50 epochs initially with the Massachusetts building detection dataset and secondly with a combination of Massachusetts and Inria datasets to perform a comparative evaluation. According to the independent testing results with data from Massachusetts, Inria, Pleiades and Google Earth, both datasets provided satisfactory IoU scores ranging between 0.71 and 0.89, except for the first dataset testing with Pleiades images that provide a 0.51 IoU score.

1. Introduction

Up to date building information has an important role in several applications such as population estimation, change monitoring, urban planning, smart city applications, map services, and disaster management, thus the extraction of building boundary lines from high-resolution images has always been the main research topic for remote sensing research projects (Xie et al. 2020). The emergence of high spatial resolution satellite images due to current satellite technologies made it possible to extract buildings from these images and to perform useful analyzes by using them in applications such as geographic information systems.

The initial afford in building footprint extraction from satellite images was based on the spectral characteristics and geometric features of the objects on the image, such as spectral information, colors, textures, and geometric shapes, and algorithms were mainly designed as defining thresholds on these parameters to differentiate the buildings from their environment. With the recent advances in hardware and software environments, machine learning-based classification approaches have

become popular. The main algorithms for this purpose can be listed as, K-means, support vector machines, random forest, adaptive boosting, and conditional random fields (Liu et al. 2018). The drawbacks of the above-mentioned methods are that they require a high degree of prior knowledge and parameter selection and, accordingly, require a significant amount of time and labor (Liu et al. 2020; Yang et al. 2020).

In recent years, deep learning (DL) networks, especially convolutional neural networks, have been used frequently in remote sensing applications such as classification, change detection, artificial object detection, and extraction (Bakirman et al. 2022; Ekim and Sertel, 2021; Zhang et al. 2020). Over half a decade, the use of DL networks for building detection has frequently been encountered. In the study of Li et al. (2018), Unet and Deeplabv3+ architectures were applied to SpaceNet 2 dataset for the same purpose and their results provided that Unet is more efficient. Bischke et al. (2019) used SegNet architecture and Inria dataset for building segmentation and footprint extraction and they presented high IoU scores for different regions. Another study by Zhang et al. (2019) used Web-net architecture

* Corresponding Author

(volkandagdelen@gmail.com) ORCID ID 0000 – 0001 – 7563 – 8111
*(alganci@itu.edu.tr) ORCID ID 0000-0002-5693-3614
(sertele@itu.edu.tr) ORCID ID 0000-0003-4854-494X

Cite this study

Dağdelen, V., Alganci, U., & Sertel, E. (2022). Automated building extraction from very high-resolution remote sensing data with deep learning approaches. 4th Intercontinental Geoinformation Days (IGD), 127-130, Tabriz, Iran

on Inria and Wuhan University (WHU) datasets and could reach over 0.85 IoU scores.

Inspired by the latest DL-based research for building extraction, this study aims to perform a comparative experiment to evaluate the effects of the training dataset on building extraction using DL-based approaches. Moreover, it presents independent testing to measure the extendability of the trained network in building extraction from different sensor data.

2. Method

In this study, Unet architecture with Resnet 50 backbone was used for building extraction purposes. The Massachusetts and Inria datasets were used for training, while Massachusetts, Inria, Pleiades, and Google Earth data were used for testing.

2.1. Data and preprocessing

The Massachusetts dataset consists of 1500 x 1500 pixel-sized 151 RGB aerial images of Boston with 1m spatial resolution. The footprints of the buildings for this dataset are extracted from OpenStreetMap. The Inria dataset includes 30 cm spatial resolution RGB aerial images with their label data (building – not building). The training and validation data of this dataset covers different cities, which makes the data suitable for such research applications. The test data used in this study includes 10 images from the Massachusetts dataset, 10 images from the Inria dataset. Additionally, 10 images from 50cm spatial resolution Pleiades satellite images and 10 images from Google Earth were used for independent testing. Building footprint labels for Pleiades and Google Earth images were manually generated in the QGIS environment.

This study uses the Google Colab and Kaggle platform to perform the analysis, thus all image sets and the label masks were cropped to create patches with 512 x 512 dimensions in order to minimize the computation bottleneck. After this process, the datasets were augmented to synthetically increase the training data amount, which is proved to improve the learning performance (Roh et al. 2019). Data augmentation parameters applied via “albumations” toolset are provided in Table 1.

Table 1. Hyperparameter set used to train the Unet Resnet 50 model.

Augmentation Method	Parameters
Horizontal Flip	p: 0.5
Offset and Scale	0.2 scale limit, 0.1 sliding limit, p:1
Gaussian Noise	p: 0.2
Perspective	p: 0.5
CLAHE	p: 1
Sharpness	Selection probability: 0.9, p:1
Blurriness	Selection probability: 0.9, blur ratio: 3, p:1
Random Brightness	Selection probability: 0.9, p: 1
Random Gamma	Selection probability: 0.9, p: 1
Random Motion	Selection probability: 0.9, p: 1
Blur	
Random Contrast	Selection probability: 0.9, p: 1
HSV	Selection probability: 0.9, p: 1

2.2. Model training and validation

Within the scope of the study, the Unet segmentation architecture was used as the basic architecture. The U-Net architecture is a semantic segmentation architecture proposed for biomedical purposes (Ronneberger et al. 2015). The architecture consists of two phases. The first stage is the encoder stage and consists of convolution and max-pooling layers as in classical convolutional neural networks (CNN). In this layer, there are 3x3 convolution layers, followed by corrected linear unit (ReLU) activation functions, followed by max-pooling layers containing two 2x2 sized strides for downsampling. Feature channels are doubled at each downsampling. The second stage is the decoder stage and uses transposed convolutions for precise positioning. Transposed convolutions are used for up-sampling. These convolution layers are 3x3 in size and each convolution layer is followed by the ReLU activation function. This structure is called an end-to-end fully convolutional network, since it has no density layers and only convolutional layers, it accepts any size image as input.

The python programming language and the Pytorch segmentation model library were used to implement the Unet architecture. The hyperparameters used to train Unet Resnet 50 are provided in Table 2.

Table 2. Hyperparameter set used to train the Unet Resnet 50 model.

Parameters	Used Values
Loss Function	Dice
Evaluation Metric	IoU
Optimizer	Adam
Activation Function	Sigmoid
Encoder	Resnet50
Pre Trained Weights	ImageNet
Batch Size	16
# Epochs	50
Learning Rate	0.0001 till 25 th epoch, 0.00001 after 25 th epoch

This study uses the intersection over Union (IoU) score metric to evaluate the model results. The IoU metric can be calculated as Formulae 1.

$$\text{IoU} = (\text{TP}) / (\text{TP} + \text{FP} + \text{FN}) \quad (1)$$

Where TP represents true-positive, FP represents false-positive and FN represents false-negative extractions.

3. Results

When the model results are investigated, the highest score was obtained by the model trained with only the Massachusetts dataset and tested with the Massachusetts test set with a 0.8923 IoU score. On the other hand, the model trained with the Massachusetts + Inria dataset provided the highest scores for the remaining test sets (Table 3 and Table 4).

The most critical stage of evaluation is to test the models with data that are not available in both training models. One of the aims of this study is to detect different

building types in images obtained from different satellites, with different resolutions, containing different regions. When the test data containing the images of the Pleiades satellite were examined, a 0.5123 IoU score was obtained only in the Massachusetts trained model and a 0.7073 IoU score in the Massachusetts + Inria trained model. When the results on the Google Earth test images were examined, a 0.8393 IoU score was obtained in the model trained with only the Massachusetts dataset, and a 0.8144 IoU score in the model trained with the Massachusetts + Inria dataset.

These results suggest that the model trained with a combination of two datasets provided more generalized performance across different image sources. Especially the improvement in building extraction from Pleiades image points out the advantage of training a model with data from different sensors for extendability requirements.

In order to evaluate the model, it is necessary to examine and interpret the images as well as the scores. Fig. 1 provides visuals from the testing results of the study. In this figure, green circles represent the better-extracted regions by the model trained with only the Massachusetts dataset and red circles represent the better-extracted regions by the model trained with Massachusetts + Inria dataset. When these visuals are interpreted, it can be asserted that both models provided similar performances for Massachusetts and Inria test sets, on the other hand, there is an obvious gain by training with the Massachusetts + Inria dataset for Pleiades images. For Google Earth test data, the model trained with only the Massachusetts dataset surprisingly provided better extractions.

Another important aspect that should be considered here is that IoU values in the training phase and validation phase converged for the Unet model trained with only the Massachusetts dataset at the 50 epochs, while a 2 percent difference was observed for the model with the combined dataset, which indicates lower learning performance on a more complicated dataset.

Table 3. Performance results of the Unet model trained with only the Massachusetts dataset

Test	#of image	Encoder	Dice Loss	IoU Score
Massachusetts	10	Resnet50	0.0626	0.8923
Google Earth	10	Resnet50	0.0924	0.8393
Inria	10	Resnet50	0.0846	0.8500
Pleiades	10	Resnet50	0.3247	0.5123

Table 4. Performance results of the Unet model trained with the Massachusetts + Inria dataset

Test	#of image	Encoder	Dice Loss	IoU Score
Massachusetts	10	Resnet50	0.0645	0.8796
Google Earth	10	Resnet50	0.1044	0.8144
Inria	10	Resnet50	0.0691	0.8742
Pleiades	10	Resnet50	0.1766	0.7073

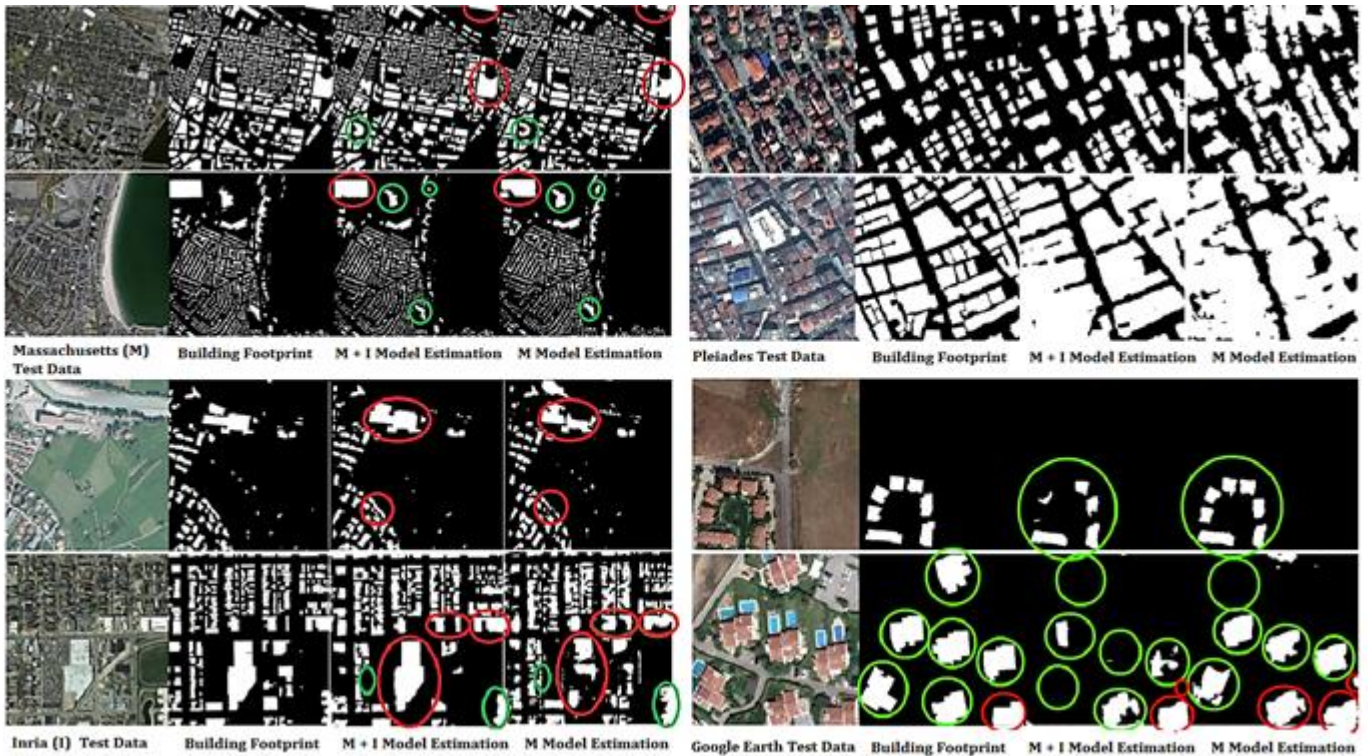


Figure 1. Sample visuals from test results. Green circles represent the better-extracted regions by the model trained with only the Massachusetts dataset and red circles represent the better-extracted regions by the model trained with Massachusetts + Inria dataset

4. Discussion

When the metric scores and test images were examined as a result of all tests, it was found that the model trained with Massachusetts + Inria dataset provided improved performance with the same hyperparameters and architecture. As a result of this study, it is observed that improved results are obtained by increasing the training data. In addition, it may be possible to obtain better results by using different segmentation architectures and encoders. The increase in the number of parameters in different encoders and the extraction of different features can affect the model performance.

It is obvious that there is a benefit in diversifying data sources, but it is also worth mentioning that this increase may not always have positive effects, as in the example of Google Earth images. This situation points out the importance of the test data set in examining the model results and that its diversity is of great importance for the interpretation and accuracy assessment of the model results.

5. Conclusion

This study evaluated the effects of the training dataset on the building extraction from very high-resolution remote sensing data by performing two experiments with different training data setups on the same Unet architecture. Trained models were evaluated across different test data setup two of which is completely independent and sourced by different sensors. Results provided that the model trained by a combination of two datasets provided comparatively higher performance and more importantly the accuracy levels seemed more stable across different test data. This finding points to the expendability of the model with combined training to be used in building extraction from multisensory datasets.

References

- Bakirman, T., Komurcu, I., & Sertel, E. (2022). Comparative analysis of deep learning-based building extraction methods with the new VHR Istanbul dataset, *Experts Systems with Applications*, 202, 117346, <https://doi.org/10.1016/j.eswa.2022.117346>.
- Bischke, B., Helber, P., Folz, J., Borth, D., & Dengel, A. (2019). Multi-Task Learning for Segmentation of Building Footprints with Deep Neural Networks. *AI4SocialGood. International Conference on Learning Representations (ICLR-2019) May 6-9 New Orleans Louisiana United States arXiv 2019*.
- Ekim, B., & Sertel, E. (2021). A Multi-Task Deep Learning Framework for Building Footprint Segmentation, *International Geoscience and Remote Sensing Symposium (IGARSS-2021)*, 11-16 July, Brussels, Belgium.
- Liu, Y., Zhou, J., Qi, W., Li, X., Gross, L., Shao, Q., Zhao, Z., Fan, X., & Li, Z. (2020). ARC-Net: An Efficient Network for Building Extraction from High-Resolution Aerial Images, *IEEE Access*, 8, 154997-155010. <https://doi.org/10.1109/ACCESS.2020.3015701>
- Li, W., He, C., Fang, J., & Fu, H. (2018). Semantic Segmentation Based Building Extraction Method Using Multi-source GIS Map Datasets and Satellite Imagery. *2018 IEEE/CVF Conference on Computer Vision and Pattern Recognition Workshops (CVPRW)*, 233 – 236. <https://doi.org/10.1109/CVPRW.2018.00043>.
- Ronneberger, O., Fischer, P., & Brox, T. (2015). U-net: Convolutional networks for biomedical image segmentation. *International Conference on Medical image computing and computer-assisted intervention*, 234-241.
- Xie, Y., Zhu, J., Cao, Y., Feng, D., Hu, M., Li, W., Zhang, Y., & Fu, L. (2020). Refined Extraction of Building Outlines from High-Resolution Remote Sensing Imagery Based on a Multifeature Convolutional Neural Network and Morphological Filtering, *IEEE Journal of Selected Topics in Applied Earth Observations and Remote Sensing*, 13, 1842-1855. <https://doi.org/10.1109/JSTARS.2020.2991391>.
- Yang, G., Zhang, Q., & Zhang, G. (2020). EANet: Edge-Aware Network for the Extraction of Buildings from Aerial Images. *Remote Sensing*, 12 (13), 2161. <https://doi.org/10.3390/rs12132161>
- Zhang, Y., Gong, W., Sun, J., & Li, W. (2019). Web-Net: A Novel Nest Networks with Ultra-Hierarchical Sampling for Building Extraction from Aerial Imageries. *Remote Sensing*, 11, 1897, <https://doi.org/10.3390/rs11161897>.
- Zhang, Y., Li, W., Gong, W., Wang, Z., & Sun, J. (2020). An Improved Boundary-Aware Perceptual Loss for Building Extraction from VHR Images. *Remote Sensing*, 12, 1195. <https://doi.org/10.3390/rs12071195>.



4th Intercontinental Geoinformation Days

igd.mersin.edu.tr



Comparison of open-source and commercial software for 3 modeling with terrestrial photogrammetry

Muhammed Enes Atik^{*1} , Zaide Duran ¹

¹Istanbul Technical University, Faculty of Civil Engineering, Geomatics Engineering Department, Istanbul, Türkiye

Keywords

Photogrammetry
3D modelling
Camera calibration
Open-source
Accuracy analysis

Abstract

Thanks to advancing computer technologies, computer programs are used in many fields instead of classical methods. Photogrammetry has become a technique accessible to many users, especially with the introduction of open-source software as well as commercial software. Thus, the use of photogrammetry in different fields is becoming widespread. In this study, a miniature statuette and calibration cube made of wood is modeled in 3D with Meshlab and Visual SFM, which are Open-Source software. On the other hand, the same small object is modeled in 3D using the commercial software Agisoft Photoscan and 3DF Zephyr. Accuracy analysis was carried out with the measured lengths on the models. RMSE was calculated as ± 0.7 mm for Agisoft Photoscan, ± 5.3 mm for MeshLab and ± 1.5 mm for 3DF Zephyr.

1. Introduction

As computer vision algorithms and photogrammetric technologies are combined, procedures that automate the image-based 3D modeling process become more common. Photogrammetry's main goal is to create a three-dimensional model from terrestrial or aerial pictures (Duran and Atik, 2021). The open-source software and software enhanced over the last 25 years is one of the most essential factors that fasten this cycle. Today, Information is accessible at any time. Producing an application with the open-source software using this information, processes such as product and result analysis can be commonly improved and shared. Open-source software attracts attention in many areas thanks to the freedom of use it provides, the freedom to interfere with the source code, and the freedom to use and distribute it free of charge. (Weber, 2004).

In this study, a miniature figurine and calibration cube made of wood is modeled in 3D with Meshlab and Visual SFM, which are Open-Source software. On the other hand, the same small object is modeled in 3D using the commercial software Agisoft Photoscan and 3DF Zephyr. RMSE (Root Mean Square Error) and MAE (Mean

Absolute Error) values were compared between the points determined on these 3D models obtained with Agisoft Photoscan, 3DF Zephyr, and Visual SFM + Meshlab. Finally, this software is compared with each other in terms of performance, ease of operation, processing time, and accuracy.

2. Method

2.1. Data used

In this study, historical artifact figurine and wooden cube were modeled. A mobile phone camera (Samsung Galaxy J7) was used to obtain the images. The camera has a 3.7 mm focal length and 13 megapixels resolution. A total of 36 pictures were taken from around the object (Fig. 1).

2.2. Software Used

The VisualSFM program that was developed by Chang chang Wu, is a graphical user interface (GUI) application that provides 3D modeling with images using the SFM technique (Wu, 2011).

* Corresponding Author

(atikm@itu.edu.tr) ORCID ID 0000-0003-2273-7751
(duranza@itu.edu.tr) ORCID ID 0000-0002-1608-0119

Cite this study

Atik, M. E., & Duran, Z. (2022). Comparison of open-source and commercial software for 3 modeling with terrestrial photogrammetry. 4th Intercontinental Geoinformation Days (IGD), 131-134, Tabriz, Iran

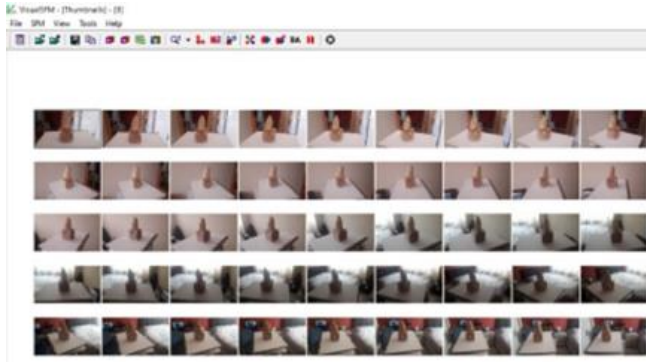


Figure 1. Captured photos.

MeshLab is a 3D mesh processing software system aimed at organizing and processing huge unstructured meshes, with capabilities for editing, cleaning, healing, inspecting, rendering, and converting them. (Cignoni *et al.*, 2008).

Agisoft photoscan is commercial software based on SFM for point clouds, mesh models, DSMs / DTMs and orthophotos from images. (Agisoft, 2014).

3DF Zephyr is commercial photogrammetry and 3D modeling software. It's a software suite that includes various post-processing tools for post-processing, measuring, 3D modeling, and content production. It enables for 3D reconstruction from photographs or movies by automatically removing frames and selecting the ones that are most suited for calculation.

2.3. Camera Calibration

The calculation of the camera's internal orientation parameters using the 3D coordinates of a point in space and the related picture coordinates is known as camera calibration (Song *et al.*, 2013). Agisoft Lens software used as the first camera for the calibration. Photos taken chessboards to add chunk and add photos were installed by performing the steps respectively. Then the camera Calibration tool was opened and the calibration file was loaded, evaluated in Agisoft Lens software and saved in xml format (Table 1). This way, the camera type used was introduced to the program and calibrated. For calibration, 13 images were taken from different angles of the software's chessboard (Fig. 2).

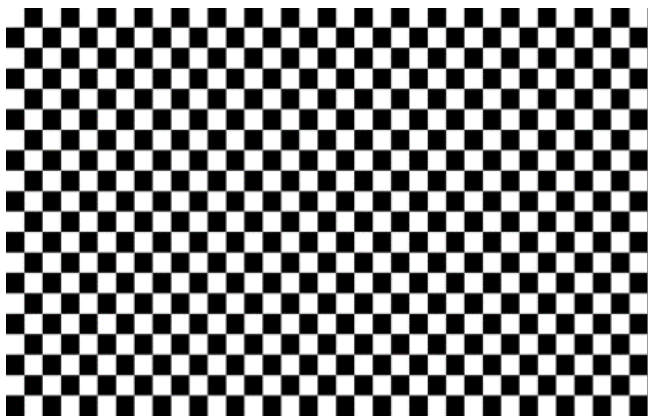


Figure 2. Agisoft Lens Calibration Chessboard

Table 1. Camera interior orientation parameters.

Parameter	Value
f	3.78 mm
c _x	0.074 mm
c _y	-0.003 mm
k ₁	0.362182
k ₂	-1.96877
k ₃	3.84656
k ₄	-2.18084
b ₁	-1.36718
b ₂	3.77981
p ₁	-0.00019
p ₂	-0.00166

2.4. Structure from Motion (SfM)

The software based on the Structure-from-Motion (SfM) method, which uses photogrammetric principles to derive the 3D coordinates of an object by measuring the corresponding points between two overlapping photos. Contrary to traditional photogrammetry, SFM creates object geometry by autonomously resolving camera locations and orientation without the need of a target network with specified 3D coordinates. Camera pose and scene geometry are reconstructed in real time by automatically matching points in several photos, and camera positions and object coordinates are calculated using these points' coordinates (Duran *et al.*, 2021). Initial values are iteratively improved by applying linear least-squares adjustment (Westoby *et al.*, 2012).

2.5. Experiment

After calibration, 36 images were transferred to softwares for photogrammetric model generation. Images were matched to each other using automatically generated key points. The camera's resolution was used as full capacity and 60,000 was selected as the key point limit. Then, tie points were determined among the key points for matching, and thus, all images were aligned. The tie point limit is set to 10,000. The lengths on the cube were used to scale the model. The lengths were measured with caliper and defined on the software. Thus, it was ensured that the generated point cloud was formed on a real-world scale. Dense point cloud was produced by using the resulting sparse point cloud. In order to pass from the point cloud to the mesh model, the surface is passed through the points with interpolation. The model was produced literally by adding the texture produced from the images. All processes for Photoscan and 3D Zephyr have been completed via software. On the other hand, scaling and point cloud generation were performed in VisualSfM, then the model was produced by transferring the point cloud to MeshLab. The visual of the produced model is shown in Fig. 3.

3. Results

Mesh model generation and scaling have been completed in three software. The visuals of the produced models are shown in Fig. 4.

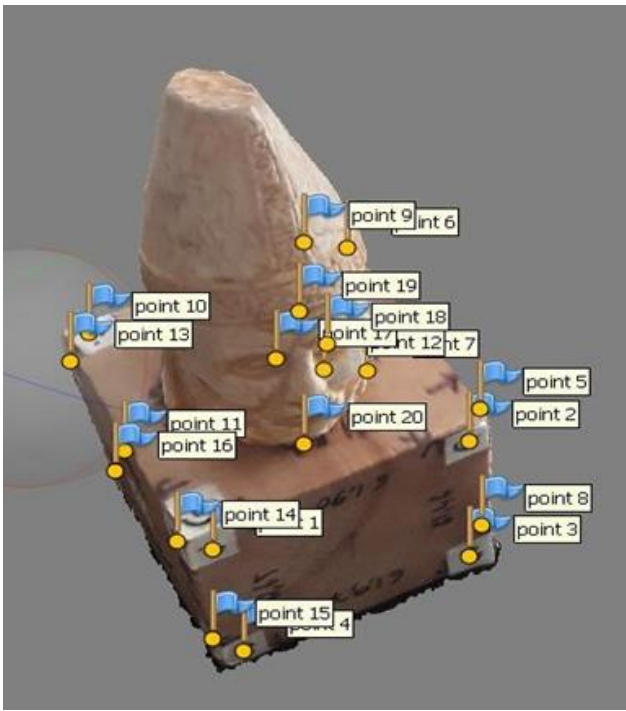


Figure 3. Produced 3D model and marked points.



(a)



(b)



(c)

Figure 4. Produced 3D models. (a) Photoscan; (b) 3DF Zephyr; (c) VisualSFM+MeshLab

A total of 26 length were measured on the model. Absolute error was calculated as the actual values were measured with a caliper. RMSE was calculated as ± 0.7 mm for Agisoft Photoscan, ± 5.3 mm for MeshLab and ± 1.5 mm for 3DF Zephyr (Table 2).

Table 2. Comparison of reference lengths and accuracy analysis.

Length	Absolute Error		
	Photoscan (mm)	VisualSFM (mm)	3DF Zephyr (mm)
1	-1	-1.1	0.3
2	0.4	0.5	0.2
3	1.7	2.2	2.6
4	-1.2	-2.9	-1.4
5	-1.1	-0.7	-0.3
6	-0.5	-1.5	0.5
7	-1	-1.1	-1.8
8	-0.5	-0.3	0.5
9	-0.3	-0.4	1
10	-1.2	-2.1	-1.1
11	-0.2	0.3	0.2
12	0.2	1.4	0.4
13	-0.7	5.6	0.9
14	-0.2	3.2	-0.4
15	-0.3	4	1.5
16	-1.3	1.9	-3.4
17	0.1	2.1	0.7
18	-0.5	0.9	-0.4
19	-0.8	1.1	-2.2
20	-0.4	3.2	0.2
21	-0.8	2.2	-0.3
22	-0.5	4.2	-0.2
23	-0.6	1.2	0.2
24	-0.7	0.3	0.9
25	0.2	-0.9	-0.2
26	-1.5	-1.8	-0.7
RMSE	± 0.7 mm	± 5.3 mm	± 1.5 mm

4. Discussion

In the studies carried out in the commercial software of Agisoft Photoscan, it is seen that the photos with regular cover rates give good results in the software and the 3D models formed are true to reality. Furthermore, as the number of photos used for the 3D model in Agisoft software is increased, it is seen that the model accuracy increases in direct proportion to the Tie Points and Key Points limit, but the processing time is extended and the unnecessary points occur.

Although increasing the number of images increases the visual completeness and accuracy of the models, it prolongs the processing time. For this reason, an optimum balance must be achieved between the image capture parameters and the processing time.

When Meshlab software, Agisoft Photoscan and 3DF Zephyr software were compared in terms of obtaining Texture Clothed Model and their performance, it was observed that Agisoft and Zephyr commercial software performed the processes faster. In contrast, in the Meshlab Open-Source Software, the processes were slower as they were done in steps and manually.

Although the Dense cloud created in Visual SFM contains a lot of unnecessary points and as a result, the

defects occurring in the modeling made in Meshlab software are tried to be eliminated by filtering and cleaning processes

5. Conclusion

In this study, the performance of Open-Source Software is evaluated as an alternative to commercial software used in modeling small objects. The accuracy, convenience and processing times between 3D models produced with open-source software and 3D models obtained with commercial software are evaluated. In this study, Zeus miniature statuette and a calibration cube made of wood of a specific size are used as small objects. The photographs of the objects were taken from different angles and saved for 3D modeling. Photos are used to produce 3D models in Agisoft Photoscan, Visual SFM + Meshlab and 3DF Zephyr software.

Even if Agisoft Photoscan and 3DF Zephyr are better than MeshLab and Visual SFM, which are Open-Source software in terms of ease of processing, shorter processing time and accuracy, Open-Source software can be used as an alternative to Commercial software as it is used and developed by many users. As more information is shared among users and the number of people using for photogrammetric purposes, the processing times of these software will be shortened, and their accuracy will increase.

References

- Agisoft, L. L. C. (2014). Agisoft Photoscan Pro. St. Petersburg, Russia. Disponível em: <http://www.agisoft.com>.
- Cignoni, P., Callieri, M., Corsini, M., Dellepiane, M., Ganovelli, F., & Ranzuglia, G. (2008, July). Meshlab: an open-source mesh processing tool. In Eurographics Italian chapter conference (Vol. 2008, pp. 129-136).
- Duran, Z., & Atik, M. E. (2021). Accuracy comparison of interior orientation parameters from different photogrammetric software and direct linear transformation method. *International Journal of Engineering and Geosciences*, 6(2), 74-80.
- Duran, Z., Ozcan, K., & Atik, M. E. (2021). Classification of photogrammetric and airborne lidar point clouds using machine learning algorithms. *Drones*, 5(4), 104.
- Song, L., Wu, W., Guo, J., & Li, X. (2013, August). Survey on camera calibration technique. In 2013 5th International conference on intelligent human-machine systems and cybernetics (Vol. 2, pp. 389-392). IEEE.
- Weber, S. (2004). The success of open source. Harvard University Press.
- Westoby, M. J., Brasington, J., Glasser, N. F., Hambrey, M. J., & Reynolds, J. M. (2012). 'Structure-from-Motion' photogrammetry: A low-cost, effective tool for geoscience applications. *Geomorphology*, 179, 300-314.
- Wu, C. (2011). VisualSFM: A visual structure from motion system.



4th Intercontinental Geoinformation Days

igd.mersin.edu.tr



Air pollution analysis in Istanbul between January 2019 and April 2022 through remote sensing technology

HamedReza Vafa ^{*1}, Ahmet Ozgur Dogru ², Dursun Zafer Seker ²

¹Istanbul Technical University, Graduate School, Geographical Information Technologies Program, Istanbul, Türkiye

²Istanbul Technical University, Civil Engineering Faculty, Department of Geomatics Engineering, Istanbul, Türkiye

Keywords

Google Earth Engine (GEE)
Remote sensing imagery
Java script
Air pollution
COVID-19 pandemic

Abstract

The need to study air pollution and its connection to human health is no longer a strange idea. Despite the fatalities and illnesses caused by COVID-19, the quarantines significantly decreased air pollution and deaths during this period. Today, satellites can monitor air pollution with great precision, and the research process has quickened, providing professionals with helpful information. This research analyzed six air contaminants using the Sentinel 5P satellite and the Google Earth Engine platform in Istanbul, Türkiye. January 2019 to January 2020, as before COVID—the pandemic period, and January 2020 to April 2022, during and somehow after the pandemic period. The data revealed a notable upward trend in air pollution and pinpointed hot spots. It should be mentioned that the whole city is now affected by different types of air pollution. The issue has been exacerbated in districts like Fatih, bey, and Bayrampasa, where air pollution decreased during COVID's quarantine. Meanwhile, Asian neighborhoods of Istanbul, such as Kadikoy and Uskudar, have been identified as new hotspots where air pollution has also reached severe levels recently.

1. Introduction

Due to industrialization and globalization over the last several decades, air pollution has become one of the world's most significant challenges, threatening many elements of human existence, such as health, and directly influencing and triggering illnesses such as cancer. According to the World Health Organization (WHO), 90% of the world population lives in areas where air pollution exceeds the guideline and 4.2 million people die as a consequence. Air pollution consists of a spectrum of hazardous gases with varying concentrations, reflecting the extent of exposure to these pollutants (Moghimi et al., 2020). The deterioration of public health produces several challenges for communities, including economic concerns and problems with the healthcare system, such as inadequate medical facilities (Kermani et al., 2017).

COVID-19 is a sort of respiratory illness that might not be an exception to the impact of air pollution on diseases. COVID-19 pandemic resulted in extensive quarantines across the globe and also Türkiye, particularly in Istanbul which plays a vital role in the country, from the perspective of tourism attraction to

industry and education. The first case of COVID patient was recorded in Türkiye on March 10, 2020, and it reached its first peak in April 2020 with more than 37000 daily new cases. As a result of the infection peak, the government enacted several quarantines to combat the rising mortality. Türkiye's president officially announced the first public closure from 26 April to 17 May 2020.

Many forms of air pollution might be specified. The first kind consists of exhaust fume pollutants such as Nitrogen dioxide (NO₂), Sulfur dioxide (SO₂), Carbon monoxide (CO), and Carbon dioxide (CO₂). The second category of pollutants is those produced by the interaction of water, temperature, and sunlight with the first type, which includes ozone (O₃) (Moghimi et al., 2020). In addition, the relationship between COVID-19 and CO₂ concentration in an area's environment has been established, and CO₂ concentration has a protracted effect on humans' health (Mehta et al., 2020). These air pollutants cause cardiovascular disorders, high blood pressure, and diabetes, which are underlying conditions for respiratory diseases such as influenza and COVID-19. NO₂, a pollutant of the first kind that leads to respiratory

* Corresponding Author

^{*}(vafa21@itu.edu.tr) ORCID ID 0000-0002-8171-9206
(dogruahm@itu.edu.tr) ORCID ID 0000-0001-7415-1862
(seker@itu.edu.tr) ORCID ID 0000-0001-7498-1540

Cite this study

Vafa, H., Doğru, A. O., Seker, D. Z. (2022). Air pollution analysis in Istanbul between January 2019 and April 2022 through remote sensing technology. 4th Intercontinental Geoinformation Days (IGD), 135-138, Tabriz, Iran

illnesses, generates second-type pollutants such as ozone and nitric acid (Huang et al., 2018; Shin et al., 2020). It was demonstrated by (Li et al., 2021) that significantly decreasing the number of cars leads to NO_x reduction. However, (Wang et al. 2020) note that considerable reductions in emissions would not prevent severe air pollution in China when meteorological conditions are adverse. Formaldehyde (HCHO) may also be formed from automobile gasoline; however, the use of tobacco in homes, the combustion of wood, and the use of natural gas in industrial areas are its principal sources. If this material is in the air, a person will have a cough, runny nose, or watery eyes. Since June 2011, formaldehyde also has become a compound known to cause human cancer (US Department of Health and Human Service).

Remote sensing using satellite data and images appears to be a viable tool for monitoring air pollution. Additionally, they are free and straightforward for people to use and process. Satellites such as Sentinel-5P with the TROPOMI onboard sensor presented vast data by viewing the whole planet multiple times. Google Earth began storing Landsat satellite data in 2008 and built an open-source cloud or internet platform (Shami et al., 2021). The Google Earth Engine (GEE) platform has collected data from satellites such as Landsat and Sentinel to benefit users. This platform can effectively handle metadata, eliminating the requirement for a powerful processor when dealing with vast amounts of data. Environmental research necessitates acquiring brand-new technology and techniques for data processing that can combine many disciplines, such as location or remote sensing data, on a worldwide scale. The GEE benefits in this sector give a mix of images that can be quickly arranged and filtered to make them user-friendly (Ghasempour et al., 2021). (Vafa et al., 2021) studied air pollution in the Khuzestan province of Iran during the COVID-19 pandemic and revealed how partial quarantine led to a decreasing pattern of various types of air pollution.

This study aims to explore the effects of COVID-19 quarantines on air pollution in Istanbul, particularly nitrogen dioxide, using remote sensing technology. This paper represents the first step of a bigger environmental investigation of Istanbul's air pollution. NO₂, SO₂, CO, HCHO, O₃ percentage, and Aerosol Indexes, referred to as particulate matter (PM_{2.5}), were retrieved from Sentinel-5P data packages using Java scripts written in the GEE IDE environment. The observation period extends **from January 1, 2019, to April 30, 2022**, corresponding to the time before and following the epidemic.

2. Materials and method

This research focuses on Istanbul, located at 41° 0' 49.82" N, 28° 56' 58.78" E. (Figure 1). Istanbul, one of the most important cities in Turkiye's northwestern region, has an estimated 5,343 km² with more than 15 million people population and plays a critical role in Turkiye. Its climate may be described as the transitional Mediterranean; in reality, it has cold winters, but otherwise, it has Mediterranean characteristics: autumn and winter are the wettest seasons, while summer is bright and sunny. GEE is the fundamental technology

used to implement remote sensing technologies. The Code Editor, a web-based Integrated Development Environment (IDE) for creating and executing detailed data using Python or JavaScript, was utilized to perform the technique. The GEE data catalog has been updated with Copernicus Data, allowing users to access random data using its explorer. Table 1 summarizes this research's data-related information (GEE Catalogue).



Figure 1. Study Area, Istanbul, Turkiye

Figure 2 depicts the main phases of the employed approach. The picture also depicts the temporal and geographical distribution of air pollution in Istanbul from 2019 to 2022, before, during, and after the COVID-19 epidemic, using data taken from the Sentinel-5P satellite on Google Earth Engine.

Table 1. Tropomi Data Information

Data	Unit	Lowest	Highest	Accuracy
Absorbing_aerosol_index		-21	39	0.01 arc degree
CO_column_number_density	(mol / m ²)	-34.43	5.71	0.01 arc degree
NO2_column_number_density	(mol / m ²)	-0.00051	0.0192	0.01 arc degree
O3_column_number_density	(mol / m ²)	0.025	0.3048	0.01 arc degree
SO2_column_number_density	(mol / m ²)	-0.4051	0.2079	0.01 arc degree
Tropospheric_HCHO_column_number_density	(mol / m ²)	-0.0172	0.0074	0.01 arc degree

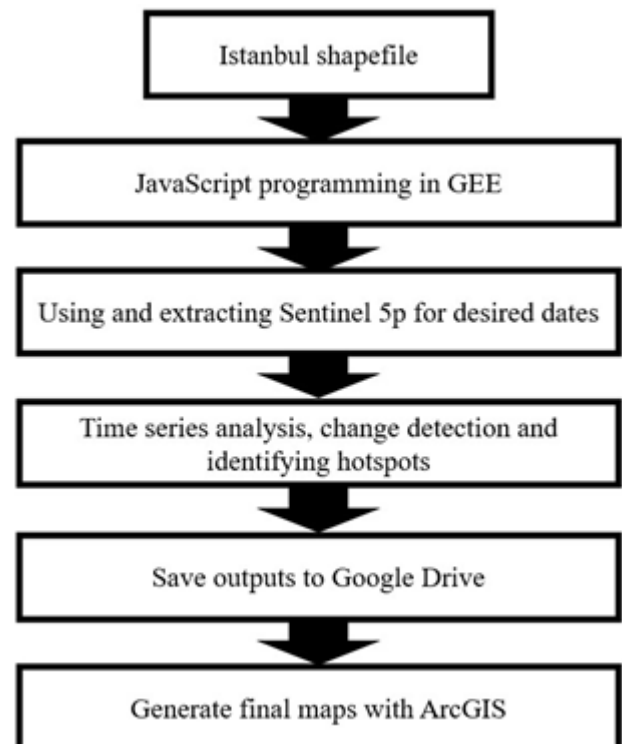


Figure 2. Project process flowchart

3. Results and discussion

Significant results of the study are presented for each parameter. Besides thematic maps and charts that show the daily changes in Nitrogen Dioxide are presented in Figure 3 and Figure 4 respectively. Figure 3 depicts the average levels of Nitrogen Dioxide in 2019, 2020, and 2021, from low (white) to very high (black), using themed maps. According to the thematic maps given in Figure 3 and the diagrams in Figure 4, it is

evident that, despite a declining trend in 2020, the NO_2 concentration in Istanbul will increase in 2021. The dark patches are recognized as hotspots.

As shown in Figure 3, a2, and c2, the amount of nitrogen dioxide pollution in hotspots fell in 2020, increased in 2021, and surpassed its former levels in 2019. Despite this, the rise in air pollution is visible in all parts of Istanbul, necessitating immediate preventative action.

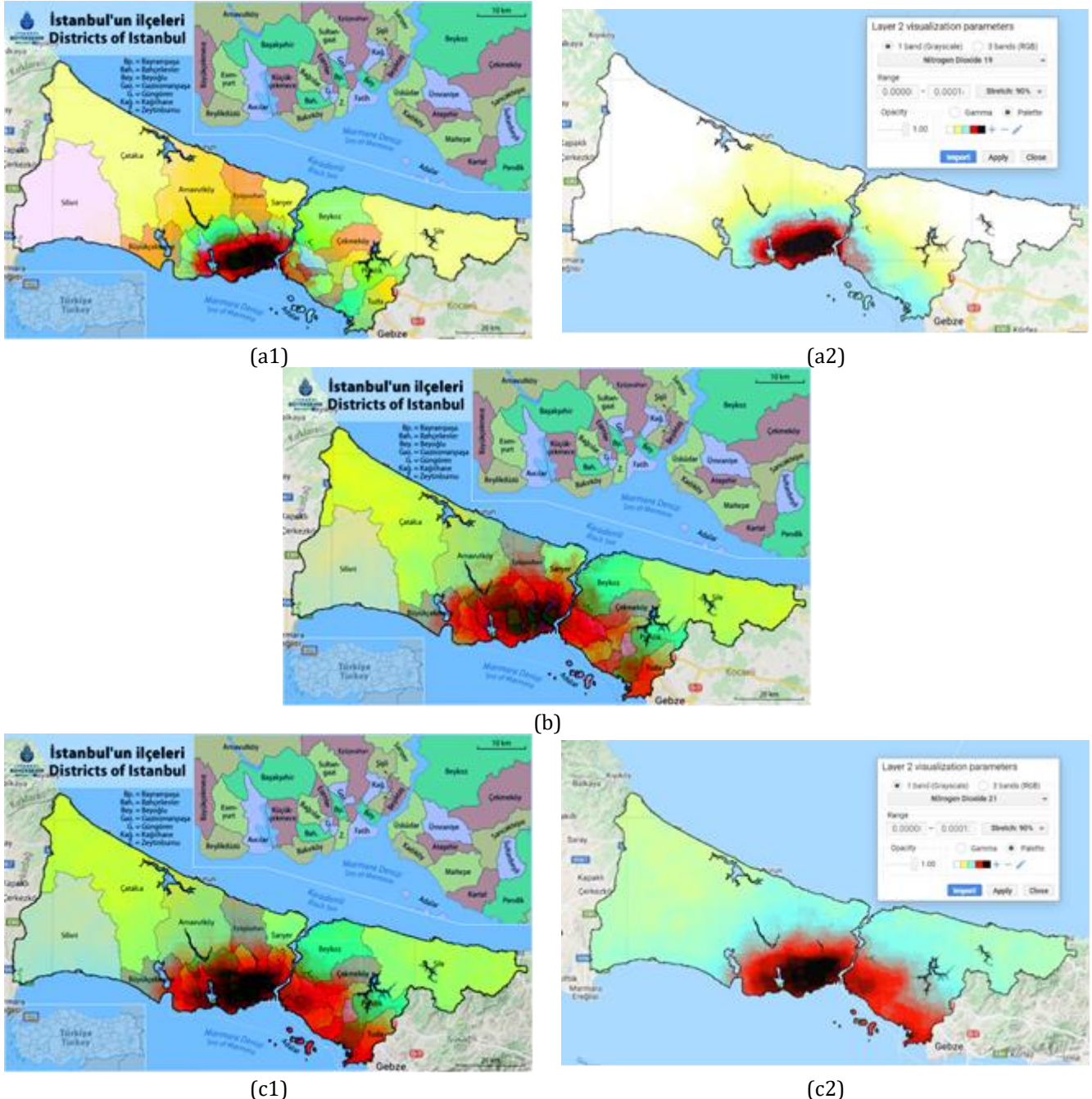


Figure 3. Comparative Average Nitrogen Dioxide in Istanbul for the years 2019, 2020, and 2021.

4. Conclusion

In this study, with the aid of Sentinel 5P satellite imagery and Java programming in the IDE of the GEE platform, six types of pollution in the Istanbul of Türkiye from 2019 to 2022 were studied. Summarizing all cases can be concluded that most parts of Istanbul are affected

by NO_2 . Fatih, bey, Bayrampasa, and neighbor districts have been identified as hotspots. It can be logically understood that all the hotspots are affected by different types of pollution due to the number of cars and industries in the region. Similar to previous studies, this study could point out that the emergence of the COVID-19 could reduce air pollution mortality. It can be noted

that satellite studies can be done faster, and it is better to repeat the air pollution at regular intervals for all regions of the country. In the continuation of this study, data retrieved from the ground bases of air pollution purification, wind velocity, air temperature, and the number of patients in various Istanbul neighborhoods could be analyzed. Using the AHP method and co-kriging interpolation, and despite comparing Google Earth engine results with ground bases, there is a significant relationship between wind intensity, air temperature, increasing pollution, and the number of patients with respiratory diseases such as Covid 19 could be defined.

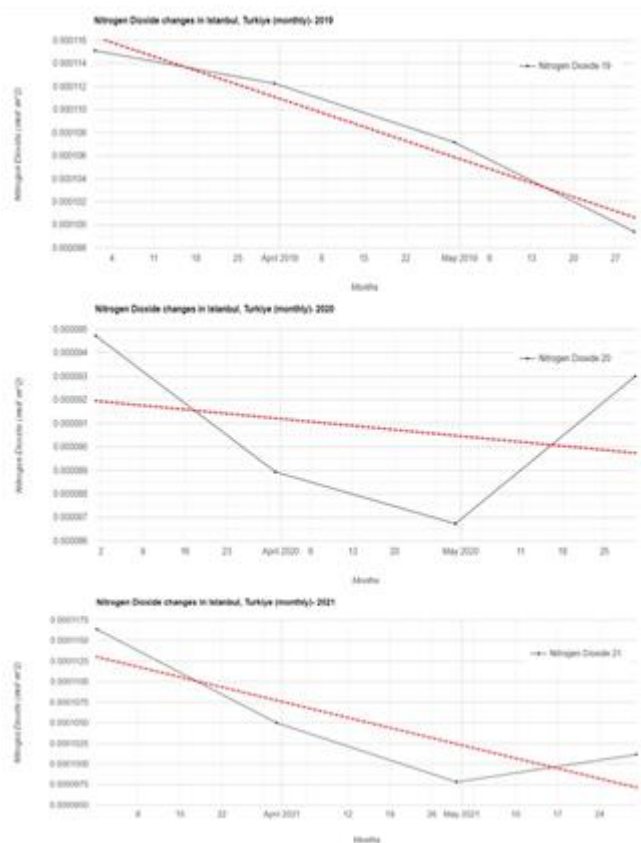


Figure 4. Comparative dynamics of monthly Nitrogen Dioxide values from a) 1 January 2019 to 1 January 2020, b) 1 January 2020 to 1 January 2021 c) 1 January 2021 to 1 January 2022

References

- Amani, M., Ghorbanian, A., Ahmadi, S. A., Kakooei, M., Moghimi, A., Mirmazloumi, S., Alizadeh Moghaddam, S. H., Mahdavi, S., Ghahremanloo, M., Parsian, S., Wu, Q., & Brisco, B. (2020). Google Earth Engine Cloud Computing Platform for Remote Sensing Big Data Applications: A Comprehensive Review. *IEEE Journal of Selected Topics in Applied Earth Observations and Remote Sensing*, 13, 5326-5350.
- Ghasempour, F., Sekertekin, A., & Kutoglu, S. H. (2021). Google Earth Engine Based Spatio-Temporal Analysis of Air Pollutants before and during the First Wave COVID-19 Outbreak over Türkiye via Remote Sensing. *Journal of Cleaner Production*, Volume 319, 128599, ISSN 0959-6526, <https://doi.org/10.1016/j.jclepro.2021.128599>.
- Huang, Y., Hickman, J. E. & Wu, S. (2018). Impacts of enhanced fertilizer applications on tropospheric ozone and crop damage over sub-Saharan Africa. *Atmospheric Environment*, Volume 180, Pages 117-125, ISSN 1352-2310, <https://doi.org/10.1016/j.atmosenv.2018.02.040>.
- Kermani, M., Dowlati, M., Jonidi Jafari, A., & Rezaei Kalantari, R. (2017). Number of Total Mortalities, Cardiovascular Mortality and Chronic Obstructive Pulmonary Disease due to Exposure with Nitrogen Dioxide in Tehran during 2005-2014. *The Journal of Urmia University of Medical Sciences*, 28, 4, 22.
- Li, D., Wu, Q., Wang, H., Xiao, H., Xu, Q., Wang, L., Feng, J., Yang, X., Cheng, H., Wang, L. & Sun, Y. (2021). The Spring Festival Effect: The change in NO₂ column concentration in China caused by the migration of human activities. *Atmospheric Pollution Research*, Volume 12, Issue 12, 101232, ISSN 1309-1042, <https://doi.org/10.1016/j.apr.2021.101232>.
- Mehta, P., McAuley, D. F., Brown, M., Sanchez, E., Tattersall, R. S. & Manson, J. J. (2020). COVID-19: Consider Cytokine Storm Syndromes and Immunosuppression. *The Lancet* 395, 10229, 1033-1034.
- National Toxicology Program (June 2011). Report on Carcinogens, Twelfth Edition. Department of Health and Human Services, Public Health Service, National Toxicology Program. from: <http://ntp.niehs.nih.gov/go/roc12>.
- Shami, S., Khoshlahjeh, M., Ghorbani, Z., Moghimi, A., Mohammadzadeh, A. & Sabet Ghadam, S. (2021). Evaluation of Air Pollution Contributes for the COVID-19 Pandemic in Iran using Sentinel 5 Satellite Data. *JGST*, 10 (3), 135-146.
- Shin, S., Li, B., Oiamo, T. H., Burnett, R. T., Weichenthal, S., Jerrett, M., Kwong, J. C., Goldberg, M. S., Copes, R., Kopp, A., & Chen, H. (2020). Association between Road Traffic Noise and Incidence of Diabetes Mellitus and Hypertension in Toronto, Canada: a Population-Based Cohort Study. *Journal of the American Heart Association* 9, 6, 013021.
- Vafa, H., Dogru, A. O., & Seker, D. Z. (2021). Monitoring Air Pollution in Khuzestan Before and During the Covid-19 Pandemic Through Remote Sensing Technology. *ISAG, International Symposium on Applied Geoinformatics*, Riga, Latvia.
- Wang, S., Zhang, Y., Ma, J., Zhu, S., Shen, J., Wang, P. & Zhang, H. (2021). Responses of decline in air pollution and recovery associated with COVID-19 lockdown in the Pearl River Delta. *Science of The Total Environment*, Volume 756, 143868, ISSN 0048-9697, <https://doi.org/10.1016/j.scitotenv.2020.143868>.
- World Health Organization. Available Online: <https://www.who.int/> (accessed on 18 June 2021).



4th Intercontinental Geoinformation Days

igd.mersin.edu.tr



Land use change forest scenarios on the Horizon 2025

Maryam Sadeghi¹, Khalil Valizadeh Kamran¹, Sayed Asadollah Hejazi²

¹University of Tabriz, Department of Remote Sensing and GIS, Tabriz, Iran

²University of Tabriz, Department of Geomorphology, Tabriz, Iran

Keywords

Scenario Wizard
Key factors
MICMAC
Land Change Use
Forest Fandoghlo

Abstract

The purpose of this research is to identify the key factors affecting the land use that changes in the forest area of Fandoghlo. At the beginning of the research, 19 factors are designed in forest that use in various economic, social, natural and political dimensions in a 19-19th dimension questionnaire and provided experts to weigh from numbers 3 to 0, with three highlights. The effect and effectiveness of variables were analyzed directly and indirectly in MICMAC software. Finally, eight effective factors were determined in changing the forest use of the Fandoghlo area. At last, among the key factors of land use, distance from the village and population, cutting and harvesting, vegetation, motivation for agriculture to residential and height are the most important key factors in the future of the region's system. After that with the opinion of experts and solutions were designed in three favorable, static and critical spectrum. And after the final confirmation a questionnaire was designed and re-addressed to the research experts, which was used to weigh the numeric between 3- and 3+ Used, and finally the results were entered into the wizard scenario software and the result was obtained in three spectres, 2 favorable scenarios to strong scenarios 5 scenarios and 275 poor scenarios, and ultimately scenarios are achieved as favorable scenarios in three rating spectres. Of these, seven scenarios were selected as the most desirable scenario for planning for the future of forest use and in line with its protection.

1. Introduction

Forest is one of the most important and valuable natural resources that is urgent in the world for environmental balance (Bell 2003). Deforestation, especially in developing countries, is the largest threats for biodiversity protection from carbon watershed and storage (Kramer et al. 2004; Hansen et al. 2013). The reasons for deforestation come from several local stimuli and regional scales related to human population for example growth, politics, technology, and cultural norms (Hesenama 2002; Gist and Lambin 2005). The differences are the result of interaction in space and time in human and biological-physical dimensions. Therefore, it also has works on natural and social land (Veldkamp and Verburg 2004). Land use changes are mainly influenced by large scale factors such as global economy and climate issues, and issues such as demographic changes and local policies, along with the factors, have a decisive role (Geist and Lambin. 2006). And including climate change, water and soil and the loss of environmental diversity, which is

the largest concern of today's population. Therefore, the management and monitoring of the negative consequences of changing land coverage for the continuation of essential resources production has become an important issue. Performing land use researchers for researchers and politicians around the world over time is very necessary (Mishra 2014; Li 2011). In a dynamic space system, by changing the forces and stimulus processes, another challenge is that the design of integrated systems to deal with uncertainty about the future process that has no historical background is a constant challenge to create models that are directly planned to plan. And environmental management is related to (Paegelowa 2013). One of the right tools of the future architecture in terms of uncertainty and in terms of our world is full of surprises of various instruments is the scenario planning. Scenario planning is a method for future paradigms that have been developed in response to the main challenges of the present age, such as the instability of the future environment, the presence of magnates and the future of

* Corresponding Author

(sadehi.maryam92@gmail.com) ORCID ID xxxx – xxxx – xxxx – xxxx
(valizadeh@tabrizu.ac.ir) ORCID ID xxxx – xxxx – xxxx – xxxx
(s.hejazi@tabrizu.ac.ir) ORCID ID xxxx – xxxx – xxxx – xxxx

Cite this study

Sadeghi, M., Kamran, K. V., Hejazi, S. A. (2022). Land use change forest scenarios on the Horizon 2025. 4th Intercontinental Geoinformation Days (IGD), 139-146, Tabriz, Iran

deep uncertainties (Volkery 2009). Futurist futures is an appropriately approach to defining strategic development priorities that are systematically discovered by combining elements .2012 Weber). One of the most common means of futurism is to climb by entering the arena of a cytological approach from the 1960s. Theodore Gordon and Alfa Helmar also raised the analysis of structural effects, interactions in 1966 and an analysis of the interactive structural effects method for analyzing the probability of occurrence of a subject in a set forecast. The probabilities of this issue can be adjusted with judgments of the potential interaction between the subject, with the judgments of the potential, the interaction between the predicted issues. Planning based on scenario is a systematic way for creative thinking about uncertain future and possible (Peterson, 2003). The purpose of this scenario is based on the probable future and purpose of making scenarios, reveal the dominant trends. and possible data rupture is the competitive environment of the future (Goodet et al. 2008). (1994 Gordon). In their research examined the factors affecting the urban future and economic factors of social impact on deforestation (Benzhaf and Lowry 2010) in an article entitled Can Land Taxes Prevent Distribution? Using demographic data and land use information and examines the Pennsylvania city pattern those taxes can reduce land. Taghi Lou (2018) examines the changing scenarios of rural areas of Qala-e-Dehstan-Urmia with the aim of determining land use change scenarios. Mick Mac software and Scenario Wizard software were used to analyze the data. Lands were in that place.

Rostami Kia and Sharifi (2017) examined the causes of Fandoghlo Forest's change in the world's largest forest storage, and the conversion of forest and rangelands into agriculture, deliberate and unusual fire and cutting of trees from the main factors influencing the destruction of the forest of Fonaxel they said. 1399, Mozhgan Arasteh et al), with the futures approach to identifying the status of the metropolitan resilience system of Mashhad with a futuristic method with MICMAC and SCENARIO WIZARD software, identifying key factors and analyzing Mashhad metropolitan patterns. According to studies, further use of future research methods with urban issues has not been associated with environmental planning and research forest which is considered to be a research innovation. This research aims to identify the factors affecting the change in forest use of Fandoghlo and the analysis of the probable status of forest jungle changes in the wizard scenario in 2025.

2. Method

2.1. Study area

The studied area is the tropical trail of tropical forests of Guilan province, located 25 kilometers northeast of Ardebil city to Astara and 10 km from the city. The study area is 1322 to 2345 meters in terms of height from sea level. Fadoghlo Ardabil Forest in Geographical Coordinates 38° 29' 4.70" Up to 38° 9' 16.75" North Width and 48° 40' 32.55" E up to 48° 32' 84" Has been placed. The area of the study area

179/3288 Kilometer. It is 32 kilometers from its area (Valizadeh Kamran et al, 2021).

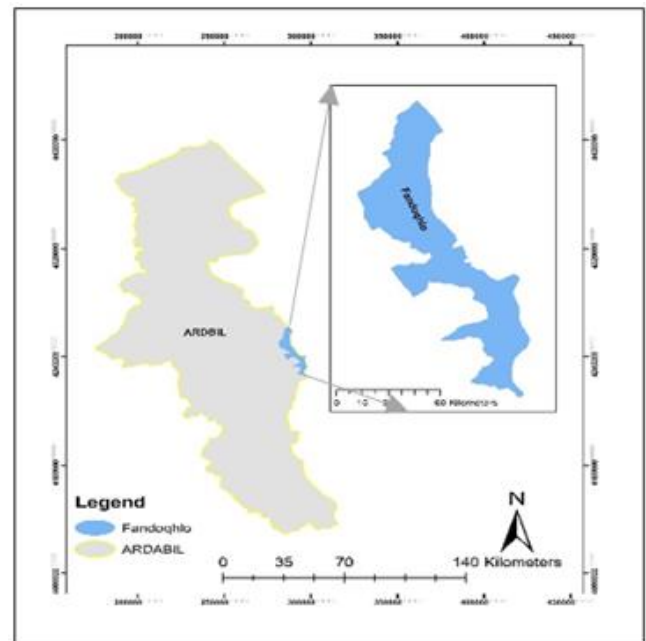


Figure 1. Study area

2.2. Data used

The data used in the present study is descriptive in terms of purpose, user of nature. The necessary information was collected based on the nature of the research in two libraries and questionnaires. To collect data and identify the initial variables. after examining the various studies of decorated and colleagues, 1399 on average, with 30 questionnaires in Among specialists, the average results of about 20 completed questionnaires in Mac MIC software (structural analysis of the severity of influence and relationships that exist between factors. In the next round, the Delphi method of the questionnaire was designed in the form of structural analysis. those were experts and a slight weight between zero and three, which is zero as a non-impact, three with high impact, two and one, with moderate and low impact, which occurs on average with 30 questionnaires among specialists. The mean results from about 20 questionnaires completed by experienced professors specializing in this field, the factors of the Organization of Natural Resources and Watershed of Ardabil and the city of Namin, PhD students and Masters in MICMAC software (structural analysis) are severely influenced and relationships between There are factors and factors that have high impact were extracted as key factors.

In the next step, after identifying key factors, by importing them in the Scenario Wizard software, system-compatible scenarios in a range of the most desirable conditions may be presented within the framework of the moderate, desirable and disaster scenarios.

3. Results

3.1. Justifiability Stability analysis

In the previous stages, with the average examination of expert theories, the results for extracting key

propellers entered the Mick Mac software based on the number of input matrix input variables 19*19, with the results of matrix stability in Table (1) it has been shown. The degree of desirability and optimization of the 96% impact matrix\|r and 99% and the impact is 98% and 100%.

Table 1. Results of the direct effects of the Mick Mac matrix

Ingredient	Number
Dimension matrix	19
Number of Iteration	2
Number of 1	36
Number of 0	114
Number of 1	130
Number of 2	81
Number of all	325
Percent of Fill Homes	90

3.2. Indirect Impact and Impact Assessment (MDI) Evaluation Results (MII)

The relationships between variables in MICMAC software provide two types of graphs and analyzes, one direct impact and other indirect effects on each other. The dispersion analysis of variables is based on direct and indirect effects. The dispersion of variables around the influence-effectiveness indicates the status of the system because in stable devices and the role of each of the factors is clear; But in unstable systems, the situation is complex and variables are distributed around the diagonal axis. Due to the dispersion of variables in Figure (1), the system of the study area was considered unstable system (figure on the right).

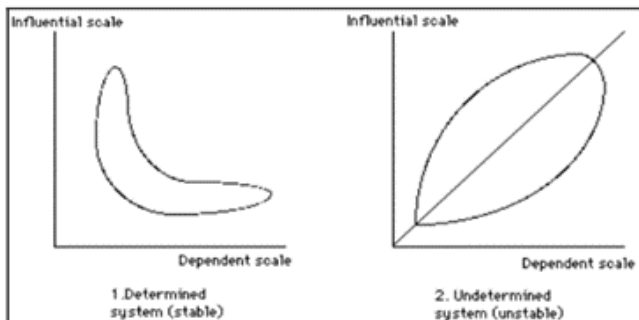


Figure 2. the shape of the unstable system key factors affecting forest land use change in Fandoqhlo region

3.3. Before situations for key factors

Previous situations for general factors in the previous stage were determined using a structural analysis method in Mac software software. Out of the total 19 primary factors influencing the future of the use of the forest area of the forest area, 8 factors were selected as key factors, but at this stage, research scenarios should determine the first step in defining probable situations; Therefore, with theoretical studies on each of these factors and also the opinion of experts for each of these key factors, three conditions in the desired, neutral and

undesirable spectra were defined. It is the change of use of the forest. Possible situations for each factor are different from other factors and the only common feature between them is the existence of a range of favorable to unfavorable situations. is the situation in front of each of the key drivers of possible situations for screenwriting (Table 2).

Table 2. Results of the key facture

Row	Variable	Direct (MDI)	Variable	Indirect (MI)
1	land use	696	land use	745
2	Herbaceous covering	680	Herbaceous covering	648
3	Visitor	538	Number of the households (population)	632
4	Motivation to change from agricultural to residential	583	slop	599
5	Village of Space	567	Fire point	538
6	Outage and Removal	567	slop	551
7	Number of households (population)	551	Number of households (population)	551
8	High	534	Variable	534

After analyzing the analysis of the structural analysis of the results, there are eight key factors in three different situations: he proper solution for each of the situations was collected in a questionnaire of experts. The questionnaire was designed and available to experts. Experts with the plan that if any of the 24 situations occur, what impact does it affect? To complete the weighted questionnaire between 3 and 3, the effect of each situation on the system identified the system. Finally, the results of analysis were analyzed and accompanied by probable determinants entered the Scenario Wizard software. Results from analyzing analysis in scenario software.

3.4. The results of the analysis in the scenario software

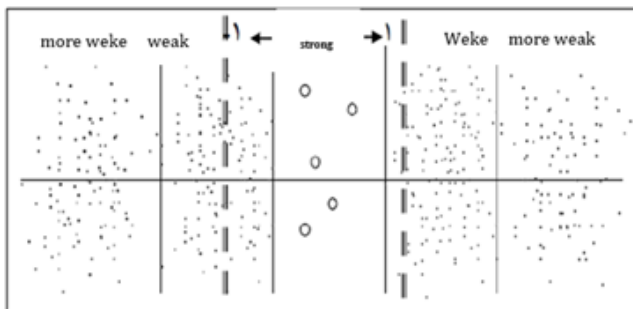
In general, the results of analysis are subject to 3 scenario categories: a) Strong scenarios: 5, B) Bacaladic scenarios or high compatibility scenarios: 27 and c) Weak scenarios: 275.

3.5. How to categorize scenarios

The nature of the software scenario software is its nature as the dimensions. In these meanings, it seems reasonable and between strong limited scenarios and poor scenarios are, scenarios with compatibility one. The distance in a fact is the expansion of strong scenarios as a unit towards weak scenarios.

Table 2. Results of the key facture

Key factors	of possible situations
Land use(a)	Favourable : Coordination of organizations and government agencies not to issue any permits for land use change Static : Preserving current landscapes Undesirable and critical: Lack of monitoring and unprincipled use of applications
Herbaceous covering (b)	Favourable : Cut down dried trees and rehabilitate them by planting Static: Maintain the status quo Undesirable and critical: Inability to manage crisis in the region (such as fire)
Visitor (c)	Favourable: planning to develop and preserve the natural landscape Static : Continuation of the current situation Undesirable and critical: development of recreational facilities without ecotourism empowerment
Motivation to change from agricultural to residential (d)	Favourable: Establishment of production workshops and greenhouses with the cooperation of local people and under the supervision of Jihad Keshavarzi Static: if necessary and with minimal environmental degradation Undesirable and critical: selling to local investors (non-permanent residents) and non-locals due to financial needs of residents
Outage and Removal (e)	Favourable felling and harvesting: Cutting down dried trees and planting and rehabilitating by planting Static : Creating integrated agriculture Undesirable and critical : cutting down forest trees for agricultural development
Height (f)	Favourable : protection of vegetation and trees of the slopes and its non-plowing Static : Optimal use of environmental capabilities for optimal production Undesirable and critical: Destruction by overgrazing of slopes
Village of distance (g)	Favourable Determine the buffer or privacy for the development of the village and determine the pattern appropriate to the environment Static Support plans for the livelihood of local people and reducing the pressure of destruction Undesirable and critical development of the village into forested areas
Number of households (population)(h)	Favourable : Failure to issue a construction permit for a non-resident population Static : : Continuation of normal growth process Undesirable and critical : Lack of supervision and neglect of village development

**Figure 3.** How to select compatibility scenarios 1 from a multitude of scenarios (Zali 2009).

Strong scenarios derived from the scenario of Wizard based on this feature, the possibility of increasing the domain of strong scenarios may be possible and therefore with a unit of increase that the standard unit increases this domain based on the software is 23 logical scenarios for planning and policy was obtained.

Analysis of selected and probable scenarios for the future of the forest use of the Fandoghlo Ardabil region that according to the previous explanation of 27 scenarios, as the most probable scenario for the future of the Change Forest District, was evaluated by wizard scenario software. These scenarios are also derived from the occurrence between the status of each of the factors in relation to the status of each factor that the occurrence of a situation on the probability of occurrence by strengthening and empowering other situations or even limiting other situations. The impact can have the main base of the formation on scenarios that require the same time as they are known the scenario table. The possible

situations clearly show the scenario and the key factor to facilitate understanding of the scenario and weight conditions. The desired and undesirable page of this page was divided into three situations based on key factors status and defined by specified colors.

Table 4. Defining the concept of colors, numbers and situations on the scenario page

Feature	status	color	rating
Optimal approach in order to protect the process of forest land use change	Optimal	green	+3
Continue the approach the current trend	static	yellow	1
Critical and undesirable approach in order to protect forest land use change	Critical and undesirable	red	-3

3.6. Poor scenarios

24 * 24 cross matrix obtained in 275 scenarios. These scenarios, which are unlikely to occur, were not logical to analyze, and a large number of them were omitted from their analysis. Analysis of high compatibility scenarios (believable scenarios).

3.7. Scenarios analysis whit Strong Adaptability

Analysis of data related to different situations with the advanced scenario software has evaluated the probability of occurrence of 27 scenarios more than other scenarios. These scenarios are interconnected between the status of each of the factors associated with the status of each of the factors are no longer extracted that happening The situation on the likelihood of occurrence or strengthening and empowering other situations, or even limiting other situations that can be the main base of the formation of scenarios, which requires simultaneous factors and complex situations that can be analyzed from mind and the human ability is out and only smart processors are able to analyze their simultaneously. According to the previous explanation of 27 scenarios as the most probable scenario for the future of changing, the forest area is evaluated by Vizard Scenario Software as you seen clearly depending on the scenario and key factor Gives to facilitate understanding of the scenario page and Weight of favorable and undesirable conditions on this page statements of key factors to three situations as described the following was divided and defined with specific colors. Results from the analysis of wizard scenario provided that a combination of purposes especially static and desirable situations in scenarios. In general, 216 situations for 27 scenarios have been identified that 89 of these 216 cases are defined in favorable condition, which form 41% of these scenarios. 116 cases and status of 27 scenarios based on the number of replicates of the 3 spectra for each static status scenario with 46% scenarios. They have had an undesirable scenario of 26 cases with 12 percent of scenarios, which figure 4 also shows the frequency of scenarios status.

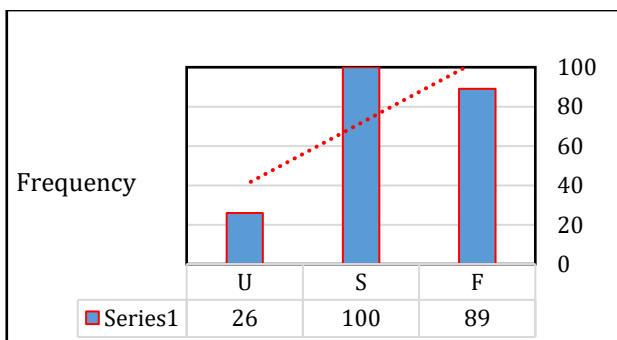


Figure 4. Graphic representation of the frequency of each of the three optimal, static, and critical states

Table 5. Scenario status table guide

Static	Unfavorable	Favorable
S	U	F

Prioritizing each scenario according to the results of Table 4-31 based on the number of each situation is calculated compared to the numerical sum of eight key factors with multiplication of 100 and the status of each scenario is marked with the star sign. According to the results of the first, second and sixth scenarios and Tajiri scenarios. The desired process of the future in line with the forest changes in the area of the Fandoghlo (Namin) region shows that the scenario results are not quite

optimal and 100%, but 75% are acceptable for the desirability of a scenario, and this is the reason for the score of the scenario, but the scenario 21 quite static and there is not any good or bad feature.

Table 7. Determine the status of each scenario based on the triple spectrum

scenario	a	b	c	d	e	f	g	h
s1	F	S	F	F	F	U	F	F
S2	F	S	F	F	S	U	F	F
S3	F	S	F	S	S	U	F	F
S4	S	S	F	S	S	U	F	F
S5	F	S	F	S	S	S	F	F
S6	F	S	F	F	S	S	F	F
S7	F	S	F	S	S	S	F	F
S8	S	S	F	S	S	S	F	F
S9	F	S	F	S	S	U	S	F
S10	F	S	F	S	S	U	S	F
S11	F	S	F	S	S	U	S	F
S12	F	S	F	S	S	S	S	F
S13	S	S	F	S	S	S	S	F
S14	S	S	F	S	S	U	S	F
S15	F	S	F	F	S	S	F	S
S16	F	S	S	F	S	S	F	S
S17	S	S	S	F	S	S	F	S
S18	S	S	F	S	S	S	F	S
S19	S	S	F	S	S	S	F	S
S20	S	S	S	S	S	S	F	S
S21	S	S	S	S	S	S	S	S
S22	S	S	S	F	S	S	S	S
S23	S	S	S	F	S	S	S	S
S24	S	U	S	F	S	U	S	S
S25	S	U	S	F	S	U	S	S
S26	S	S	S	F	S	U	S	S
S27	U	U	U	U	U	U	U	U

Table 7. Determining the optimal, static and critical states in each scenario

Scenario number	Frequency situation for each scenario			Percent			Situation final		
	F	S	U	F	S	U	F	S	U
s1	6	1	1	75	13	13	*	-	-
S2	6	1	1	75	25	13	*	-	-
S3	4	3	1	50	38	13	*	*	-
S4	3	4	1	38	50	13	-	*	-
S5	4	4	0	50	50	0	*	*	-
S6	5	3	0	63	38	0	*	-	-
S7	4	4	0	50	50	0	*	*	-
S8	3	5	0	38	38	0	-	*	-
S9	3	4	1	38	50	13	-	*	-
S10	3	4	1	38	50	13	-	*	-
S11	3	4	1	38	50	13	-	*	-
S12	3	5	0	38	63	0	-	*	-
S13	2	6	0	25	75	0	-	*	-
S14	2	5	1	25	63	13	-	*	-
S15	4	3	1	50	38	13	*	*	-
S16	4	4	0	50	50	0	*	*	-
S17	2	6	0	25	75	0	-	*	-
S18	2	6	0	25	75	0	-	*	-
S19	2	6	0	25	75	0	-	*	-
S20	1	7	0	13	88	0	-	*	-
S21	0	8	0	0	100	0	-	*	-
S22	1	7	0	13	88	0	-	*	-
S23	1	7	0	13	88	0	-	*	-
S24	1	7	0	13	88	0	-	*	-
S25	1	5	2	13	63	13	-	*	-
S26	1	6	1	13	75	13	-	*	-
S27	0	0	8	0	0	10	-	-	*

The desired future trend in integrate changes forest user changes. They are quite desirable and 100% in the scenario results is not observed, but 75 percent for the desirability of the scenario is acceptable and this is the reason for the score of the scenario shows, but 21 scenarios are completely static and there is no desirable and negative feature, and scenario 27 that all its features are in critical state and 100% will occur in the event of destruction and change. In general, it can be concluded. Most scenarios obtained to manage stable user change the forest of the Fandoghlo area is in the middle. This indicates that in the planning area and there is no coherence. Sustainability conditions of the area with attention to the rapid changes today in all areas of existence it can cause an incorrect action become the critical situation of the region and if attention and systematic planning in the desired status area to see acceptance.

3.8. Grouping and scenario analysis

Grouping and analyzing scenarios a total of 27 incredible scenarios can be divided into three groups according to Table (7), each of which groups with several scenarios almost common features and Low difference in one or more situations of 8 key factors are that these groups are as follows desirable

Favorable scenario: including first, second and sixth scenarios. It is almost identical in terms of rank lack of licensing to change applications, planning sustainable development of tourism and protection natural landscapes of the region, determining the privacy for the future development of the village proportional to the environment returns of agricultural lands around villages, lack of Issuing construction permits for non-resident population permanent, creating workshops and total manufacturing homes with with the collaboration of local people and agricultural jihad, increasing coordination between local people and organizations, creating integrated agriculture and increasing interest but preventing agricultural production and destruction Forest, optimal use of environmental resources for optimal production and change of use if necessary.

Static scenarios: all three to 26 scenarios except sixth scenario that is desirable and has features natural population growth, coordination of organizations and governmental organs of not being licensed for changing user, determining the privacy and future growth pattern fits the environment, continue the current trend, planning for sustainable tourism development, land use change in the event of necessity and with the minimum destruction of the environment integrated agriculture and cutting harvesting of tree, bushes near the forest development of culture protection vegetation covering area of forest trees and vegetation of slopes and lack of plowing it cut off dry trees and resuscitation with seedlings, lack of supervision and disregard to the development of the village and there is too much sliver and the development of the village into the forest areas.

Undesirable and critical scenario: where 27 scenario That's all the negative elements. they cutting the trees Forest and digging tree plants for development agricultural land and inability to organizations in district crisis management, forest destruction and loss of vegetation and agriculture region of non-monitoring or disregard to the development of the village, too much sliver and the development of the village into the forest areas.

These three groups represent the overall trend framework forest changes status for the horizon of 2025 in the study area.

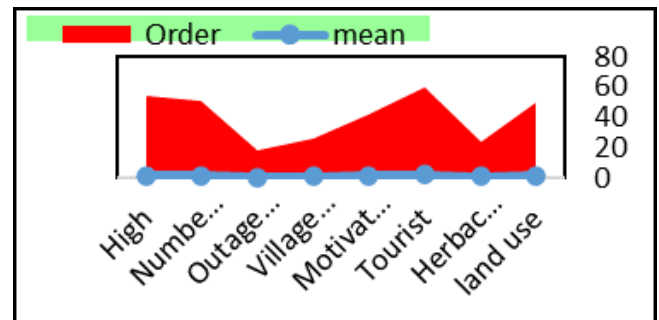


Figure 6. The importance of key factors in the composition of scenarios

Table 8. Ranking of key factors based on the triple status of 27 scenarios

Situation key factor in 27 scenario	Mean	Key factor
47	1/6	land use
21	0/7	Herbaceous Covering
57	1/9	Tourist
39	1/3	Motivation to change from agricultural to residential
23	0/8	Village of Space
15	0/5	Outage and Removal
48	1/6	Number of households (population)
51	1/7	High

According to the results of Table (8) key tourist factors, households, distance the village and land use were identified as the most influential or golden factors in the process of forest use change in the horizon of 2025. In fact, the sustainable future of forest use change depends on how these factors are managed and planned systematically.

4. Discussion and conclusion

Protection and maintenance of natural and environmental cause resources require systematic and prospective reviews. Due to the rate of destruction of natural resources and changes in land cover, due to the effect of different factors over time and human interference, it has led to natural environmental instability; Therefore, identifying the factors affecting environmental changes can be effective for conscious planning in order to protect and sustain the region's system. This research was conducted with the aim of an

overview and identifying factors affecting the use of Fadoghlo Regional Media, which to choose its effective factors and weighing. The peripheral scanning method and structural analysis of bad use in this regard questionnaire to dimensions 19 was designed and completed by expert experts. Then, according to the weight obtained, their relationships were decomposed in the micrograph software environment, resulting in key factors of cutting, harvesting, height and distance from tourist village, the motivation of people to change from agriculture to residential in the category of influential variables they got. Then for each of these factors the overall three situations were defined in desirable, neutral and undesirable spectra. These probable situations are for the future of the study area of the study area, which is the base of the scenario for the future of forest use. In the next step, possible situations were provided to experts as a questionnaire to choose the most appropriate solution and in the round last due to eight key factors and three possible matrix conditions with dimensions: experts based on weight

and the influence of each situation on the system identified the system finally obtained the results of the analysis and with probable determinant situations. In general, the results of Scenario Wizard software analysis in Floy's strong 27 belief scenarios or high adaptation scenarios and 75 poor Narives. To facilitate the understanding of the scenario page and the weight of the desired and undesirable conditions of this page, according to key factors, three specified states were defined and based on the rank of each of the factors in direct influence that these factors play an effective role in this region in the future. They play that land use variables have the highest rank as a key factor, namely any change in work. the expansion of human construction areas can affect the environment. These eight key factors in different natural, physical and empathy dimensions were determined as an effective key factor in changing the forest use of the Fadoghlo region that manages these factors in different dimensions will have a direct impact on the sustainable development of this forest area and also for each of these key factors, liberation was presented by experts who are among the social factors, population changes are the most important factor affecting anabestani to change land use that matches the results. In (2020) and Jafariaarasth et al, the ultimate scenarios for the future of the space system of the region were obtained for sustainable management and development. This area can have a favorable effect.

5. References

- Banzhaf, H.S., & Lavery, N. (2010). Can the Land Tax Help Curb Urban Sprawl? Evidence from Growth Patterns in Pennsylvania, *Journal of Urban Economics*. Vol 67, 169-179. 2009 Elsevier Inc. All rights reserved. doi:10.1016/j.jue.2009.08.005.
- Bell, W. (2003). *Foundations of Futures Studies: History, Purposes, and Knowledge*. Transaction Publishers.
- Bonyad Tose Farda (2005). *Technology foresight methods* Tehran. Bonyad Tose Publishers [In Persian].
- Caldas, M. M., Simmons, C., Walker, R., Perz, S., Aldrich, S., Pereira, R., Leite, F. & Arima, E. (2010). Settlement Formation and Land Cover and Land Use Change: A Case Study in the Brazilian Amazon. *Journal of www.SID.ir Archive of SID American Latin Geography*, 9(1).
- Dong, C., Scopus, G., & van de Giesen, N. (2013). Scenario development for water resource planning and management: a review. *Technological forecasting and Social change*, 80(4), 749-761. DOI:10.1016/j.techfore.2012.09.015
- Fahey, L., & Randall, R. M. (1998). *Learning from the Future: Competitive Foresight Scenarios*. Wiley Publications: New York, 13.
- Geist, H. J., & Lambin, E. F. (2006). Proximate causes and underlying driving forces of tropical deforestation tropical forests are disappearing as the result of many pressures, both local and regional, acting in various combinations in different geographical locations. *BioScience*, 52(2), 143-150.
- Godet, A. J., Meunier, M. F., Roubelat, F. (2003). Structural analysis with the MICMAC method & actors' strategy with MACTOR method. *Futures Research Methodology*, No. 2.
- Godet, M. (2006). Effective strategic management the prospective approach. *Technology Analysis & Strategic Management*, vol,1, No,1.
- Gordon, T. (1994). *Trend Impact Analysis*. Futures Research Methodology.
- Kameoka, A., Yokoo, Y., Kuwahara, T. (2004). A challenge of integrating technology foresight and assessment in industrial strategy development and policymaking. *Technological Forecasting and Social Change*, 71(6), 579-598.
- Krawczyk, E. (2006). *Futures thinking in city planning processes: the case of Dublin*, PhD. Dublin Institute of Technology School of Environmental Planning and Management Faculty of Built Environment.
- Lambin, E. F., Baulies, X., Bockstael, N., Fischer, G., Krug, T., Leemans, R., Moran, E. F., Rindfuss, R. R., Sato, Y., Skole, D., Turner, B. L. II, & Vogel, C. (1999). Land-use and land-cover change (LUCC): Implementation strategy. IGBP Report No,48, IHDP Report No. 10
- Martin, B. R. (1995). Foresight in science and technology. *Technology Analysis and Strategic Management*, 7(2), 139-168.
- Mertnes, & Lambin, E. F. (2000). Land-Cover Change Trajectories in Southern Cameroon, *Annals of the Association of American Geographers*, 90 (3). <http://dx.doi.org/10.1111/0004-5608.00205>
- Mishra, V., Kumar, Rai P. & Mohan, M. (2014). Prediction of Land use changes based on change modeler (LCM) using Remote sensing: a case study of study of muzaffarpur (BIHAR), India. *Original scientific paper. J. Geogr. Inst. Cvijic*, 64(1), 111-127. <https://doi.org/10.2298/IJGI1401111M>
- Naimi, K. & Pourmohammadi, M. (2016). Identifying the key factors affecting the future status of low-income urban settlements in Sanandaj with emphasis on the application of futures studies. *Quarterly Journal of Urban Studies*, No. (In Persian).

- Ndubisi, F. (1997). Landscape Ecological Planning. In: Thompson, G.F., Steiner, F.R. (Eds.). Ecological Design and Planning, Wiley, New York.
- Paegelowa, M., Camacho Olmedob, M. T., Masc, J. F, Houetd, T. & Pontius, Jr. R. G. (2013). Land change modelling: moving beyond projections. International Journal of Geographical Information Science, Vol. 27, No. 9, 1691–1695.
- Rostami Kia Y, Little Tabari, M., Ahmadzadeh, A, Rahmani, A. (2017). The effect of growth-promoting bacteria on vegetative traits and nutrients of hazelnut seedlings in Ardabil hazelnut nursery. Iranian Journal of Forest and Poplar Research, 25 (1), 116-126. https://irannature.areeo.ac.ir/article_118216_101456ac2011556504cf51ae786afb80 [In Persian].
- Taghilou, A. (2018). Land use Changes Scenarios for Rural Areas (Case study: Bash Qaleh Dehestan –Urmia County). Journal of Research and Rural Planning, Volume 7, No. 3, Autumn 2018, Serial No.23 eISSN: 2383-2495 ISSN: 2322-2514 <http://jrrp.um.ac.ir> [In Persian].
- Torahi, A., Chand, rai S. (2011). Land Cover Classification and Forest Change Analysis. Using Satellite Imagery-A Case Study in Dehdez Area of Zagros Mountain inIran, Journal of Geographic Information System, 3, 1-11. DOI: 10.4236/jgis.2011.31001
- Valizadeh, Kamran, Kh, Sadegih, M., Hejazi, S. A. (2021). Modeling SA (2021). Land Changes forest Using by LCM in Fandoqhlo Forest Area (Ardabil). Journal of Civil and Environmental Engineering Volume, Issue 10.22034/JCEE.2021.43502.1984 [In Persian].
- Veldkamp, A., & Verburg, P. H. (2004). Modelling land use change and environmental impact. Journal of Environmental Management, 72, pp: 1-3.
- Volkery, A., Riberio, H. (2009). Scenario planning in public policy: Understanding use, impacts and the role of institutional context factors. Tecnological Forecasting & social change, 76, 1198-1207. 10.1016/j.techfore.2009.07.009
- Wang, Y., Li, Sh. (2011). Simulating multiple class urban land-use/cover changes by RBFN-based CA model. Computers and Geosciences, 37 (3), 111–121.
- Wang, Yang & Li, Shuangcheng, (2011). Simulating multiple class urban land-use/cover changes by RBFN-based CA model. Computers & Geosciences, 37, 111–121. 10.1016/j.cageo.2010.07.006
- Weber, M. (2012). FLAs and new patterns of governance of research and innovation. In S. Giessecke, A., van der Gießen, & S. Elkins (Eds.). The role of forward-looking activities for the governance of Grand Challenges. Insights from the European Foresight Platform, (pp. 4-11). Retrieved from: [https:// ec.europa.eu/ jrc/ en/scientific-tool/ european-foresight-platform](https://ec.europa.eu/jrc/en/scientific-tool/european-foresight-platform).



4th Intercontinental Geoinformation Days

igd.mersin.edu.tr



Impact of Climatic Change on the Irrigated Agriculture–Case Study: Seyhan River Basin

Burçak Kapur*¹, Bülent Özekici ¹

¹Çukurova University, Department of Agricultural Structures and Irrigation, Adana, Türkiye

Keywords

ICCAP
Irrigation projects
Lower Seyhan Irrigation
Climate Change
Precipitation

Abstract

Climate change will have an especially negative impact on the Mediterranean region in the twenty-first century. Rising temperatures and more severe droughts will have an impact on precipitation patterns and, as a result, on water resources. The temperatures in the Mediterranean region are expected to rise +3 to 5 °C by 2100. The water-poor countries are likely to be the most affected by 2100, and rainfall is likely to decrease by 20–30% in the countries to the south of Mediterranean. Against these challenges, countries invest in large irrigation projects to increase welfare and to alleviate economic disparities within regions. Lower Seyhan Irrigation Project (LSIP) in southern Turkey is such a project initiated for hydro-energy, irrigation, drainage and flood control. This paper evaluates the adaptation capacity of the Lower Seyhan Irrigation Project area to the future climate change as a case study. The case study reflects the outcomes of the Turkish Japanese bi-lateral project entitled “Impact of Climate Changes on the Agricultural Production System in Arid Areas - ICCAP”. The surface temperature may increase by 2.0 °C to 3.5 °C respectively by 2070. The total precipitation will decrease by 25% in the LSIP area.

1. Introduction

Over the last century, rainfall has decreased throughout the Mediterranean region. The impact of climate change and temperature increases has received the majority of the recent attention paid to global warming or the greenhouse effect by relevant sciences.

Adana region -located on the eastern Mediterranean-with its fertile lands and abundant water resources play a foremost role in Turkish agriculture. It produces, for example, 55% of total maize and 60% of total citrus production of Turkey. Its farmers are one of the most productive and efficient as well as modern, eager to adapt to new technology. Average yields are one of the highest in Turkey. The farmers of this region can and do compete with farmers of richer nations in terms of quality and quantity.

Large scale irrigation projects increase food and fiber production, improve welfare and also alleviate economic disparities between developed and underdeveloped regions, thus providing social and economic justice. Lower Seyhan Irrigation Project (LSIP) located in central-south Turkey on Eastern Mediterranean initiated in the late 1950's is a pioneer in Turkey's huge scale irrigation projects. Considered as one of the most

progressive and exclusive investments the country has undertaken, LSIP is a multipurpose project put into operation for irrigation, drainage, flood control and hydroelectric energy production.

In spite of all the positive achievements, LSIP just like other huge scale irrigation investments also have many shortcomings and deficiencies. Determining the strengths, accomplishments as well as degree of realization of the irrigation project's initial objectives, weaknesses, failures, insufficiencies and project's limitations, therefore, are of utmost importance in the planning, implementation and supervision of such intended projects. Such an evaluation may help shed light for future irrigation and drainage investments elsewhere in the country and thus improve the performance of large-scale public irrigation projects. With this objective in mind, this study was undertaken to assess the performance of irrigation and drainage systems in LSIP under Impact of Climate Change on Agricultural Production) project which is a multidisciplinary cooperative research project with Japanese (RIHN, Research Institute for Humanity and Nature, Kyoto, Japan) and Turkish (TUBITAK, Turkish Scientific and Technical Research Council, Ankara, Turkey) scientists.

* Corresponding Author

(bkapur@cu.edu.tr) ORCID ID 0000 – 0001 – 6131 – 4458
(e-mail) ORCID ID xxxx – xxxx – xxxx – xxxx

Cite this study

Kapur, B. & Özekici, B. (2022). **Impact of Climatic Change on the Irrigated Agriculture–Case Study: Seyhan River Basin**. 4th Intercontinental Geoinformation Days (IGD), 147-150, Tabriz, Iran

2. Projection of air temperature and precipitation

Climate change in the Seyhan basin was projected by Yano et al. (2007) as part of the ICCAP project. They revealed variations of annual mean temperature and precipitation collected from four GCM-based models for 111 years from 1990 to 2100 in Adana are shown in Fig. 1 as the difference from 1990 – 2004 mean. Four models tested are: CGCM2 model of Canadian Center for Climate Modeling and Analysis (CCCma), ECHAM4/OPYC3 model of Max Planck Institute für Meteorologie (MPIfM), CGCM2.2 model of Meteorological Research Institute (MRI) and AGCM + CCSR OGCM model of Center for Climate System Research and National Institute for Environmental Studies (CCSR/NIES). The MRI data are not available at the IPCC web-site. The inverse distance weighted approach was used to calculate these statistics for Adana using predicted values at the four nearest surrounding grid points. Annual temperature increases gradually. According to the linear regression equation, averaged surface temperature is estimated to increase by 3.1-8.6 °C over the period of 1990 to 2100. The CCSR/NIES and MRI results show the highest and lowest increases, respectively, among the four models. Although annual precipitation denotes noticeable variations year by year, it is not likely that it will have increased in the future (Yano et al. 2007).

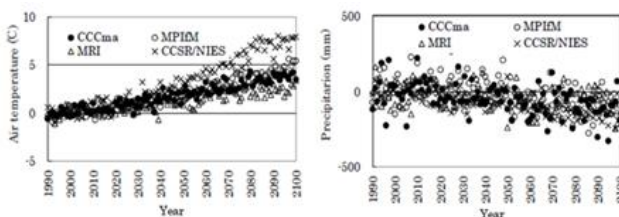


Figure. 1. Projections of air temperature and precipitation difference from 1990 – 2004 mean (Yano et al., 2007).

Figure 2 illustrates monthly fluctuations in potential evapo-transpiration from a reference crop (ET_{ref}) to represent the atmosphere's evaporative demand. ET_{ref} was calculated with the Penman-Monteith equation based on the GCM and RCM data and the observed data. Calculated potential ET from the different climate data shows the similar monthly variations with the air temperature variations. Because potential ET is the most important parameter for predicting water demand, it's assumed that using the original GCM and MRI data will yield incorrect findings (Yano et al. 2007).

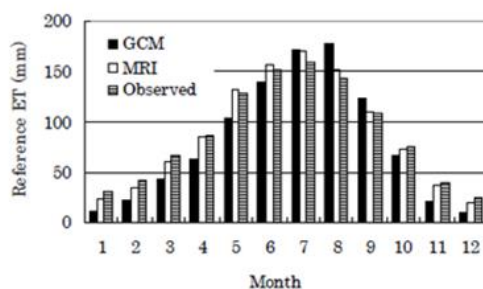


Figure. 2. Calculated reference ET from the GCM, MRI and observed data (Yano et al., 2007).

3. Water Balance Change Due to Global Warming

Table 1 and Table 2 show the average values and standard deviations of the water balance components for the periods of 10 years beginning in 1994 and ending in 2070, as well as biomass, grain yield, and growing duration for wheat and second crop maize, respectively. Since CO₂ concentration in 2070s is estimated to increase up to doubling concentration under SRES A2 scenario, calculations were done for under doubling CO₂ concentration condition. In doing calculation, the percent change in acclimatized photosynthesis rate was assumed to be +27% and +4% for wheat and maize, respectively (Cure and Acock, 1986). It is well-known that actual ET decreases considerably due to stomata closure under elevated CO₂ concentration (e.g. Ainsworth and Long, 2005; Yano et al. 2007).

For the period 2070-2079, the percent change in transpiration for wheat and maize was reduced by 17 percent and 26 percent, respectively (Cure and Acock, 1986; Yano et al. 2007). Comparison of calculated actual ET between the current climatic condition and the future for the GCM, MRI and CCSR/NIES data shows the decrease of 28%, 8% and 16%, respectively for wheat and 24%, 28% and 26%, respectively for maize, reflecting the different rises in air temperature in the future (Yano et al. 2007).

The evaporative demand of the atmosphere will increase as the temperature of the atmosphere rises in the future. However, decrease in actual ET for both wheat and maize shown in Tables 1 and 2 can be attributed to reduction of growing days and LAI due to temperature rise and transpiration reduction due to stomata closure regardless of increase in evaporative demand (Yano et al. 2007).

Table 1. Predictions of the combined effects of projected climate change with elevated air temperature and doubling CO₂ concentration with transpiration reduction due to stomata closure for wheat (Yano et al. 2007)

Model	Period	Precipitation (mm)	ET (mm)	Irrigation (mm)	Biomass (ton/ha)	Grain yield (ton/ha)	Growth days
GCM	1994–2003	535.0 ± 186.3	349.2 ± 35.2	0 ± 0	17.5 ± 1.8	5.0 ± 0.9	198.5 ± 7.8
	2070–2079	503.6 ± 211.8	250.9 ± 32.1	16.6 ± 36.9	16.8 ± 2.0	5.8 ± 0.8	174.1 ± 6.6
MRI	1994–2003	597.9 ± 190.1	301.8 ± 30.1	24.8 ± 45.3	16.9 ± 1.7	4.5 ± 0.9	188.1 ± 5.8
	2070–2079	313.9 ± 82.5	276.6 ± 20.9	68.9 ± 56.8	23.3 ± 0.9	6.1 ± 1.3	181.3 ± 4.1
CCSR	2070–2079	308.0 ± 88.1	252.5 ± 26.7	79.2 ± 88.1	19.0 ± 2.1	5.6 ± 0.9	167.6 ± 4.5

Table 2 Predictions of the combined effects of projected climate change with elevated air temperature and doubling CO₂ concentration with transpiration reduction due to stomata closure for maize (Yano et al. 2007)

Model	Period	Precipitation (mm)	ET (mm)	Irrigation (mm)	Biomass (ton/ha)	Grain yield (ton/ha)	Growth days
GCM	1994–2003	47.5 ± 23.8	414.1 ± 26.1	375.5 ± 51.7	27.3 ± 1.5	15.1 ± 1.3	115.9 ± 3.8
	2070–2079	24.9 ± 18.0	314.0 ± 23.7	318.4 ± 27.6	22.6 ± 1.6	11.4 ± 1.2	106.7 ± 0.7
MRI	1994–2003	9.8 ± 6.0	439.8 ± 5.8	423.1 ± 7.8	30.1 ± 1.0	16.4 ± 0.9	118.8 ± 2.9
	2070–2079	8.5 ± 8.0	317.6 ± 5.9	331.4 ± 36.0	31.0 ± 1.0	16.9 ± 0.8	115.8 ± 2.4
CCSR	2070–2079	10.7 ± 17.1	326.6 ± 5.2	328.2 ± 24.8	29.2 ± 0.8	15.5 ± 0.7	109.8 ± 1.3

4. Description of Lower Seyhan Irrigation Project (LSIP)

LSIP area is located on the southern part of Turkey on the eastern Mediterranean (Figure 3). Seyhan Plain is the largest and the most important deltaic plane in southern

Turkey. This important project covers an area of 204,000 ha of which 174,000 ha is irrigable. The area is bordered by the Mediterranean Sea on the south, by the foot hills of the Taurus Mountains on the north and by Berdan River on the west and Ceyhan River on the east. The area is divided in two parts by the Seyhan River which flows from north to south through the plain. The part between Seyhan and Berdan Rivers is known as "Seyhan Right Bank" or "Tarsus Plain" with a completed irrigation network for 64,400 ha, and the other part located between Seyhan and Ceyhan Rivers is called "Seyhan Left Bank" or "Yuregir Plain" with a completed network for 68,200 ha. The average slope varies between 1% and 0.1% from north towards south.

LSIP area with its fertile lands and abundant water resources plays a foremost role in Turkish agriculture. It produces, for example, 55% of total maize, 60% of total citrus and 25% of total watermelon production of Turkey. Favorable climate conditions permit cropping year around allowing both single (wheat, corn, cotton, soybeans, onions, potatoes, melons, etc.) and double cropping (usually corn or soybeans after wheat harvest in late May or after onion harvest in April). Note that wheat is seldom irrigated, it is mainly rainfed.



Figure 5. Map of Turkey (Seyhan Basin in box), Seyhan Basin and LSIP

5. Climate Change Adaptation of The LSIP Results

ICCAP's General Circulation Models (GCMs) reflects snow storage and stream runoff in the Seyhan Basin are likely to decline in the future (2070–2100) due to a warmer environment (Fig. 3) (Kanber et al. 2019). The LSIP considers three future scenarios: (a) Land and water use will be the same as now, (b) Adaptation 1: land and water use will be under low-investment conditions, and (c) Adaptation 2: land and water use will be under high-investment conditions. Figure 3 illustrates that in the current climate, the maximum snow water equivalent (SWE) is around 0.4 Gt, but in the future climate, it will drop to 0.1 Gt. The yearly evaporation rate for the Seyhan delta (irrigated region) is over 800 mm, requiring nearly 500 mm of irrigation water during the hot and dry summer growing season. As a result of the decreasing snow cover, these areas will be exposed to greater shortwave sunlight (albedo effect), which will lead to higher evaporation in the spring. According to Fujinawa et al. (2007), more energy will result in a shorter crop maturity period, but the amount of irrigation water required will rise due to higher evaporation demand during the growing season and lower soil moisture at the start of the growing season. According to the results given by Tezcan et al. (2007), the decrease in the mean

annual snow storage is about 14.56 km³ in the warming up period. The major decrease will occur in Aladağlar, the south-east slopes of the Erciyes and the north of the Göksu Basin. Reduced snow storage will have an impact on spring discharge in the Zamanti and Göksu Basins, which feed the Seyhan River.

Similarly, future inflows will be far lower than current levels. Furthermore, the drops in inflow expected for April, May, and June will be higher than those predicted for the other months, and the peak monthly inflow will occur earlier than it does now, resulting in a drastic reduction in inflow. Fewer flood events are estimated to occur during the warm season, when the decreased river flow may lead to water scarcity in the LSIP area (Watanabe 2007). However, Tezcan et al. (2007) have reported that the months for peak flow will be the same in both the present and warm up periods using the Mike-She simulation program.

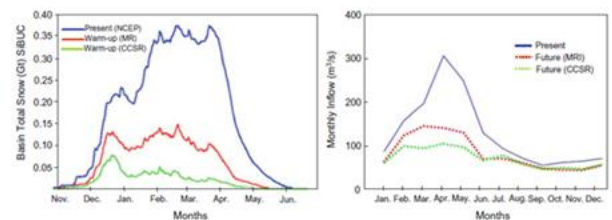


Figure. 3 Total snowfall in volume equivalent to water (Gt) (left) and the changes in Seyhan River flow (right) predicted from different models of MRI (red), CCSR (green) and present (blue). Source Fujinawa et al. (2007: 56)

The reliability index, defined as the ratio of water supply to water demand, is a measure of whether or not water demand can be met by a reservoir's supply or the degree of water scarcity. Currently, the dependability index is around 0.4, indicating minimal water stress; however, in the future, it will vary from 0.4 to 0.7 for Adaptation 1 (high water stress) and 0.5–1.0 for Adaptation 2 (very high-water stress) (Fujinawa et al. 2007). As a result, the reservoir volume in the future and Adaptation 1 will be lower than it is now, and the reservoir will be devoid of water in a few circumstances. Based on the precipitation estimates of the MRI and CCSR models, the dam reliabilities in the future and Adaptation 1 will change from 0.95 to 1.0. In Adaptation 2, the reservoir is frequently empty and reliability ranges from 1.0 to 0.7 according to future data projected by the MRI and CCSR models (Kanber et al. 2019).

Climate change, on the other hand, is expected to reduce the water budget elements in the warm-up period compared to now. The CCSR climate data reveal a greater decrease than those of the MRI data. Reduced precipitation limits the decline in actual evapotranspiration. During the warm-up phase, precipitation may drop by 29.4% (MRI) and 34.7 percent (CCSR), reducing river flow by 37.5 and 46.4 percent, respectively. As a result, groundwater recharge in the Seyhan Basin will drop by 24.7 and 27.4%, respectively. The majority of the springs in the basin will become dry due to the decline of the groundwater level below the spring level.

Climate change will have a significant impact on groundwater supplies in the LSIP area. Reduced Seyhan River recharge will result in a reduction in subsurface recharge to the LSPP area from higher elevations in the north of the region. The change in groundwater storage in the LSIP area as a result of climate change. The most major effects are a decrease in recharge at higher elevations and an increase in abstraction due to surface water resource constraints. As the head degrades, salty water will infiltrate the LSIP area. In the case of a 50% increase in the groundwater abstraction in the warm-up period of 2080, the seawater intrusion will reach 10 km inland (Tezcan et al. 2007). At the same time, groundwater salinity in the LSIP area's coastal zone will reach 25% of the seawater composition.

6. Conclusion

Implementation of Lower Seyhan Irrigation Project has increased agricultural production considerably, thereby affecting the livelihood of many people in a positive way. However, introduction of irrigated agriculture has also brought problems related to irrigation, drainage and high-water tables due to inadequate management and excess water use. Evaluation of LSIP reveals that expected full productivity has not been realized yet and that this huge investment has many shortcomings which should be monitored carefully and closely in order to shed light for similar future investments. Water should be considered as an important and valuable input through effective measures and should be efficiently utilized by the users. Volume based water charges should be preferred over area-crop basis for conserving this valuable commodity.

The conclusion of this chapter, based on the research and modeling studies indicated above, is that agriculture in the LSIP area may be impacted by future expected climate change. Precipitation in Adana is expected to fall by 42–46 percent by the 2070s. The reduced precipitation would primarily occur throughout the winter. To deal with the dry winter, irrigation would be required in the early spring for tree crops and vegetables. In addition, as a result of the predicted climatic change, irrigation demand would rise and the irrigation season would lengthen. As a result, the LSIP may need to adjust crop and irrigation management in order to react to situations where water is scarce. The LSIP features two large-scale reservoirs as water sources upstream. Climate change-related decreases in river discharge would entail determining a resource-wise adaptive capability. The 30,000 hectares of increased irrigation expansion in the Phase IV area, on the other hand, will result in an additional water shortfall in the future.

In addition, effective changes in water consumption and irrigation system management should be made to improve the LSIP area's adaptive capacity to climate change. The gravity water distribution system should be converted to a closed system, and emergency measures to avoid erosion and sedimentation in the water basin and water storage buildings should be performed. As a result of this work, high levels of efficacy in terms of water supply and utilization would be achieved.

Acknowledgement

This article summarized some of the works from the ICCAP (Impact of Climate Change on Agricultural Production) project which is a multidisciplinary cooperative research project with Japanese (RIHN, Research Institute for Humanity and Nature, Kyoto, Japan) and Turkish (TUBITAK, Turkish Scientific and Technical Research Council, Ankara, Turkey) scientists. The authors would like to thank all those involved in ICCAP, and RIHN and TUBITAK for their support in this presentation.

References

- Ainsworth, E.A. & Long, S. P. (2005). What have we learned from 15 years of free-air CO₂ enrichment (FACE)? A meta-analytic review of the responses of photosynthesis, canopy properties and plant production to rising CO₂. *New Phytologist*, 165, 351-372.
- Cure, J. D., & Acock, B. (1986). Crop responses to carbon dioxide doubling: A literature survey. *Agric. For. Meteorol.*, 38: 127-145.
- Fujinawa, K, Tanaka, K., Fujihara, Y., & Kojiri, T. (2007). The impacts of climate change on the hydrology and water resources of Seyhan River Basin, Turkey. The Research Project on the Impact of Climate Changes on Agricultural Production System in Arid Areas. ICCAP Publication 10, Kyoto, Japan, pp 53–58.
- Kanber, R., Ünlü, M., Kapur, B., Özekici, B., & Donma, S. (2019). Adaptation of Contemporary Irrigation Systems to Face the Challenges of Future Climate Changes in the Mediterranean Region: A Case Study of the Lower Seyhan Irrigation System. Springer Nature Switzerland AG 2019 T. Watanabe et al. (eds.), *Climate Change Impacts on Basin Agro-ecosystems, The Anthropocene: Politik—Economics—Society—Science* 18, https://doi.org/10.1007/978-3-030-01036-2_7
- Tezcan, L., Ekmekçi, M., Atilla, Ö., Gürkan, D., Yalçınkaya, O., Namkhay, O., Soylu, E. M., Donma, S., Yilmazer, D., Akyatan, A., Pelen, N., Topaloğlu, F., & İrvem, A. (2007) Assessment of climate change impacts on water resources of Seyhan River Basin. The Research Project on the Impact of Climate Changes on Agricultural Production System in Arid Areas. ICCAP Publication 10, pp 59–72, Kyoto, Japan.
- Watanabe, T. (2007) Summary of ICCAP: Framework, outcomes and implication of the project. The final report of ICCAP. The Research Project on the Impact of Climate Changes on Agricultural Production System in Arid Areas. ICCAP Publication 10, Kyoto, Japan, pp 1–14.
- Yano, T., Tomokazu, H., Masumi, K., & Mehmet, A. (2007). Prediction of Future Change of Water Demand Following Global Warming in the Cukurova Region, Turkey. The Research Project on the Impact of Climate Changes on Agricultural Production System in Arid Areas. ICCAP Publication 10, pp 185–190, Kyoto, Japan.



4th Intercontinental Geoinformation Days

igd.mersin.edu.tr



Evaluation of land consolidation impact criteria for rural development

Halil Burak Akdeniz^{*1}, Tayfun Çay¹, Şaban İnam¹

¹ Konya Technical University, Engineering and Natural Sciences Faculty, Geomatics Department, Konya, Türkiye

Keywords

Rural development
Land consolidation
Rural area regulation

Abstract

Land consolidation is one of the most important means of rural development practices. In order for land consolidation studies to successfully achieve rural development-oriented goals, they must be carried out “with the feature and content that responds to the expectations in the most appropriate quality”. In this study, the effect of the land consolidation and on-farm development projects, which were implemented and approved in two separate units in the Manyas district of Balıkesir province of Turkey, on rural development was examined. As a result of land consolidation, it was determined that the average size of the parcels in the study areas increased, the average number of parcels per enterprise decreased, all parcels benefited from the transportation and irrigation system, the parcel shapes were made suitable for modern agriculture, the amount of border area loss decreased and public investments were made without paying any price.

1. Introduction

Today, the continuous increase in the world population increases the importance of soil and water, which are limited natural resources. Global warming, climate change and epidemic diseases that have increased in the last 10 years have revealed the importance of agricultural production. All these developments increase the importance of rural development policies that directly affect food production (Yoğunlu 2013). One of the important criteria of a correct rural development planning is the efficient and effective use of agricultural lands. Among these, “Land Consolidation (LC)” is an important and effective tool. LC has become an effective tool used to improve the quantity and quality of cultivated lands, reduce land fragmentation, regulate land shape and property structure, increase modern agricultural development, improve rural environment, realize public investments without expropriation, support rural development and poverty reduction (Jiang et al. 2017; Zhou et al. 2020).

LC is important not only for increasing agricultural production, but also for solving the socio-economic problems of rural areas. Therefore, LC should not be accepted as a practice for agricultural production only. Land consolidation is also a versatile rural area planning that will improve the living standards of the population living in rural settlements and slow down the migration from villages to cities.

In this study, the effects of land consolidation and on-farm development projects implemented in the Manyas district of Balıkesir province of Turkey on rural development were examined.

2. Materials and methods

2.1. Materials

Eskiçatal and Kayaca neighborhoods, which are connected to the Manyas district of Balıkesir province in the northwest of Turkey, constitute the study areas (Fig. 1). The study areas are 5 km away from Manyas district and 80 km away from the city center of Balıkesir. The altitude of the region above sea level is about 50 meters and the slope value is low. According to the census data of 2021, the total population of both neighborhoods is 600. In the area with Mediterranean climate characteristics, the winters are cool and rainy, and the summers are hot and dry. The average annual precipitation is 700 mm. As its lands are very fertile, the main livelihood of the people in the region is agriculture and animal husbandry. It is possible to get crops from irrigated land twice a year. Mostly wheat, rice, corn, sunflower, tomato and cabbage are grown in agricultural production areas. Small cattle breeding also has a special place in the region, which is famous for its milk and dairy products.

* Corresponding Author

(hbkakdeniz@ktun.edu.tr) ORCID ID 0000 – 0002 – 9504 – 051X
(tcay@ktun.edu.tr) ORCID ID 0000 – 0002 – 4661 – 5583
(sinam@ktun.edu.tr) ORCID ID 0000 – 0002 – 9101 – 6109

Cite this study

Akdeniz, H. B., Çay, T., & İnam, Ş. (2022). Evaluation of land consolidation impact criteria for rural development. 4th Intercontinental Geoinformation Days (IGD), 151-154, Tabriz, Iran

Land consolidation and on-farm development services in Kayaca and Eskiçatal neighborhoods were completed in 2014 and 2015. In the study, numerical and attribute data obtained before and after the land consolidation projects were used.

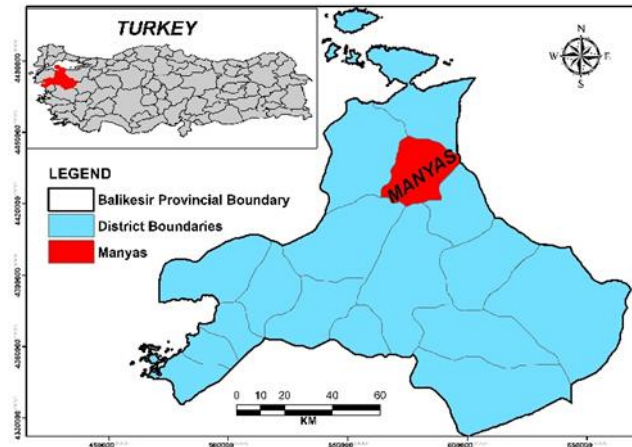


Figure 1. Study area

2.2. Methods

In this study, in which the effects of land consolidation and on-farm development services on rural development were evaluated, the issues determined were

- Consolidation rate of LC projects,
- Change in average parcel size and average number of parcels per enterprise before and after LC,
- Number and rate of parcels directly benefiting from the transportation and irrigation system before and after LC,
- The size of the parcels before and after LC,
- Change of parcel geometry,
- The amount of area loss caused by the inability to approach the parcel border, and
- The area to be expropriated by the public finance, and the expropriation cost to be paid if infrastructure and superstructure investments are made without the implementation of the LC project

Netcad 8.5 software was used in the production of spatial analysis, and ArcMap 10.5 software was used in the display of thematic maps. Subdivision maps before and after LC for each study area are shown in Fig. 2 and Fig. 3.

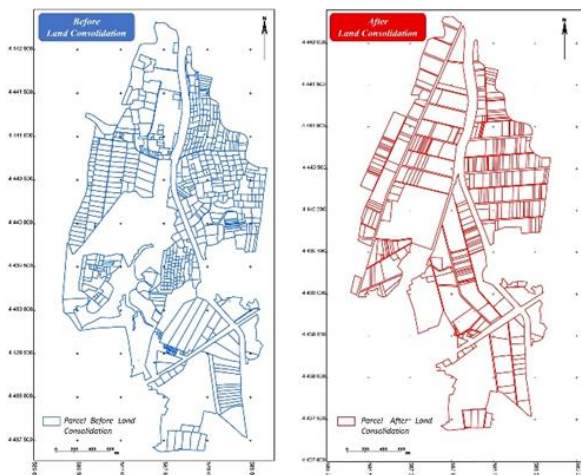


Figure 2. Eskiçatal parcellation maps before and after LC

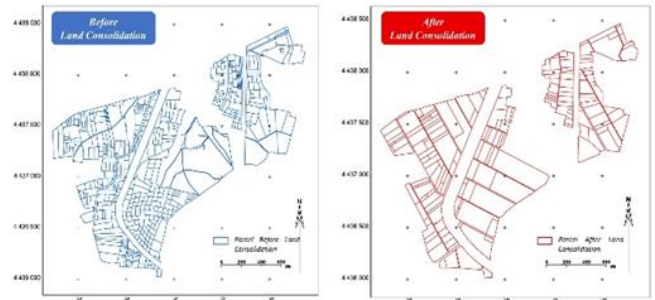


Figure 3. Kayaca parcellation maps before and after LC

3. Results

3.1. Consolidation rate

There are a total of 344 private enterprises within the scope of the Eskiçatal LC project. While the total number of parcels belonging to private enterprises was 626 before LC, the total number of parcels decreased to 373 after LC and the consolidation rate was calculated as 40.41% (Table 1). There are a total of 194 private enterprises within the scope of the Kayaca LC project. While the total number of parcels belonging to private enterprises was 470 before LC, the total number of parcels decreased to 177 after LC and the consolidation rate was calculated as 62.34% (Table 1). Considering that the consolidation rate in the land consolidation projects in Turkey is 42.4% on average [Yağanoğlu et al. 2000; Döner and Kaya 2021], it is observed that the consolidation rate value in both projects is similar to the country average.

3.2. Average parcel size and average number of parcels per enterprise

While the average parcel size in the Eskiçatal project site was 9.79 da before LC, it was 16.43 da after LC (Table 1). The average parcel size increased by 67.82% before and after LC. While the average parcel size in the Kayaca project site was 4.96 da before LC, it was 13.17 da after LC (Table 1). The average parcel size increased by 62.33% before and after LC.

Table 1. Information before and after consolidation of Eskiçatal and Kayaca neighborhoods

		ESKİÇATAL	KAYACA
Project implementation period		2010-2015	2011-2014
Project area (da)		24585.0	23317.0
Number of parcel	Before LC	626	470
	After LC	373	177
Average parcel size (da)	Before LC	9.79	4.96
	After LC	16.43	13.17
Number of enterprises		344	194
Average number of parcels of the enterprise	Before LC	1.82	2.42
	After LC	1.08	0.91
	Reduction ratio (%)	40.66	62.40
Consolidation rate (%)		40.41	62.34

3.3. Transportation and irrigation system

When Table 2 is examined, while 156 of the 626 parcels (24.92%) in the Eskiçatal neighborhood have direct access to the transportation system before LC, 113 (24.04%) of the 470 parcels in the Kayaca neighborhood have direct access to the transportation system. It was determined that all parcels (100%) in both neighborhoods have direct access to the transportation system after LC.

While none of the parcels in the Eskiçatal neighborhood had an irrigation system before LC, 153 (32.55%) parcels in the Kayaca neighborhood benefited from the irrigation system. It was determined that all parcels (100%) in both neighborhoods directly benefited from the irrigation system after LC. The number and rates of parcels benefiting from the transportation and irrigation system before and after LC are given in Table 2.

Table 2. Number and rate of parcels direct access to the transportation and irrigation system before and after LC

	Status	Transportation System		Irrigation System	
		Number of parcels	Parcel rate (%)	Number of parcels	Parcel rate (%)
Eskiçatal	<i>Before LC</i>	156	24.92	0	0.00
	<i>After LC</i>	373	100.0	373	100.0
Kayaca	<i>Before LC</i>	113	24.04	153	32.55
	<i>After LC</i>	177	100.0	177	100.0

3.4. The effect of land consolidation on parcel size

Parcel sizes (da) were divided into six groups as 0-5, 6-10, 11-20, 21-50, 51-100 and 100<. The number and rates of parcels belonging to the parcel size groups before and after LC are given in Table 3.

While 57.67% of the parcels in the Eskiçatal project site were in the range of 0-5 before LC, this rate became 39.41% after LC. A decrease was observed in the rate of parcels between 0-5 da size after consolidation, while an increase was observed in all other sizes.

While 74.90% of the parcels in the Kayaca project site were in the range of 0-5 decare before LC, this rate was 38.42% after LC. The rate of parcels over 20 decare increased after LC.

Table 3. Distribution of parcel size in Eskiçatal and Kayaca project area before and after LC

Parcel size (da)	ESKİÇATAL		KAYACA	
	<i>Before LC (%)</i>	<i>After LC (%)</i>	<i>Before LC (%)</i>	<i>After LC (%)</i>
0-5	57.67	39.41	74.90	38.42
6-10	24.60	26.01	17.23	28.25
11-20	12.94	19.57	5.96	22.60
21-50	2.56	9.92	1.49	7.91
51-100	1.28	3.48	0.21	2.26
100<	0.95	1.61	0.21	0.56

3.5. The effect of land consolidation on parcel shape

Parcel shapes were divided into five groups as rectangular, square, amorphous, triangular and trapezoidal. The number and rates of parcels belonging to these groups before and after LC are given in Table 4.

While the rate of rectangular parcels in Eskiçatal neighborhood was 53.03% before LC, it increased to 69.44% after LC. It was determined that while the rate of amorphous parcels was 36.10% before LC, it decreased to 9.65% after LC.

While the rate of rectangular parcels in Kayaca neighborhood was 37.23% before LC, it increased to 60.45% after LC. While the rate of trapezoidal parcels was 29.36% before LC, it decreased to 14.69% after LC.

Table 4. Changes of parcel shape

Parcel shape		Neighborhoods			
		ESKİÇATAL		KAYACA	
		<i>Before LC</i>	<i>After LC</i>	<i>Before LC</i>	<i>After LC</i>
Rectangle	Number	322	259	175	107
	%	53.03	69.44	37.23	60.45
Square	Number	4	1	9	4
	%	0.64	0.27	1.91	2.26
Amorphous	Number	226	36	132	36
	%	36.10	9.65	28.09	20.34
Triangular	Number	6	5	16	4
	%	0.96	1.34	3.41	2.26
Trapezoidal	Number	58	72	138	26
	%	9.27	19.20	29.36	14.69

3.6. Border area losses

In agricultural production, a strip of land with a width of about 40 cm parallel to the parcel border cannot be planted (Demirel 1997). While the non-cultivation area of the enterprises in the Eskiçatal and Kayaca project sites due to the parcel border facilities was 93.45 da and 52.83 da before LC, it decreased to 72.44 da and 30.45 da after LC. The 21.01 da and 22.38 da lands in the Eskiçatal and Kayaca project sites were made available for agricultural production after consolidation.

An area gains of 9.60% and 8.55% was achieved in Eskiçatal and Kayaca project sites due to the loss of border area after LC.

3.7. The amount and cost of expropriation

One of the benefits of the implementation of the LC project is the acquisition of public common-use areas by consolidation instead of expropriation. The area required for public investments in Eskiçatal and Kayaca project sites was calculated as 590.93 da and 219.65 da. According to the decision of the 25th Regional Directorate of State Hydraulic Works (DSI) dated 06.01.2020, the expropriation unit price in the irrigated agricultural lands of Eskiçatal and Kayaca neighborhoods in Manyas district was determined as 10 TL/m². In line with this value, with the assumption that there were no

buildings and facilities on the areas to be allocated for public investments, the expropriation cost of Eskiçatal and Kayaca project sites was calculated as 8,105,800 TL. Such a situation would put an additional burden on public finances and cause a waste of resources.

4. Discussion and Conclusion

This study has been evaluated on the basis of 7 criteria, the impact criteria of the land consolidation project in ensuring rural development, as "consolidation rate, average number and size of parcels, number of parcels benefiting from the transportation and irrigation system, parcel geometry, the amount of border area loss and the amount of expropriation".

By decreasing the number of enterprise parcels and increasing the average parcel size after LC, the number of labor and workdays decreased while agricultural productivity and efficiency increased. With LC, it was ensured that all parcels in the project sites benefit directly from the road and irrigation network. Thus, it became easier and more economical for enterprise owners to access their lands, and damages caused by transportation to the parcel and disputes between property owners were prevented. One of the benefits of LC projects is the correction and improvement of the parcel geometry in a way that is suitable for agricultural mechanization. The most suitable parcel geometry for agricultural mechanization is rectangular (Boztoprak et al. 2015). Agricultural mechanization will be facilitated in the parcels formed in this way, and productivity will increase with the reduction in processing cost and time. The increase in the rate of rectangular parcels in both study areas after LC is an important gain in terms of rural development. Large number of enterprise parcels per unit area and the amorphous parcel geometry cause a certain section parallel to the parcel border not to be used in agricultural production. With the decrease in the number of parcels and the improvement of the parcel geometry after LC, border area losses will decrease and production will become more efficient in vacant areas. In the application areas that are the subject of the study, a total of 43.39 da of land was brought into agricultural production after LC. This will increase agricultural production, enterprise income and country added value. For rural development, accelerating public investment

costs is as important as reducing them. With LC projects, public common-use areas were created both quickly and holistically and were obtained without paying the expropriation price. Thus, the public finances gained 8,105,800 TL.

As a result, it is necessary to develop and support land consolidation projects that accelerate the achievement of rural development goals and contribute to sustainability in rural areas.

Acknowledgement

Acknowledgements of support for 25th Regional Directorate of State Hydraulic Works are welcome.

References

- Boztoprak, T., Demir, O., Çoruhlu, Y. E., & Nişancı, R. (2015). Arazi toplulaştırmasının tarımsal işletmelere etkilerinin araştırılması. *Selçuk Üniversitesi Mühendislik, Bilim ve Teknoloji Dergisi*, 3(3), 1-11.
- Demirel, Z. (1997). Kırsal toprak düzenlemesi. Y.T.Ü. Basım Yayın Merkezi, İstanbul.
- Döner, H., & Kaya, S. (2021). Bingöl ili merkez ilçe köylerinde uygulanan arazi toplulaştırma projesinin kırsal alan planlaması yönüyle değerlendirilmesi. *Türk Doğa ve Fen Dergisi*, 10(2), 34-41, <https://doi.org/10.46810/tdfd.839340>.
- Jiang, G., Zhang, R., Ma, W., Zhou, D., Wang, X., & He, X. (2017). Cultivated land productivity potential improvement in land consolidation schemes in Shenyang, China: assessment and policy implications. *Land Use Policy*, 68, 80-88, <https://doi.org/10.1016/j.landusepol.2017.07.001>.
- Yağanoğlu, A. V., Okuroğlu, M., & Hanay, A. (2000). Arazi toplulaştırması. Atatürk Üniv. Ziraat Fak. Ders Yay. No: 159, Erzurum.
- Yoğunlu, A. (2013). Arazi Toplulaştırma Faaliyetleri. TRB1 Bölgesi (Bingöl, Elazığ, Malatya, Tunceli), Fırat Kalkınma Ajansı.
- Zhou, Y., Li, X., & Xu, C. (2020). Land consolidation and rural revitalization in China: Mechanisms and paths. *Land Use Policy*, <https://doi.org/10.1016/j.landusepol.2019.104379>.



4th Intercontinental Geoinformation Days

igd.mersin.edu.tr



Challenges of integrating cadastral map and urban data infrastructure in Iran

Alireza Hajiheidari ^{*1}, Mahmoud Reza Delavar ², Abbas Rajabifard ³

¹ University of Tehran, College of Engineering, School of Surveying and Geospatial Engineering, Tehran, Iran

² University of Tehran, College of Engineering, Center of Excellence in Geospatial Eng. in Disaster Management, School of Surveying and Geospatial Engineering, Tehran, Iran

³ University of Melbourne, Department of Infrastructure Engineering, Center for Spatial Data Infrastructures and Land Administration, Victoria, Australia

Keywords

Digital cadastre
Data integration
Spatial data fusion
Geospatial data sharing
Spatial data infrastructure

Abstract

Producing rich cadastral maps of megacities is time-consuming and imposes exorbitant costs on the concerned organizations. Due to rapid urban expansion and development, keeping maps up-to-date is a significant challenge for spatially enabled government and land administration affairs. Therefore, in order to keep urban cadastral maps up-to-date and enrich their content geometrically and thematically, a number of issues should be resolved. In this research, challenges in integrating and enriching the urban and cadastral map data of different organizations in some parts of a District of the mega city of Tehran, the capital of Iran, have been investigated. Some of the important challenges are the heterogeneous methods of map production, inconsistency in the employed maps currency, existence of a variety of map scales produced in different urban organizations, lack of coordination and cooperation in map data formats, production methods, and standardization. This paper has attempted to overcome these challenges.

1. Introduction

It is believed that having rich, up-to-date and reliable urban cadastral maps is essential for urban management organizations to make reliable, informed and timely decisions. Increasing the complexity of cities, the needs and opportunities of the cities in the context of smart cities, the availability of more stakeholders than before, and also increasing urbanization in the world by 70% by 2050, increases the need for an intelligent urban cadastre (Rajabifard, 2015). This urban expansion and development increase the need for management organizations to have up-to-date and rich urban and cadastral maps. In addition, production of new maps takes much time and cost for the urban management organizations and makes maps out-of-date almost soon after their production. Therefore, urban management organizations can update their cadastral maps and spatial data infrastructure (SDI) to make the right decisions in various issues by enriching their maps through integrating their spatial and legal information. Sharing the latest spatial data facilitates urban sustainable development, have created a win-win

situation for all actors in the urban management organizations such as spatial data providers, service providers, and end users (Olufunmilayo Akinyemi and Uwayezu, 2011).

Data sharing prevents duplication of data collection efforts and reduces resource waste. It may also improve data quality because it enables users to review, correct, and improve the data (Gelagay, 2017). The geospatial community needs a suitable space for sharing and accessing geospatial assets to take full advantage of their socio-economic benefits because meeting users' needs in a spatial community is beyond an organization's ability (Rajabifard et al., 2005). Some research has been conducted in different countries to examine the challenges for data integration and the creation of an SDI. Similarities and differences between cadastral maps in 8 states of Australia and New Zealand have been examined. Finally, a new cadastral framework has been considered across Australia and New Zealand (Atazadeh et al., 2021). In Ethiopia, poor organizational coordination, poor data quality and compatibility as well as institutional, legal, policy, and technological issues have been identified as significant challenges to geospatial data sharing barriers

* Corresponding Author

^{*}(aliz.hajiheidari@ut.ac.ir) ORCID ID 0000-0002-6138-8657
(mdelavar@ut.ac.ir) ORCID ID 0000-0002-9654-6491
(abbas.r@unimelb.edu.au) ORCID ID 0000-0002-4256-3173

Cite this study

Hajiheidari, A., Delavar, M. R., Rajabifard, A. (2022). Challenges of integrating cadastral map and urban data infrastructure in Iran. 4th Intercontinental Geoinformation Days (IGD), 155-158, Tabriz, Iran

among organizations (Gelagay, 2017). Gózdź and van Oosterom (2016) have examined the development of SDIs in Poland. This paper discusses the possibilities of developing a national information infrastructure using the Land Administration Domain Model (LADM) (Gózdź and van Oosterom, 2016). Kafashan (2020) has studied the challenges in the Iranian two-dimensional cadastral maps mainly in spatial information, descriptive information, shortages and shortcomings of urban coverage and land use. Most of the urban management organizations are incapable of meeting their spatial data needs alone. In addition, sharing geospatial data faces several mega challenges including scattering data across its respective organizations, duplication efforts in the production of spatial data, and the existence of outdated data and the problems in finding available, qualified, and sharable data (Pierre, 2016). In the data integration process, it is always necessary to preprocess and harmonize the data to become at the same format and scale as well as eliminate their errors. The data will then be combined using specific international spatial data standards and frameworks which will be evaluated at using some specifications such as ISO/TC 211 and federal geographic data committee (FGDC) standards.

2. Method

An initial review of the organizations and their data should be done in the integration process. After providing data, it should be quality controlled and pre-processed. Their format, scale, symbols, and definitions should be harmonized and then their errors should be removed and corrected. Furthermore, they eventually are integrated by global frameworks and standards. Finally, they must be evaluated. At the end, the enriched maps are obtained. The integration workflow is shown in "Fig. 1".

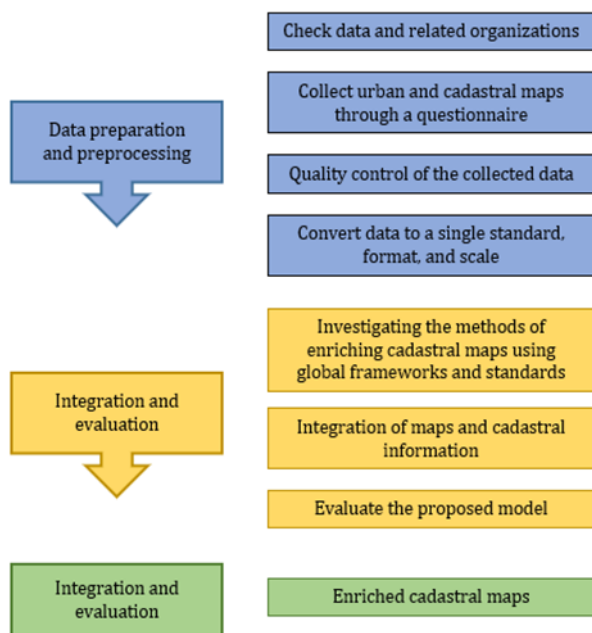


Figure 1. Cadastral and urban map integration framework.

The purpose of this study is to investigate the challenges in enriching urban and cadastral maps in

District 6 of Tehran Municipality, the capital of Iran, by combining urban maps of the concerned organizations and departments of this megacity. In this research, the existing challenges in preparing and integrating data of Iran's Deed and Property Registration Organization, National Cartographic Center (NCC), and Tehran Municipality have been studied. This research has been undertaken by checking the data of these organizations and filling the questionnaires during the preparation of the data. Finally, different data from these organizations have been compared with each other to find the difficulty of map integration and suggest a way to prepare a map from different sources. The research methodology is illustrated in "Fig. 2".

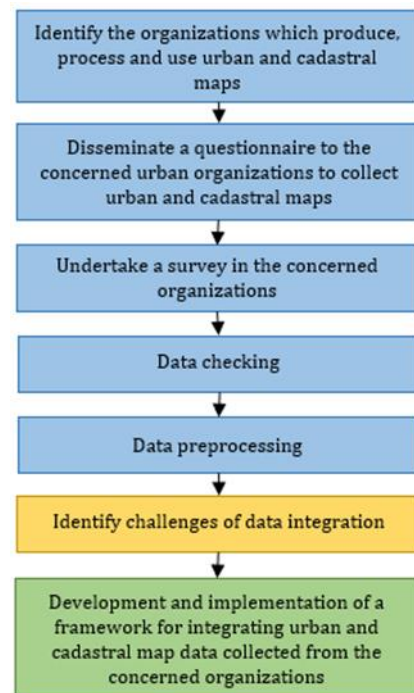


Figure 2. Research methodology.

2.1. Implementation

In this paper, the aforementioned steps have been followed according to "Fig. 2", which are elaborated in sections 2.1.1 to 2.1.5. Finally, the challenges and solutions have been addressed in the result section.

2.1.1. Identification of organizations which have cadastral and urban maps

In metropolitan areas, various organizations require cadastral and urban maps to manage the cities and provide smart services to citizens. Thus, they collect and maintain cadastral and urban maps for their organizations with appropriate accuracy for other organizations.

National Cartographic Center (NCC) of Iran is a public organization that produces national and urban topographic maps. It is worth mentioning that in 2010, NCC was appointed as the custodian of developing National Spatial Data Infrastructure (NSDI).

The Deed and Registration Organization which include Iranian Cadastral Organization, prepares judicial

cadastral maps and documents property registration records. This organization has urban cadastral maps and their registration information.

Tehran Municipality has also produced urban maps for the urban organizations in Tehran that govern and manage the city. Utility organizations are also producing some urban maps with appropriate accuracy for their intended use. These organizations usually use the municipality's maps as base maps and add their features and information to those maps.

In this study, National Cartographic Center, Cadastral Organization and Tehran Municipality have been considered as the main organizations under study, and their maps have been compared. Tehran District 6 has been considered as the study area as shown in "Fig. 3".

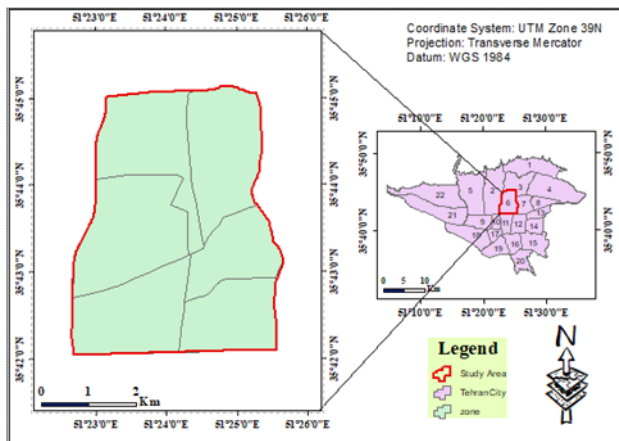


Figure 3. Study area

2.1.2. Development of the questionnaire

To examine the differences and processes followed by the organizations for urban cadastral and spatial data infrastructure production and enrichment, a questionnaire has been prepared with the following questions as mentioned in "Table 1".

Table 1. Questions considered for identifying the available data in the concerned organizations

Number	Questions
1	How to store and share cadastral and urban map data in your organization?
2	What does your organization's metadata include?
3	What is your organization's standard for urban and cadastral map data preparation?
4	What information has been added to the urban and cadastral maps for the spatial and thematic data enrichment in your organizations?
5	What is your organization's data sharing limitation?

2.1.3. Survey of experts in organizations

Some questionnaires in the concerned organizations have been completed with the assistance of some senior experts and examined in order to obtain and check the employed data. The employed process has been mentioned in the following sections. Because of poor metadata for each organization's data and a number of different overlapped data in organizations, this survey is

essential to decide which data are more matches to the urban cadastral and spatial data enrichment process.

2.1.4. Data cheking

National Cartographic Center has produced maps at a scale of 1:2000 in 2002 from a number of urban areas using photogrammetric technique. Various information is available at different map layers.

One of the basic maps of the Cadastre organization is the 1:2000 maps produced by NCC in 2002 to which the registration information has been added. In addition, new properties for which a deed is required to be issued will be re-registered and their maps updated. In order to prepare maps in the Cadastre organization, judicial permits are required to access the registration information. In order to access the geometric data, the desired area must be specified according to the registration areas, and a request must be sent to the Cadastre organization. The registration information is stored in a system designed for this organization. This information is based on the quadruple and boundaries of the property, and there is also information about the whole property that requires registration knowledge and designed software.

Tehran Municipality has also urban maps at different scales that have been produced in different years. Their most recent maps are at the scale of 1:1000 produced in 2014 using photogrammetric and ground surveying methods. In case of modification or change of a property, this item is updated. These maps can be produced according to the municipality's zoning on the intended site. Updated information is added to the maps in the form of different layers and databases.

2.1.5. Data preprocessing

At this stage, the geometric information of the organizations is pre-processed for urban and cadastral map integration and enrichment. Data preprocessing varies according to the map production standards, data format, and scales which suffer from the challenges outlined in "Section 3".

3. Results

The available information about the data is given in "Table 2".

Following standards such as International Organization for Standardization (ISO) and Open Geospatial Consortium (OGC) leads to standardization of definitions and facilitates for the urban and cadastral map integration. The data of Tehran municipality and National Cartographic Center have the same standard, and the basic maps of the Cadastre organization follow these standards. However, the standard for updating the cadastral maps has not been indicated to the users. Tehran municipality still uses Organization for the Advancement of Structured Information Standards (OASIS) open-source data standards. For this research, ISO and OGC standards are considered as final data standards. Different data formats, make it difficult to display and integrate the data with each other.

Furthermore, in the format such as DWG (AutoCAD Drawing Format) used in the National Cartographic Center and the Cadastre Organization, descriptive information cannot be added to features and data must be layered and symbolized to distinguish from each other. However, GIS formats such as shapefile (shp), which is used in Tehran Municipality, support descriptive information for each feature to separate the employed data and the symbology. So, all of the data is converted to shapefile and added attributes based on different layers and labels in AutoCAD. Different years and methods of map data production cause differences in the contents of the maps and their accuracies. Using ground-based methods reasonably enhances the map accuracy. It is necessary for Tehran Municipality and the Cadastre Organization to update their maps due to the new constructions or transfer of property rights. Examining the topology of features identifies inconsistencies in data and makes data more consistent. In addition, modifying the data, makes it possible to implement spatial and thematic analysis on the updated cadastral and urban map data.

Table 2. The employed urban and cadastral maps

Organization	NCC	Cadastre organization	Tehran municipality
Standard	OGC, ISO	Unknown	OGC, ISO, OASIS Open
Scale	1:2000	1:2000	1:1000
Data format	DWG	DWG	SHP
Production year	2002	Since 2002	2014
Production method	Photogram-metric and ground surveying methods	Updating the base map	Photogram-metric and ground surveying methods
Terminated/ Updated?	Terminated	Updated	Updated
Topology correction	No	Yes	Yes

4. Discussion

These differences pose challenges such as the need to harmonize the implemented standards, formats, and scales, as well as validating data topology in the data preprocessing stage. Following a single standard and preparing data in the same format and scale reduces the challenges of data integration and having complete metadata accelerates this process.

5. Conclusion

Unprecedented urbanization necessitates the production, revision and enrichment of urban and cadastral maps for informed urban management. The integration of existing urban and cadastral maps will save cost and time to develop a complete urban data infrastructure. In this study, the existing challenges in integrating the urban and cadastral map of District 6 of Tehran Municipality of the three organizations including Cadastral Organization, NCC and Tehran Municipality, were investigated. The most important challenges

include implementation of inconsistent mapping methods, map scales, data formats, production years, data preparation, sharing standard, and incomplete metadata employed by the concerned organizations. Having a unified map production standard and specifications and production of the harmonized and integrated spatial, semantic and thematic urban and cadastral map data overcome these problems in the urban map data enrichment phase. Furthermore, having complete metadata accelerates the urban and cadastral map preparation and integration. In this research, ISO and OGC standards have been used and tackled. All of the data have been converted to the shapefile format, topologies corrected, and maps generalized to a 1:2000 scale to prepare them for their integration in order to produce an enriched urban and cadastral map.

At the future steps of this research, the data will be examined from semantic differences, descriptive information, and features' spatial boundaries of the urban and cadastral maps collected from organizations. Finally, the preprocessed data will be combined by smart spatial fusion methods such as Rough Set Theory (RST), Dempster-Shafer Theory (DST) and Granular Computing (GrC) enabling a reliable assessment of the enrichment and fusion process.

References

- Atazadeh, B., Olfat, H., & Rajabifard, A. (2021). 3D Cadastre in Australian and New Zealand Jurisdictions: Similarities and Differences. 7th International FIG 3D Cadastre Workshop. New York, 153-184.
- Gelagay, H. (2017). Geospatial Data Sharing Barriers across Organisations and the Possible Solution for Ethiopia. International Journal of Spatial Data Infrastructure Research, (12), 62-84. <https://doi.org/10.2902/1725-0463.2017.12.art4>
- Gózdź, K. J., & van Oosterom, P. J. M. (2016). Developing the information infrastructure based on LADM – the case of Poland. Survey Review, 48(348), 168-180. <https://doi.org/10.1179/1752270615Y.0000000018>
- Kafashan, M. R. (2020). 'Creating a Three-Dimensional Cadastral System for Spatial Reflection of the Third Dimension in Legal Laws: Case Study of Real Estate Parking Documentation, Master's thesis (In Persian with English abstract), Islamic Azad University, Science and Research Branch, Tehran, Iran.
- Olufunmilayo Akinyemi, F., & Uwayezu, E. (2011). An Assessment of the Current State of Spatial Data Sharing in Rwanda. International Journal of Spatial Data Infrastructures Research, (6), 365-387. <https://doi.org/10.2902/1725-0463.2011.06.art16>
- Pierre, E. H. J. (2016). Analysis of data sharing environment and major challenges currently being faced in data sharing in Rwanda.
- Rajabifard, A. (2015). Smart future cities—The role of 3D land & property & cadastre information. The World Cadastre Summit, Congress & Exhibition, Turkey.
- Rajabifard, A., Binns, A., & Williamson, I. (2005). Creating an enabling platform for the delivery of spatial information. The national biennial Conference of the Spatial Sciences Institute, Melbourne, 11.

4th Intercontinental Geoinformation Days

igd.mersin.edu.tr



Mapping urban land use and land cover variations based on support vector machine algorithm: A case study of Sowme'eh Sara County

Khalil Valizadeh Kamran^{*1}, Behnam Khorrami², Hadi Beygi Heidarlou³, Asma Karamat Mirshekarlou⁴

¹University of Tabriz, Faculty of Planning and Environmental Sciences, Department of Remote sensing & GIS, Tabriz, Iran

²Dokuz Eylul University, Graduate School of natural and Applied Sciences, Department of GIS, Izmir, Türkiye

³Transilvania University of Brasov, Department of Forest Engineering, Forest Management Planning and Terrestrial Measurements, Faculty of Silviculture and Forest Engineering, Sirul Beethoven 1, 500123 Brasov, Romania

⁴Urmia University, Forestry Department, Faculty of Natural Resources, Urmia, Iran

Keywords

Land Use/Cover
Support Vector Machine
Classification,
Change Detection
Guilan

Abstract

Land-use change processes present a variety of trajectories depending on local conditions, the regional context, and external forces. Uncontrolled and imprudent alteration of the Land-Cover and Land-Use Change (LCLUC) brings about serious problems in terms of environmental damages. Taking the scale of the LCLUC changes into account, remote sensing technology can be used efficiently and affordably to monitor and detect such large-scale changes. This study is an in-depth analysis of spatial and temporal LCLUC variations in an urban area (Sowme'eh Sara) in Guilan province, northwest Iran. Support Vector Machine (SVM) algorithm and Landsat imageries were utilized to derive the LCLUC variations between 19889 to 2021. The accuracy of the classification was investigated through ground truth data, Google Earth images, and aerial photographs. The results indicate that the SVM-based classification of TM and OLI imageries gives an overall precision of 93%, and 95% respectively which manifests the high feasibility of this technique for deriving LCLUC. According to the mapping results, a distinctive evolution in LCLUC is seen over the study area where consistent urban consolidation with changes of the wetland typology involving marsh degradation, gains from agro-forest land, or sparsely vegetated areas.

1. Introduction

Land-Cover and Land-Use Change (LCLUC) mapping and assessment are among the core areas of remote sensing data applications (King 2002; Foody 2002). Remote sensing data has been an attractive source in the determination of land cover thematic mapping, providing valuable information for delineating the extent of LCLUC classes, as well as LCLUC analysis and risk analysis at various scales (Kavzoglu and Colkesen 2009). Producing LCLUC thematic maps using remote sensing data is commonly performed by digital image classification (Chintan et al. 2004). Generally, a widely used categorization of classification techniques includes three main groups of approaches: pixel-based, sub-pixel, and object-based classification techniques. Pixel-based techniques perform classification by assigning pixels to land cover classes and this is achieved by either

supervised or unsupervised classifiers. Sub-pixel classification approaches are generally divided into linear and non-linear unmixing, depending on whether it is assumed that the reflectance at each pixel of the image is a linear or a non-linear respectively combination of the reflectance of each material present within the pixel (Plaza et al. 2009). In object-based classification, each classification task addresses a specific scale, and image information can be represented in different scales based on the average size of image objects. In contrast, the same imagery can be segmented into smaller or larger objects.

Support Vector Machine (SVM) is a learning technique based on Statistical Learning Theory (SLT) which has been introduced for the classification of remote sensing data (Dixon and Candade 2008; Yao et al. 2008). The SVM methods are used to recognize text in images (to convert documents into computer text), handwritten digital and face recognitions (Vapnik 1995;

* Corresponding Author

^{*}(valizadeh@tabrizu.ac.ir) ORCID ID 0000-0003-4648-842X
(khorrami1987@gmail.com) ORCID ID 0000-0003-3265-372X
(hadibeygi@gmail.com) ORCID ID 0000-0002-7070-6178
(karamat6776@gmail.com) ORCID ID 0000-0003-1241-5505

Cite this study

Kamran, K. V., Khorrami, B., Heidarlou, H. B., & Mirshekarlou, A. K. (2022). Mapping urban land use and land cover variations based on support vector machine algorithm: A case study of Sowme'eh Sara County. 4th Intercontinental Geoinformation Days (IGD), 159-162, Tabriz, Iran

Joachims 1998). The results derived from various tests show that the SVM algorithm is capable for comparison with the best classification methods such as artificial neural networks (ANNs), tree classification and so on. Since remote sensing systems are the most common instruments used for LCLUC information, evaluating the performance of the SVM algorithm using images obtained from such systems can have practical applications for land cover classification in this respect. The SVM algorithm has been used in this study to monitor changes related to the 1988, 2001, and 2007.

2. Method

2.1. Overview of the Study Area

Sowme'eh Sara region is located in Guilan Province, between 49°02' to 49°32' E longitude and 37°30' to 37°30' N latitude. The mean height above sea level of the study area is 6 m (Figure 1).

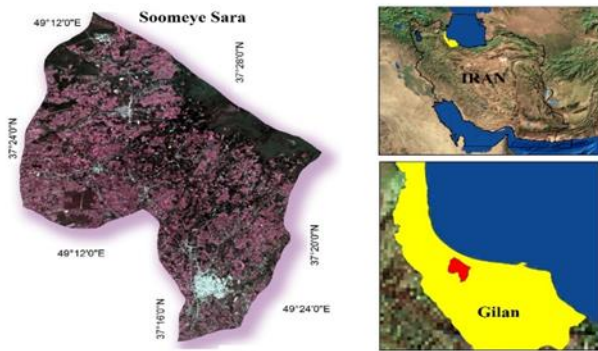


Figure 1. Geographic location of the study area

2.2. Satellite images and reference data

In this study, three predominantly cloud-free Landsat scenes of the Sowme'eh Sara region are used. The first is Landsat TM data obtained on April 24, 2020, and the others are Landsat OLI data on May 05, 2021. The other data used in this study mainly include: (1) aerial photographs of 1994; (2) digitized topographic maps and (3) ground reference data obtained from the land survey with hand-held GPS to determine the characteristics of sampling points.

2.3. Image classification

In order to demonstrate the effectiveness of SVM for heterogeneous land cover mapping, we implemented SVM to map land cover types in the study area. The study area covers a mosaic of different land use cover types. In this study, we utilized training data obtained from intensive field survey, and available 1:50,000 scale topographic maps. Furthermore, we collected additional training data and ground control points for image classification in the entire period by visually interpreting the desired Landsat images and confirming each point's land cover attribution whenever possible with high-resolution imagery in the Google Earth (Beygi Heidarlou et al. 2019). Then, we used the training data to classify our Landsat imageries using a supervised classification maximum likelihood algorithm (MLA) (ENVI, 2014) and

SVM classifier in four classes: (1) wetland, (2) croplands, (3) Marsh, and (4) built-up areas.

2.4. Image classification

Measuring accuracy is important not only for understanding the results derived but also for using these results for decision making process. In this study, we used total accuracy and kappa coefficient for measuring the accuracy of the classified images (Beygi Heidarlou et al. 2020).

2.5. LCLUC detection

The cross-tabulation analysis is carried out to analyze the spatial distribution of different land cover classes and LCLUC. The CROSSTAB module of IDRISI Selva software is employed for performing crosstabulation analysis. Cross classification can be described as a multiple overlay showing all combinations of the logical AND operation. The result is a new image that shows the locations of all combination categories in the original images. Cross classification thus produces a map representation of all non-zero entries in the cross-tabulation table.

3. Results

The SVM method (radial basis function kernel) is used in the study area to monitor changes in land use and land cover during the periods from 1989 to 2021. The land use and land cover classes are determined in four classes including wetland, marsh, croplands, and built-up areas. The training samples are then collected using visual interpretation of satellite images, aerial photographs, and Google Earth image and field observations. The land cover classes, in the next step, are considered in the study area using image characteristics. The separability of classes is also computed using Jefferies- Matusita method. The derived results are shown in Table 1 and 2. Additionally, the land cover maps are prepared for the 1989, 2021 (Figure 2). The statistical parameters related to accuracy measurement including total accuracy and kappa coefficient are extracted for each map as described in Table 3.

Table 1. Separability amount for land cover map classes derived from TM image (1988)

Land use/cover	Wetland	Marsh	Cropland	built-up areas
Wetland	1			
Marsh	1.97	1		
Cropland	1.99	1.87	1	
built-up areas	1.93	2	2	1

3.1. LCLUC analysis

One of the results derived from supervised classification for 1989 and 2021 is the possibility of determining the LCLUC using the map difference method. For this purpose, the land use/cover maps derived from the supervised classification of 1989 are subtracted from

2021. The results derived from this method are shown in Table 4.

Table 2. Separability amount for land cover map classes derived from Landsat 8 (OLI) image (2021)

Land use/cover	Wetland	Marsh	Cropland	Built-up areas
Wetland	1			
Marsh	1.56	1		
Cropland	2	1.87	1	
Built-up areas	1.93	1.93	1.74	1

Table 3. Accuracy statistics for the classification result during the years 1988, 2021

Image	Overall accuracy	Kappa coefficient
TM (1989)	95.60	0.94
OLI (2021)	94.40	0.93

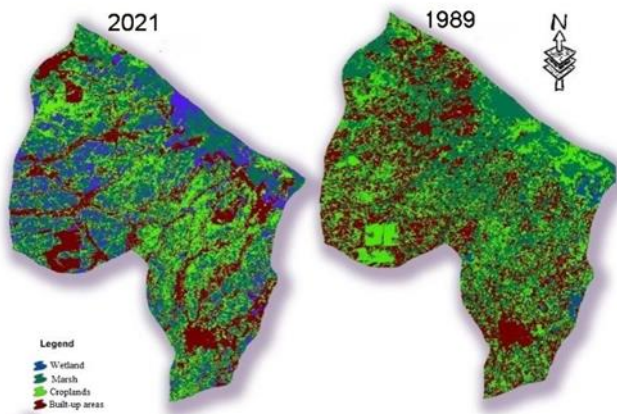


Figure 2. Land use/cover maps of the study area

Table 4. Cross-tabulation of land cover classes between 1989 and 2021 (in percentage)

Image	Wetland	Marsh	Cropland	Built-up areas
Wetland	78.43	35.50	2.08	11.34
Marsh	19.50	98.04	86.33	0
Cropland	2.05	66.20	12.70	94.35
Built-up areas	4.58	2.45	89.60	99
Class change	26.55	38.30	35.60	48.95
Map difference	1.60	4.05	21.80	32.45

3.2. Monitoring changes

The new map is created by crossing of two classified maps during the periods 1989 and 2021 (Figure 3), which helps to compare the changes in land use and land cover classes during 1989 to 2021. Table 4 includes the results derived from the figure. The most positive change (increase) has occurred for built-up areas due to construction and the most negative change (decrease) occurred for croplands.

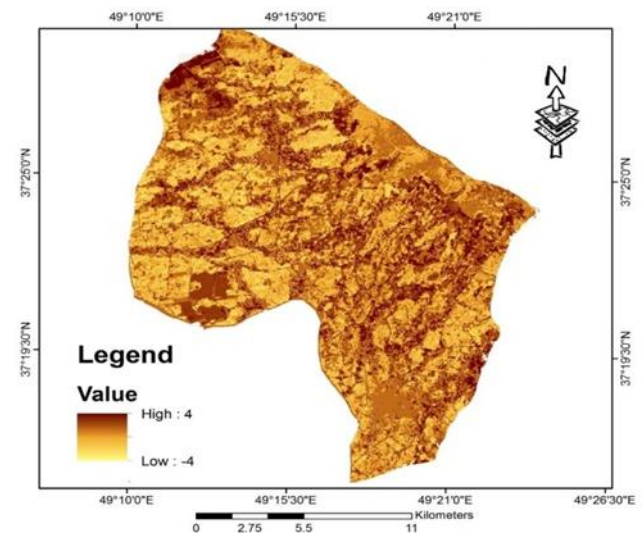


Figure 3. Change detection map- Differencing between the two classified maps related to 1988 -2021

4. Discussion

The results of this study clearly show how planning instruments, whether sectoral or territorial, influence the dynamics of land-use change in a township area with mountain characteristics. In this study, post-classification comparison method is applied to monitor changes. Since the changes in land use and land cover of Sowme'eh Sara dam watershed are evident, an attempt is made in this study to detect them using the aforementioned method. Many researchers have shown in their studies that post-classification comparison method is one of the most accurate approaches to monitor the changes in land use and land cover.

The land use and land cover information can be extracted from past and present using satellite images. The results can be combined with other data and map information. The effects of land use and land cover development on other uses and changes can be evaluated and determined specially by using the post-classification comparison method and also binary combination of land use maps. One of the objectives of this study is to determine the nature of changes in land use and land cover. However, the traditional classification algorithms such as statistical methods cannot provide the optimum results due to low flexibility and parametric varieties, just like the maximum likelihood method, which is not able to provide optimum results in the absence of normal training data due to its dependence on Gaussian statistics model.

In recent years, accordingly, a new technique based on statistical learning theory called Support Vector Machines (SVM) has been devised to classify the remote sensing data. The SVM, in this study, is adopted to classify the land use and land cover of Sowme'eh Sara township during the periods 1998-2021. Four types of kernels (linear, polynomial, radial and sigmoid) are considered for SVM classifications. Among them, the radial basis function (RBF) kernel is used and the results derived are for the post-classification comparison.

The most positive change (increase), in Sowme'eh Sara township, has occurred for built-up areas, during

the period 1988 to 2021. The percentages of conversion into built-up areas are 40.20%, 30.85%, 9.39%, 5.20% and 29.07%, respectively, for wetland, croplands and marsh. Meanwhile, the most negative change (decrease has occurred for wetland during the period. In this period, 65.90% of wetland has remained unchanged; however, 7.50 % has been converted to built-up areas, 5.08% to marsh, 18.98% to croplands. After all, it can be stated that if the purpose of changes monitoring is to detect the nature of changes (type and direction of changes), then the post-classification comparison is the best method in this regard. The accuracy values of land cover maps derived from satellite data classification by using the support vector machine algorithm are equal to 93%, 95% for TM and OLI, respectively. This indicates a high accuracy of SVM algorithm in satellite data classification studies.

5. Conclusion

The management of common land, even in an informal way, introduces differences to land-use trajectories, involving the development of wetland and marsh through the introduction of new species and wetland (shore line) maintenance, leading to smaller subdivisions in patterns of land use. Therefore, it is local factors, whether emerging from planning methods or community involvement in land management, which explain land-use change and create greater benefits for the communities, and may also lead to future forms of intervention in this township mountainous community.

References

- Beygi Heidarlou, H., Banj Shafiei, A., Erfanian, M., Tayyebi, A., & Alijanpour, A. (2019). Effects of preservation policy on land use changes in Iranian Northern Zagros forests. *Land use policy*, 81, 76-90.
- Beygi Heidarlou, H., Banj Shafiei, A., Erfanian, M., Tayyebi, A., & Alijanpour, A. (2020). Armed conflict and land-use changes: Insights from Iraq-Iran war in Zagros forests. *Forest Policy and Economics*, 118, 102246.
- ENVI User's Guide (2014). ENVI user's manual, ITT Visual Information Solutions. Fassnacht, K. S., Cohen, W. B., & Spies, T. A. 2006. Key issues in making and using satellite-based maps in ecology: A primer. *Forest Ecology and Management*, 222, 167-181.
- Foody, G. M. (2000). Mapping land cover from remotely sensed data with a softened feedforward neural network classification. *Journal of Intelligent and Robotic Systems*, 29(4), 433-449.
- Joachims, T. (1998, April). Text categorization with support vector machines: Learning with many relevant features. In *European conference on machine learning* (pp. 137-142). Springer, Berlin, Heidelberg.
- Kavzoglu, T., & Colkesen, I. (2009). A kernel functions analysis for support vector machines for land cover classification. *International Journal of Applied Earth Observation and Geoinformation*, 11(5), 352-359.
- King, R. B. (2002). Land cover mapping principles: a return to interpretation fundamentals. *International Journal of Remote Sensing*, 23(18), 3525-3545.
- Plaza, J., Plaza, A., Perez, R., & Martinez, P. (2009). On the use of small training sets for neural network-based characterization of mixed pixels in remotely sensed hyperspectral images. *Pattern Recognition*, 42(11), 3032-3045.
- Shah, C. A., Arora, M. K., & Varshney, P. K. (2004). Unsupervised classification of hyperspectral data: an ICA mixture model-based approach. *International Journal of Remote Sensing*, 25(2), 481-487.
- Vapnik, V. (1999). *The nature of statistical learning theory*. Springer science & business media.

4th Intercontinental Geoinformation Days

igd.mersin.edu.tr



Optimal weighting approach for real-time positioning with Android smartphones

Berkay Bahadur *¹ ¹ Hacettepe University, Department of Geomatics Engineering, Ankara, Türkiye**Keywords**

GNSS
Android
Smartphone
Weighting
Carrier to noise ratio

Abstract

The performance of real-time positioning with Android smartphones is evaluated in this study considering two fundamental weighting approaches, which rely on satellite elevation angle and carrier to noise ratio (C/N₀) values, respectively. The experimental test conducted in this study includes the observation dataset of Xiaomi Mi 8 and Google Pixel 4 smartphones collected by the Android GPS team in the kinematic environment. First, this study analyzes the observation dataset to understand the stochastic characteristics of observations acquired from smartphones. The analyses revealed that the dependency of smartphone observations on satellite elevation angle is considerably lower compared with high-grade geodetic receivers. The experimental tests indicated that it is possible to obtain more accurate positioning solutions when applying the C/N₀-dependent weighting approach. Compared with the elevation-dependent weighting approach, the C/N₀-dependent weighting approach improves the positioning performance of Xiaomi Mi 8 and Google Pixel 4 smartphones by 30.1% and 36.5%, respectively.

1. Introduction

The raw GNSS (Global Navigation Satellite System) observations collected from Android devices have been accessible since 2016. From this date on, positioning, navigation, and timing applications with Android devices, especially smartphones, have received considerable interest from the GNSS community. The main reason behind this substantial attention is that low-cost chipsets on smart devices still dominate the GNSS mass market (GSA 2019). However, due to the specific restrictions, such as the high noise level of observations, low protection against the multipath effect, and discontinuities in carrier phase observations, it is very demanding to achieve high positioning performance with smartphones (Paziewski et al. 2019). As a result, many studies have been made in recent years to evaluate and advance the positioning performance of smartphones based on the positioning techniques of real-time kinematic (RTK), single- and dual-frequency Precise Point Positioning (PPP) (Robustelli et al. 2019; Odolinski and Teunissen 2019; Liu et al. 2021).

In the current literature, many studies have analyzed the performance of smartphones with relative or differential positioning techniques that depend on

reference stations equipped with geodetic receivers (Geng and Li 2019; Gao et al. 2021). Besides, some studies employ another smartphone as the reference station, named smartphone-to-smartphone positioning (Paziewski et al. 2021). As revealed by these studies, it is possible to reach relatively high positioning accuracy with smartphones using relative or differential positioning techniques. Still, the base station(s) requirement is the main limitation of these techniques. Also, relative or differential positioning techniques require carrier phase observations to achieve high positioning accuracy, although carrier phase observations acquired from smartphones are usually disrupted because of missing phase observations and abrupt phase shifts (Paziewski et al. 2019; Zangenehnejad and Gao 2021). On the other side, absolute positioning applications that include a single GNSS receiver are of great interest to GNSS users. This substantial interest is mainly because of eliminating the requirement for a simultaneous reference station or network. In addition, absolute positioning techniques can present the desired positioning accuracy for most location-based services applied with smartphones. Therefore, a considerable number of studies have recently been conducted for standalone positioning

* Corresponding Author

* (berkaybahadur@hacettepe.edu.tr) ORCID ID 0000-0003-3169-8862

Cite this study

Bahadur, B. (2022). Optimal weighting approach for real-time positioning with Android smartphones. 4th Intercontinental Geoinformation Days (IGD), 163-166, Tabriz, Iran

applications with smartphone observations in the literature (Aggrey et al. 2020; Wang et al. 2020; Robustelli et al. 2021).

Regardless of the applied positioning technique, the application of a proper stochastic model is one of the most critical points for achieving high positioning accuracy with smartphones. Since smartphones generally contain relatively low-cost antennas, the stochastic characteristics of observations acquired from smartphones are quite different from those of geodetic GNSS receivers. Therefore, it is crucial to apply an optimal weighting scheme that is able to reflect actual stochastic characteristics of observations in smartphone positioning. In the current literature, there has been a limited number of studies that specifically analyzed the positioning performance of smartphones in terms of observation weighting approaches. In this regard, this study aims at analyzing the performance of real-time standalone positioning with smartphones on the basis of observation weighting approaches. Firstly, this study evaluates the characteristics of smartphone observations collected in the challenging environment, i.e., in the urban area and kinematic mode. Also, two fundamental weighting approaches, which are respectively dependent on elevation angle and carrier to noise ratio (C/N0), are assessed for real-time positioning performance with smartphones.

2. Method

This study includes the standalone positioning that relies on single-frequency code pseudorange observations. Basically, code pseudorange observation (P) on the i th frequency can be expressed by the following equation:

$$P_{i,r}^{s,k} = \rho_r^{s,k} + c(dt_r^s - dT^{s,k}) + T_r^{s,k} + I_i^{s,k} + c(b_{i,r}^s - B_i^{s,k}) + \varepsilon(P_{i,r}^{s,k}) \quad (1)$$

where subscript r indicates the receiver, while superscripts s and k demonstrate the GNSS index and satellite number. Additionally, ρ is the geometric range between the receiver and satellite, c is the velocity of light, dt and dT are the receiver and satellite clock offsets, T is the tropospheric delay, I is the first-order ionospheric delay on i th frequency, b and B are the receiver and satellite code hardware biases, respectively and ε indicates the observation noise and multipath for the related observation.

In this study, single-frequency code observations on L1, G1, E1, and B1 frequencies are employed for GPS, GLONASS, Galileo, and BeiDou satellites, respectively. The International GNSS Service (IGS) Real-time Service (RTS) products are also used to obtain real-time satellite orbits and clock corrections. Besides, the ionospheric delay is mitigated using the ionospheric corrections provided in IGS-RTS products. On the other side, the tropospheric delay is corrected by the Saastamoinen model (1972) combined with the VMF3 (Vienna Mapping Functions 3) and GPT3 (Global Pressure and Temperature 3) model (Landskron and Böhm 2018). In this study, an extended version of PPPH is used to

conduct all real-time processes (Bahadur and Nohutcu 2018).

When it comes to observation weights, two weighting approaches, which respectively rely on elevation angles and C/N0 values, are employed in this study. Traditionally, the elevation-dependent weighting method is expressed as follows:

$$\sigma_P^2 = \sigma_{P_0}^2 + \sigma_{P_0}^2 \cos(E^2) \quad (2)$$

where $\sigma_{P_0}^2$ denotes the initial observation variance, E is the satellite elevation angle and σ_P^2 represents the related observation variance. The standard deviation of code pseudorange observations is typically used as 0.3 m.

On the other hand, the C/N0 dependent weighting method can be given as follows:

$$\sigma_P^2 = \frac{\alpha \beta_L}{c/n_0} \lambda_c \quad (3)$$

where c/n_0 indicates the carrier-to-noise density calculated as $10^{(C/N0)/10}$ in dB-Hz for C/N0 values, λ_c is the wavelength of P- or C/A-code (29.305 and 293.05 m). α and β_L represent the dimensionless delay lock loop discriminator correlator factor and equivalent code loop noise bandwidth, which are approximated as $\alpha = 0.5$ and $\beta_L = 0.8$ Hz (Langley 1996).

3. Results and Discussion

In this section, the observation dataset utilized in the experimental tests is introduced. Afterward, the observations collected from smartphones are analyzed in several aspects. Finally, this section provides the results obtained from the experimental tests conducted for evaluating the impact of weighting approaches on the performance of real-time positioning with smartphones.

3.1. Observation dataset and analysis

In recent years, the Android GPS team has provided the benchmark dataset so that researchers can test their algorithms and positioning models with Android smartphones. This study employs the benchmark dataset collected from two different smartphones, Xiaomi Mi 8 and Google Pixel 4, placed above the dashboard of the test vehicle moving along a highway in the US San Francisco Sunnyvale on January 5, 2021. The smartphones contain GNSS receivers that can collect dual-frequency multi-GNSS observations with a sampling interval of 1 second. Besides, the dataset provides the ground truth information obtained from an external positioning system that combines the NovAtel SPAN IMU (Inertial Measurement Unit) with RTK positioning. The external coordinates can be used as a reference for assessing the positioning performance of smartphones. Figure 1 indicates the geometry of the experimental setup, including the positions of smartphones, GNSS antenna, and SPAN IMU (Fu et al. 2020).

The observations collected from two different smartphones in the kinematic environment are evaluated in several aspects. These smartphones can collect dual-frequency observations on civilian GNSS

signals only. As an example, code and phase observations on L1 and L5 frequencies can be collected by smartphones for GPS satellites. In this regard, Table 1 indicates the average number of tracked satellites on the corresponding frequencies of GPS, GLONASS, Galileo, and BeiDou constellations per epoch for two smartphones.

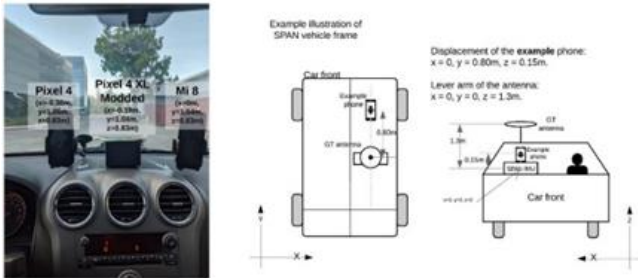


Figure 1. Geometry of the experimental setup used for the observation dataset (Fu et al. 2020).

Table 1. Average number of tracked satellites per epoch for two smartphones.

System	Frequency	Smartphone MI8	PIXEL 4
GPS	L1	8.07	7.93
	L5	5.38	5.36
GLO	G1	4.28	5.80
	E1	4.47	5.96
GAL	E5	4.59	5.60
	B1	3.74	2.68

To evaluate the quality of observations acquired from smartphones, C/N0 values that represent the GNSS signal strength are analyzed as a part of this study. Figure 2 illustrates the C/N0 values of specific GNSS satellites obtained from the Xiaomi Mi 8 and Google Pixel smartphones during the observation period. In this figure, the y-axis represents the C/N0 values (dB-Hz), while the x-axis represents the elevation angle of the corresponding satellite in degree. As can be seen from the figure, there is no considerable dependency between C/N0 values and satellite elevation angle, which is a very different situation from the high-grade geodetic receivers. These results show that the traditional weighting approaches which mainly rely on the satellite elevation angle can be insufficient in representing the actual stochastic characteristics of smartphone observations.

3.2. Positioning performance

The observation dataset was processed based on the elevation- and C/N0-dependent weighting approaches, separately. To evaluate the positioning accuracy, positioning errors were computed as the difference between the acquired coordinates and ground truth from the related positioning process for each epoch in the local coordinate system (North, East, and Up). The epoch-wise coordinates obtained from the external IMU system were used as the ground truth in the computation of positioning errors. Figure 3 indicates the scatter plots of three-dimensional (3D) positioning errors obtained from two weighting approaches for the Mi 8 and Pixel 4 smartphones. In addition, Table 2 shows RMS values of horizontal, vertical, and 3D positioning errors obtained

from the Mi 8 and Pixel 4 smartphones with the elevation- and C/N0-dependent weighting approaches. It can be seen from the table that the C/N0-dependent weighting approach provides a better positioning performance for both smartphones. When compared with the elevation-dependent weighting approach, the C/N0-dependent weighting method improves the 3D positioning accuracy by 30.1% and 36.5% for Mi 8 and Pixel 4 smartphones, respectively.

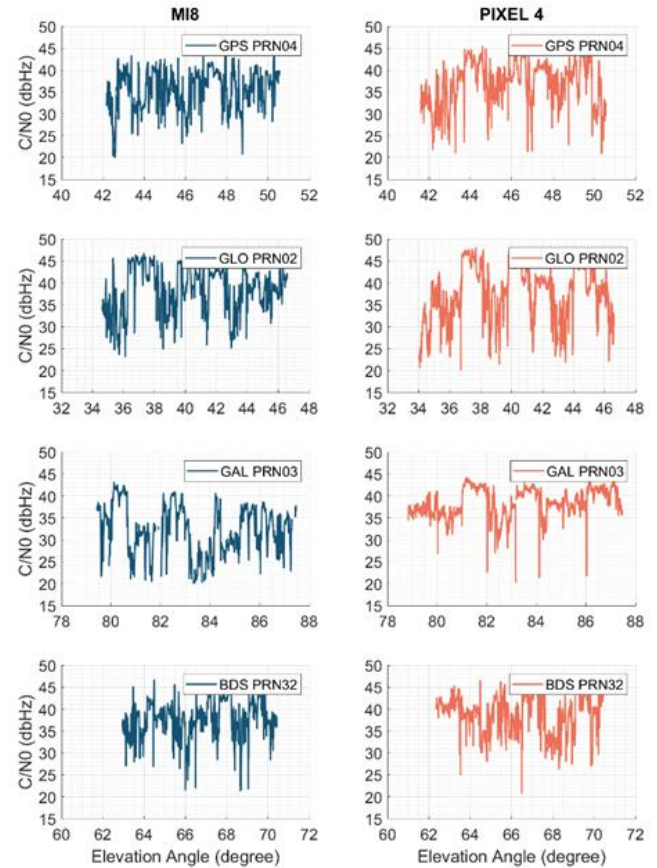


Figure 2. C/N0 values of specific GNSS satellites for Xiaomi Mi 8 and Google Pixel 4 smartphones

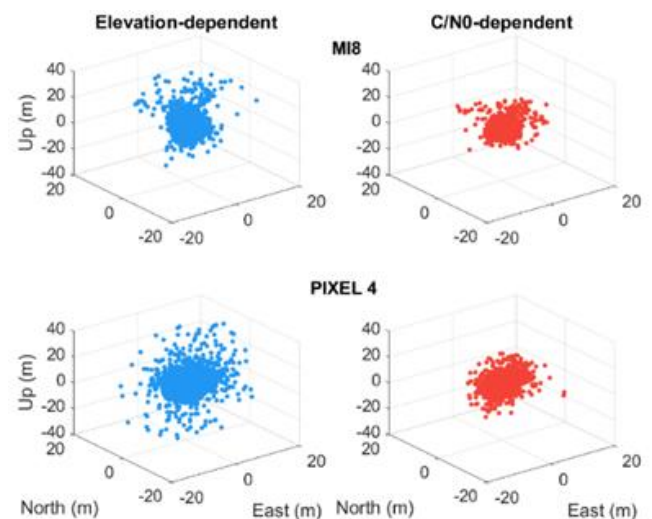


Figure 3. 3D positioning errors of Mi 8 and Pixel 4 smartphones for elevation- and C/N0-dependent weighting approaches

Table 2. RMS values of horizontal, vertical, and 3D positioning errors for Mi 8 and Pixel 4 smartphones with elevation- and C/N0-dependent weighting approach

	Weighting approach	Positioning error		
		Horizontal	Vertical	3D
MI8	Elevation	3.720	4.992	6.673
MI8	C/N0	2.902	3.231	4.663
PIXEL 4	Elevation	5.134	7.483	9.640
PIXEL 4	C/N0	3.344	4.689	6.119

4. Conclusion

This study evaluates the performance of real-time positioning with smartphone observations collected in the kinematic environment using two fundamental weighting approaches, namely elevation- and C/N0-dependent. The observation dataset of two smartphones, including Xiaomi Mi 8 and Google Pixel 4, is utilized in this study to evaluate the impact of two weighting approaches. The results revealed that C/N0 values acquired from smartphones are not significantly dependent on satellite elevation angle, which is a very different situation from the high-grade geodetic receivers. As a result, the traditional weighting approaches which mainly rely on the satellite elevation angle can be insufficient in representing the actual stochastic characteristics of smartphone observations. The experimental tests proved that the C/N0-dependent weighting approach provides considerably better positioning performance for both smartphones when compared with the elevation-dependent weighting strategy. Considering the 3D positioning errors, the C/N0-dependent weighting approach enhances the positioning accuracies of the Mi 8 and Pixel 4 smartphones by 30.1% and 36.5% in comparison with the elevation-dependent weighting approach.

References

- Aggrey, J., Bisnath, S., Naciri, N., Shinghal, G., & Yang, S. (2020). Multi-GNSS precise point positioning with next-generation smartphone measurements. *Journal of Spatial Science*, 65(1), 79-98. <https://doi.org/10.1080/14498596.2019.1664944>
- Bahadur, B., & Nohutcu, M. (2018). PPPH: a MATLAB-based software for multi-GNSS precise point positioning analysis. *GPS Solutions*, 22(4), 1-10. <https://doi.org/10.1007/s10291-018-0777-z>
- Bahadur, B. (2022). A study on the real-time code-based GNSS positioning with Android smartphones. *Measurement*, 194, 111078. <https://doi.org/10.1016/j.measurement.2022.111078>
- Fu, G. M., Khider, M. & van Diggelen, F. (2020). Android Raw GNSS Measurement Datasets for Precise Positioning. In *Proceedings of the 33rd International Technical Meeting of the Satellite Division of The Institute of Navigation* (2020), pp. 1925-1937
- Gao, R., Xu, L., Zhang, B., & Liu, T. (2021). Raw GNSS observations from Android smartphones: Characteristics and short-baseline RTK positioning performance. *Measurement Science and Technology*, 32(8), 084012. <https://doi.org/10.1088/1361-6501/abe56e>
- Geng, J., & Li, G. (2019). On the feasibility of resolving Android GNSS carrier-phase ambiguities. *Journal of Geodesy*, 93(12), 2621-2635. <https://doi.org/10.1007/s00190-019-01323-0>
- GSA, European GNSS Agency (GSA) GNSS Market Report Issue 6, European GNSS Agency: Prague, Czech Republic, 2019. <https://doi.org/10.2878/031762>
- Landskron, D., & Böhm, J. (2018). VMF3/GPT3: refined discrete and empirical troposphere mapping functions. *Journal of Geodesy*, 92(4), 349-360. <https://doi.org/10.1007/s00190-017-1066-2>
- Langley, R. B. (1996). GPS receivers and the observables, in: A. Kleusberg, P.J.G. Teunissen (Eds.), *GPS for Geodesy*, Lecture Notes in Earth Sciences, vol. 60, Springer, Berlin.
- Liu, Q., Gao, C., Peng, Z., Zhang, R., & Shang, R. (2021). Smartphone positioning and accuracy analysis based on real-time regional ionospheric correction model. *Sensors*, 21(11), 3879. <https://doi.org/10.3390/s21113879>
- Odolinski, R., & Teunissen, P. (2019). An assessment of smartphone and low-cost multi-GNSS single-frequency RTK positioning for low, medium and high ionospheric disturbance periods. *Journal of Geodesy*, 93(5), 701-722. <https://doi.org/10.1007/s00190-018-1192-5>
- Paziewski, J., Sieradzki, R., & Baryla, R. (2019). Signal characterization and assessment of code GNSS positioning with low-power consumption smartphones. *GPS Solutions*, 23(4), 1-12. <https://doi.org/10.1007/s10291-019-0892-5>
- Paziewski, J., Fortunato, M., Mazzoni, A., & Odolinski, R. (2021). An analysis of multi-GNSS observations tracked by recent Android smartphones and smartphone-only relative positioning results. *Measurement*, 175, 109162. <https://doi.org/10.1016/j.measurement.2021.109162>
- Robustelli, U., Baiocchi, V., & Pugliano, G. (2019). Assessment of dual frequency GNSS observations from a Xiaomi Mi 8 Android smartphone and positioning performance analysis. *Electronics*, 8(1), 91. <https://doi.org/10.3390/electronics8010091>
- Robustelli, U., Paziewski, J., & Pugliano, G. (2021). Observation quality assessment and performance of GNSS standalone positioning with code pseudoranges of dual-frequency Android smartphones. *Sensors*, 21(6), 2125. <https://doi.org/10.3390/s21062125>
- Saastamoinen, J. (1972). Contributions to the theory of atmospheric refraction. *Bulletin Géodésique* (1946-1975), 105(1), 279-298. <https://doi.org/10.1007/BF02522083>
- Wang, G., Bo, Y., Yu, Q., Li, M., Yin, Z., & Chen, Y. (2020). Ionosphere-Constrained Single-Frequency PPP with an Android Smartphone and Assessment of GNSS Observations. *Sensors*, 20(20), 5917. <https://doi.org/10.3390/s20205917>
- Zangenehnejad, F., & Gao, Y. (2021). GNSS smartphones positioning: Advances, challenges, opportunities, and future perspectives. *Satellite Navigation*, 2(1), 1-23. <https://doi.org/10.1186/s43020-021-00054-y>



4th Intercontinental Geoinformation Days

igd.mersin.edu.tr



Land-use change on Peri-Urban: The role of rural-urban centralized and segregated planning strategy

Naser Shafieisabet^{*1} , Sogand Khaksar¹

¹ Shahid Beheshti University, Faculty of Earth Science, Department of Human Geography and Spatial Planning, Tehran, Iran

Keywords

Government
Local planning
Planning goals

Abstract

The growth and development of urban spaces worldwide have led to dramatic changes in the landscape of peri-urban villages. In Iran, rapid urban sprawl has also reduced agricultural land and increased scattered construction. In this study, the sprawl and its effects on land-use change periphery of the city were measured by satellite imagery using remote sensing (RS) and Geographic Information System (GIS) analysis. Thus, the trend of land-use change periphery the city of Hamedan from 1990 to 2020 separately in 7 types of land use, i.e., residential construction, non-residential construction, convertible wasteland, arable land, garden land, pastures, and the road was inspected. The present survey findings show that the adoption of centralized settlement strategies and separate rural and urban planning in Iran, especially in rural- interconnected urban areas such as the study area, causes land-use change and subsequent spatial anomalies in the city and rural settlements.

1. Introduction

Urbanization is the most important social and economic phenomenon taking place on a large scale worldwide (Sun et al., 2013). In large cities and towns in developing countries, uneven population growth and unplanned activities have led to a lack of infrastructure facilities in cities (Chetty and Surawar 2021, Theobald 2001). However, urban centers cover a small part of the earth's surface. But the rapid expansion of cities has dramatically changed the natural landscape and led to huge changes in the ecosystem of the peripheral (Berling-Wolff and Jianguo 2004, Kappas et al. 2020); It also discusses the natural resources and changes in the valuable agricultural lands of that area (Hart and Milstein 1999). Also, major global trends that have increased competition for land have led to uneven urban development, with half of the world's population living in densely populated cities. The ratio is still increasing (Ludlow and Jupova 2016). In this regard, the adoption of economic adjustment policy, the "top-down development approach," and the accelerated industrialization of the peripheral rural economy with the growth-oriented attitude of urban economies have transformed cities into unplanned areas (Chambers

1994), with the inevitable consequences of uncontrolled expansion. Population growth and migration to urban areas have caused "urban sprawl" (Club 1999). In recent decades, the imposition of new maps and functions by cities on the surrounding spaces has led to disorders in the economic, social, and spatial organization of the surrounding areas (Ebrahimi and Talebi 2013). In other words, the outsourcing of activities and the subsequent uncontrolled expansion of urban constructions to their surrounding spaces, as well as the irregular and irregular growth of these constructions have caused changes in the spatial structure of the suburbs. So that this imbalance in the spatial structure in terms of order and size of settlements, urbanization of rural landscape, change in the basic economy of villages, change of land use, composition of population and activity, are the most important manifestations of change. In addition, due to population density and resource pressure in rapidly expanding cities, destructive environmental damage remains, including the loss of valuable agricultural land, the loss of pristine landscapes, and eventual destruction. Hence, the change of agricultural land use due to the rapid urbanization and its consequence of "urban sprawl" and its environmental and socio-economic consequences is a question that can be answered around

* Corresponding Author

^{*}(n-shafiei@sbu.ac.ir) ORCID ID 0000-0003-3444-6652
(Sogandkhak@yahoo.com) ORCID ID 0000-0002-0439-9608

Cite this study

Shafieisabet, N., & Khaksar, S. (2022). Land-use change on Peri-Urban: The role of rural-urban centralized and segregated planning strategy. 4th Intercontinental Geoinformation Days (IGD), 167-170, Tabriz, Iran

the metropolises and large cities of each country. Thus, the present study has tried with a new approach; In addition to analyzing the change of agricultural land use affected by the consequences of urban sprawl, pay attention to the role of separate rural-urban planning and centralized settlement policies and environmental capacities and internal capabilities of villages in accelerating urban sprawl; And analyze its impact on land-use change; And to provide a scientific solution to reduce the effects of centralist policies.

2. Method

The study area of this research is the southwestern and southeastern part of the city of Hamadan in Iran. In terms of relative position in the study area, the location of rural settlements is different from other rural settlements in Hamadan province. This difference is due to its proximity to Hamedan and its place in its area of direct influence. Also, the existence of wide flatlands, the significant expansion of the network of roads and highways, etc., has given a particular position to the rural settlements of the study area in terms of rising land prices. A descriptive-analytical method was used to measure the consequences of urban sprawl phenomena in the study area. In other words, the method of analysis of land-use changes trends during the three periods of 1990, 2006, and 2020, by satellite imagery and remote sensing (RS) and the GIS analysis. According to US Geological Survey (USGS) standards, analyses were performed on seven types of land use: residential construction, non-residential construction, convertible wasteland, arable land, garden land, and pastures and roads. The consequences of urban sprawl in rural settlements periphery Hamedan city and its effective factors were studied. Data were collected, including Landsat TM Year 1990 and ETM + the Year 2006, OLI 2020, and 1:50000 map of Hamadan, to identify the

phenomena better and compare them with subsequent land-use changes.

3. Results

In recent decades, due to the proliferation of scattered construction and urban sprawl periphery the city of Hamadan, the problem of demolition and alteration of agricultural land and unauthorized construction has occurred, with consequences such as changes in the natural landscape, construction in lands, indiscriminate exploitation of natural resources resulting in ecosystem imbalances. The implementation of urban and rural development projects such as rural, detailed, and comprehensive urban conduction plans and the construction of roads and highways by official and governmental organizations to protect the land ignored agricultural lands. In this way, much of the agricultural land has been legally demolished and altered as part of their implementation. This subject has caused severe changes in the environmental and ecological dimensions of the area.

The results showed that in the Hamadan area, due to urban development and the highest rate of land-use change was observed over 30 years, namely from 1990 to 2020, in arable, horticultural, and pasture lands, respectively, with a total area of 1017 hectares, there were 272 hectares and 189 hectares (Fig. 1). In contrast, residential construction increased by 805 hectares, non-residential construction increased by 346 hectares, and road network increased by 20 hectares. In addition, 307 hectares out of 6446 hectares have become a wasteland, transformed into different construction uses. The statistics show that residential construction is still increasing, with the number of construction sites in the study area increased by about 17.8% from 1990 to 2020. But in contrast, agricultural land declined from 71.2 percent to about 51 percent.

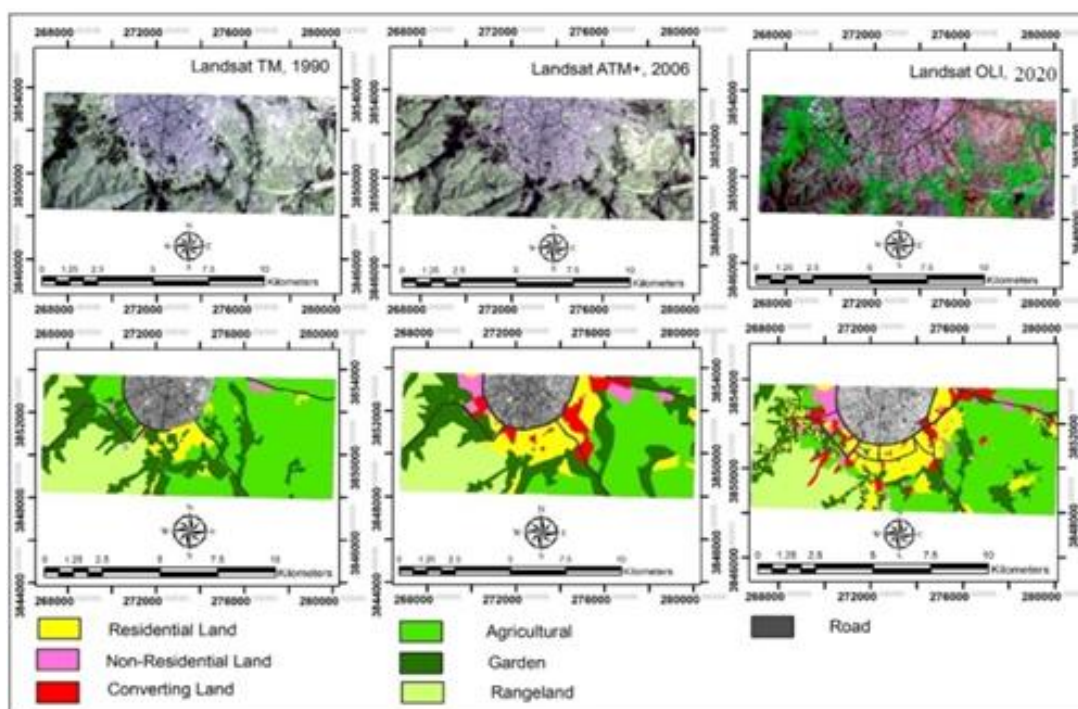


Figure 1. Distribution of the extracted classes in the three study periods from 1990 to 2020

The study of land-use changes in the periphery villages of Hamadan revealed. The rapid spread of the city of Hamedan to the suburbs and surrounding areas was more in the villages that had more cultivated and abandoned agricultural lands and gardens. In addition to the centralized settlement policies that accelerate the city's expansion to the suburbs and periphery areas, this land-use change is more observed in villages with more internal capacity, such as: 1. more extensive cultivation and gardening 2. More extensive abandoned farmland and gardens due to lack of water 3. Nearer to the city and more accessible 4. Broader infrastructure and services 5. The people in their villages were more willing to sell land and convert the agricultural land 6. The fragmentation of agricultural land whose economic surplus from their sales price for construction and machinery is much greater than the surplus from the production and sale of agricultural products. Thus, the negative socio-economic and environmental-ecological consequences of urban sprawl in these villages have been more pronounced due to severe land-use changes and subsequent agricultural performance changes.

3.1. Centralized settlement policies and accelerated urbanization expansion

In the last few decades, the rapid growth and development of urban centers in developing countries, especially Iran, has led to unrest and imbalances in their rural settlements. This phenomenon has been influenced mainly by socio-economic developments and the nature of the political economy in Iran. Rapid migration and population movement to the city of Hamedan increased the need for land for residential and non-residential construction. Therefore, the rapid urbanization has caused a change in the quantity and quality of rangeland and forest lands, soil, surface and groundwater, waste and sewage disposal, changes in the area of agricultural and garden lands, etc., in the study area. Also, the study of demographic changes in rural settlements in the study area has revealed an increasing trend from 1996 to 2016. In other words, 15 villages in the study area were affected by urban sprawl (Table 1).

Table 1. Evolutionary trend of rural settlements population in the study area during 1986-2016

Row	Village	1986	1996	2006	2016
1	Cheshin	1313	1366	1447	1804
2	Cheshmeh Malek	333	242	252	266
3	Silvar	589	467	373	282
4	Sangestan	1324	1227	1127	1195
5	Tafrijan	2410	2404	2134	2149
6	Shourin (on the verge of conversion into city)	3703	3800	4021	4473
7	Ali Abad Taghipour	2510	2598	4453	7759
	Total	12182	12104	13807	17928

It is worth mentioning that between 1986 and 2016, 4 villages in the study area were annexed to Hamedan.

Economic and demographic loads in these settlements are affected mainly by the concentration of many facilities, activities, and services in Hamadan and its surroundings. Due to the high cost of land and housing in Hamadan, job seekers and low-income immigrants are forced to move to the larger rural settlement's periphery, where agricultural lands have been abandoned due to lack of water. Accommodation without a plan has caused an imbalance in the urban-rural space organization. It has led to the duality of traditional and modern texture in the periphery of the village of Hamedan.

3.2. Changes in the amount of garden land

The calculations of the cultivated area of horticultural crops during the last four decades (1973, 1983, 1993, 2003, and 2014) showed that out of the total of 15 villages in the study area, in 1973, the total area of irrigated (irrigated and dry-farming) lands was about 1760 hectares. It was reduced to 1214 hectares in 2014 (Table 2). The amount of garden land calculated based on satellite images in 2020 compared to the Statistics Center of Iran data was about 240 hectares. This difference was due to the drying up of garden lands.

Table 2. Fertile cultivable horticultural land area (irrigated/dry farming) in the rural settlements in the study area per hectare from 1973 to 2013

Row	Village	1973	1983	1993	2003	2013
1	Cheshin	0	20	24	60	54
2	Cheshmeh Malek	27	17	19	45	40
3	Silvar	50	33	27	35	31
4	Tafrijan	6	63	79	67	55
5	Sangestan	200	57	33	54	50
6	Shourin	100	62	57	82	72
	The villages converted into a city	1377	1274	1184	976	912
	Total	1760	1526	1423	1319	1214

4. Conclusion

It is essential to study spatial evolution and change in agricultural land use, which changes slowly and which elements change more rapidly. This study found that agricultural (agricultural and horticultural) land had no significant changes to other areas. However, lands without vegetation (rock mass) and pasture have changed to a lesser extent. Also, the roads' width is noticeable with the increase in construction and the entrance of buildings to the roadside. Because of the use of the road, there has been no significant increase in periphery Hamadan. The sharp increase in urban and residential construction has led to a decrease in arable and garden land and an increase in land abandoned. Another reason for urban sprawl in the study area is the expansion of the roads. The development of roads and public transport has made it easier and less time-consuming to move the rural and urban areas. People go to urban centers for work and money every day and return to their neighborhoods at night to settle in the suburbs.

According to the study's findings, rural immigrants who come to the area's central city, whose income level does not meet the city's cost, turn to suburbs where economic conditions are more favorable. It is noteworthy that, due to ethnic and religious beliefs, many rural residents in some settlements close to the city did not wish to sell the land. The sprawl in the study area was discrete. More urban and rural sprawl has also occurred in settlements with greater intrinsic capacity in irrigated land abandoned and more fragmented agricultural lands. For this reason, the influx of population in these rural hubs is accompanied by discrete urban sprawl. Discrete sprawl periphery of the urban area in the study area has led to a severe decline in agricultural land resulting in severe agricultural instability and numerous environmental and socio-economic issues. Also, it has changed the economic performance of the villages from agricultural to non-productive and mainly false services, which has had many negative spatial and socio-economic consequences.

Therefore, the local government will abandon previous measures of centralized residential policies, separate urban and rural planning with a "top-down" approach to Urban expansion, and thus intensify the discrete urban sprawl. Policies and measures are needed to integrate the local government's urban and rural land use planning to prevent this process from continuing. To preserve the environment of rural settlements periphery the city, sustain their natural, social and economic dimensions, and preserve valuable agricultural land, the local government must enforce rigorous and stringent land-use change laws and strict controls. On such constructions, it will prevent any exploitation of landowners and speculators in destroying such areas.

References

- Berling-Wolff, S. & Jianguo, W. (2004) Modeling urban landscape dynamics: A review. *Ecological Research* 19(1), 119-129.
- Chambers, R. (1994) Participatory rural appraisal (PRA): Analysis of experience. *World Development* 22(9), 1253-1268.
- Chetry, V. & Surawar, M. (2021) Assessment of urban sprawl characteristics in Indian cities using remote sensing: case studies of Patna, Ranchi, and Srinagar. *Environment, Development, and Sustainability*, 1-23.
- Club, S. (1999) the dark side of the American Dream: the costs and consequences of suburban sprawl, The Sierra Club San Francisco, CA.
- Ebrahimi, A. & Talebi, J. (2013). Software training in Arc GIS 10.1, Dabigatran bookmaker. p.70.
- Hart, S. L. & Milstein, M. B. (1999) Global sustainability and the creative destruction of industries. *MIT Sloan Management Review* 41(1), 23.
- Kappas, M., Degener, J., Klinge, M., Vitkovskaya, I. & Batyrbayeva, M. (2020) Landscape Dynamics of Drylands across Greater Central Asia: People, Societies and Ecosystems, pp. 143-189, Springer.
- Ludlow, D. & Jupova, K. (2016) URBIS Decision Support for Integrated Urban Governance, pp. 769-776, CORP–Competence Center of Urban and Regional Planning.
- Sun, C., Wu, Z.-f., Lv, Z.-q., Yao, N. and Wei, J.-b. (2013) Quantifying different types of urban growth and the change dynamic in Guangzhou using multi-temporal remote sensing data. *International Journal of Applied Earth Observation and Geoinformation* 21, 409-417.
- Theobald, D. M. (2001). Quantifying urban and rural sprawl using the sprawl index. In *annual conference of the Association of American Geographers in New York, on March 2nd*.



4th Intercontinental Geoinformation Days

igd.mersin.edu.tr



Ecological-geomorphological analysis of surface processes in the Kura-Araz lowland and adjacent territories on the base of remote sensing data

Gasimov Jeyhun Yashar *¹

¹ Institute of Geography named after academician H.A. Aliyev ANAS, Baku, Azerbaijan

Keywords

Exodynamic processes
NDVI
NDMI
NDSI
NBal

Abstract

The relief of the earth's surface is the result of a continuous interaction of endogenous and exogenous forces. This law follows from the general provisions of materialistic dialectics about the unity and conflict of opposites and expresses the basic axiom of geomorphology about the joint action of the main forces of morphogenesis. The purpose of the study is to analyze the distribution and dynamics of exodynamic processes that form ecogeomorphological conditions under the influence of natural and anthropogenic factors. Natural factors include endogenous, such as mud volcanism, modern tectonic movements, buried high, tectonic faults on sediments and the crystalline basement of the territory, exogenous, such as linear and planar erosion, deflation and eolian accumulation, waterlogging, salinization, abrasion, floods, anthropogenic, such as irrigation erosion, intensive grazing, exploitation of oil and gas fields, production of building materials, accelerating unfavorable exodynamic processes. In the study, land use and land cover maps were composed using supervised and unsupervised classification, and different normalized vegetation, humidity, salinity and erosion indices were built using a combination of red, infrared, shortwave infrared spectral channels of the Landsat space image taken in 1976-2017 on the base of aerospace methods and GIS technologies. Based on the interpretation of satellite images and a digital terrain model, the flood process on the Kura and Araz rivers in May 2010, which caused serious damage to the country's economy, was analyzed in detail. The total area of flooding was calculated and the degree of flooding of settlements was assessed. In different years (1976-2017), reductions in the areas of fluvial, arid-denudation and accumulative processes (linear and surface erosion, salinization, deflation and aeolian accumulation, etc.) were revealed based on the analysis of compiled maps of land use and land cover and the construction of normalized vegetation, humidity, salinity and erosion indices. This was due to the expansion of arable land due to anthropogenic activities.

1. Introduction

The unity of endogenous and exodynamic processes on the earth's surface is formed by landscape forms of the earth's crust and geomorphological formations of the environment. Exodynamic processes are activated as a result of a number of natural factors, such as: seismotectonic, tectonic-geomorphological, geological-lithological, hydrogeological and climatic (Fedotov 2019; Jashi et al. 2012). Exodynamic processes of morphogenesis, characterized by high destructive and creative activity, significantly changed the initial appearance of morphostructures formed as a result of endogenous processes, which led to the emergence of

new morphogenetic types of relief - morphosculptures (Chalov 1988). Exodynamic processes interacting with static and endodynamic relief factors, as well as other components of the physical and geographical conditions of the area, play an important role in the formation of the ecological and geomorphological conditions of the area (Khalilov, Gasimov 2017). The nature and intensity of exogenous processes depend on tectonic movements, surface slope, rock lithology, climatic conditions, hydrographic network, vegetation, etc. sedimentation (accumulation) took place in negative landforms with a small slope. With the weakening and stabilization of tectonic movements, the destructive and constructive activity of exogenous processes is gradually balanced,

* Corresponding Author

^{*}(jeyhungasimov@mail.ru) ORCID ID 0000-0001-7516-9319

Cite this study

Yashar, G. J. (2022). Ecological-geomorphological analysis of surface processes in the Kura-Araz lowland and adjacent territories on the base of remote sensing data. 4th Intercontinental Geoinformation Days (IGD), 171-174, Tabriz, Iran

planation and smoothing of the relief occur (Shirinov 1973). Exodynamic processes that represent geomorphological risk and danger in the study area include floods, coastal erosion, gully erosion, surface runoff, clayey karst, deflation, eolian accumulation, salinization, and waterlogging. There are constructive relief-forming processes of exogenous origin, such as alluvial, alluvial-proluvial, alluvial-deltaic, alluvial-lake-former river beds, deluvial, proluvial-deluvial, alluvial-marine accumulation.

2. Method

The purpose of the study is to analyze the distribution and dynamics of exodynamic processes that form ecological and geomorphological conditions under the influence of natural and anthropogenic factors. To achieve this goal, the following tasks were performed: 1) literary sources were analyzed, the reasons for the formation and distribution patterns of exodynamic processes that create geomorphological risks were studied; 2) an information base was created consisting of Landsat satellite images relating to 1976-2017, a digital elevation model (SRTM); 3) The gradations of surface (exodynamic) processes were determined, reflecting the degree of influence on ecological and geomorphological conditions; 4) On the basis of cartographic generalization, the total area of exodynamic processes in the study area was determined.

In the study, supervised and unsupervised classification was performed. Maps of land use and land cover were composed, vegetation, humidity, salinity and erosion indices were built, the flooding process on the Kura and Araz rivers in May 2010 was analyzed based on the analysis of satellite images, a digital elevation model and using GIS technologies. The total area of flooding was calculated and the degree of flooding of settlements was assessed.

2.1. Flood monitoring

Flood processes that occurred in May 2010 were studied on the basis of unsupervised classification of the Landsat-5 TM satellite image (2010) with a resolution of 30 m in the spectral channels: near-infrared (0.76-0.90 μm), mid-infrared (1.55-1.75 μm) and red (0.63-0.69 μm) and digital terrain model (SRTM) analysis.

2.2. Vegetation, humidity, salinization and erosion indices

The study also calculated the vegetation index (1), which indicates the density of vegetation on the site, and identified areas with sparse vegetation (in the range: -1-0.2) and relatively dense (in the range: 0.2-1) gradations:

$$\text{NDVI} = (\text{NIR} - \text{RED}) / (\text{NIR} + \text{RED}) \quad (1)$$

During the study, the normalized differential humidity index (2) was calculated for the summer season of 2002 and 2017:

$$\text{NDMI} = (\text{NIR} - \text{SWIR-1}) / (\text{NIR} + \text{SWIR-1}) \quad (2)$$

To analyze the dynamics of salinity in the study area for 1976-2017, the normalized differential salinity index was established (3):

$$\text{NDSI} = (\text{RED} - \text{NIR}) / (\text{RED} + \text{NIR}) \quad (3)$$

In order to conduct a comparative analysis of areas where erosion, salinization and clayey karst processes occur in the area, the exposure index (4) was used:

$$\text{NBal} = (\text{NIR} - \text{SWIR-1}) / (\text{NIR} + \text{SWIR-1}) \quad (4)$$

In formulas (1)-(4): NIR - near infrared, RED - red, SWIR - shortwave channel of the spectrum.

2.3. Land-use land cover map

The study provided a supervised classification of multispectral space images Landsat 2 MSS (1976) and Landsat 8 OLI & TIRS (2017) at wavelengths of near infrared (NIR - 0.7-0.8 μm), red (Red - 0.6-0.7 μm) and green (Green) (0.5-0.6 μm).

3. Results

In different years (1976-2017), reductions in the areas of fluvial, arid-denudation and accumulative processes (linear erosion, surface washout, salinization, deflation and aeolian accumulation, etc.) were revealed based on the analysis of compiled maps of land use and land cover and the construction of normalized indices vegetation, humidity, salinity and erosion. This was due to the expansion of arable land due to anthropogenic activities.

In areas of intense uplift, valley erosion is developed, in areas with a small slope subject to subsidence, lateral erosion is developed (Shirinov, 1973). They are found in the cones of rivers and their tributaries, in the valleys of the Kura and Araz rivers and in the foothills.

Ravine erosion together with clayey karst led to the formation of areas with the so-called badlands, characterized by high ecological and geomorphological tension, devoid of soil and vegetation, completely unsuitable for economic purposes (Shirinov, 1973). We explain this with breccias of mud volcanoes, characterized by a high degree of mineralization, flowing in the foothills along a dense network of ravines developed on the northeastern slope of the depression and causing salinization in these areas.

Gorge erosion is developed in areas with weak tectonic uplift and a relatively humid climate (warm-temperate climate with 400-600 mm of precipitation per year, dry winters). The soil and vegetation in these areas are not completely degraded, but partially preserved (Shirinov, 1973). In our opinion, gully erosion is characterized by moderate ecological and geomorphological intensity compared to gully erosion.

According to observations, planar washout in all flat and adjacent areas is subject to relative uplift and lacks conditions for accumulation (a slight slope, the presence of silt and a small amount of surface runoff) (Shirinov, 1973). We explain this with the flow of water covering

the surface with a thin layer and leading to erosion of the fertile soil layer.

The Kura-Araz lowland and adjacent areas were a zone of marine and continental accumulation, inherited from the Pliocene and Quaternary period. There are the following genetic types of accumulation prevailing in the study area according to their origin: alluvial, alluvial-proluvial, proluvial, proluvial-deluvial, deluvial, marsh-lake, lake, eolian and saline. In the study area, the area of alluvial accumulation is limited in the deposits of modern river valleys (Kura, Araz and their tributaries), alluvial-proluvial is limited in river fans, and the accumulation of proluvial, proluvial-deluvial and deluvial deposits is limited in the foothills and low-slope areas of the plain (Shirinov, 1973).

Floods in the valleys of the Kura and Araz rivers and their tributaries in March-June are characterized as a destructive natural process. 33.3% of cities and towns, 44.1% of rural settlements, 29.8% of agricultural land, 53% of transport roads, 62.2% of the collector-drainage network, 45.6% of irrigation canals were periodically flooded. In general, during the floods in 2000-2010, the economy of the republic was damaged in the amount of 1.9 billion dollars (66.7% of which was due to floods that occurred only in 2010) (Musayeva, 2013). Flooding in the lower reaches of the Kura River, in 2003 alone, caused about \$65 million in damage to the population (Budagov et al. 2008).

Eolian processes in the form of deflation and eolian accumulation are widespread in areas characterized by arid climate, strong winds, poor vegetation cover, salinity of surface sediments (Shirinov, 1973). As a result of the deflation process, over large areas suitable for use as winter pastures, the soil cover loses its fertility and productivity, and in some cases, as a result of complete absorption, loose sediments that are not resistant to denudation have formed. Fine dust particles with a high degree of mineralization, carried by the wind from salt-ridden lands, settle in the adjacent territories, as well as in the sown fields, causing salinization of these territories as a result of eolian accumulation. According to our observations, eolian accumulation creates positive landforms such as sand dunes and dunes.

Approximately 60% of the lands of the Kura-Araz lowland, which make up an area of 2.2 million hectares, consist of medium and highly saline soils (Mammadov, Khalilov, 2005). In our opinion, both natural and anthropogenic factors influence the development of salinization in the deposits of the Kura-Araz lowland and adjacent territories. Natural factors include arid climatic conditions (temperate semi-desert and dry steppe climate), a high degree of mineralization and filtration capacity of sediments, the proximity of water-resistant strata and groundwater to the surface, and anthropogenic factors include irrigation measures without taking into account physical and geographical conditions (irrigation water infiltration into unconcrete canals and subsequent rise in groundwater levels).

Underground erosion (clay karst) in the Kura-Araz lowland and adjacent territories is observed in the areas of occurrence of Pliocene sandy-argillaceous deposits, mud volcanic breccias and deluvial clays.

Floods and inundations in the Kura and Araz rivers in May 2010 were analyzed by us on the basis of uncontrolled and controlled interpretation carried out on the Landsat-5 TM satellite image (Fig. 1). According to the calculations performed on the digital elevation model (SRTM), the absolute height in the flooded areas varies in the range: -27-0 and 0-219 m, the average height is -14.88 m, the slope varies in the range of 0-40°, and the average the slope reaches 0.98°. In total, more than 610 sq.km of the study area was found to be flooded by the waters of the Kura and Araz rivers. More than 26 sq.km of the flooded area, falls on 159 settlements (9 cities, 5 towns, 145 villages) with a population of more than 565 thousand people (2009). The degree of flooding of settlements was calculated (Table 1).

Table 1. Flooding of settlements in 2010

Degree	City	Settlement	Village	Common	Population	S, km ²
Weak	8	2	121	131	456788	7,25
Moderate	1	2	11	14	91271	8,61
Medium	-	1	4	5	7950	2,37
High	-	-	9	9	9330	8,34
Sum	9	5	145	159	565339	26,6

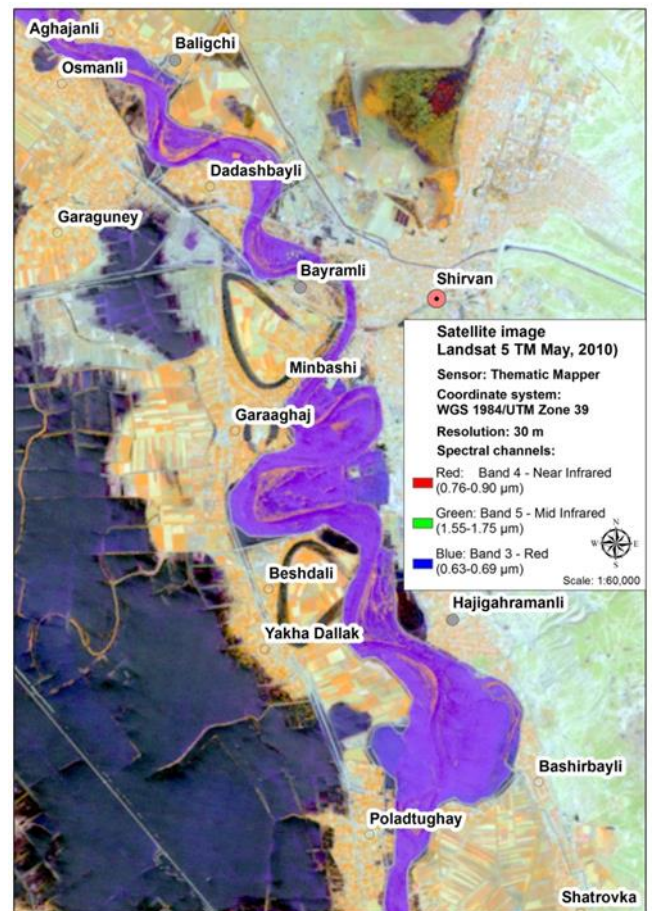


Figure 1. Flooding process in Kura-Araz lowland in May, 2010

4. Conclusion

Due to anthropogenic influence, the area of fluvial, arid-denudation and accumulative processes in the territory is decreasing. Based on the interpretation of the satellite image, it was revealed that as a result of the flood that occurred in May 2010, more than 610 sq.km of the territory adjacent to the floodplains of the Kura and Araz rivers were flooded and caused enormous damage to the population. The degree of flooding was assessed by the area of flooding of 159 settlements and four degrees were divided: weak, moderate, medium and high. 9 settlements with a population of about 10 thousand people were classified as high, as more than 30% of the area of these settlements were flooded. According to the interpretation and comparative analysis of space images, the area of erosion, salinization and eolian processes for 1976-2017 decreased by 2596.0 sq.km, and the average annual decrease for 41 years reached 63.32 sq.km. The average annual decrease of exodynamic processes in the study area was 25.26 sq.km according to the estimated vegetation index (NDVI) for 1976-2017, 30.01 sq.km according to the salinity index (NDSI), 80.77 sq.km according to the moisture index (NDMI), 192.43 sq.km according to the erosion index (NBaI).

In conclusion, let us note that anthropogenic influence plays an important role in the development of such processes as salinization, waterlogging, etc. The failure of main, inter-farm and intra-farm canals, as well as improper irrigation and drainage, led to the infiltration of irrigation water into irrigated areas, an increase in the level of groundwater, swamping and salinization processes. In conclusion, we note that all harmful exodynamic processes create geomorphological risk and danger. But the potential damage can be quite different. The whole complex of these exodynamic processes leads to desertification. This study can serve as a theoretical and practical basis for monitoring and taking measures to protect the environment in various areas with similar environmental problems.

In order to regulate the level of groundwater and prevent the development of the processes of re-

salinization and waterlogging caused by them in the study area, abandoned, main and inter-farm canals and collectors should be concreted, drip irrigation should also be introduced, and in areas with intensive development of wetlands and saline lands to expand a closed horizontal collector-drainage system and vertical drainage to flush soils.

References

- Budagov, B. A., Mamedov, R. M., Alizade, E. K. et al. (2008). Natural and anthropogenic disasters in the territory of Azerbaijan. *Proceedings of the National Academy of Sciences of Azerbaijan Earth Sciences* No. 1: 121-133.
- Mammadov, G. Sh, & Khalilov, M. Y. (2005). *Ecology and environmental protection*. Elm, Baku.
- Musayeva, M. R. (2013). *Economic and geographical study of the impact of floods on the development of the economy and the territorial organization of the Republic of Azerbaijan*. Abstract of the dissertation of Doctor of Philosophical Sciences in Geography, Baku.
- Fedotov, V. I., & Fedotov, S. V. (2019). Modern exodynamic processes in the Voronezh Don region. *Bulletin of VSU, Series: Geology*, No. 1: 15-20.
- Khalilov, H. A., & Gasimov, J. Y. (2017). Assessment of ecogeomorphological conditions of the eastern part of the Kura depression based on exodynamic processes. *Bulletin of the Baku University, Series of Natural Sciences*, No. 1: 151-158.
- Chalov, R. S. (1988). *Laws of fluvial geomorphology. Problems of Theoretical Geomorphology*, Nauka, Moscow: 111-121.
- Shirinov, N. Sh. (1973). *Geomorphological structure of the Kuro-Araks depression (Morphosculptures)*, Elm, Baku.
- Jashi, G., Chelidze, T., & Chichinadze, V. (2011-2012). Seismotectonic movements – one of the main receptors in exodynamic processes. *Journal of Georgian Geophysical Society, Issue (A), Physics of Solid Earth*, v.15a: 138-141.



4th Intercontinental Geoinformation Days

igd.mersin.edu.tr



Land cover classification in an arid landscape of Iran using Landsat 8 OLI science products: Performance assessment of machine learning algorithms

Ali Keshavarzi¹, Fuat Kaya^{*2}, Gordana Kaplan³, Levent Başayığit²

¹University of Tehran, Laboratory of Remote Sensing and GIS, Department of Soil Science, Karaj, Iran

²Isparta University of Applied Sciences, Faculty of Agriculture, Department of Soil Science and Plant Nutrition, Isparta, Türkiye

³Eskisehir Technical University, Institute of Earth and Space Sciences, Eskişehir, Türkiye

Keywords

Remote sensing
Landsat 8 OLI
Land cover class
Machine learning
Agricultural areas

Abstract

The spatial variation of several dynamic chemical soil characteristics is greatly influenced by land cover and land use. High-accuracy land use and land cover (LULC) classification have enormous promise for temporal scale evaluation of soil characteristics. The study aims to evaluate the performance of linear and non-linear classification methods in determining land cover classes by using remotely sensed time-series Landsat 8 OLI satellite data in an area where semi-arid agricultural activities are active. Four LULC classes were identified, and Landsat 8 images were classified using three supervised machine learning classifiers. When the producer's accuracy, user's accuracy, overall accuracy, and Cohen kappa coefficient were taken into account, it was observed that support vector machines (SVMs) and random forest (RF) algorithms produced more accurate results than multinomial logistic regression (MNL). The SVMs had the highest overall classification accuracy of 96.00 % and a kappa coefficient of 0.93 on the test set. It is recommended to compare the efficiency of satellite data with different spectral and spatial resolutions.

1. Introduction

Analysts and decision-makers in government, civil society, industry, and finance rely on land use/land cover (LULC) maps to keep tabs on global environmental change and assess the risk to long-term livelihoods and development (Karra et al. 2020). Typically, land use classification schemes include agricultural areas, forests, grassland, water, and artificial regions. Land-use type information is critical for the spatial study of soil attributes because it reflects the different effects of organism-associated factors on soil (Yigini et al. 2018; Shi et al. 2021). Land cover/land use maps can be beneficial for constructing land-use sensitive contextual indicators of soil and ecosystem health that are valid for spatially explicit monitoring of ecosystem health (Vågen et al. 2016). Land use maps are an important determinant in the spatial prediction of soil organic carbon in Mediterranean biogeography (Schillaci et al. 2017). Land use data collected during soil sampling can

serve as training examples for land use classification. With this format, the land use maps that are eventually produced can be beneficial for the qualitative assessment of soil scientists.

In different geographies, machine learning algorithms enabled the generation of large-scale spatial maps with the integration of remote sensing, taking into account a certain number of field observations (training data) to map land use and land cover classes (Shih et al. 2019). In this regard, considering the complexity of geography, algorithms that have the potential to reveal linear and nonlinear relationships are studied comparatively and their results are evaluated (Bouaziz et al. 2017).

This research focused on the application and evaluation of different classification algorithms in obtaining LULC in Northeast Iran. It was conducted to test the potential of machine learning algorithms to classify LULC in areas where active agricultural production is maintained in arid regions.

* Corresponding Author

(alikesavarzi@ut.ac.ir) ORCID ID 0000-0003-3330-6500
*(fuatkaya@isparta.edu.tr) ORCID ID 0000-0003-0011-9020
(kaplangorde@gmail.com) ORCID ID 0000-0001-7522-9924
(leventbasayigit@isparta.edu.tr) ORCID ID 0000-0003-2431-5763

Cite this study

Keshavarzi, A., Kaya, F., Kaplan, G., & Başayığit, L. (2022). Land cover classification in an arid landscape of Iran using Landsat 8 OLI science products: Performance assessment of machine learning algorithms. 4th Intercontinental Geoinformation Days (IGD), 175-179, Tabriz, Iran

2. Method

2.1. Study area

The investigated area was located in northeastern Iran. This area was selected because of the importance of agriculture in this region. Rain harvested water collection ponds, which are particularly useful in Iran's dry regions and may be found in abundance in the study area, also play a significant role in the study. This covers an area of approximately 85 km² located between the coordinates of UTM Northern Zone 40, epsg:32640, 3992370 to 4005540 North, and 668891 to 687491 East (Fig. 1). The climate is characterized as semi-arid with a mean daily temperature of 14.5 °C and mean annual precipitation of 233.7 mm.

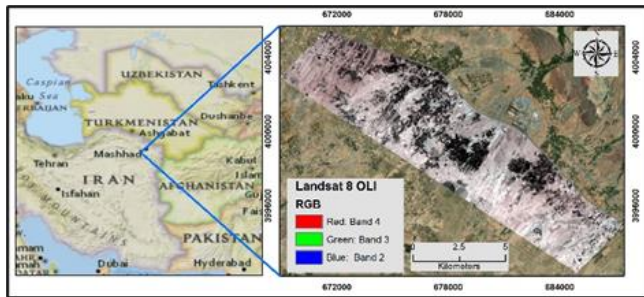


Figure 1. Location of the study area: Landsat 8 natural colors (right); Geographical location in Iran (left)

2.2. Remote sensing data

The Landsat 8 OLI science products multispectral data used in this study was acquired from <https://earthexplorer.usgs.gov> on 30 June 2018, 03 July 2019, 21 July 2020, and 25 August 2021. Before using data from Collection 2 Landsat Level-2 surface reflectance, a scaling factor must be applied. Landsat Collection 2 has a scale factor of SR 0.0000275 and an extra pixel offset of -0.2. (Saylor and Zanter 2021). ArcGIS 10.8-Arctoolbox-related tools (ESRI, 2021) were utilized for the visualization in this study.

2.3. Data collection

Observational data from the ground were gathered from the study region. In addition, the dataset was determined by photo-interpreting the "historical images" in Google Earth®, which was then used to classify the dataset. A total of 1323 observations representing four land cover types were gathered (Table 1). The land cover class was determined using the CORINE level 1 classification nomenclature (CLC 2018; Kozstra et al. 2019). The land use map was created using band 2-7 averages of four linked Landsat 8 OLI images. We used Multinomial logistic regression (Venables and Ripley 2002), Support vector machines (Meyer et al. 2020), and Random Forest (Liaw and Wiener 2002) algorithm from machine learning algorithms that give reliable results in producing land cover or land use maps.

2.4. Modelling process

For classification analyses, the sampled dataset was split into two subsets of training and then tested. Yigini

et al. (2018) recommended splitting criterion of 70% ($n = 926$) for training and 30% ($n = 397$) for validation. Similar data splitting techniques have been common practice in land cover classification studies (Thenkabail et al. 2021). Classification results were evaluated by considering general accuracy and kappa coefficients (Congalton, 1991). R Core Environment and related packages were used for data extraction, modeling, and spatial mapping (R Core Team 2022). The methodological flow chart is present in Fig. 2.

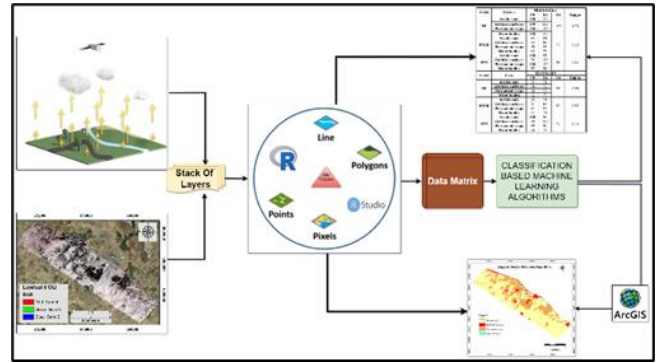


Figure 2. Flowchart of the methodology of the study

Table 1. Number of observations in the training and test sets

Class_Type	TRAINING	TESTING
Arable Lands	316	145
Artificial Surfaces	105	46
Permanent Crops	453	181
Water Bodies	52	25

The spectral signatures from the investigated classes are shown in Fig. 3, where it can be seen that arable lands and artificial surfaces have similar values, while permanent crops and water bodies have significantly lower spectral values in all bands, except for the permanent crops in band 5. The peak of the reflection in the 5th band must have occurred due to the chlorophyll content. This is an expected result for permanent crops.

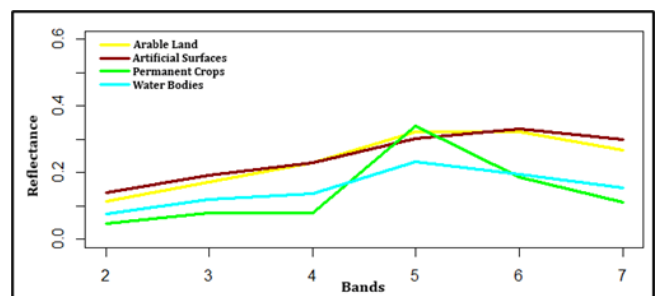


Figure 3. Spectral profile of land cover classes

3. Results

The results from the investigation made in this study are presented in Fig. 4, while the accuracy assessment results are in Table 2. In this study, we compare three different machine learning algorithms for producing land cover over the semi-arid area in Iran. For this purpose, we have classified the study area into four classes, Arable land, Artificial surfaces, Permanent crops, and Water

bodies. The accuracy assessment from the training set showed high accuracy using the RF classifier, followed by SVM. MNLr performed last, especially in the water class, where the producer accuracy was 62%. The testing set, on the other hand, showed the best result with the SVM algorithm, followed by RF. Here also MNLr performed last. Permanent crops were classified with the highest accuracy in all tested models, followed by arable lands, and artificial surfaces. Water class was classified with poor accuracy.

Table 2. Comparisons of the performance of random forest (RF), support vector machines (SVM) and multinomial logistic regression (MNLr) models for the training and the validation datasets (O: Overall, A: Accuracy, P: Producer's, U: User's)

Model	Class ^[1]	TRAINING SET			
		PA	UA	OA	Kappa
RF	Arable land	100	100		
	Artificial surfaces	100	100		
	Permanent crops	100	100	100	1.00
	Water bodies	100	100		
MNLr	Arable land	94	91		
	Artificial surfaces	84	88		
	Permanent crops	98	97	93	0.88
	Water bodies	62	79		
SVM	Arable land	100	97		
	Artificial surfaces	93	100		
	Permanent crops	100	100	99	0.97
	Water bodies	87	98		
Model	Class	TESTING SET			
		PA	UA	OA	Kappa
RF	Arable land	96	91		
	Artificial surfaces	74	92		
	Permanent crops	98	97	93	0.88
	Water bodies	72	79		
MNLr	Arable land	96	91		
	Artificial surfaces	81	87		
	Permanent crops	97	97	92	0.87
	Water bodies	57	74		
SVM	Arable land	100	96		
	Artificial surfaces	83	100		
	Permanent crops	99	98	96	0.93
	Water bodies	76	76		

4. Discussion

In this study, we use Landsat – 8 data for land use mapping of four different classes in a semi-arid area in Iran. For this purpose, we use three different machine learning algorithms, RF, MNLr, and SVM. For the classification, we use a dataset of 1323 points collected from the field and high-resolution imagery. The dataset

was divided into 70% samples for training and 30% for testing.

The results showed the significant success of both SVM and RF algorithms in the classification accuracy assessment parameters. Surprisingly, the water class was the least accurate classified class. Due to the water sensitivity in the green and NIR bands, water is usually classified with high accuracy. It is possible that the accumulated water has been inactive for a certain period and has affected the reflection as a result of the development of biological organisms due to the high organic content (Fig. 3). However, in our study area, not many water bodies can be found. Thus, the training and testing data for the water class is very limited. The water bodies might be also confused with freshly watered croplands, thus, lowering the producer and user accuracy of the water class, and affecting the overall classification accuracy. This problem might be solved using higher spatial resolution imagery, like Sentinel-2, or fusing Landsat-8 and/or Sentinel-2 with Sentinel-1, a microwave active radar sensor, which is very sensitive to water bodies. Also, for relatively small areas like the one selected in the presented study, a UAV of high-spatial resolution imagery might be considered for more accurate mapping. However, as UAV and high-resolution imagery require additional funding, and are more time-consuming for processing, the results obtained in this study are sufficient for drawing a general frame of the study area.

5. Conclusion

This study investigates different machine learning algorithms for land cover classification. We have selected a relatively small area in Iran for this purpose, using Landsat-8 imagery. The four investigated classes were Arable land, Artificial surfaces, Permanent crops, and Water bodies. Two of the investigated algorithms showed high and similar results, RF and SVM. MNLr on the other hand performed last in the overall accuracy and the single class assessment. As there are small water bodies in the study area, the accuracy of the water bodies was not as high as in the other classes. Considering that the water in the area is rain harvested water collection ponds, organic developments are expected to be high. Nature is dynamic and has a complex interaction within itself. When it comes to the detection and identification of natural objects, the selection of satellite images and band preferences affect accuracy more than classification methods. The capability of approaches based on simple mathematics or complex algorithm is controversial. For future studies, we recommend using imagery with higher spatial and temporal resolution, such as Sentinel-2, and for the water bodies, Sentinel-1 can be considered, as it is highly sensitive to water areas.

Acknowledgment

We acknowledge the usage of Landsat Collection 2 L2SP Surface Reflectance data from A subcategory of the Landsat category is Landsat 8 OLI/TIRS C2 L2, which contains the files for each sensor (160 path, 35 Row).

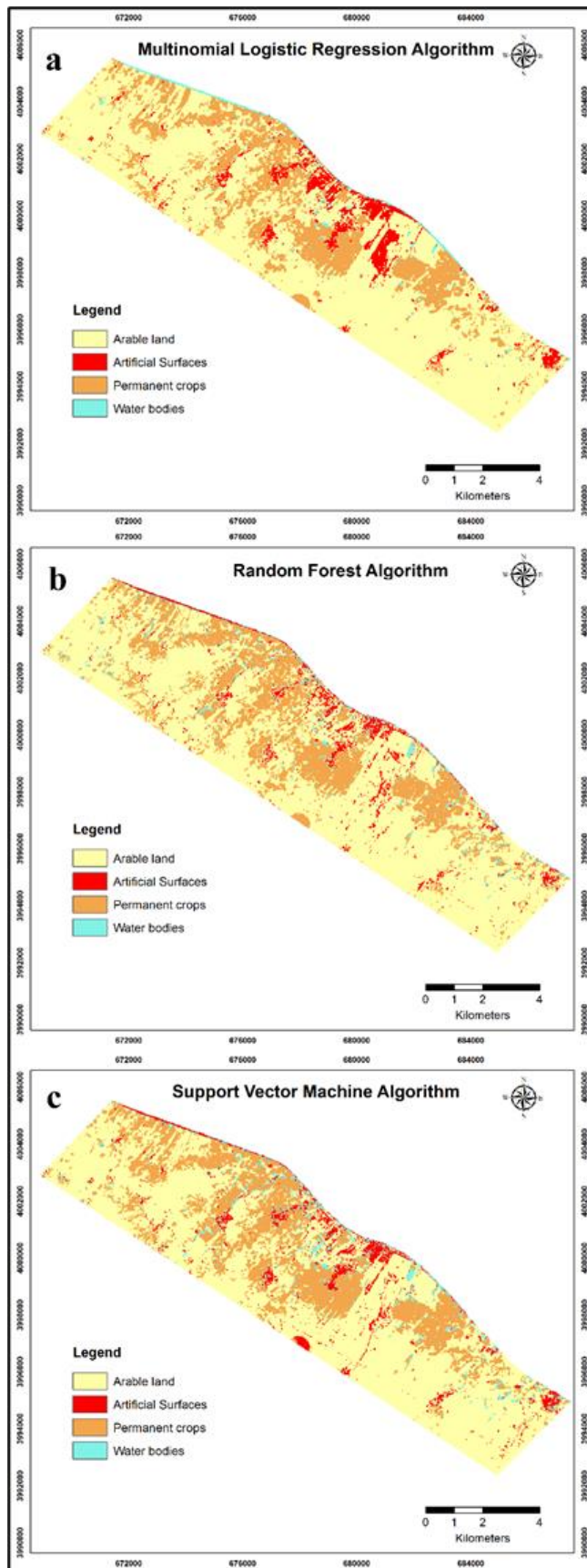


Figure 4. Comparison between a) MNL, b) RF, and c) SVM classification results for land cover types

References

- Bouaziz, M., Eisold, S., & Guermazi, E. (2017). Semiautomatic approach for land cover classification: a remote sensing study for arid climate in southeastern Tunisia. *Euro-Mediterranean Journal for Environmental Integration*, 2(1), 1-7. <https://doi.org/10.1007/s41207-017-0036-7>
- CLC (2018). CORINE land cover-CLC2018 Technical Guidelines. 25 October 2017. Environment Agency Spittelauer Lände 5 A-1090 Wien, Austria.
- Congalton R, (1991). A review of assessing the accuracy of classifications of remotely sensed data. *Remote Sensing of Environment*, 37, 35-46. [https://doi.org/10.1016/0034-4257\(91\)90048-B](https://doi.org/10.1016/0034-4257(91)90048-B).
- ESRI, (2021). ArcGIS user's guide, <http://www.esri.com>.
- Vågen, T. G., Winowiecki, L. A., Tondoh, J. E., Desta, L. T., & Gumbrecht, T. (2016). Mapping of soil properties and land degradation risk in Africa using MODIS reflectance. *Geoderma*, 263, 216-225. <https://doi.org/10.1016/j.geoderma.2015.06.023>
- Karra K, Kontgis C, Statman-Weil Z, Mazzariello J C, Mathis M, Brumby S P, (2021). Global land use/land cover with Sentinel 2 and deep learning. 2021 IEEE International Geoscience and Remote Sensing Symposium IGARSS, pp. 4704-4707. Brussels, Belgium. <https://doi.org/10.1109/IGARSS47720.2021.9553499>
- Kosztra, B., Büttner, G., Hazeu, G., & Arnold, S. (2019). Updated CLC illustrated nomenclature guidelines. European Environment Agency: Wien, Austria, 1-126.
- Meyer D, Dimitriadou E, Hornik K, Weingessel A, Leisch F, (2020). e1071: Misc Functions of the Department of Statistics, Probability Theory Group (Formerly: E1071), TU Wien. R package version 1.7-4.
- R Core Team., 2022. R: A language and environment for statistical computing. R Foundation for Statistical Computing, Vienna, Austria
- Sayler K, Zanter K, (2021). Landsat 8 Collection 2 (C2) Level 2 Science Product (L2SP) Guide LSDS-1619 Version 2.0, EROS Sioux Falls, South Dakota
- Schillaci, C., Acutis, M., Lombardo, L., Lipani, A., Fantappie, M., Märker, M., & Saia, S. (2017). Spatio-temporal topsoil organic carbon mapping of a semi-arid Mediterranean region: The role of land use, soil texture, topographic indices and the influence of remote sensing data to modelling. *Science of the total environment*, 601, 821-832. <https://doi.org/10.1016/j.scitotenv.2017.05.239>
- Shi, T., Hu, X., Guo, L., Su, F., Tu, W., Hu, Z., Liu, H., Yang, C., Wang, J., Zhang, J., & Wu, G. (2021). Digital mapping of zinc in urban topsoil using multisource geospatial data and random forest. *Science of Total Environment*. 148455. <https://doi.org/10.1016/j.scitotenv.2021.148455>
- Shih, H. C., Stow, D. A., & Tsai, Y. H. (2019). Guidance on and comparison of machine learning classifiers for Landsat-based land cover and land use mapping. *International Journal of Remote Sensing*, 40(4), 1248-1274. <https://doi.org/10.1080/01431161.2018.1524179>
- Thenkabail P S, Teluguntla P G, Xiong J, Oliphant A, Congalton R G, Ozdogan M, Foley, D (2021). Global cropland-extent product at 30-m resolution (GCEP30) derived from Landsat satellite time-series data for the year 2015 using multiple machine-

- learning algorithms on Google Earth Engine cloud.
<https://doi.org/10.3133/pp1868>
- Venables W N, Ripley B D, (2002). Modern Applied Statistics with S. Fourth Edition. Springer, New York
- Liaw A, Wiener M, (2002). Classification and regression by randomForest. R News. 2,18-22.
- Yigini, Y, Olmedo G F, Reiter S, Baritz R, Viatkin K, Vargas R, (2018). Soil Organic Carbon Mapping Cookbook 2nd edition. Rome, FAO. 220 pp.



4th Intercontinental Geoinformation Days

igd.mersin.edu.tr



Estimation of land use and land cover changes in Konya Closed Basin

Hüseyin Emre Kaya¹, Vahdettin Demir*¹

¹KTO Karatay University, Engineering and Natural Sciences Faculty, Civil Engineering Department, Konya, Türkiye

Keywords

Remote sensing
CORINE
Konya
Estimation

Abstract

In this study, 28-year change of land cover in Konya Closed Basin between 1990-2018 was examined with CORINE data and mapped with geographic information systems. In addition, using the obtained data and linear regression method, predictions were made for the years 2024, 2030 and 2036. As a result of the study, it was seen that the biggest changes in the Konya Closed Basin were in the wetlands. In addition, artificial areas have also increased significantly. With the decrease in water areas, it has been seen that the basin may face drought problems in the future. As a result of the negative linear relationship in agricultural areas, it was observed that while the cultivated areas decreased, the uncultivated areas increased. On the other hand, there has been a slight decrease in forest areas.

1. Introduction

The land change of the world has been going on for centuries. It has always been a difficult issue for humanity to adapt. Science tried to understand and make sense of this land change, but these studies were very incomplete due to the inadequacy of technology.

CORINE (Coordination of Information on the Environment), is the land cover and usage data produced by computer aided visual interpretation method over satellite images according to the Land Use and Land Cover Use (LULC) Classification determined by the European Environment Agency. Launched in 1985, the project aimed to gather information for the European Union. In 1994, the European Environment Agency included the project in its program. The project, which covers an area of approximately 5.8 million km² and includes 39 countries, is responsible for collecting impartial information about the environment (LULC 2022).

When some important studies in the literature are examined Ateşoğlu (2016), 2006 CORINE data and the western Black Sea Region, Aegean coasts and Central Anatolian Google Earth data were compared and it was determined that the similarities were low. Başayığit (2004), a land use map was created in the Isparta region by using the landsat data of the year 2000. Bayar and

Karabacak (2017), using the 2000, 2006 and 2012 CORINE data, the land change of Ankara province was examined and predictions were made for 2030 according to the Puyravaud formula. Butner et al. (2004) described the methodology of CORINE databases. The results reveal significant land cover changes in some countries. Gençer and others (2015), Lake Eğirdir was compared using the Spot-4 satellite image and the CORINE 2006 map. It was concluded that the 2006 CORINE information should be updated for the whole of Turkey. Gezici and Maktav (2012), change analysis was made in Konya province by using landsat images of 1985, 2000 and 2011. The results obtained in this study showed that controlled and uncontrolled classification methods can be used effectively in the monitoring and management of the urbanization process. Özür and Ataol (2018) applied CORINE data in different parts of Turkey and emphasized the deficiencies of the project data in terms of resolution, accuracy, currency, and classification. Sarı and Özşahin (2016), within the scope of the study, the changes that took place in Tekirdağ province between 2000 and 2015 and the reasons for these changes were investigated. It has been determined that the most obvious change is in continuous city structures.

In this study, unlike the literature, LULC maps and change as well as future LULC situations were tried to be estimated.

* Corresponding Author

(sadeceemre166@gmail.com.tr) ORCID ID 0000-0002-0824-0071
*(vahdettin.demir@karatay.edu.tr) ORCID ID 0000-0002-6590-5658

Cite this study

Kaya, H. E., & Demir, V. (2022). Estimation of land use and land cover changes in Konya Closed Basin. 4th Intercontinental Geoinformation Days (IGD), 180-183, Tabriz, Iran

2. Method

In this study, satellite images and utilities were used to observe and analyze the changes in Konya Closed Basin in different years. CORINE land cover 1990 to 2018 maps were used. The workflow of this study is given in Figure 1.

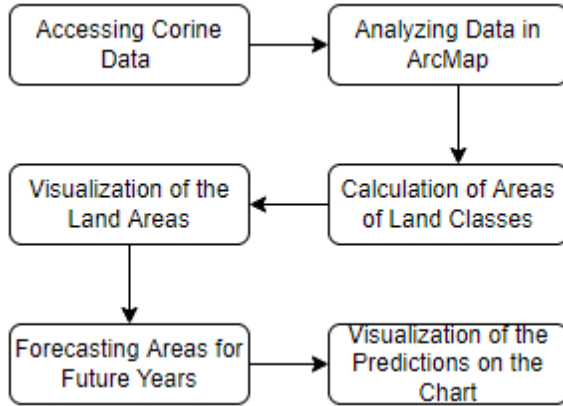


Figure 1. Work flow chart

2.1. Study area

Konya Closed Basin is located in the Central Anatolian borders of Turkey and covers 7% of the country with an area of approximately 5 million hectares (Özür and Ataol 2018). It is located between latitudes 36°51' N and 39°29' N, longitudes 31°36' and 34°52' E. The main river basins of Turkey are given in Figure 2 and the Location of Konya Closed Basin in Figure 3.

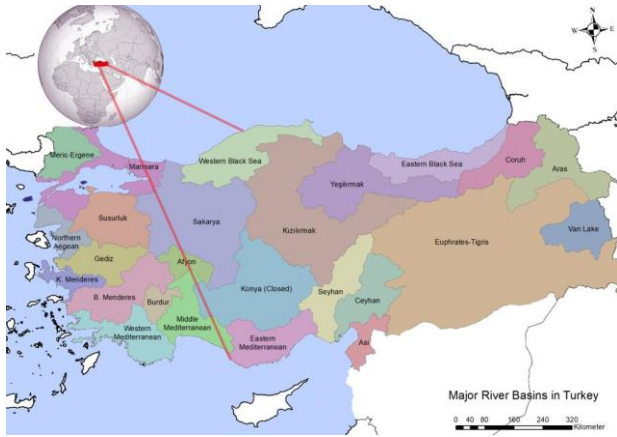


Figure 2. Major River Basins in Turkey



Figure 3. Konya Closed Basin

3. Results

The maps of Konya Closed Basin in different years were prepared in the ArcGIS program using CORINE data and their areas were calculated. The classification map of the Konya Closed Basin in 1990 is given in Figure 4.

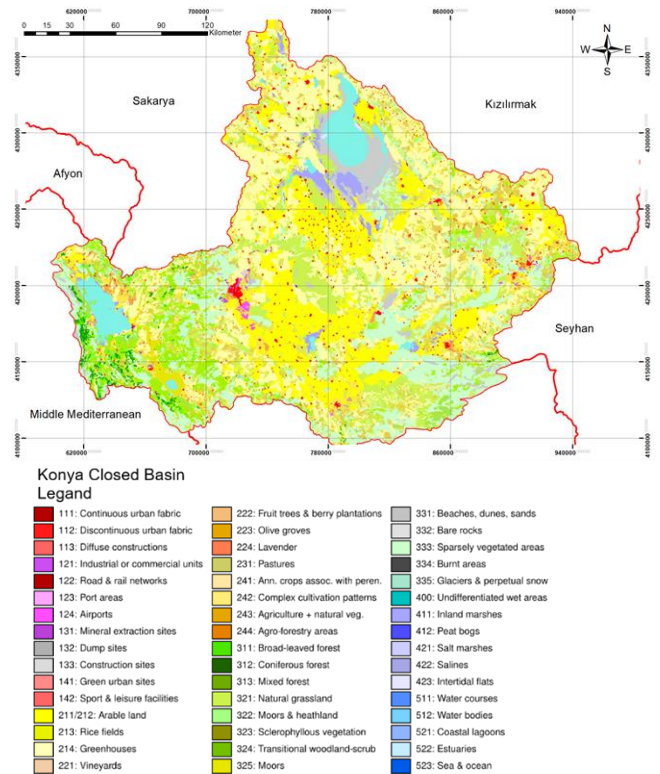


Figure 4. Classification of the year 1990

The classification map of the Konya Closed Basin in 2018 is given in Figure 5.

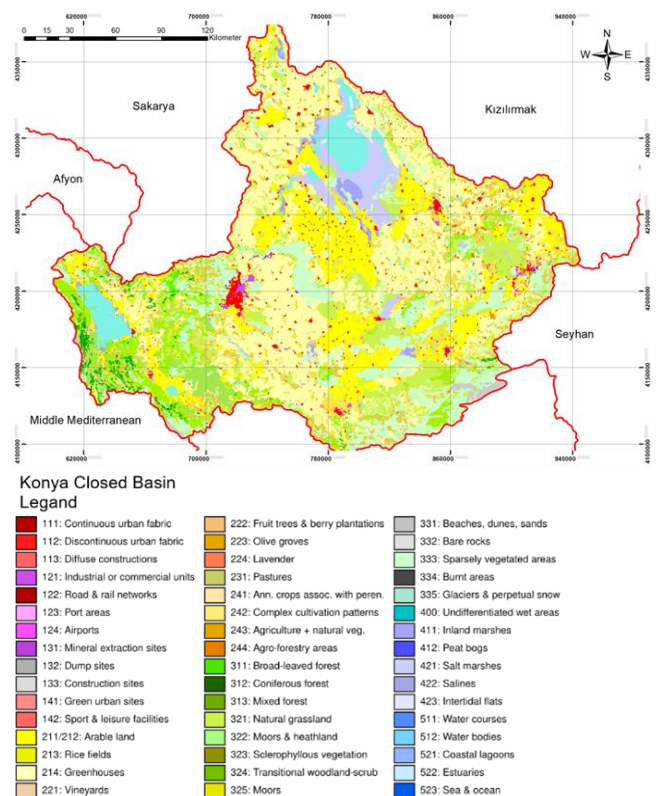


Figure 5. Classification of the year 2018

The areas are gathered under 5 general headings as is given in Table 1.

Table 1. CORINE Areas of Konya Closed Basin

Year	Artificial Surfaces (ha)	Agricultural Areas (ha)	Forest Areas (ha)
1990	81,230	2,779,074.42	1,866,756.45
2018	111,503.75	2,825,881.77	1,662,546.78
Year	Wetlands (ha)	Water Bodies (ha)	
1990	74,589.08	190,191.54	
2018	207,584.14	184,325.28	

Using the analysis, the areas that are likely to occur in the coming years were calculated with the linear regression method. The data obtained as a result of this method are given in table 2 for each title.

Table 2. Linear Regression Data

	R ²	Intersection Coefficient	Year Coefficient
Artificial Surfaces	0.9469	-1977327	1035,63
Agricultural Areas	0.7414	-1317939,7	2056,66
Forest Areas	0.7800	19261604,28	-8734,23
Wetlands	0.7229	-11545993	5833,92
Water Bodies	0.8380	571495.7	-191,98

The estimation of 2024, 2030 and 2036 using linear regression data is given in Table 3.

Table 3. Forecasts for the coming years

Year	Artificial Surfaces (ha)	Agricultural Areas (ha)	Forest Areas (ha)
2024	118,807.21	2,844,750.80	1,583,509.54
2030	125,021.05	2,857,090.79	1,531,104.12
2036	131,234.88	2,869,430.78	1,478,698.70
Year	Wetlands (ha)	Water Bodies (ha)	
2024	261,861.52	182,912.47	
2030	296,865.05	181,760.54	
2036	331,868.57	180,608.62	

Graphs were created for the found areas. These graphs are given in Figure 6, Figure 7, Figure 8, Figure 9, and Figure 10.

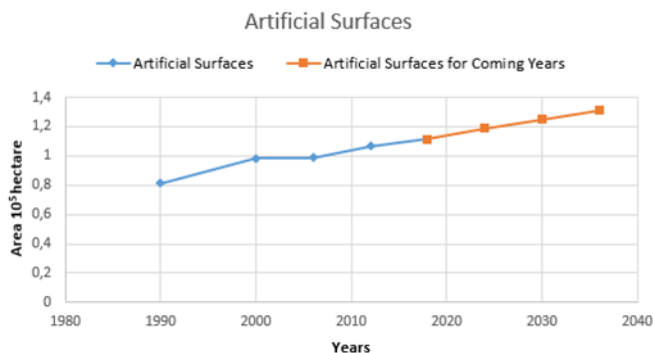


Figure 6. Artificial Surfaces of Konya Closed Basin

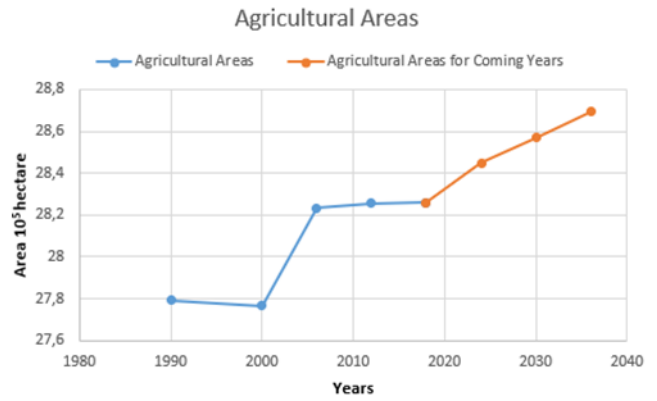


Figure 7. Agricultural Areas of Konya Closed Basin

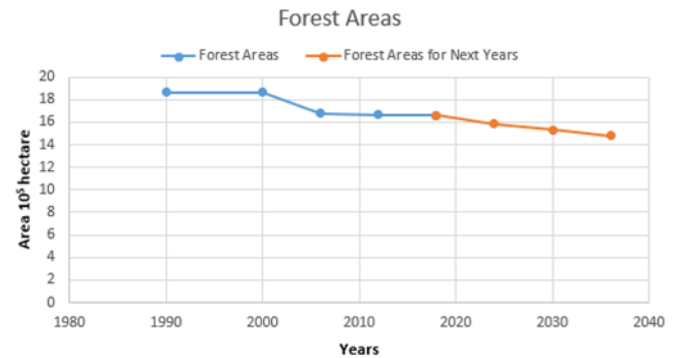


Figure 8. Forest Areas of Konya Closed Basin

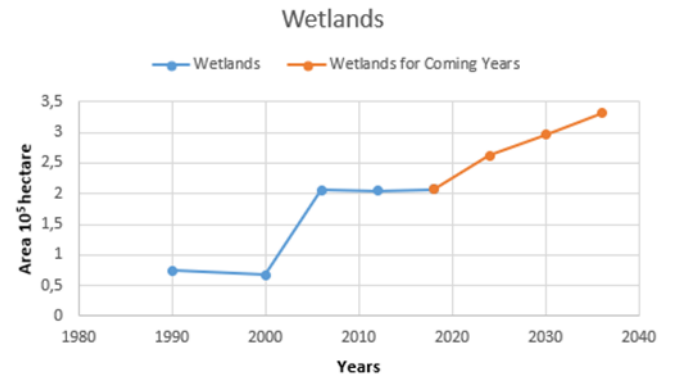


Figure 9. Wetlands of Konya Closed Basin

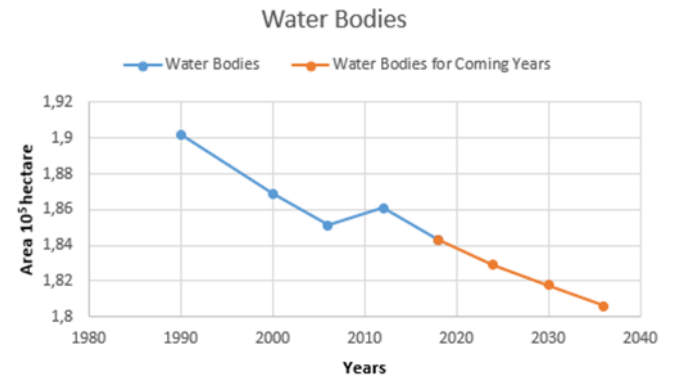


Figure 10. Water Bodies of Konya Closed Basin

4. Conclusion

As a result of this research, it was seen that artificial areas increased rapidly and these artificial areas were mostly formed as a result of the expansion of city centers. Artificial areas, which covered approximately 81

thousand 230 hectares and 1.63% of the total catchment area in 1990, reached 111 thousand 500 hectares in 2018. This area corresponds to 2.23% of the total basin. As a result of the calculations, if the increase continues at the same rate, it is predicted that there will be 131 thousand 234 hectares of artificial land in 2036. With this number, artificial areas will cover 2.63% of the total catchment area in 2036. In agricultural areas, reductions were observed in all areas except irrigated arable land. The biggest decrease is in rice fields, while there were 30 thousand 428 hectares of rice fields in 1990, this number was only 354 hectares in 2018. On the other hand, there is an increase of approximately 250 thousand hectares in 28 years in irrigated arable land. Agricultural lands, which covered 55.67% of the total basin with 2 million 779 thousand hectares in 1990, became 2 million 825 thousand hectares with an increase of 55 thousand hectares in 2018. In 2018, agricultural areas constitute 55.61% of the basin. It is predicted by the analysis that agricultural lands will reach 2 million 869 thousand hectares and 57.48% of the total basin area in 2036. A slight increase was observed in broad-leaved and coniferous forests in forest areas. Arid vegetation has increased from 39 thousand 333 hectares to 94 thousand 545 hectares in 28 years. On the other hand, natural grasslands, bare cliffs and sparse vegetation areas have experienced a great decline. While there was 1 million 866 thousand hectares of forest area in Konya Closed Basin in 1990, approximately 200 thousand hectares of forest were lost in 2018 and 1 million 662 thousand hectares of forest area remained. With this decrease, the forest areas that covered 37.40% of the total area in the basin in 1990 could have an area of 33.31% in 2018. As a result of the analyzes, it is predicted that forest areas will have 1 million 478 thousand hectares in 2036. This area will be equivalent to 29.62% of the total catchment area. With proper city planning, unplanned urbanization can be reduced and thus cities can be prevented from occupying forest areas. Wetlands have been the land cover in which the highest increase has been observed in this 28-year period. Particularly, the withdrawal of water bodies as a result of drought in the basin and leaving swamps as a result of these withdrawals have been effective in this area increase. Salt marshes, which were hardly observed in 1990, reached 151,901 hectares in 2018. The total wetlands in 1990 was 74 thousand 589 hectares. This area is equal to 1.49% of the area in the basin in 1990. In 2018, the wetlands was 207 thousand 584 hectares with an increase of approximately 3 times, which is equal to 4.16% of the total area. With the analyzes made, it has been seen that this area will reach 331 thousand 868 hectares in 2036. Under the conditions at that time, this number would be equivalent to 6.65% of the total area. Water bodies have decreased with the effect of drought and unconscious agriculture. While there were 190 thousand 191 hectares of water bodies in 1990, 184 thousand 235 hectares of water bodies remained in 2018. In this process, some lakes such as Lake Meke dried up and with the withdrawal of Tuz Gölü, large

salt marshes were formed. While wetlands accounted for 3.81% of the total basin in 1990, it decreased to 3.69% in 2018. In line with the analyzes made, it has been predicted that the decrease in wetlands will continue steadily and 180 thousand 608 hectares of wetland will remain in 2036. This area will be equivalent to 3.62% of the total basin. Efforts should be made to prevent unconscious agricultural irrigation, and the drought that will occur due to global warming should not be fueled by incorrect irrigation. Farmers can be trained on this subject and the amount of water used in agricultural areas can be better controlled.

Acknowledgement

The authors thank to CORINE Project and KTO Karatay University for their support.

References

- Ateşoğlu A. (2016) Investigation of accuracy of CORINE 2006 land cover data used in watershed studies. *Journal of the Faculty of Forestry Istanbul University* 66(1), 173-183. (in Turkish)
- Başayığıt, L. (2004). Producing of land use map according to the CORINE Land Use Classification System: Isparta Case, *Journal of Agricultural Sciences* 10 (4), 366-374. (in Turkish)
- Bayar, R. & Karabacak, K. (2017). Land cover changes of Ankara Province (2000-2012). *Journal Of Geographical Sciences*, 15 (1), 59-76. (in Turkish)
- Büttner, G., Feranec, J., Jaffrain, G., Mari, L., Maucha, G., & Soukup, T. (2004). The CORINE land cover 2000 project. *EARSeL eProceedings*, 3(3), 331-346.
- Gençer, M., Başayığıt, L., & Akgül, M. (2015). CORINE land use classification of Eğirdir Lake protection zones. *Journal of Agricultural Sciences*, 21(1), 26-38. (in Turkish)
- Gezici, A., & Maktav, D. (2012). Land cover / use change detection assessment with the integration of remote sensing and GIS: Konya case study, *IV. Remote Sensing and Geographic Information Systems Symposium (UZAL-CBS 2012)*, 16-19 October 2012, Zonguldak (in Turkish)
- LULC (2022), CORINE land cover, <https://land.copernicus.eu/pan-european/corine-land-cover> (Access date: 06.06.2022)
- Özür, N. K. & Ataol, M. (2018). Using CORINE data in geography surveys. *International Geography Symposium on the 30th Anniversary of TUCAUM 3-6 Ekim 2018 /3-6 October 2018, Ankara* (in Turkish)
- Özür, N. K. & Ataol, M. (2018). Assessment on the use of CORINE data in Turkey, *Journal of Institute of Social Sciences*, 9 (2), 110-130. (in Turkish)
- Sarı, H. & Özşahin, E. (2016). Analysis of LULC (Landuse/Landcover) Characteristics of Tekirdag Province based on the CORINE System. *Alinteri Journal of Agriculture Science*, 30 (1), 13-26. (in Turkish)

4th Intercontinental Geoinformation Days

igd.mersin.edu.tr



Effects of Urban Vegetation in Mitigating Land Surface Temperature (LST) in Kaduna Metropolis, Nigeria

Bello Abubakar Abubakar^{*1} , Sani Abubakar Abubakar²

¹Nigerian Defence Academy, Faculty of Arts and Social Sciences, Department of Geography, Kaduna, Nigeria

²Kaduna Polytechnic, School of Geodesy and Land Administration, Department of Photogrammetry and Remote Sensing, Kaduna, Nigeria

Keywords

Land Surface Temperature
Vegetation
NDVI
Kaduna

Abstract

Urban vegetation plays a vital role in mitigating higher temperature through shade, evapotranspiration and high albedo. Replacement of vegetation with urban land uses results in the increase in Land Surface Temperature (LST). This study analyses the effects of urban vegetation in mitigating LST in Kaduna metropolis, Nigeria. Landsat 8 data was used to classify the area into built-up area, vegetation, bare land and water bodies using random forest supervised classification. Information on the vegetation density was obtained using Normalized Difference Vegetation Index (NDVI), while single channel algorithm was used for the retrieval of LST. The effect of vegetation on LST was quantified using correlation analysis. The results showed that built-up area was the largest land cover, occupying 157.99km² (46.53%), followed by vegetation with 143.34km² (42.22%). Bare land had 34.26km² (10.09%), while water bodies occupied 3.95km² (1.16%). The vegetation density that mitigates LST indicated by NDVI showed higher values (0.38-0.69) in the suburb with higher vegetation density, which resulted in low LST range (22°-26°C). Lower NDVI values (0.05-0.38) were recorded in the bare land and built-up area with sparse vegetation. This resulted in moderate (28°-30°C) and high (30°-34°C) LST respectively. Lowest NDVI (-0.26 – 0.05) and LST (22°C – 26°C) were recorded in the water bodies. There was negative correlation (-0.55) between NDVI and LST, indicating the effect of vegetation in mitigating LST. Proper urban planning is necessary by planting more trees in the metropolis as part of LST mitigation strategies.

1. Introduction

Urbanization is a leading factor responsible for land use/land cover change, where vegetation cover is replaced with buildings and impervious surfaces like concrete and asphalt, which are responsible for higher temperature in urban areas (Sadroddin et al., 2015). Reduction in vegetation cover as a result of urban expansion and increase in human activities increase Land Surface Temperature (LST) (Bokaie et al., 2016; Pal and Ziaul, 2017; Yin et al., 2020). LST changes due to alteration of urban surface albedo, roughness and heat flux exchanges (Estoque et al., 2017; Singh et al., 2017; Zhu et al., 2022). Buildings and impervious surfaces in the urban built-up areas store and emit heat resulting in the increase in sensible heat flux and decrease in the latent heat flux compare with the pervious and vegetated surfaces (Liu et al., 2012; Zhan et al., 2012; Rogan et al., 2013). High temperature causes human discomfort and increases disease and mortality (Basara

et al., 2010; Sadroddin et al., 2015). For instance, in 2003, there was an increase in mortality by 7.6% in Munich, Germany as a result of heat wave (D'Ippoliti et al., 2010; Sadroddin et al., 2015). Urban vegetation has a role to play in mitigating high temperature through shading, and increasing evapotranspiration and albedo (Armson et al., 2012; Rogan et al., 2013). The spatial variation in the urban LST depends on the land cover type, with higher temperature in impervious surfaces and lowers in vegetation cover (Rogan et al., 2013). Remote Sensing is a significant tool used for the study of spatial distribution of LST and vegetation. Kaduna Metropolis is witnessing urbanization causes replacement of vegetation cover with buildings and impervious surfaces (Alamin and Dadan-Garba, 2014). This led to increase in the LST that is detrimental to human health and environment. Excessive heat exposure results in medical condition like heat cramp, heat exhaustion and heat stroke. High urban temperature can be mitigated through proper urban

* Corresponding Author

^{*}(abubakarbello1064@gmail.com) ORCID ID 0000 – 0003 – 3959 – 876X
(abu86sani@gmail.com) ORCID ID 0000 – 0002 – 7521 – 7365

Cite this study

Bello, A. A., Sani, A. A. (2022). Effects of Urban Vegetation in Mitigating Land Surface Temperature (LST) in Kaduna Metropolis, Nigeria. 4th Intercontinental Geoinformation Days (IGD), 184-187, Tabriz, Iran

planning. This study examines the role of vegetation cover in mitigating LST in the metropolis.

2. Method

2.1. Study Area

The study area is located between Latitudes 10°25' and 10°72' North of the Equator, and Longitudes 7°25' and 7°75' East of the Greenwich Meridian (Figure 1). The metropolis occupies almost 260 km², and it is made up of Kaduna North and South local government areas, and parts of Igabi and Chikun local government areas. It is the capital city, economic, and financial centre of Kaduna State (Aliyu and Suleiman, 2006). It is drained by River Kaduna and its tributaries, which takes its source from Sherri Hill in Plateau State (Folorunsho, 2004; Folorunsho et al., 2012). The climate of the area is tropical continental with distinct rainy and dry season. The rainy season is shorter and lasts from April to October, while the dry season starts from November to March (Orogade et al., 2016). The annual rainfall values range between 1500mm and 2000mm (Alamin and Dadan-Garba, 2014). The temperature is high throughout the year, with a mean annual temperature between 26°C and 34°C (Bununu et al., 2015). The natural vegetation of the area is Sudan savannah which is characterised by grasses and scattered trees (Amadi et al., 2014). The tree species found include *Azadirachta indica*, *Mangifera indica*, *Eucalyptus* sp, *Tamarindus indica*, and *Parkia biglobosa* (Ogunkalu et al., 2017).

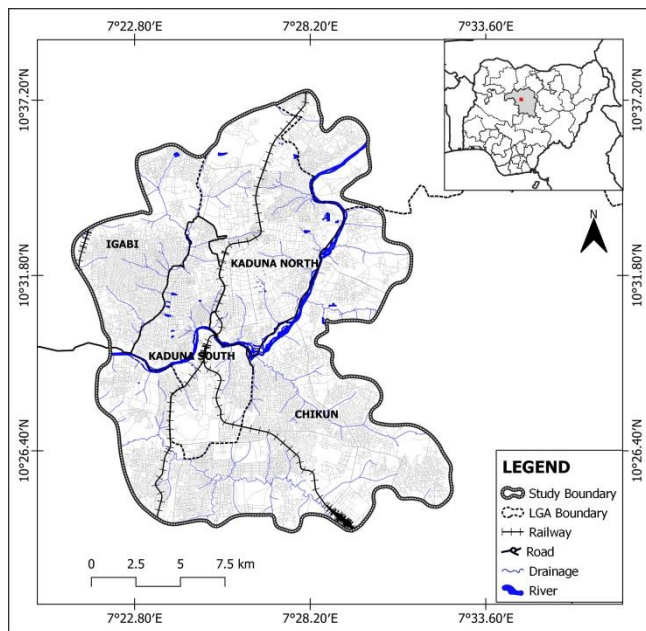


Figure 1. The Study area

2.2. Material and Methods

In this research, we used Landsat 8 Operational Land Imager and Thermal Infrared Sensors (OLI/TIRS) obtained on 8th November, 2021. It was downloaded freely from the United States Geological Survey's website. The data was used for land use/land cover classification, extraction of vegetation density and retrieval of Land Surface Temperature (LST),

Random Forest (RF) supervised machine learning algorithm was used for image classification to classify

the study area into built-up area, bare land, vegetation, and water bodies.

Normalized Difference Vegetation Index (NDVI) was used to quantify the vegetation greenness and density. It is the ratio between the red and near infrared band, with values range between -1.0 and +1.0. It was calculated using the following algorithm:

$$NDVI = \frac{NIR - Red}{NIR + Red} \quad (1)$$

Where

NIR is the near infrared band of the image

Red is the red band of the image

Single channel algorithm was used to retrieve the LST from thermal band 10 of the imagery. Finally, the effect of vegetation on LST was quantified by correlation analysis. The satellite imagery was processed using Semi-Automatic Classification Plugin (SCP) for QGIS.

3. Results

The classified imagery (Figure 2) displayed the four major land cover classes, namely built-up area, bare land, vegetation, and water bodies. Built-up area was the largest land cover class, occupying 157.99km² (46.53%). It covered most of the centre of the metropolis and extended to the northern and southern parts. Vegetation was the second-largest land cover with an area of 143.34km² (42.22%). It was sparse in the built-up area and bare land, and dense mostly around the built-up area. Bare land covered 34.26km² (10.09%) found mostly within the vegetation area. Water bodies were the smallest land cover class that occupied 3.95km² (1.16%). It was found mostly in River Kaduna and its tributaries that nearly divide the metropolis into two.

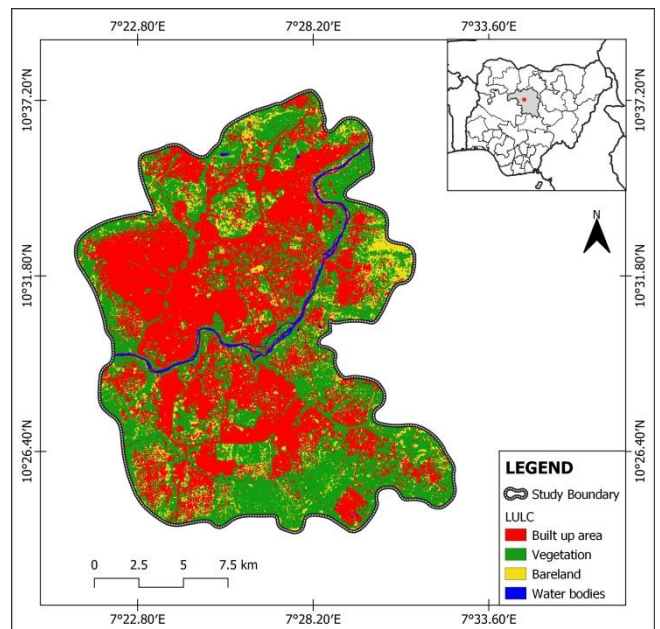


Figure 2. Land use/land cover

The vegetation density displayed by the NDVI values ranges from -0.26 to 0.69 (Figure 3). The lowest values range from -0.26 – 0.05 were found in the water bodies. Average NDVI values between 0.05 – 0.38 were found in

the built-up area and bare land, while the highest values from 0.38 – 0.69 in the vegetation.

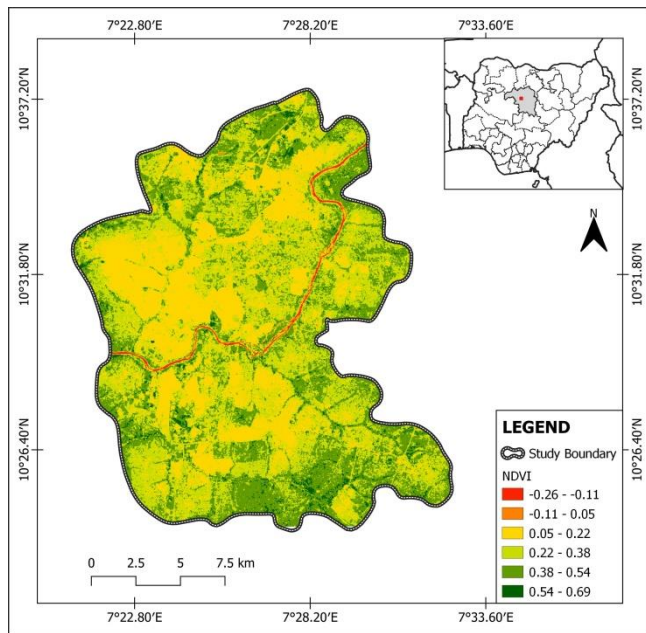


Figure 3. Normalized Difference Vegetation Index

The LST retrieved from the image showed spatial variability, with 22°C as the lower value and 34°C as the highest (Figure 4). Lowest temperature range (22-26°C) was recorded in the water bodies. Vegetation exhibited a low range of between 26 to 28°C. Higher temperature range (28-32°C) was found in the bare land and built-up area. Hotspots of LST (32-34°C) were found in the built-up areas in different locations of the metropolis. The relationship between LST and NDVI showed a moderate negative correlation (-0.55).

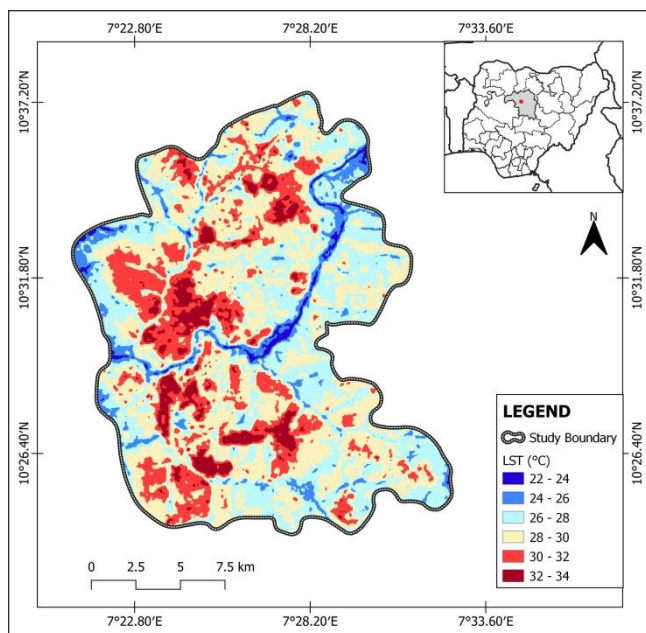


Figure 4. Land surface temperature

4. Discussion

The land use/land cover indicated built-up area, bare land, vegetation, and water bodies. The built-up area was the dominant land cover because of urban

expansion, where other land cover classes were converted to urban land uses. Urban expansion is caused by increase in population as a result of rural-urban migration and high birth rate. Currently, more than half of the world population is currently living in the urban areas (United Nations, 2011; Uysal and Polat, 2015). The centre of the metropolis is the Central Business District (CBD), which is the commercial and administrative hub that consists of markets and offices. The northern part was dominated by low and high density residential areas, while the southern part comprises of industrial and residential areas. The low NDVI values in the built-up area showed low vegetation density because of the replacement of trees with buildings and impervious surfaces. Reduction in vegetation exposed the buildings and pavements to sunlight, increasing the amount of energy absorbed and radiated in the air. This is because of the decrease in shed and evapotranspiration. Moreover, release of heat from anthropogenic activities contributed to the higher LST.

The bare land showed the pervious areas of exposed soil and impervious rock surfaces found in undeveloped lands that were not put to urban uses. The bare land had scattered trees with grasses and shrubs that dried up because of the dry season and exposed the land. This led to the low NDVI values recorded. Moreover, the exposure of the bare land to solar radiation resulted in the high temperature because of reduction in shade and evapotranspiration. Furthermore, the impervious nature of the rock surfaces and the properties of the soil like the color contributed to the higher LST.

The vegetation showed the assemblage of plants in the area found along the streets, in the residential and commercial areas, and other green areas. The replacement of vegetation cover with buildings and other impervious surfaces led to the sparse vegetation at the centre of the metropolis. Dense vegetation found around the built-up area indicated the suburb area with higher NDVI values. The surface temperature in the vegetated areas was low because of the abundant shade and evapotranspiration that mitigates LST.

River Kaduna and its tributaries that mainly drained the metropolis showed a very low NDVI values indicating the absence of vegetation in the water bodies. The lower LST exhibited by water was as a result of evaporation that takes heat from water. Moreover, water heats slower than land. Finally, the negative correlation between NDVI and LST demonstrated the effect of vegetation in mitigating LST. Therefore, the increase in vegetation density leads to decrease in LST as a result of increase in shade and evapotranspiration.

5. Conclusion

Remote sensing is an essential tool for studying land use/land cover change and LST spatial variability. The role of urban vegetation in mitigating LST in Kaduna metropolis, Nigeria was analysed. Landsat 8 data was used to classify the area into built-up area, bare land, vegetation and water bodies using random forest algorithm. Moreover, vegetation density and LST were derived from the imagery using NDVI and single channel

algorithm respectively. The effect of vegetation on LST was quantified by correlation analysis. The results revealed that built-up area was the largest land cover followed by vegetation, bare land and water bodies. Highest NDVI values and lower LST were found in vegetation. In contrast, lower NDVI values with higher LST were recorded in built-up area and bare land. Lowest NDVI and LST were found in the water bodies. Increase in vegetation density, resulted in decrease in LST. Proper urban planning is required for sustainable development.

Acknowledgement

We wish to thank the United States Geological Survey (USGS) for the satellite imageries made freely available.

References

- Alamin, M. A. & Dadan-Garba, A. (2014) Urban Vegetation Study of Kaduna Metropolis Using GIS and Remotely Sensed Data, *Journal of Natural Sciences Research*, 4 (2),160-171.
- Aliyu, H. I. and Suleiman, Z. A. (2006). Flood Menace in Kaduna Metropolis: Impacts, Remedial and Management Strategies, *Science World Journal*,11(2),16-22
- Amadi, A. N., Okoye, N. O., Alabi, A. D., Tukur, A. & Angwa, E. M. (2014) Quality Assessment of Soil and Ground Water Near Kaduna Refinery and Petrochemical Company, Northwest Nigeria, *Journal of Scientific Research and Reports*, 3 (6), 884-893
- Armson D., Stringer P. & Ennos A. R. (2012) The Effect of Tree Shade and Grass on Surface and Globe Temperatures in an Urban Area, *Urban Forestry and Urban Green*, 11(3), 245-255.
- Basara J. B., Basara H. G., Illston B. G. & Crawford K. C. (2010) The Impact of the Urban Heat Islands During an Intense Heat Wave in Oklahoma City, *Adv. Meterol*, doi:10.1155/2010/230365.
- Bokaie M., Zarkesh M. K., Arasteh P. D. & Hosseini A. (2016) Assessment of urban heat island based on the relationship between land surface temperature and land use/land cover in Tehran, *Sustainable Cities and Society*, 23, 94-104
- Bununu, Y. A., Ludin, A. N. M. & Hosni, N. (2015) City profile: Kaduna, *Cities*, 49, 53-65.
- D'Ippoliti D., Michelozzi P., Marino C., de'Donato C., Menne B., Katsouyanni K., Kirchmayer U., Analitis A., Medina-Ramon M., Paldy A., et al. (2010) The Impact of Heatwaves on Mortality in 9 European Cities: Results from the EuroHEAT Project, *J. environ. Health*, 9
- Estoque R. C., Murayama Y. & Myint, S. W. (2017) Effects of Landscape Composition and Pattern on Land Surface Temperature: An Urban Heat Island Study in the Megacities of Southeast Asia, *Sci. Total Environ*, 577, 349-359
- Folorunsho, J. O. (2004) An Examination of Some Stream Flow Characteristics of River Kaduna State. Unpublished M.Sc. Thesis, Geography Department, Ahmadu Bello University, Zaria-Nigeria.
- Folorunsho, J. O., Iguisi, E. O., Mu'azu, M. B. & Garba, S. (2012) Application of Adaptive Neuro Fuzzy Inference System (Anfis) in River Kaduna Discharge Forecasting, *Research Journal of Applied Sciences, Engineering and Technology*, 4 (21),4275-4283.
- Liu Y., Shintaro G., Zhuang D. & Kuang W. (2012) Urban Surface Heat Fluxes Infrared Remote Sensing Inversion and their Relationship with Land Use Types, *Journal of Geographical Sciences*, 22(4), 699-715.
- Ogunkalu, O. A., Sodimu, A. I, Sulaiman, R. A. & Adedire, O. O. (2017) Survey of Benefits and Constraints of Urban Trees in Kaduna Metropolis, *World News of Natural Sciences*, 11,19-27.
- Orogade, S. A., Owoade, K. O., Hopke, P. K., Adie, D. B., Ismail, A. & Okuofu, C. A. (2016) Source Apportionment of Fine and Coarse Particulate Matter in Industrial Areas of Kaduna, Northern Nigeria, *Aerosol and Air Quality Research*, 16,1179-1190.
- Pal, S. & Ziaul, S. (2017) Detection of land use and land cover change and land surface temperature in English Bazar urban centre, *The Egyptian Journal of Remote Sensing and Space Science*, 20(1), 125-145
- Rogan, J., Ziemer M., Martin D., Ratick S., Cuba N. & DeLauer V. (2013) The Impact of Tree Cover Loss on Land Surface Temperature: A Case Study of Central Massachusetts Using Landsat Thematic Mapper Thermal Data, *Applied Geography*, 45, 49-57.
- Sadroddin A., Martin W., Salman Q., Qihao W. & Thomas K. (2015) The Role of Vegetation in Mitigating Urban Land Surface Temperatures: A Case Study of Munich, Germany during Warm Season, *Sustainability*, 7, 4689-4706.
- Singh, P., Kikon N. & Verma P. (2017) Impact of Land Use Change and Urbanization on Urban Heat Island in Lucknow City, Central India. A Remote Sensing Based Estimate, *Sustainable Cities Soc.*, 32, 100-114
- United Nations (2011). *World Urbanization Prospects the 2011 Revision*, Department of Economic and Social Affairs, Population Division, NewYork
- Uysal, M. & Polat, N. (2015). An Investigation of the Relationship Between Land Surface Temperatures and Biophysical Indices Retrieved from Landsat TM in Afyonkarahisar (Turkey), *Technical Gazette*, 22(1),177-181
- Yin Z., Liang S., Lina K., & Ruxin Y. (2020) Analysis of Land Surface Temperature Driving Factors and Spatial Heterogeneity Research Based on Geographically Weighted Regression Model. *Hindawi Complexity*, 2862917, 1-9
- Zhan, W., Chen Y., Voogt J., Zhou J., Wang J., Liu W., et al. (2012) Interpolating Diurnal Surface Temperatures of an Urban Facet Using Sporadic Thermal Observations, *Building and Environment*, 57, 239-252
- Zhu, Y., Myint, S. W., Schaffer-Smith, D., Muenich, R. L. Tong D. & Li Y. (2022) Formulating Operational Mitigation Options and Existing Intra-Urban Social Inequality Using Evidence-Based Urban Warming Effects, *Front. Environ. Sci.*, 9,795474, 1-16.

4th Intercontinental Geoinformation Days

igd.mersin.edu.tr



Assessing the importance of variable selection in land subsidence susceptibility mapping

Sepideh Tavakkoli Piralilou ^{*1,2}, Golzar Einali ³, Shokrolah Kiani ⁴, Khalil Gholamnia ³¹University of Salzburg, Department of Geoinformatics—Z_GIS, Salzburg, Austria²Institute of Advanced Research in Artificial Intelligence (IARAI), Vienna, Austria³University of Tabriz, Department of Remote Sensing and GIS, Tabriz, Iran⁴University of Yazd Department of Geography, Yazd, Iran

Keywords

Remote sensing
Land Subsidence
machine learning (ML)
Random Forest (RF)
Damaneh Plain

Abstract

In the domain of land subsidence risk science, Land Subsidence Susceptibility Mapping (LSSM) aids in spatially identifying regions prone to subsidence. This study used a multi-collinearity analysis through the variance inflation system (VIF) and tolerance (TOL) and a machine learning (ML) model of Random Forest (RF) for LSSM in the Damaneh Plain, Isfahan Province, Iran. The study investigated the importance of the conditioning variables in predicting Land Subsidence occurrences using an ML model. An ML model's prediction capabilities and performance were evaluated using conditioning variables in this paper. Using VIF, we eliminated the least "important" variables related to the LSSM. Conclusively, we found that removing the least "important" variables improves the accuracy of the resulting LSSMs. Based on the results of our study, using VIF could increase the predictive performance of the RF model by three percentage points in the applied accuracy assessment metric.

1. Introduction

Land subsidence is a geological phenomenon that is considered a natural disaster caused by human activities (O. Ghorbanzadeh, Rostamzadeh, Blaschke, Gholamnia, & Aryal, 2018). In most cases, the underground layers compact after natural and manufactured factors work together to cause their downward movement (O. Ghorbanzadeh, Feizizadeh, & Blaschke, 2018). In addition to changing the environment, this phenomenon has significant economic and social repercussions. There have been many causes of land subsidence worldwide, such as earthquakes, extraction of natural gas, mineral exploration, dissolution of limestone, and extraction of groundwater (Tien Bui et al., 2018). In Iran, many land subsidences have occurred on several plains due to the high extraction of groundwater for agriculture and urban consumption during the last few decades. Land subsidence is one of the most frequently occurring natural disasters that cause significant human casualties and infrastructure destruction in this country. Many problems are associated with land subsidence, including damage to public and private infrastructure, power lines, roads, settlements, sinkholes, and soil erosion (Ranjgar, Razavi-Termeh, Foroughnia, Sadeghi-Niaraki, & Perissin,

2021). Thus, generating the LSSM and modeling variables affecting land subsidence are important approaches that incorporate potential land subsidence locations. The LSSM refers to the likelihood of a land subsidence occurring in a particular region due to several causative factors. Land subsidence risk management is an essential step towards reducing subsidence risk and assists in mapping the spatial distribution of probable manifestations of subsidence (Mohammady, Pourghasemi, & Amiri, 2019).

In land subsidence susceptibility studies, satellite data and geographic information system (GIS) tools and machine learning (ML) models are instrumental in acquiring satisfactory resolution remote sensing and other relevant data, evaluating variables that affect this phenomenon (Omid Ghorbanzadeh, Blaschke, Aryal, & Gholamnia, 2020; Omid Ghorbanzadeh, Crivellari, Ghamisi, Shahabi, & Blaschke, 2021). In the past, researchers have used various models to generate LSSMs using the technologies mentioned above. An adaptive neuro-fuzzy inference system has been evaluated by (O. Ghorbanzadeh, Rostamzadeh, et al., 2018) for LSSM generating for Marand Plain, the East Azerbaijan Province in Iran, using six different membership functions (MF). Two of the six LSSMs, the DsigMF (0.958),

* Corresponding Author

(sepideh.tavakkoli-piralilou@stud.sbg.ac.at) ORCID ID 0000-0002-1188-8290
(Golzar.einali@yahoo.com) ORCID ID 0000-0002-0679-8370
(arashkiani97rs@gmail.com) ORCID ID 0000-0001-9292-3694
(khalil.gh3@gmail.com) ORCID ID 0000-0002-3860-8674

Cite this study

Piralilou, S. T., Einali, G., Kiani, S., & Gholamnia, G. (2022). Assessing the importance of variable selection in land subsidence susceptibility mapping. 4th Intercontinental Geoinformation Days (IGD), 188-191, Tabriz, Iran

and the GaussMF (0.951) yielded very high prediction values based on the calculated areas under the curves (AUC) of the receiver operating characteristic (ROC) analyses. The same model was integrated with two models of imperialist competition algorithms and gray wolf optimization by (Tien Bui et al., 2018) to calculate LSSM for Shahryar County, Iran. The resulting maps were evaluated based on the inventory data set of land subsidence locations and the root mean square error value and the ROC, which showed that the integration with imperialist competitive algorithm had the best accuracy with a 0.932 AUC value.

On the one hand, although ML models show acceptable performance and have high accuracy, they are dependent on a precise land subsidence inventory map, which is somewhat challenging in Iran (Arabameri et al., 2020). On the other hand, the ML models are sensitive regarding the input data set for training. A selection of important ones is essential to get the best accuracy for the modeling (Saha et al., 2021). This matter is more evident for modeling and mapping the susceptibility of land subsidence because there are two leading causes of land subsidence: natural and human activities that disrupt the underground layers (Arabameri et al., 2021; Ranjgar et al., 2021). However, land subsidence can be attributed to a variety of geological and hydrological factors in different parts of the world.

We aim to use the most current ML models and analyze the importance of each variable prior to training. Thus, it is possible to examine how each of the land subsidence relevant variables can affect the performance of the ML models for having the best prediction. This approach in research can lead to the use of variables that contribute more to the modeling goal and avoid data duplication that complicates computation and results in ambiguous conclusions.

2. Study area and Data set

We studied the Damaneh Plain in Faridan County, Isfahan Province, Iran. Figure 1 shows the boundaries of the study area, which is located between longitudes $30^{\circ}50'$ to $35^{\circ}50'$ and latitudes 50° to $35^{\circ}50'$. The plain covers an area of more than 2651057 ha. The climate in Damaneh plain is mild in spring and summer and cold in winter. The coldest month of the year is January with an average of -3.1°C . As July approaches, the temperature rises to an average of 23°C , making it the hottest month of the year. (<http://www.esfahanmet.ir/>). The study area receives an average annual rainfall of 317.4 mm and average annual temperatures of 10.4°C . This plain sees about 48% of its total rainfall in winter, the wettest season of the year (<https://www.esrw.ir/>). There have been significant land subsidence issues in Damaneh plain, especially in Damaneh city, resulting in most houses being cracked and destroyed, forcing local people to leave their homes.

2.1. Land subsidence inventory data set

To predict and evaluate the LSSMs, 2667 land subsidence occurrence locations were collected through a comprehensive field survey. 70% and 30% of the points

in this inventory data set have been used to train and validate the models, respectively.

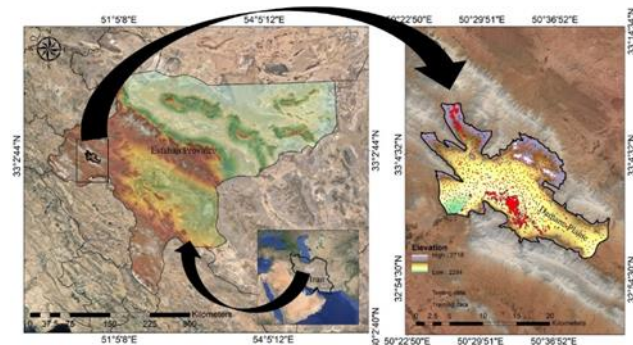


Figure 1. The location of the Damaneh Plain in Faridan County, Isfahan Province, Iran

2.2. Conditioning variables

Fourteen inter-related variables have been selected based on the literature review in the present land subsidence study. The prepared conditional variables are distinct from rivers, Landover, the topographic wetness index (TWI), distance to villages, slope, aspect, catchment slope, rainfall, elevation, groundwater depth, soil, lithology, distance to roads, and well density. These variables are derived from different sources, which are fully explained by (Arabameri et al., 2021; Omid Ghorbanzadeh et al., 2020).

3. Methods

All prepared variables were once used to train the ML model of RF. Following are the results of evaluating the fixed and dependent variables in the multi co-linearity analysis among the factors was done through the variance inflation system (VIF) and tolerance (TOL). For the training of the models, we selected variables with a VIF value greater than two for the ML training process. We evaluated the validity of the LSSMs from each model using the ROC curve. The applied multivariate linear regression (MLR), and the VIF and RF models are explained as follows.

3.1. Multi-collinearity analysis

The probability estimation model uses this criterion to exclude co-linearity and select influential variables. In particular, the multi-collinearity among the conditional variables is more likely to be error-prone if the VIF is greater than five and the TOL is less than 0.1 (Lei et al., 2020).

3.2. Random Forest (RF)

Breiman and Cutler created the RF ML model, developed by Ho (1994) (Ho, Hull, & Srihari, 1994). RF estimates the final result based on most votes instead of relying on a decision tree. Using this approach will enhance accuracy and prevent overfitting. In this work, in both the 11 and 14 variable models, the maximum number of variables is designed upon the square root of the total number of variables.

4. Results

In this study, 14 conditional variables were generated for the LSSM. An essential part of this study was identifying the key variables, which are illustrated in the following "Table 1". To evaluate the relationship between the conditional variables, we used the multi-collinearity test considering VIF and the TOL. The results show that this test assigns more than 5 VIF values to variables of distance to villages, aspect, and distance to roads.

Table 1. Collinearity results among the variables. The red highlighted rows with more than 5 VIF resulting values represent the least "important" related variables to the LSSM.

Conditional variables	TOL	VIF
Distinct to rivers	0.52	1.92
Landover	0.29	3.44
TWI	0.22	4.54
Distance to villages	0.17	5.87
Slope	0.38	2.63
Aspect	0.16	6.25
Catchment slope	0.79	1.26
Rainfall	0.52	1.92
Elevation	0.59	1.69
Depth of GW	0.45	2.22
Soil	0.54	1.85
Lithology	0.49	2.04
Distance to roads	0.18	5.37
Well Density	0.39	2.56

The resulting LSSM from the RF model is classified into five classes, very low class with 65.94%, low class with 14.33%, medium class with 8.41%, high class with 5.48% and very high class with 5.84% of the area (see "Figure 2"). Model RF-VIF, with a very low-class area of 51.81%, a high-class area of 18.55%, a medium class area of 11.53%, a high-class area of 9.62%, and a very high-class area of 8.48%, contained a larger area and focused more on the center and types of land use, primarily agricultural land. We evaluated the performance of the applied ML model using a standard accuracy assessment method. The calculated areas under the curves (AUC) of the receiver operating characteristic (ROC) analyses discovered that the LSSM predicted by the RF-VIF got a higher AUC value of 92.29%. In comparison, that of the RF model was 89.89%.

5. Discussion

Considering a wide variety of land subsidence triggers, many variables are involved in LSSM generating. This variation can affect modeling and lead to errors (Lei et al., 2020). Modeling should therefore avoid these problems to the extent possible. Therefore, using the multi-collinearity analysis, we eliminated the least "important" three variables and trained the RF model with 11 remaining conditional variables. According to

the present study, land subsidence in Damaneh Plain is significantly related to the river's distance, landcover, TWI, slope, catchment slope, rainfall, elevation, depth of ground water, soil lithology, and well density. There are 572 wells in the study area, 200 illegally drilled. Moreover, all the region slopes have been cultivated for agriculture, and water consumption has increased.

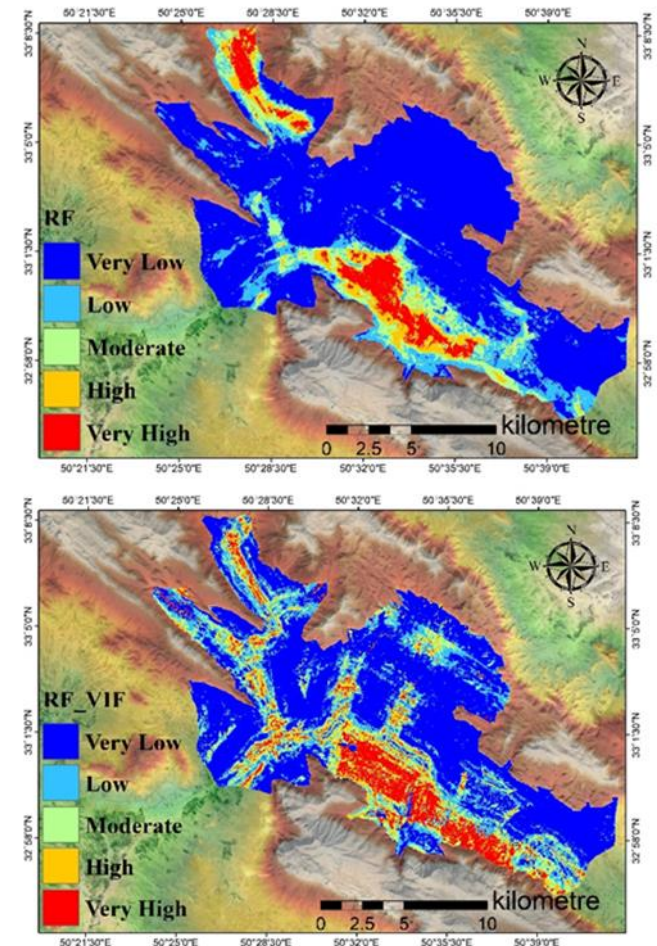


Figure 2. The resulting LSSMs predicted using the RF model based on all conditional variables and based on the selected variables derived from the VIF for Damaneh Plain.

6. Conclusion

To conclude, the results overall showed the effectiveness of the RF model in LSSM generation and the multi-collinearity method for assessing the importance of the conditioning variables. The integrated approach can be reproduced and applied to other land subsidence susceptible plains with different environmental indicators.

Acknowledgement

The authors are grateful for the support of the University of Salzburg, and the Institute of Advanced Research in Artificial Intelligence (IARAI) GmbH, Vienna, Austria.

References

- Arabameri, A., Pal, S. C., Rezaie, F., Chakraborty, R., Chowdhuri, I., Blaschke, T., & Ngo, P. T. T. (2021). Comparison of multi-criteria and artificial intelligence models for land-subsidence susceptibility zonation. *Journal of Environmental Management*, 284, 112067.
- Arabameri, A., Saha, S., Roy, J., Tiefenbacher, J. P., Cerda, A., Biggs, T., ... Collins, A. L. (2020). A novel ensemble computational intelligence approach for the spatial prediction of land subsidence susceptibility. *Science of The Total Environment*, 726, 138595.
- Ghorbanzadeh, O., Feizizadeh, B., & Blaschke, T. (2018). An interval matrix method used to optimize the decision matrix in AHP technique for land subsidence susceptibility mapping. *Environmental Earth Sciences*, 77(16). <https://doi.org/10.1007/s12665-018-7758-y>
- Ghorbanzadeh, O., Rostamzadeh, H., Blaschke, T., Gholaminia, K., & Aryal, J. (2018). A new GIS-based data mining technique using an adaptive neuro-fuzzy inference system (ANFIS) and k-fold cross-validation approach for land subsidence susceptibility mapping. *Natural Hazards*. <https://doi.org/10.1007/s11069-018-3449-y>
- Ghorbanzadeh, Omid, Blaschke, T., Aryal, J., & Gholaminia, K. (2020). A new GIS-based technique using an adaptive neuro-fuzzy inference system for land subsidence susceptibility mapping. *Journal of Spatial Science*, 65(3), 401–418.
- Ghorbanzadeh, Omid, Crivellari, A., Ghamisi, P., Shahabi, H., & Blaschke, T. (2021). A comprehensive transferability evaluation of U-Net and ResU-Net for landslide detection from Sentinel-2 data (case study areas from Taiwan, China, and Japan). *Scientific Reports*, 11(1), 1–20.
- Ho, T. K., Hull, J. J., & Srihari, S. N. (1994). Decision combination in multiple classifier systems. *IEEE Transactions on Pattern Analysis & Machine Intelligence*, (1), 66–75.
- Lei, X., Chen, W., Avand, M., Janizadeh, S., Kariminejad, N., Shahabi, H., ... Mosavi, A. (2020). GIS-based machine learning algorithms for gully erosion susceptibility mapping in a semi-arid region of Iran. *Remote Sensing*, 12(15), 2478.
- Mohammady, M., Pourghasemi, H. R., & Amiri, M. (2019). Land subsidence susceptibility assessment using random forest machine learning algorithm. *Environmental Earth Sciences*, 78(16), 1–12.
- Ranjgar, B., Razavi-Termeh, S. V., Foroughnia, F., Sadeghi-Niaraki, A., & Perissin, D. (2021). Land subsidence susceptibility mapping using persistent scatterer sar interferometry technique and optimized hybrid machine learning algorithms. *Remote Sensing*, 13(7), 1326.
- Saha, S., Arabameri, A., Saha, A., Blaschke, T., Ngo, P. T. T., Nhu, V. H., & Band, S. S. (2021). Prediction of landslide susceptibility in Rudraprayag, India using novel ensemble of conditional probability and boosted regression tree-based on cross-validation method. *Science of the Total Environment*, 764, 142928.
- Tien Bui, D., Shahabi, H., Shirzadi, A., Chapi, K., Pradhan, B., Chen, W., ... Saro, L. (2018). Land subsidence susceptibility mapping in south korea using machine learning algorithms. *Sensors*, 18(8), 2464.



4th Intercontinental Geoinformation Days

igd.mersin.edu.tr



Comparison of photogrammetric software using the terrestrial photogrammetric method: The case of Hüsrev Paşa Mosque

Fatih Pulat ^{*1}, Murat Yakar ², Ali Ulvi ³

¹Siirt University, Department of Architecture and Urban Planning, Map and Cadastre Program, Siirt, Türkiye

²Mersin University, Faculty of Engineering, Department of Surveying Engineering, Mersin, Türkiye

³Mersin University, Department of Geographic Information Systems and Remote Sensing, Mersin, Türkiye

Keywords

3D Model
Photogrammetry
Cultural Heritage

Abstract

From the past to the present, very few cultural artifacts have survived to the present day by preserving their own characteristics. These artifacts undergo structural deterioration due to the destruction they have suffered as a result of natural events, the damages caused by human hands, and since the necessary repairs have not been made in accordance with their structural characteristics, although they are under protection, so they are devastated and demolished. In this study, the detail measurements of the Hüsrev Paşa Mosque, which is located in the Merkez İpekyolu district of Van province and which has survived as a work of Mimar Sinan, were made with the terrestrial photogrammetric method in three dimensions, and the pictures of the building were taken. Thus, by evaluating the data obtained in the computer environment, it is aimed to obtain a three-dimensional model with all the building details such as the size, type of structural material, and visual of the building for every desired point on the building. In the study, comparison will be made using different photogrammetric software.

1. Introduction

It is aimed to keep the cultural and natural assets alive by taking many precautions to protect them and to transfer them to the next generations. In line with this purpose, all kinds of technological developments brought by the age lived since the past have been followed. The most fundamental element in the protection and preservation of cultural and natural heritage is the preservation of the structural integrity of the property. When we look at the assets that have not preserved their structural integrity, natural disasters such as earthquakes, floods, landslides, weather events such as wind, storm, rain, and human-made damages intentionally or unintentionally (intentional damages and unintentional damages during renovation-repair) are the reasons why the structure has not survived until today. and is one of the biggest reasons why it cannot be passed on to the next generations. Another major reason for this destruction is the failure to take adequate measures to protect these structures and the failure to use scientific and technical methods to keep these cultural heritages alive.

1.2. Resources Research

In the light of the technological developments experienced today, it is necessary to protect our cultural heritage both structurally and digitally record all the norms and features (shape, size, detail, building material, etc.) of the building. In this sense, there are many techniques developed for the preservation and survival of cultural heritage. One of these techniques that is widely used is photogrammetry technique. Thanks to the photogrammetry technique, all assets subject to cultural heritage can be geodesically measured with all their detail points, and a three-dimensional model can be obtained by combining the images obtained by the picture shooting process. Photogrammetry is the creation of a three-dimensional model of any object or structure with pictures and determining its location (Kraus, 1993).

In parallel with the continuous development of technology in our age, photogrammetry technique has also shown continuous improvement. Analogue methods have been replaced by analytical photogrammetry, especially with the development of cameras and the use

* Corresponding Author

(fatih.plt.65@siirt.edu.tr) ORCID ID 0000-0002-4043-9654
(myakar@mersin.edu.tr) ORCID ID 0000-0002-2664-6251
(aliulvi@mersin.edu.tr) ORCID ID 0000-0003-3005-8011

Cite this study

Pulat, F., Yakar, M., & Ulvi, A. (2022). Comparison of photogrammetric software using the terrestrial photogrammetric method: The case of Hüsrev Paşa Mosque. 4th Intercontinental Geoinformation Days (IGD), 192-195, Tabriz, Iran

of computers. With the developments in the digital sense in a short time, the photogrammetry technique has also developed rapidly, and today, wearable technologies with laser scanners, unmanned aerial drones (UAVs), mobile vehicles with terrestrial laser scanning are experiencing a very strong age in terms of technology (Caglayan, 2020).

1.3. Local Photogrammetry

Photogrammetry can be studied in three main steps by looking at its components. These steps are listed as obtaining the data, evaluating the data, and obtaining a final product by utilizing these data. These steps are also valid for terrestrial photogrammetry (Hanke and Grussenmeyer, 2002).

The most important part of these steps is the acquisition of data. The data obtained in this step are of two types. These data are; triangulation, polygon etc. established in the field and called ground control points. These are the measurement data obtained based on geodetic points such as geodetic points and photographic data obtained by taking pictures (Karslı, 2016).



Figure 1. Digital cameras used in terrestrial photogrammetry

2. Method

The work on which the study will be carried out is located in the south of the old city of Van, within the borders of the historical Van Castle, which dates back to 840 BC from the Urartian civilization. The work was commissioned by the Governor of Van, Köse Hüsrev Pasha, in 1567 by Mimar Sinan, one of the most famous architects of his time and one of the best architects of all time. Hüsrev Pasha Mosque is square in shape and was built with a large dome on thick walls. The walls of the work are made of cut stone and squinches, and the dome is made of brick. Today, it has still managed to preserve its beauty and robustness to a large extent.



Figure 2. Study area

The method used in this study is called the terrestrial photogrammetry method. In this method, studies are carried out in a place-based manner. Aim; is to produce a 3D and measurable model of the work by using the 2D photographs of the work and the measured points on the work.

Scope of the study, photographing and measuring processes of the work were carried out in the field. Obtained 3D point data using Netcad 5.1 software, Photomodeler UAS and Agisoft It has been evaluated to provide base data for Metashape software. This data, together with the uploading of the photographs of the work to the software, 3D drawing and point production were provided, and a 3D model of the work was obtained through both software.

Terrestrial photogrammetry work consists of successive stages within the discipline, starting with the work in the field and ending with the office work in the office environment. The work flow chart showing these stages is given in Figure 3.

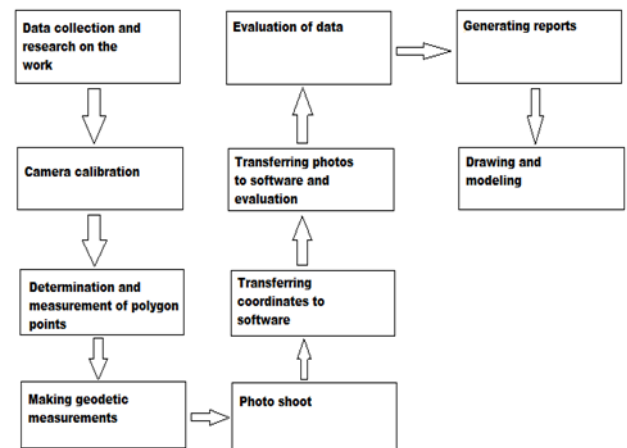


Figure 3. Work flow chart of the study

2.1. Office Studies

2.2. Photogrammetric Drawing Stage of the Artwork with Photomodeler UAS Software

The measurement values obtained from the field were transferred to the computer environment and recorded in Netcad 5.1 software. ncn file format for later evaluation in Photomodeler software. txt format has been converted. The parameters of the camera from which the photographs were taken were introduced in the Photomodeler (PM) software and the calibration process was carried out before proceeding to the drawing process.

In Photomodeler UAS software, the work of obtaining a 3D model was started by creating a point cloud in the same software. After the selection of parameters related to the sensitivity of the work, the photos of the work are uploaded to the software, respectively. detection (feature detection), matching (matching), matching and Marking (matching and marking), orientation (orientation) operations are done.

Thus, as a result of the process, a point cloud consisting of 61337 3D points belonging to the work was obtained. Using the generated point cloud 3D viewer

options menu, surface and point mesh parameters were determined.

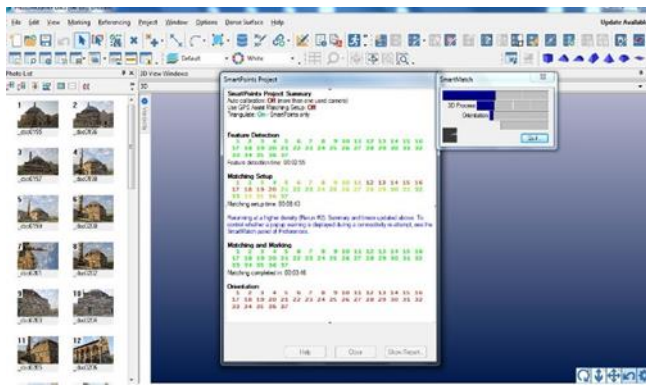


Figure 4. Point cloud generation phase

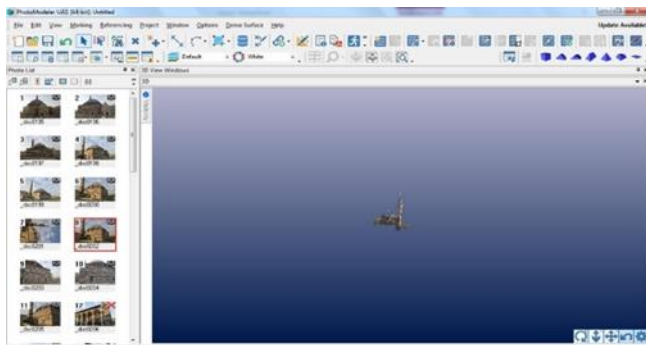


Figure 5. Model created with sparse point cloud

It has been observed that the point cloud of the 3D model obtained with the sparse point cloud does not have a homogeneous structure, so an even sparse point cloud is obtained in some parts of the work. In order to obtain a dense point cloud of the work, a dense point cloud surface was created by using the 'Create Dense Surface' tab of the 'Dense Surface' menu by selecting the photos with even less sparse point cloud over the software.

In order to create the dense point cloud, the number of dense point clouds created for a selected surface of the work was 447,063 and the creation time took 2 minutes and 5 seconds. Thus, a 3D model of the artifact was obtained by obtaining dense point clouds belonging to each surface.

2.3. Photogrammetric Drawing Stage of the Artwork with Agisoft Software

To the work After the field operations carried out on the land belonging to the company, work began in the office environment. Agisoft, the latest version of Agisoft software First of all, camera calibration processes were performed with Metashape software. In order to calibrate the camera, at least 3 photographs of the checkerboard calibration test paper taken from different angles must be used. For this study, 12 photographs of the camera calibration paper taken from different angles were used.

Photographs of the work after the camera calibration processes Agisoft The evaluation phase was started by transferring it to the Metashape software. This

evaluation phase is on the Add Workflow menu on the software. It is done with the Photos command.

With the transfer of the photos to the software, the alignment of the photos is done by clicking the Align tab on the Workflow menu. Here, the frequency of the point cloud to be created and the features of the photographs to be studied are determined by choosing the appropriate parameters according to the nature of the work to be done and the desired sensitivity.

Alignment _ After the Photos) process, the control points marked and measured on the artifact were loaded into the software, and matches were made with the marked points on the artifact very precisely.

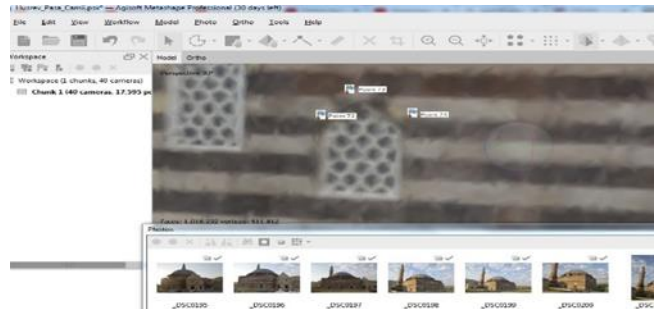


Figure 6. Matching points

After the point matching process, a point cloud was obtained by tightening the points of the artifact by clicking on the Build Dense Cloud tab from the Workflow menu to tighten the points on the artifact.

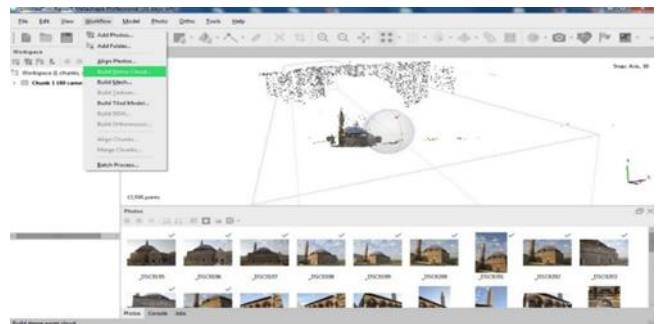


Figure 7. Point cloud

The solid model obtained from the work will be able to have its real texture with the painting process. Therefore, texture coating processes are started by clicking Model Shaded and then model textured on the software. (Fig. 8.). As a result, a 3-dimensional model of the work is obtained (Fig. 9.). The file of the model can be viewed in 3D with different software by obtaining the 3D file with the Export Model operation from the File menu.

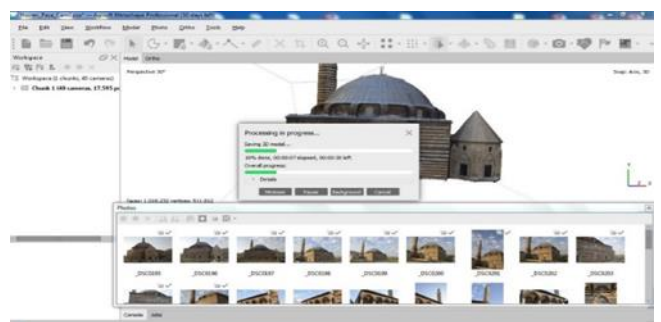


Figure 8. The texture coating process of the work



Figure 9. 3D view of the work from different angles

3. Results

V max, V min and V avg values in the x, y and z directions of the location data of both software were determined and position error were calculated.

$$m = \pm \sqrt{([vw]) / (n-1)} \quad (1)$$

$$m(xyz) = \pm \sqrt{(m_x^2 + m_y^2 + m_z^2)} \quad (2)$$

Table 1. Coordinate differences obtained from software

	Photomodels UAS				Agisoft metashape		
	Vi Differences (cm)				Vi Differences (cm)		
	Vx (±)	Vy (±)	Vz (±)		Vx (±)	Vy (±)	Vz (±)
vmin	0.1	0	0.3	vmin	0.1	0.4	0.5
vmax	7.1	4.1	2.8	vmax	4.9	3.4	3
vort	1.9	1.7	1.5	vort	1.7	1.6	1.6
	VxVx	VyVy	VzVz		VxVx	VyVy	VzVz
	181.42	146.69	115.33		158.77	137.66	130.89
m	2.2	1.8	1.2	m	1.7	1.9	1.1
m(xyz) (±)	3.08			m(xyz) (±)	2.78		

Agisoft in terms of the calculated mean square error and position error of the data obtained through both software. It has been determined that the data obtained from the Metashape software are more sensitive data (Table 1). In addition, the 3D model obtained by Photomodeler UAS and Agisoft The data on the number of sparse points, the number of dense points and the creation times of these point clouds are given in Table 2 comparatively.

Table 2. Data of the 3D model obtained from the software

	Photomodels UAS		Agisoft metashape	
	Sparse Spot	Dense Spot	Sparse Spot	Dense Spot
Number	61,337	6,675,987	17,595	5,168,153
Total Number of Points	6,737,324		5,185,748	
Pairing Time	00:20:02	00:18:38	00:03:26	09:50:08
The total time	00:38:40		09:53:34	
Used your computer Properties	Intel Core 2 Duo Processor		237Gb Hard Disk Capacity	
	2.0 GHz Processor Speed		Windows 7 64 Bit Operating System	
	2.0 RAM			

As seen in Table 2, Agisoft While the total number of points produced in the Metashape software was 5,185,748, the total number of points produced in the Photomodeler UAS software was 6,737,324. Thus, the number of dots produced in Photomodeler UAS software It has been observed that the Metashape software creates extra points, approximately 30% of the number of points. This shows that more detail points can be obtained with Photomodeler UAS software, especially in the modeling of artifacts with intense detail features, and the features of the artifact can be modeled better.

4. Discussion

Photomodeler UAS software from Agisoft Another advantage over Metashape software is that this software allows 3D modeling in the form of hand drawing. Making manual drawings in Photomodeler UAS software is one of the extra advantages of this software. In addition, it has been observed that the lines of the building model obtained by hand drawing are smoother and sharper than the lines of the model obtained through the point cloud. This is the point of the modeling work of this work, considering the time and effort spent on drawing, the parts (minaret) of the work that cannot be measured and photographed, although the software provided an advantage in the drawing phase, since the work that is the subject of this study has a relatively flat architecture. Creating the cloud creates a greater advantage.

5. Conclusion

The terrestrial photogrammetry technique applied in the study area, and the measurement processes, especially together with the laser measuring instrument, enabled the study to be carried out much faster than the classical methods, to require shorter time, to be carried out with less personnel and less costly equipment. It is seen that the precision quality of the measurement results obtained with both software is high, but compared to each other, Agisoft It was determined that the Metashape software gave better results (Table 1).

The measurement results obtained were compared and it was determined that the error amount of the measurement process made with the total station measuring instrument was below 5 mm, thus giving more accurate results than the GPS measuring instrument. The building does not have complex surfaces, but generally has a flat surface. This has been an important factor in keeping the amount of error low in drawing processes.

References

- Çağlayan, U., (2020) Agisoft Based on UAV Data, Context 3D Position Accuracy Analysis of Capture and Pix4d Image Matching Software, Master Thesis, Bülent Ecevit University, Zonguldak.
- Hanke, K., & Grussenmeyer, P. (2002). Architectural Photogrammetry: Basic theory, Procedures, Tools, ISPRS Comission 5 Tutorial, Corfu, September.
- Karşlı, F. (2016). Photogrammetry I Lecture Notes (Unpublished), Karadeniz Technical University, Trabzon, p 6.
- Kraus, K. (1993). Photogrammetry, Fundamentals and Standard Processes. Volume 1; Bonn, p 23.



4th Intercontinental Geoinformation Days

igd.mersin.edu.tr



Modelling a landslide site using UAV photogrammetry in Değirmençay village, Mersin

Aydın Alptekin^{*1}, Murat Yakar²

¹Mersin University, Geological Engineering Department, Mersin, Türkiye

²Mersin University, Geomatics Engineering Department, Mersin, Türkiye

Keywords

Landslide
UAV
Photogrammetry
DSM
Orthomosaic

Abstract

Natural disasters cause loss of life and property. This situation causes both economic and psychological problems on the society. Developing countries' economies are more affected by disasters than developed countries. Turkey is frequently exposed to natural disasters due to its geological, geomorphological and hydrogeological features. Landslide is the most common natural disaster. Modeling and regular monitoring of disaster risk areas is necessary to reduce disaster risk. The development of remote sensing techniques facilitates the work of engineers. Creating a three-dimensional (3D) model of the terrain can be done practically by modeling the pictures taken from unmanned aerial vehicles (UAVs) in computer environment. The current status of the land can be documented. In this study, a flight was carried out with a UAV in order to determine the current status of the land after the landslide that occurred as a result of heavy rains in the Değirmençay Village of Mersin in January 2021. The images were combined using the structure from motion algorithm and a 3D model of the land was created. Using the 3D model, the Digital Elevation Map, and orthophoto maps of the terrain were created with high precision and resolution. With future UAV flights, the condition of the land will be re-documented. By using the difference between point clouds, the amount of sliding and volume change in the region will be determined.

1. Introduction

Natural hazards cause loss of life and property. This situation causes both economic and psychological problems on the society. The economy of developing countries is more affected by disasters than developed countries. Natural hazards are seen all over the world. There is no place where natural disasters are not seen.

Turkey is frequently exposed to natural disasters due to its geological, geomorphological and hydrogeological characteristics. Landslide is the most seen natural disaster. Landslide may occur due to change of forces acting on the soil and rock mass. Heavy rainfall, tectonic movements, uncontrolled excavations and stream erosion are the main factors causing landslide.

Field study performed by well-trained geologist is essential to understand landslide dynamics. However, it is time consuming and labor intensive. Fine-scale terrain structures may be omitted with the traditional mapping.

The development of remote sensing techniques demystifies the mechanism of landslides. Satellite

images, unmanned aerial vehicles (UAV) and light detection and ranging (Lidar) have been used frequently in natural disaster studies since last decade.

Data can be obtained easily from rough and inaccessible terrain using UAV with centimeter accuracy. High-resolution 3D model can be generated using pictures taken from UAV. Geomorphologic features can be extracted from 3D model.

A low-cost UAV can obtain pictures from inaccessible terrain. This facilitates the job of engineers. Data from dangerous steep slopes can be obtained in a practical way.

In December 2019, heavy rainfall caused landslide in Değirmençay village. In this study, we model the using UAV photogrammetry.

2. Study area

Değirmençay village is located in the northern part of Mersin (Figure 1). The study area is characterized by Mediterranean climate. Rainfall amount is increasing

* Corresponding Author

^{*}(aydinlptekin@mersin.edu.tr) ORCID ID 0000-0002-5605-0758
(myakar@mersin.edu.tr) ORCID ID 0000-0002-2664-6251

Cite this study

Alptekin, A. & Yakar, M. (2022). Modelling a landslide site using UAV photogrammetry in Değirmençay village, Mersin. 4th Intercontinental Geoinformation Days (IGD), 196-198, Tabriz, Iran

each year (Figure 2). The average rainfall amount is 972.26 kg/cm² between 2015 and 2019. The monthly rainfall amount of 2019 is shown in Figure 3. In January

and December, most rainfall is seen. The average rainfall amount is 98.89 kg/cm².

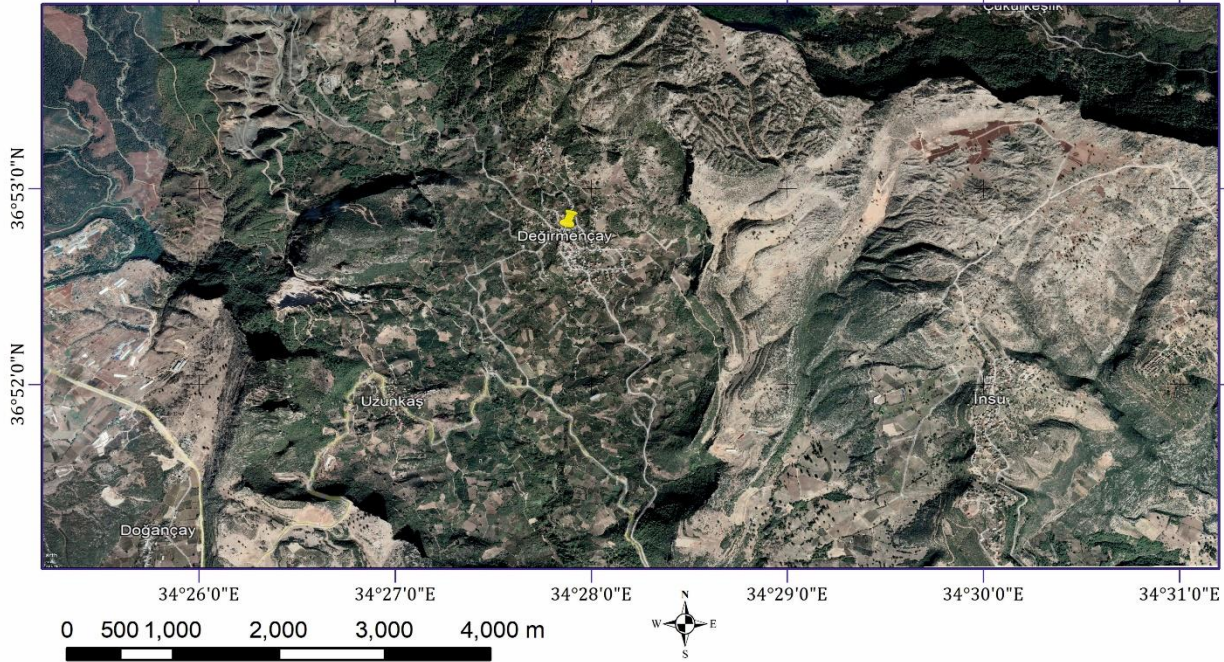


Figure 1. Location map of the study area

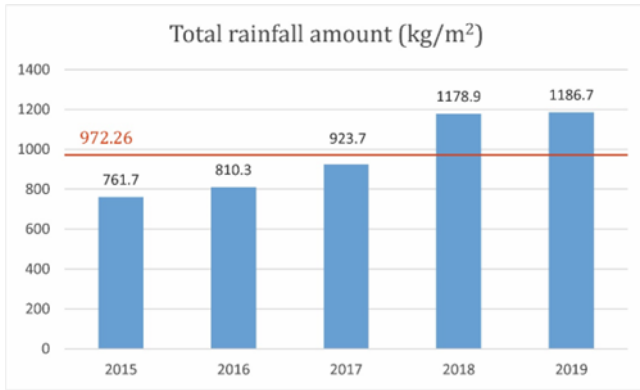


Figure 2. Rainfall amount per year

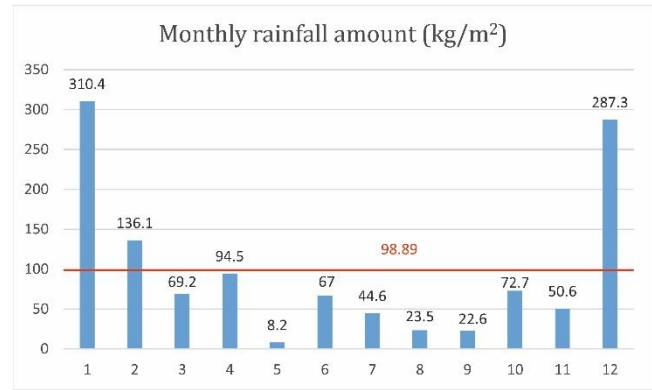


Figure 3. Rainfall amount per month

3. Methods

Unmanned aerial vehicles contribute to the modern solution of many engineering problems. 3D model of the terrain can be obtained in high resolution using the point clouds obtained from the photographs. Structure from motion algorithm enable us to construct 3D models from 2D pictures.

UAV has been used in many engineering projects since last decade. Landslide site mapping (Alptekin and Yakar 2020a; Kuşak et al. 2021), rockfall site mapping (Alptekin et al. 2019), shoreline detection (Unel et al. 2020), pond volume measurement (Alptekin and Yakar 2020b), cultural heritage modelling (Alptekin and Yakar 2021; Kanun et al. 2021)

In this study, Anafi Parrot (Figure 4), which is a low-cost UAV, was used to obtain pictures. The flight information is given in Table 1.

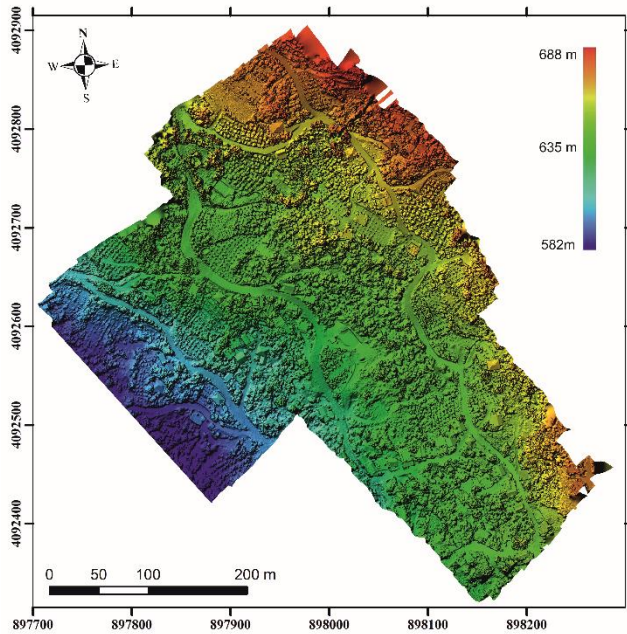
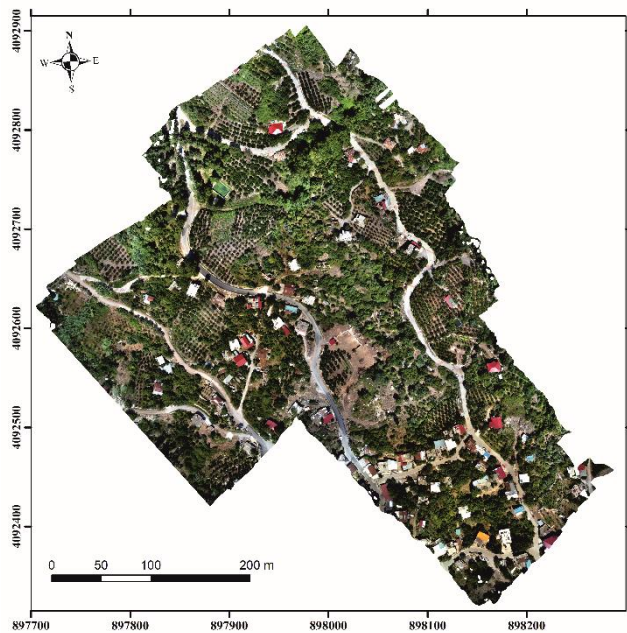
The pictures were processed in Agisoft Metashape software. We modelled the landslide site to characterize landslide dynamics. We created Digital Surface Model (DSM) (Figure 3) and ortho-mosaic (Figure 4) of the study area.



Figure 4. Anafi Parrot set

Table 1. Flight information

Item	Number
Ground Control Points	7
Pictures	1053
Flight height	40 m
Coverage area	0.166 km ²

**Figure 4.** Digital surface map**Figure 5.** Orthomosaic

4. Discussion

UAV photogrammetry is very useful for geoscientists. Creating terrain model is very practical.

High-resolution models enable us to interpret the fissures, displacements and geomorphologic structures.

The flight height is very important to produce models. The lower flight height enables us creating more detailed map (Çelik et al. 2020). However, when we take pictures from low height, we get too many pictures. This will be a problem for modelling. A high standard computer will be needed as there will be too many point clouds.

DSM shows us how the elevation changes in the landslide site. Slope and rainfall are the main reasons of this landslide event.

5. Conclusion

In this study, we modelled the landslide site with high-resolution. In order to be prepared for natural disasters, dangerous areas should be modeled at regular intervals. In near future, we will repeat the field study and determine the displacement amount.

References

- Alptekin, A., Çelik, M. Ö., Doğan, Y., & Yakar, M. (2019). Mapping of a rockfall site with an unmanned aerial vehicle. *Mersin Photogrammetry Journal*, 1(1), 12-16.
- Alptekin, A., & Yakar, M. (2020a). Heyelan bölgesinin İHA kullanarak modellenmesi. *Türkiye İnsansız Hava Araçları Dergisi*, 2(1), 17-21.
- Alptekin, A., & Yakar, M. (2020b). Determination of pond volume with using an unmanned aerial vehicle. *Mersin Photogrammetry Journal*, 2(2), 59-63.
- Alptekin, A., & Yakar, M. (2021). 3D model of Üçayak Ruins obtained from point clouds. *Mersin Photogrammetry Journal*, 3(2), 37-40.
- Çelik, M. Ö., Alptekin, A., Ünel, F. B., Kuşak, L., & Kanun, E. (2020). The effect of different flight heights on generated digital products: DSM and Orthophoto. *Mersin Photogrammetry Journal*, 2(1), 1-9.
- Kanun, E., Alptekin, A., & Yakar, M. (2021). Cultural heritage modelling using UAV photogrammetric methods: a case study of Kanlıdivane archeological site. *Advanced UAV*, 1(1), 24-33.
- Kusak, L., Unel, F. B., Alptekin, A., Celik, M. O., & Yakar, M. (2021). Apriori association rule and K-means clustering algorithms for interpretation of pre-event landslide areas and landslide inventory mapping. *Open Geosciences*, 13(1), 1226-1244.
- Ünel, F. B., Kuşak, L., Çelik, M., Alptekin, A., & Yakar, M. (2020). Kıyı çizgisinin belirlenerek mülkiyet durumunun incelenmesi. *Türkiye Arazi Yönetimi Dergisi*, 2(1), 33-40.

4th Intercontinental Geoinformation Days

igd.mersin.edu.tr



Comparison of shoreline extraction indexes performance using Landsat 9 satellite images in the heterogeneous coastal area

Çiğdem Esendağlı¹, Serdar Selim^{*2}, Nusret Demir²

¹Akdeniz University, Institute of Science, Department of Space Science and Technologies, Antalya, Türkiye

²Akdeniz University, Faculty of Science, Department of Space Science and Technologies, Antalya, Türkiye

Keywords

Water indexes
Landsat 9
Shoreline extraction
Coastal area
Performance analysis

Abstract

In this study, automatic shoreline extraction was performed using different indexes in the coastal region containing different land cover types and their performances were compared. For this purpose, Landsat 9 Satellite images, the newest satellite of Landsat, were used. Normalized Difference Vegetation Index (NDVI), Normalized Difference Water Index (NDWI), Automated Water Extraction Index (AWEI), Water Ratio Index (WRI), and Normalized Difference Moisture Index (NDMI), which are frequently preferred in the literature, are used automatically to determine the shoreline. The obtained shorelines were compared with the reference shoreline and their performances were evaluated. In the performance evaluation phase, the behavior of the shoreline inference indices in different land cover types adjacent to the shore was examined and their advantages and disadvantages compared to each other were revealed. The results showed that AWEI, NDWI, WRI, NDMI and NDVI gave the most accurate results in automatic shoreline inference across the study area, respectively. Although AWEI still gives a high accuracy in different land cover types, it is seen that the accuracy of NDVI increases in the region where vegetation is adjacent to the shore.

1. Introduction

Coastal regions, where a large part of the world's population live, are changing rapidly due to their dynamic structure. Various natural and cultural factors accelerate this change, and therefore, obtaining up-to-date information about coasts quickly and reliably is of great interest (Zollini et al. 2019; Demir et al. 2016). The priority in determining the change in coasts is the determination of the coastline. Accurate determination of the shoreline, coastal zone management, etc. extremely useful for various applications (Ghorai and Mahapatra 2020).

Coastline extraction with conventional methods is very difficult, costly, time consuming and sometimes impossible for the entire coastal system (Aedla et al. 2015). In this context, coastlines can be detected quickly and accurately with the integration of Geographic Information System (GIS) and Remote Sensing (RS) technologies (Selim et al. 2016; Hossain et al. 2021). Automatic shoreline extraction indexes also make this detection much easier. However, it is known that

different land cover types adjacent to the shoreline directly affect the performance of the indexes used in the shoreline extraction (Li and Gong 2016; Wicaksono and Wicaksono 2019; Selim et al. 2021). Therefore, advantages and disadvantages of shoreline inference indexes on non-homogeneous shores constitute the motivation of this study. In this study, the performances of the shoreline extraction indexes, which are frequently used in the literature, on the inhomogeneous coastal region were compared. In this context, Landsat 9 satellite images, the newest satellite of Landsat, were used. Using edge detection technology, Landsat 9 collects the highest quality data ever recorded by a Landsat satellite (Masek et al. 2020; NASA 2021). Landsat 9 carries two devices, Operational Land Imager 2 (OLI-2) and Thermal Infrared Sensor 2 (TIRS-2) (Masek et al. 2020). These devices are optical sensors that detect 11 wavelength bands of visible, near infrared, shortwave infrared, and thermal infrared light as it is reflected or emitted from the planet's surface (NASA 2021). Data from these devices can be accessed free of charge. The OLI sensor that produces images used in this study has 9 bands, 8 of

* Corresponding Author

(cigdemesendagli@hotmail.com) ORCID ID 0000-0003-4379-2178
(serdarselim@akdeniz.edu.tr) ORCID ID 0000-0002-5631-6253
(nusretdemir@akdeniz.edu.tr) ORCID ID 0000-0002-8756-7127

Cite this study

Esendağlı, Ç., Selim, S., & Demir, N. (2022). Comparison of shoreline extraction indexes performance using Landsat 9 satellite images in the heterogeneous coastal area. 4th Intercontinental Geoinformation Days (IGD), 199-202, Tabriz, Iran

which are 30 m ground sample distances (GSD) and 1 is 15 m GSD.

Among the shoreline extraction indexes that can be calculated using relevant bands of Landsat 9, Normalized Difference Vegetation Index (NDVI), Normalized Difference Water Index (NDWI), Automated Water Extraction Index (AWEI), Water Ratio Index (WRI) and Normalized Difference Moisture Index (NDMI) were calculated, the performances and accuracy of these indexes were compared.

2. Method

The working method consists of 4 basic stages: area definition, data preparation, index calculation and the accuracy analysis.

2.1. Study area

The study was carried out in Antalya Province, which is one of the most important tourism destinations in Turkey and known for its coastal regions. The working area is located at 36°53'1.04"N and 30°41'14.30"E (Figure 1).



Figure 1. Location of the study area

The coastline covering the study area is approximately 8.5 km long. The land uses adjacent to the coastline, on the other hand, show different characteristics. In this context, approximately 3 km of it consists of sand dunes, 4 km of which consists of stony-rocky and the remaining 1.5 km of which consists of vegetation cover.

2.2. Data preparation

In the study, Landsat 9 satellite images on 28 April, 2022 which can be accessed free of charge, were used. Landsat's newest satellite, Landsat 9, has a resolution of 30 m and has 9 bands. Atmospheric correction was applied to the images using Quantum GIS (QGIS 3.6.3) software and they were made ready for analysis.

2.3. Shoreline Extraction Indexes

In this study, shoreline extraction indexes, which are frequently preferred in the literature, were used and their performances were compared.

2.3.1 NDVI

The Normalized Difference Vegetation Index is an index that reveals the density of vegetation by analyzing its health or unhealthy state. It is also used in shoreline extraction (El Kafrawy et al. 2017; Gonçalves et al. 2019). The NDVI formula is shown below.

$$NDVI = \frac{NIR - Red}{NIR + Red}$$

2.3.2 NDWI

The Normalized Difference Water Index is used to highlight open water features in satellite images and allows a body of water to be highlighted against soil and vegetation (Xu 2006). It also effectively measures the moisture content (McAllister et al. 2022). NDWI is calculated by the following method;

$$NDWI = \frac{Green - NIR}{Green + NIR}$$

2.3.3 AWEI

Automatic Water Extraction Index enables shoreline determination by increasing the contrast between water and other surfaces, maximizing the separability of water and non-water pixels (Feyisa et al. 2014). Index formula shows as below:

$$AWEI = 4 \times (Green - SWIR2) - (0.25 \times NIR + 2.75 \times SWIR1)$$

2.3.4 WRI

The Water Ratio Index is an index based on the dominant spectral reflection of water in the green and red bands and using 4 spectral reflectance bands (Guatam et al. 2015). The formula shown as below;

$$WRI = \frac{Green + Red}{NIR + SWIR}$$

2.3.5 NDMI

The Normalized Difference Moisture Index is often used to determine vegetation water content. It is calculated as the ratio between NIR and SWIR values (Naik and Anuradha 2018). The formula shown as below;

$$NDMI = \frac{NIR - SWIR}{NIR + SWIR}$$

2.4. Performance Analysis

First of all, the reference coastline was obtained by precisely drawing the coastline of the study area with manual digitation on the Google Earth satellite image. Then, each index was calculated using the relevant bands of the Landsat 9 image and the shorelines were automatically extracted. The extracted shorelines were converted into points with a distance of 30 m based on the pixel resolution, and nearest analysis was applied with the reference shoreline. Then, the mean and standard deviation values were calculated with the following formulas and their performance was evaluated.

$$\begin{aligned} \text{Mean formula} \quad \bar{x} &= \frac{\sum x}{N} \\ \text{Standard deviation formula} \quad s &= \sqrt{\frac{\sum (x - \bar{x})^2}{N - 1}} \\ \text{Median formula} \quad \mu(x) &= \frac{N + 1}{2} \end{aligned}$$

here;

- \bar{x} : arithmetic mean of values
- s : standard deviation
- x : each shoreline value
- μ : median
- $\sum x$: the sum of x
- N : number of data

3. Results

In the study area, where different land covers are adjacent to the coast, the coastline was automatically determined and mapped on the Landsat 9 images of the water-based indexes (Figure2).

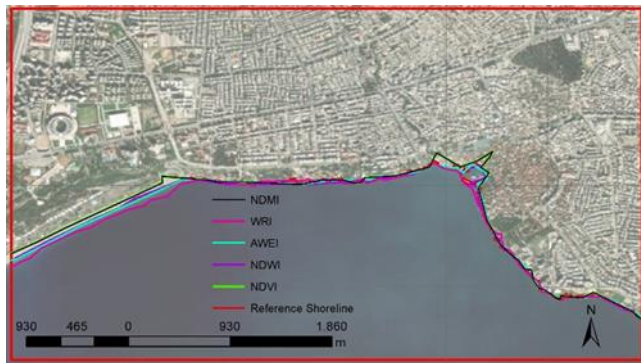


Figure 2. Shorelines created with indexes

In the map created, it is seen that for 5 different index coastlines can be drawn automatically, but there are differences in certain regions. Indexes that give the closest and farthest results based on the reference coastline are shown with mean, median and standard deviation in Table 1.

Table 1. Index performance data

Indexes	Mean (m)	Median (m)	Standart deviation (m)
AWEI	6,256	4,441	5,284
NDWI	8,883	6,661	6,694
WRI	18,814	13,053	17,527
NDMI	20,873	7,864	26,568
NDVI	21,071	8,168	26,585

As can be seen from the table, it is understood that AWEI is the most compatible index with the reference coastline in the relevant study area. The AWEI index automatically determined the shoreline in the best way with an average difference of 6 m and a standard error about 5 m. Then, NDWI gives the best result by about 9 m. Again, the standard error of NDVI has a value similar to the AWEI. It is understood that these two indices are very close to the reference line with their median values of 4.4 m and 6.6 m, respectively. WRI gives the best result following these indexes. It is seen that mean, median and standard deviation are high in this index. NDMI with a mean value of 20,873 m and NDVI with a mean value of 21,071 m gave the worst results in the related field. The median and standard deviation values of NDMI and NDVI were also quite high. Related indexes differ in areas where different types of land cover are adjacent to the coast. In the area where the waterline is adjacent to the dune, AWEI and NDWI give the closest results, while other indexes seem to be quite far from the reference shoreline (Figure 3).

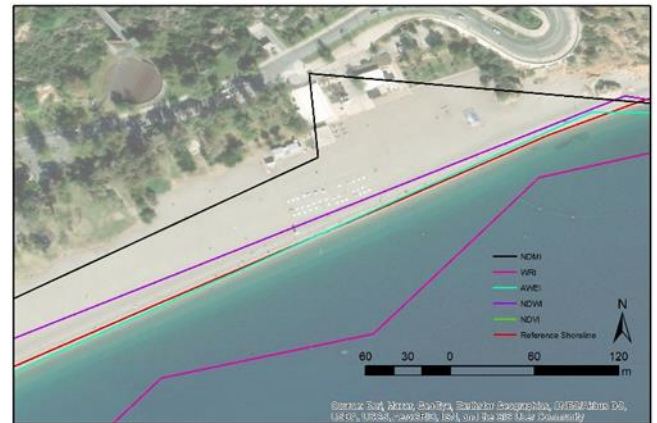


Figure 3. Behavior of indexes on the beach coast

In the area where the stony-rocky land cover borders the waterline, it is seen that WRI is superior to other indexes (Figure 4). In this region, other indices show similar behaviors.



Figure 4. Behavior of indexes on the rocky shore

In the parts where the vegetation cover is adjacent and close to the waterline, WRI gave the worst results, in this part NDMI and NDVI showed results close to the shoreline (Figure 5).



Figure 5. Behavior of indices on the vegetation shore

The obtained results show that in the study area where there are different land cover types adjacent to the coast, when the entire study area is evaluated, indexes that best extract the coastline are AWEI, NDWI, WRI, NDMI and NDVI, respectively.

4. Discussion and Conclusion

In the study area where different land cover types border the waterline, the performance of the shoreline extraction indexes were compared, and it was seen that AWEI and NDWI were more advantageous than other indexes in the whole area. According to Selim et al. (2021) stated that AWEI gave better results compared to other indexes El Kafrawy (2017) stated that NDWI provides higher accuracy than NDVI in the coastline extraction. In the literature, the results of many studies using shoreline extraction indices are largely in line with this study. However, since NDVI and NDMI make a classification based on moisture content, it has been observed that they do not produce very good results in shoreline extraction (Magloine et al. 2014). It was determined that the accuracy of NDVI and NDMI slightly increased only in the vegetation cover adjacent to the waterfront, and in this context, it was predicted that it could be used in a controlled manner in such areas.

References

Aedla, R., Dwarakish, G. S. & Reddy, D. V. (2015). Automatic shoreline detection and change detection analysis of netravati-gurpurrivermouth using histogram equalization and adaptive thresholding techniques. *Aquatic Procedia*, 4, 563-570.

Demir, N., Kaynarca, M. & Oy, S. (2016). Extraction of coastlines with fuzzy approach using SENTINEL-1 SAR image. *The International Archives of Photogrammetry, Remote Sensing and spatial Information Sciences*, 41, 747.

El Kafrawy, S. B., Basiouny, M. E., Ghanem, E. A. & Taha, A. S. (2017). Performance evaluation of shoreline extraction methods based on remote sensing data. *Journal of Geography, Environment and Earth Science International*, 11(4), 1-18.

Feyisa, G. L., Meilby, H., Fensholt, R., & Proud, S. R. (2014). Automated Water Extraction Index: A new technique for surface water mapping using Landsat imagery. *Remote Sensing of Environment*, 140, 23-35.

Ghorai, D., & Mahapatra, M. (2020). Extracting shoreline from satellite imagery for GIS analysis. *Remote Sensing in Earth Systems Sciences*, 3(1), 13-22.

Gonçalves, R. M., Saleem, A., Queiroz, H. A., & Awange, J. L. (2019). A fuzzy model integrating shoreline changes, NDVI and settlement influences for coastal zone human impact classification. *Applied Geography*, 113, 102093.

Gautam, V. K., Gaurav, P. K., Murugan, P., & Annadurai, M. J. A. P. (2015). Assessment of surface water Dynamicsin Bangalore using WRI, NDWI, MNDWI, supervised classification and KT transformation. *Aquatic Procedia*, 4, 739-746.

Li, W., & Gong, P. (2016). Continuous monitoring of coastline dynamics in western Florida with a 30-year time series of Landsat imagery. *Remote Sensing of Environment*, 179, 196– 209

Masek, J. G., Wulder, M. A., Markham, B., McCorkel, J., Crawford, C. J., Storey, J., & Jenstrom, D. T. (2020). Landsat 9: Empowering open science and applications through continuity. *Remote Sensing of Environment*, 248, 111968.

Maglione, P., Parente, C., & Vallario, A. (2014). Coastline extraction using high resolution WorldView-2 satellite imagery. *European Journal of Remote Sensing*, 47(1), 685-699.

McAllister, E., Payo, A., Novellino, A., Dolphin, T., & Medina-Lopez, E. (2022). Multispectral satellite imagery and machine learning for the extraction of shoreline indicators. *Coastal Engineering*, 104102.

NASA (2021). National Aeronautics and Space Administration, Landsat 9 Mission Brochure, 8p.

Naik, B. C., & Anuradha, B. (2018). Extraction of water-body area from high-resolution Landsat imagery. *International Journal of Electrical and Computer Engineering (IJECE)*, 8(6), 4111-4119.

Selim, S., Çoşlu, M., Sönmez, N. K., & Karakuş, N. (2016). Köyceğiz Gölü ve Dalyan Kanallarında Kıyı Kenar Çizgisinin UA ve CBS Teknikleri ile Belirlenmesi, *Alanda Karşılaşılan Sorunlar. Süleyman Demirel Üniversitesi Fen Bilimleri Enstitüsü Dergisi*, 20(2).

Selim, S., Esendağlı, Ç., Dönmez, B. (2021). Comparison of Different Indices Used for Shoreline Extraction from Landsat 8 Operational Land Imager in the context of Coastal Planning, *Recent Studies in Planning and Design*, IKSAD International Publishing House, Ankara, ss.3-24, 2022

Zollini, S., Alicandro, M., Cuevas-González, M., Baiocchi, V., Dominici, D., & Buscema, P. M. (2019). Shoreline extraction based on an active connection matrix (ACM) image enhancement strategy. *Journal of Marine Science and Engineering*, 8(1), 9.

Xu, H. (2006). Modification of Normalised Difference Water Index (NDWI) to Enhance Open Water Features in Remotely Sensed Imagery. *International Journal of Remote Sensing* 27, No. 14 (2006): 3025-3033.

Wicaksono, A., & Wicaksono, P. (2019). Geometric accuracy assessment for shoreline derived from NDWI, MNDWI, and AWEI transformation on various coastal physical typology in Jepara Regency using Landsat 8 OLI imagery in 2018. *Geopanning Journal of Geomatics and Planning*, 6(1), 55-57



4th Intercontinental Geoinformation Days

igd.mersin.edu.tr



Detection of surface algae blooms using the Sentinel 2A: An algorithm of the best strip ratio for a freshwater lake

Pathmalal M. Manage*¹, Gamage Charith Madushanka ²

¹University of Sri Jayewardenepura, Faculty of Applied Sciences, Department of Zoology, Center for Water Quality and Algae Research, Nugegoda, Sri Lanka

²University of Sri Jayewardenepura, Faculty of Graduate Studies, Nugegoda, Sri Lanka

Keywords

Remote sensing
Algal blooms
Chlorophyll-a
Sentinel 2A

Abstract

Harmful Algal Blooms (HABs) are problematic algal blooms that cause toxicity and associated environmental impacts on freshwater, marine and coastal ecosystems. HABs produce strong toxins that pose a threat to humans and wildlife, with significant negative impacts i.e., food web vectoring, airborne toxic events, decay of algal blooms resulting in low oxygen or hypoxia and killing fish and birds. Measurement of algae concentrations has conventionally relied on direct water sampling for lab-based cell enumeration. These traditional approaches are extremely labor-intensive, tedious, and limited spatially and temporally. Remote sensing (RS) based methods are capable to handle these complications in inland and near-coastal waters (consistent revisit rate for well-structured time series analyses, regular and reliable observations over a large area). The Multispectral Instrument (MSI) onboard European Space Agency's (ESA) Sentinel 2 satellite initiates a new era in high-to-moderate resolution (10, 20, 60 m) of earth observation data. Sentinel 2A (S2A) satellites launched in 2015 as a part of the ESA's Copernicus program. S2A filter-based push-broom imager, measures the reflected solar spectral radiances in 13 spectral bands ranging from the visible-near infrared (VNIR) (0.4422-0.8640 μm) to the short-wave infrared (SWIR) (0.9432-2.1857 μm) bands. This study aims to develop a method to estimate Chlorophyll-a (Chl-a) concentration in freshwater lake waters using in situ data of Chl-a, water reflectance, and contemporaneous S2A imagery over the Kotmale reservoir Sri Lanka.

1. Introduction

Algae are neither homogenous organisms, nor belong to natural taxonomic grouping. They are eukaryotic organisms that has permanent plastid, Chl-a as their primary photosynthetic pigment (Granéli and Turner, 2006). Algae are unicellular prokaryotes, their growth is driven by light, nutrient (nitrate and phosphates) and temperature. These organisms are primary producers; produce food via photosynthesis and key foundation of marine and freshwater food chains and webs (Klemas, 2012). Freshwater ecosystems provide unique habitats, supports high level of biodiversity. These ecosystems occupy approximately 0.8% of the Earth's surface but support almost 6% of all known species, i.e., more than 10, 000 fish species live in freshwaters, which is about 40% of the global fish species. Moreover, these freshwater ecosystems provide irreplaceable goods and

services. Inland lakes, rivers are among the most threatened freshwater ecosystems on the Earth. Besides, biodiversity losses in freshwaters are much faster or even worse (Xiong et al., 2020).

HABs are ubiquitous (Clark et al., 2017; Liang et al., 2017; Torbick and Corbiere, 2015), posing serious threats to marine and freshwater aquatic ecosystems and causes significance health consequences. HABs are an issue in marine, brackish, and freshwater systems. Large and tiny lakes, reservoirs, rivers, ponds, dugouts, and wide selection of other surface waters were affected worldwide. HABs and toxic algae kill fish and birds, food web vectoring, airborne toxic events, decay of algal blooms resulting in low oxygen or hypoxia, impede visual predators, attenuate light to submerged aquatic vegetations, distress in humans resulting respiratory

* Corresponding Author

*(pathmalal@sjp.ac.lk) ORCID ID 0000-0002-2014-2060
(charithmadups@gmail.com) ORCID ID 0000-0003-2195-3655

Cite this study

Manage P. M & Madushanka G.C (2022). Detection of surface algae blooms using the Sentinel 2A: An algorithm of the best strip ratio for a freshwater lake. 4th Intercontinental Geoinformation Days (IGD), 203-206, Tabriz, Iran

irritations, breathing difficulties, and even mortality (Xu et al., 2019; Palacios et al., 2017).

Microcystis aeruginosa is considered as a Cyanobacterial HAB organism which impede recreational use of waterbodies, reduce esthetics, lower dissolved oxygen concentration and cause taste and odor issues in drinking water. They also produce microcystins (MC-LR) which are powerful hepatotoxins. Long-term exposure to MC-LR causes development of liver cancer and liver tumors under low-level exposure (Metcalf et al., 2018; Palacios et al., 2017). Yet not all cyanobacterial genera are toxic. Different cyanobacteria produce similar toxins i.e., *Microcystis* sp, *Anabaena* sp, and *Anabaenopsis* sp all have been capable of producing microcystin (Torbick and Corbiere, 2015). Furthermore, cyanobacterial toxins also implicated among the factors contributing to chronic kidney disease of uncertain etiology in Sri Lanka. Thus, presence of cyanobacterial harmful algal bloom formation in freshwaters is a serious concern (Kulasooriya, 2017).

HABs are extremely patchy, they often remain unobserved by current monitoring programs, and spatial and temporal frequencies of conventional water sampling programs are not adequate to report changes in phytoplankton biomass, bloom conditions. Conventional in situ sampling and laboratory measurements comprise of physical, chemical and biological properties and indicators. Though, the in situ measurements of water quality parameters only represent point estimates of water quality conditions in time and space nevertheless, obtaining spatial-temporal variations in large waterbodies are almost impossible, conventional methods are extremely labor-intensive, tedious, monitoring and forecasting of entire waterbodies might be unapproachable, due to water surface extent and topographic characteristics (Gholizadeh et al., 2016; Ouma et al., 2018).

RS become an effective tool to derive the spatial and temporal behavior of aquatic ecosystems (Liang et al., 2017; Neil et al., 2019). Combination of RS with conventional in situ sampling methods coupled with laboratory measurements and analysis may provide effective approach (Bonansea et al., 2018). Numerous algorithms have been developed to estimate Chl-a concentrations. Namely, Sea-viewing Wide Field-of-view Sensor (SeaWiFS), Moderate Resolution Imaging Spectroradiometer (MODIS), Medium-spectral Resolution Imaging Spectrometer (MERIS), Sentinel 2 and 3, Landsat Operational Land Imager (OLI) and Enhanced Thematic Mapper Plus (ETM+) which are spaceborne missions that have been frequently used in deriving the information on Chl-a concentrations.

Chl-a taken as the index of phytoplankton abundance, and may result in visible changes in water bodies. HABs have distinct spectral characteristics i.e., significant absorption bands around 500 nm, 675 nm and reflectance peaks 550 nm, and 700 nm; which is caused due to dramatic increase of phytoplankton biomass. When a HAB dominates the phytoplankton biomass, Chl-a concentration has the advantage of providing an estimate of the total concentration of the bloom (Kutser, 2004).

2. Method

The datasets in this research include S2A satellite imagery of Kotmale reservoir, Sri Lanka acquired on July 21, 2020, approximately at 05:06 GMT. Level -1C MSI data downloaded from the Copernicus Open Access Hub (<https://scihub.copernicus.eu/dhus>) provided by European Space Agency. Water samples at 45 study points were collected randomly. Coordinates for water sample stations were recorded using a global positioning system (GPS). The in-situ data and corresponding satellite image pixels were used to develop and evaluate the supervised learning method for retrieval of the Chl-a concentration in the lake.

2.1. Laboratory Analysis of Chlorophyll-a

Chl-a quantification, used to estimate the total phytoplankton biomass, was carried out according to the Lorenzen, 1967 method. Each sample was filtered using 0.8 µm pore size filters under vacuum pressure that were then kept frozen at 253.15K for 8-12 hours in darkness. Chl-a was extracted from these filters in methanol by ultrasonication and agitation. The extracts were centrifuged at 13300 rpm for 10 minutes to reduce the turbidity. The Chl-a concentration of the extracts was determined spectrophotometrically using a Labomed UV-VIS RS spectrometer. Chl-a concentration was calculated accordingly.

2.2. Atmospheric Correction

Removing the intervening atmosphere effect from S2A satellite imagery is vital for the accurate estimation of Chl-a concentration in the reservoir. In this research, the Rayleigh correction is carried out to obtain the Rayleigh-corrected reflectance. The reflectance to radiance results from the below formula:

$$L_{TOA}(\lambda) = \frac{Q_{cal} E(\lambda) \cos\theta_i}{\pi d^2} \quad (1)$$

Where $L_{TOA}(\lambda)$ is Rayleigh adjusted radiance ($Wm^{-2}sr^{-1}$), Q_{cal} is the pixel value, θ_i is the incidence angle (radians), $E(\lambda)$ mean solar irradiance for each band (Wm^{-2}) and d is the sun-earth distance in astronomical units (AU). For Sentinel 2 the incidence angle is substituted with the values from the sun zenith band θ_s .

Undetected clouds can produce misleading results in the analysis of surface and atmospheric parameters. Water color RS products requires reliable cloud detection and cloud shadow detection and classification before atmospheric correction. The SHIMEZ method assumes that clouds are grey to white. Assumption is made that the mean of the red, blue, and green bands greater than a defendable threshold (B) (0.25), and that the difference between each of two bands lower than a pre-determined threshold (A) (0.15 over the day).

2.2.1. Algorithms for Chlorophyll-a

All available band ratios, frequently used for Chl-a estimation were assessed in this study, including two blue-green band ratios (B1/ B3 and B2/B3, respectively) one green-red band ratio (B3/B4), two NIR-red band

ratios (B5/ B4 and B6/B4, respectively) one NIR-Red three-band ratio ((B5 + B6) /B4) and Normalized Difference Chlorophyll Index (B4-B6/B4+B6).

2.2.2. Quantifying the Quality of Predictions

Standard statistical metrics were used to evaluate the empirical model to estimate Chl-a in the reservoir. The Root Mean Square Error (RMSE), Normalized Root Mean Square Error (NRMSE), Mean Absolute Percentage Error (MAPE) metrics were used.

3. Results

All cross-regression analyses between Chl-a and sensor radiance that corresponds to the band ratios shown in Table 1 and Table 2 including the locations under semitransparent clouds and cloud shadows.

Table 1. Performance of selected Chlorophyll-a estimation algorithms and results of the best-fit curve analyses

S2A band ratio	Regression equation coefficients	
	$\ln Y = \beta_0 + \beta_1 x$	
	β_0	β_1
B1/B3	17.5	-12.6
B2/B3	21.2	-18.0
B3/B4*	-36.8	22.3
B5/B4	-22.7	24.6
B6/B4	-10.9	7.7
B5+B6/B4	-15.7	6.5
B4-B6/B4+B6	-3.3	18.6

Table 2. Selected Chlorophyll-a estimation algorithms and results of the best-fit curve analyses for in situ measurements of Chlorophyll-a located under semitransparent clouds and cloud shadows

S2A band ratio	Regression equation coefficients			
	$Y = \beta_0 + \beta_1 x + \beta_2 x^2 + \beta_3 x^3$			
	β_0	β_1	β_2	β_3
B1/B3	-2105.9	4421.6	-3090.8	719.4
B2/B3	-9827.0	23674.9	19007.1	5085.2
B3/B4*	-927.7	1775.4	-1133.0	241.12
B5/B4	1762.6	-5470.8	5659.6	-1951.4
B6/B4	457.5	-1162.9	98.3	-277.4
B5+B6/B4	1592.4	-2227.4	1038.0	-161.6
B4-B6/B4+B6	1.9	75.3	954.6	3857.5

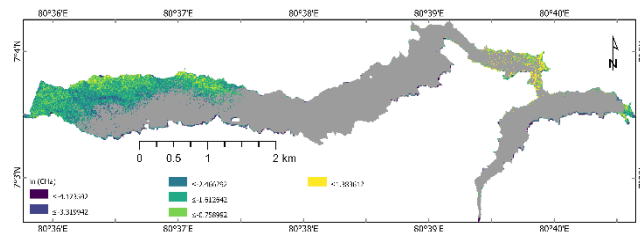


Figure 2. Chl-a retrieved from S2A MSI (B3/B4 Exponential curve fitted) in Kotmale reservoir. Areas covered with semitransparent clouds and cloud shadows are masked in color gray

The summarized statistical analyses of the S2A MSI derived Chl-a concentrations over the locations including

study points under semitransparent cloud cover are listed in Table 3 and Table 4 respectively.

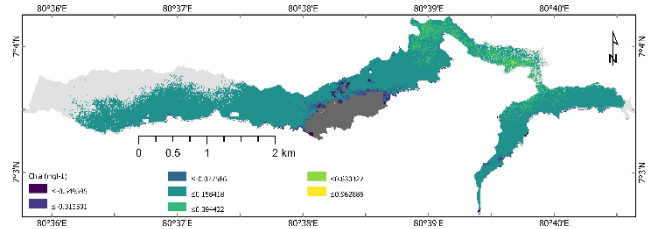


Figure 3. Chl-a retrieved from S2A MSI for study points under the semitransparent cloud and loud shadows (B3/B4 Polynomial curve fitted) in Kotmale reservoir. Dense clouds and cloud shadows are masked in dark gray.

Table 3. Validation of Sentinel 2A band ratio models considering RMSE, NRMSE and MAPE

S2A band ratio	RMSE	NRMSE	MAPE
B1/B3	0.180	0.454	0.534
B2/B3	0.190	0.478	0.853
B3/B4*	0.092	0.233	0.255
B5/B4	0.149	0.374	0.914
B6/B4	0.167	0.422	0.749
B5+B6/B4	0.163	0.410	0.799
B4-B6/B4+B6	0.167	0.421	0.758

Table 4. Validation of S2A band ratio models considering RMSE, NRMSE and MAPE for in situ measurements located under semitransparent clouds

S2A band ratio	RMSE	NRMSE	MAPE
B1/B3	0.154	0.591	12.696
B2/B3	0.091	0.349	2.019
B3/B4*	0.055	0.213	3.142
B5/B4	0.116	0.447	6.167
B6/B4	0.120	0.463	6.167
B5+B6/B4	0.120	0.463	6.554
B4-B6/B4+B6	0.110	0.421	6.022

4. Discussion

Evaluation on the performances of frequently used band ratio algorithms for estimating Chl-a in Kotmale reservoir, demonstrated the appropriateness of green-red two band ratio to estimate Chl-a in the reservoir using S2A data. The cross-relationship of Chl-a and band ratios for non-cloudy locations, with the strongest correlation, was detected between under exponential curve fit of Chl-a and band ratio of B4/B4. Measurements located under clouds and cloud shadows show a correlation with Chl-a and band ratio of B3/B4 under polynomial fit.

5. Conclusion

The main aim of this study was to evaluate the suitability of S2 MSI imagery for mapping lake water quality parameters (Chl-a) by means of band ratio type algorithms, which has demonstrated good performance in previous water color remote sensing studies.

The clouds' interference can cause lowering of the signal to noise ratio of reflectance, especially in blue and green bands, which were used to calculate the calibrated spectral radiance, which might be problematic for predicting low spectral band ratio derived Chl-a in the study points which are located under clouds and cloud shadows.

The second prominent reflectance peak around 700 nm occurred because of minimal absorption of water constituents i.e., Chl-a, Colored Dissolved Organic Matter (CDOM), non-algal particles (NAP) and particulate backscattering, which controls the reflectance variations in this region. While the peak magnitude; near 700 nm vs. Chl-a concentration indicated a very poor relationship, the increase in the Chla concentration caused the displacement of the peak position in the red region which is usually observed in turbid and productive waters. The NIR-Red band ratio algorithms did not result in a significant improvement in performance relative to the green-red two band ratio model feasibly because of the effect of absorption by CDOM NAPs.

References

- Bonansea, M., Rodriguez, C. and Pinotti, L. (2018), "Assessing the potential of integrating Landsat sensors for estimating chlorophyll - A concentration in a reservoir", *Hydrology Research*, Vol. 49 No. 5, pp. 1608-1617
- Clark, J.M., Schaeffer, B.A., Darling, J.A., Urquhart, E.A., Johnston, J.M., Ignatius, A.R., Myer, M.H., et al. (2017), "Satellite monitoring of cyanobacterial harmful algal bloom frequency in recreational waters and drinking water sources", *Ecological Indicators*, Vol. 80 No. November 2016, pp. 84-95
- Gholizadeh, M.H., Melesse, A.M. and Reddi, L. (2016), "A comprehensive review on water quality parameters estimation using remote sensing techniques", *Sensors (Switzerland)*, Vol. 16 No. 8, available at: <https://doi.org/10.3390/s16081298>
- Granéli, E. & Turner, J. T. (2006), *Ecology of Harmful Algae - Analysis and Synthesis*.
- Klemas, V. (2012). *Remote Sensing of Algal Blooms: An Overview with Case Studies*. *Journal of Coastal Research*
- Kulasooriya, S. A. (2017), Toxin producing freshwater cyanobacteria of Sri Lanka. *Ceylon Journal of Science*, 46(1), p. 3.
- Kutser, T. (2004). Quantitative detection of chlorophyll in cyanobacterial blooms by satellite remote sensing. *Limnology and Oceanography*, 49(6), 2179-2189.
- Liang, Q., Zhang, Y., Ma, R., Loisel, S., Li, J. and Hu, M. (2017). A MODIS-based novel method to distinguish surface cyanobacterial scums and aquatic macrophytes in Lake Taihu. *Remote Sensing*, available at: <https://doi.org/10.3390/rs9020133>.
- Metcalf, J.S., Banack, S.A., Powell, J.T., Tym, F.J.M., Murch, S.J., Brand, L.E. and Cox, P.A. (2018). Public health responses to toxic cyanobacterial blooms: Perspectives from the 2016 Florida event. *Water Policy*, 20(5), 919-932.
- Neil, C., Spyros, E., Hunter, P.D. and Tyler, A.N. (2019), "A global approach for chlorophyll-a retrieval across optically complex inland waters based on optical water types", *Remote Sensing of Environment*, Elsevier, Vol. 229 No. May, pp. 159-178.
- Ouma, Y.O., Waga, J., Okech, M., Lavisa, O. and Mbuthia, D. (2018), "Estimation of Reservoir Bio-Optical Water Quality Parameters Using Smartphone Sensor Apps and Landsat ETM+: Review and Comparative Experimental Results", *Journal of Sensors*, Vol. 2018, available at: <https://doi.org/10.1155/2018/3490757>
- Palacios, S., Mehta, A., Anderson, C., Kudela, R., Bahr, F., Chao, Y., Kahru, M., Robinson, D., Stumpf, R., Salls, W. (2017). *Introduction to Remote Sensing of Harmful Algal Blooms*. NASA Applied Remote Sensing Training Program (ARSET). <https://appliedsciences.nasa.gov/join-mission/training/english/arset-introduction-remote-sensing-harmful-algal-blooms>
- Torbick, N. & Corbiere, M. (2015). A multiscale mapping assessment of lake champlain cyanobacterial harmful algal blooms. *International Journal of Environmental Research and Public Health*, 12(9), 11560-11578
- Xiong, W., Huang, X., Chen, Y., Fu, R., Du, X., Chen, X. and Zhan, A. (2020). Zooplankton biodiversity monitoring in polluted freshwater ecosystems: A technical review. *Environmental Science and Ecotechnology*, Elsevier Ltd, Vol. 1 No. December 2019, p. 100008.
- Xu, M., Liu, H., Beck, R., Lekki, J., Yang, B., Shu, S., Kang, E.L., et al. (2019). A spectral space partition guided ensemble method for retrieving chlorophyll-a concentration in inland waters from Sentinel-2A satellite imagery. *Journal of Great Lakes Research*, Elsevier B.V., 45(3), 454-465

4th Intercontinental Geoinformation Days

igd.mersin.edu.tr



Global scale-biomass estimation based on a deep learning method

Somayeh Talebiesfandarani ^{*1}, Ali Shamsoddini ¹¹Tarbiat Modares University, Department of Remote sensing and GIS, Tehran, Iran

Keywords

Biomass
CNN
Microwave
Feature Selection

Abstract

Modeling accurate above-ground biomass (AGB) maps is a critical issue in remote sensing research. Since the relationship between biomass and environmental variables are usually complex, because of being affected by many factors, using non-parametric methods like Convolutional Neural Network (CNN) to estimate biomass on the global scale is convenient. To choose the most significant variables to enter to the AGB estimation model two feature selection techniques were applied, Support Vector Machine for Regression Feature Selection (SVRFS) and Random Forest Feature Selection (RFFS) techniques. The optimum AGB model was created using the training dataset and the predicted model was created using the test dataset. The results showed CNN with the SVRFS technique, achieved the highest RMSE values (31.22 Mg/ha). This study highlighted the capability of the deep learning algorithm to improve AGB estimates on a global scale.

1. Introduction

Biomass is a good measure of plant domination in research. Remote sensing technology is a powerful tool in biomass estimation in regional and global scale (Lu 2006). Passive microwave observations can provide data from both green and non-green vegetation components (Liu, Van Dijk et al. 2015, Talebiesfandarani, Zhao et al. 2019) and can take information from a deeper layer of vegetation, depending on the frequency. Besides, passive microwave observations are insensitive to cloud cover. Biomass estimation using passive microwave data is based on Vegetation Optical Depth (VOD) (Ulaby, Kouyate et al. 1986, Momen, Wood et al. 2017). The VOD retrieved at lower frequencies like L-band has special relationship to the vegetation features of the whole canopy. Beside VOD, there are many variables that are important in biomass estimation (Rodríguez-Fernández, Mialon et al. 2018, Vittucci, Laurin et al. 2019). In this research, beside VOD, precipitation, temperature, tree height, NDVI, EVI, climatic water availability (CWA) and evapotranspiration were used to enter to the models.

Recently, Non-parametric models like convolutional neural network (CNN) as a deep learning approach are a popular way to analyze complex environment relationships (Chen, Ren et al. 2018, Jin, Li et al. 2020, Kattenborn, Leitloff et al. 2021).

It's clear that in a deep learning model, all the input variables in the biomass estimation dataset are not helpful to build the model. Furthermore, adding many variables from different datasets to the model can cause model complexity and reduce the overall accuracy of the model. Efforts were made to mitigate these problems using some feature selection techniques to find the best series of features and build an effective biomass model. Here Random Forest Feature Selection (RFFS) and Support Vector Regression Feature Selection (SVRFS) were used to find how the accuracy of the biomass estimation is affected by the different combinations of feature selection techniques.

The main goals of this study were:

- Using feature selection techniques to select the most influential variables in biomass estimation.
- Investigating the ability of a deep learning method on biomass estimation in the global scale and comparing the models.

2. Method

2.1. Input Data

To take climatic variables the Climatic Research Unit Time Series (CRU TS) 4.05 diffusion (Harris et al., 2014) has been utilized in the present study. The CRU TS dataset that used here consists of precipitation,

* Corresponding Author

(so.talebi@modares.ac.ir) ORCID ID 0000-0001-6141-6489
(ali.shamsoddini@modares.ac.ir) ORCID ID 0000-0002-4559-7563

Cite this study

Talebiesfandarani, S., & Shamsoddini, A. (2022). Global scale-biomass estimation based on a deep learning method. 4th Intercontinental Geoinformation Days (IGD), 207-210, Tabriz, Iran

temperature (air temperature at 2m above the soil) and evapotranspiration. In addition to CRU TS, the climatic water availability (CWA) was used as one of the inputs to the models. CWA [mm/yr.], show the amount of water lost during the dry season. Here is supposed CWA not to change during the period of this research (2000-2019).

The VOD data (SMOS-IC), used in this study, at L band was obtained from SMOS which operate at 1.2 GHz. It is a global product with 25-km spatial and one-day temporal resolution.

The input data consist of yearly, seasonal and monthly data.

AGB map was derived as a part of the Climate Change Initiative, CCI project (CCI AGB D4.3, 2020)(Santoro, Cartus et al. 2021). NDVI, EVI and tree high also were used as the input data to the CNN model.

2.2. CNN

Our CNN model consists of 5 convolution layers. Each convolution layer extracts a special-spectral feature. To avoid overfitting, dropout function was used but no special improvement in the test data. Stepwise learning rate was used to avoid overfitting during training the model. All the layers of the network performed the feature extraction. In the first layers, low-level features and in the last layers high-level features was extracted. Here, a fully connected neural network is used. Adjusting the optimal hyperparameters for CNN was based on random search, because the grid search was time consuming. Table 1 shows the configurations of the tuning hyperparameters for CNN algorithm.

The original data are divided into training dataset (80%) and testing dataset (20%). The training data are classified into five folds (five-fold cross-validation), four folds chosen for training and one left signified for validation. Each of the five folds operates once as validation set and four times as training data. The minimum average RMSE in the five validation datasets is a key specifying the optimal combination of hyperparameters.

Table 1. The procedure of tuning the hyperparameters adjusted for each model

Algorithm	Hyperparameters Tuned	Hyperparameter Configurations
CNN	Epoch	10000,30000,
	H	70000,100000
	Kernel	[299, 24, 5, 3, 1],
	Learning rate	[299, 24, 8, 2, 1],
	seed	3*3, 5*5, 7*7 0.1, 0.2, .0.3 10-100interval 10

2.3. Feature Selection Techniques

Here RFFS and SVRFS are chosen to apply to the original dataset to specify suitable variables. RFFS is an embedded algorithm that utilizes random forests as the base arranger(Rodríguez-Fernández, Mialon et al. 2018). Firstly, the random forest was fitted for all the AGB features. In every run, one variable is permuted by random permutation model and other variables are entered in to the model without permutation. This

process was implemented for all input variables one by one. Paying attention to RMSE values from permutations and sorting them showed the most important variables were those with greater RMSE values. Then, 20% of the less important attributes were removed, and again, the model fitted with other variables. This step was repeated and the process was done until the least numbers of variables with the highest RMSE values were left. In the final step, the most important features were ranked(Shamsoddini, Trinder et al. 2013, Shamsoddini and Raval 2018).

In the SVRFS technique, the process was done the same as RFFS technique, and the SVR model was used as the base arranger to choose appropriate variables to enter the models(Lal, Chapelle et al. 2006, Rodriguez-Galiano, Luque-Espinar et al. 2018).

Biomass estimation has been done using two feature selection techniques with a combination of CNN model (RFFS-CNN SVRFS-CNN respectively).

2.4. Evaluation of the AGB estimation models

The AGB models trained with all training data (80%) and 20% of the initial data as an independent-test dataset were used to estimate the coefficient of determination (R^2), root mean square error (RMSE), relative RMSE (RMSE%), and bias. Paired samples t-test also was used for statistically comparing the efficiency of different AGB models.

3. Results

3.1. The primitive AGB estimation models result with all layers as inputs

Table 2 represented the distribution of the R^2 , RMSE, RMSE%, and bias for CNN biomass estimation model in the case of entering all the input data to the models (without using feature selection techniques).

Table 2. The performance metrics for CNN algorithm with all input variables

	R^2	RMSE(Mg/ha)	RMSE%	bias (Mg/ha)
CNN	0.8795	40.5700	30.1041	0.50

3.2. Specifying the optimal number of input variables (implementation of feature selection techniques)

The trend of RMSE values of RFFS-CNN SVRFS-CNN models as the input variable numbers changed is represented in fig. 1. Input data started from about 300 variables and low-scoring features were removed until eight variables left. In general, in the figure, by decreasing the number of variables, RMSE values decreased.

Tree height, average EVI index in autumn 2017, average EVI index in winter in 2017, average evapotranspiration in winter 2017, average temperature in spring 2004, average NDVI in August 2017, average optical depth in January 2017 and mean NDVI in October in 2017were included in 8 most effective variables when use RFFS respectively.

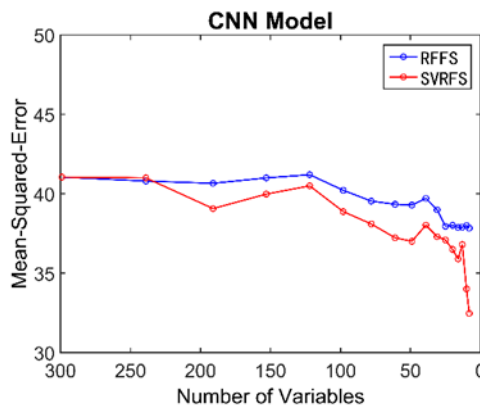


Fig.1. The trend of RMSE values for different number of variables for the CNN model

When SVRFS model was used as feature selection model tree height, Average spring rainfall in 2004, Average optical depth in November 2017, average NDVI in August 2017, average NDVI in autumn 2017, average optical depth in January 2017, average spring precipitation in 2016 and average optical depth in spring 2017 were the 8 most significant variables in AGB estimation. Tree Hight, mean NDVI in August 2017 and mean optical depth in January 2017 were the same variables in two feature selection models. The most important variable in two feature selection models was tree height. It shows tree height variables are fundamental variable in AGB estimation regardless of the method is used.

Since the most important target in using feature selection technique is reducing the RMSE value, precise attention to the accuracies, indicated SVRFS technique compared to RFFS could reduce RMSE value appropriately in AGB estimation model (31.2209 Mg/ha, for SVRFS-CNN, compare to 36.6764 Mg/ha, for RFFS-CNN). Here also SVRFS technique could reduce overestimation and underestimation of the models more significant than RFFS.

3.1. Evaluation of the Model

Statistical comparison of different models was done using the paired sample t-test (Shamsoddini and Raval, 2018). Table 3 indicated the p-value derived from paired sample t-test. No statistical differences were between the CNN model and CNN in combination with two feature selection techniques. RFFS-CNN and SVRFS-CNN also have no statistically difference but SVRFS-CNN outperformed better than RFFS-CNN (Table 3).

Table3. P-value related to paired sample t-test to compare two models

	CNN	RFFS-CNN	SVRFS-CNN
CNN	*	0.94	0.20
RFFS-CNN		*	0.17
SVRFS-CNN			*

4. Discussion

CNN model could predict biomass well (Kussul, Lavreniuk et al. 2017). One of the important issues in taking the best results from the CNN model depended on

choosing the optimal scale for it. The optimal scale depends on many factors like the appropriate number and type of samples, spatial and spectral resolution, sensor and land cover type (Dong, Du et al. 2020). Another important issue in CNN model precision for biomass monitoring is adjusting and tuning the hyperparameters properly (Dong, Du et al. 2020, Gupta, Rajnish et al. 2021). In this research, many efforts been made in choosing optimal scale and tuning the hyperparameters.

In this research SVRFS technique outperformed RFFS in the AGB mode (Tuong, Tani et al. 2020). It means that the SVRFS technique could retain more convenient information from the original data set. Also, compared to the AGB models with all variables as inputs, the least overestimations and underestimations related to the CNN model with combination of feature selection techniques (Li, Li et al. 2020). Here, tree height was the most practical feature in both feature selection techniques (Wang, Zhang et al. 2021). It is noteworthy that reliable reference biomass maps such as Saatchi (Saatchi, Harris et al. 2011) and Glob biomass (Santoro, Cartus et al. 2018, Santoro, Cartus et al. 2021) were produced based on tree height measurements (Nogueira, Engel et al. 2014). The other joint selected variables were VOD and NDVI. VOD has coarse spatial resolution but its high sensitivity to AGB makes it suitable indicator for biomass monitoring in large scale (Chaparro, Duveiller et al. 2019). AGB also has a significant relationship with NDVI, especially in shorter vegetation cover (Goswami, Gamon et al. 2015).

Finally, it should be noted that improving AGB estimation for landcovers and ecoregions can investigate more details in biomass estimation and provide stable results in contributions of the predictor variables to the AGB estimation model and is necessary in the future.

5. Conclusion

This study compared CNN AGB estimation model with and without feature selection techniques. The outcomes of this study were as follows:

- CNN model could predict biomass well on the global scale.
- Feature selection techniques were an effective tool in choosing the best variables to enter into the AGB model and improved estimation results. SVRFS technique outperformed RFFS.
- The jointly selected variables in two feature selection techniques were tree height, VOD and NDVI.
- The best models to estimate AGB with the combination of feature selection techniques were SVRFS-CNN with the lowest RMSE values.

References

- Chaparro, D., G. Duveiller, M. Piles, A. Cescatti, M. Vall-Llossera, A. Camps and D. Entekhabi (2019). "Sensitivity of L-band vegetation optical depth to carbon stocks in tropical forests: a comparison to higher frequencies and optical indices." *Remote sensing of environment* **232**: 111303.

- Chen, L., C. Ren, B. Zhang, Z. Wang and Y. Xi (2018). "Estimation of forest above-ground biomass by geographically weighted regression and machine learning with sentinel imagery." *Forests* **9**(10): 582.
- Dong, L., H. Du, N. Han, X. Li, D. e. Zhu, F. Mao, M. Zhang, J. Zheng, H. Liu and Z. Huang (2020). "Application of convolutional neural network on Lei Bamboo above-ground-biomass (AGB) estimation using Worldview-2." *Remote Sensing* **12**(6): 958.
- Goswami, S., J. Gamon, S. Vargas and C. Tweedie (2015). Relationships of NDVI, Biomass, and Leaf Area Index (LAI) for six key plant species in Barrow, Alaska, PeerJ PrePrints.
- Gupta, M., K. Rajnish and V. Bhattacharjee (2021). "Impact of Parameter Tuning for Optimizing Deep Neural Network Models for Predicting Software Faults." *Scientific Programming* **2021**.
- Jin, X., Z. Li, H. Feng, Z. Ren and S. Li (2020). "Deep neural network algorithm for estimating maize biomass based on simulated Sentinel 2A vegetation indices and leaf area index." *The Crop Journal* **8**(1): 87-97.
- Kattenborn, T., J. Leitloff, F. Schiefer and S. Hinz (2021). "Review on Convolutional Neural Networks (CNN) in vegetation remote sensing." *ISPRS Journal of Photogrammetry and Remote Sensing* **173**: 24-49.
- Kussul, N., M. Lavreniuk, S. Skakun and A. Shelestov (2017). "Deep learning classification of land cover and crop types using remote sensing data." *IEEE Geoscience and Remote Sensing Letters* **14**(5): 778-782.
- Lal, T. N., O. Chapelle, J. Weston and A. Elisseeff (2006). *Embedded methods. Feature extraction*, Springer: 137-165.
- Li, Y., M. Li, C. Li and Z. Liu (2020). "Forest aboveground biomass estimation using Landsat 8 and Sentinel-1A data with machine learning algorithms." *Scientific reports* **10**(1): 1-12.
- Liu, Y. Y., A. I. Van Dijk, R. A. De Jeu, J. G. Canadell, M. F. McCabe, J. P. Evans and G. Wang (2015). "Recent reversal in loss of global terrestrial biomass." *Nature Climate Change* **5**(5): 470-474.
- Lu, D. (2006). "The potential and challenge of remote sensing-based biomass estimation." *International journal of remote sensing* **27**(7): 1297-1328.
- Momen, M., J. D. Wood, K. A. Novick, R. Pangle, W. T. Pockman, N. G. McDowell and A. G. Konings (2017). "Interacting effects of leaf water potential and biomass on vegetation optical depth." *Journal of Geophysical Research: Biogeosciences* **122**(11): 3031-3046.
- Nogueira, L. R., V. L. Engel, J. A. Parrotta, A. C. G. d. Melo and D. S. Ré (2014). "Allometric equations for estimating tree biomass in restored mixed-species Atlantic Forest stands." *Biota Neotropica* **14**.
- Rodríguez-Fernández, N. J., A. Mialon, S. Mermoz, A. Bouvet, P. Richaume, A. Al Bitar, A. Al-Yaari, M. Brandt, T. Kaminski and T. Le Toan (2018). "An evaluation of SMOS L-band vegetation optical depth (L-VOD) data sets: high sensitivity of L-VOD to above-ground biomass in Africa." *Biogeosciences* **15**(14): 4627-4645.
- Rodriguez-Galiano, V. F., J. A. Luque-Espinar, M. Chica-Olmo and M. P. Mendes (2018). "Feature selection approaches for predictive modelling of groundwater nitrate pollution: An evaluation of filters, embedded and wrapper methods." *Science of the total environment* **624**: 661-672.
- Saatchi, S. S., N. L. Harris, S. Brown, M. Lefsky, E. T. Mitchard, W. Salas, B. R. Zutta, W. Buermann, S. L. Lewis and S. Hagen (2011). "Benchmark map of forest carbon stocks in tropical regions across three continents." *Proceedings of the national academy of sciences* **108**(24): 9899-9904.
- Santoro, M., O. Cartus, N. Carvalhais, D. Rozendaal, V. Avitabile, A. Araza, S. de Bruin, M. Herold, S. Quegan and P. Rodríguez-Veiga (2021). "The global forest above-ground biomass pool for 2010 estimated from high-resolution satellite observations." *Earth System Science Data* **13**(8): 3927-3950.
- Santoro, M., O. Cartus, S. Mermoz, A. Bouvet, T. Le Toan, N. Carvalhais, D. Rozendaal, M. Herold, V. Avitabile and S. Quegan (2018). A detailed portrait of the forest aboveground biomass pool for the year 2010 obtained from multiple remote sensing observations. EGU general assembly conference abstracts.
- Shamsoddini, A. and S. Raval (2018). "Mapping red edge-based vegetation health indicators using Landsat TM data for Australian native vegetation cover." *Earth Science Informatics* **11**(4): 545-552.
- Shamsoddini, A., J. C. Trinder and R. Turner (2013). "Non-linear methods for inferring lidar metrics using SPOT-5 textural data." *ISPRS Annals of Photogrammetry, Remote Sensing and Spatial Information Sciences* **2**: 259-264.
- Talebiesfandarani, S., T. Zhao, J. Shi, P. Ferrazzoli, J.-P. Wigneron, M. Zamani and P. Pani (2019). "Microwave vegetation index from multi-angular observations and its application in vegetation properties retrieval: Theoretical modelling." *Remote Sensing* **11**(6): 730.
- Tuong, T. T. C., H. Tani, X. Wang, N. Q. Thang and H. M. Bui (2020). "Combination of SAR Polarimetric Parameters for Estimating Tropical Forest Aboveground Biomass." *Polish Journal of Environmental Studies* **29**(5).
- Ulaby, F. T., F. Kouyate, B. Brisco and T. L. Williams (1986). "Textural information in SAR images." *IEEE Transactions on Geoscience and Remote Sensing*(2): 235-245.
- Vittucci, C., G. V. Laurin, G. Tramontana, P. Ferrazzoli, L. Guerriero and D. Papale (2019). "Vegetation optical depth at L-band and above ground biomass in the tropical range: Evaluating their relationships at continental and regional scales." *International Journal of Applied Earth Observation and Geoinformation* **77**: 151-161.
- Wang, Y., X. Zhang and Z. Guo (2021). "Estimation of tree height and aboveground biomass of coniferous forests in North China using stereo ZY-3, multispectral Sentinel-2, and DEM data." *Ecological Indicators* **126**: 107645.

4th Intercontinental Geoinformation Days

igd.mersin.edu.tr



Relationship between net primary production (NPP) and dust storms in different land cover classes

Ali Shamsoddini ^{*1}, Ali Sadeghnezhad ¹

¹ Tarbiat Modares University, Department of Remote Sensing and GIS, Tehran, Iran

Keywords

NPP
AOD
Dust storm
Google Earth Engine
MODIS
Linear Regression

Abstract

Iran has been a prime target of dust storms, mostly with exogenous origins arising from its neighboring countries. Dust storms generally depend on two factors, namely wind speed and soil erosion threshold, the latter being highly dependent on vegetation. Meanwhile, remote sensing data and imagery allow for monitoring vegetation changes in different spatial and temporal scales, particularly through vegetation indices commonly found in the literature. Still, these indices suffer from certain shortcomings such as a lack of quantitative outcomes and sensitivity to greenness. Net primary production (NPP) is a measure of carbon content absorbed by plants through photosynthesis and is not affected by the shortcomings seen in vegetation indices. This study explored the relationship between NPP and dust storms in the Tigris and Euphrates basin. AOD values derived from MODIS data were used to measure dust and NPP values for different land cover types. The research findings showed that the highest correlation between AOD and NPP was found in the evergreen coniferous forest class with a Pearson correlation coefficient of negative 0.5326.

1. Introduction

Most countries located to the west of Iran are covered with vast deserts that serve as potential sources of sand and dust storms (SDS), which sometimes surpass political borders and affect neighboring countries (Al-Dabbas et al., 2012; Griffin et al., 2002). Dust storms are not limited to specific regions or climates and can affect any place with unprotected soil surfaces. Hence, vegetation, water, and rock covers can effectively protect the soil against wind erosion (Qian et al., 2002). Some of the main contributors to wind erosion are drought, low precipitation, rangeland plowing, and land-use change from forest to rangeland or from rangeland to agricultural lands (Haghighi et al., 2018; N. Middleton & Kang, 2017). Vegetation is much more effective than other factors since plants not only strengthen the soil through their roots but also reduce evaporation by providing shading (N. J. Middleton, 1986). Furthermore, plant litter decomposes into organic matter, which can increase the soil's erosion threshold. Vegetation, however, is severely sensitive to drought and low precipitation and more rangelands and forests are being

destroyed with population expansion worldwide (Rivera et al., 2021). In addition, land cover changes can have positive or negative effects on SDS. Overall, forest and tree cover boost soil consistency and prevent wind erosion by reducing wind speed, creating shade, and developing roots (Youlin, 2001). Vegetation monitoring through field surveys is rarely cost-effective and often impossible in certain cases. Satellite data and imagery present a suitable alternative thanks to their regular and long-term acquisitions, allowing for the analysis of land surface phenomena over long periods from the past to the present. The most common remote sensing method for monitoring vegetation is using vegetation indices such as NDVI. This method has also been used for investigating the effect of vegetation on dust events (Li et al., 2020; Ranjbar et al., 2020; Rivera et al., 2021). These indices are not perfect either and suffer from flaws such as lack of quantitative results, sensitivity to greenness, and high dependence on image acquisition angle and time. This study used net primary production (NPP) instead of vegetation indices to overcome these issues. NPP is an indicator of the carbon absorbed by plants through photosynthesis minus autotrophic respiration.

* Corresponding Author

^{*}(ali.shamsoddini@modares.ac.ir) ORCID ID 0000-0002-4559-7563
(alisadeghnezhad@modares.ac.ir) ORCID ID 0000-0002-6469-0616

Cite this study

Shamsoddini, A., & Sadeghnezhad, S. (2022). Relationship between net primary production (NPP) and dust storms in different land cover classes. 4th Intercontinental Geoinformation Days (IGD), 211-214, Tabriz, Iran

NPP is a quantitative indicator of vegetation growth and depends on factors such as leaf area, woody/herbaceous plant type, and perennial/annual plant type (Gulbeyaz et al., 2018; Ruimy et al., 1999). These features also affect sand and dust storms and so NPP monitoring can shed light on the relationship between vegetation and SDS. This study used the NPP index to determine the effect of different land cover classes on the amount of dust in the Tigris and Euphrates basin. AOD was used to measure variations in dust levels. Considering that variations in vegetation affect the level of dust at different intervals and with delay, the relationship between AOD and NPP was investigated using different delay intervals.

2. Research Data and Method

2.1. Study area

The Tigris and Euphrates basin with an area of 935,400 km² is located between longitude 36-51° E and latitude 27-40° N. The study area covers parts of Iran, Turkey, Syria, Jordan, Iraq, and Saudi Arabia, located 9 m below sea level at the shallowest and 4305 m above sea level at the highest point. A variety of climates can be seen across the region with the lowest and highest annual precipitation rates recorded at 18 and 376 mm, respectively.

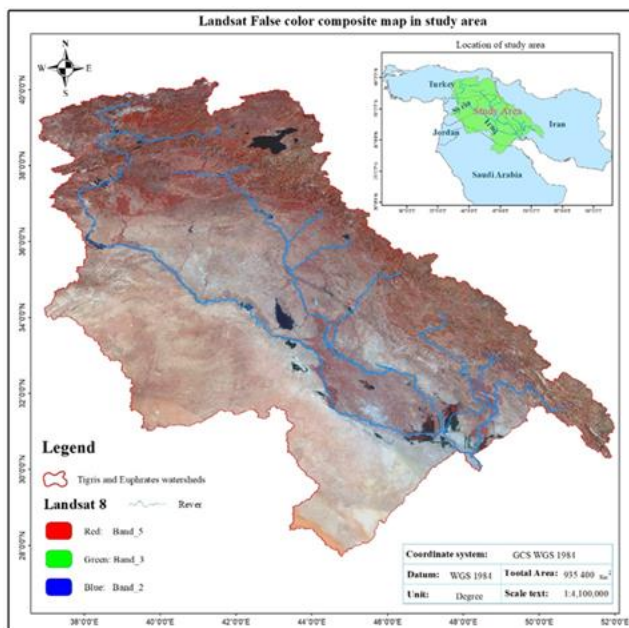


Figure 1. Landsat 8 false-color composite image of the study area (RGB with a band combination of 5, 3, and 2, respectively).

2.2. Research Data

NPP and AOD are among the most commonly used MODIS products for monitoring the carbon cycle and sand and dust storms. NPP is the amount of carbon absorbed by the plant during photosynthesis minus the amount released during respiration. It is called MOD17A3HGF V6 in the Google Earth Engine (GEE), which is a cumulative eight-day composite of MOD17A2H product (i.e., pure photosynthesis). AOD, another MODIS product, is also available in GEE (MCD19A2 V6) and provides daily estimates of optical depth at 0.47 and 0.55

μm wavelengths using the Terra and Aqua sensors. MCD12Q1 V6 product of MODIS supplies six types of global maps of land cover at annual time steps, the fourth being the carbon cycle, which enables NPP monitoring and was used in this study.

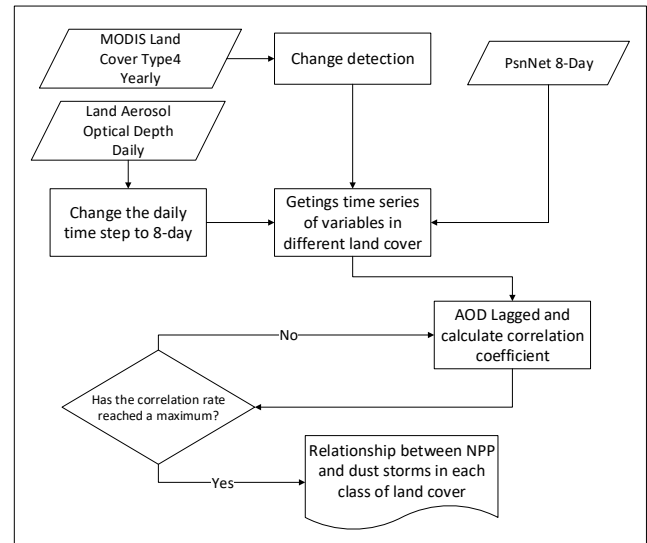


Figure 2. Flowchart of this study

2.3. Methodology

As shown in Figure 2, first, the 20-year MODIS land cover images were retrieved and the changes were enhanced. Then, two classes, namely change from vegetation to other classes and change from one type of vegetation to another vegetation class, were identified. Next, the samples were randomly selected from each class and uploaded to the GEE platform for pre-processing of satellite data and extraction of time series data. After extracting the time series of NPP and AOD samples, the Pearson correlation coefficient values and the time delays were computed in Python.

3. Results

3.1 Twenty-year land cover and land use changes

According to the results, land cover and land use classes in the study area included water bodies, evergreen coniferous forests, evergreen broad-leaved forests, broad-leaved deciduous forests, annual broad-leaved plants, grasslands, barren lands, and built-up lands (eight classes). The highest land use change was from different vegetation classes to barren (112,193 km²) and the lowest from rangeland to built-up (478 km²). The total land use changes over 20 years amounted to 122,000 km². Change from one vegetation class to another was approximately 91,239 km² and from vegetation to other classes stood at about 11,2671 km².

3.2 Area of SDS and monthly NPP over 22 years

AOD measures the optical depth of the atmosphere (i.e., the extent of sunlight prevented from reaching the ground), and AOD values above 0.5 mark the occurrence of a dust event. By retrieving the AOD from the MODIS data in GEE and creating a threshold, areas with an AOD

value above 0.5 were selected and their area was calculated for each month. Figure 3a shows the area of land affected by dust on a monthly basis over a 22-year period. Accordingly, large areas were affected by SDS in the 2000–2002 and 2008–2012 periods.

MODIS NPP is an 8-day product, and the monthly NPP is the cumulative value of each month's images. The total NPP for each month is presented in Figure 3b, showing a declining trend in 2007 and 2008, which is consistent with the significant rising AOD trends.

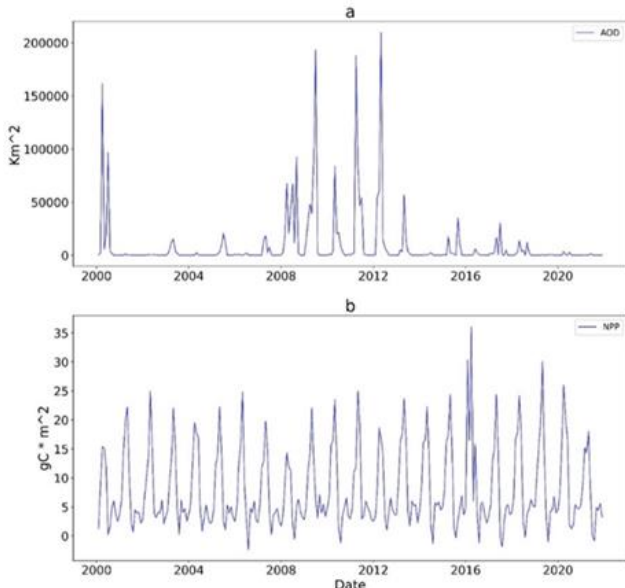


Figure 3. (a) The area of land affected by sand and dust storms per month and (b) the monthly NPP in a 22-year period.

3.3 Relationship between NPP and AOD in each land cover class

Five vegetation land cover classes were found in the study area. After the enhancement of changes, each class was sampled separately and randomly, and the SDS and NPP time series were extracted using GEE. Overall, there were no high correlation coefficients in any of the land use classes, with the highest observed in the evergreen coniferous forest (-0.5326) and the lowest in the evergreen broad-leaved forest class (-0.4320). The highest correlation among all classes was obtained with a 10-month delay, indicating that a rise in dust storms was seen after 10 months since declining NPP trends. An example of the AOD and NPP time series in the evergreen coniferous forest class is presented in Figure 4a. It can be seen that a declining AOD has led to an increasing NPP. Figure 4a shows the correlation coefficient of these variables in 0–25-month time delays. Moreover, 4c and 4d demonstrate the variable scatter plots in zero and 10-month delays. In the 10-month delay, the relationship between the variables was in its most regular state.

Interestingly, in the 10-month delay (4d), no dust storm has occurred with NPP values above 2 since AOD values above 0.5 signal dust storms (Yue et al., 2017). The same result was obtained in other classes except for the evergreen broad-leaved forest class, in which no storms occurred with NPP values above 3.

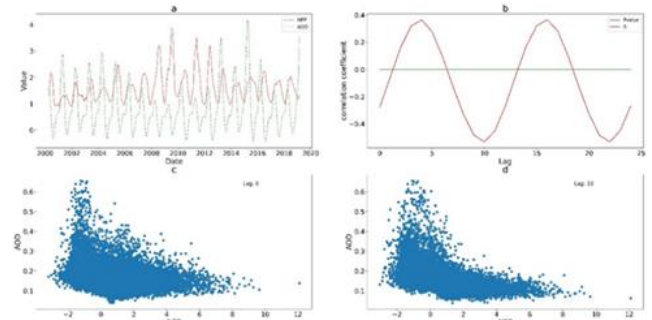


Figure 4. AOD and NPP time series with a 22-year correlation for the evergreen coniferous forest class; (a) the NPP and AOD time series and (b) the correlation coefficient at 0–24-month time delays. Figure 4c and 4d, respectively, show the relationship between the variables in zero and 10-month delays (highest correlation).

4. Discussion

There is an increasing urbanization trend in the Tigris and Euphrates basin (Attiya & Jones, 2020). Over the last 20 years, built-up lands have expanded by 478.25 km² while 112,193.75 km² have turned into barren lands. The vegetation status is changing drastically with 91,239 km² experiencing changes in the vegetation type over the past 20 years, mostly from forests and rangelands to agricultural lands. The research by Xu et al. (2015) revealed that vegetation change from woody to herbaceous led to a severe fall in NPP (Xu et al., 2015). The analysis of the study area showed that in the 20-year period, NPP values were the lowest in 2008 and dust storms were highest from 2008 to 2012 covering large portions of the study area in most months. These findings are consistent with those of many studies (Albarakat & Lakshmi, 2019; Boloorani et al., 2020; Broomandi et al., 2017a, 2017b). Although the fall in NPP cannot be seen as directly affecting the rise in SDS, it can be associated with the rise in AOD considering the effect of vegetation on dust storms as confirmed by previous studies. Zou and Zhai (2004) concluded that former declines in vegetation (e.g., the last summer) can increase dust storms in later times (e.g., the next spring) (Zou & Zhai, 2004). The findings of the present study also showed that the time delay for the highest correlation between the variables was 10 months, which is also consistent with Zou and Zhai (2004).

The separation of land cover classes increased the correlation between NPP and AOD in the evergreen coniferous forest class, whereas a lower correlation was obtained for other tree cover classes due to their low area and distribution.

5. Conclusion

This study used MODIS products, namely AOD, NPP, and land use data to investigate the relationship between AOD and NPP in different land uses and time delays. The research results can be summarized as follows:

- The relationship between NPP and AOD varies in different land cover classes.

- In the study area, the NPP of the evergreen coniferous forest class had the highest correlation with AOD.
- The effect of increasing or decreasing NPP on dust storms reached its highest level 10 months after the land use change.
- A dust storm event is very unlikely if the NPP level has not been less than 2 g of carbon per m² in the previous 10 months.

References

- Al-Dabbas, M. A., Ayad Abbas, M., & Al-Khafaji, R. M. (2012). Dust storms loads analyses—Iraq. *Arabian Journal of Geosciences*, 5(1), 121–131. <https://doi.org/10.1007/s12517-010-0181-7>
- Albarakat, R., & Lakshmi, V. (2019). Monitoring dust storms in Iraq using satellite data. *Sensors (Switzerland)*, 19(17). <https://doi.org/10.3390/s19173687>
- Attiya, A. A., & Jones, B. G. (2020). Climatology of Iraqi dust events during 1980–2015. *SN Applied Sciences*, 2(5). <https://doi.org/10.1007/s42452-020-2669-4>
- Bolloorani, A. D., Kazemi, Y., Sadeghi, A., Shorabeh, S. N., & Argany, M. (2020). Identification of dust sources using long term satellite and climatic data: A case study of Tigris and Euphrates basin. *Atmospheric Environment*, 224, 117299. <https://doi.org/10.1016/j.atmosenv.2020.117299>
- Broomandi, P., Dabir, B., Bonakdarpour, B., & Rashidi, Y. (2017a). Identification of the sources of dust storms in the City of Ahvaz by HYSPLIT. *Pollution*, 3(2), 341–348. <https://doi.org/10.7508/pj.2017.02>
- Broomandi, P., Dabir, B., Bonakdarpour, B., & Rashidi, Y. (2017b). Identification of dust storm origin in South - West of Iran. *Journal of Environmental Health Science and Engineering*, 15(1). <https://doi.org/10.1186/s40201-017-0280-4>
- Griffin, D. W., Kellogg, C. A., Garrison, V. H., & Shinn, E. A. (2002). The global transport of dust. *American Scientist*, 90(3), 228–235. <https://doi.org/10.1511/2002.3.228>
- Gulbeyaz, O., Bond-Lamberty, B., Akyurek, Z., & West, T. O. (2018). A new approach to evaluate the MODIS annual NPP product (MOD17A3) using forest field data from Turkey. *International Journal of Remote Sensing*, 39(8), 2560–2578. <https://doi.org/10.1080/01431161.2018.1430913>
- Haghighi, S., Akhzari, D., Attaeian, B., & Bashir Gonbad, M. (2018). The effect of drought in the source area of dust storms on vegetation change (case study: western parts of Iran). *Environmental Resources Research*, 6(2), 195–200.
- Li, J., Garshick, E., Al-Hemoud, A., Huang, S., & Koutrakis, P. (2020). Impacts of meteorology and vegetation on surface dust concentrations in Middle Eastern countries. *Science of the Total Environment*, 712, 136597. <https://doi.org/10.1016/j.scitotenv.2020.136597>
- Middleton, N. J. (1986). Dust storms in the Middle East. *Journal of Arid Environments*, 10(2), 83–96. [https://doi.org/10.1016/s0140-1963\(18\)31249-7](https://doi.org/10.1016/s0140-1963(18)31249-7)
- Middleton, N., & Kang, U. (2017). Sand and dust storms: Impact mitigation. *Sustainability (Switzerland)*, 9(6), 1–22. <https://doi.org/10.3390/su9061053>
- Qian, W., Quan, L., & Shi, S. (2002). Variations of the dust storm in China and its climatic control. *Journal of Climate*. [https://doi.org/10.1175/1520-0442\(2002\)015<1216:VOTDSI>2.0.CO;2](https://doi.org/10.1175/1520-0442(2002)015<1216:VOTDSI>2.0.CO;2)
- Ranjbar, A. A., Imani, A., Abdoosi, V., Fruits, T., Branch, A., Attiya, A. A., Jones, B. G., Yang, B., Bräuning, A., Zhang, Z., Dong, Z., Esper, J., Sun, J., Du, W., Lane, Diana R., Debra P, Lauenroth, & William K, ... Ranjbar, A. A. (2020). The key role of water resources management in the Middle East dust events. *Atmospheric Environment*, 187(5), 139. <https://doi.org/10.1007/978-3-662-45737-5>
- Rivera, J. A., Marianetti, G., Hinrichs, S., Liu, Y., Ju, W., He, H., Wang, S., Sun, R., Zhang, Y. Y., Zhang, N., Hong, Y., Qin, Q., Liu, L., Iwasaka, Y., Minoura, H., Nagaya, K., Bousbih, S., Zribi, M., Pelletier, C., ... Wang, Y. Y. (2021). Light-Use Efficiency Across the Oregon Transect'. *Remote Sensing*, 12(3), 284–295. <https://doi.org/10.1002/ecs2.3578>
- Ruimy, A., Kergoat, L., & Bondeau, A. (1999). Comparing global models of terrestrial net primary productivity (NPP): Analysis of differences in light absorption and light-use efficiency. *Global Change Biology*, 5(SUPPL. 1), 56–64. <https://doi.org/10.1046/j.1365-2486.1999.00007.x>
- Xu, J., Dong, J., Wu, L., Shao, G., & Yang, H. (2015). Land Use/Cover Change and its Impact on Net Primary Productivity in Huangfuchuan Watershed Temperate Grassland, China. *Communications in Computer and Information Science*, 482, 664–683. https://doi.org/10.1007/978-3-662-45737-5_65
- Youlin, Y. (2001). Global Alarm: Dust and Sandstorms from the World's Drylands. *Global Alarm: Dust and Sandstorms from the World's Drylands*, 345. http://www.preventionweb.net/files/1800_VL102211.pdf
- Yue, H., He, C., Zhao, Y., Ma, Q., & Zhang, Q. (2017). The brightness temperature adjusted dust index: An improved approach to detect dust storms using MODIS imagery. *International Journal of Applied Earth Observation and Geoinformation*, 57, 166–176. <https://doi.org/10.1016/j.jag.2016.12.016>
- Zou, X. K., & Zhai, P. M. (2004). Relationship between vegetation coverage and spring dust storms over northern China. *Journal of Geophysical Research: Atmospheres*, 109(3), 1–9. <https://doi.org/10.1029/2003jd003913>



4th Intercontinental Geoinformation Days

igd.mersin.edu.tr



Study of land subsidence by INSAR time series of ALOS-2, Sentinel-1 and GNSS CORS stations in Chaopraya basin, samutprakan, Thailand

Adisorn Sittiwong*¹

¹Wuhan University, The State Key Laboratory of Information Engineering in Surveying, Mapping and Remote Sensing (LIESMARS), Wuhan, Hubei, China

Keywords

INSAR time series
Land subsidence
ALOS-2
Sentinel-1
CORS station

Abstract

Samutprakan province is the most important industrial province and one of the main ports of Thailand, located in the north coast of Thailand near Bangkok. This area is receiving the impact of climate change from sea level rise and land subsidence, caused by many factors such as use of ground water from many industries in this province and surrounded area, the movement of earth surface and the numerous constructions in this area. This study will identify the movement ratio of land subsidence rate in last six years by using Interferometric Synthetic Aperture Radar (InSAR) time series technique from ALOS-2 satellite, Sentinel-1 and Precise Point Positioning (PPP) from GNSS CORS stations to identify the rate of land subsidence and compare the land subsidence with three difference methods above in last 6 years of Samutprakan province Thailand.

1. Introduction

Samutprakan province is one of the economically most important provinces in Thailand. The province is located in the northern gulf of Thailand near Bangkok. This province is facing flooding from sea level rise. This problem is getting closer to the capital city: Bangkok. Samutprakan and surrounding provinces are facing sea level rise, flooding, and land subsidence. The land subsidence is an important factor of flooding in Samutprakan, shown by case studies showing that the land subsidence in Samutprakan is caused by many factors such as the use of ground water, land reclaiming, and movements of the Earth surface. The Department of Groundwater Resources started to do research between 1978 - 1981 and they found land subsidence of more than 10 cm per year in Bangkok and Samutprakan. After that, the study of land subsidence has been widespread to many Universities in Thailand such as King Mongkut University of Technology vicinity (Bangmod), Chulalongkorn University, and Kasetsart University to

work on monitoring land subsidence in the central part of Thailand.

2. Method

This study will identify the movement ratio of land subsidence rate in the last six years by using Interferometric Synthetic Aperture Radar; InSAR time series technique from ALOS-2 satellite, Sentinel-1 and Precise Point Positioning (PPP) from GNSS CORS stations to identify the rate of land subsidence and compare the land subsidence with three difference methods above in last 6 years of Samutprakan province Thailand. Both techniques are used to identify data from difference sources to find the subsidence rates of the study area in Samutprakan, in order to allocate the suitable area for industrial constructions and farming areas. The result from this thesis will benefit the residents in Samutprakan and the planning of industrial areas in the next 6 to 12 years and indicate the most accuracy methods from these three methods.

* Corresponding Author

^{*}(Adisorn.dui48@gmail.com) ORCID ID 0000-0002-7819-9967

Cite this study

Sittiwong, A. (2022). Study of land subsidence by INSAR time series of ALOS-2, Sentinel-1 and GNSS CORS stations in Chaopraya basin, samutprakan, Thailand. 4th Intercontinental Geoinformation Days (IGD), 215-217, Tabriz, Iran

2.1. Equations and analysis

The SAR system transmits the microwave pulse that consists of amplitudes and phases. The difference phases represent the Earth's surface movement by using the phase difference between two SAR acquisitions ($\Delta\phi$), as shown in Equation 1. Hence, $\Delta\phi$ can calculate the ground surface movement in LOS of a satellite (Δr), but $\Delta\phi$ is wrapped difference phase form. So, measuring the deformation, the interferometric phase needs to be unwrapped. Simultaneously, the fundamental InSAR principle is used differential SAR interferometry (DInSAR) by a spatial ground surface of a stable object. The phase difference ($\Delta\phi$) (A. Ferretti et al., 2001; Hanssen, 2001) as shown in Equation 2 is the summation of a phase of surface movement, or phase contribution of the pixel in the satellite LOS direction relate to ground deformation (ϕ_{def}), phase of orbit error (ϕ_{orbit}), topographic effect phase (ϕ_{topo}), phase of noise (ϕ_{noise}), and atmospheric phase delay (ϕ_{atm}). The phase difference is calculated based on Equation 1 and Equation 2.

$$\Delta\phi = \phi_1 - \phi_2 = 4\pi \lambda \Delta r \quad (1)$$

where

ϕ_1, ϕ_2 : the phase of each acquisition

λ : wavelength of radar

Δr : the difference in range (LOS) between two SAR acquisitions

$$\Delta\phi = \phi_{atm} + \phi_{def} + \phi_{topo} + \phi_{orbit} + \phi_{noise} \quad (2)$$

where

$\Delta\phi$: interferometric phase (or phase difference)

ϕ_{atm} : Atmospheric Delay

ϕ_{def} : phase contribution related to ground deformation

ϕ_{topo} : Topographic Effect

ϕ_{orbit} : Orbit Error

ϕ_{noise} : Noise

3. Results

The validation of results between Sentinel-1 images ascending mode and BPLE CORS station from 2014-2020 can be interpreted in results of land subsidence velocity in mm/year. Both results retrieved from different sensors and programs. The results of Ps points from Sentinel-1 represented the velocity of BPLE CORS station leveled up 47.7 mm/year in blue points of map in figure 28. The results from GNSS CORS station by AUSPOS online processing is 27.5 mm/year. The difference land subsidence velocity of 2 sources indicated in 20.2 mm/year or 2 cm/year. The trend of 2 sources has relative in results and graph in figure 28. Thus, the result of 2 different sources presented in the same of land subsidence in trend that relate to results of DPT CORS station with level down in Sentinel-1 and DPT CORS station.

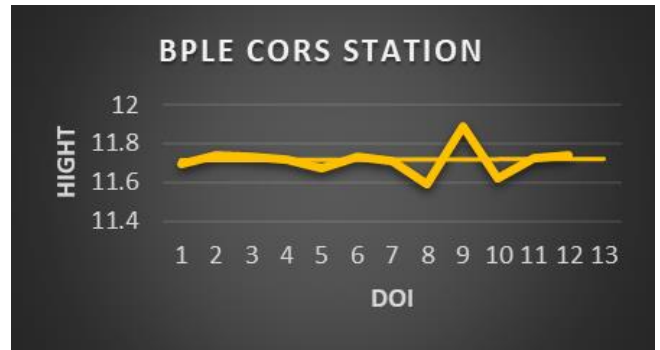


Figure 1. Height and trend of BPLE CORS station in Samutprakan

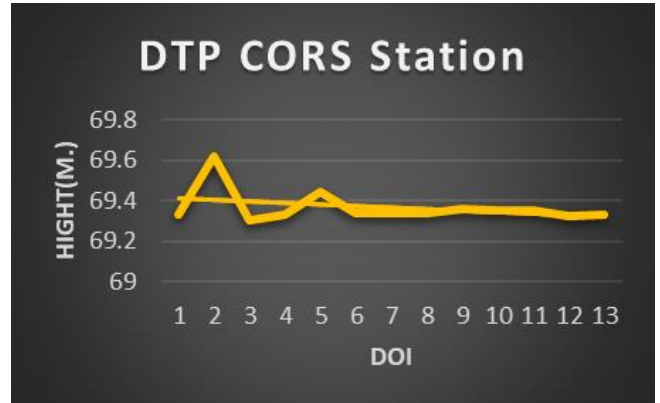


Figure 2 Height and trend of DPT CORS station in Samutprakan

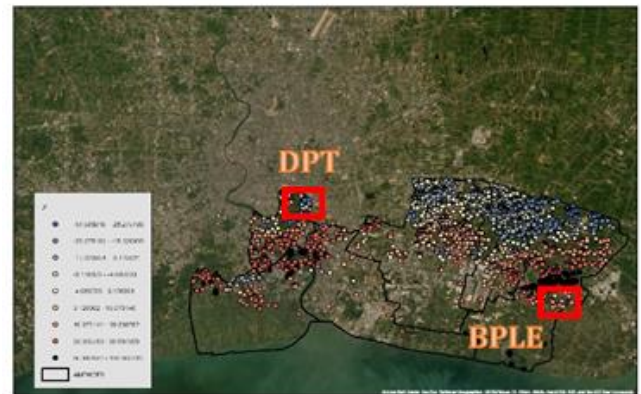


Figure 3. The land deformation spots in Samutprakan

4. Discussion

This research has studied the land subsidence in the most high-risk area in Thailand, Samutprakan by trying to use different of methodology and different sources such as satellite data from ALOS-2 and Sentinel-1 with SAR images that can detect the different of phases of radar energy on the earth surface. There are many studies of land subsidence in many places throughout the world that used InSAR time series of land deformation to study the trend of land deformation in the future for their interest and the change of disasters such as earthquake, volcano eruption, and ground water. In Samutprakan is also the area that is facing land subsidence and sea level raise every year. This research has provided the value,

numbers, and trend of land subsidence in Samutprakan in order to know the change of earth surface movement in specific area to concern in some high-risk area of land subsidence. This study also used many different sources to present the numbers of land subsidence in Samutprakan to be various of options and find the most suitable methods and sources for further study.

5. Conclusion

All results have answered of this thesis that want to know the influence of land subsidence in Samutprakan. The influent of land subsidence came from the use of ground water, the city grows up with more populations. These reasons cause the land subsidence in Samutprakan. For the rate of land subsidence in Samutprakan have different rate in different area. In this study we focused on two CORS stations to be the ground base reference for land subsidence by two satellites. The land subsidence rate in the middle of Samutprakan; the location of DPT is going down because constructions, use of ground water, and higher populations. The land subsidence rate in BPLE CORS station is going up because the city from Samutprakan has been expanding to the urban area, so the leveling of BPLE CORS station is having the level up. The different of three sources in results are not highly different. The results from all sources presented in the same trend of land subsidence velocity. The different in numbers of millimeters that reliable accurate.

Acknowledgement

I would like to thank and appreciate my supervisor Prof.Dr. Timo Balz, Dr Phattraporn Soyong, Dr. Anuphao Aobpaet, Dr. Kitsanai Charoenjit. I would also thank you to my classmates, SCGI batch 3, Master Program Student and the other members of my Master's, Ph.D. classmate and SAR team in Faculty of Geoinformatics, Burapha University and State Key Laboratory of Information Engineering in Surveying, Mapping and Remote Sensing, Wuhan University. The source of data of this research consists of Department of Public Works and Town & Country Planning (DPT), Department of Land (DOL), Kasetsart University, Sentinel-1 website, and AUSPOS online software.

References

- Aobpaet, A. (2012). InSAR time series analysis for land subsidence monitoring in Bangkok and its vicinity area. (Doctoral dissertation), Chulalongkorn University, Bangkok.
- Balz, T. (2019). Surface Motion Estimation: Lecture Note for Summer School 2019. LIESMARS, Wuhan University, China.
- Bo Hu, Junyu Chen & Xingfu Zhang. (2019). Monitoring the Land Subsidence Area in a Coastal Urban Area with InSAR and GNSS.
- Hooper, A., Bekaert, D., Spaans, K., & Arikian, M. (2012). Recent advances in SAR interferometry time series analysis for measuring crustal deformation. *Tectonophysics*, 514-517, 1-13. <https://doi.org/10.1016/j.tecto.2011.10.013>
- Morishita, Yu & Lazecky, Milan & Wright, & Weiss, & Elliott, & Hooper, Andy. (2020). LiCSBAS: An Open-Source InSAR Time Series Analysis Package Integrated with the LiCSAR Automated Sentinel-1 InSAR Processor. *Remote Sensing*. 12. 424. <https://doi.org/10.3390/rs12030424>.
- Phien-wej, N. & Gao, P. & Nutalaya, P. (2006). Land subsidence in Bangkok, Thailand. *Engineering Geology*. 82. 187-201. [10.1016/j.enggeo.2005.10.004](https://doi.org/10.1016/j.enggeo.2005.10.004).
- Somchai Kriengkraiwasin, Chaiyut Charoenphon, Korakod Butwong, Vichien Kovitpongkajorn, Peera Yomwan, Thayathip Thongtan & Chalermchon Satirapod (2021) Unification of GNSS CORS coordinates in Thailand, Survey Review, <https://doi.org/10.1080/00396265.2021.198702>
- Dardanelli, g., lo Brutto, m., & Pipitone, c. (2020). GNSS CORS network of the University of Palermo: Design and first analysis of data. *Geographia Technica*, 15(1).
- Werner, C., U. Wegmuller, T. Strozzi, A. Wiesmann. (2003). Interferometric Point Target Analysis for Deformation Mapping. Paper presented at the interferometric Point Target Analysis for Deformation Mapping." In *International Geoscience and Remote Sensing Symposium (IGARSS)*, Toulouse, France



4th Intercontinental Geoinformation Days

igd.mersin.edu.tr



Determination of the conversion of the stone fields into potential agricultural lands using Sentinel-2 satellite

Hasan Lafcı¹ , Halil İbrahim Şenol¹ , Nizar Polat¹

¹Harran University, Faculty of Engineering, Department of Geomatics Engineering, Şanlıurfa, Türkiye

Keywords

Remote sensing
Agriculture
Sentinel-2
Satellite

Abstract

The Sentinel-2A satellite is a medium spatial resolution (10-60) multispectral instrument developed by ESA. In recent years, it has been seen that different studies have been carried out to demonstrate the competence and potential of Sentinel-2A MSI (Multispectral Instrument) satellite sensors. The aim of this study is to determine the temporal change in the acquisition of stone fields related to the rural neighborhood of Arabuk, Hilvan district of Şanlıurfa, to agricultural areas by using Sentinel-2A satellites. In this context, satellite images from the Sentinel-2A satellite of 2017 and 2022 were obtained from the data provider web address of the European Space Agency (ESA). The land cover changes for these five years were determined and the agricultural area gains were calculated. In the practice, which was carried out on an area of approximately 1925 hectares, it was determined that the lavas sprayed by Karacadağ, which is a volcanic mountain, cooled over time and turned into basalt stones. The lands that could be cultivated turned into a large stone area. As a result, the usability of Sentinel-2A satellite images, which provide free access, in the determination of the terrain pattern and determination of its use has been demonstrated.

1. Introduction

Although the agricultural activities in the world have increased over time, they cannot meet the needs and it is predicted that the increase in the world population will continue to increase in the future. On the other hand, reaching the border point of arable lands in countries that meet the demand for agricultural products and the decrease in the possibilities of increasing agricultural production further increase the importance of the issue. In parallel with these developments, the importance of developing countries with arable land and agricultural potential is increasing in terms of agricultural production. Karacadağ, which is a volcanic mountain located in the middle of the Southeastern Anatolia Region, transformed a large area into stony lands as the lavas it sprayed cooled over time and turned into basalt stones. There are dense stony areas in Şanlıurfa, especially in Siverek, Hilvan and Viranşehir districts. Since stones are scattered on fertile soils in a large part of the said lands, they can be easily cleaned and opened for agriculture.

Satellite images, which are remote sensing data, provide data with sufficient spatial resolution for many years in frequent periods (Dereli, 2019; Oğraş, 2018; Yiğit & Kaya, 2020). Determining and comparing the satellite images archived for many years with the land data belonging to the same area in repetitive periods is useful for the maps to be created in the detection of new agricultural areas (İrfanoğlu & Balçık, 2018; Aghlamand et al., 2019).

The main purpose of this study is to reveal the usability of the data obtained with Sentinel-2. For this purpose, using Sentinel-2 data, it reveals results related to the determination of the clearing of the stones on the land and opening it for agriculture in the rural neighborhood of Arabuk in Hilvan district of Şanlıurfa (Figure 1).

2. Method

Satellite images used in the detection study were obtained from the Sentinel-2A satellite. The areas covered by the stony areas of the lands determined from

* Corresponding Author

*(hasanlafci.02@gmail.com) ORCID ID 0000-0002-2049-9940
(hsenola@gmail.com) ORCID ID 0000-0003-0235-5764
(nizarpolat@harran.edu.tr) ORCID ID 0000-0002-6061-7796

Cite this study

Lafcı, H., Şenol, H. İ., & Polat, N. (2022). Determination of the conversion of the stone fields into potential agricultural lands using Sentinel-2 satellite. 4th Intercontinental Geoinformation Days (IGD), 218-220, Tabriz, Iran

2 satellite images detected in different time periods were determined and the situation before and after the stony areas were determined.



Figure 1. Study area

In the study, Sentinel-2 data from two different years was used and the changes between them were examined. First of all, a satellite image of May, 2017 was used to show the stony area before it was cleared (Figure 2). Then, a second satellite image of May, 2022 was used to show the state of the stony area after cleaning (Figure 3).



Figure 2. Map showing the study area in 2017



Figure 3. Map showing the study area in 2022

With this study, the area covered by the stony areas was determined quickly by remote sensing methods and the areas suitable for agriculture were reached instantly

and accurately. On the Sentinel-2 images, the stony area and the area brought to agriculture were determined and the area brought to agriculture was determined through the image. The areas where the stony areas were cleared and collected are shown in Figure 4.



Figure 4. Areas where stony areas are cleared and collected

The accuracy assessment was made with the differences between the terrain images and the satellite images of 2017 and 2022. Evaluations of the produced maps were carried out with controls on the existing ground (Figure 5).



Figure 5. After stones are collected (up) and before stones are collected (down)

3. Results

In the study, the land cover changes for the years 2017 and 2022 were determined, and the agricultural area gains of the stony areas were calculated. In the applications performed on images with a spatial resolution of 10 m with Sentinel-2A satellites, it is seen that 740,000 m² of stony area is cleared and brought to agricultural areas.

If the above-mentioned areas are opened to agriculture and dry wheat farming is considered to be used once a year, if we calculate the income to be obtained from 1 decare of land (for the year 2021);

Annual expense for 1 decare;

-(Seed 100 TL + Fertilizer 220 TL + Fuel expenses 50 TL + Harvest 50 TL + Agricultural Protection 160 TL) = 580 TL

-Annual income for 1 decare (Main product sales 1 decare average 400 kg = 400×2.40 TL=960 TL + By-product Straw $350 \times 0.4=140$ TL) = 1100 TL

-Annual net income for 1 decare = 520 TL

According to this calculation, it is seen that the cleaning cost of 1 decare of stony land is 1500 TL/da, and the income to be obtained from 1 decare of cleared and dry wheat farming land is 520 TL. 1 decare of land pays for itself in 2.8 years.

Fertilizer cost was also calculated in the above calculation. However, when we consider that the lands are uncultivated lands and do not require fertilizer, and we exclude that cost from the calculation, the amortization period can be reduced to 2 years for 1 decare, even in dry wheat farming that does not require only water. If different products and the second product account are added to the said calculation, it will be seen that the cleaning cost can be amortized in a very short time.

In addition, when the fact that the stones collected from the lands can also be processed and evaluated economically, it is clear that stone collection works will contribute greatly to the economy of the region.

4. Conclusion

The important point here is to determine the effectiveness of Sentinel-2 satellite images in areas such as this study. For this reason, as it is understood from the study, since Sentinel-2 satellites provide high resolution data, interpretation can be made on the resulting images. In change detection studies, satellite images of at least two different times should be used. The use of long-term data, especially in the evaluations of land change and use, yields clear results.

References

- Dereli M., (2019). Sentinel-2A uydu görüntüleri ile Giresun il merkezi için kısa dönem arazi örtüsü değişiminin belirlenmesi, Afyon Kocatepe Üniversitesi Fen ve Mühendislik Bilimleri Dergisi, 19(2), 361-368.
- Oğraş, S. (2018). Dicle Nehri'nin Taşkın Analizinin HEC-RAS Programıyla Yapılması. Yüksek Lisans Tezi, Dicle Üniversitesi, Diyarbakır.
- Yiğit, A.Y., & Kaya, Y (2020). Sentinel-2A uydu verileri kullanılarak sel alanlarının incelenmesi: Düzce örneği. Türkiye Uzaktan Algılama Dergisi, 2(1), 1-9.
- İrfanoğlu, F., & Balçık, F. B., 2018. Arazi örtüsü ve arazi kullanımı sınıflarının sentinel-2 görüntüsü ve nesne tabanlı sınıflandırma yöntemiyle belirlenmesi. VII. Uzaktan Algılama-CBS Sempozyumu.
- Aghlamand M., Kalkan K., & Onur M., (2019). Sentinel 2 Uydusunun Orman Sınıflandırma Kabiliyetinin İncelenmesi k Creek (Çınar Region) in Diyarbakır

4th Intercontinental Geoinformation Days

igd.mersin.edu.tr



Preliminary results of surface displacement of the Elazığ Sivrice region by comparing D-InSAR and SBAS methods

Dilara Solmaz^{*1}, Furkan Veziro², Nusret Demir²

¹Akdeniz University, Institute of Science and Technology, Department of Space Sciences and Technologies, Antalya, Türkiye

²Akdeniz University, Faculty of Science, Department of Space Sciences and Technologies, Antalya, Türkiye

Keywords

Remote sensing
Radar
D-InSAR
SBAS

Abstract

Earthquakes, which are caused by cracks in the earth's crust, are a type of natural disaster that can result in loss of life and property as well as economic damage. Earthquakes also induce ground surface displacements. In Turkey, the North Anatolian Fault Line, the East Anatolian Fault Line, and the West Anatolian Fault Line all experience continuous ground movements. The displacement caused by the earthquake that struck the Elazığ-Sivrice region on the Eastern Anatolian fault line on January 24, 2020 was calculated using D-InSAR (Differential Interferometric Synthetic Aperture Radar) and SBAS (Sort Baseline Subsets) methods using Radar data from the Sentinel-1 satellite. compared and computed.

1. Introduction

Earthquakes are described as the shaking of the environment caused by the vibrations of the earth's crust breaking. Varying soils experience different deformations as a result of the earthquake effect. Surface rupture, regional collapse, slope movements, volumetric compression, liquefaction, settling and bearing failures, flow slides, lateral spreading, and sand volcanoes are some of the deformations that can occur (Onur, 2007). Since Turkey is located on the North Anatolian Fault Line, East Anatolian Fault Line, and West Anatolian Fault Zones, it is subject to earthquakes. Turkey, which is located on the Eurasian-Arab-African plate, has been subjected to destructive earthquakes throughout history due to its tectonic structure. Since the 1900s, these seismic movements in the square have been recorded with instruments. The two primary seismic network operators in Turkey are the Ministry of Interior, Disaster and Emergency Management Presidency (AFAD) and Boaziçi University Kandilli Observatory and Earthquake Research Institute (KRDAE) (Kadirliolu et al., 2018). The 1999 Gölcük and Düzce, 2011 Van, and 2020 Elazığ earthquakes are among the most catastrophic earthquakes in Turkey, according to records. Elazığ is a province in Turkey's Eastern Anatolia region, bordered on the north by Tunceli and on the west by Malatya. The

East Anatolian Fault Zone runs across this province, with Diyarbakır in the south and Bingöl in the east. In the last hundred years, 299 earthquakes larger than 4.0 have occurred in this region, which is still on this fault line and is still quite active today (AFAD, 2020). According to AFAD statistics, the epicenter of the 6.8 magnitude earthquake that struck on January 24, 2020 at 20:55 and lasted 20.04 seconds was located in the evrimtaş village of Elazığ province, Sivrice district, around 800 meters distant. The earthquake occurred in the Sivrice-Pötürge segment of the left-lateral Eastern Anatolian Fault zone, according to the research. After the earthquake, there is expected to be a 50-55 km rupture. 41 people were killed and 1600 more were injured in this earthquake, which demolished 547 structures and badly damaged 6247 others. With technical advancements, the use of remote sensing tools in the analysis and monitoring of natural disasters has increased. Change detection analysis usually employs RADAR/SAR, LIDAR, and UAV technologies, which are commonly utilized in the field of active remote sensing. It is critical to properly and swiftly assess the changes that occur as a result of the disaster (Turker and San (2003), Turker and San (2004), Gince and San (2018)). Artificial Aperture Radar (SAR) approaches, in particular, are one of the most effective remote sensing instruments available today since they are unaffected by environmental conditions, are an active

* Corresponding Author

^{*}(dilarasolmaz02@gmail.com) ORCID ID 0000-0002-5555-1761
(furkanveziro@gmail.com) ORCID ID 0000-0002-1940-6970
(nusretdemir@akdeniz.edu.tr) ORCID ID 0000-0002-8756-7127

Cite this study

Solmaz, D., Veziro, F., & Demir, N. (2022). Preliminary results of surface displacement of the Elazığ Sivrice region by comparing D-InSAR and SBAS methods. 4th Intercontinental Geoinformation Days (IGD), 221-224, Tabriz, Iran

system, and can collect data at any period (Gunce and San, 2018). Mamolu et al. (2020) analyzed a general geodetic event that occurred in Bolvadin using the interferometry technique, and displacement time series were acquired by creating the region's velocity map (Mamolu et al., 2020). The SAR image records the amplitude and phases of the reflected signals from the targets in the study region. The phase is a value that is proportional to the target's distance. The target's reflectance values are used to calculate the amplitude. Using SAR data and D-InSAR and SBAS methodologies, the displacement analysis that happened after the earthquake in the Elazığ Sivrice region was carried out in this work. D-InSAR uses the phase difference of two SAR images to calculate the difference in distances between targets on the ground. The SBAS method of Berardino et al. (2002) was used, as well as the advanced D-InSAR approach. In terms of providing temporal and spatial analysis, this approach is an important and powerful tool in the analysis of disasters that occur on Earth. This method can be used to see the spatial development of the deformation, which occurs over a long period of time and develops slowly.

2. Test Site and Methods

2.1. Test Site

According to AFAD data, the epicenter of the 6.8 magnitude earthquake that struck on January 24, 2020 at 20:55 and lasted 20.04 seconds was located in the evrimtaş village of Elaz province, Sivrice district, around 800 meters distant. The earthquake occurred in the Sivrice-Pötürge segment of the left-lateral Eastern Anatolian Fault zone, according to the research. After the earthquake, there is expected to be a 50-55 km rupture.

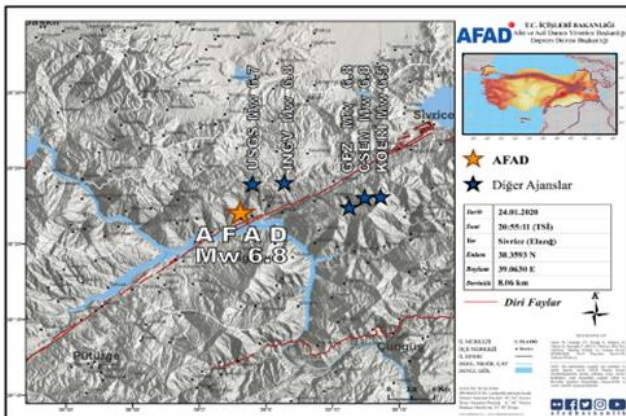


Figure 1. Sivrice (Elazığ) earthquake location map (AFAD, 2020)

2.2. Methods

2.2.1. D-InSAR

SAR data acquired by the Sentinel-1 satellite on the 22nd of January and the 3rd of February 2020 were used in the research. These photos are in SLC format and are stored in IW mode. An image created at an oblique range distance along the azimuth direction is stored in SLC

format. Complex values (I and Q) including amplitude and phase information are used to represent each pixel in the image. SLC products are processed to produce a single view of any size that uses the entire signal bandwidth. The satellite's orbit and altitude data are used to geo-reference the images (Bourbig et al., 2016). The SAR image records the amplitude and phases of the reflected signals from the targets in the study area. The phase is a value that is proportional to the target's distance. The target's reflectance values are used to calculate the amplitude.

Based on the phase difference of two SAR images, D-InSAR is used to measure displacements in the study area with very low precision. The interferogram used in this case provides information on the target area's high difference. A one-dimensional measure of surface collapses in the satellite line of sight direction corresponds to a portion of the phase difference between the two SAR images obtained before and after the earthquake.

2.2.2. SBAS

Another method, known as the SBAS method, obtains displacement over time by stacking conventional D-InSAR interferograms (Berardino et al. 2002, Schmidt and Bürgmann 2003, 30 Hooper 2008).

When compared to D-InSAR, the SBAS approach has two distinct features. Multiple SAR images taken at different times in the same area are required to get started. Second, only stable scattering signals are extracted.

3. Results

The data from February 3, 2020 and January 22, 2020 were utilized to analyze the earthquake that occurred on January 24, 2020 in Elazığ Sivrice district, and the phase difference between the data was used to create the interferogram displayed in Figure 2. The slump values in the displacement map developed varied from +25.4 cm to -17.9 cm, according to this interferogram. Figure 3 depicts the displacement map that was developed. Furthermore, the displacement map developed with the LICSBAS tool (Morishita, et al., 2020), which is a SAR interferometry time series analysis software, is consistent with the results obtained from the D-InSAR study.

The SBAS study determined that the subsidence in the Elazığ Sivrice region was between +11.73 cm and -11.92 cm, based on a displacement map developed on the same platform as the D-InSAR displacement map. Figure 4 shows the resulting displacement map.

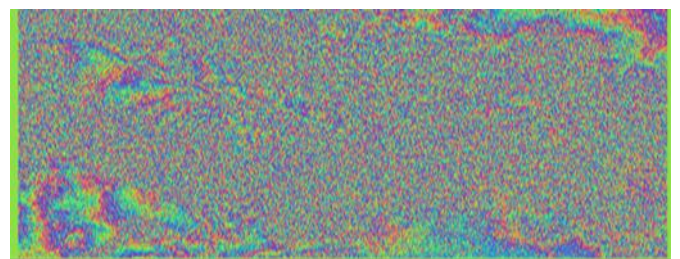


Figure 2. Interferogram

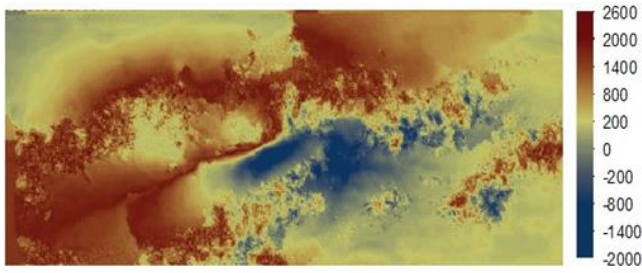


Figure 3. Displacement Map in mm (D-InSAR)



Figure 4. Displacement Map in mm (SBAS)

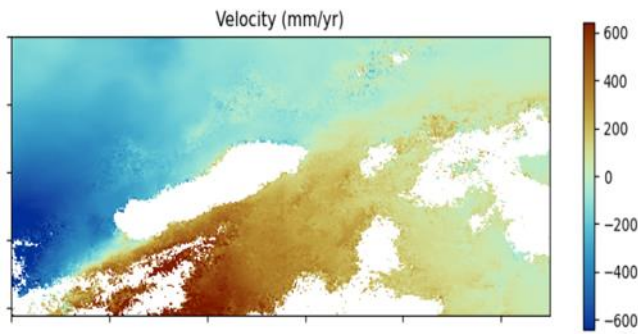


Figure 5. Displacement Map in mm (SBAS)

The minimum, maximum mean and standard deviation values of the obtained analysis results are given in Table 1.

Table 1. Values obtained as a result of analysis

	Minimum value	Maximum value	Mean value	Standard deviation
D-InSAR	-1799,979	2545,0082	-24,8119	240,8371
SBAS	-1094,050903	1173,7658	-37,8196	347,8103

4. Discussion and Conclusions

Karşlıoğlu et al. determined the collapse values between +25.4 cm and -17.9 cm as a result of the earthquake that occurred in the Sivrice district of Elazığ province in January 2021 as a result of the study. The earthquake-induced subsidence analysis of the Sentinel-1 satellite: Sivrice-Doğanyol-Pütürge sample agrees well with the study's collapse values, confirming the study's findings.

It has been determined that the displacement values obtained as a result of the SBAS analysis using interferogram stacks give more sensitive results than the values found by the D-InSAR method, as shown in the table 1.

Acknowledgement

This work has been supported by the Disaster and Emergency Management Authority (AFAD) by the project no. UDAP-Ç-21-34.

References

- Berardino P, Fornaro G, Lanari R and Sansosti E (2002) A New Algorithm for Surface Deformation Monitoring Based on Small Baseline Differential SAR Interferograms. *IEEE Transactions on Geoscience And Remote Sensing*, 40: 2375-2383.
- Gunce, H. B., San, B. T. "Measuring Earthquake-Induced Deformation in the South of Halabjah (Sarpol-e-Zahab) Using Sentinel-1 Data on November 12, 2017", *Proceedings* (2018), 2, 346; doi:10.3390/ecrs-2-05159.
- Gökçeoğlu, C., Yürür, T., Kocaman, S., Nefeslioğlu, H.A., Durmaz, M., Tavus, B., Karakaş, G., Büyükdemircioğlu, M., Atasoy, K., Yörük, İ., Can, R., Yalçın, İ., (2020) , "Hacettepe Üniversitesi Mühendislik Fakültesi RADAR İnterferometri ve Stereo hava fotogrametrisi ile Elazığ Sivrice depreminin (24 Ocak 2020, M W = 6.8) incelenmesi", February, 2020, <https://www.researchgate.net/publication/339596648>.
- Karşlıoğlu, A., Alkayış, M.H., Kalkan, K., Onur, M.İ., (2020), "Sentinel-1 uydusu ile Konya Karapınar ilçesi bölgesel çökme analizi", *Disaster Science and Engineering*, 6 (2)-2020.
- Karşlıoğlu, A., Alkayış, M.E., Onur, M.İ., (2021.) "Sentinel-1 Uydusu ile Deprem Kaynaklı Yüzey Çökme Analizi: Sivrice-Doğanyol-Pütürge Örneği", *Gümüşhane University, Institute of Science, Journal*, 11(2) 510-521.
- Köse, O., Yürür, M.T., Chorowich, J., "Sismotektoniğe ve sismik boşluğa DInSAR yaklaşımı: Kuzey Anadolu Fay Zonunun Erzincan havzası kesimi (doğu Türkiye)", *Yer Bilimleri*, 2019, 40 (3), 326-351.
- Kutoğlu, Ş.H., Özölçer, İ.H., Kemaldere, H., "Radar interferometri tekniği ile kıyı yapılarındaki deformasyonların izlenmesi", *8.Kıyı Mühendisliği Sempozyumu*, 7-9 Kasım 2014, s: 919-928.
- Li, S., Xu, W., Li, Z., Review of the SBAS InSAR Time-series algorithms, applications, and challenges, *Geodesy and Geodynamics*, Volume 13, Issue 2, 2022, Pages 114-126, ISSN 1674-9847,
- Mancini, F., Grassi, F., Cenni, N., "A Workflow Based on SNAP–StaMPS Open-Source Tools and GNSS Data for PSI-Based Ground Deformation Using Dual-Orbit Sentinel-1 Data: Accuracy Assessment with Error Propagation Analysis", *Remote Sensing*, 2021, 13, 753.
- Morishita, Y.; Lazecky, M.; Wright, T.J.; Weiss, J.R.; Elliott, J.R.; Hooper, A. LiCSBAS: An Open-Source InSAR Time Series Analysis Package Integrated with the LiCSAR Automated Sentinel-1 InSAR Processor. *Remote Sens.* 2020, 12, 424, <https://doi.org/10.3390/RS12030424>.
- Onat, E., "Sentetik açıklıklı RADAR görüntülerinde interferometri ve radargrametri tekniklerinin füzyonu", PhD Thesis, Istanbul, 2020.

- Onur, M. İ., (2007). "Dinamik etkiler altında zemin deformasyonunun incelenmesi." Master Thesis, Anadolu University, İnstitute of Science Eskişehir.
- Thomas, A., (2021). Mapping of surface deformation associated with the 5.2 magnitude Stilfontein earthquake of 3 April 2017 using radar interferometry. *The Egyptian Journal of Remote Sensing and Space Sciences*, 2021, 24, 85–108.
- Turker, M., San, B.T. "Detection of collapsed buildings caused by the 1999 Izmit, Turkey earthquake through digital analysis of post-event aerial photographs". *Int. J. Remote Sens.* 2004, 25, 4701–4714, doi:10.1080/01431160410001709976.
- Vajedian, S., Motagh, M., Mousavi, Z., Motaghi, K., Fielding, E., Akbari, B., Wetzel, H., Darabi, A., Coseismic Deformation Field of the Mw 7.3 12 November 2017 Sarpol-e Zahab "(Iran) Earthquake: A Decoupling Horizon in the Northern Zagros Mountains Inferred from InSAR Observations", 2018.

4th Intercontinental Geoinformation Days

igd.mersin.edu.tr



Evaluation of U-Th enrichments in QGIS platform; Example of Arıklı (Çanakkale, Turkey) district

Cihan Yalçın^{*1}, Sercan Öztürk², Mustafa Kumral²

¹ Ministry of Industry and Technology, World Bank Project Implementation Unit, Ankara, Türkiye

² Istanbul Technical University, Faculty of Mines, Department of Geological Engineering, İstanbul, Türkiye

Keywords

Remote sensing
GIS
U-Th
Arıklı
Fault

Abstract

Uranium (U) and Thorium (Th) are strategically important elements worldwide. For this reason, exploring these elements, which are enriched in many geological environments, is exceedingly significant. U-Th enrichments in Turkey were usually discovered in the Western Anatolian geography. U-Th anomalies were still observed in the Arıklı region south of Çanakkale. In this study, remote sensing and Geographical Information Systems (GIS) were utilized in the QGIS program to carry out the geochemical data obtained in the field more understandable. U-Th values, which show high values in the fault zones in the Arıklı region, are immediately related to the CaO values. As in many geological studies, remote sensing and GIS studies suggest the opportunity to check out field data with a significant quality in exploring ore deposits.

1. Introduction

Uranium and Thorium are significant and strategic radioactive elements. For this reason, applications are carried out to explore these elements, which are enriched in many geological environments. Granite and volcanic rocks are essential sources of Uranium enrichment (Zhang and Zhang 1991; Qin and Liu 1998). U deposits are divided into four groups corresponding to the host rock lithology (Li et al. 2002). These are granite-rock type (G-type), sandstone type, volcanic-rock type (V-type), and carbonaceous-silica-pelitic-rock type (CSP-type), respectively. It has been described that the significant uranium enrichments in Turkey are situated in western Anatolia (Şaşmaz 2008).

MTA started uranium exploration activities in Turkey in 1953, and after that, exploration studies continued (Contencin 1960; Günaydın 2017). In the Ayvacık-Küçükkuyu field near Çanakkale province, the U₃₀₈ value was 0.08% in Miocene carbonate rocks (MTA, 2009, MTA 2010c). There are phosphate nodules and natural radiation sources in the volcanic tuffs between Küçükkuyu and Ayvacık (Atabey 2006). On the Geyikli coast, near the region, there are minerals (taurite and uraninite) consisting of heavy metals, uranium and

Thorium in the sands (Andaç 1971). These radioactive minerals originate from the granitic rocks outcropping around Geyikli (Andaç 1971). Günaydın (2017) explained that there is a U enrichment in the composition of bayleite and ningyoite in and around Arıklı. High natural radiation values were also reached in the fault zones around Örencik and Feyzullah Tepe, northwest of Arıklı (Atabey 2006). The effect of hydrothermal waters forms magnesite breccias located in the northwest of Arıklı, and there are U up to 700 ppm and Th greater than 1000 ppm in this fault zone (Günaydın 2017). Öztürk et al. (2021) examined microthermometric measurements from magnesite observed in these fault zones and determined that (Th, °C) was between 282-348 °C and % NaCl salinity equivalents were between 4.2-8.0. They also stated that the solution system of liquid inclusions is in the form of H₂O-MgCl₂-CaCl₂, and the density of liquids is between 0.58-0.74 g/cm³.

In recent years, high-resolution digital applications have been widely used in geological studies. Remote sensing (RS) and geographic information systems (GIS) are principles for map-based interpretation of many geological structures. With scientific advances in spatial analysis techniques, linearity, ore exploration, and morphological investigations have become practical.

* Corresponding Author

*(cihan.yalcin@sanayi.gov.tr) ORCID ID 0000-0002-0510-2992
(sercanozturk@hotmail.com) ORCID ID 0000-0003-4478-2908
(kumral@itu.edu.tr) ORCID ID 0000-0001-7827-8721

Cite this study

Yalçın, C., Öztürk, S., & Kumral, M. (2022). Evaluation of U-Th enrichments in QGIS platform; Example of Arıklı (Çanakkale, Turkey) district. 4th Intercontinental Geoinformation Days (IGD), 225-228, Tabriz, Iran

Geographic Information Systems (GIS) have also been used in mineral exploration studies and mine probability maps (Porwall et al. 2001; Joly et al. 2012; Lindsay et al. 2014).

This study evaluated the analysis results obtained in the survey by Öztürk et al. (2021). Samples collected in the field, geological maps, satellite images and thematic maps were evaluated together.

2. Method

The DEM image of this geologically significant region has been downloaded from the United States Geological Survey (USGS) website. Aspect, 3D map and slope map of the region was created by evaluating the downloaded images in the QGIS environment. The geological map prepared by Öztürk et al. (2021) was digitized in the GIS environment, and sample points were located. Afterwards, heat maps dwelling on major oxide and trace elements were made.

2.1. Regional Geology

The application area is south of the Biga Peninsula in Western Anatolia. The application area in the Ayvacık district of Çanakkale is tectonically located in the Sakarya Zone (Fig 1). Okay et al. (1990) described the units in the Çanakkale region as pre-tertiary and post-Tertiary units, respectively. Their subsequent studies divided it into three pre-tertiary tectonic zones observed in the NE-SW direction (Okay et al. 2001; Okay and Altınır 2004). These zones are Ezine Zone, Ayvacık-Karabiga Zone and Sakarya Zone respectively.

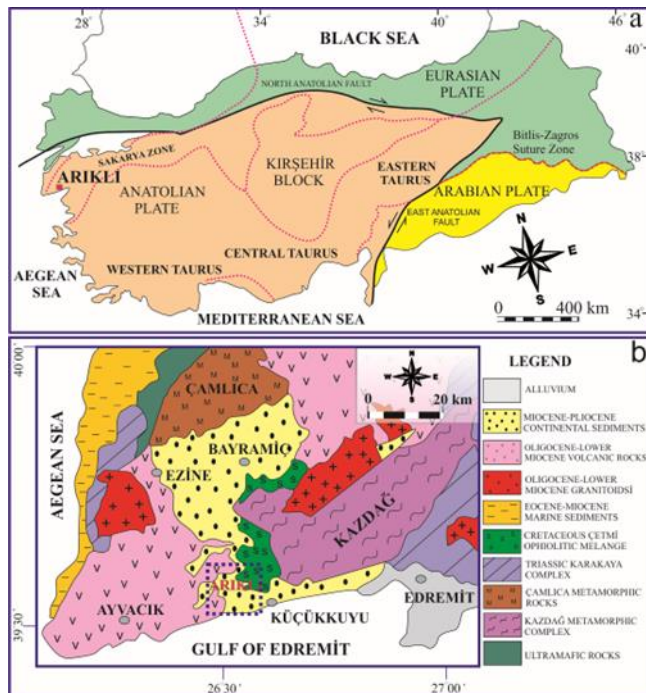


Figure 1. a. Tectonic location of the study area (modified from Işık 2016), b. Generalized geology map of the Biga region and location of the study area (modified from Okay and Satır 2000a; Şengün et al. 2011).

Many metamorphic facies and magmatic, ophiolite, sedimentary and volcanic rock groups are established

north of the Gulf of Edremit (Fig 1) (Okay and Satır 2000a; Şengün et al. 2011). In the vicinity of Arıklı, the Miocene Pliocene aged continental sediments and Cretaceous aged Çetmi melange are outcrop (Fig 1).

The Cretaceous Aged Çetmi Ophiolitic Melange, Küçükkuyu Formation and Quaternary aged alluvial deposits are located in the study area. In the Küçükkuyu formation, shale-sandstone member and Arıklı tuff member were separated, and diabases that cut these units were mapped on the Örencik Tepe (Fig 2).

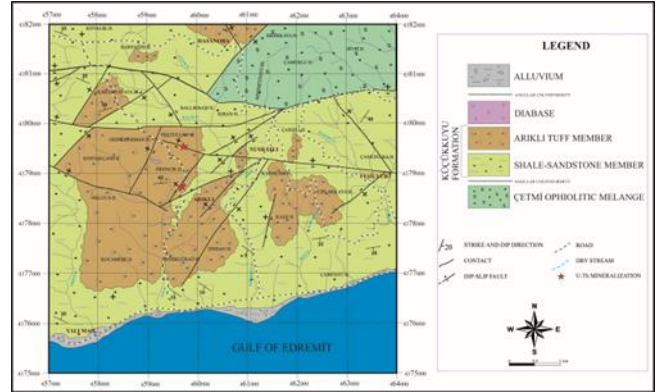


Figure 2. Geological map of the study area.

3. Results

3.1. Ore Geochemistry

Öztürk et al. (2021) collected 48 samples in the field. XRF and ICP-MS methods analyzed these collected samples in Istanbul Technical University Geochemistry Research Laboratory (ITU-JAL). Corresponding to the results of the analysis, U and Th anomalies are observed in the dip-slip fault zones. U is between 64-1640 ppm in these fault zones, and Th is between 302-11813 ppm, respectively. As a result of these data, U and Th mineralizations in the region are related to fault zones observed in Arıklı ignimbrites.

3.2. Remote Sensing

Topographical approaches were obtained with the DEM image of Arıklı and its vicinity. The downloaded DEM images were evaluated in the QGIS environment, an open-source Geographical Information System.

The images of the region generally obtained by remote sensing were evaluated in the QGIS environment. DEM data was classified and coloured in the QGIS environment with a single band pseudocolour application. Then 3D map of the region was created to obtain a more understandable image (Fig 3).

3.3. GIS Application

Sample points of major oxide and trace elements are yielded in Fig 4. Heat maps were established corresponding to spatially major oxide and trace element values appropriately. CaO and U-Th enrichments are observed strongly in similar areas, and a direct ore-fault-and lithology relationship is observed. There are U-Th enrichments exclusively in CaO-rich and faulted areas. This relationship still shows pretty usefully in the GIS environment.

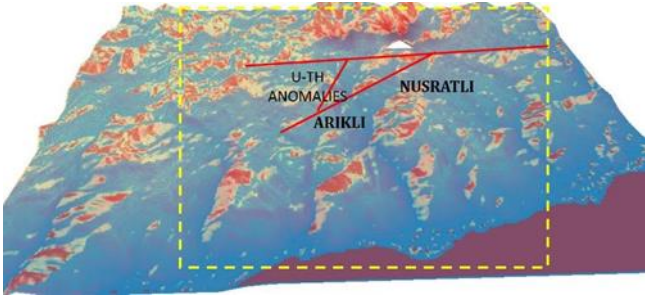


Figure 3. 3D-map of the study area and surroundings

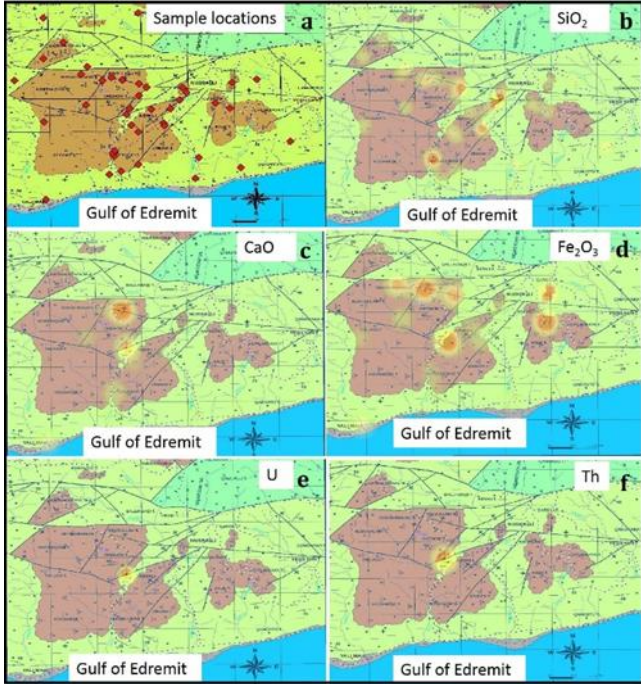


Figure 4. GIS applications of the study area.

4. Discussion and Conclusion

Many GIS-based applications have been carried out in uranium exploration studies. On the principle of these, GIS-based modelling has been proposed in addition to geology-geochemistry studies (Brown et al. 2003; Partington 2008).

Mapping minerals, elements or oxides based on multi-source geoscience data (geology, geochemistry, and remote sensing) and computer technology is an effective technique that merges information and data-driven production (Bonham-Carter 1994; Zhao 2002; Cheng et al. 2007; Asadi et al. 2016; Ford et al. 2016; Wang et al. 2016). For this reason, the data of the study conducted by Öztürk et al. (2021) in the Arıklı region were re-evaluated in the QGIS environment. Field data, remote sensing and GIS data were correlated. In the evaluations prepared, field and spatial data are consistent and supported by thematic maps.

References

- Andaç, M. (1971). Biga yarımadasında tarihi Truva harabelerinin güneyindeki radyoaktif sahil kumlarının mineralojisi ve bunların ana kayaçlarının petrolojisi, MTA Dergisi, 95, 75-79.
- Asadi, H. H., Sansoleimani, A., Fatehi, M., & Carranza, E. J. M. (2016). An AHPeTOPSIS predictive model for district-scale mapping of porphyry Cu-Au potential: a case study from salafchegan area (Central Iran). *Nat. Resour. Res.* 25, 417.
- Atabey, E. (2006). Çanakkale'nin Ayvacık-Küçükkuyu arası kayaların özellikleri, MTA'nın uranyum-fosfat aramaları ve doğal radyoaktivite. *Radyasyon ve Çevre Sempozyumu Bildiriler kitabı* (s.1), Çanakkale
- Bonham-Carter, G. F. (1994). *Geographic information systems for geoscientists: modelling with GIS*. Pergamon Press, Oxford, p. 398.
- Brown, W., Groves, D. I., & Gedeon, T. (2003). Use of fuzzy membership input layers to combine subjective geological knowledge and empirical data in a neural network method for mineral-potential mapping. *Natural Resources Research* 12, 183-200.
- Cheng, Q., Chen, Z., & Khaled, A. (2007). Application of fuzzy weights of evidence method in mineral resource assessment for gold in Zhenyuan district, Yunnan province, China. *Earth Sci. J. China Univ. Geosci.* 32 (2), 175-184.
- Contencin, G. (1960). Sivrihisar Beylikahır radyoaktif emaresi [Radioactive signs of Sivrihisar Beylikahır]. General Directorate of Mineral Research and Exploration Report, no 3167 (in Turkish, unpublished).
- Ford, A., Miller, J. M., & Mol, A. G. (2016). A comparative analysis of weights of evidence, evidential belief functions, and fuzzy logic for mineral potential mapping using incomplete data at the scale of investigation. *Nat. Resour. Res.* 25, 19-33.
- Günaydın, A. (2017). Geology and geochemistry of nodular-phosphate and fault-controlled hydrothermal-phosphate mineralizations in Arıklı and Nusratlı villages (Ayvacık-Çanakkale, NW Turkey). *Bulletin of the Mineral Research and Exploration*, 155 (155), 131-146. <https://doi.org/10.19111/bulletinofmre.314197>.
- İşık, V. (2016). *Torosların Jeolojisi; Türkiye Jeolojisi Ders Notu*. Ankara Üniversitesi, Jeoloji Mühendisliği Bölümü, Ankara.
- Joly, A., Porwal, A., & McCuaig, T. C. (2012). Exploration targeting for orogenic gold deposits in the Granites-Tanami Orogen: mineral system analysis, targeting model and prospectivity analysis, *Ore Geology Reviews* 48, 349-383.
- Li, J., Zhou, M., Li, X., Fu, Z., & Li, Z. (2002). Structural control on uranium mineralization in South China: Implications for fluid flow in continental strike-slip faults. *Science in China (Series-D)*, 45, 851-864. <https://doi.org/10.1007/BF02879519>.
- Lindsay, M., Betts, P. G., & Ailleres, L. (2014). Data fusion and porphyry copper prospectivity models, southeastern Arizona, *Ore Geology Reviews* 61, 120-140.
- MTA. (2009). *Mineral resources of Turkey (According to Province)*. Publication of Mineral Research and Exploration, Earth Science and Culture Series-5, Ankara, p 602. ISBN 978-605-4075-32-4.
- MTA. (2010c). *Maden Tetkik ve Arama Genel Müdürlüğü websitesi*, (Accessed 22 Oct 2015).

- http://www.mta.gov.tr/v2.0/turkiye_maden/maden_potansiyel_2010/Canakkale_Madenler.pdf.
- Okay, A. I., Siyako, M., & Bürkan, K. A. (1990). Geology and tectonic evolution of the Biga peninsula. *Association Of Turkish Petroleum Geologists Bulletin*, 2, 83-121.
- Okay, A. İ., & Satır, M. (2000a). Upper Cretaceous Eclogite-Facies Metamorphic Rocks From the Biga Peninsula, Northwest Turkey. *Turkish Journal of Earth Sciences*, 9, 47-56.
- Okay, A. I., Tansel, I., & Tuysuz, O. (2001). Obduction, subduction and collision as reflected in the Upper Cretaceous-Lower Eocene sedimentary record of western Turkey. *Geological Magazine*, 138(2), 117-142.
- Okay, A. I., & Altınır, D. (2004). Uppermost Triassic limestone in the Karakaya Complex stratigraphic and tectonic significance. *Turkish Journal of Earth Sciences*, 13, 187-199.
- Öztürk, S., Yalçın, C., & Kumral, M. (2021). Microthermometric characteristics of vein type U-Th enrichment observed in the Fault Zones in Northwest Of Arıklı (Çanakkale-Turkey), *Gümüşhane Üniversitesi Fen Bilimleri Enstitüsü Dergisi, GÜFBED/GUSTIJ*, 11 (3), 729-743. DOI: 10.17714/gumusfenbil.866085.
- Partington, G. (2008). Prospectivity analysis in action: the Auzex Resources Ltd (AZX) story as applied to granite related mineral systems in Eastern Australia and New Zealand. *Australian Earth Sciences Convention*, Perth, July 20-24, p. 195.
- Porwal, A., Carranza, E. J. M., & Hale, M. (2001). Extended weights-of-evidence modelling for predictive mapping of base metal deposit potential in Aravalli Province, Western India, *Exploration and Mineral Geology* 10, 273-287.
- Qin, M. T., & Liu, S. X. (1998). Granite- and volcanic rocks-type uranium deposits in the Nanling region (in Chinese with English abstract), Beijing: Geological Publishing House, 147-155.
- Şaşmaz, A. (2008). Determination of uranium occurrences from soil, water and plant samples and possible environmental effects around Köprübaşı (Manisa) uranium bed. Scientific and Technical Research Council of Turkey, Project no 107Y226, 82 p (in Turkish, unpublished).
- Şengün, F., Yiğitbaş, E., & Tunç, İ. O. (2011). Geology and tectonic emplacement of eclogite and blueschists, Biga peninsula, northwest Turkey. *Turkish Journal of Earth Science*, 20, 273-285. <https://doi: 10.3906/yer-0912-75>.
- Wang, G. W., Du, W., & Carranza, J. M. (2016). Remote sensing and GIS prospectivity mapping for magmatic-hydrothermal base and precious-metal deposits in the Honghai district, China. *J. Afr. Earth Sci.* xxx, 1e19.
- Zhang, Z. H., & Zhang, B. T. (1991). Studies of U-bearing granites and associated uranium ore deposits in south China (in Chinese with English abstract), Beijing: Atomic Energy Publishing House, 70-105.
- Zhao, P. D. (2002). Three Component quantitative resource prediction and assessments: theory and practice of digital mineral prospecting. *Earth Sci. J. China Univ. Geosci.* 27 (5), 482e490 (in Chinese).



4th Intercontinental Geoinformation Days

igd.mersin.edu.tr



Applications of machine learning and deep learning techniques in smart agriculture: A review

Mehran Dadashzadeh^{*1}, Kosar Sakhaeian²

¹University of Tabriz, Faculty of Civil Engineering, Department of Water Resources Engineering, Tabriz, Iran

²University of Tabriz, Faculty of Planning and Environmental Sciences, Department of Urban Planning, Tabriz, Iran

Keywords

Smart agriculture
Machine learning
Deep learning
Land cover identification
Diseases management

Abstract

Smart farming is a novel concept that makes agriculture more productive by employing up-to-date information technologies. The most recent developments in automation and artificial intelligence empower farmers better to monitor all procedures and exert accurate treatments determined by machines with great precision. Farmers, experts and data scientists keep on dealing with techniques that allow for optimizing the human labor required in farming. Machine Learning (ML) and Deep Learning (DL) networks that do not need human intervention while performing automatic feature extraction have a significant advantage over previous algorithms. ML and DL allow performing continuous decision-making based on data analysis. Nowadays these techniques have been applied in many applications of smart agriculture such as land cover identification, crop disease detection, weeds removal, and pest recognition. The focus of this study is to review the potential of using ML and DL techniques in agricultural applications and focus on how they are used for smart agriculture.

1. Introduction

Agriculture ensures food security for the country that's why it is the backbone of the country. It plays a vital role in the external trade of most of the country. In most parts of the world, approximately 75% of people rely on agriculture as a livelihood. Due to the boom in population, farmers are looking for efficient ways to increase crop production with less expense and efficient utilization of available resources. This contributes new implementation of digital technologies in the agriculture field to help the farmers to make better decisions and increase yields. Nowadays artificial intelligence techniques are utilized to overcome various problems and challenges in agriculture fields (Dhayabarani et al. 2018). Therefore, many researchers have focused on intelligent systems that monitor and control agricultural parameters by increasing productivity and efficiency. Intelligent systems collect data for measurements and get accurate results that can take the appropriate action. The most common subsets of artificial intelligence, Machine Learning (ML) and Deep Learning (DL), have a considerable potential to handle numerous challenges in the establishment of knowledge-based farming systems (Benos et al. 2021). A vast range of ML and DL applications are also existing in smart agriculture and

farming. Land cover identification, disease management and weed management are a few examples of the application of these techniques in this field. This study aims at shedding light on ML and DL applications in agriculture by reviewing the recent scholarly literature. It is expected that the present study will constitute a lucrative guide towards enhancing awareness of the potential benefits of using artificial intelligence techniques in agriculture and contributing to more structured research on this issue.

2. General Considerations on Machine Learning and Deep Learning

Artificial intelligence (AI) includes several tools and algorithms to computationally imitate human intelligence. AI might use various algorithms derived from the subfields of ML or DL to push forward the computerization of human experts' tasks.

Overall, ML aims at generating informed evaluations by detecting relationships in information employing numerical algorithms, with these procedures presenting the advantage of being able to computerize the method of hypothesis construction. ML algorithms have integrated and, in some instances, modified the

* Corresponding Author

^{*}(mehrandadashzadeh@tabrizu.ac.ir) ORCID ID 0000-0001-9521-7330
(k.sakhaeian31@gmail.com) ORCID ID 0000-0002-7983-8441

Cite this study

Dadashzadeh, M., & Sakhaeian, K. (2022). Applications of machine learning and deep learning techniques in smart agriculture: A review. 4th Intercontinental Geoinformation Days (IGD), 229-232, Tabriz, Iran

conventional statistical methodologies (Lynch and Liston 2018).

DL is a subfield of ML enthused by the configuration of the brain relying on the so-called artificial neural networks (ANNs). Basically, it structures algorithms into layers in order to create ANNs, able to learn and take an intelligent decision on their own (Deng and Yu 2014).

3. Machine Learning and Deep Learning Applications in Smart Agriculture

ML and DL could be considered as novel ways for machines to simulate human learning activities, gain new knowledge, continually improve performance, and achieve unique maturity. In the past few years, these techniques have been very successful in algorithms, theories, and applications, combined with other agricultural techniques to minimize crop costs and maximize yield. ML and DL applications on agricultural farms can be widely used in areas such as land cover identification, disease detection, crop detection, weed detection, soil conditions, crop quality, weather forecasting, etc. The most prominent areas are reviewed in more detail below.

3.1. Land Cover Identification

Land cover and crop type maps have emerged as an area where ML and DL could be used efficiently. Several studies used these techniques for land productivity assessment and land cover classification. Kussul et al. (2019) presented a workflow for developing sustainable goals indicators assessment using high-resolution satellite data. Persello et al. (2019) combined a full CNN with globalization and grouping to detect field boundaries. Zhou et al. (2019) presented a DL-based classifier that learns time-series features of crops and classifies parcels of land. Using these parcels, a final classification map was produced. Zhao et al. (2019) proposed a method for rice mapping which combined a decision tree method and a CNN model.

3.2. Diseases Management

In agriculture, it is critical to monitor the condition of the products and to control the spread of diseases. ML and DL techniques can be used to identify and manage diseases in agricultural fields. ML methods further stimulate appropriate pesticides to protect crops from these infections and reduce labor. Such a system assists producers by obtaining statistics and planning fertilizers, pesticides, and irrigation accordingly. For instance, by accurately identifying the disease and providing accurate pesticide application and irrigation schemes, grape visibility and volume have been increased and extreme pesticide use reduced (Adedola et al. 2019). Fuentes et al. (2017) introduced a DL-based detector for recognizing diseases and pests in tomato plants. Kerkech et al. (2018) proposed DL approaches for vine disease detection using vegetation indices and colorimetric spaces, applied to images collected by UAV. A low shot learning method for disease identification in tea leaves was proposed by Hu et al. (2019). Coulibaly et al. (2019) suggested an

approach for the identification of mildew disease in pearl millet, which is using transfer learning with feature extraction. An artificial intelligence-based approach for detecting grapevine yellows symptoms was proposed by Cruz et al. (2019). Picon et al. (2019) proposed a deep convolutional neural network-based approach for crop disease classification on wheat images.

3.3. Weed Management

Ever since humans first attempted the cultivation of plants, they have had to fight the invasion by weeds into areas chosen for crops. Weed recognition is one of those essential that requires digitization and automation. Therefore, data-driven and image processing-based techniques need to be developed. In recent years, various studies have been carried out for the automation of the process of identification and classification of weeds. Tang et al. (2017) proposed a new approach that combined CNN and K-means feature learning for weed identification and control. The application of DL and K-means pre-training resulted in an accuracy of identification of 92.89%. Santos Ferreira et al. (2017) used CNN to perform weed detection in soybean crop images and classify them as grass and broadleaf weeds. Moshia and Newete (2019) proposed a DL neural network, for the automatic identification of weeds from the main crop using row-guided robots. Bah et al. (2018) proposed a learning method using CNN for weed detection from images collected by UAV that automatically performed unsupervised training dataset collection. Kounalakis et al. (2019) combined a classifier for weed recognition with transfer learning techniques for DL-based feature extraction. Partel et al. (2019) developed a smart sprayer using machine vision and artificial intelligence. This smart sprayer distinguishes target weeds from crops and precisely sprays the targeted weed. Subeesh et al. (2022) investigated the feasibility of DL-based techniques in weed identification from RGB images of bell pepper fields.

3.4. Pest Recognition

Pest attack is one of the significant problems in the agriculture sector that results in the degradation of crop quality. These destructive insects, known as agricultural pests, need to be correctly identified and treated according to their species to minimize the damage they cause. Recently, many developments have been made in the agriculture sector, using ML and DL techniques to detect and classify insects under stored grain conditions. Cheng et al. (2017) performed pest identification via deep residual learning in a complex background. Ding and Taylor (2016) proposed an automatic detection pipeline based on DL for identifying and counting pests in images taken inside field traps. Shen et al. (2016) exerted a deep neural network for the detection and identification of stored-grain insects. Partel et al. (2019) used artificial intelligence to develop an automated vision-based system that can be utilized for monitoring pests, such as the Asian citrus psyllid. Li et al. (2019) proposed an effective data augmentation strategy for CNN-based pest recognition and localization in the field.

Kasinathan et al. (2021) presented the insect pest detection algorithm that consists of foreground extraction and contour identification to detect the insects in a highly complex background. They used different shape features for insect classification by applying ANN, SVM, KNN, NB, and CNN models.

4. Conclusion

Due to the population growth in the world, there is a great demand for agricultural products. That's why it is necessary to increase the production in agriculture. Nowadays the latest technologies such as ML and DL are used to increase agriculture production, reduce production costs and increase income. Applying ML algorithms to data generated from various inputs from farms can make the system smarter and provide definitive information and make predictions.

The focus of the present study is to identify where ML and DL techniques have been used for improving various agricultural practices. Applications of these techniques in the most prominent areas of agriculture are reviewed in this study. It is anticipated that the present review motivates more researchers to focus on AI topics, related to data analysis, image analysis and computer vision, applying it for classification or prediction in smarter farming.

References

- Adedoja, A., Owolawi, P. A., & Mapayi, T. (2019). Deep Learning Based on NASNet for Plant Disease Recognition Using Leaf Images, *International Conference on Advances in Big Data, Computing and Data Communication Systems (icABCD)*, Winterton, South Africa, 1-5.
- Alvarez-Gila, P., Seitz, M., Ortiz-Barredo, A., Echazarra, J., Johannes, A. (2019). Deep convolutional neural networks for mobile capture device-based crop disease classification in the wild, *Computers and Electronics in Agriculture*, (161), 280-290.
- Bah, M. D., Hafiane, A., & Canals, R. (2018), Deep learning with unsupervised data labeling for weed detection in line crops in UAV images. *Remote sensing*, (10), 16-90.
- Benos, L., Tagarakis, A. C., Dolias, G., Berruto, R., Kateris, D., & Bochtis, D. (2021). Machine Learning in Agriculture: A Comprehensive Updated Review, *Sensors (Basel)*, (21): 37-58.
- Cheng, X., Zhang, Y., Chen, Y., Wu, Y., & Yue, Y. (2017). Pest identification via deep residual learning in complex background, *Computers and Electronics in Agriculture*, (141), 351-356.
- Coulibaly, S., Kamsu-Foguem, B., Kamissoko, D., & Traore, D. (2019). Deep neural networks with transfer learning in millet crop images. *Computers in Industry*, (108), 115-120.
- Cruz, A., Ampatzidis, Y., Pierro, R., Materazzi, A., Panattoni, A., De Bellis, L., & Luvisi, A. (2019). Detection of grapevine yellows symptoms in *Vitis vinifera* L with artificial intelligence. *Computers and electronics in agriculture*, (157), 63-76.
- Deng, L., & Yu, D. (2014), Deep learning: methods and applications: Foundations and Trends in Signal Processing, (7), 197-387.
- Dhayabaran, A., Aravinth, K., Gowtham, M., Gowtham, D., & Balakrishnan, (2018), Detection of Weed using Neural Networks. *International Journal of Engineering Research and Technology*, (6), 1-5.
- Dimitriadis, S., & Goumopoulos, C. (2008). Applying Machine Learning to Extract New Knowledge in Precision Agriculture Applications, *Panhellenic Conference on Informatics*, Samos, 100-104.
- Ding, W., & Taylor, G. (2016), Automatic moth detection from trap images for pest management, *Computers and Electronics in Agriculture*, (123), 17-28.
- Ferreira, d. S., Freitas, D. M., da Silva, G. G., Pistori, H., Folhes, M. T. (2017). Weed detection in soybean crops using ConvNets. *Computers and Electronics in Agriculture*, (143), 314-324.
- Fuentes, A., Yoon, S., Kim, S. C., & Park, D. S. (2017). A robust deep-learning-based detector for real-time tomato plant diseases and pests' recognition, *Sensors*, (17), 1-21.
- Fyfe, C. (2000), *Artificial Neural Networks and Information Theory*, Department of Computing and Information System, The university of Paisley, Paisley, UK.
- Goodfellow, I., Bengio, Y., & Courville, A. (2016). Deep learning, USA: MIT Press, 1-15.
- Hu, G., Wu, H., Zhang, Y., & Wan, M. (2019). A low shot learning method for tea leaf's disease identification, *Computers and Electronics in Agriculture*, (163), 104-852.
- Kamilaris, A., & Prenafeta-Boldú, F. X. (2018). Deep learning in agriculture: A survey, *Computers and Electronics in Agriculture*, (147), 70-90.
- Kasinathan, T., Singaraju, D., & Reddy, S. (2021), Insect classification and detection in field crops using modern machine learning techniques, *Information Processing in Agriculture*, (8), 446-457.
- Kavitha, A. (2021). Deep Learning for Smart Agriculture. *International Journal of Engineering Research & Technology (IJERT)*, (9), 132-134.
- Kounalakis, T., Triantafyllidis, G. A., & Nalpantidis, L. (2019). Deep learning-based visual recognition of rumex for robotic precision farming, *Computers and Electronics in Agriculture*, (165), 104-973.
- Kerkech, M., Hafiane, A., & Canals, R. (2018). Deep leaning approach with colorimetric spaces and vegetation indices for vine diseases detection in UAV images, *Computers and electronics in agriculture*, (155), 237-243.
- Kussul, N., Lavreniuk, M., Kolotii, A., Skakun, S., Rakoid, O., & Shumilo, L. (2019). A workflow for Sustainable Development Goals indicators assessment based on high-resolution satellite data, *International Journal of Digital Earth*, 1-13.
- Li, R., Wang, R. R., Zhang, J., Xie, C., Liu, L., Wang, F., Chen, H., Chen, T., Hu, H., X. J., Hu, M., Zhou, M., Li, D., & Liu, W. (2019). An Effective Data Augmentation Strategy for CNN-Based Pest Localization and Recognition in the Field, (7), 274-283.

- Lynch, C. J., Liston, C. (2018). New machine-learning technologies for computer-aided diagnosis, *Nat. Med.*, (24), 1304–1305.
- Maduranga, P., & Abeysekera, R. (2020). Machine learning application in IoT base agriculture and smart framing: A Review, *International Journal of Engineering Applied Sciences and Technology*, (4), 24-27.
- Mahdavinejad M S et al (2018), Machine learning for internet of things data analysis: a survey in proc, *Digital Communications and Network*, 161–175.
- Medela, et al (2013), IoT Multiplatform networking to monitor and control wineries and vineyards, *Future Network and Mobile Summit*, 1–10.
- Moshia, M. E., Newete, S. W. (2019). Mexican poppy (*Argemone mexicana*) control in cornfield using deep learning neural networks: a perspective, *Acta Agriculturae Scandinavica, Section B-Soil and Plant Science*, (69), 228-234.
- Partel, V., Kakarla, S. C., & Ampatzidis, Y. (2019). Development and evaluation of a low-cost and smart technology for precision weed management utilizing artificial intelligence, *Computers and electronics in agriculture*, (157), 339-350.
- Partel, V., Nunes, L., Stansly, P., & Ampatzidis, Y. (2019). Automated vision-based system for monitoring Asian citrus psyllid in orchards utilizing artificial intelligence. *Computers and Electronics in Agriculture*, (162), 328-336.
- Persello, C., Tolpekin, V. A., Bergado, J. R., de By, R. A. (2019). Delineation of agricultural fields in smallholder farms from satellite images using fully convolutional networks and combinatorial grouping, *Remote sensing of environment*, (231), 111-253.
- Picon, A., Alvarez-Gila, A., Seitz, M., Ortiz-Barredo, A., Echazarra, J., & Johannes, A. (2019), Deep convolutional neural networks for mobile capture device-based crop disease classification in the wild, *Computers and Electronics in Agriculture*, (161), 280-290.
- Popa, M., Prostean, O., & Popa, A. S. (2019). Machine Learning Approach for Agricultural IoT in Proc. *International Journal of Recent Technology and Engineering (IJRTE)*, 22-29.
- Raschka, S., & Mirjalili, V. (2017). *Machine Learning and Deep Learning with Python. scikit-learn and TensorFlow*, Birmingham, İngiltere: Packt Publishing, 2-6.
- Santos Ferreira, A., Freitas, D. M., da Silva, G. G., Pistori, H., & Folhes, M. T. (2017). Weed detection in soybean crops using ConvNets, *Computers and Electronics in Agriculture*, 314-324.
- Shakoor, M. T., Rahman, K., Rayta, S. N., & Chakrabarty, A. (2017). Agricultural production output prediction using Supervised Machine Learning Siddique T, Barua D, Ferdous Z, Chakrabarty A (2017), *Automated farming prediction. Intelligent Systems Conference (IntelliSys)*, 757-763.
- Shen, Y., Zhou, H., Li, J., Jian, F., & Jayas, D. (2018). Detection of stored-grain insects using deep learning. *Computers and Electronics in Agriculture*, 145, 319-325.
- Subeesh, Bhole S, Singh K, Chandel N S, Rajwade Y A, Rao K V R, Kumar S P, Jat D (2022), Deep convolutional neural network models for weed detection in polyhouse grown bell peppers. *Artificial Intelligence in Agriculture*, (6), 47-54.
- Tang, J. L., Wang, D., Zhang, Z. G., He, L. J., Xin, J., & Xu, Y. (2017). Weed identification based on K-means feature learning combined with convolutional neural network, *Computers and Electronics in Agriculture*, (13), 63–70.
- Thenmozhi, Reddy U S (2019), Crop pest classification based on deep convolutional neural network and transfer learning, *Computers and Electronics in Agriculture*, (164), 104-906.
- Techniques, 1st International Conference on Next Generation Computing Applications (NextComp), Mauritius, 182-187.
- Ünal, Z. (2020). Smart Farming Becomes Even Smarter with Deep Learning: A Bibliographical Analysis, *IEEE Access*, (8), 105587 – 105609.
- Varman, S. A. M., Baskaran, A., Baskaran, A. R., & Prabhu, E. (2017). *International Conference on Computational Intelligence and Computing Research (ICCIC)*.
- Zhu, N., Liu, X., Liu, Z., Hu, K., Wang, Y., Tan, J., Huang, M., Zhu, Q., Ji, X., Jiang, Y., Guo, Y. (2018). Deep learning for smart agriculture: Concepts, tools, applications, and opportunities. *International Journal of Agricultural and Biological Engineering*, (11), 32-44.
- Zhou, Y. N., Luo, J., Feng, L., Yang, Y., Chen, Y., & Wu, W. (2019). Long-short-term memory-based crop classification using high-resolution optical images and multi-temporal SAR data, *GIScience and Remote Sensing*, (56), 1170-1191.
- Zhao, S., Liu, X., Ding, C., Liu, S., Wu, C., & Wu, L. (2019). Mapping Rice Paddies in Complex Landscapes with Convolutional Neural Networks and Phenological Metrics. *GIScience & Remote Sensing*, 1-12.



4th Intercontinental Geoinformation Days

igd.mersin.edu.tr



Monitoring of growth of wheat's height using time series analysis of synthetic aperture radar (SAR) images and the corresponding parameters

Ahya Rezaei ^{*1}, Sadra Karimzadeh ¹, Khalil Valizadeh Kamran ¹

¹University of Tabriz, Environmental and Planning Science, Tabriz, Iran

Keywords

Radar Images
Google Earth Engine
Precision Agriculture
Time Series Analysis
Sentinel-1

Abstract

In today's word, precision agriculture is one of the practical solutions in increasing agricultural products and timely monitoring to increase food security in today's world. Today, remote sensing technology and GIS are used for this purpose. Classification of various crops, especially wheat, in order to monitor its growth stages in multispectral images due to limitations such as dependence on weather conditions and lack of night imaging. At the same time, SAR images are capable of capturing images in all weather conditions, as well as day-to-day imaging, overcoming the limitations of optical images. Due to the identification of the phenomenon based on the geometry, hardness and orientation of objects, it provides us with a lot of information. Therefore, the main purpose of this study is to evaluate the feasibility of using RADAR images to monitor the growth cycle of wheat. For this study, a bipolar radar image of Sentinel 1 with polarization (VV and VH) will be used to obtain plant growth parameters such as height and biomass. Then, the parameters obtained in order to analyze the time series to understand the plant growth cycle will be performed unsupervised in the Google Earth Engine system. The results will show that band C in the early stages of wheat growth is most sensitive to wheat height and have appropriate information. Field data will then be used to assess accuracy. Final result demonstrates that VV polarization is far better indicator of Wheat growth in early stage, however, VH polarization is more sensitive to middle stage of plant growth cycle. Moreover, neither VV nor VH can detect Wheat growth cycle in their last stage. Both VV and VH showed high connection with the peak of Wheat growth in early May. In fact, it is said that it would be better way to use L band and longer wavelength for Wheat growth in its last stages.

1. Introduction

Agriculture is one of the most important infrastructures of any society and the food security of nations depends on it. So, get the information When pests and plant diseases occur, especially strategic crops such as wheat, it is considered necessary and important. In addition, this is agriculture as a growth engine for most communities in terms of basic human needs (including food and fiber), (Awokuse T.O, 2015 and Gillespie, S, 2017).

Precision farming is the right management in making decisions such as the use of pesticides and pesticides, chemical fertilizers, irrigation rates. And seeks the required labor force for the farm through information analysis, which always leads to increased production and

reduced Water loss and reduction of destructive effects on the environment (2010, R, Gebbers and 2012, A B, Aubert).

Remote sensing is one of the most important techniques used in precision agriculture in monitoring the vegetation of the land surface and today the development of large-scale monitoring of agricultural products with the help of remote sensing techniques to implement reasonable management in relation to resources Natural land is especially important for populous countries that rely on agricultural products. Ability of radar sensors compared to optical sensors to provide images in different polarization channels with high spatial accuracy and wide coverage, penetration, sensitivity to roughness and humidity, and day-to-day

* Corresponding Author

(ahya1996rz@gmail.com) ORCID ID xxxx – xxxx – xxxx – xxxx
(sadra.karimzadeh@gmail.com) ORCID ID 0000-0002-5645-0188
(valizadeh@tabrizu.ac.ir) ORCID ID 0000-0003-4648-842X

Cite this study

Rezaei, A, Karimzadeh, S., & Kamran, K. V. (2022). Monitoring of growth of wheat's height using time series analysis of synthetic aperture radar (SAR) images and the corresponding parameters. 4th Intercontinental Geoinformation Days (IGD), 233-238, Tabriz, Iran

imaging and night and all-weather conditions have made it a key tool for agricultural applications.

The sunlight reflected from the plant depends on the morphological and chemical structure of the plant. In fact, the type of product, the amount of water stored in the plant, the canopy and the health status of the plant in terms of photosynthesis depends on the reflection of sunlight from the plant and causes differences in energy received recorded in different visible and infrared bands. And this has led to the creation of various plant indices to monitor the condition of the plant (2017, J, Xue) so having up-to-date information about the plant growth cycle and changes in this cycle can make timely and cost-effective decisions.

Optical images are used in many fields related to precision agriculture, but due to the limitation of imaging in cloudy conditions, they do not have the necessary efficiency, and this leads to precision agriculture in the field of using radar images that can capture images in any water conditions. And are airborne. Optical images are completely affected by environmental factors such as smoke, rain, fog, dust, clouds and so on. In contrast, optical images are SAR images that have removed the limitations that existed in optical images. SAR images are independent of weather conditions and use replication and redistribution properties. Provides rich information about the object's texture and structure to a variety of components, including: shape, moisture, roughness, and directions (Garcia, F W, 2002).

Various studies conducted in agricultural applications indicate the very good ability of radar remote sensing to monitor plant growth stages. These studies are often very complex because radar systems provide different information at different wavelengths, polarizations, and angles of impact. Different characteristics of plants such as: plant mass, structure) leaf size, stem density, leaf area, etc. (as well as soil moisture, surface unevenness, etc. have different effects on the return signal from plant surfaces. Interaction of radar parameters) Wavelength, polarization and angle of impact (with each other as well as its interactions with the plant, It can lead to the useful use and interpretation of this information and at the same time it is very complex. For this reason, in agricultural studies, radar parameters that signal relay and target-related parameters should be carefully studied (Karjalainen et al, 2008).

In Iran, however, the issue of monitoring agricultural products has been considered due to its importance and place in planning to ensure food security (Gozar Jomhor, 1311) and so far various studies in the field of agriculture have been conducted using optical sensors (Mirbagheri et al. 1310; Asadi Rashed et al. 1311; Jahan Afrooz et al. 1315, Roghan Cheraghi et al., 1344.) But radar remote sensing tools have received less attention due to limited access to data and radar software. In this research, Tal is based on the use of radar sensor data such as Sentinel-1 in monitoring dryland wheat. Changes due to plant phenological characteristics in specific geographical conditions of the country and the variety of environmental parameters in agricultural areas along with the multiplicity of species and species used, the issue of using new radar remote sensing techniques to

monitor wheat production is important. . This strategic product is widely cultivated in Iran and has stages of germination and emergence, stem elongation and rivet development, maturation and seed formation and development.

The purpose of this study is to use radar data to analyze the sensitivity of this data in different polarizations to the height of wheat crop at different growth stages. Since the redistribution of radar waves is different in different polarizations and in different bands (2019, N, Rouhollah), so by comparing the data in polarizations (VH and VV) with ground data to the best parameter to determine the height of wheat and finally the growth stages of wheat We will arrive. Dual redistributions have greater potential for detecting biophysical parameters and phenological stages of plants (2014, all et Nelson).

The Google Earth Engine Web site has become a very useful platform for beginners and professionals in the field of remote sensing. It leads to this functional cloud environment and with the help of this system, different polarizations can be done without the need for

2. Method

In this study, we will use the advantage of remote sensing and different polarizations of Sentinel-1 GRDH format images to detect the plant phenological cycle. The study area is located in the northwestern part of Hamedan province and dryland wheat products are cultivated in it. Due to the presence of clouds during the plant season, more accurate results can be obtained if radar images are used. Therefore, radar images were used and to perform time series analysis, Sentinel-1 images were called to the online platform of Google Earth Engine to increase the speed of work and do not need desktop software. Finally, by comparing the redistribution in different bands and in different stages of growth, the best band composition can be achieved to better show the plant growth cycle.

The study field is under dryland wheat cultivation, so the possibility of errors in radar images due to excessive irrigation is reduced.

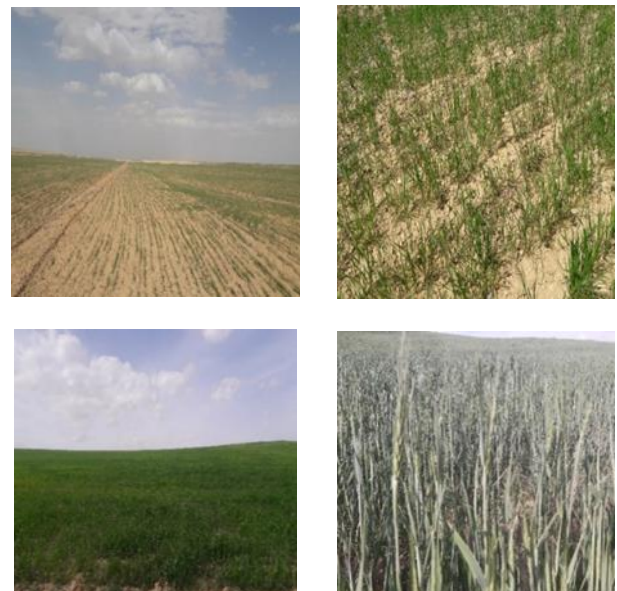


Figure 1. Wheat in different stage of its growth

Table 1. Wheat growth stages

Field survey	Growth Stage	Height
3 April 2021	Emerging	4cm
2 May 2021	Heading	15cm
9 May 2021	Filling	21cm
1 June 2021	Harvesting	36cm

The current study focuses mainly on images of the Sentinel-1 satellite from the European Space Agency (ESA), which is a collection of SAR observations from the Sentinel-1 project (two satellites). October 3, 2014. The project involves combining two platforms A and B in a circuit board with a phase difference of 182 degrees.

has it. This age sensor can receive radar images in the form of HH, HV, VV and VH polarization. The Sentinel-1 satellite can cover the entire planet once every 12 days, which is reduced to 6 days using both Sentinel-1 projects. The angle of impact of this sensor is between 29.1 to 46 degrees and the image bandwidth is 252 km. Spatial resolution in azimuth and slope directions are 5 m and 22 m, respectively) (Lazecky, et al., 2017).

Sentinel-1 images are taken from radar for analysis. Sentinel-1 images, in GRDH format in IW sensor mode, are wide-angle interferometers.

Figure 2. Image information in Google Earth Engine

Date of acquiring image	Satellite pass	Polarization	orbit number
3 April 2021	Ascending	VH and VV	108
2 May 2021	Ascending	VH and VV	108
9 May 2021	Ascending	VH and VV	108
1 June 2021	Ascending	VH and VV	108

Processors were performed in the Google Earth engine block and the amount of redistribution and the type of polarization were investigated in selecting the best parameter to avoid the plant growth cycle. VV polarization actually performed best in showing plant growth.

After entering the account and calling the data with the desired specifications, we apply spatial and temporal filters. Then, by averaging the images in the intervals in which the ground data were collected, we calculate their time series in VV and VH re-representations, as well as in the pass-through and down-pass modes.

In this study, images of Sentinel-1 have been prepared. Necessary filters were also applied. Sentinel-1 images were prepared for time series analysis after calling. Google Earth system engine performed time series analysis at high speed and the results were shown as a chart. Then the redistribution of radar images in different bands was compared.

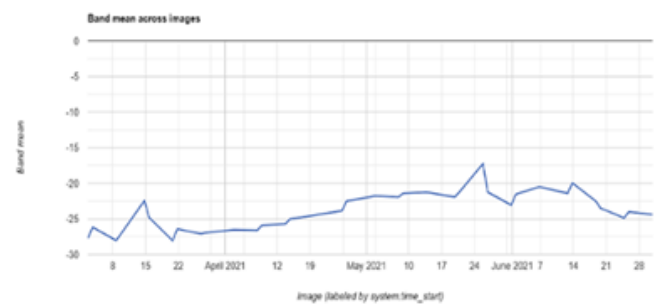
3. Results

The study was conducted to analyze the time series of Sentinel-1 satellite images to study the phenological cycle of the wheat plant and was conducted in the context of the online platform of Google Earth Engine. Sedeps were compared with ground data to obtain the best redistribution in showing the phenological cycle of the plant.

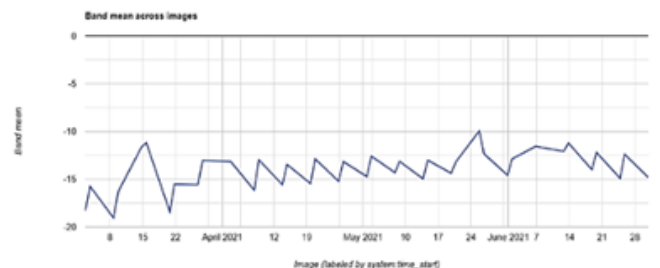
The Google Earth Engine online system was able to process data in a very short time, as well as obtain time series diagrams. Another advantage of Google Earth Engine is shown in the following figures. Since bad time series requires several images from different times and downloading a large number of images also requires high storage space on the user's computer, Google

Inheritance of the engine has overcome all these limitations and provided the best to achieve the desired time series with the least form.

In Figure 1, we can see the redistribution changes according to the plant growth stages, which reached its maximum height in late May and has the highest redistribution on the graph.

**Figure 3.** VV polarisation in ascending mode

According to Figure 3, it can be understood that there is still a direct relationship between plant height at its maximum and the rate of redistribution. VV redistribution has fluctuations that can be due to wind and bending of wheat ears or due to field spraying that has added a little moisture to the wheat ears.

**Figure 4.** VH polarisation in ascending mode

VV images fluctuate more in high-pass and low-pass modes because the wave redistribution in Co-Polarize mode has more contrast and is more sensitive to factors affecting redistribution such as surface roughness and moisture. What is evident in both types of redistribution is that the redistribution of radar images is directly related to the rate of product growth. Thus, with increasing plant height and density, volumetric redistribution occurs and causes more redistributions to reach the satellite sensor.

After downloading the numerical values of the VV and VH redistributions in the transient state and normalizing the numbers (placing the numbers on a scale between 0-1 were compared with the ground-based values) Figure 5.

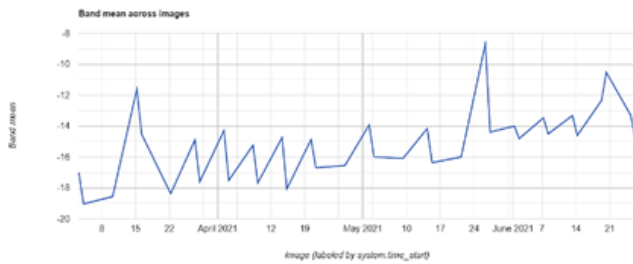


Figure 5. VV polarisation in decending mode

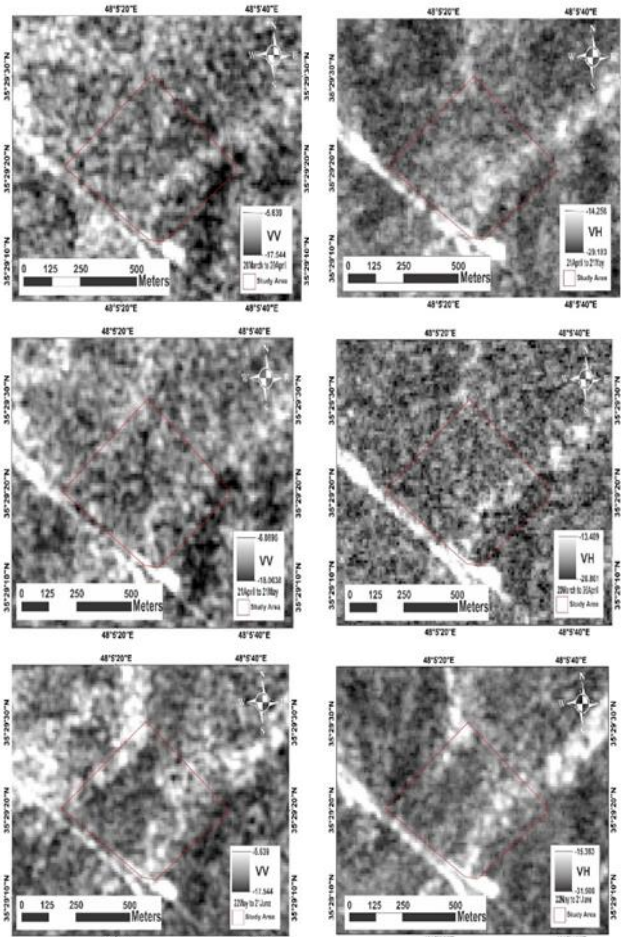


Figure 6. VV and VH in 3 time period (April-May-June 2021)

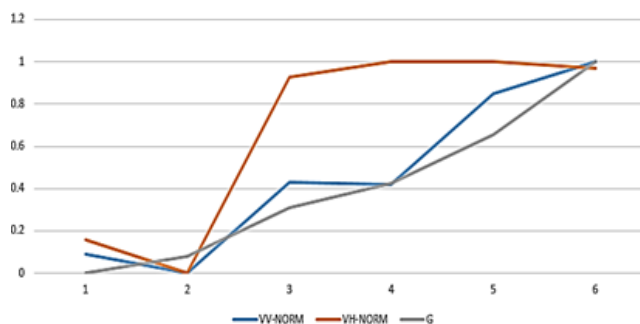


Figure 7. VV, VH and Ground truth data

In the image above, the blue line represents the VV redistribution, the orange line represents the VH redistribution, and the gray line represents the amount of ground data collected. Depending on the shape, it can be understood that the reason for redistribution in both VV and VH in the early stages of plant growth, which is less than 3 cm, may be due to soil moisture due to rainfall

or uneven ground surface due to seeding. It can also be claimed that redistribution in VV mode is closer to the harvested terrestrial values and therefore can better describe the phenological growth cycle of the wheat plant. The Google Earth online engine system was used to show the time series diagrams shown above. With the help of Google Earth Engine system, according to the stages of plant growth, three-time intervals of one month were considered to determine the average redistribution in these intervals. The images below are a visual representation of the same diagrams.

Then, with the help of redistribution in three values, the color band composite was performed to show the best values in the plant phenological cycle in each redistribution. Dedicated to May 22-June 22. And the visualization results are as follows.

According to Figure 1, it can be concluded that the VH band has performed better than other bands in showing the middle stages of crop growth. On the other hand, VV band, as it is taken from time series diagrams, is more sensitive to the growth stages of wheat, and therefore shows the first stages of wheat growth well, and the blue diagram shows it. It should also be noted that neither VV nor VH performed well in the final stages of wheat plant growth. Due to the volumetric redistribution that has occurred and the inability of C-band to penetrate into the dense plant canopy, they do not represent a good indication for the final stages of plant growth. It is suggested to use bands with longer wavelengths to show the final stages of wheat growth. Better results will be obtained.

4. Discussion

We conclude that the use of redistribution of Sentinel-1 images with VV band specificity for wheat production and personalization of its phenological cycle has better results because in polarizations of the same name, the image contrast is usually higher. Also, using the online platform of Google Earth Engine has made the work much easier by being able to process several images simultaneously in the shortest time and without the need for storage space inside the computer.

It has also made it possible for all users to submit their code in the form of an online software so that other users can perform the necessary processes just by entering the study area. C-band Sentinel-1 images are available in GRDH format (SLC mode is not available), and then applying the relevant parameters and comparing all three with the ground samples, we conclude that due to volumetric redistribution occurs, the amount of signal penetration into the plant canopy in the last stages is reduced due to crop density.

5. Conclusion

In this study, by using the analysis of temporal cedars in intensifying intervals and in accordance with the ground visit, the stages of phonological development of wheat crop were obtained. This operation was performed with the help of block chain under the Google Earth Engine Web, and finally, by comparing the normalized numbers to a hundred diagrams with ground data, the inaccurate results showed that the VV

polarization is higher. Also, by obtaining the color band compounds, it can be claimed that the C band performs well in showing the phenological cycle, provided that the plant is in its early stages. Because of the occurrence of volumetric redistribution, the amount of signal penetration into the plant canopy in the last stages due to crop density is reduced.

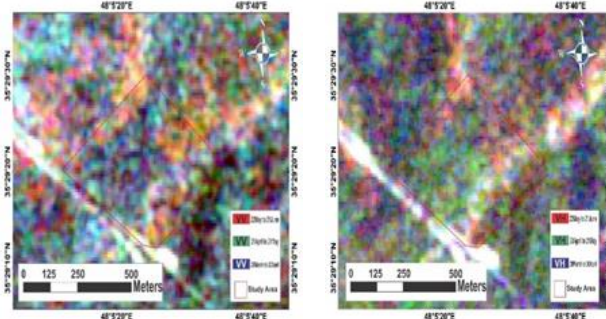


Figure 8. Color composite of VV and VH

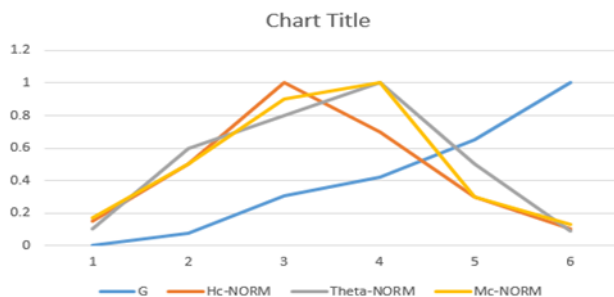


Figure 9. VV, VH and Ground truth data after normalized (the numbers between 1-0)

Acknowledgement

Thanks to professor Karimzadeh and professor Valizadeh Kamran for all their support

References

- Awokuse, Titus O., and Ruizhi Xie. "Does agriculture really matter for economic growth in developing countries?." *Canadian Journal of Agricultural Economics/Revue canadienne d'agroeconomie* 63.1 (2015): 77-99.
- Aubert, Benoit A., Andreas Schroeder, and Jonathan Grimaudo. "IT as enabler of sustainable farming: An empirical analysis of farmers' adoption decision of precision agriculture technology." *Decision support systems* 54.1 (2012): 510-520.
- Amazirh, Abdelhakim, et al. "Retrieving crop albedo based on radar sentinel-1 and random forest approach." *Remote Sensing* 13.16 (2021): 3181.
- Argenti, Fabrizio, et al. "A tutorial on speckle reduction in synthetic aperture radar images." *IEEE Geoscience and remote sensing magazine* 1.3 (2013): 6-35.
- Bhogapurapu, Narayanarao, et al. "Dual-polarimetric descriptors from Sentinel-1 GRD SAR data for crop growth assessment." *ISPRS Journal of Photogrammetry and Remote Sensing* 178 (2021): 20-35.
- Bhogapurapu, Narayanarao; Dey, Subhadip; Bhattacharya, Avik; Mandal, Dipankar; Sanchez, Juan M Lopez; McNairn, Heather; et al. (2021): Dual-polarimetric descriptors from Sentinel-1 GRD SAR data for crop growth assessment. TechRxiv.
- Baghdadi, Nicolas, et al. "Potential of SAR sensors TerraSAR-X, ASAR/ENVISAT and PALSAR/ALOS for monitoring sugarcane crops on Reunion Island." *Remote sensing of environment* 113.8 (2009): 1724-1738.
- Colin Koeniguer, Elise, and Jean-Marie Nicolas. "Change Detection Based on the Coefficient of Variation in SAR Time-Series of Urban Areas." *Remote Sensing* 12.13 (2020): 2089.
- Cotterman, Kayla A., et al. "Groundwater depletion and climate change: future prospects of crop production in the Central High Plains Aquifer." *Climatic change* 146.1 (2018): 187-200.
- Connor, Melanie, et al. "When climate change is not psychologically distant—Factors influencing the acceptance of sustainable farming practices in the Mekong River Delta of Vietnam." *World Development Perspectives* 18 (2020): 100204.
- Chang, Jisung Geba, Maxim Shoshany, and Yisok Oh. "Polarimetric radar vegetation index for biomass estimation in desert fringe ecosystems." *IEEE Transactions on Geoscience and Remote Sensing* 56.12 (2018): 7102-7108.
- Delgado, Jorge A., et al. "Big data analysis for sustainable agriculture on a geospatial cloud framework." *Frontiers in Sustainable Food Systems* 3 (2019): 54.
- Feng, Lei, et al. "Wind field distribution of multi-rotor UAV and its influence on spectral information acquisition of rice canopies." *Remote Sensing* 11.6 (2019): 602.
- Gebbers, Robin, and Viacheslav I. Adamchuk. "Precision agriculture and food security." *Science* 327.5967 (2010): 828-831.
- Gillespie, Stuart, and Mara van den Bold. "Agriculture, food systems, and nutrition: meeting the challenge." *Global Challenges* 1.3 (2017): 1600002.
- Gamba, Paolo, Massimiliano Aldrighi, and Mattia Stasolla. "Robust extraction of urban area extents in HR and VHR SAR images." *IEEE Journal of Selected Topics in Applied Earth Observations and Remote Sensing* 4.1 (2010): 27-34.
- Gibson, Paul Jude, and John Keating. *Introductory Remote Sensing: Introduction to and historical development of remote sensing*. Routledge, 2000.
- Gumma, Murali Krishna, et al. "Mapping irrigated areas of Ghana using fusion of 30 m and 250 m resolution remote-sensing data." *Remote Sensing* 3.4 (2011): 816-835.
- Hirooka, Yoshihiro, et al. "Applicability of synthetic aperture radar (SAR) to evaluate leaf area index (LAI) and its growth rate of rice in farmers' fields in Lao PDR." *Field Crops Research* 176 (2015): 119-122.
- Han, Dong, et al. "Improving Wheat Yield Estimates by Integrating a Remotely Sensed Drought Monitoring Index Into the Simple Algorithm for Yield Estimate Model." *IEEE Journal of Selected Topics in Applied*

- Earth Observations and Remote Sensing* 14 (2021): 10383-10394.
- Holtgrave, Ann-Kathrin, et al. "Comparing Sentinel-1 and-2 data and indices for agricultural land use monitoring." *Remote Sensing* 12.18 (2020): 2919.
- Jensen, John R. "Digital image processing: a remote sensing perspective." *Upper Saddle River, NJ: sPrentice Hall* (2005).
- Jensen, John R. *Remote sensing of the environment: An earth resource perspective 2/e*. Pearson Education India, 2009.
- Jensen, Ryan R., and Perry J. Hardin. "Estimating urban leaf area using field measurements and satellite remote sensing data." *Journal of Arboriculture* 31.1 (2005): 21-27.
- Karimzadeh, Sadra, and Masashi Matsuoka. "Ground displacement in East Azerbaijan Province, Iran, revealed by L-band and C-band InSAR analyses." *Sensors* 20.23 (2020): 6913.
- Karjalainen, Mika, Harri Kaartinen, and Juha Hyyppä. "Agricultural monitoring using Envisat alternating polarization SAR images." *Photogrammetric Engineering & Remote Sensing* 74.1 (2008): 117-126.
- Kurosu, Takashi, Masaharu Fujita, and Kazuo Chiba. "Monitoring of rice crop growth from space using the ERS-1 C-band SAR." *IEEE Transactions on Geoscience and Remote Sensing* 33.4 (1995): 1092-1096.
- Kuhl, Alexandria, et al. "Estimating Soil and Root Parameters of Biofuel Crops using a Hydrogeophysical Inversion." *AGU Fall Meeting Abstracts*. Vol. 2017. 2017.
- Lazecký, Milan, et al. "Displacements monitoring over Czechia by IT4S1 System for Automatised Interferometric measurements using sentinel-1 data." *Remote Sensing* 12.18 (2020): 2960.
- Lee, Jong-Sen, Mitchell R. Grunes, and Gianfranco De Grandi. "Polarimetric SAR speckle filtering and its implication for classification." *IEEE Transactions on Geoscience and remote sensing* 37.5 (1999): 2363-2373.
- Liaghat, Shohreh, and Siva Kumar Balasundram. "A review: The role of remote sensing in precision agriculture." *American journal of agricultural and biological sciences* 5.1 (2010): 50-55.
- Lasko, Kristofer, Michael Laurence Humber, and Sean P. Griffin. "A combined Radar and optical algorithm for refining temporal information in the MODIS burned area product using Sentinel-1 Synthetic Aperture Radar (SAR) Imagery." *AGU Fall Meeting Abstracts*. Vol. 2018. 2018.
- Lasko, Kristofer, et al. "Mapping double and single crop paddy rice with Sentinel-1A at varying spatial scales and polarizations in Hanoi, Vietnam." *IEEE journal of selected topics in applied earth observations and remote sensing* 11.2 (2018): 498-512.
- Lee, Jong-Sen, et al. "Speckle filtering and coherence estimation of polarimetric SAR interferometry data for forest applications." *IEEE Transactions on Geoscience and Remote Sensing* 41.10 (2003): 2254-2263.
- Mascaro, Joseph, et al. "Controls over aboveground forest carbon density on Barro Colorado Island, Panama." *Biogeosciences* 8.6 (2011): 1615-1629.
- Mirasi, Asadollah, et al. "Evaluation of sum-NDVI values to estimate wheat grain yields using multi-temporal Landsat OLI data." *Geocarto International* 36.12 (2021): 1309-1324.
- McNairn, Heather, et al. "Estimating canola phenology using synthetic aperture radar." *Remote sensing of environment* 219 (2018): 196-205.
- Nystuen, Jeffrey A., and F. W. Garcia. "Sea ice classification using SAR backscatter statistics." *IEEE Transactions on Geoscience and Remote Sensing* 30.3 (1992): 502-509.
- Nasirzadehdizaji, Rouhollah, et al. "Sensitivity analysis of multi-temporal Sentinel-1 SAR parameters to crop height and canopy coverage." *Applied Sciences* 9.4 (2019): 655.
- Nasrallah, Ali, et al. "Sentinel-1 data for winter wheat phenology monitoring and mapping." *Remote Sensing* 11.19 (2019): 2228.
- Nystuen, Jeffrey A., and F. W. Garcia. "Sea ice classification using SAR backscatter statistics." *IEEE Transactions on Geoscience and Remote Sensing* 30.3 (1992): 502-509.
- Patel, Raj. "The long green revolution." *The Journal of Peasant Studies* 40.1 (2013): 1-63.
- Pingali, Prabhu L. "Green revolution: impacts, limits, and the path ahead." *Proceedings of the National Academy of Sciences* 109.31 (2012): 12302-12308.
- Richards, John A., and J. A. Richards. *Remote sensing digital image analysis*. Vol. 3. Berlin: springer, 1999.
- Schlund, Michael, and Stefan Erasmi. "Sentinel-1 time series data for monitoring the phenology of winter wheat." *Remote Sensing of Environment* 246 (2020): 111814.



4th Intercontinental Geoinformation Days

igd.mersin.edu.tr



HYSPLIT algorithm in dust source Identifying and modeling

Behnaz Ghaderi¹ , Zahra Azizi ^{*1}

¹ Islamic Azad University, Science and Research Branch, Faculty of Natural Resources and Environment, Department of Remote Sensing and GIS, Tehran, Iran

Keywords

Modis
Dust index
HYSPLIT
Correlation

Abstract

Dust storms are one of the most important natural disasters and can strike due to different reasons, the phenomenon of dust is one of the most important sources of pollution in the world. This paper was used to identify dust hotspots in southwestern of Iran using Modis satellite images with appropriate temporal and spatial resolution. Modis images of MOD021KM were taken on dates corresponding to dust days and a true color combination and index (BTD) were used to identify dust. After dust detection, the main source and modeling of dust was performed by HYSPLIT algorithm at three heights and 48-hour return path. By tracking and identifying the source of dust storms, investigation of vegetation changes was carried out as this research was being done and the correlation between dust index and vegetation was also investigated. The results demonstrated that the dust source originates from neighboring countries such as Iraq, Syria, Jordan and Libya, and the increase in the occurrence of dust storms has had negative impacts on vegetation changes and plant loss.

1. Introduction

Dust is considered one of the biggest environmental issues in arid and semi-arid regions of the world today that every year it causes a lot of damage to sectors such as industry, transportation, agriculture, tourism and human health. (Baaghideh and Ahmadi, 2014).

Furthermore, it has disturbed the environment and reduced the growth of plants, this phenomenon has a strong negative impact on natural resources and vegetation (Baaghideh et al. 2014; Hao et al. 2007).

Previous research has shown that dust has become widespread, thus it has turned into an uncontrollable phenomenon (Taghavi et al., 2013).

Remote measuring and spatial information system have the ability to identify the center and source of the dust storm as well as tracking and predicting the direction of dust movement.

2. Method

Khuzestan province is a vast plain which is one of the richest provinces in Iran in terms of fertility.

The latitude and longitude of the study area is, 47°, 50° E and 30° 33' N respectively. It is the fifth most populous province of Iran with an area of 640057 square kilometers, it is located in the southwest of Iran on the shores of the Persian Gulf and the Arvand River. Due to the proximity to the Persian Gulf and the dry and burning winds of the Arabian Peninsula, it is a dry region and has a desert climate.

This study aims at monitoring and tracking the dust source related to the years 2010 and 2017. By examining the recorded data of dust in 20 synoptic stations and matching the time of recording the occurrence of dust phenomenon in the station with the imaging time of Modis sensor (MODIS), suitable data were obtained for this study.

Two methods of true color combination (TCC) and dust index (BTD) were used to monitor dust storms. In the color combination method, (3-4-1) dust is seen as a cloud mass in the image (Karimi et al. 2012; Ghaderi et al. 2019; Ghaderi et al 2020). In the BTD index method, dust has a higher temperature in bands 31 and 32 than other phenomena and the difference in radiance temperature between these two bands in the detection of dust phenomenon is the BTD index (Ghaderi et al. 2019 and samadi, 2019). Finally, using the Hysplit method, the

* Corresponding Author

(ghaderi6719@gmail.com) ORCID ID 0000- 0001 - 6924 -6920
*(zazizi@srbiau.ac.ir) ORCID ID 0000- 0001 - 8572 - 7134

Cite this study

Ghaderi, B., & Azizi, Z. (2022). HYSPLIT algorithm in dust source Identifying and modeling. 4th Intercontinental Geoinformation Days (IGD), 239-241, Tabriz, Iran

sources of dust in the study area (Khuzestan) were tracked. Then, correlation and vegetation analysis with dust in the area was performed.

2.1. Meteorological Model HYSPLIT

HYSPLIT is one of the most commonly used atmospheric models to specify the backward trajectories to determine the origin of air masses. One of the tools used in this research is the Hybrid Single Particle Lagrangian Integrated Trajectory (HYSPLIT) meteorological model.

Modeling by tracking and reversing method, in 48 hours before the occurrence of dust phenomenon in Khuzestan province, at three altitudes of 100, 500 and 1000 meters to determine the path of dust particles was done.

2.2. Vegetation changes and its correlation with dust phenomenon

In this section, by analyzing and evaluating two vegetation maps in 2010 and 2017, the impact and role of dust storm in vegetation changes and plant loss were investigated.

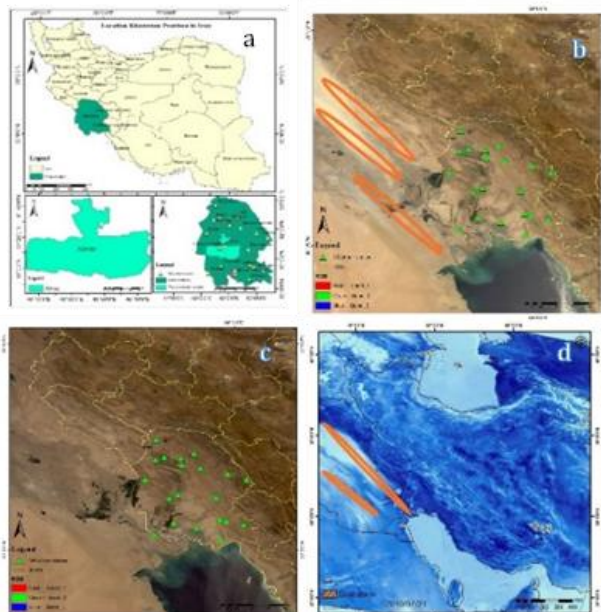


Figure 1. Study area, b, c) TCC image July/07/2010 and June/22/2017 d) BTD index.

Based on the NDVI index, the origin of dust was identified and the relationship between vegetation and dust in the study area was determined.

3. Results

The BTD dust index was used to identify the dust storm and the true color composition (TCC) was interpreted visually. Therefore, dust was identified in the west and north of Khuzestan province.

In order to modeling from meteorological model, the HYSPLIT was performed backwards from the starting point in Khuzestan province with three altitude trajectories.

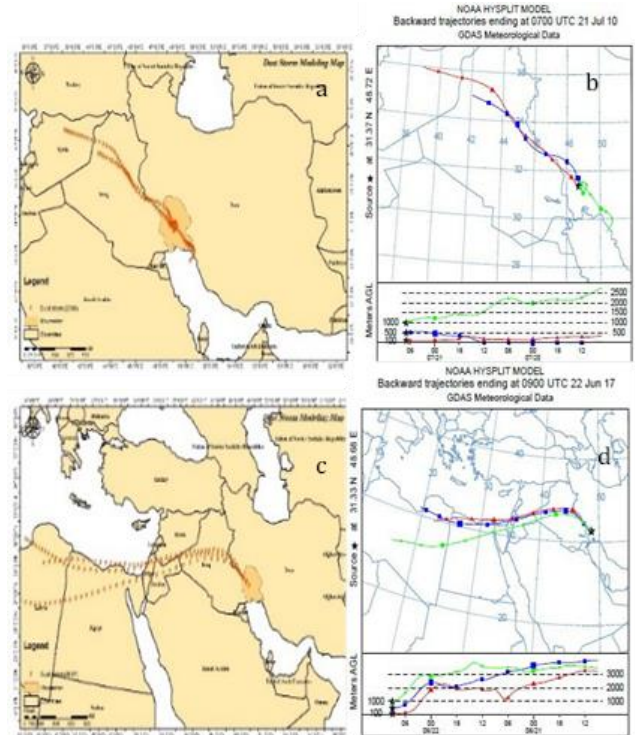


Figure 2. a, c) Hysplit model b, d) Hysplit model results to show dust cloud at three altitudes and validation.

The results of the meteorological model showed that the source of dust is from the west and northwest of Khuzestan province and the main source of foreign dust is from Iraq, Syria, Jordan and Libya.

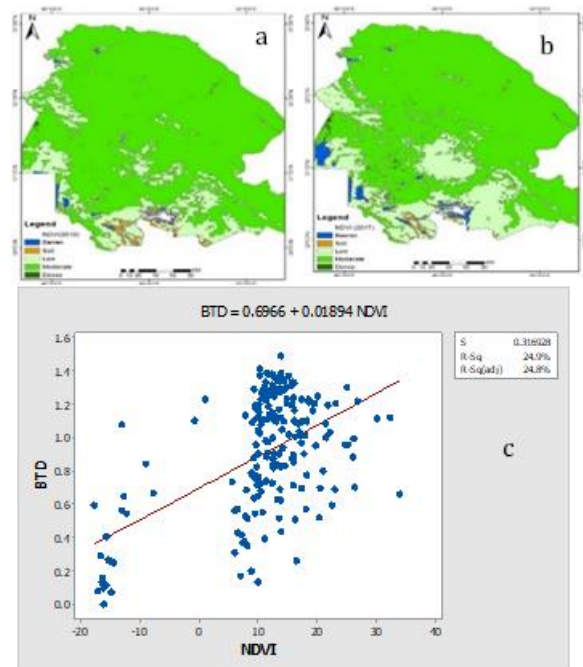


Figure 3. a, b) Map NDVI 2010&2017 c) Correlation of btd variable with ndvi.

Vegetation in 2010, according to the map of the southern regions of Khuzestan province is low. During the 8-year period of research, the vegetation of the areas with the most dust is reduced by vegetation. By analyzing the correlation between vegetation index and dust, it is stated that dust has a negative relationship with

vegetation. That is, with increasing dust, the vegetation decreases. Therefore, dust causes vegetation to disappear. Optical depth of aerosols (AOD) shows the density and depth of dust particles in the Earth's atmosphere and shows the aerosols in the atmosphere. (b).

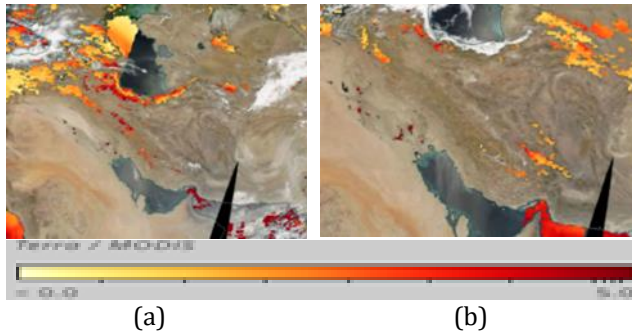


Figure 4. a) Aerosol optical depth (AOD) in 2010, b) Aerosol optical depth (AOD) in 2017

4. Discussion

Dust storms usually occur in arid and semi-arid regions of the world, and in recent years have created many problems for people living in arid regions. Therefore, many studies have been carried out with different methods to monitor, prevent and predict the occurrence of storms. Remote measuring and GIS are widely used in identifying and analyzing changes and monitoring meteorological phenomena.

5. Conclusion

This paper applies remote sensing and spatial information systems, data and the images of Terra/Modis were acquired on 21 July 2010, 22 June 2017, at 07.30 hrs. Then the necessary corrections were made in the images, and by using BTM index method the difference in dust brightness temperature was identified. With the HYSPLIT ventilation model, the return route to 48 hours before and three altitude trajectories of dust source and its accuracy were performed. Finally, the vegetation in southern Khuzestan was correlated with dust. As a result, with the increase of dust storm, vegetation was decreasing from 2010 to 2017.

References

- Baaghdeh, M., Ahmadi, H. (2014). Dust and Detector Analysis of the Changes in the West and Southwest of Iran. *Journal of Rescue and Rescue*, Year 6, No
- Hao, x., Qu, J, (2007). saharnm dust storm detection using moderate resolution imaging spectroradiometer thermal infrared bands. *Journal of Applied Remote Sensing*. vol, 1.
- Taghavi, F., Olad, E., Safarrad, T., Irannejad, P. (2013). Detection and monitoring of dust storms in western Iran using remote sensing methods. *Journal of Physics of Earth and Space*, 39(3), 96-83.
- Karimi, K., Taheri, H., Hafezi Moghaddas, N., Habibi Nokhandan, M. (2012). "Identifying and Classifying the Dust lands in the Middle East Using the Combination of MODIS Sensing Reflective and Infrared Thermal Characteristics". *Journal of Iranian Engineering Society of Geology*, Vol. 5, No. 1 & 2, Page 121 93-83, Spring & Summer.
- Ghaderi, B., Azizi, Z (2019). Detecting and monitoring dust storm and studying the effect of temperature and relative humidity parameters using remote sensing. 2ND Conference of the Arabian journal of geosciences (cajg) 25-28 november 2019, sousse, Tunisia.
- Ghaderi, B., Azizi, Z. (2020). Monitoring of dust phenomenon and investigate its correlation with temperature and humidity parameters (Case study: Khuzestan Province). *Journal of Geomatics Science and Technology*.
- Ghaderi B., Azizi, Z. (2020). Identification and zoning of dust phenomena using satellite remote sensing (Case study: Khuzestan Province). *Journal of Environmental Science and Technology*.
- Samadi, M. (2011). Detection and origination of dust storms using satellite imagery. Master thesis, Department of Cartography, University of Tehran.

4th Intercontinental Geoinformation Days

igd.mersin.edu.tr



The effect of Covid-19 epidemic on the Land surface temperature of Asaluyeh Industrial City with an approach to image processing in Google Earth Engine Platform

Mostafa MahdaviFard ¹, Shahin Jafari ^{*2}, Khalil Valizadeh Kamran ¹, Seyed Kazem Alavipanah ²

¹ University of Tabriz, Department of Remote Sensing and GIS, Tabriz, Iran

² University of Tehran, Department of Remote Sensing and GIS, Tehran, Iran

Keywords

Land Surface Temperature
Covid-19
Google Earth Engine
Landsat Series
Remote Sensing

Abstract

At the end of 2019, the world became infected with the Covid-19 virus. In Iran, public places were declared quarantined and closed due to policy-making and social distancing. Land surface temperature is an important variable for the environment. The purpose of this study is to compare the LST extracted from Landsat 8 images in the new GEE for Asaluyeh Industrial City before, during and after the outbreak of Corona virus in April-May 2018, 2019, 2020 and 2021. The results of this study showed that the maximum temperatures in 2018, 2019, 2020 and 2021 for the city of Asaluyeh are 74.4, 61.2, 58.8 and 58.7 degrees Celsius, respectively. In fact, the city of Asaluyeh in the pre-Covid period experienced relatively high temperatures in residential areas and industrial towns, respectively, which were seen as hot spots in this period, but during the prevalence and epidemic of Corona due to closure and quarantine of cities, especially transportation, Factories and industries The LST has decreased significantly compared to the previous year, and after the normalization of epidemic conditions, ie in the post-corona period, due to the reduction of quarantine restrictions, we are witnessing an increase in temperature again in this city.

1. Introduction

Covid-19 virus was first reported in late December 2019 in the Huanan Seafood Market in Wuhan, China (Wuhan Municipal Health Commission, 2019). This nasty virus has spread rapidly worldwide and its epidemic has caused deaths worldwide (WHO, 2020). One effective way to reduce the effect of this virus is to apply quarantine. Quarantine conditions have led to the closure of academic institutions, public and private offices, restaurants, banks, public and private transport, factories, shops, etc. (Guha & Govil, 2021).

From the effects of urban blockage and environmental quarantine, decrease in air temperature and land surface temperature (LST) has been observed (Shi et al., 2020). Land surface temperature plays an important role in many studies such as climate change, agriculture, hydrology, land use and Land cover (LULC) (Avdan & Jovanovska, 2016). In general, heat in cities is caused by tire friction and smoke emissions from cars, as

well as industrial sectors and areas such as power plants and petrochemicals, which affect air temperature and surface temperature (LST) in industrial cities (Phelan et al., 2015).

The city of Asaluyeh in Iran is known as an industrial city that was directly affected during the outbreak of Covid-19 virus, which resulted in the closure of factories, industries and petrochemicals and reduced human activities. These conditions cause the LST to change, so monitoring the LST is more important than before for environmental planners and managers. The quick development of remote sensing technology has made it possible to estimate the LST with satellite time series data, which has given rise to the online Google Earth engine (GEE) platform.

GEE is a computing platform for processing satellite imagery and spatial and geographic data in the cloud to integrate big data Petabyte-scale, including Landsat satellite data (Shelestov et al., 2017; Mahmoudzadeh et al., 2021).

* Corresponding Author

(mostafamahdavi842@gmail.com) ORCID ID 0000-0001-9811-5428
*(Shahin.jafari75@ut.ac.ir) ORCID ID 0000-0001-8593-7131
(valizadeh@tabrizu.ac.ir) ORCID ID 0000-0003-4648-842X
(salavipa@ut.ac.ir) ORCID ID 0000-0002-3554-111X

Cite this study

MahdaviFard, M., Jafari, S., Kamran, K. V., & Alavipanah, S. K. (2022). The effect of Covid-19 epidemic on the Land surface temperature of Asaluyeh Industrial City with an approach to image processing in Google Earth Engine Platform. 4th Intercontinental Geoinformation Days (IGD), 242-245, Tabriz, Iran

The aim of this study was to investigate the effect of Covid-19 virus on the surface temperature of Asaluyeh Industrial City. In line with the purpose of the study, surface temperature before, during and after Covid-19 were obtained from Landsat 8 images in the new GEE system.

2. Method

This section describes the steps of preprocessing and data processing in the GEE cloud space. Figure 1 shows the research processing flowchart.

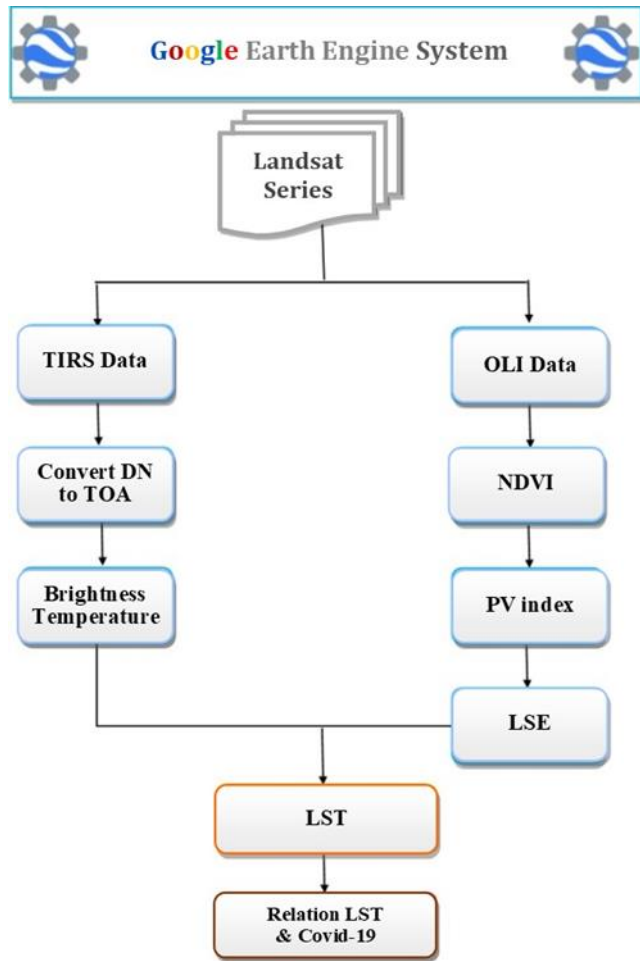


Figure 1. Flowchart of research process

2.1. Study area

Asaluyeh city is known as an industrial city in Iran. The geographical location of this city is located between north latitude 27° 29' and 52° 37' east longitude (Figure 2) and is located at an altitude of 5 meters above sea level. Content should be written in 2 columns with Cambria 10 font size.

The city has moderate and scattered vegetation with some dense palm lands and mangrove shrubs. The relative humidity of this region is between 59 to 88% and it receives 180 mm of rainfall annually. The population of this city is about 65 thousand people (Mokhtari Malek Abadi et al., 2016).

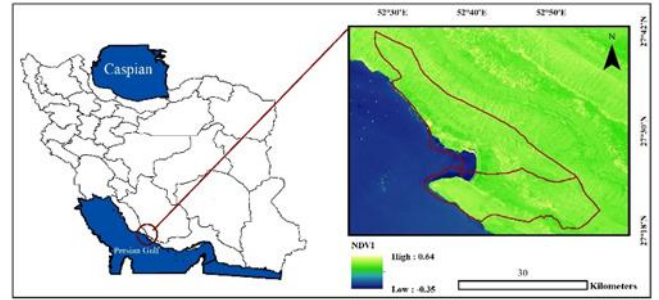


Figure 2. Geographical location of the study area

2.2. Datasets

To create a surface temperature map, satellite images of OLI and TIRS sensors in Landsat 8 related to 4 time periods were used on the Google Earth Engine platform. The criterion for selecting the date of satellite images in this study was the first quarantine apply In April and May 2020).

In order to validate the LST maps, the synoptic station data of 2018, 2019, 2020 and 2021 in the pre-, during and post-Covid-19 periods, respectively, were used. Table 1 shows the characteristics of the data used.

Table 1. Specifications of the data used

Image Satellite	Date of Acquisition	Climate Data	Temperature (°C)
Landsat-8	2018-5-13	Climate Station (CS)	36
	2019-5-15		35
	2020-5-16		33
	2021-5-19		34

2.3. Data Processing

In order to obtain the amount of spectral radiation above the atmosphere of band 10 of TIRS sensors, Equation 1 is used. Using this relation, the DN of the image can be converted to spectral radiation (USGS, 2020).

$$L\lambda = M_L \times Q_{cal} + A_L \quad (1)$$

Where $L\lambda$ high-spectral atmospheric radius, M_L specific band scaling factor, A_L specific band cumulative scaling factor, Q_{cal} specific band digital value (DN), M_L and A_L values are extracted from the MTL file (Ghorbannia et al., 2017).

Brightness temperature (BT) is the microwave radiation radiance traveling upward from the top of Earth's atmosphere. Equation 2 is used to convert spectral reflection to brightness temperature.

$$BT = \frac{K2}{\ln \left[\left(\frac{K1}{L\lambda} \right) + 1 \right]} - 273.15 \quad (2)$$

Where BT is the brightness temperature of the satellite in Kelvin unit, K1 is the first thermal constant (specific band thermal conversion of the MTL file equivalent to 774.89), K2 is the second thermal constant (specific band thermal conversion of the MTL file is equal

to 1321.08) and L_λ radiance Spectrum is the top of atmosphere (Xu & Chen, 2004).

The NDVI index is based on the relationship between energy absorption in the red range by chlorophyll and increased reflectance in the near infrared range for healthy vegetation. This index is calculated from Equation 3 (Rouse et al., 1974).

$$NDVI = \frac{Band5 - Band4}{Band5 + Band4} \quad (3)$$

NDVI is the normalized vegetation index, which is calculated using near-infrared (band 5) and red (band 4).

PV is a ratio of the vertical projection area of vegetation (leaves, stalks, and branches) on the ground to the total vegetation area (Neinavaz et al., 2020). The proportion of vegetation (Pv) calculated using the Equation 4 (Bendib et al., 2017):

$$NDVI = \left(\frac{NDVI - NDVI_{min}}{NDVI_{max} - NDVI_{min}} \right)^2 \quad (4)$$

where Pv = Proportion of vegetation, $NDVI_{max}$ = maximum value of $NDVI = NDVI_v$ (NDVI Vegetation), and $NDVI_{min}$ = minimum value of $NDVI = NDVI_s$ (NDVI Soil).

To obtain the surface temperature, it is important to calculate the surface emission. The ratio between emissions from an object to its emission from a black body at a constant temperature is called emission. Surface emission is a comparative factor that expresses the brightness of black body (Planck's law) to predict emitted radiation and is calculated from Equation 5 (Ghorbannia et al., 2017).

$$LSE = 0.004 \cdot Pv + 0.986 \quad (5)$$

In this equation LSE is the land emission temperature and Pv is the Proportion of vegetation.

Land Surface temperature (LST) is a constant temperature that is calculated using the calculated parameters of thermal radiation, TOA radiation, and land surface emissivity from Equation 6 (Stathopoulou & Cartalis, 2007).

$$LST = \frac{BT}{\{1 + [(\lambda BT/p) \ln \epsilon]\}} \quad (6)$$

In this equation, BT is the brightness temperature, λ is the TOA radiation, ϵ is the emission of phenomena, p is a constant coefficient equal to 1.4388.

3. Results and Discussion

The results of comparing synoptic station data with satellite LST map are given in Table 2.

The data recorded by the meteorological station in Table 2 have a difference of about 11 minutes with the satellite passing through the study area, which can be the reason for the difference of about 2 to 3 degrees Celsius. Because of the heterogeneity of the pixels and the changes of the surfaces in the urban area cause the value

of the pixels to interfere and, consequently, there is a possibility of errors and differences in the estimation of the Land surface temperature. In general, both the meteorological station and the estimated temperature by satellite in the study city show the maximum temperature in 2019 (before Covid-19) and the minimum temperature in 2020 (during Covid-19).

Table 2. Comparison of estimated temperature from satellite and synoptic station

Date	LST Landsat (°C)	CS Temperature (°C)
2018-5-13	39	36
2019-5-15	37	35
2020-5-16	35	33
2021-5-19	36	34

The results (Figure 2) show that the surface temperature in the pre-Covid-19 period (2018 and 2019) has been increasing, while during Covid-19 (2020) the temperature of these areas has decreased significantly. On the other hand, during the normalization of coronavirus conditions (2021), the earth's surface temperature has increased relative to the period during Covid-19.

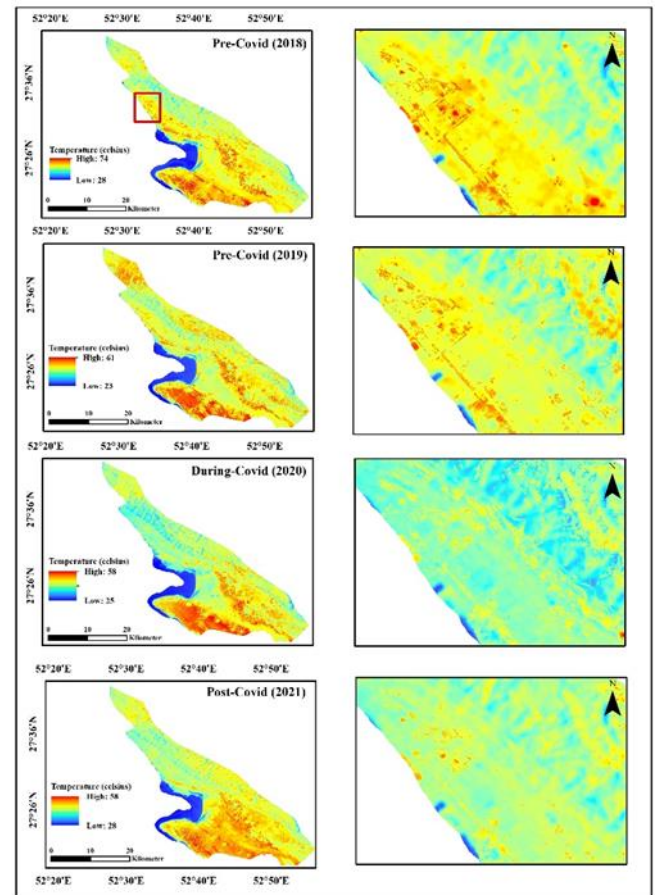


Figure 2. LST map before, during and after Covid-19

4. Conclusion

In this study, it was tried to investigate the changes in land surface temperature before, during and after Covid-19 in Assaluyeh industrial city. In order to conduct this research, Landsat-8 time series images were processed for extract LST in the Google Earth Engine platform (GEE). The results show that in the pre-covid-

19 period, the northern, western and eastern regions of Assaluyeh, where the factories, industries and residential areas of the city are located, respectively, had a temperature of more than 60 to 70 degrees Celsius, while the rate has decreased to about 58 ° C during and after the normalization of Covid-19 conditions in the country. In general, industrial activities, tourism, transportation have a direct impact on surface temperature and indirectly on the environment.

Nowadays, using remote sensing data can make the connection between Covid-19 and the LST easier, but processing this amount of satellite data into one piece of software is not easy, so in the end, researchers recommend using the new Google Earth Engine system. Because time series processing of LST changes on a monthly and annual basis provides easy.

References

- Avdan, U., & Jovanovska, G. (2016). Algorithm for automated mapping of land surface temperature using LANDSAT 8 satellite data. *Journal of sensors*, 2016. <https://doi.org/10.1155/2016/1480307>
- Bendib, A., Dridi, H., Kalla, M. I., (2017). Contribution of Landsat 8 data for the estimation of land surface temperature in Batna city, Eastern Algeria. *Geocarto Int.* 32, 503–513. <https://doi.org/10.1080/10106049.2016.1156167>
- Ghorbannia, V., Mirsanjari, M., Liaghati, H. and Armin, M., (2017). Estimating land surface temperature of land use and land cover in Dena County using single window algorithm and landsat 8 satellite data. *Environmental Sciences*, 15(2), 55-74.
- Guha, S., & Govil, H. (2021). COVID-19 lockdown effect on land surface temperature and normalized difference vegetation index. *Geomatics, Natural Hazards and Risk*, 12(1), 1082-1100.
- Mahmoudzadeh, H., Mahdaviard, M., Azizmoradi, M., & Zanjani Sani, Z. (2021). Modeling physical development by combining the capabilities of Google Earth Engine (GEE) and Artificial Neural Network (MLP) the Case Study: Tabriz. *Geography and Planning*, 24(74), 215-232. <https://doi.org/10.22034/gp.2021.10780>
- Mokhtary Malek Abadi, R., Marsosi, N., Hosaini, A. & Gholami, M., (2016). Assessing social & cultural sustainability in the extractive cities (Case: extractive city Asalooeye). *Spatial Planning*, 5(4), 1-16.
- Phelan, P. E., Kaloush, K., Miner, M., Golden, J., Phelan, B., Silva, H., & Taylor, R. A. (2015). Urban Heat Island: Mechanisms, Implications, and Possible Remedies. *Annu. Rev. Environ. Resour.* 40, 285–307. <https://doi.org/10.1146/annurev-environ-102014-021155>
- Rouse, J. W., Haas, R. H., Schell, J. A., & Deering, D. W. (1974). Monitoring vegetation systems in the Great Plains with ERTS. *NASA special publication*, 351(1974), 309.
- Shelestov, A., Lavreniuk, M., Kussul, N., Novikov, A., & Skakun, S. (2017). Exploring Google earth engine platform for big data processing: Classification of multi-temporal satellite imagery for crop mapping. *Frontiers in Earth Science*, 5, 17. doi.org/10.3389/feart.2017.00017.
- Shi, P., Dong, Y., Yan, H., Zhao, C., Li, X., Liu, W., He, M., Tang, S., & Xi, S. (2020). Impact of temperature on the dynamics of the COVID-19 outbreak in China. *Science of the total environment*, 728, 138890. <https://doi.org/10.1016/j.scitotenv.2020.138890> Get rights and content.
- Stathopoulou, M. & Cartalis, C. (2007). Daytime urban heat islands from Landsat ETM+ and Corine land cover data: An application to major cities in Greece. *Solar Energy*, 81(3), 358-368. <https://doi.org/10.1016/j.solener.2006.06.014>
- World Health Organization, (2020). Considerations for quarantine of individuals in the context of containment for coronavirus disease (COVID-19): interim guidance, 19 March 2020 (No. WHO/2019-nCoV/IHR Quarantine/2020.2). World Health Organization.
- Wuhan Municipal Health Commission: Report on current pneumonia epidemic situation in the city. 2019. <http://wjw.wuhan.gov.cn/front/web/showDetail/2019123108989>
- Xu, H. Q., & Chen, B. Q. (2004). Remote sensing of the urban heat island and its changes in Xiamen City of SE China. *Journal of Environmental Sciences*, 16(2), 276-281. [https://doi.org/10.1016/S1001-0742\(004\)02-0276-06](https://doi.org/10.1016/S1001-0742(004)02-0276-06).

4th Intercontinental Geoinformation Days

igd.mersin.edu.tr



Vis-NIR spectroscopy coupled with machine learning algorithms to predict soil gypsum in calcareous soils, southern Iran

Monire Mina¹ , Mahrooz Rezaei^{*2} , Leila Hossein Abadi³ , Abdolmajid Sameni¹

¹Shiraz University, School of Agriculture, Department of Soil Science, Shiraz, Iran

²Wageningen University, Meteorology and Air Quality Department, Wageningen, the Netherlands

³Shahid Beheshti University, Remote Sensing and GIS Center, Tehran, Iran

Keywords

PLSR model
Savitzky-Golay filter
Spectral reflectance

Abstract

The use of soil spectral reflectance, which has been introduced as a new method in soil science, is widely used in estimating the physicochemical properties of soil. The aim of this study was to estimate the amount of gypsum in surface soils of Fars province. Based on random sampling method, 100 soil samples were collected and measured by standard method. Spectral analysis of soil samples was performed using a spectrophotometer in the range of 2500-400 nm. After this stage, various preprocessing methods were evaluated and finally the percentage of soil gypsum was modeled using two models of partial least squares regression (PLSR) and support vector regression (SVR). The results showed that the best results for estimating the percentage of soil gypsum are related to the SVR model with Preprocessing Savitzky- Golay Filter with the first derivative. Also, according to RPIQ statistics, the estimation of PLSR model for the percentage of soil gypsum in the weak class is 1.02% and for the SVR model in the moderate class is 1.54%.

1. Introduction

The use of visible-near-infrared spectroscopy has been introduced as a fast, inexpensive and non-destructive method that has a good capability in estimating different soil properties (Cambou et al., 2016). One of the most important characteristics of soil is the amount of soil gypsum. Gypsum has more solubility than carbonates and therefore, is under the influence of leaching process, and this resulted in less amount in the soil (Chaternour et al., 2020). The amount of gypsum has significant effect on soil properties such as soil water retention, aggregate stability and soil structure; More than 25% gypsum has a negative effect on plant growth and soil resilience (Smith and Robertson., 1962). Due to the cost, time and difficulty of direct measurement of soil gypsum, the use of indirect methods such as soil spectral behavior and spectroscopy has become common (Khayamim et al., 2015). So far, many studies have been done in this field, most of which have been researched on soil particle size, CaCO₃ (Gomez et al., 2008), the soil organic matter (Ostovari et al., 2018) and soil moisture (Mina et al., 2021). In these studies, methods such as

partial least squares regression, principal component regression, and support vector machine have been used to estimate the correlation between soil properties and spectral data (Farifteh et al., 2007). Also, studies have been reported in estimating the amount of soil gypsum using spectral reflections. Among these studies is a study by Chaternor et. al., 2020, they used PLSR and SVR models to estimate the amount of gypsum using spectral reflections of soil. Their results showed that the SVR model has a higher accuracy than the PLSR model. In another study, some chemical properties of soils in Isfahan province were estimated by spectroscopy. The properties of calcium carbonate, gypsum and organic matter were obtained with optimal accuracy with coefficients of determination of 0.45, 0.8 and 0.61, respectively (Khayamim et al., 2015). Hassani et al. (2014) estimated the properties of gypsum (RPD = 2.65), organic matter (RPD = 1.64) and calcium carbonate (RPD = 2.86) using spectral reflections. Gohari et al. (2017) used visible-near-infrared spectroscopy to estimate the amounts of gypsum, organic matter and carbonates. their research showed better result in the percentage of gypsum and organic matter in the good class, while it

* Corresponding Author

(monireh.mina@gmail.com) ORCID ID xxxx – xxxx – xxxx – xxxx
(mahrooz.rezaei@wur.nl) ORCID ID xxxx – xxxx – xxxx – xxxx
(leilahosseinabadi1993@gmail.com) ORCID ID xxxx – xxxx – xxxx – xxxx
(majid.baba@gmail.com) ORCID ID

Cite this study

Mina, M., Rezaei, M., Abadi, L. H., & Sameni, A. (2022). Vis-NIR spectroscopy coupled with machine learning algorithms to predict soil gypsum in calcareous soils, southern Iran. 4th Intercontinental Geoinformation Days (IGD), 246-249, Tabriz, Iran

showed worse result in the carbonates in the weak class due to the relative deviation of the model prediction.

Due to the importance of gypsum content, this study was conducted to estimate the percentage of soil gypsum with PLSR and SVR models using spectral data by applying Savitzky -Glaze filters with the first derivative.

2. Method

2.1. Study area

The study area was Fars province which is located in the south-central region of Iran with coordinates 27° 2' to 31° 42' latitude and 50° 42' to 55° 36' longitude.

2.2. Soil sampling and soil analysis

Soil sampling was done randomly from a depth of 0 -10 cm. 100 soil samples were collected and then the samples were transferred to the laboratory, air dried and passed through a 2 mm sieve. The gypsum content was determined by acetone method (Nelson,1982).

2.3. Spectral reflectance measurement

Soil spectral data were determined using a spectroscopy device (NIRS-XDS) in the range of visible and near-infrared wavelengths (2500-400 nm). 20 g of each sample of air-dried soil with a size of less than 2 mm was placed in a special container and then 5 scans were performed on them (Figure 1, a). Due to the high noise at the beginning and end of the spectral data, the range of 449-400 and 2500-2451 nm was removed from the modeling process and then the preprocessing of the Savitzky and Glaze filters with the first derivative was applied to the spectral data of soil samples (Figure 1, B).

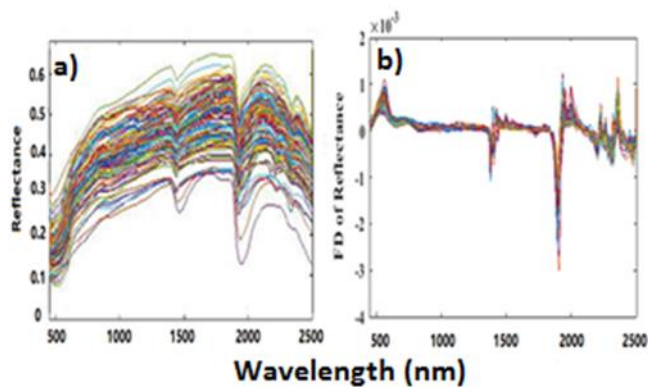


Figure 1. The a) raw and b) preprocessed spectral reflectance data.

2.4. Model evaluation

To predict the percentage of soil gypsum based on soil spectral reflectance, partial least squares regression and support vector regression were used. To evaluate the accuracy of the models, three statistical criteria including coefficient of determination (R^2), root mean square error (RMSE) and ratio of performance to the interquartile range (RPIQ) were used (Mina et al., 2022).

3. Results

For the purpose of modeling, the data were randomly divided into two sets of training (70% of data) and testing (30% of data). Using t-test, no significant difference was observed between the two data sets. Table 1 shows the statistical summary of the measured soil gypsum for both train and test datasets. All soil samples had a low amount of gypsum with a mean of 0.97% and 0.99% for train and test datasets, respectively.

Table 1. Statistical analysis of the soil gypsum, minimum, maximum (Range), mean values, standard deviation (SD) and coefficient of variation (CV).

soil parameter	Gypsum	
	Train	Test
Unit	%	%
Range	0.2-3.98	0-3.90
Mean \pm SD	0.97 ^a \pm 0.64	0.99 ^a \pm 0.68
CV (%)	65.97	68.68

a-significant difference ($p < 0.05$)

The values of R^2 , RMSE and RPIQ from modeling in estimating soil gypsum based on soil spectral reflections are presented in Table 2. The results of Table 2 show that the SVR model can have a higher performance in estimating the amount of soil gypsum than the PLSR model. The SVR model has the highest R^2 (0.85, 0.73%) and RMSE (0.22, 0.39%) in both training and testing stages, respectively. In addition to RMSE, the accuracy of the model predicted by RPIQ was also evaluated. Classification is done by Lacerda et al., 2016 into 6 classes: Very Poor with $RPIQ < 1$, weak with $RPIQ = 1 - 1.4$, Moderate with $RPIQ = 1.4-1.8$, Good with $RPIQ = 1.8-2$, Very Good with $RPIQ = 2-2.5$ and Excellent with $RPIQ > 2.5$. The SVR model has a moderate performance using spectral reflectance with Savitzky- Glaze filter with the first derivative, and the PLSR model has a poor performance in estimating the amount of soil gypsum.

Table 2. Prediction result for gypsum using partial least squares regression (PLSR) and support vector regression (SVR) model.

Method		Train			Test	
Model	R ²	RMSE	RPIQ	R ²	RMSE	RPIQ
PLSR	0.74	0.30	1.97	0.57	0.48	1.02
SVR	0.85	0.22	2.10	0.73	0.39	1.54

R^2 - coefficient of determination, RMSE - root mean square error, and RPIQ - ratio of performance to the interquartile range.

Figure 2 depicts the measured gypsum versus the predicted gypsum using the PLSR and SVR models in both train and test datasets. In both datasets, the points are well-scattered around 1:1 line for SVR compared to PLSR, which shows the better performance of the SVR model.

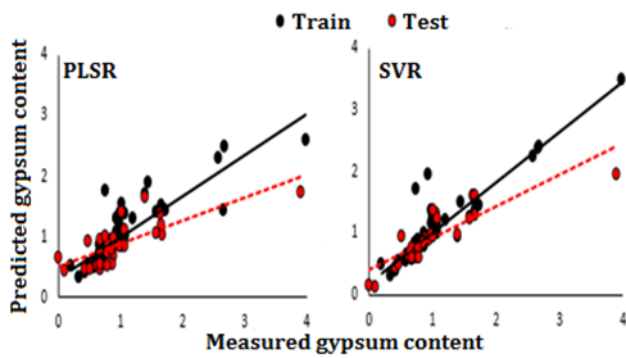


Figure 2. Scatter plots of predicted versus measured gypsum by PLSR and SVR. a) Train set (N=70), b) Test set (N=30). PLSR: Partial least squares regression; SVR: Support vector regression.

4. Discussion

The t-test showed that there was no significant difference between soil gypsum in the train and test datasets. Table 1 shows the statistical description of soil properties in two sets of training and testing. The standard deviation of the amount of gypsum in the training set is 0.64 and, in the test, set is 0.68. This clearly shows that the test dataset is a good representation of the dataset.

It has been used as an input parameter in PLSR and SVR models to estimate soil gypsum using wavelengths of the visible-near-infrared range (400-2500 nm). In predicting the percentage of gypsum by two models PLSR and SVR, the highest value of R^2 and the lowest value of RMSE were obtained in each training and test sets (Table 2). The results of this study are consistent with the study by Chaternor et al., 2020. The results clearly show that the SVR model is better for estimating soil gypsum than the PLSR model. Research has been conducted using PLSR and SVR models in 72 soil spectral samples in Iran. Their results showed that the SVR model has the highest performance in estimating soil CEC.

In another study, Khayamim et al. (2015) obtained an excellent yield ($RPIQ > 2$) for the amount of soil gypsum using the PLSR model.

Also, the SVR model had the shortest distance from the line (1: 1) and the best fit (Figure 2).

In general, according to Table 2 and Figure 2, the results clearly show that the performance of the SVR model is better than the PLSR model in estimating soil gypsum. Therefore, it can be concluded that SVR is a more suitable multivariate method for soil spectral data.

According to Nawar et al. 2016 research, the range of changes in the concentration of soil properties has an important role in the accuracy of the regression model and with an increase in changes and data breadth and also an increase in range, the model's accuracy estimation increases.

Also, according to the Wilding (1985), the extent of the data with the coefficient of variation (CV) in the range of > 35 is considered as a large extent. In the present study, the CV for the training and test data sets is 65.97% and 68.68 % respectively, which indicates the appropriate breadth in the Collected data and has improved the accuracy of gypsum estimation in both models.

5. Conclusion

In this study, we explored the ability of reflectance spectroscopy to estimate gypsum. Generally, the results showed that there is a correlation between the gypsum and soil spectral reflectance. Among the two predictive models, the machine learning algorithm performed better compared to the common PLSR method. Our results proved that spectral reflectance is a promising tool for efficiently assessing large areas.

Therefore, it can be said that soil spectral reflections can be used as a rapid and alternative method in soil.

To get a better view of the performances of machine learning methods in soil science studies, we recommend comparing other data mining approaches such as random forest and artificial neural networks, for the future studies.

References

- Cambou, A., Cardinael, R., Kouakoua, E., Villeneuve, M., Durand, C., & Barthès, B. G. (2016). Prediction of soil organic carbon stock using visible and near infrared reflectance spectroscopy (VNIRS) in the field. *Geoderma*, 261, 151-159.
- Chatrenor, M., Landi, A., Farrokhan Firouzi, A., Noroozi, A., & Bahrami, H. A. (2020). Application of hyperspectral images in Quantification of soil gypsum in center areas of Khuzestan province prone to dust generation. *Applied Soil Research*, 8(3), 1-13.
- Farifteh, J., Van der Meer, F., Atzberger, C., & Carranza, E. J. M. (2007). Quantitative analysis of salt-affected soil reflectance spectra: A comparison of two adaptive methods (PLSR and ANN). *Remote Sensing of Environment*, 110(1), 59-78.
- Hassani, A., Bahrami, H., Noroozi, A., & Oustan, S. (2014). Visible-near infrared reflectance spectroscopy for assessment of soil properties in gypseous and calcareous soils. *Watershed Engineering and Management*, 6(2), 125-138.
- Khayamim, F., Wetterlind, J., Khademi, H., Robertson, A. J., Cano, A. F., & Stenberg, B. (2015). Using visible and near infrared spectroscopy to estimate carbonates and gypsum in soils in arid and subhumid regions of Isfahan, Iran. *Journal of Near Infrared Spectroscopy*, 23(3), 155-165.
- Lacerda, M. P., Demattê, J. A., Sato, M. V., Fongaro, C. T., Gallo, B. C., & Souza, A. B. (2016). Tropical texture determination by proximal sensing using a regional spectral library and its relationship with soil classification. *Remote Sensing*, 8(9), 701.
- Mehrabi Gohari, E., Matinfar, H. R., Jafari, A., Taghizadeh-Mehrjardi, R., & Khayamim, F. (2020). Comparing Different Statistical Models and Pre-processing Techniques for Estimation several chemical properties of the soil Using VNIR/SWIR Spectrum. *Iranian Journal of Remote Sensing & GIS*, 11(4), 47-60.
- Mina, M., Rezaei, M., Sameni, A., Moosavi, A. A., & Fallah Shamsi, R. A. S. H. I. D. (2022). Using Soil Pedotransfer and Spectrotransfer Functions to Estimate Cation Exchange Capacity in Calcareous Soils, Fars Province. *Iranian Journal of Soil and Water Research*, 52(11), 2911-2922.

- Mina, M., Rezaei, M., Sameni, A., Moosavi, A. A., & Ritsema, C. (2021). Vis-NIR spectroscopy predicts threshold velocity of wind erosion in calcareous soils. *Geoderma*, 401, 115163.
- Nawar, S., Buddenbaum, H., Hill, J., Kozak, J., & Mouazen, A. M. (2016). Estimating the soil clay content and organic matter by means of different calibration methods of vis-NIR diffuse reflectance spectroscopy. *Soil and Tillage Research*, 155, 510-522.
- Nelson, R. E. (1982). Carbonate and gypsum. In: Page, A.L. (Ed.), *Methods of Soil Analysis: Part 1 Agronomy Handbook 9. American Society of Agronomy and Soil Science Society of America, Madison (WI)*. 6, 181–197.
- Ostovari, Y., Ghorbani-Dashtaki, S., Bahrami, H. A., Abbasi, M., Dematte, J. A. M., Arthur, E., & Panagos, P. (2018). Towards prediction of soil erodibility, SOM and CaCO₃ using laboratory Vis-NIR spectra: A case study in a semi-arid region of Iran. *Geoderma*, 314, 102-112.
- Smith, P. A., & Robertson, J. E. (1962). Some factors affecting the site of alkylation of oxime salts. *Journal of the American Chemical Society*, 84(7), 1197-1204.
- Wilding, L. P. (1985). Spatial variability: its documentation, accomodation and implication to soil surveys. In *Soil spatial variability, Las Vegas NV, 30 November-1 December 1984* (pp. 166-194).

4th Intercontinental Geoinformation Days

igd.mersin.edu.tr



Heavy vehicle detection using optical remote sensing images and deep learning

Roya Talebi¹, Sadra Karimzadeh¹, Gordana Kaplan²¹University of Tabriz, Department of Remote Sensing and GIS, Tabriz, Iran²Eskisehir Technical University, Institute of Earth and Space Sciences, Eskisehir, Türkiye**Keywords**Remote sensing
Object detection
YOLOv5
CNNs
Heavy vehicle**Abstract**

Recently, object detection has experienced significant progress. However, in the field of remote sensing, it is still under investigation for real-time detection of small objects because of the limited resolution and information. The detection of a predefined object, such as heavy vehicle, is vital in some applications. This study aims to improve the detection accuracy of the heavy vehicle. We train the latest model, YOLOv5 on our dataset in this paper. The results show that YOLOv5 can be well applied in the field of heavy vehicle detection.

1. Introduction

Today, the automobile industry of any country is one of the essential indicators for the development of that country. This industry is considered a key industry in terms of extensive relationship with its upstream and downstream chains. It has an important place in industrial development and production prosperity as it plays an effective role in economic growth and development. Thus, reviewing the activities of these industrial poles with the help of remote sensing data and techniques can significantly reduce the need for human monitoring and save time and money for various organizations. On the other hand, this method can be used to check other collections as well. For example, identifying heavy goods vehicles in rest areas (Kasper-Eulaers et al., 2021).

A large number of remote sensing images have been generated regularly, and due to the rapid development of satellite and imaging technology, the task of object detection has gained significant attention of researchers (Zakria et al., 2022).

In this paper, we used the latest version of the You Only Look Once (YOLO) object detection algorithm (Jocher et al., 2020) to detect vehicles. Our focus was on applying the algorithm, data acquisition, data annotation and Data counting.

YOLOv5 is the fifth generation of YOLO, written in Python programming language (Thuan, 2021). According to various studies YOLOv5 outperforms the rest of the

YOLO model in terms of accuracy and speed (Thuan, 2021); (Cengil & Çınar, 2021).

YOLOv5 proposed by Ultralytics LLC is an improved version based on YOLOv4. It is a one-stage detection network regarding accuracy and detection speed (Wu et al., 2020). After learning from the advantages of the previous version and other networks, YOLOv5 changes the characteristics of the previous YOLO target detection algorithm that the detection speed is faster but the accuracy is not high. YOLOv5 has improved detection accuracy and real-time performance, which meets the needs of real-time image detection and has a smaller structure. Therefore, this article uses YOLOv5 as the detection model. Its network model is divided into 4 parts, namely Input, Backbone, Neck and Prediction, and its network structure is shown in Fig. 1 (Tan et al., 2021). Input includes mosaic data enhancement, adaptive anchor frame calculation, and adaptive image scaling. The input terminal of YOLOv5 adopts the same mosaic data enhancement method as YOLOv4. The random clipping, scaling, and distribution are used to splice the images. The four images are spliced, which enriches the detection data set, improves the robustness of the network, reduces the calculation of GPU, and increases the universal applicability of the network; Adaptive anchor frame calculation sets the initial anchor frame for different data sets, outputs the prediction frame based on the initial anchor frame, and then compares it with the real frame. After calculating the gap, it updates the network parameters reversely and iterates the network

*** Corresponding Author**

*(roya.talebi1399@gmail.com) ORCID ID 0000-0002-1553-1678
(sadra.karimzadeh@gmail.com) ORCID ID 0000-0002-5645-0188
(kaplangorde@gmail.com) ORCID ID 0000-0001-7522-9924

Cite this study

Talebi, R., Karimzadeh, S., & Kaplan, G. (2022). Heavy vehicle detection using optical remote sensing images and deep learning. 4th Intercontinental Geoinformation Days (IGD), 250-253, Tabriz, Iran

parameters continuously. The anchor frame parameters are (Gao et al., 2021). Adaptive image scaling is to scale

the image to a uniform size, which has been implemented in the data preprocessing stage (Luo et al., 2022).

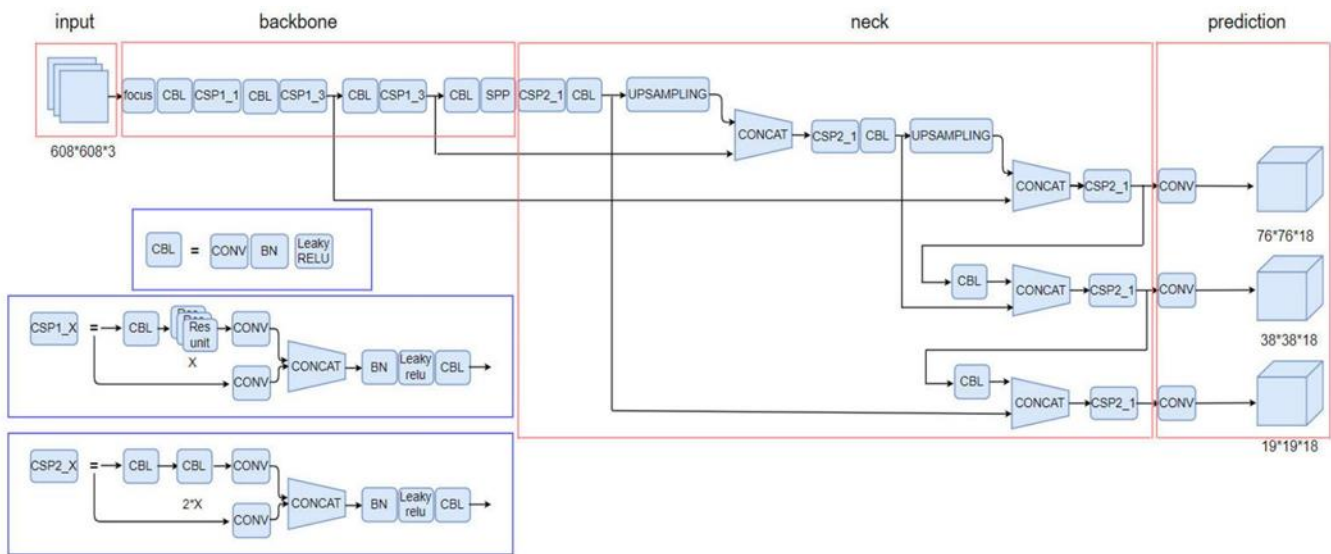


Figure 1. The main modules of YOLOv5 network

2. Materials and Method

2.1. Study area

Tehran is located within latitude of $35^{\circ}40'18''$ and longitude of $51^{\circ}25'27''$ with an altitude of 1,191 m above the mean sea level in a semi-arid region of Iran. Iran Khodro Diesel Company is the study area in this article, which is located in Tehran.



Figure 2. Study Area

2.2. Selection of Algorithm

The decision to use a convolutional neural network (CNN) was made due to their ease of use. There are a number of pre-trained models that can be tuned for a variety of tasks. They are also readily available, computationally inexpensive and show good performance metrics. Object recognition systems from the YOLO family are often used for vehicle recognition tasks, e.g., (Fachrie, 2020); and have been shown to outperform other target recognition algorithms (Benjdira et al., 2019). YOLOv5 has proven to significantly improve the processing time of deeper networks (Jocher et al., 2020).

2.3. Evaluation metric

In order to evaluate performance of the algorithm, results of the model should be compared to the ground truth. In this paper, Precision and recall are used to evaluate the similarity and diversity between detection results and ground truth in test dataset. Also, the overall accuracy and F-Score have been calculated for the accuracy assessment (Kaplan et al., 2021).

$$P = \frac{TP}{TP + FP} \quad (1)$$

$$R = \frac{TP}{TP + FN} \quad (2)$$

$$Accuracy = \frac{TP + TN}{TP + FP + FN + TN} \quad (3)$$

$$F - score = \frac{2 \times Precision \times Recall}{Precision + Recall} \quad (4)$$

Where,

TP = true positive
 FP = false positive
 FN = false negative
 TN = True negative.

3. Experiments

3.1. Experimental process

The experimental process can be divided into four steps:

(i) Dataset construction. The remote sensing images (gain from open-source data source such as GoogleEarth are animated using imgLabel to obtain standard YOLO format dataset. Tzutalin's (Tzutalin, 2018) popular annotation tool Labellmg was used to cautiously label the images in this final phase. First, each image is opened in this tool one at a time. Then, a rectangular shape was manually drawn to the boundary of an object in order to specify its exact location in that image by x_center y_center width height. Finally, each object has been given a label, such as 'heavy vehicle'. In Labellmg, annotated values were saved as txt files in YOLOv5 format. Divide labeled dataset into training, validation, and test sets.

(ii) Model construction. Constructing a CNN structure and setting its hyperparameters.

(iii) Model training. Training with training sets and validation sets.

(iv) Model prediction. Testing with the test set, and the result is used for evaluates model.

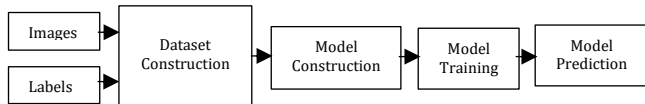


Figure 3. Experimental Process

3.2. Dataset

For this study, 1000 images of the study area were prepared by Google Earth Pro software. Imglabel software is used for manual annotation of heavy vehicles in the images. Fig. 4 shows one demos of image label. 800 images have been used for practice. To test the work, 20% of the images selected for the exercise and another 150 images from the image collection have been selected. Finally, the proposed method is tested with the remaining 50 images.

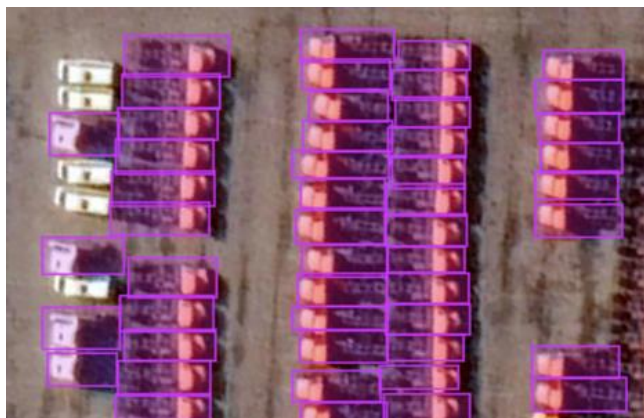


Figure 4. Demo of image label

3.3. Training

The model was trained using Google Colab, which provides free access to powerful GPUs and requires no configuration. We used a notebook developed by Roboflow.ai (Li et al., 2021) which is based on YOLOv5 (Jocher et al., 2020) and uses pre-trained COCO weights. We added the desired area dataset and adjusted the number of epochs to be trained as well as the stack size to train the upper layers of the model to detect our classes. Training a model for 500 epochs takes about 150 min.

3.4. Experimental Analysis

After training our model, we made predictions for our test set's new and unseen pictures. The examples in Fig. 5 show that the algorithm can detect the heavy vehicle to a higher degree of certainty. However, it has difficulty the Data counting, especially when the data is in the corner of the image.

3.5. Results

The YOLOv5 model performs really well with 230 epochs. After that with the increase of epochs all the losses like classification loss, box loss and objectness loss were increased and the model performance was decreased. YOLOv5 was tested on other images to detect heavy vehicles. To train the model, various image resolutions were used.

The mold dataset was designed to train by using Google Colab, which provides free access to powerful GPUs. We used a notebook developed by Roboflow.ai which is based on YOLOv5 (Roboflow, 2016) and uses pre-trained COCO weights. Suitable number of epochs was chosen to train newly developed mold dataset. To train the model 205 epochs was selected which was taken approximately 40 min.



Figure 5. Results of heavy vehicle detection

According to the results shown in Table 1, the proposed method has identified the heavy vehicle in the study area with high accuracy. A total of 45 heavy vehicles were identified in the first image and 64 heavy vehicles in the second image. The number of TP (heavy vehicles is correctly identified) was 43 for the first image and 59 for the second image. In order to evaluate the results, accuracy assessment was performed using Equations 1 and 2. The values of P (Precision) and R (Recall) for the first image were 1.0 and 0.95, respectively, and for the second image were 1.0 and 0.92, which indicates the efficiency of the proposed method in this field.

Table 1. Performance of heavy vehicle detection

Items	TP	TN	FP	FN	P	R	OA	F-s
a	43	0	0	2	1.0	0.95	0.95	0.97
b	59	0	0	5	1.0	0.92	0.92	0.95

Results and performances of heavy vehicle detection are shown in Fig. 5 and Table 1.

4. Discussion

Although tremendous progress has been made in the field of object detection recently, it remains a difficult task to detect and identify objects accurately and quickly. Yan et al. (2021) named the YOLOv5 as the most powerful object detection algorithm in present times.

We see the greatest potential for improving performance in adjusting the physical data collection and in improving the data annotation. For most applications, changes to the physical data collection cannot be influenced.

However, as this is a pilot project running on only one Automotive company, there is the possibility of changing the physical setup for data collection if more Automotive companies are added.

In order to get closer to the goal of identifying all the heavy vehicles in the image, we need to train the sample with more images.

5. Conclusion

In order to achieve the accurate and real-time intelligent detection of heavy vehicles in Google Earth images, a real-time heavy vehicle detection method based on YOLO v5 was proposed in this study. The method of using YOLO v5 algorithm was proposed to identify heavy vehicles in the study area. According to the results shown in Fig. 5, the proposed method is able to detect heavy vehicles with an accuracy of 78%. We are confident that with a bigger training set and the implementation of the changes suggested in Section 4, the algorithm can be improved even further.

References

Benjdira, B., Khursheed, T., Koubaa, A., Ammar, A., & Ouni, K. (2019). Car detection using unmanned aerial vehicles: Comparison between faster r-cnn and yolov3. 2019 1st International Conference on Unmanned Vehicle Systems-Oman (UVS),

Cengil, E., & Çınar, A. (2021). Poisonous mushroom detection using YOLOV5. *Turkish Journal of Science and Technology*, 16(1), 119-127.

Fachrie, M. (2020). A Simple Vehicle Counting System Using Deep Learning with YOLOv3 Model. *Jurnal RESTI (Rekayasa Sistem Dan Teknologi Informasi)*, 4(3), 462-468.

Gao, S.-H., Han, Q., Li, D., Cheng, M.-M., & Peng, P. (2021). Representative batch normalization with feature calibration. *Proceedings of the IEEE/CVF Conference on Computer Vision and Pattern Recognition*,

Jocher, G., Stoken, A., & Borovec, J. (2020). NanoCode012, ChristopherSTAN, L. Changyu, Laughing, tkianai, A. Hogan, lorenzomammanna, yxNONG, AlexWang1900, L. Diaconu, Marc, wanghaoyang0106, ml5ah, Doug, F. Ingham, Frederik, Guilhen, Hatovix, J. Poznanski, J. Fang, L. Yu, changyu98, M. Wang, N. Gupta, O. Akhtar, PetrDvoracek, and P. Rai, "ultralytics/yolov5: v3, 1.

Kaplan, O., & Kaplan, G. (2021). Response Spectra-Based Post-Earthquake Rapid Structural Damage Estimation Approach Aided with Remote Sensing Data: 2020 Samos Earthquake. *Buildings* 2022, 12, 14.

Kasper-Eulaers, M., Hahn, N., Berger, S., Sebulonsen, T., Myrland, Ø., & Kummervold, P. E. (2021). Detecting heavy goods vehicles in rest areas in winter conditions using YOLOv5. *Algorithms*, 14(4).

Li, B., Fu, M., & Li, Q. (2021). Runway Crack Detection Based on YOLOV5. 2021 IEEE 3rd International Conference on Civil Aviation Safety and Information Technology (ICCASIT),

Luo, S., Yu, J., Xi, Y., & Liao, X. (2022). Aircraft Target Detection in Remote Sensing Images Based on Improved YOLOv5. *IEEE Access*.

Roboflow. How to Train YOLOv5 on Custom Objects. 2016. Available online: <https://colab.research.google.com/drive/1gDZ2xcTOgR39tGGs-EZ6i3RTs16wmzZQ> (accessed on 3 February 2021)

Tan, S., Bie, X., Lu, G., & Tan, X. (2021). Real time detection of personnel mask wearing based on yolov5 network model. *Laser magazine*, 42(2), 147-150.

Thuan, D. (2021). Evolution of yolo algorithm and yolov5: the state-of-the-art object detection algorithm.

Tzutalin. 'Labellmg'. 2018. Available at: <https://github.com/tzutalin/labellmg>. (Accessed on November 2020)

Wu, D., Lv, S., Jiang, M., & Song, H. (2020). Using channel pruning-based YOLO v4 deep learning algorithm for the real-time and accurate detection of apple flowers in natural environments. *Computers and Electronics in Agriculture*, 178, 105742.

Yan, B., Fan, P., Lei, X., Liu, Z., & Yang, F. (2021). A real-time apple targets detection method for picking robot based on improved YOLOv5. *Remote Sensing*, 13(9), 1619.

Zakria, Z., Deng, J., Kumar, R., Khokhar, M. S., Cai, J., & Kumar, J. (2022). Multi scale and direction target detecting in remote sensing images via modified YOLO-v4. *IEEE Journal of Selected Topics in Applied Earth Observations and Remote Sensing*.



4th Intercontinental Geoinformation Days

igd.mersin.edu.tr



Remote sensing of nighttime light

Samaneh Bagheri ^{*1}, Hooman Moradpour¹, Khalil Valizadeh Kamran ¹, Sadra Karimzadeh ¹

¹University of Tabriz, Faculty, Department of Remote Sensing and GIS, Tabriz, Iran

Keywords

Remote sensing
Night time
DMSP/OLS
VIIRS

Abstract

Night light observations through remote sensing allow us to make accurate measurements of the location of human activities, so we can in various fields such as urban tracking and economic dynamism, conflict assessment and armed incidents, fisheries study, emission assessment. They used greenhouse gases and energy consumption and analyzed light pollution and health effects. New and improved sensors, algorithms, and products for night lights, in conjunction with other ground observations and ancillary data (e.g., geographic location data), have great potential for in-depth understanding of human activities and their environmental consequences. This paper examines the advancement of night light sensors and products, and examines the contribution of night light remote sensing to the perception of a changing world with an emphasis on DMSP / OLS and VIIRS night light data.

1. Introduction

In general, the rapid growth of the human population has profound implications for land-based processes, both locally and globally, and poses great challenges for scientists and policymakers to understand and address global change and its consequences (Zhao, et al., 2019).

Today, as we grow and innovate in tools and techniques, our understanding of issues such as urbanization, environmental change, and global change will emerge deeper and more comprehensible. Undoubtedly, the most important indicator of the impact on the environment and ecosystem is human activities. Ground-based imaging from space, due to its high potential, provides the possibility of analyzing, evaluating and predicting unprecedented changes that occur on the surface of the earth, and is a great help in tracking human activities and environmental impacts. It has. In this regard, the role of satellite remote sensing in the comprehensive understanding of the changes facing the Earth and humans in the 21st century has been very colorful (Zhao, et al, 2019).

At the beginning of the 21st century, people realized that satellite remote sensing technology would play a key role in Earth observation. One of the most important ways to detect human footprints on the ground, light

measured from the ground is very useful for identifying human habitats and economic dynamics. This will show the potential for continuous monitoring and monitoring of human activities and the identification and understanding of environmental effects of night light data compared to other satellite products used to monitor human activities [He et al., 2017].

Global nighttime running lights are one of the most important and well-known satellite data products that provide an accurate measure of human presence and activity across the globe. In addition, the mapping of light regions and their illumination levels are used by scientists in a variety of fields. [Levin, et al., 2020].

In this paper, we aim to examine the potential and effectiveness of NTL remote sensing in understanding human activities and related environmental changes in a changing world. As such, this paper will provide a comprehensive review of night-time remote sensing (NTL) data from data sets to applications and challenges and perspectives.

2. Method

Examining various studies that have been done using night light images, it is clear that each of these data sets has advantages and disadvantages that in

* Corresponding Author

(samanehbagheri99@gmail.com) ORCID ID 0000-0003-3889-6685
(moradpourhooman@gmail.com) ORCID ID 0000-0003-2466-8489
(valizadeh@tabrizu.ac.ir) ORCID ID 0000-0003-4648-842X
(sadra.karimzadeh@gmail.com) ORCID ID 0000-0002-5645-0188

Cite this study

Bagheri, S., Moradpour, H., Kamran, K. V., & Karimzadeh, S. (2022). Remote sensing of nighttime light. 4th Intercontinental Geoinformation Days (IGD), 254-257, Tabriz, Iran

combination with a series of data and ancillary information provide the desired result. In the following, we will introduce the main data of night light and review the summary of studies performed using these images.

3. An Overview of Major Nighttime Light Datasets

This section provides an overview of the main NTL datasets collected from the various sensors and operating systems and their features. DMSP-OLS and VIIRS sensors are the two main sensors in the field of night light images, which we will introduce in full below.

3.1. DMSP-OLS & NPP-VIIRS

The Defense Meteorological Satellite Program (DMSP) was launched in 1962, and since then its satellites have been using the Ground Surface Scanning System (OLS) as a valuable source of night light data (NTL). Since 1992, DMSP satellites have been broadcasting digital images, which, after being processed by NOAA (now Colorado Mining School), the Earth Observatory (EOG) became the global average of the year, and the NTL map background was removed. With the expansion of annual data from 1992 to 2013, DMSP turns night light into the longest range of remote sensing data available in human activities (Elvidge, et al., 1997). In 2011, the Suomi NPP satellite (SNPP) was launched with a set of Visible Infrared Imaging Radiometers (VIIRS). The VIIRS tool is also able to detect dim light sources at night. VIIRS annual maps of night lights have been published from 2013 to 2022 (Elvidge, et al, 2019). NTL maps made with DMSP (DNL) or VIIRS (VNL) are widely used in human activities, economics and environmental research (Levin, et al., 2020).

The DMSP-OLS nighttime stable light (NSL) data have a spatial resolution of 30 arc-seconds, a coverage spanning 180 to 180 degrees longitude and 65 to 75 degrees latitude. The digital number (DN) value for pixels ranges from 0 to 63. This means that value 0 represents the unlit area and the greater the value, the higher the light level of the region will be. VIIRS, a 22-band visible/infrared sensor, has a same swath width (i.e., 3000 km) as DMSP and a higher spatial resolution (i.e., 375 m and 750 m at nadir). Similar to OLS, VIIRS observes NTLs of the Earth every 24 hours, with the local overpass time after midnight—near 01:30. Among the 22 bands of VIIRS instrument, the Day/Night Band (DNB) with a spectral range of 0.5–0.9 μm shows an unprecedented capability of night observations (Zhao, et. al., 2019).

4. The contributions of night lights to various studies to understand the changing world

Through a range of new applications, NTL remote sensing improves our understanding of the rate of land change. In this section, we briefly review the major contribution of satellite NTLs in previous studies for various purposes.

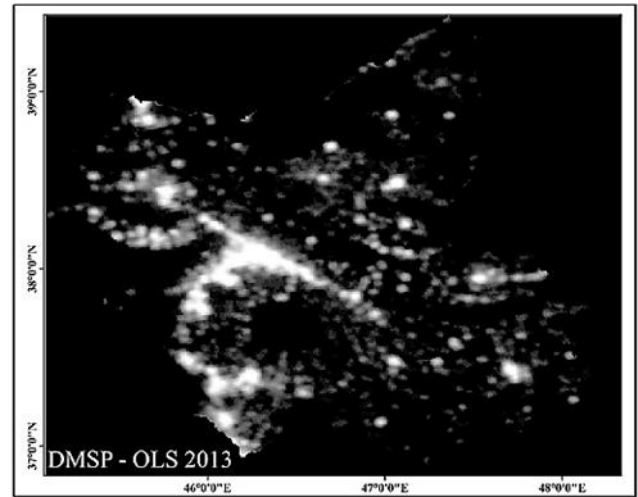


Figure 1. VIIRS Nighttime Light image for East Azerbaijan province

4.1. Urban studies

The use of artificial light data measured from satellites has made it possible to change research methods in geography and urban planning. The DMSP-OLS and VIIRS night optical data sets provide consistent and valuable data sources for the study of urbanization processes. To better understand, we summarize a number of studies conducted in this field.

Luqman et al. 2019 in their study. They introduced a new algorithm called BUNTUS (indoor areas, night light and travel time for urban size) using remote sensing techniques to draw urban boundaries. This method combines land cover data, night light and travel time to extract the boundaries of urban areas. This method is a universal method and uses data sets with sufficient time to create the process. They used Landsat-8 OLI images to confirm their work, and the results showed an overall accuracy of 60 to 95 percent. Therefore, this method is a practical method in collecting information from the urban area and in accordance with its criteria.

In their study, Dou et al 2017. Noted that the timely and accurate extraction of urban land using night light data from Visible Infrared Imaging Radiometers (VIIRS) is important for the national participation of the third polar orbit for urban studies. Extraction of urban land using VIIRS night light data requires consideration of various methods. Therefore, they first reviewed the relevant methods and selected three common methods for extracting urban areas using night light data. These methods included Local Optimal Threshold (LOT), Plant Adjusted Night Light Index (VANUI), Integrated Night Lights, Normalized Plant Index, and Surface Temperature Support Vector Classification (INNLSVM). They evaluated the performance of these methods for extracting urban land area based on VIIRS night light with seven assessment areas with different economic and socio-economic conditions in China. The results showed that among the mentioned methods, INNLSVM method has more potential for effective extraction of urban land from VIIRS data.

He, et al. 2017, colleagues have stated in their study that Quantifying the spatial and temporal changes of urban extent is important for understanding the burgeoning process of urbanization. Among the excellent methods used to map urban areas and detect urban change using night light data, many assume that the urban area is equivalent to areas with a high percentage of impenetrable surfaces or developed terrain. They selected the appropriate boundary criteria and urban indicators based on understanding the current urban situation of the study area and after object-based segmentation and identification of primary urban centers, urban plots were identified and urban centers through grouping algorithm, relative margins of urban area. The results showed that this method is able to identify urban plots with reliable accuracy on a regional scale.

4.2. Modeling GDP

Another application of night light images is to evaluate GDP. Many studies have been done in this regard. Zhao et al. 2019 Noted in their study that night light data from the Defense Meteorological Meteorological Program (DMSP-OLS) line-scan operating system in conjunction with the Visible Infrared Imaging Radiometer (NPP-VIIRS) with the participation of the Third National Polar Orbit Is obtained. It has great potential for measuring large-scale GDP dynamics (GDP). DMSP-OLS data coverage covers the period between 1992 and 2013, while NPP-VIIRS data are available from 2012. The integration of these two datasets has been important for the production of a time series of continuous and continuously monitored data since the 1990s. Understanding the Dynamics of Long-Term Economic Development In addition, since patterns of economic development vary with physical environment and geographic location, the quantitative relationship between night light and GDP should be designed for separate areas. Through a case study in China, this study attempted to integrate the DMSP-OLS and NPP-VIIRS databases, as well as to identify an optimal model for the long-term dynamics of spatio-temporal GDP in different parts of China.

4.3. Light pollution

A comprehensive definition of light pollution is that light pollution is the presence of unwanted, inappropriate, or excessive artificial light. In a descriptive sense, the term "light pollution" refers to the effects of any dim light during the day or night. Light pollution can not only be understood as a phenomenon caused by a particular source or type of pollution, but also can be considered as an effective factor in various studies.

Bagheri et al 2022. In their study. They have studied light pollution and pointed out that due to the increasing expansion of urbanization and the consequences of urbanization and uncontrolled migration of light, this pollution has also increased. Although this contamination is not comparable to the naked eye, it is an unfortunate environmental fact that has devastating

effects on the health of organisms and humans. Using new methods and techniques for measuring distance, these pollutants can be mapped and appropriate measures can be taken to control and reduce them. For example, in an area with high light pollution and its negative effects, extinction of individuals and organisms may be prevented. Or moved them.

5. Result

By examining night light data and various studies performed using these data, it was found that night light data have a very high potential and efficiency in various fields such as urban studies, economics, light pollution, traffic, etc. These data, when combined with other data, give very accurate results that can be used in important planning, especially urban planning.

6. Discussion

Universal night light received by satellites shows us the location and brightness of light in different regions. In low light conditions, only specialized imaging sensors are able to receive source information for night light. To produce a universal product without additional features requires dozens of views per year. From the mid-1970s to 2011, the only instrument that met these criteria was the US Air Force DMSP OLS, which collected a complete set of night-time images of the Earth every 24 hours. NOAA builds a time series of annual global night light products with OLS data from 1992 to 2013. OLS products have been widely used by scientists and economists; however, OLS data has several drawbacks, including dynamic range limited by six-bit quantization, large spatial resolution, and in-flight calibration. In 2011, NASA and NOAA launched the SNPP satellite with VIIRS, which compared low-light imaging data with 14-bit quantization, fewer detection limits, wider dynamic range, and 45x smaller pixel footprint compared to DMSP OLS. Collects with OLS. VIIRS, like OLS, collects a complete set of Earth images every 24 hours. The purpose of this study was to investigate the applications and potentials of night light data in various studies (Elvidge, et al, 2017). In all these studies, the effective role of these data was proven. The point that should be considered and mentioned in almost all studies is the choice of the optimal method in these studies.

7. Conclusion

The results of these studies show that by combining night light data with a set of other information and data, various phenomena such as urban growth trends can be easily calculated. Due to the quality and availability of this data and available methods, this data can be used in many studies.

References

Bagheri, S., Karimzadeh, S., & Feizizadeh, B. Investigation and modeling of physical development of urban areas and its effects on light pollution using night light

- data. *International Journal of Engineering and Geosciences*, 8(1), 98-110.
- Dou, Y., Liu, Z., He, C., & Yue, H. (2017). Urban Land Extraction Using VIIRS Nighttime Light Data: An Evaluation of Three Popular Methods. *Remote Sensing*, 9(2), 175. <https://doi.org/10.3390/rs9020175>
- Elvidge, C. D., Zhizhin, M., Ghosh, T., Hsu, F. C., Taneja, J. (2021). Annual Time Series of Global VIIRS Nighttime Lights Derived from Monthly Averages: 2012 to 2019. *Remote Sens.* 2021, 13, 922.
- Elvidge, C. D., Baugh, K. E, Kihn E A, Kroehl H W & Davis E R (1997). Mapping city lights with nighttime data from the DMSP Operational Linescan System. *Photogramm. Eng. Remote Sens.* 1997, 63, 727–734.
- Elvidge, Ch., Baugh, K., Zhizhin, M., Chi Hsu, F. Ghosh, T. (2017). VIIRS night-time lights, *INTERNATIONAL JOURNAL OF REMOTE SENSING*, 2017, 38(21), 5860–5879
- He, CH., Yue, H., Dou, Y., & Liu, Zh. (2017). Urban Land Extraction Using VIIRS Nighttime Light Data: An Evaluation of Three Popular Methods. *Remote Sensing*, 9, 175. <https://doi.org/10.3390/rs9020175>
- Levin, N., Kyba, C., C Zhang, Q, de Miguel, A. S Román M. O., Li, X., & Elvidge C. D. (2020). Remote sensing of night lights: A review and an outlook for the future. *Remote Sensing of Environment*, 237, 111–443.
- Luqman, M., J. Rayner, P., & R. Gurney K. (2019). Combining Measurements of Built-up Area, Nighttime Light, and Travel Time Distance for Detecting Changes in Urban Boundaries: Introducing the BUNTUS Algorithm. *Remote Sens.* 2019, 11, 2969; <https://doi.org/10.3390/rs11242969>
- Hu, X., Qian, Y., Pickett, S. T., & Zhou, W. (2020). Urban mapping needs up-to-date approaches to provide diverse perspectives of current urbanization: A novel attempt to map urban areas with nighttime light data. *Landscape and Urban Planning*, 195, 103709. <https://doi.org/10.1016/j.landurbplan.2019.103709>
- Yang, H., Ma, M., Ge, W., & Zhu, X. (2017). Modeling the Spatiotemporal Dynamics of Gross Domestic Product in China Using Extended Temporal Coverage Nighttime Light Data. *Remote Sens.* 2017, 9, 626; <https://doi.org/10.3390/rs9060626>
- Yu, B. D., Elvidge, Ch, He Ch, Zhou, Ch., Zhao, M., Cao, W., Cheng, W., Li, X., Li, X., & Zhou, Y. (2019). Applications of Satellite Remote Sensing of Nighttime Light Observations: Advances, Challenges, and Perspectives. *Remote Sens.* 2019, 11, 1971; <https://doi.org/10.3390/rs11171971>
- Zhao, M., Cheng, W., Zhou, C., Li, M., Huang, K., & Wang, N. (2018). Assessing spatiotemporal characteristics of urbanization dynamics in Southeast Asia using time series of DMSP/OLS night-time light data. *Remote Sensing*, 10(1), 47.

4th Intercontinental Geoinformation Days

igd.mersin.edu.tr



Applying object-oriented processing techniques for investigating land use/land cover changes and predicting future changes (Case study: Miandoab, Iran)

Abolfazl Ghanbari ^{*1} , Khalil Valizadeh Kamran ¹ , Arezoo Rahimi ¹

¹University of Tabriz, Department RS & GIS, Tabriz, Iran

Keywords

Land cover
Changes Predict
Object-oriented Processing
Camera calibration
Markov Chain Model
Miandoab

Abstract

Assessing the dynamic changes in land use/land cover in the management and sustainability of natural ecosystems is important. This study aims to investigate the ability of object-oriented processing of satellite images for land cover detection and prediction of future changes using CA Markov model in the township of Miandoab. For this purpose, land cover maps were obtained for the years 1984, 1994, 2004, 2014, and 2018 using the threshold setting method in eCognition 9.1 software and Landsat satellite images of TM, + ETM and OLI. The CA-Markov model was used to predict future changes for 2032. The accuracy of the forecast model was obtained by matching the predicted map of 2018 with its real value. This value represents the validity of modeling results. The results showed that during the period of 34 years (1984-2018), gardens and human-made lands have been improved significantly, so the area of the gardens grew 45 km² between 1984-2018 and human-made lands increased from 6.21 km² in 1984 to 27.55 km² in 2018. In recent years, compared to previous years, the water bodies have diminished, and if the management and resources planning are not altered in the region, this trend of change will have irreparable consequences soon.

1. Introduction

Land use/cover can be considered as a combined concept in terms of physical, social, cultural, economic and information of any country. In fact, land use maps include how to use the land for various human needs (Fezizadeh et al., 2021). Rapid urbanization leads to rapid land use/cover change that can cause a severe deterioration of living environment in urban areas (Sun et al., 2016). One of the effects of urban growth is destroying the environment around the city and changing the agricultural lands to urban usage. Land-use changes are a dynamic and complex process that interconnects natural and human systems (Koomen, et al, 2007). Monitoring land use and land cover changes (LULCC) is an important part of ecological planning in areas with rapid changes. The rapid development of industry, local phenomena such as internal security problems and hard living conditions in rural areas can directly affect LULCC (Satir and Erdogan, 2016). LULCC influences forests by deforesting for agricultural use or other uses are elements that contribute to global environmental change. Therefore, knowing the process

of these changes in the past, present and future are essential for decision-making of sustainable development (Nguye, 2018). Land use refers directly to human activities on the earth, while land cover identifies the natural properties of the earth (Ozdogan, 2016; Singh and Singh, 2011). LULCC is the result of human activities that affect both terrestrial surface and atmospheric region (Pielke et al., 2011). LULCC is a significant factor in global changes and has a notable impact on ecosystem processes, biological cycles, and biodiversity (Basommi et al., 2016; Verburg et al., 2004). In recent years, depending on the type of land use and the growing population of the world and economic growth, identification of effective LULCC has become a global concern (Jia et al., 2015). Factors and influential forces in the formation and expansion and land use change can be considered as a result of natural, social, economic and other conditions and characteristics. (Moazeni, 2015). Human activities are reshaping the terrestrial environment (Seto et al., 2011). With the development of remote sensing technology, abundant spatial data is available now. Satellite data is the fastest and affordable method available for researchers to produce a land-use

* Corresponding Author

^{*}(a_ghanbari@tabrizu.ac.ir) ORCID ID 0000-0001-6225-0433
(valizadeh@tabrizu.ac.ir) ORCID ID 0000-0003-4648-842X
(arezoo.rahimi.9121@gmail.com) ORCID ID 0000-0002-4442-9453

Cite this study

Ghanbari, A., Kamran, K. V., & Rahimi, A. (2022). Applying object-oriented processing techniques for investigating land use/land cover changes and predicting future changes (Case study: Miandoab, Iran). 4th Intercontinental Geoinformation Days (IGD), 258-261, Tabriz, Iran

map (Pal & Mather, 2005). In recent years, satellite image analysis has been proposed as a tool for identifying and extracting LULCC (Szuster et al., 2011). Remote sensing and GIS data are extensively used to identify and analyze the LULCC (Hua, 2017). Remote sensing data can effectively record the location of land cover and it is a marvelous source of data for extracting, analyzing and simulating LULCC (Pradhan et al., 2008; Singh et al., 2018). Different methods have been proposed for extracting land cover information from satellite images. Object-based processing of satellite images (OBIA), has overcome the weakness of the pixel-based approach which refuse to use side information in the process of satellite image classification (Blaschke, 2010). Object-based techniques use more data including geometric information related to the shape of features and their placement, various side information (digital elevation models, various mathematical indicators) for the classification of phenomena and side effects compared to the traditional methods of classification. The satellite image classification using object-based techniques has been widely used so far (Blaschke, 2014): also, many approaches have been used in the framework of OBIA techniques to classify satellite imagery (Benz et al., 2004; Tiede et al., 2010 and Strasser & Lang, 2015). Regarding the LULCC, most of the desirable agricultural lands are located around cities, therefore, uncontrolled urban expansion with low population density destroys agricultural lands. Environmental, economic and social effects caused reduction of agricultural activity. The city of Miandoab, with the population of 134,000 in 2016, has experienced widespread growth over the past few decades. In addition, because the city is located in an alluvial plain and between two permanent rivers, it is surrounded by high-quality agricultural lands and numerous villages; therefore, it is essential to pay attention to the development of the city and its effects on the surrounding areas as the transition areas of the city and the village. Recent advances in tools and remote sensing techniques have enabled researchers to make effective modelling for future land cover changes. In this context, many models have been created to simulate the dynamics of landscape change. One of these models is the combined cellular automata model and Markov chain analysis. Markov chain analysis states that the future status of a system can be modeled solely based on immediate past status. The cellular automata model is used to allocate a spatial dimension to modeling dimension. Therefore, in this research, for modeling the land-use change of the city and its surrounding areas, the CA-Markov model has been used. The simulation method is divided into two sections: prediction of quantitative changes by Markov.

2. Method

In this study, two types of data including satellite imagery and GPS data, which were obtained from field operations, were used. Satellite images used include Landsat satellite imagery between 1984-2018 with a period of 10 years and rows and path of 168-34 for the months of July and August. It should be noted that the images related to TM Landsat 5, ETM Landsat 7 and OLI

Sensors relates to Landsat 8, and due to the presence of information gap in most of the Landsat 7 images, it is tried to use Landsat 5 images as far as possible. According to the purpose of the study, first, the images were pre-processed in the ENVI 5.1 software environment; then, the GIS images and layers included topographic data obtained from the DEM 30, normalized difference vegetation index (NDVI) and other information layers, were entered into the eCognition developer software for database classification and the application of different algorithms. These processes include algorithms (Brightness, NDVI, SI, GLCM ...) to identify existing applications and select the most appropriate indicator for the study area. In the post-processing stage, the land-use change trend has been evaluated and the results have been analyzed. It should be noted that in this study to evaluate the accuracy of classification in different years, in addition to land harvest points, Google Earth images were also used.

3. Results

In the preprocessing stage, all Landsat satellite bands were stacked and cut in ENVI software. After performing various studies and testing the scales, coefficient of shape and compression of scale 10 with 0.2 and 0.5 for Landsat 5 and 7, and the scale 170 with 0.3 and 0.5 for Landsat 8 images were selected as the appropriate scale for extraction of the complications in the image. In this research, various functions and capabilities of OBIA (Object-Based Image Analysis) techniques are used to extract land cover with high accuracy; these functions include texture information (GLCM), average of image bands, normalized difference vegetation index (NDVI), normalized difference water index (NDWI), and brightness index. To implement object-based processing, suitable criteria and algorithms were selected for extraction of each land use/land cover based on ground control points, and then the spatial thresholds, as well as thresholds based on the calculated indexes, were applied to extract the desired applications. This processing method was applied to all images in virtually identical conditions.

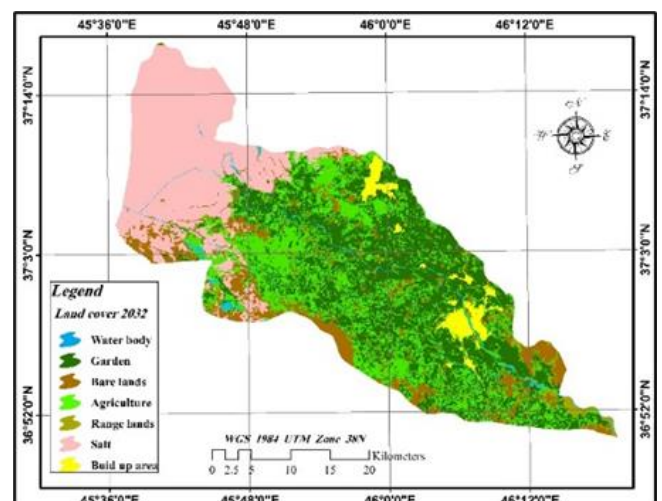


Figure 1. Predicting Future Land Cover Change with CA – Markov Model- 2032

4. Discussion and Conclusion

In this research, the land cover map in was created using object-based processing of satellite images for 34 years (1984-2018) with a general accuracy of 0.89 and Kappa coefficient of 0.8770 in seven classes (water, garden, pasture, agriculture, bare lands, salt, and building area). The analysis of the results showed that at the beginning and in the period of 1994 due to increased rainfall in the study area, farming and water have increased; then, due to the reduced rainfall in the area and the beginning of the drought, the agricultural land area and water have decreased. In the following years, since 2004, with the beginning of irrigation networks, the exploitation of the agricultural land and garden area has increased. Nevertheless, in the same years, due to the reduction of rainfall and mismanagement of water resources, the water bodies of the region have been reduced, and due to the salinity of Urmia Lake, with decreasing the water level and drying of the lake, Salt field of the region is expanding. Following the research process, the map of future changes of 2032 was obtained using the Cellular automate Markov chain model in the Terrset software. To evaluate the accuracy of the prediction model map, first, using the images of 1994 and 2004, the map of change was predicted for 2018, and then the predicted model of land cover changes was compared with real land cover values in 2018. The consistency of the predicted values with the real values of 2018 represents the high accuracy of the prediction model. Accordingly, future changes in land cover are expected in the next 13 years (2032). Evaluation of the prediction model for 2032 indicates significant growth in the constructed areas and salt marshes. Increasing salt marshes can have devastating effects on the environment, agriculture, and gardens. We also see these effects in the study area. As a result, the area of agricultural lands and gardens has decreased in the last period of the total study period. Because of an increase in population, pressure on natural resources and the growth of agricultural and garden lands, man-made lands are also increasing in the study area. On the other hand, agricultural and pasture usage show negative growth. Significant growth of saline lands in the coming years in the region will change the landscape of the land and will bring irreparable damage to the environment. Considering the changes in land use / cover in the eastern part of the study area, it can be said that this part of the study area in the current conditions, due to past degradation and conversions, is disruptive and indicates the development of degradation. Since one of the consequences of the destruction and transformation of land over a period of time is increased desertification and destruction of biodiversity, it can be concluded that due to the drying of Urmia Lake, probably, the destruction of natural vegetation, increased size of barren lands by decreasing vegetation and decreasing preservation capacity, have increased dust and reduced soil fertility in the region. Therefore, modifying management and conservation plans for the ecosystem of the region is essential.

References

- Basommi, L. P., Guan, Q. F., Cheng, D. D., & Singh, S. K. (2016). Dynamics of land use change in a mining area: a case study of Nadowli District, Ghana. *Journal of mountain science*, 13(4), 633-642.
- Benz, U. C., Hofmann, P., Willhauck, G., Lingenfelder, I., & Heynen, M. (2004). Multi-resolution, object- oriented fuzzy analysis of remote sensing data for GIS-ready information. *ISPRS Journal of photogrammetry and remote sensing*, 58(3-4), 239-258.
- Blaschke, T. (2010). Object based image analysis for remote sensing. *ISPRS journal of photogrammetry and remote sensing*, 65(1), 2-16.
- Blaschke, T., Hay, G. J., Kelly, M., Lang, S., Hofmann, P., Addink, E., ... & Tiede, D. (2014). Geographic object-based image analysis-towards a new paradigm. *ISPRS journal of photogrammetry and remote sensing*, 87, 180-191.
- Fezizadeh, B., & Taheri, A. (2021). The Application Of Object-Based Image Analysis Approach For Land Use/Cover Change Modeling Of Urban Growth Within The City Of Maragheh. *Journal environmental based territorial planning (AMAYESH) winter 2021*, Volume 13, Number 51; Page(s) 1 To 22.
- Hua, A. K. (2017). Land use land cover changes in detection of water quality: a study based on remote sensing and multivariate statistics. *Journal of environmental and public health*, 2017.
- Jia, K., Liang, S. L., Liu, J. Y., Li, Q. Z., Wei, X. Q., Yuan, W. P., & Yao, Y. J. (2015). Forest Cover Changes in the Three-North Shelter Forest Region of China during 1990 to 2005. *Journal of Environmental Informatics*, 26(2).
- Koomen, E., & Stillwell, J. (2007). Modelling land-use change. In *Modelling land-use change* (pp. 1-22). Springer, Dordrecht.
- Moazeni, M., Aghayi, V., Badali, A., Pari, H. 2015. Study of land use changes in Parsabad Moghan city using satellite imagery, 1st International Congress of Earth, Clean Space and Energy, Ardebil, University of Mohaghegh Ardabili, https://www.civilica.com/Paper-ATTITTDE01-ATTITTDE01_379.html.
- Nguyen, T. T. H., & Ngo, T. T. P. (2018). Land use/land cover change prediction in Dak Nong Province based on remote sensing and Markov Chain Model and Cellular Automata. *Journal of Vietnamese Environment*, 9(3), 132-140.
- Özdoğan, M. (2016). Image classification methods in land cover and land use. In *Remote Sensing Handbook-Three Volume Set* (pp. 265-280). CRC Press.
- Pal, M., & Mather, P. M. (2005). Support vector machines for classification in remote sensing. *International Journal of Remote Sensing*, 26(5), 1007-1011.
- Pielke Sr, R. A., Pitman, A., Niyogi, D., Mahmood, R., McAlpine, C., Hossain, F., ... & Reichstein, M. (2011). Land use/land cover changes and climate: modeling analysis and observational evidence. *Wiley Interdisciplinary Reviews: Climate Change*, 2(6), 828-850.
- Pradhan, B., Lee, S., Mansor, S., Buchroithner, M., Jamaluddin, N., & Khujaimah, Z. (2008). Utilization of optical remote sensing data and geographic

- information system tools for regional landslide hazard analysis by using binomial logistic regression model. *Journal of Applied Remote Sensing*, 2(1), 023542.
- Satir, O., & Erdogan, M. A. (2016). Monitoring the land use/cover changes and habitat quality using Landsat dataset and landscape metrics under the immigration effect in subalpine eastern Turkey. *Environmental Earth Sciences*, 75(15), 1118.
- Seto, K. C., Fragkias, M., Güneralp, B., & Reilly, M. K. (2011). A meta-analysis of global urban land expansion. *PloS one*, 6(8), e23777.
- Singh, P., & Singh, S. (2011). Landuse Pattern Analysis Using Remote Sensing: A Case Study of Mau District, India". *Archives of Applied Science Research*, 3(5), 10-16.
- Strasser, T., & Lang, S. (2015). Object-based class modelling for multi-scale riparian forest habitat mapping. *International Journal of Applied Earth Observation and Geoinformation*, 37, 29-37.
- Sun, A., Chen, T., Niu, R. Q., & Trinder, J. C. (2016). Land use/cover change and the urbanization process in the Wuhan area from 1991 to 2013 based on MESMA. *Environmental Earth Sciences*, 75(17), 1214.
- Szuster, B. W., Chen, Q., & Borger, M. (2011). A comparison of classification techniques to support land cover and land use analysis in tropical coastal zones. *Applied Geography*, 31(2), 525-532.
- Tiede, D., Lang, S., Albrecht, F., & Höbling, D. (2010). Object-based class modeling for cadastre-constrained delineation of geo-objects. *Photogrammetric Engineering & Remote Sensing*, 76(2), 193-202.



4th Intercontinental Geoinformation Days

igd.mersin.edu.tr



GNSS-R of soil moisture content in Khuzestan for optimal crop distribution

Andres Calabia¹, Iñigo Molina^{*2}, Catherine Jones³

¹ Nanjing University of Information Science and Technology, School of Remote Sensing and Geomatics Engineering, Nanjing, China

² School of Land Surveying, Geodesy and Mapping Engineering, Universidad Politécnica de Madrid, Madrid, Spain

³ Sunnyside Rural Trust, Northchurch, United Kingdom

Keywords

GNSS-R
Soil Moisture
Agriculture
Remote Sensing

Abstract

A new technology based on the reflection of Global Navigation Satellite Systems (GNSS) signals, namely GNSS-Reflectometry (GNSS-R), can monitor soil moisture content (SMC) and provide very valuable data for agriculture and hydrology at a regional and larger scales. In this paper, GNSS-R SMC estimates in the Khuzestan Province of Iran are estimated from the NASA's Cyclone GNSS (CYGNSS) data through the bistatic radar equation and the Fresnel coefficients. We identify a set of optimal areas for agriculture with CYGNSS SMC estimates ($SMC > 0.1$) during the dry season of 2021. We compare the results with the actual distribution of wheat, and provide some suggestions and recommendations for future works on using GNSS-R SMC in agriculture. We provide the first insights of the possible benefits that GNSS-R SMC can deliver to farmers and national government.

1. Introduction

Monitoring and predicting soil moisture content (SMC) is very important for social economy and human activity, while it plays a crucial role in the characterization of the Earth's climate and its hydrological cycle. SMC is a key parameter for planning irrigation strategies, while it simultaneously regulates energy and water exchange between the land and the atmosphere, and other hydrological and climate processes.

Disasters on agriculture and food security need to be mitigated using models that can predict the state of the land held; different crops require different conditions for growing optimally. Some crops need dry climates to mature for harvest. These mainly include crops from the grass family, which are staple food source. For example, the agriculture in Iran uses the climate as an advantage, to grow and harvest crops depending on available soil moisture along the seasons. That being said, all crops require water at the sowing or planting, and become well established. In addition, Iran also may grow crops that require more moisture that that is available for the characteristics of the area, such as rice or sunflowerseed

crops, but it is difficult to identify the optimal locations for crops that require more water.

At a local scale, farmers have a large wealth of knowledge of growing crops in their own country. However, at a regional and larger scales, it is difficult to characterize the land held in terms of SMC. Fortunately, with the recent satellite technology developments with Earth's observation through remote sensing from space, more insights on soil and climate conditions at regional and larger scales allow farmers and national governments to further benefit from agricultural strategies.

In this paper, we estimate SMC using a new technology based on the reflection of Global Navigation Satellite Systems (GNSS) Reflectometry, namely GNSS-R [Carreño-Luengo et al. 2018; Privette et al. 2011, Clarizia et al. 2019; Calabia et al. 2020]. This is a new remote sensing method that is accurate and much cheaper than traditional satellite microwave instruments, such as NASA's SMAP (Soil Moisture Active Passive), or other terrestrial data collection methods marketed to farmers. This technology uses an L frequency band that is suitable for assessing the SMC in the first 10 cm of the soil surface. In this work, we study the region of Khuzestan in Iran during the driest period of 2021, so that it is possible to

* Corresponding Author

(andres@calabia.com) ORCID ID 0000-0001-6779-4341
(inigo.molina@upm.es) ORCID ID 0000-0002-6223-6874
(catherine.cmjones@gmail.com) ORCID ID xxxx-xxxx-xxxx-xxxx

Cite this study

Calabia, A., Molina, I., & Jones, C. (2022). GNSS-R of soil moisture content in Khuzestan for optimal crop distribution. 4th Intercontinental Geoinformation Days (IGD), 262-265, Tabriz, Iran

characterize the optimal location of crops depending on their SMC requirements. In the next section, we introduce the study area with its details on climate and crop calendar. Then in section 3, we describe the methods and data used to obtain the results, which are presented in section 4. Final discussion and conclusions are given in the last sections.

2. Study Area

The Khuzestan Province is located in the southwest of Iran, bordering Iraq and the Persian Gulf. Figure 1 shows the climograph of Khuzestan, where the mean temperature in summer routinely approaches 38°C, and in the winter drops down to 12°C. In general, the climate of Khuzestan in Summer is hot and dry, with almost no precipitation from June to September.

In Iran, wheat, rice, and barley are the country's major crops. Figure 2 shows the crop calendar of Iran, where rice and Sunflowerseed are planted up to June, Sorghum, soybean, corn, and cotton are mid-season growing crops, and wheat, rapeseed, and barley are harvested in August.

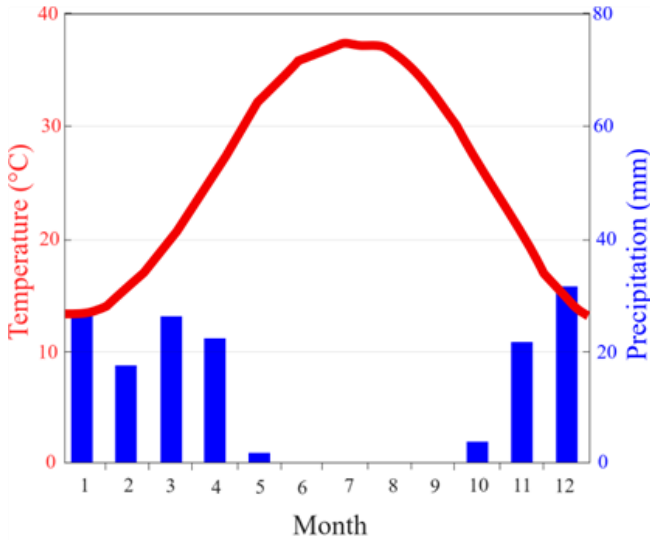


Figure 1. Climograph of Khuzestan (Iran). Data from climatecharts.net

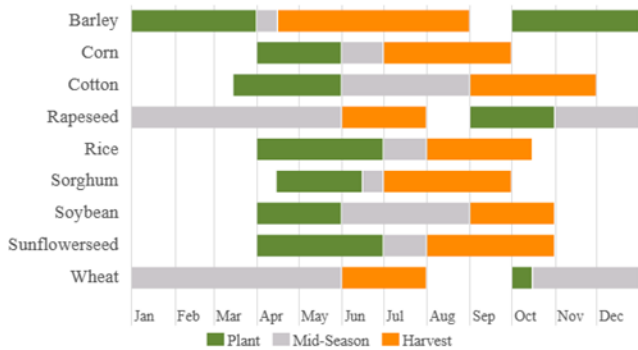


Figure 2. The crop calendar of Iran. From: ipad.fas.usda.gov.

3. Data and Methods

In this study, we employ the NASA's Cyclone GNSS (GYGNSS) data during the month of August 2021. The

GNSS-R SMC retrieval approach of Calabria et al. [2020] employs a modification of the bistatic radar model [Masters et al., 2004] for the coherent component of smooth surfaces [Clarizzia et al., 2019]:

$$\Gamma_{lr}(\theta) = \frac{(4\pi)^2 (P_{DDM} - N)(R_t + R_r)^2}{\lambda^2 G_t G_r P_t} \quad (1)$$

where P_{DDM} is the peak value from the analog scattered power. The subscript rl stands for a scattering mechanism when the incident right hand circularly polarized (RHCP) signal is scattered by the surface and inverts the polarization to left hand circularly polarized (LHCP) at the receiver position. Γ_{lr} is the surface reflectivity for the received lr polarization from which the SMC can be estimated.

Land surfaces' reflectivity is affected by its corresponding bare soil roughness (BSR) and vegetation optical depth (VOD) parameters, and their implementation in Equation 1 is as follows:

$$\Gamma_{lr} = |R_{lr}(\theta_i)|^2 e^{(-2k\sigma \cos \theta_i)^2} e^{-2\tau/(\cos \theta_i)^2} \quad (2)$$

where $R_{lr}(\theta)$ is the Fresnel reflection coefficient for the given polarization, τ stands for the VOD and $h=4k^2\sigma^2$, with $k=2\pi/\lambda$, where λ is the wavelength of the system, and σ is the standard deviation of the surface roughness. Here, NASA's SMAP VOD and BSR ancillary data are used to correct for their corresponding attenuation effects. The soil permittivity (ϵ_r) is estimated by means of the Fresnel reflection coefficients, that are related to the reflectivity linear polarization modes [Jia and Pei, 2018]:

$$R_{lr} = R_{rl} = \frac{1}{2}(R_{vv} - R_{hh}) \quad (3a)$$

$$R_{rr} = R_{ll} = \frac{1}{2}(R_{vv} + R_{hh}) \quad (3b)$$

where R_{vv} , and R_{hh} are the Fresnel coefficients for vertical and horizontal co-polarization, respectively. The subscripts, lr and rl hold for circular cross-polarized reflections, while rr and ll for co-polarized reflections. For soil surfaces, the Fresnel reflectivity (R_{vv} and R_{hh}) is function of soil permittivity or dielectric constant ϵ_r and the incidence angle (θ), from which SMC is retrieved. The conversion from the Fresnel reflectivities to the real part of permittivity (ϵ_r) is based on the model of Jackson et al. [2004]. Once the dielectric constant is retrieved, the volumetric SMC can be derived from the Topp model [Topp et al., 1980]. These models are suitable for low incidence or high elevation angles, which is the case of satellite viewing properties and, particularly, for observations of GYGNSS.

4. Results

The SMC estimates at the specular points of the CYGNSS data for the period of August 2021 are shown in

Figure 3. In this figure, the false color image of land surface heights is shown in the background. Note that data points with heights above 700 m are not suitable for GNSS-R SMC retrieval. Note the geometric distribution of the observed points follows a quasi-random spatiotemporal distribution, due to the changing geometry of GNSS and CYGNSS satellites. Each point in this figure shows the corresponding SMC estimated at each location. We can observe a large number of values below 0.2, while values above 0.2 are more infrequent, forming clear areas of agricultural interest. In Figure 4,

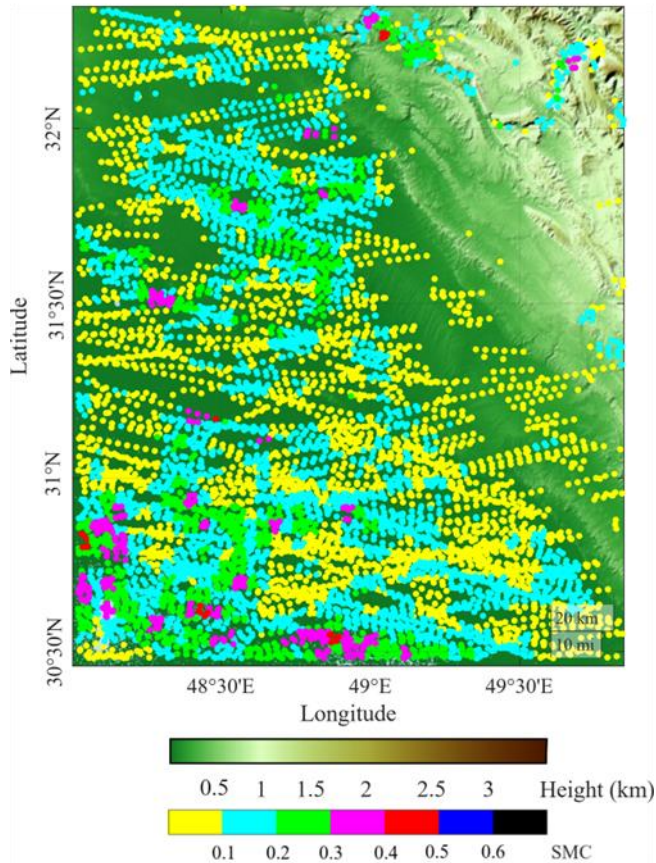


Figure 3. The GYGNSS SMC data during August 2021. The false color image of land surface heights is shown in the background. Note: height data from Beauducel [2022].

Table 1. Usual crops seen in Khuzestan categorized depending on SMC requirements.

Range	Crop Types	Comments
0.4 - 0.5	Rice, Sunflowerseed	Planted up to June
0.3 - 0.4	Sorghum, soybean	Mid-season growing
0.2 - 0.3	Corn, cotton	Mid-season growing
0.1 - 0.2	Wheat, rapeseed, barley	Harvest in August

Table 1 shows the main crops in Iran classified in terms of the available SMC during August. This classification is based on the crop calendar in Figure 2. According to this table, wheat, rapeseed and barley requires lower amount of SMC than the other crops. In this table, the comments show the stage of growth during

these areas have been grouped and segmented for a better identification of the optimal locations with elevated SMC. In this figure, we also include the areas of most frequent crop used in this area, i.e. the wheat pattern shows the areas with the actual production of wheat. We can clearly observe some similarities between the wheat production and the areas with $SMC > 0.1$. However, in several locations, we can observe for a possible optimization by relocating the crops into areas with higher SMC.

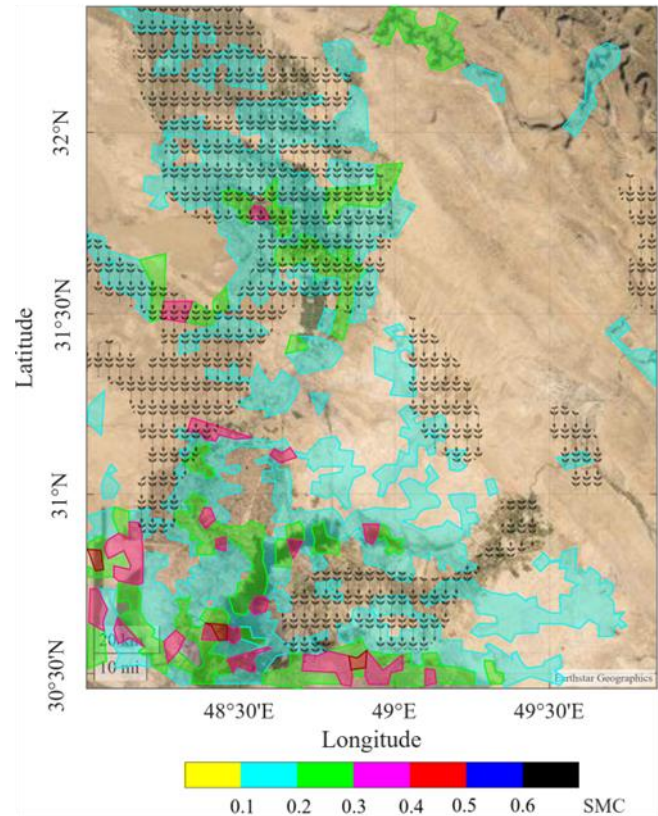


Figure 4. Optimal areas ($SMC > 0.1$) for agriculture classified in terms of SMC levels during August 2021. The true color image is in the background, and the wheat pattern shows the areas with the actual production of wheat. Table 1 shows the optimal crops for each range. Note: wheat data from ipad.fas.usda.gov.

the period investigated in this study. This table along with the map in Figure 4 is an example of crop optimization which could be applied in future strategies.

5. Discussion

Ground sensors only provide discrete SMC measurements for one point, and the real irrigation needs of other areas are unknown. Compared with the traditional monostatic remote sensing, a GNSS-R platform just need to carry a delay/Doppler receiver (low cost, low mass, and low power consumption). The installation of a GNSS-R receiver can be done in any kind of platform (drones, airplanes, satellites, etc.). In this

way, GNSS-R has a wider and flexible coverage, ranging from middle scales to larger scales.

However, in order to provide a suitable SMC product that is beneficial and useful for society, several factors need to be addressed. For example, an interesting issue is how farmers can access to the data, and which scale is the most appropriate for the final products. We want assist both local farmers and national governments with this new data, but also it should be suitable for researchers and climate change decision makers. Note also the governmental issues with existing economic support and regulations to farmers. There may be no grants or support to adopt the crop to new strategies. Another factor for agriculture and food supply is that additional ancillary data such as topography, soil chemistry and composition, are required for accurate studies. Finally, long-term temporal series of GNSS-R data from space can help to climate-change and hydrological-cycle studies at a regional and global scales.

6. Conclusion

In this paper, we have estimated GYGNSS SMC in the region of Khuzestan (Iran) during the dry season of 2021. We have identified a set of optimal areas for different crops and compared the results with the actual distribution of wheat. These results prove that SMC from GNSS-R can be used to help farmers and national governments to take decisions at a regional and larger scales. This promising technique is also very useful for hydrological-cycle and climate-change studies, in which desertification trends and fertilization strategies must be taken into account.

Acknowledgement

Great appreciation is extended to NASA for providing the CYGNSS data access. Special thanks are given to IGD for making possible this intercontinental meeting.

References

- Beauducel, F. (2022), READHGT: Import/download NASA SRTM data files, MATLAB Central File Exchange. Retrieved: 1 March 2022.
- Calabia, A, I Molina, & SG Jin (2020), Soil Moisture Content from GNSS Reflectometry using Dielectric Permittivity from Fresnel Reflection Coefficients, *Remote Sens.*, 12(1), 122, doi: 10.3390/rs12010122.
- Carreño-luengo, H, G Luzi, & M Crosetto (2018), Sensitivity of CyGNSS Bistatic Reflectivity and SMAP Microwave Radiometry Brightness Temperature to Geophysical Parameters Over Land Surfaces. *IEEE J. Sel. Top. Appl. Earth Obs. Remote Sens.* 12(1), 1-16.
- Clarizia, M. P, N Pierdicca, F Costantini, & N Floury (2019), Analysis of CyGNSS Data for Soil Moisture Retrieval. *IEEE J. Sel. Top. Appl. Earth Obs. Remote Sens.*, 12(7), 2227-2235.
- Jackson, T. J., R Hurkmans, A Hsu, M. H. Cosh (2004), Soil moisture algorithm validation using data from the Advanced Microwave Scanning Radiometer (AMSR-E) in Mongolia. *Ital. J. Remote Sens.*, 30, 23–32.
- Jia, Y, Y Pei (2018), Remote Sensing in Land Applications by Using GNSS-Reflectometry. In *Recent Advances and Applications in Remote Sensing*; Ming-Chih Hung and Yi-Hwa Wu Eds.; IntechOpen, London. UK.
- Masters, D, P Axelrad, S Katzberg (2004), Initial results of land-reflected GPS bistatic radar measurements in SMEX02. *Remote Sens. Environ.*, 92, 507–520.
- Privette, C. V, A Khalilian, O Torres, S Katzberg (2011), Utilizing space-based GPS technology to determine hydrological properties of soils. *Remote Sens Environ.*, 115, 3582–3586.
- Topp, G. C, J. L. Davis, AP Annan, (1980). Electromagnetic determination of soil water content: Measurements in coaxial transmission lines. *Water Resour. Res.*, 16, 574–582



4th Intercontinental Geoinformation Days

igd.mersin.edu.tr



Due to the drop in the level of the Caspian Sea evaluation of the geomorphologic properties of the coastal region based on the processing of satellite images

Turkan Mamishova*¹

¹National Aerospace Agency (NASA), Baku, Azerbaijan

Keywords

Remote sensing
DSAS
Shoreline
Morphology
Satellite images

Abstract

The fall in the level of the Caspian Sea in recent years has a serious impact on the infrastructure of the coastal zone. In this work, based on the processing of images taken from the Sentinel 2 satellite, the influence of the level drop on the morphometric characteristics of the coastal zone from the cape Bandovan to Astarachay river of the Azerbaijan water area of the Caspian Sea is estimated. The images were processed using the Tasseled Cap and DSAS-Digital Shoreline Analysis System software. The results are presented in the form of maps and tables, graphically showing the changes occurring in the coastal zone as a result of falling sea level.

1. Introduction

The coastal zones are environmentally and economically important regions. Monitoring of the coastal zone and, in particular, the precise demarcation of the coastline is important as a fundamental research object in solving problems such as environmental protection in the context of *global* climate change. Shorelines are important particular qualities for land/water resources management, geographical mapping, safe navigation and coastal monitoring.

The coastal zone is located in the zone of contact of the atmospheric system, hydrosphere, lithosphere and biosphere. Coastal zones formed as a result of geomorphological processes, such as abrasion and accumulation, have different characteristics from the points of view of the landscape structure, geomorphological process, relief and its constituents (Yamamoto and Finn 2012).

2. Method

The most common methods for shoreline extraction involve visual interpretation from conventional ground surveys or aerial photographs (Boak and Turner 2005, GENS 2010). These methods are, by definition, subjective and depend on the interpreter's individual abilities, often requiring the operator to be familiar with the locale (Boak and Turner

2005). Using tidal datum indicators is a better method to identify the shoreline, but it's limited when determining the historical shoreline (GENS 2010). In recent years, there has been an increase in the use of remote sensing data using

Accuracy plays a crucial role in determining the shoreline using satellite imagery, and several factors make it difficult: sea level changes, coastline movement due to swells and surges, the presence of waves, the presence of watters and swamps along the coast (is incorrectly classified as a part of water).

In this research work, the pre-processing steps are applied for the automatic extraction of coastline by using the ArcGis 10.5 software. The shoreline change analysis was performed using ArcGIS 10.5 and DSAS 5.0. Furthermore, the erase tool of ArcGIS practiced for the calculation of erosion-accretion of the study area. The database used in this study to determine the coastline is the 2016-2021 Sentinel 2A satellite imagery.

Sentinel-2A MS image, covering an area of 100 km x 100 km, were used for a shoreline extraction. The high-resolution MSI data include 13 spectral bands from Visible and Near-Infrared (VNIR) to Short-wave infrared (SWIR) region, fine spatial resolution (10, 20 and 60 m), and 12 bit (Drusch, Del, Carlier, Colin, Fernandez, Gascon, Hoersch, Isola, Laberinti and Martimort 2012). For extract of the shoreline, we used the Tasseled cap transformation method and NDVI (Normalized

*Corresponding Author

*Turkan.memishova@gmail.com) ORCID ID 0000-0003-2729-5067

Cite this study

Mamishova, T. (2022). Due to the drop in the level of the Caspian Sea evaluation of the geomorphologic properties of the coastal region based on the processing of satellite images. 4th Intercontinental Geoinformation Days (IGD), 266-269, Tabriz, Iran

Difference Vegetation Index). Determining the Normalized Difference Vegetation Index (NDVI) in this technique uses a composite Red band and Near Infrared (NIR) to determine the level of greenness and classification of vegetation areas. The next step uses Tasseled Cap to convert band channel into a new band set with clear interpretation for vegetation mapping, this transformation already proven fit for shoreline extraction (Safyanov 1996). Tasseled cap transformation (TCT) is a usually used remote-sensing technique and has been successfully used in various remote sensing-related applications. However, the TCT coefficient set is sensor-specific, and therefore, in this article, we developed the TCT coefficients specifically for Sentinel-2 multispectral instrument at-sensor reflectance data (Thieler, Himmelstoss, Zichichi and Ergul 2009). Tasseled Cap process are using composite bands of red, green, blue, NIR, short wave infrared-1 (SWIR-1) and short wave infrared-2 (SWIR-2) to find out the level of brightness, greenness and wetness of an object. Brightness, a measurement value for the ground; greenness, a measured value for the vegetation; wetness, a measured value for interactions of soil and canopy moisture (Wang 2018). After this analysis shoreline was extracted (Figure 1).



Figure 1. Shoreline extraction results for 2016 to 2021

2.1. Study area

The study area is located coastal zone from the Cape Bandovan to Astarachay river of the Azerbaijan water area of the Caspian Sea. The coastline is approximately 300 km.

2.2. Data

The Sentinel-2A product has radiometric and geometric corrections. An atmospheric correction operation was performed by applying a Sen2Cor

processor to the satellite image in the SNAP software package provided by ESA (European Space Agency). Satellite imagery was analyzed on two different dates (19/08/2016 and 20/05/2021).

Optical and synthetic aperture radar (SAR) satellites to extract and mapping the shoreline automatically or semi-automatically (DI 2003). Several methods have been proposed to accurately locate the position of the shoreline and are based on the use of supervised and unsupervised classification or thresholding techniques (Garcia-Rubio, Huntley and Russell 2015, GENS 2010, Tingting and Hanqiu 2019). Regardless of the method the classification of the pixels in water or land will depend, among other factors, on the resolution of the input data used.

In the study, various semi-automated methods such as Tasseled Cap (Brightness, Greenness, Wetness) and DSAS (Digital Shoreline Analysis System) were used to identify and dynamic the coastal zone and coastline, the areas of impact and quantitative indicators of geomorphological processes were determined. For this study, used high-resolution Sentinel 2 satellite images for 2016–2021.

3. Results

The shoreline is constantly influenced by sea level variations, climate and ecosystems that occur over a wide range of time-scales. The combination of natural and manmade activities often exacerbates the shoreline change and increases the risk factors to coastal community. According to the results, in period form, 2016 to 2021 the rates of shoreline position changes indicate that all transects are accretional and less erosion was observed.

Study area shoreline is changing over time because of accretion and erosion process. However, the whole area of the coastline is almost gone through the accretion process whereas the erosion also occurred but not like the accretion through the entire period. From 2016-2021 most of the accretion took place having 8052 ha of the net gain of the area although in this period coastline has lost about 71.47 ha of the land. Kura island gain of the area 623.66 ha lost of 220 ha.

The assessment of the coastline variation was accomplished in present research work for the from the Bandovan to river of Astarachay coastline integrating GIS. Total 2 years (2016 to 2021) data was evaluated coastline, using the DSAS application and satellite data. For the automatic extraction of the study area, TCT and NDVI is proposed in this research work. This method outperforms by providing accurate and finer edges of the coastline. The coastline change rates were measured based on EPR and NSM statistical techniques to evaluate the short term trends. The results obtained indicate that there is a change in shoreline from 2016-2021 it shows an mean accretion of 230 m. mean of erosion 23,14 m.

4. Discussion

In Caspian Sea, the minimum sea level for the past years was registered in 1977 by a ground station at -29 m. Since 1978, the sea level has risen, and in 1995 it was

registered at -26.66 m and whereupon the sea level was almost stable with slight decrease. In 2016-2020, a 0.2-meter descent was observed in the Caspian Sea (Figure 2).



Figure 2. Sea level changes in the Caspian Sea (1837-2019)

The Digital Shoreline Analysis System (DSAS) is a GIS-based system established by the USGS. DSAS5.0 has six statistical methods to measure variations. In this study, Net Shore Movement (NSM), End Point Rate (EPR) approaches were used. NSM measuring net shoreline change according to distance rather than mean value. NSM relates to date and only two shorelines requires, i.e. total distance among the earliest and the latest of coastline in each transect. The End Point Rate (EPR) was selected as the statistical parameter describing the spatial patterns of shoreline change (Scott, Moore, Harris and Reed 2003). EPR measures shoreline change by dividing the distance of the coastline among its initial and the most current position of coastline. Where, the EPR and NSM positive and negative value shows seaward and landward movement of the coastline respectively (Figure 3; 4). Baseline, historical seashores and coastlines uncertainty are input data delivered in the model for during simulation phase. The spaces among transects alongside the baseline and transects length were demarcated based on the coastline pattern. DSAS creates transects that are cast perpendicular to the baseline at a user definite spacing along the coast. The transect coastline intersections along this baseline are then used to compute the rate of change statistics. Based on the logical conditions in DSAS, 2446 transects has been created that are oriented perpendicular to the baseline at each 500 m spacing along from Cape Bandoan to Astarachay river.

Four scenes of Sentinel 2 sensors, covering the period between 2016 and 2021, were used to demarcate shoreline positions and estimate shoreline change rates from the Bandoan to Astarachay river of Azerbaijan. The method relies on image processing techniques using the IDRISI software, and the Digital Shoreline Analysis System for ArcGIS software, which provides a set of tools permitting transects-based calculation of shoreline displacement. First, the Sentinel images were radiometrically and geometrically corrected. Second, band ratioing, reclassification, raster to vector conversion, and smoothing techniques are applied successively to detect and extract the multi-temporal shoreline data. Third, these data are overlaid and the changes are calculated using the end points and net shoreline movement and end point rate methods. The results indicate significant shoreline changes

ranging from 1559.6 to -41.7 m/year, while some parts remained unchanged.

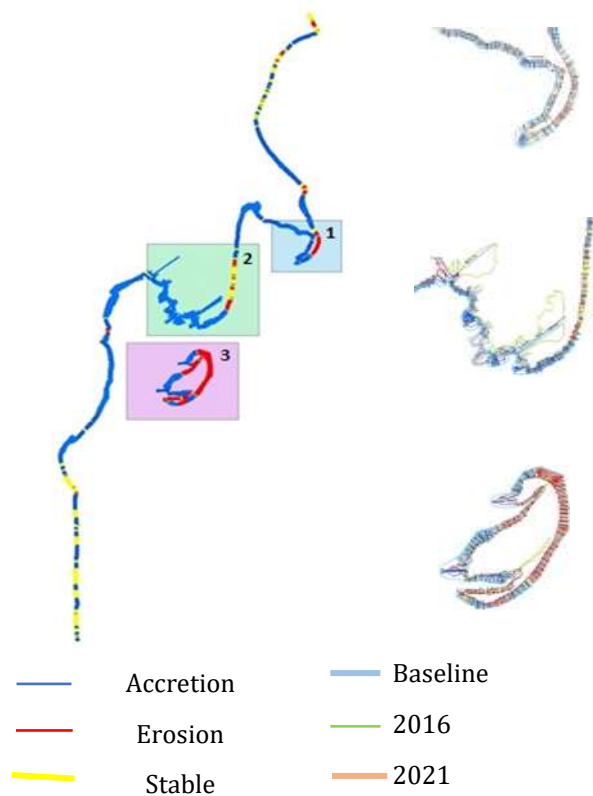


Figure 3. Areas where the coastline is subject to maximum erosion (1) and accretion (2) and result of Kura language island (3).

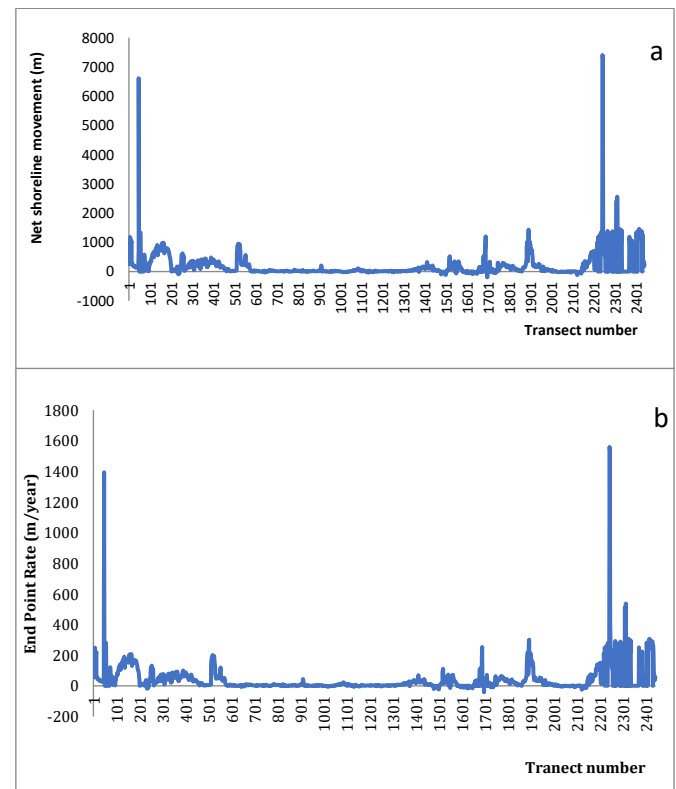


Figure 4. Rate of shoreline change a (NSM in m), b) (EPR in m/yr) for the year 2016 to 2021.

5. Conclusion

The presented results are clearly indicative of a coastline shift. This was particularly noticeable between 2016 and 2021 when the shoreline moved on average 197.12 m towards the Caspian sea. As the coastline moves away from the land, a continuous increase in the beach surface in from the Bandovan to river of Astarachay was observed. Based on conducted analyses, the sandy area increased by 7980.53 ha. The area of the Kura language island has expanded by 403.66 hectares (Figure 5).

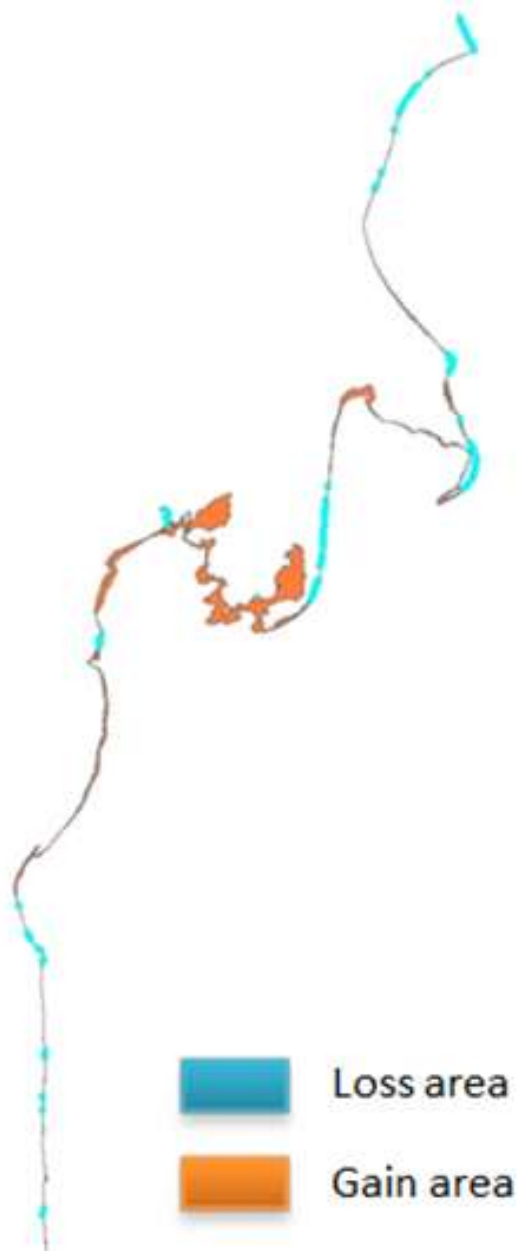


Figure 5. Fragments showing land gain and loss

References

- Boak, E. H. & Turner, I. L. (2005). Shoreline definition and detection: A review. *Journal of Coastal Research*, 21(4); 688–703. West Palm Beach (Florida), ISSN 0749-0208.
- DI, K. (2003). Automatic shoreline extraction from highresolution IKONOS satellite imagery. In: *Proceedings of ASPRS 2003 Annual Conference*. [S.l.: s.n.]; 5–9.
- Drusch, M., Del Bello, U., Carlie, S., Colin, O., Fernandez, V., Gascon, F., Hoersch, B., Isola, C., Laberinti, P. & Martimort, P. (2012). Sentinel-2: ESA's Optical High-Resolution Mission for GMES Operational Services. *Remote Sens. Environ.* 120; 25–36.
- Garcia-Rubio, G., Huntley, D. & Russell, P. (2015). Evaluating shoreline identification using optical satellite images. *Marine Geology*, v. 359; 96–105.
- GENS, R. (2010). Remote sensing of coastlines: detection, extraction and monitoring. *International Journal of Remote Sensing*, v. 31, n. 7; 1819–1836.
- Pardo-Pascual, J. E. (2012). Automatic extraction of shorelines from Landsat TM and ETM+ multi-temporal images with subpixel precision. *Remote Sensing of Environment*, v. 123; 1–11.
- Safyanov, G. A. (1996). *Geomorphology of seashores*. Moscow 400.
- Scott, J. W., Moore, L., Harris W. M. & Reed, M. D. (2003). Using the Landsat Enhanced Thematic Mapper Tasseled Cap Transformation to Extract Shoreline (US: Geological Survey Open File Report OF) 03-272.
- Thieler, E. R., Himmelstoss, E. A., Zichichi, J. L. & Ergul, A. (2009). The digital shoreline analysis system (DSAS) version 4.0 an ArcGIS extension for calculating shoreline change," U.S. Geol. Surv., Reston, VA, USA, Tech. Rep.
- Tingting, S. & Hanqiu, X. (2019). Derivation of Tasseled Cap Transformation Coefficients for Sentinel-2 MSI At-Sensor Reflectance Data *IEEE Journal of Selected Topics in Applied Earth Observations and Remote Sensing* (Volume: 12), 4038 – 4048.
- Wang, X. (2018). Fine spatial resolution coastline extraction from Landsat-8 OLI imagery by integrating downscaling and pansharpening approaches. *Remote Sensing Letters*, v. 9, n. 4; 314–323.
- Yamamoto, K. H., & Finn, M. P. (2012). Approximating tasseled cap values to evaluate brightness, greenness, and wetness for the Advanced Land Imager (ALI): U.S. Geological Survey Scientific Investigations Report 5057, 9.

4th Intercontinental Geoinformation Days

igd.mersin.edu.tr



Aircraft detection in very high-resolution satellite images using YOLO-based deep learning methods

Berkay Yaban¹, Ugur Alganci^{*2}, Elif Sertel²

¹ Istanbul Technical University, Graduate School, İstanbul, Türkiye

² Istanbul Technical University, Civil Engineering Faculty, Geomatics Engineering Department, İstanbul, Türkiye

Keywords

Remote sensing
Deep Learning
Convolutional Neural Network

Abstract

With the recent developments in remote sensing technology, satellite images with high spatial and temporal resolution have been becoming widely available. Very high resolution (VHR) satellite images are very appropriate data sources for geospatial object detection using deep learning algorithms. Airplane detection from satellite images is one of the significant application areas to support airspace inspection, airline traffic control, and defense applications. In this study, we compared various variants of YOLOv5 (You Only Look Once) models and the Scaled-YOLOv4 model for aircraft detection from satellite images. We implemented different hyperparameters, optimization algorithms, and data augmentation methods. Finally, based on the results of numerous experiments, we evaluated the advantages and disadvantages of both methods. Our analysis illustrated that the best mAP@0.50:0.95 value of 0.865 belongs to the YOLOv5x model with 16 batch sizes. Whereas, in terms of computational efficiency, the Scaled-YOLOv4 model has the shortest duration in the training.

1. Introduction

Aircraft detection from satellite images is an important topic since obtained information is used for traffic control, airport activity monitoring, environmental impact assessments, and defense applications. Satellite systems with their capabilities of covering large areas, including high spatial details, fast data collection, and processing times are important sources of information for the geospatial object detection such as planes, ships, storage areas, and buildings (Alganci et al., 2020; Bakirman et al., 2022; Cheng and Han, 2016; Psiroukis et al. 2021).

Manual digitization of geospatial objects from satellite images is highly dependent on the experience of the operator and it is time-consuming. Therefore, it is essential to develop accurate automatic approaches for geospatial object detection. Deep learning-based approaches have become widespread in 2012 and later, especially after the successful conclusion of the ImageNet competition.

Different disciplines and applications have benefited from DL methods. In the Remote Sensing (RS) domain, DL methods are also used for the detection of different geospatial objects, land cover/use segmentation, and

pan-sharpening. For the object detection tasks, You Only Look Once (YOLO) models are common since accurate and fast results could be obtained using YOLO models (Redmon et al., 2016; Li et al., 2017; Krizhevsky et al., 2012; Wang et al., 2021).

In recent years, with the developments in graphics cards and the production of GPU-based solutions, deep learning-based methods have become more common. In addition, the Google Colab platform has made a significant contribution to deep learning studies with its cloud-based computing environment and efficiency to implement different DL frameworks and libraries.

In this study, we aimed to automatically detect airplanes from very high-resolution satellite images using the High Resolution Planes (HRPlanes) data set and a new test data set generated from satellite images of different airports and air bases obtained from the Google Earth platform.

We implemented different experimental designs for YOLOv5 variations and Scaled-YOLOv4 models, and these compared two YOLO models. For experimental designs, we tried various hyperparameter values, optimization functions, and data augmentation methods. We compared the results of our experiments based on Mean Average Precision (mAP) values.

* Corresponding Author

(yaban20@itu.edu.tr) ORCID ID 0000-0002-5648-8506
(alganci@itu.edu.tr) ORCID ID 0000-0002-5693-3614
(sertele@itu.edu.tr) ORCID ID 0000-0003-4854-494X

Cite this study

Yaban, B., Alganci, U., & Sertel, E. (2022). Aircraft detection in very high-resolution satellite images using YOLO-based deep learning methods. 4th Intercontinental Geoinformation Days (IGD), 270-273, Tabriz, Iran

2. Method

2.1. Data and Environment

We used the HRPlanes dataset that includes high-resolution satellite images from various airports across the world (Bakirman & Sertel, 2022). The sizes of the images are 4800 x 2703 pixels. HRPlanes dataset was divided into 1686 training and 404 validation images. In addition to this dataset, we also collected 100 images from Google Earth and used them as the independent test set.

We implemented our experiments in the Google Colab Pro development platform, in which we could able to use an Nvidia P100 graphics card. We used YOLOv5x and YOLOv5l variants of YOLO5 and the Scaled- YOLOv4 models (Mahendrakar et al., 2021; Wang et al., 2021).

2.2. Data Augmentation

We used Hue, Saturation, Value (HSV), and mosaic data augmentation methods to synthetically increase the dataset. HSV specifies colors based on hue, saturation, and brightness values rather than Red, Green, and Blue (RGB) values. HSV provides better results for the object with a specific color. The mosaic method, on the other hand, combines 4 training images into one image with certain ratios. Thus, the trained model can learn the identification of objects at a smaller scale than normal (Hao & Zhili, 2020).

2.3. YOLOv5 Algorithm

In region-based algorithms, possible positions of individual objects are fed into the network. For this reason, the processing load increases, and it takes a long time to get results from the model. The most important feature of the YOLO algorithm is that it works fast because it passes through the neural network at once by dividing the image into grids (Jocher et al., 2022). The purpose of gridding is to detect the object and enclose it in a bounding box. If both grids detect an object, it uses a non-maximum suppression method to eliminate clutter. With this method, the bounding box with the smaller probability value is removed (Krizhevsky et al., 2012)

The difference between YOLOv5 from older YOLO algorithms is that it uses the Pytorch framework (Jocher et al., 2022). In architecture, the backbone is the feature extraction layer. An interlayer called BottleNeck is used

to obtain more information while estimating objects (Figure 1).

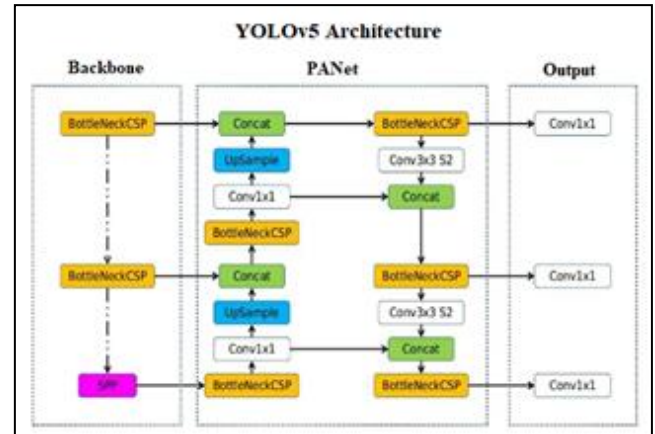


Figure 1. YOLOv5 Architecture [2]

2.4. Scaled-YOLOv4 Algorithm

Scaled-YOLOv4, which is a different version of YOLOv4, aims to improve the training time by scaling the model. To ensure this, both the depth, width, and resolution values of the model and the structure of the network are scaled using the Cross Stage Partial (CSP) approach (Mahendrakar et al., 2021). CSP divides the input into two different paths and convolutions to one path (Jocher et al., 2022; Wang et al., 2020). In the output part; combining these two paths provides the result.

2.5. Experiment Design

In this study, we conducted and evaluated 11 experiments with different settings including various model, network, optimizer batch size, and data augmentation combinations. YOLOv5 and Scaled-YOLOv4 tests were performed using the Pytorch library. 1686 training images and 404 validation images were used in each test. The network sizes were 640x640, 960x960, and 1280x1280 in YOLOv5 tests and 416x416 in Scaled-YOLOv4 tests. In order to make comparisons between the tests, the iteration number was kept constant at 100, but different hyperparameters and augmentations were used. While 16 and 8 values are used as batch size, mosaic and HSV (hue, saturation, value) are used as data augmentation. These configurations are summarized in Table 1.

Table 1. Experimental setup

No	Model	Network	Optimizer	Batch Size	Augmentation
Exp-1	YOLOv5m	1280x1280	SGD	8	Image HSV-Saturation(0,7)- Hue(0,015)-Value(0,4)
Exp-2	YOLOv5m	1280x1280	Adam	8	Image HSV-Saturation(0,7)- Hue(0,015)-Value(0,4)
Exp-3	YOLOv5x	960x960	SGD	16	Image HSV-Saturation(0,7)- Hue(0,015)-Value(0,4)-Mosaic
Exp-4	YOLOv5x	640x640	SGD	16	Image HSV-Saturation(0,7)-Hue (0,015)-Value(0,4)
Exp-5	YOLOv5l	960x960	SGD	8	-
Exp-6	YOLOv5l	640x640	Adam	8	Mosaic
Exp-7	YOLOv5l	640x640	SGD	16	Image HSV-Saturation(0,7)-Hue(0,015)-Value(0,4)
Exp-8	YOLOv5l	960x960	SGD	8	Image HSV-Saturation(0,7)-Hue(0,015)-Value(0,4)-Mosaic
Exp-9	Scaled-YOLOv4	416x416	SGD	8	Image HSV-Saturation(0,7)-Hue(0,015)-Value(0,4)
Exp-10	Scaled-YOLOv4	416x416	SGD	16	Image HSV-Saturation(0,7)-Hue(0,015)-Value(0,4), Mosaic
Exp-11	Scaled-YOLOv4	416x416	SGD	16	-

2.6. Evaluation Metrics

The results of different experiments were evaluated with mean average precision (mAP) Precision values at Union (IoU) threshold value of 0.50 (mAP@0.50), and average of AP values from IoU of 0.5 to 0.95 (mAP@0.50:0.95), Precision and Recall metrics (Henderson and Ferrari, 2016).

3. Results and Discussion

Our results showed that among the YOLOv5 models, the X and M models achieved higher mAP values. Through them, the YOLOv5x with 960x960 network size (Exp-3) yielded the best outcome (Table 2). In addition, this implementation provided higher mAP values in initial steps, which pointed out a faster learning capability with less iterations.

However, increasing the network size in the L model (Exp -8) resulted in a mAP value that was comparable to the YOLOv5x (960) model, which, while halving the training time.

When the optimization functions are compared, models trained with Adam produced lower mAP values than the models trained with Stochastic Gradient Descent (SGD). It also took longer in terms of training

time. Thus, we recommend use of SGD in similar experiments.

Increments in the batch size improved the detection accuracy, however it requires more computational power, which resulted in increased computation time in our experiment setup.

When the detection results are evaluated visually, it can be commented that, both models provided satisfactory detections, even with challenging background and atmospheric conditions. More over both models are able to detect airplanes with different sizes (Figure 3).

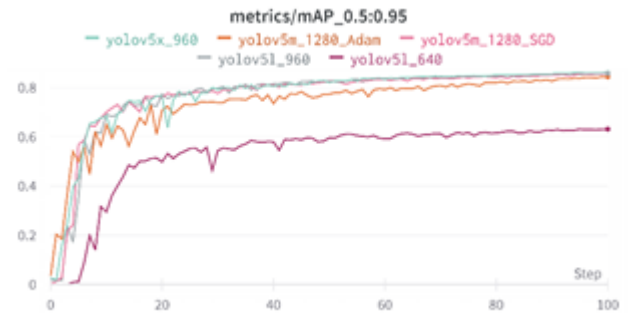


Figure 2. mAP graphic for YOLOv5 implementations.

Table 2. Evaluation metric results

No	Precision	Recall	mAP@0.50	mAP@0.50:0.95	Time
Exp-1	0.979	0.976	0.987	0.863	5h 9min 10sec
Exp-2	0.988	0.977	0.993	0.860	9h 12min 5 sec
Exp-3	0.994	0.978	0.994	0.865	16h 4min 23sec
Exp-4	0.993	0.979	0.994	0.799	12h 14min 42sec
Exp-5	0.941	0.968	0.979	0.857	8h 6min 34sec
Exp-6	0.978	0.968	0.982	0.789	7h 59min 12sec
Exp-7	0.980	0.977	0.983	0.805	5h 6min 12sec
Exp-8	0.990	0.983	0.992	0.864	8h 2min 17sec
Exp-9	0.843	0.973	0.972	0.754	1h 9min 19sec
Exp-10	0.879	0.976	0.98	0.796	1h 39min 10sec
Exp-11	0.877	0.975	0.979	0.782	1h 49min 41sec

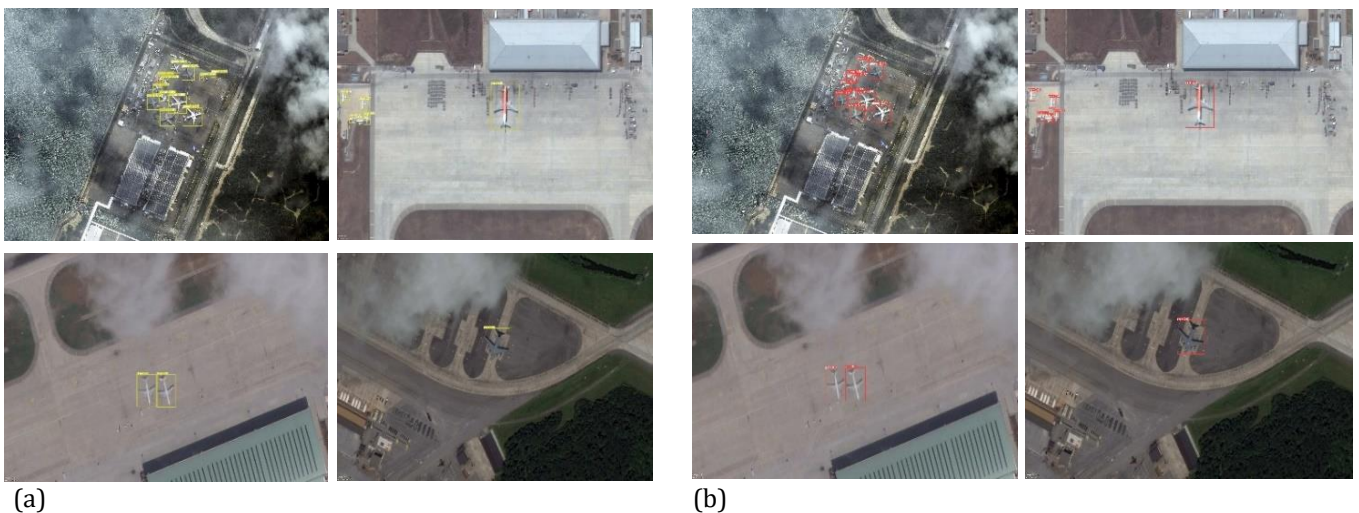


Figure 3. Detection previews from a) Scaled-YOLOv4 and b) YOLOv5 Architecture

4. Conclusion

Within the scope of this study, YOLOv5 and Scaled-YOLOv4 deep learning models were evaluated with a total of 11 tests with different hyperparameters, augmentations and network sizes. In this context, YOLOv5 models produced the highest mAP values.

In particular, increasing the number of batches (batch size) provided an increase of 0.042 at the value of mAP@0.50:0.95 for the same model. In addition, increasing the network size provided an increase the value of mAP@0.50:0.95 for the all models. Preferring smaller scale models of YOLOv5 and using more powerful graphics cards can enable model training with higher number of batch sizes, thus may result in higher success rates indirectly.

In addition, for systems that do not need very high accuracy, the Scaled-YOLOv4 model can be used to save time. It completed the model training about 4 to 6 times faster than the YOLOv5 models.

References

- Alganci, U., Soydas, M., & Sertel, E. (2020). Comparative research on deep learning approaches for airplane detection from very high-resolution satellite images. *Remote Sensing*, 12(3), 458.
- Bakirman, T, and Sertel, E. (2022). HRPlanes: High Resolution Airplane Dataset for Deep Learning. arXiv preprint arXiv:2204.10959.
- Bakirman, T., Komurcu, I. & Sertel, E. (2022). Comparative analysis of deep learning-based building extraction methods with the new VHR Istanbul dataset, *Experts Systems with Applications*, 202, 117346.
- Cheng, G., & Han, J. (2016). A survey on object detection in optical remote sensing images. *ISPRS Journal of Photogrammetry and Remote Sensing*, 117, 11-28.
- Hao, W., & Zhili, S. (2020, November). Improved Mosaic: Algorithms for more Complex Images. In *Journal of Physics: Conference Series* (Vol. 1684, No. 1, p. 012094). IOP Publishing.
- Henderson, P., & Ferrari, V. (2016, November). End-to-end training of object class detectors for mean average precision. In *Asian conference on computer vision* (pp. 198-213). Springer, Cham.
- Jocher, G., Stoken, A., Borovec, J., NanoCode012, ChristopherSTAN, Changyu, L., Laughing, tkianai, yxNONG, Hogan, A., lorenzomamma, AlexWang1900, et al (2021). "ultralytics/yolov5: v4.0 - nn.SiLU() activations, Weights & Biases logging, PyTorch Hub integration," Jan. 2021. [Online]. Available: <https://doi.org/10.5281/zenodo.4418161>
- Krizhevsky, A., Sutskever, I., & Hinton, G. E. (2012). Imagenet classification with deep convolutional neural networks. *Advances in neural information processing systems*, 25.
- Li, X., Wang, S., Jiang, B., & Chan, X. (2017, December). Airplane detection using convolutional neural networks in a coarse-to-fine manner. In *2017 IEEE 2nd Information Technology, Networking, Electronic and Automation Control Conference (ITNEC)* (pp. 235-239). IEEE.
- Mahendrakar, T., White, R. T., Wilde, M., Kish, B., & Silver, I. (2021). Realtime Satellite Component Recognition with yolov5. In *Small Satellite Conference*.
- Psiroukis, V., Malounas, I., Mylonas, N., Grivakis, K. E., Fountas, S., & Hadjigeorgiou, I. (2021). Monitoring of free-range rabbits using aerial thermal imaging. *Smart Agricultural Technology*, 1, 100002.
- Redmon, J., Divvala, S., Girshick, R., & Farhadi, A. (2016). You only look once: Unified, real-time object detection. In *Proceedings of the IEEE conference on computer vision and pattern recognition* (pp. 779-788).
- Wang, C. Y., Bochkovskiy, A., & Liao, H. Y. M. (2021). Scaled-yolov4: Scaling cross stage partial network. In *Proceedings of the IEEE/cvf conference on computer vision and pattern recognition* (pp. 13029-13038).
- Wang, C. Y., Liao, H. Y. M., Wu, Y. H., Chen, P. Y., Hsieh, J. W., & Yeh, I. H. (2020). CSPNet: A new backbone that can enhance learning capability of CNN. In *Proceedings of the IEEE/CVF conference on computer vision and pattern recognition workshops* (pp. 390-391).

4th Intercontinental Geoinformation Days

igd.mersin.edu.tr



A review of the various advances in smart cities: Application of artificial intelligence and machine learning

Mehran Dadashzadeh^{*1} , Farhad Jedari Zarezadeh²

¹University of Tabriz, Faculty of Civil Engineering, Department of Water Resources Engineering, Tabriz, Iran

²University of Tabriz, Faculty of Civil Engineering, Department of Structural Engineering, Tabriz, Iran

Keywords

Smart city
Artificial intelligence
Machine Learning
Urban planning
Urban development policies

Abstract

Artificial intelligence has played an effective role in human societies and started new concepts in community life. Meanwhile, smart cities are the new issue introduced lately. Smart cities with the aim of providing new standards of urbanization, optimal energy consumption, environment, and ameliorating the economy are propounded. The ideals of smart cities are divided into subcategories that can handle by artificial intelligence. The primary objective of this review is to explore the role of artificial intelligence and machine learning in the evolution of smart cities. In this survey, we present some details of the applications of machine learning techniques in energy grids, public lighting, natural resources, water management, environment, waste management, healthcare, public security, transport, mobility, and logistics. The result of the present study demonstrated that operating artificial intelligence methods in the field of metropolis control is very prosperous.

1. Introduction

The intelligence of a city is largely based on the ways it manages its urban resources (Fokaides et al. 2018). This fact, recently, led to the concept of “Smart Cities” in the scientific forums. The Smart City prospect preliminarily denoted initiatives that utilize digital and ICT-based inventions to ameliorate the expeditiousness of urban services and generate new economic opportunities in cities (Kamal-Chaoui. 2020). But recently Smart Cities have been defined as initiatives or approaches that effectively leverage digitalization to boost citizen well-being and deliver more efficient, sustainable, and inclusive urban services and environments as part of a collaborative. Significantly, “machine learning” is insinuated as efficient equipment to materialize targets of smart cities (Sohail Ibrahim et al. 2020).

The core of a smart city consists of the creation and use of data to generate new services and support decision-making. Data is one of the three major pillars of the Smart Cities, along with technology and people (al-kamoosi and Al-Ani. 2019). In the presence of big and complex data, it's difficult to precisely decide the most accurate and efficient actions. The best possible analysis

of the big data can be carried out using machine learning to reach an optimal decision (Liu et al. 2019). The machine learning ecosystem is both extensive and complex, with many possible ways to subdivide or classify its members (Paeglis et al. 2018).

This study focuses on clarifying the application of machine learning in smart cities by considering its characteristic features and application areas. Possible areas of smart cities are suggested to illustrate the application of innovative machine learning patterns in the empirical research presented in this study.

2. Machine Learning strategies

There are two approaches of machine learning algorithms to apply an informative classification (LeCun et al. 2015). One frequently used classification scheme outlines two broad groups of machine learning algorithms: supervised learning, where the model is presented with both a set of labeled example inputs and desired outputs (called the training dataset), with the goal to learn a mapping from inputs to outputs. The second informative approach to classifying machine learning algorithms is based on the desired type of output of the given model. Due to the wide range of

* Corresponding Author

^{*}(mehrandadashzadeh@tabrizu.ac.ir) ORCID ID 0000- 0001- 9521- 7330
(farhadjedari@yahoo.com) ORCID ID 0000- 0003- 2762- 3577

Cite this study

Dadashzadeh, M., & Zarezadeh, F. J. (2022). A review of the various advances in smart cities: Application of artificial intelligence and machine learning. 4th Intercontinental Geoinformation Days (IGD), 274-277, Tabriz, Iran

domains of a smart city, clustering is notable due to its broad and general applicability and can be employed to carry out cluster analysis on methods and algorithms.

3. Application of Machine Learning in Smart Cities

The various advances to the definition of smart cities are mainly related to two different factors, I) The way cities can steer themselves to achieve the goal of optimization, and II) The domains that are more critical for a cleverer usage of urban resources (Neirotti et al. 2014). The domains in which urban development policies are applicable can be classified as “hard” or “soft”.

Hard domains refer to energy grids, natural resources, energy and water management, waste management, environment, transport, mobility, and logistics, and by contrast, soft domains include areas such as education, culture, policies that burnish competitiveness, inventions, and social adjuncts, as well as communication between local public bureaucracies and the citizens (Neirotti et al. 2014).

In proportion to hard domains, soft domains cannot be examined by Machine Learning due to the fact that they are investigated based on urban planning and people's behavioral habits (Wataya and shaw. 2019). As a result, the hard domains are discussed in this review.

3.1. Energy grids

The machine learning applications in the smart energy grid include predictions of loads and price, cascading failure prediction, power generation and control, fault detection and diagnosis, and detection of cyberspace attacks among others (Sohail Ibrahim et al. 2020). The spectrum of machine learning applications in the smart grid is spanning from the general comprehensive perception of the underlying systems, to intelligent and adaptive decision-making and finally towards the real-time or near real-time operations in the context of smart grids.

To be detailed on this issue, energy consumption in public buildings does not fulfill the assumptions of linearity; The machine learning methods have been selected to be used due to their nonlinearity and ability to learn from historical data (recorded similar situations). Three machine learning methods have been used for creating predictive models of energy consumption and efficiency of public buildings: artificial neural networks (ANNs) and recursive partitioning methods such as CART decision trees, and random forests (Zekić-Sušaca et al. 2021).

3.2. Public lighting, natural resources, and water management

There are many challenges facing traditional public-lighting management systems, such as the number of damaged lamps that need replacement each year, the impact of extending the system by adding lamps, and lamp type on the failure rate. Generally, challenges are considered in the two sections: I) Challenges facing

lighting contractors and II) Challenges facing lighting managers (Mirzaei et al. 2020).

Due to mentioned challenges, the machine learning approach is advocated. ANN is a significant utilization of machine learning. According to this issue, some of the situations that arise with respect to street lighting include any overload in the electricity passing through the luminaries, which has to be adjusted; dimming or switching off street lights in the presence of natural light, and reducing light intensity based on the amount of illumination provided by natural light (Mohandas et al. 2019). The commodity of utilizing ANN is that once an associated situation recurs, the solutions are generalized from past data and applied instantly. Thus, ANN learns from a set of examples to manage associated situations as they occur subsequently.

In the case of natural resources and water management, Machine learning methods, particularly ANNs, have been commonly and successfully used in water systems management (Imani et al. 2021). On the other hand, resilience is an increasing idea that validated to be a conducive approach in preparing engineering systems to engage with emerging challenges. Researchers believe that the integration of machine learning techniques to predict water quality resilience can provide an opportunity for more effective adoption of resilience to tackle the emerging challenges. One potential improvement on the horizon will be using more conducive machine learning methods such as deep learning or deep reinforcement learning.

3.3. Waste management

Waste management is an essential activity and operation from the start to waste clearance. This involves trash collection, transportation, processing and disposal, monitoring, controlling, and separating waste management (Kepa et al. 2020). Artificial intelligence for smart cities plays a prominent role in taking solid waste collection seriously since it is remarkable for the environment and influences society (Chen. 2022).

Also, machine learning plays a crucial role in automated sorting techniques leading to greater precision and better waste separation quality (Ismaila et al. 2022). In addition to navigational and tracking capacity storage waste processing analysis and optimization of the required information would, in the end, enhance the entire waste management efficiency by improving the waste collection by advancing the program.

3.4. Environment

In the field of Environment, countries, and societies are paying frequent attention to the construction of ecological civilization and environmental protection (D'Amico et al. 2021). This has also been reflected to a certain extent in urban space planning. It can be seen that in the process of urban construction and development, urban space planning has more emphasis on ecological civilization and the ecological environment (Chen. 2021). Putting protection into important links and main content, it is obvious that the proportion of ecological strategies

in urban spatial planning is increasing, and it is showing an upward trend year by year.

With recent advances in environmental monitoring technologies, huge volumes of complex environmental data are being generated continuously. Because this data is dynamic, heterogeneous, multidimensional, multi-source, and extensive, it must be organized, integrated, and visualized to be informative for environmental monitoring and decision-making programs (He et al. 2010). Data mining and machine learning methods categorize this huge amount of data and provide the best output by examining the favorable conditions for the environment.

3.5. Transport, mobility, and logistics

Connected and Autonomous Vehicles, Unmanned Aerial Vehicles and Personal Aerial Vehicles, Mobility-as-a-Service, Internet of Things, and Physical Internet, approved set of definitions that critically underpins the nexus of Artificial Intelligence, transport, and the smart city (Wortmann and Fluchter 2015; Kim et al. 2018).

Smart Mobility is one of the main concerns in modern cities, which focuses on providing sustainable transport systems and logistics to allow smooth urban traffic and commuting by mainly applying information and communication technologies. They also include approaches that harness personal information to provide useful recommendations for small-scale personal management like searching for free parking spaces (Baskar et al. 2011). Some conventional control approaches such as static feedback control (SFC) and traditional Artificial Intelligence techniques based on historical data such as case-based reasoning and rule-based systems were developed to determine control actions. However, these approaches had their respective drawbacks such as trouble coping with the dynamics of the traffic networks and the techniques did not have a learning mechanism to deal with unseen situations to automatically update their model (Nallaperuma et al. 2019). The advancement of machine learning has paved the way for a generic and flexible way to develop intelligent and adaptive traffic control systems.

3.6. Healthcare

The increasing availability of electronic health data (EHR) presents a major opportunity in healthcare for discovery and practical applications to improve healthcare by providing accurate medical diagnosis, predicting diseases in the early stages, and disease analysis. Many smart devices gather data related to human health and there is a growing industry of such devices. The authenticity of information is very significant in predictive models, unfortunately, this information is not structured and cannot use in the mentioned models. Artificial Intelligence networks are known for their ability to handle large volumes of relatively messy data, including errors in labels and large numbers of input variables (Bhardwaj et al. 2017). Operators do not have to specify which variables need to be considered for prediction and in what combinations; instead, neural networks can learn representations of the

key factors and interactions from the data itself. Due to these advantages, the use of machine learning in the realm of healthcare has become prevalent. The EHR data collected can be mined for several possible applications. The entire contents of the EHR like medications, admission details, vital signs, etc. can be analyzed using machine learning algorithms to estimate the probability of a patient reacting adversely to antibiotics or to accurately measure the patient's risk of contracting common hospital spread diseases such as *Clostridium difficile* infection (Weins et al. 2014).

3.7. Public security

The smart city safeguards possible risks for residents, organizations, and other institutions. Protection measures enforcement is a significant factor to monitor city agencies and taking accountable operations in the emergency incidents (Ahmed et al. 2021). In this field, the relevant needs of public security and police affairs are met by the public security information analysis and mining system as an auxiliary analysis instrument. The effectual institution of this system means that the investigative opinion of case-handling personnel is expensive, and the case can be encountered with higher efficiency than the manual system. It can extend applicable decision-making and a basis for police work, which has very essential practical urgency (Li and Cui. 2021, Yu et al. 2021). Through the related academic research on machine learning, the police department's ability to enforce the law and combat terrorism will be greatly improved. Based on the specific characteristics of crime and associated security tools, data mining technologies primarily include the following: information sharing and collaboration, intelligent text mining, security association mining, classification and clustering, and spatial and temporal crime pattern mining. Despite the use of traditional methods, simple methods like machine learning and data mining and their impact on the proposed system will be of great importance.

4. Conclusion

A detailed evaluation is contemplated as a preparatory contribution to conceive empirical research in order to obtain a better comprehension of the current development of Smart Cities. Based on this issue, eleven main approaches to Smart Cities deployment are classified, energy grids, public lighting, natural resources, water management, environment, waste management, healthcare, public security, transport, mobility, and logistics.

In this study, the common point of mentioned approaches is the application of machine learning to obtain the targets of each field. Machine Learning strategies are used to expose a beneficial and standard alternative instead of traditional methods. The result of this study revealed that operating artificial intelligence methods in the field of metropolis control is very booming. Additionally, machine learning was found as a global algorithm to generate targets for smart cities, and machine learning behavioral filters in the various

domains mentioned are defined based on the tendencies and evolutionary patterns of each smart city, which largely depend on local context factors.

References

- Ahmed, S., Farhad Hossain Md, Kaiser M S, Taj Noor M B, Mahmud M, Chakraborty C (2021), Artificial Intelligence and Machine Learning for Ensuring Security in Smart Cities, *Advanced Sciences and Technologies for Security*, 23-46.
- Al-Kamoosi N, Al-Ani M Q (2019). The Future Initiatives of Smart communities in Baghdad as a Smart City. *Al-Nahrain Journal for Engineering Sciences*, 22(4), 259-276.
- Baskar L D (2011), Traffic control and intelligent vehicle highway systems: a survey, *IET Intelligent Transport Systems*, (5), 38-52.
- Bhardwaj R, Nambiar A R, Dutta D (2017). A study of machine learning in healthcare. *IEEE 41st Annual Computer Software and Applications Conference (COMPSAC)*.
- Chen X (2022). Machine learning approach for a circular economy with waste recycling in smart cities. *Energy Reports*, (8), 3127-3140.
- Chen Z (2021), Application of environmental ecological strategy in smart city space architecture planning, *Environmental Technology & Innovation*, (23) 101-684.
- D'Amico G, Szopik-Depczynska K, Dembinska I, Ioppolo G (2021). Smart and sustainable logistics of Port cities: A framework for comprehending enabling factors, domains and goals, *Sustainable Cities and Society* (69), 102-801.
- Fokaides P A, Apanaviciene R and Klumbyte E (2018). Energy Management in Smart Cities, *Comprehensive Energy Systems*, (5), 457-473.
- He Y, Su F, Du Y, Xiao R (2010), Web-based spatiotemporal visualization of marine environment data, *Chin. J. Oceanol. Limnol*, 28 (5), 1086-1094.
- Imani M, Mahmudul Hasan Md, Bittencourt Fernando L, McClymont K, Kapelan Z (2021). A novel machine learning application: Water quality resilience prediction Model, *Science of the Total Environment*, 768, 1-10.
- Ismaila E, Ayoub B, Azeddinea K, Hassana O (2022), Machine learning in the service of a clean city, *Procedia Computer Science*, (198), 530-535.
- Kamal-Chaoui L (2020). Smart Cities and Inclusive Growth. *Secretary-General of the OECD*, (1), 9-15.
- Kepa W, Luhach A.K, Kavi M, Fisher J, Luhach R, (2020), Gsm based remote distribution transformer condition monitoring system. In: *International Conference on Advanced Informatics for Computing Research*. Springer, 59-68.
- Khalil M I, Jhanjhi N Z, Humayun M, Sivanesan S, Mehedi M, Hossain M S. (2021). Hybrid smart grid with sustainable energy-efficient resources for smart cities. *Sustainable Energy Technologies and Assessments* (46) 101-211.
- Kim, J., Park, G., Kwon, J., & Cho E-A (2018). A captcha-like implicit authentication model for smart tv based on machine learning algorithms, *IEEE International Conference on Consumer Electronics (ICCE2018)*, 1-2.
- Li, C., & Cui, J. (2021), Intelligent sports training system based on artificial intelligence and big data, *Mobile Information Systems*, 1-11.
- LeCun, Y., Bengio, Y., & Geoffrey Hinton (2015). Deep learning. *Nature*. *Nature* 521 (7553), 436-444.
- Liu, Y., Yang, C., Jiang, L., Xie, S., & Zhang, Y. (2019). Intelligent Edge Computing for IoT-Based Energy Management in Smart Cities. *IEEE Xplore*, 33(2), 111-117.
- Mirzaei, M. J., Amiroun, M. H., Kazemi, A., & Dashti, R. (2020). Optimal contracting strategies for public-lighting asset management: A case study from Iran. *Utilities Policy*, (64), 48-101.
- Mohandasa, P., Anni Dhanarajb, J. S., & Gao, X. Z. (2019). Artificial Neural Network based Smart and Energy Efficient Street Lighting System: A Case Study for Residential area in Hosur, *Sustainable Cities and Society* (48), 1-13.
- Nallaperuma D, et al. (2019), Online incremental machine learning platform for big data-driven smart traffic management. *IEEE Transactions on Intelligent Transportation Systems*, (20), 4679-4690.
- Neirotti, P., De Marco, A., Corinna Cagliano, A., Mangano, G., & Scorrano, F. (2014). Current trends in Smart City initiatives: Some stylized facts. *Cities*, (38), 25-36.
- Paeglis, A., Strumfs, B., Mezale, D. & Fridrihsone, I. (2018), A Review on Machine Learning and Deep Learning Techniques Applied to Liquid Biopsy. *Liquid Biopsy*. ISBN: 978-1-83881-130-3.
- Renugadevi, N., Saravanan, S., & Sudha, C. (2021). IoT based smart energy grid for sustainable cities. *Materials Today: Proceedings* (47). 1-7.
- Sohail Ibrahim, M., Dong, W., & Yang, Q. (2020). Machine learning-driven smart electric power systems: Current trends and new perspectives, *Applied Energy*, (272), 1-19.
- Wataya, E., & Shaw, R. (2019). Measuring the value and the role of soft assets in smart city development, *Cities*, (94), 106-115.
- Wiens, J., Gutttag, J., & Horvitz, E. (2014), Learning Data-Driven Patient Risk Str. pagination Models for *Clostridium difficile*, *Open forum infectious diseases*, Oxford University Press.
- Wortmann, F., & Flüchter, K. (2015), Internet of Things, *Bus Inf Syst Eng*, (57), 221-224.
- Yu, X., Hu, Q., Li, H., Du, J., Gao, J., & Sun, L. (2021), Cross-domain recommendation based on latent factor Alignment Neural, *Computing & Applications*, (12), 28-43.
- Zekić-Sušaca, M., Mitrovića, S., & Has, A. (2019). Machine learning based system for managing energy efficiency of public sector as an approach towards smart cities. *International Journal of Information Management*. (57), 1-12.



4th Intercontinental Geoinformation Days

igd.mersin.edu.tr



Calculate wastage and optimize building energy consumption using GEO BIM

Saeed Rasti¹, Majid Kiyavarz^{*1}, Abbas Rajabifard²

¹ University of Tehran, Faculty of Geography, Department of Remote Sensing and GIS, Tehran, Iran

² University of Melbourne, School of Engineering (MSE), Australia

Keywords

Building Information
GIS
Lod
Energy evaluation
Building Energy Modeling

Abstract

In terms of population growth and increasing greenhouse gas emissions, urban energy planning has become a concern. And with the high speed of urban construction, it is claimed that 40% of the total energy consumption is allocated to the building sector. It is believed that energy modeling and simulation are effective in supporting urban energy planning. Today, the increasing availability of 3D models of cities has facilitated energy simulation at various scales. While the Building Information Model (BIM) allows users to explore a building's energy consumption options, GIS-based building models provide the opportunity to simulate city-wide energy demand. Given that many building energy simulations are based on existing GIS using lower-level detail (LOD) models, the aim of this study is to extract accurate geometric semantic information. Use BIM models to build GIS models with higher LOD. In order to more accurately support the energy simulation of buildings, the meanings of BIM models from various sources are consistent with GIS-based building models, and the geometry of BIM models is converted to conform to GIS-based building model standards. After conversion, the result is used to evaluate the amount of energy lost. And after calculating the energy loss, by changing the building elements, the amount of energy loss is optimized as much as possible. In this study, according to the location, climate, solar angle and various elements of the residential building, after initial calculation and optimization, the desired result was obtained up to a maximum of 50% reduction in energy loss.

1. Introduction

Kargar Sharifabad et al. The annual energy consumption index of 13 residential complexes with different characteristics was evaluated and compared. First, the method of calculating the energy intensity index was presented. Then the energy intensity index of buildings was calculated and buildings with different characteristics were compared in terms of energy intensity index. Comparison of energy intensity indicators shows that the use of new energy materials significantly reduces the intensity of energy consumption in the building.

In this article, Rahimi Nejad et al. Providing simulation software and calculating the amount of energy in office and residential buildings that has been implemented by Amirkabir University of Technology at the request of the Mahshahr Special Economic Zone Organization. The purpose of this software is to calculate the amount of building energy consumption based on

existing standards and optimally so that users and building users can be inspired by this software to minimize their building energy consumption both in the design stage and in the design stage.

Giorgio Agiaro et al. Provide the Energy Development Plan (ADE) modeling method for the CityGML standard. The purpose of this ADE extension is to provide a specific, standard-based model for solving data connection problems in heterogeneous energy applications, as well as for creating detailed details. The results show that having accurate and integrated knowledge in the three-dimensional space of the city, i.e., all the features of the city, infrastructure, functional features and their meaning and their interdependence has an important role in advanced energy simulation and analysis. has it.

Zeya Zhang et al. To calculate urban energy, a new method of integrating GIS and BIM was investigated and this research was conducted in three different buildings. The results of conversion and calculation of heat transfer through the overall shape of the building have been

* Corresponding Author

(saeedrasti13744@gmail.com) ORCID ID 0000 – 0002 – 8159 – 9144
*(kiavarzmajid@ut.ac.ir) ORCID ID 0000 – 0003 – 0335 – 3795
(abbas.r@unimelb.edu.au) ORCID ID 0000-0002-4256-3173

Cite this study

Rasti, S., Kiyavarz, M., & Rajabifard, A. (2022). Calculate wastage and optimize building energy consumption using GEO BIM. 4th Intercontinental Geoinformation Days (IGD), 278-281, Tabriz, Iran

tested at various levels. And the comparison in three scenarios shows that by not opening in the calculation of energy loss, the increase of attention can be compared with the opening scenario.

2. Method

2.1. Study area

The city of Firozabad is from the city of Fars province. The center of this city is Firozabad. Its area is 1489 hectares and its height from the sea level is 1600 meters. That Panda's main heights that are drawn from the northwest to the southeast. The city has a temperate climate that Mile is warm. The climat of this region is temperate in winter and very hot in summer and the annual rainfall is 400 mm. The study area is located the following geocoordinate (Fig. 1). The study is done in eight stages (Fig. 2).

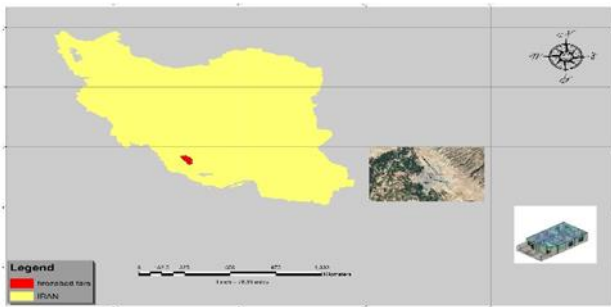


Figure 1. Geographical extent of the Building study

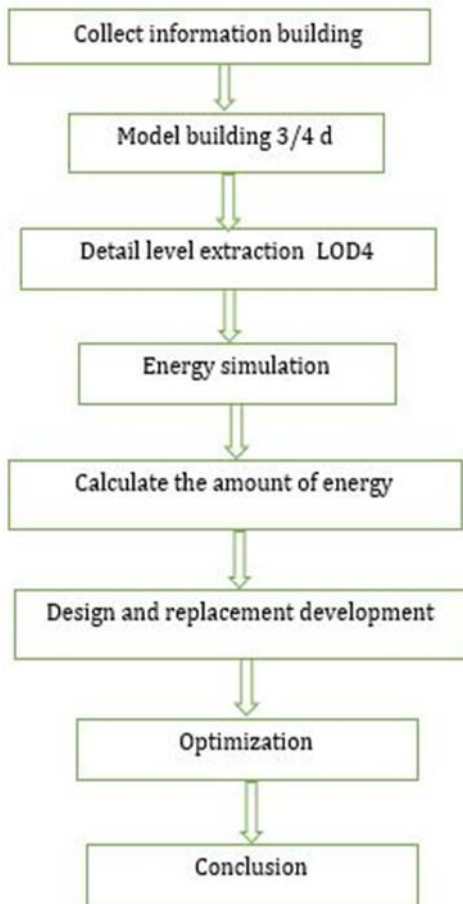


Figure 2. Stages performed in this study

2.2. Collect information building

To collect information for this research, the following criteria are considered: which is divided into three parts building information ·climatic and spatial.

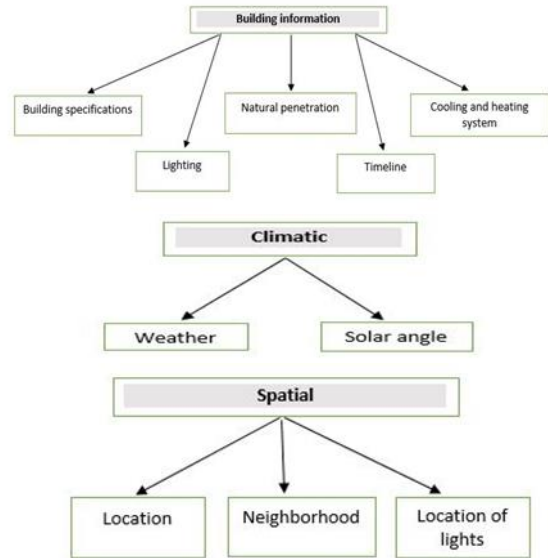


Figure 3. Building information

2.3.1. Sol-Air Values

The heat balance at a sunlit surface gives the heat flux into the surface q/A as

$$q/A = \alpha E_t + h(t_o - t_s) - \varepsilon \Delta R \quad (1)$$

α = absorptance of surface for solar radiation

E_t = total solar radiation incident on surface, Btu/h·ft²

t_o = outdoor air temperature, °F

t_s = surface temperature, °F

ε = hemispherical emittance of surface

ΔR = difference between long-wave radiation incident on surface from sky and surroundings and radiation emitted by blackbody at outdoor air temperature, Btu/h·ft²

Assuming the rate of heat transfer can be expressed in terms of the sol-air temperature t_e ,

$$\frac{q}{A} = h_o(t_e - t_s) \quad (2)$$

and from Equations (1) and (2),

$$t_e = t_o + \frac{\alpha E_t}{h_o} - \frac{\varepsilon \Delta R}{h_o} \quad (3)$$

2.3.2. Calculating Conductive Heat Gain

Conduction through exterior walls and roofs is calculated using conduction time series (CTS).

Wall and roof conductive heat input at the exterior is defined by the familiar conduction equation as

$$q_{i,q-n} = UA(t_{e,q-n} - t_{rc}) \quad (4)$$

$q_{i,q-n}$ = conductive heat input for the surface n hours ago, Btu/h
 U = overall heat transfer coefficient for the surface, Btu/h·ft²·°F
 A = surface area, ft²
 $t_{e,q-n}$ = sol-air temperature n hours ago, °F
 t_{rc} = presumed constant room temperature, °F

Conductive heat gain through walls or roofs can be calculated using conductive heat inputs for the current hours and past 23 h and conduction time series

$$q_q = C_0 q_{i,q} + C_1 q_{i,q-1} + C_2 q_{i,q-2} + C_3 q_{i,q-3} + \dots + C_{23} q_{i,q-23} \quad (5)$$

q_q = hourly conductive heat gain for the surface, Btu/h
 $q_{i,q}$ = heat input for the current hour
 $q_{i,q-n}$ = heat input n hours ago
 C_0, C_1 etc. = conduction time factors

2.3.3. Heat Gain through Interior Surfaces

Whenever a conditioned space is adjacent to a space with a different temperature (i.e. in a different zone), heat transfer through the separating physical section must be considered.

The heat transfer rate is given by

$$q = UA(t_b - t_i) \quad (6)$$

q = heat transfer rate, Btu/h
 U = coefficient of overall heat transfer between adjacent and conditional space, Btu/h·ft²·°F
 A = area of separating section concerned, ft²
 t_b = average air temperature in adjacent space, °F
 t_i = air temperature in conditioned space, °F

2.3.4. Fenestration Heat Gain

For windows and skylights, the engine uses the following equations to calculate heat gain:

Direct beam solar heat gain q_b :

$$q_b = AE_D SHGC(\theta) \quad (7)$$

Diffuse solar heat gain q_d :

$$q_d = A(E_D + E_r) < SHGC >_D \quad (8)$$

Conductive heat gain q_c

$$q_c = UA(T_{out} - T_{in}) \quad (9)$$

Total fenestration heat gain Q :

$$Q = q_b + q_d + q_c \quad (10)$$

E_D, E_d and E_r = direct, diffuse, and ground-reflected irradiance
 $SHGC(\theta)$ = direct solar heat gain coefficient as a function of incident angle θ ; may be interpolated between values
 $(SHGC)_D$ = diffuse solar heat gain coefficient (also referred to as hemispherical SHGC)

T_{in} = inside temperature, °F
 T_{out} = outside temperature, °F
 U = overall U-factor, including frame and mounting

2.3.5. Plenum Loads

The space above a ceiling, when used as a return air path, is a ceiling return air plenum. The following equations show how temperatures and heat transfer for plenums are calculated in the engine:

$$q_1 = U_c A_c (t_p - t_r) \quad (11)$$

$$q_2 = U_f A_f (t_p - t_{fa}) \quad (12)$$

$$q_3 = 1.1 Q (t_p - t_r) \quad (13)$$

$$q_{lp} - q_2 - q_1 - q_3 = 0 \quad (14)$$

$$Q = \frac{q_r + q_1}{1.1(t_r - t_s)} \quad (15)$$

q_1 = heat gain to space from plenum through ceiling, Btu/h
 q_2 = heat loss from plenum through floor above, Btu/h
 q_3 = heat gain "pickup" by return air, Btu/h
 Q = return airflow, Btu/h
 q_{lp} = light heat gain to plenum via return air, Btu/h
 q_{lr} = light heat gain to space, Btu/h
 q_f = heat gain from plenum below, through floor, Btu/h
 q_w = heat gain from exterior wall, Btu/h
 q_r = space cooling load, including appropriate treatment of q_{lr} , q_f and/or q_w , Btu/h
 t_p = plenum temperature, °F
 t_r = space temperature, °F
 t_{fs} = space temperature of the floor above, °F
 t_s = supply temperature, °F

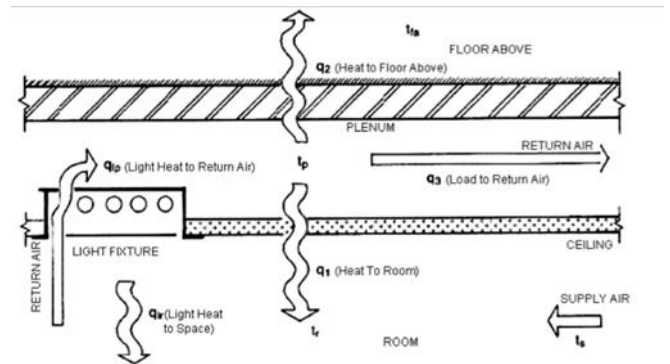


Figure 4. Plenum loads

2.3.6 Solar index calculation relationship

$$I_s = \sum (A_i \cdot S_i \cdot \sigma_i) / V \quad (16)$$

A_i = The area of the permeable part i The output shell of the building in terms of square meters

Si = solar transfer coefficient for transient light fraction i
 δ_i = The reduction coefficient is related to the position of the permeable surface
 V: The total volume of controlled space of the building or section

3. Results



Table 1. This is the example of table formatting

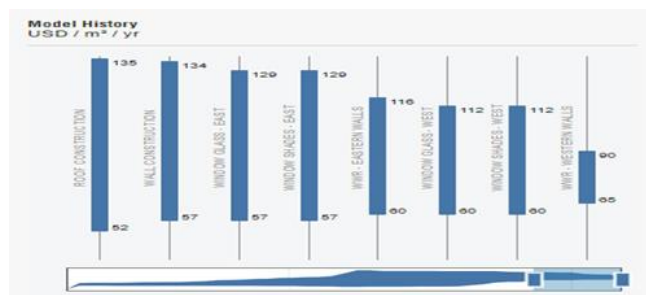


Figure 5. Graph before optimization

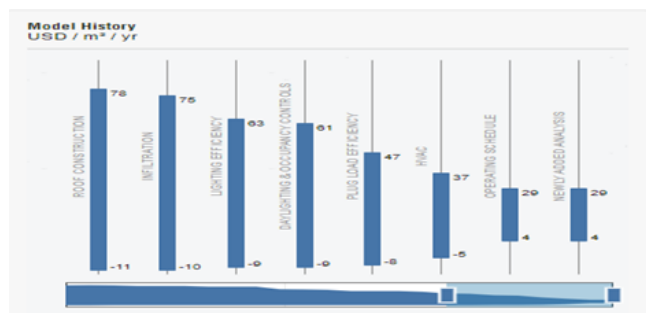


Figure 6. Graph after optimization

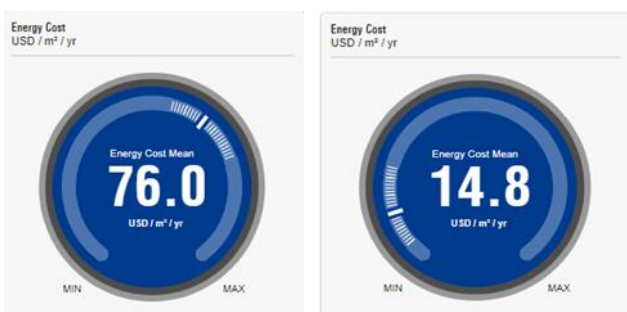


Figure 7. Cost of energy consumption before and after optimization

4. Conclusion

The issue of energy and the access of more and more industrialized countries in the world to cheap energy sources, has created many challenges and this is one of the most important and common topics in the world today. The construction sector is so concentrated that the

construction sector is the largest consumer in the country with more than 40% of energy consumption. On the other hand, various studies in different parts of the world show that buildings are the largest consumers of energy compared to other types of uses. Using simple, affordable and affordable practical strategies to reduce energy consumption and optimization solutions to reduce the demand for mechanical systems and improve the quality and thermal comfort is a way to increase the efficiency of residential buildings in terms of energy consumption. Given that in the future, most buildings will be high-rise and equipped with energy management technologies. This article examines the possibility of optimization in such buildings. Optimization of energy consumption in buildings such as the building studied in this study and providing appropriate energy saving solutions in different sectors showed that by considering different criteria in terms of building information, climate, and location as in Table (2222) presented showed that the optimal building is up to 50% possible and based on research findings. Optimal directions for the establishment of the building were estimated as south-southeast and southwest directions. Among the directions, the south direction was identified as the optimal direction due to maximum absorption in cold times of the year and less energy absorption in hot times of the year.

Table 2. Calculations wasted after wasted after optimization

Components	Cooling		Heating	
	Loads (W)	Percentage of Total	Loads (W)	Percentage of Total
Wall	882	3.10%	1,849	12.23%
Window	5,304	18.66%	1,559	10.31%
Door	170	0.60%	496	3.28%
Roof	18,177	63.93%	8,364	55.31%
Skylight	0	0.00%	0	0.00%
Partition	0	0.00%	0	0.00%
Infiltration	0	0.00%	0	0.00%
Ventilation	76	0.27%	2,854	18.88%
Lighting	878	3.09%		
Power	564	1.98%		
People	1,797	6.32%		
Plenum	0	0.00%		
Fan Heat	582	2.05%		
Reheat	0	0.00%		
Total	28,431	100%	15,123	100%

References

- Agugiario, G., Benner, J., Cipriano, P., & Nouvel, R. (2018). The Energy Application Domain Extension for CityGML: enhancing interoperability for urban energy simulations. *Open Geospatial Data, Software and Standards*, 3(1), 1-30.
- Behrouz Vahidi, Abolfazl Rahimi Nejad, Farshad Seljouki, Hamed Dehghani, Ehsan Afsharian Boys, Saeid Motie Birjandi. Design of simulator software and calculator of energy consumption in buildings Administrative and residential with the aim of promoting a culture of energy consumption management.
- Kargar Sharifabad, H., & Jalilian, M. (2016). Energy rating of residential buildings in the city of Qom according to the national standard and the effect of several factors affecting it. *Modares Mechanical Engineering*, 16(1), 361-364.
- Zeyao Zhang, (2018). BIM to GIS-based building model conversion in support of urban energy simulation.

4th Intercontinental Geoinformation Days

igd.mersin.edu.tr



Investigation of land cover change with GIS using CORINE data

Aslan Cihat Basara^{*1}, Mehmet Emin Tabar², Sumeysra Gulsun³, Yasemin Sisman¹¹Ondokuz Mayıs University, Faculty of Engineering, Department of Geomatics Engineering, Samsun, Türkiye²Bitlis Eren University, Vocational School of Technical Sciences, Department of Architecture and Urban Planning, Bitlis, Türkiye³İstanbul Ticaret University, Architecture and Design Faculty, Department of Architecture, İstanbul, Türkiye

Keywords

Land Cover
Change Detection
Urban Sprawl
CORINE
GIS

Abstract

Population growth leads to the growth of cities and the destruction of natural areas. Urban growth triggers changes in land cover. Determining the change effects in land cover is essential for sustainable policies. The temporal data were produced from the CORINE data for the years 1990, 2000, 2006, 2012 and 2018 for evaluating and understanding the land cover change. When the land cover change data of the study area were examined, an increase of 251.75% with +13.290 km² was detected in the artificial surfaces class. It is seen that from the results, The results the study area is under intense urbanization pressure.

1. Introduction

Land cover change, which affects the natural resource value, is accepted as one of the most important environmental problems globally (Guan et al. 2011; Veldkamp and Lambin 2001; Arslan and Örcü 2019). With the increasing population and developing technology, the pressure on natural resources is increasing day by day. Identifying and interpreting the problems that arise with urban sprawl and taking the necessary precautions are important in terms of effective management and planning. Therefore, investigating the degree, causes and consequences of urban sprawl is very important for human life (Uyar and Ozturk 2019).

Urban growth is a complex socio-economic process that transforms the built environment and rural areas into urban settlements with the increasing population, and also shifts the spatial distribution of the population from rural areas to urban areas (BM 2019). Land cover, on the other hand, refers to the soil layer, including the natural vegetation covering the surface of the land, agricultural products and human structures (Verburg et al. 2009; Başara and Şişman 2022). The occurrence of urban growth triggers land use as cover changes.

In this study, temporal land cover changing in Atakum district of Samsun (Turkey) were investigated. Atakum district is located at 41°19'48.4176" North and 36°17'32.9172" East coordinates. Atakum district is 7

kilometers away from Samsun city center and located in border Black Sea (Fig. 1). Atakum district has a population of 238,732 people. Atakum district has undergone a great change in residential areas due to its long coastline, university potential and important transportation networks such as the tram line, which has an important place in urban transportation in recent years.

The study area, consisting of the central areas of Atakum district along the coast, was select as of 70,937 km². The study area map is given in Figure 1.



Figure 1. Location Map

* Corresponding Author

(aslancihatbasara@gmail.com) ORCID ID 0000 – 0001 – 6644 – 6097
(metabar@beu.edu.tr) ORCID ID 0000 – 0002 – 3234 – 5340
(sumgulsun@gmail.com) ORCID ID 0000 – 0001 – 5015 – 3636
(yysisman@omu.edu.tr) ORCID ID 0000 – 0002 – 6600 – 0623

Cite this study

Basara, A. C., N, Tabar, M. E., Gulsun, S., & Sisman, Y. (2022). Investigation of land cover change with GIS using CORINE data. 4th Intercontinental Geoinformation Days (IGD), 282-285, Tabriz, Iran

2. Material and Method

While the land use/cover does not change for many years in rural areas, on the contrary, in urban areas, significant changes can be seen about it due to the pressure created by rapid population growth. The regions where this change is most rapid and evident are urban development areas (Ozturk et al. 2010).

CORINE (Coordination of Information on the Environment) data was used to determine the land cover change. CORINE Land Cover (CLC) is a 1:100,000 scale land cover map for European Union (EU) member states and all partner countries. The project was initiated by the European Union Commission in 1985 and carried out by the Commission until 1990, during which an environmental information system was established (Bruttner et al. 2000). Source attributes of CORINE data is given in Table 1.

Table 1. CORINE Data Sources (Falt'an et al. 2020)

Dataset	Spatial Resolution	Source	Format
CLC1990	≤ 50m	Landsat-5 MSS/TM	Vector
CLC2000	≤ 25m	Landsat-7 ETM	Vector
CLC2006	≤ 25m	SPOT-4/5, IRS P6 LISS III	Vector
CLC2012	≤ 25m	IRS P6 LISS III, RapidEye	Vector
CLC2018	≤ 10m	Sentinel-2, Landsat-8	Vector

The standard European CLC nomenclature is hierarchical, including three levels of thematic detail in five major groups (Heymann et al. 1993): artificial surfaces, agricultural areas, forests and semi-natural areas, wetlands, water bodies.

Level-1 and Level-2 classes of CORINE land cover classes are given in Table 2.

Table 2. CORINE Land Classes (Uyuk et al. 2020)

Level-1	Level-2
1.Artificial Surfaces	1.1. Urban Fabric
	1.2. Industrial, commercial and transport units
	1.3. Mine, dump and construction sites
	1.4. Artificial, non-agricultural vegetated areas
2.Agricultural Areas	2.1. Arable land
	2.2. Permanent crops
	2.3. Pastures
	2.4. Heterogeneous agricultural areas
3.Forest and Semi Natural Areas	3.1. Forest
	3.2. Scrub and/or herbaceous associations
	3.3. Open spaces with little or no vegetation
4.Wetlands	4.1. Inland wetlands
	4.2. Marine wetlands
5.Water Bodies	5.1. Inland waters
	5.2. Marine waters

The aim of CLC-Change creating is to produce a map of real land cover changes describing an evolution process taking place in the environment (e.g., urban sprawl, forest clearcut). Changes should be interpreted regardless of their position (Fig. 2). Change polygons should: have size at least 5 ha, have width at least 100 m, describe a real evolution process that occurred between year old and year new, and be detectable on satellite images.

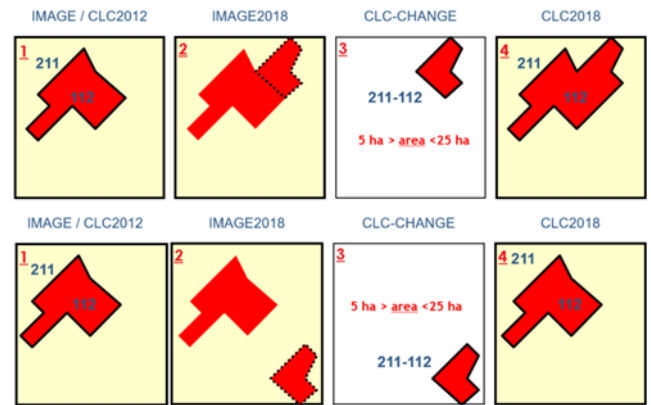


Figure 2. Consistent mapping of CLC Change

Upper row: growth of an existing settlement. Lower row: birth of a new (isolated) settlement

- First boxes in both rows show the land cover status visible on IMAGE2012 and the polygon outlines in CLC2012 database.

- Second boxes show the land cover status visible on IMAGE2018 without polygon boundaries. Dashed outline marks patches that have changed.

- Third boxes show polygons to be drawn in the CLC-Change database.

- Fourth boxes show the polygons as present in CLC2018 database (as the results of GIS addition of CLC2012 and CLC-Change 2012-2018 (CORINE 2021)).

Geographic Information System is important for collecting and processing geographic data of objects. Transforming data into geographic information with geographic analysis and viewing geographic data helps to plan activities (Başara et al. 2021). GIS software was used as a method in examining the land cover change. “Zonal toolset” and “Tabulate Area” analysis was performed from the “Spatial Analyst toolbox” menu of ArcGIS software. Calculates cross-tabulated areas between two datasets and outputs a table (Fig. 3). Land cover maps of the years 1990, 2000, 2006, 2012, 2018 were processed in accordance with the study area.

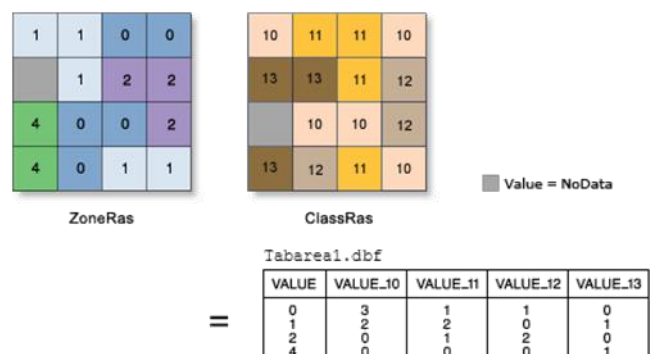


Figure 3. Tabulate Area Illustration

3. Results

Artificial surfaces, agricultural areas, forest and semi natural areas, wetlands and water bodies classes are mapped using Level-1. The produced maps were analyzed as areal and percentage. Land cover maps Fig. 4-8 and their areal distributions are given in Table 3-7.

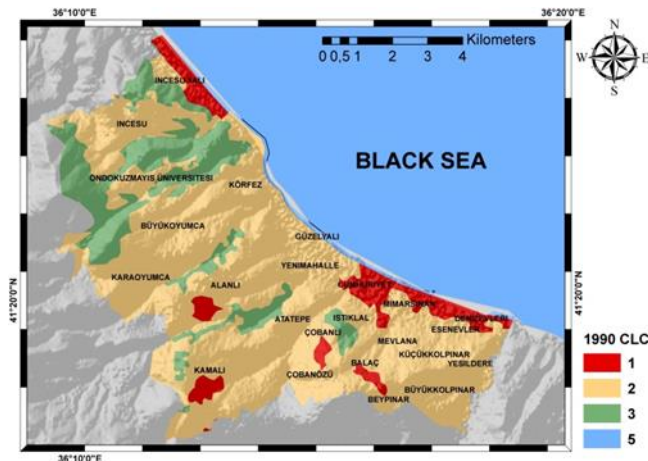


Figure 4. CORINE Land Cover Map of 1990

When the land cover data of 1990 were examined, wetlands class was not found. Artificial surfaces class is 7.44% with 5,279 km²; agricultural areas class is 52.076 km² with 73.41%; forest and semi natural areas class with 12,475 km², 17.59%; the water bodies class covers an area of 1,108 km² and with 1.56%.

Table 3. Distribution of CORINE Land Cover in 1990

Land Cover	Area (km ²)	Percent (%)
1.Artificial Surfaces	5,279	7,44
2.Agricultural Areas	52,076	73,41
3.Forest and Semi Natural Areas	12,475	17,59
4.Wetlands	0,000	0,00
5.Water Bodies	1,108	1,56

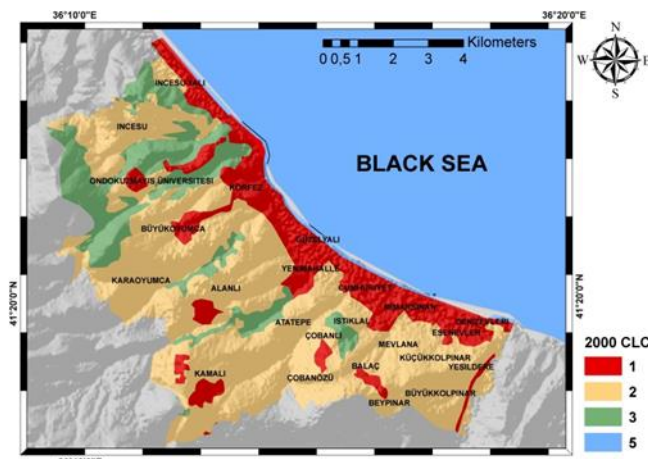


Figure 5. CORINE Land Cover Map of 2000

When the land cover data of 2000 were examined, artificial surfaces class is 19.28% with 13,677 km²; agricultural areas class is 44.261 km² with 62.39%; forest and semi natural areas class is 16.76% with 11,892 km²; the water bodies and wetlands classes is the same in 1990.

Table 4. Distribution of CORINE Land Cover in 2000

Land Cover	Area (km ²)	Percent (%)
1.Artificial Surfaces	13,677	19,28
2.Agricultural Areas	44,261	62,39
3.Forest and Semi Natural Areas	11,892	16,76
4.Wetlands	0,000	0,00
5.Water Bodies	1,108	1,56



Figure 6. CORINE Land Cover Map of 2006

When the land cover data of 2006 were examined, artificial surfaces class is 19.28% with 13,679 km²; agricultural areas class is 44,267 km² with 62,40%; forest and semi natural areas class 11,881 km² with 16.75%; the water bodies and wetlands classes is the same in 1990 and 2000.

Table 5. Distribution of CORINE Land Cover in 2006

Land Cover	Area (km ²)	Percent (%)
1.Artificial Surfaces	13,679	19,28
2.Agricultural Areas	44,267	62,40
3.Forest and Semi Natural Areas	11,881	16,75
4.Wetlands	0,000	0,00
5.Water Bodies	1,110	1,56

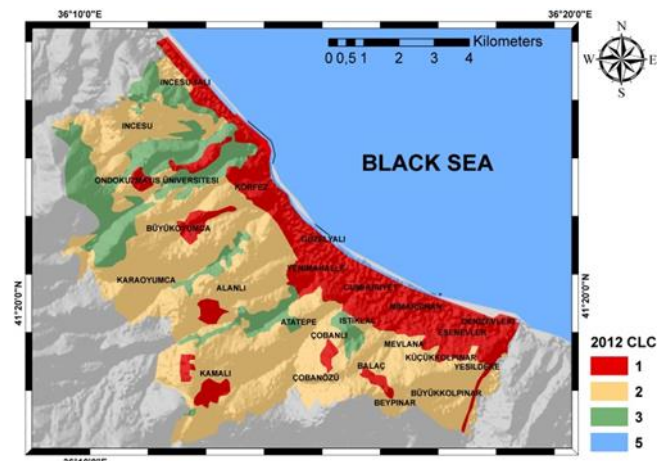


Figure 7. CORINE Land Cover Map of 2012

When the land cover data of 2012 were examined, artificial surfaces class is 23.95% with 16,987 km²; agricultural areas class is 40.865 km² with 57.61%; forest and semi natural areas class 12,114 km² with 17.08%; the water bodies class covers an area of 0.971 km² and 1.37% and the wetlands class is the same in 1990, 2000 and 2006.

Table 6. Distribution of CORINE Land Cover in 2012

Land Cover	Area (km ²)	Percent (%)
1.Artificial Surfaces	16,987	23,95
2.Agricultural Areas	40,865	57,61
3.Forest and Semi Natural Areas	12,114	17,08
4.Wetlands	0,000	0,00
5.Water Bodies	0,971	1,37



Figure 8. CORINE Land Cover Map of 2018

When the 2018 land cover data were examined, artificial surfaces class is 26.18% with 18,569 km²; agricultural areas class is 39,283 km² with 55.38%; forest and semi natural areas class 12,127 km² with 17.10%; the water bodies and wetlands classes are nearly the same the others.

Table 7. Distribution of CORINE Land Cover in 2018

Land Cover	Area (km ²)	Percent (%)
1.Artificial Surfaces	18,569	26,18
2.Agricultural Areas	39,283	55,38
3.Forest and Semi Natural Areas	12,127	17,10
4.Wetlands	0,000	0,00
5.Water Bodies	0,958	1,35

4. Discussion and Conclusion

Within the scope of this study, the urban sprawl and land cover change of Atakum district were examined using CORINE data (Table 5). Wetlands class was not found in the study area between 1990-2018. When the land cover change data is examined, an increase of 251.75% with 13,290 km² in the artificial surfaces class; A decrease of 12,793 km² and 24.57% in the agricultural areas class; a decrease of 0.347 km² and 2.78% in the forest and semi natural areas class; A decrease of 0.149 km² and 13.49% was detected in the water bodies class. The results obtained showed that the study area is under intense urbanization pressure.

Table 8. Difference Between 1990-2018

Land Cover	Difference (km ²)	Ratio (%)
1.Artificial Surfaces	+13,290	+251,75
2.Agricultural Areas	-12,793	-24,57
3.Forest and Semi Natural Areas	-0,347	-2,78
4.Wetlands	0,000	0,00
5.Water Bodies	-0,149	-13,49

Monitoring and interpreting urban changes and taking necessary precautions are of great importance for the city's developments. In this way, it will be possible to prevent environmental problems. Changes in the land cover should be examined periodically. The urban areas changing, agricultural areas, forest areas and water resources is important for planning activities. Examination of the factors that cause urban sprawl and

the consequences are among the important research topics today.

References

- Arslan, E. S., & Özücü, Ö. K. (2019). Bodrum İlçesi'nin 1990-2018 Yılları Arasındaki Arazi Örtüsü Değişimi. Mimarlık, Planlama ve Tasarım Alanında Araştırma Makaleleri (pp.181-198), Ankara: Gece Akademi.
- Başara, A. C., Tabar, M. E., & Şişman, Y. (2021). Landslide Susceptibility Mapping of Samsun (Turkey) Province Using Frequency Ratio and AHP Methods. Türkiye Coğrafi Bilgi Sistemleri Dergisi, 3 (1), 24-30.
- Başara, A. C., & Şişman, Y. (2022). Frekans oranı, kanıt ağırlığı ve lojistik regresyon yöntemleri kullanılarak heyelan duyarlılık haritalarının CBS tabanlı karşılaştırılması. Niğde Ömer Halisdemir Üniversitesi Mühendislik Bilimleri Dergisi. <https://doi.org/10.28948/ngumuh.1065284>
- BM (2019). World Urbanization Prospects: The 2018 Revision. <https://doi.org/10.18356/b9e995fe-en>
- Buttner, G., Steenmans, C., Bossard, M., Feranec, J., & Kolar, J. (2000). Land Cover - Land use mapping within the European CORINE programme. Remote Sensing for Environmental Data in Albania: A Strategy for Integrated Management, 72, 89-100.
- CORINE (2021). CORINE Land Cover Product User Manual. European Environment Agency (EEA) Kongens Nytorv 6 – 1050 Copenhagen K. – Denmark.
- Faltan, V., Petrovič, F., O'ahel', J., Feranec, J., Druga, M., Hruška, M., & Mechurová, V. (2020). Comparison of CORINE Land Cover Data with National Statistics and the Possibility to Record This Data on a Local Scale—Case Studies from Slovakia. Remote Sensing, 12(15), 2484.
- Guan, D., Li, H., Inohae, T., Su, W., Nagaie, T., & Hokao, K. (2011). Modeling urban land use change by the integration of cellular automaton and Markov model. Ecological Modelling, 222(20-22), 3761-3772.
- Heymann, Y., Steenmans, C., Croiselle, G., & Bossard, M. (1993). CORINE land cover technical guide. European Commission, CECA-CEE-CEEA, Brussels, Luxembourg.
- Öztürk, D., Şişman, A., Maraş, E. E., & Şişman, Y. (2010). Samsun-Atakum'da arazi kullanımı/arazi örtüsündeki değişimlerin uzaktan algılama ve CBS ile belirlenmesi. VI. Ulusal Coğrafya Sempozyumu, 1, 21-29.
- Uyar, A., & Öztürk, D. (2019). Fraktal Analiz Kullanılarak Arnavutköy'ün Kentsel Yayılma Özelliklerinin Zamansal Değişiminin İncelenmesi. Teknik Bilimler Dergisi, Teknik Bilimler E - Dergisi, 28-31. <https://doi.org/10.35354/tbed.516116>.
- Üyük, A., Uzun, A., & Çardak, Ç. (2020). CORINE Verileri ile Değişim Analizi, Denizli İli Örneği. Türkiye Peyzaj Araştırmaları Dergisi, 3 (2), 97-107.
- Verburg, P. H., Van de Steeg, J., Veldkamp, A., & Willemen, L. (2009). From land cover change to land function dynamics: A major challenge to improve land characterization. Journal of Environmental Management. 90(3), 1327-1335.
- Veldkamp, A. & Lambin, E. F. (2001). Predicting land-use change. In: Elsevier.

4th Intercontinental Geoinformation Days

igd.mersin.edu.tr



Fire vulnerability of Hyrcanian forests (FVHF): A conceptual framework for an enhanced forest fire risk management in northern Iran

Elnaz Nejatiyanpour ^{1,2}, Omid Ghorbanzadeh ³, Josef Strobl ², Mahmoud Daneshvar Kakhki ¹, Hamid Amirnezhad ⁴, Mahmoud Sabouhi Sabouni^{*1}

¹Ferdowsi university of Mashhad, Faculty of Agriculture, Department of Agricultural Economics, Mashhad, Iran

²University of Salzburg, Department of Geoinformatics—Z_GIS, 5020 Salzburg, Austria

³Institute of Advanced Research in Artificial Intelligence (IARAI), Landstraßer Hauptstraße 5, 1030 Vienna, Austria

⁴Sari Agricultural Sciences and Natural Resources University, Faculty of Agricultural Engineering, Department of Agricultural Economics, Sari, Iran

Keywords

GIS
Forest fire vulnerability
Socio-economic indicators
Adaptive capacity index
Exposure index

Abstract

Recently, increasing forest fires have contributed to deforestation and desertification in the Hyrcanian forests in northern Iran. It is crucial to consider the complex interactions of forest fires with particularities of the environment and the social and economic factors. This study introduces a conceptual approach to developing a comprehensive forest fire vulnerability index using both quantitative and qualitative methods. The indicators can be grouped into the three components of vulnerability (exposure, sensitivity, and adaptive capacity) based on three categories (social, economic, and environmental), resulting in three indexes: Forest Fire Exposure Index (FEI), Forest Fire Sensitivity Index (FSI) and Forest Fire Adaptive Capacity Index (FACI). Finally, we can create an integrated Forest Fire Vulnerability Index (FVI). The most vulnerable areas to forest fires can be mapped using remote sensing data, geographic information systems (GIS), the statistical data available at the Forests, Range & Watershed Management Organization (FRWO), and machine learning models. By localizing the input data and socio-economic indicators, the methodology is transferrable to other regions and helps forest fire management and prevention planning.

1. Introduction

Forest fires are a natural hazard that can begin and spread immediately and uncontrollably, causing significant losses and damages (Piralilou et al., 2022). In general, natural reasons such as lightning cause just around 4% of forest fires worldwide. In all other cases, forest fires result from human action, whether it is intentional or unintentional (Peter Hirschberger, 2016). Forest fires are not only an environmental problem but also have significant economic and social impacts, affect the quantity and quality of the forest's goods and services, and create a considerable problem related to both private owners for revenue damage and public owners for ecosystem service damage (Fagarazzi et al., 2021; Gonzalez-Caban, 2007). The forest fire also affects

urban areas, infrastructure networks, power lines, agricultural regions, and civic society. People can lose their lives or become ill, and communities can suffer from decreased well-being and economic decline due to forest fires (Mavsar et al., 2010). Moreover, both residential neighborhoods and the tourism industry are negatively impacted by forest fires. In the Western Region United States, the primary fire season intercepts the peak summer tourist season and becomes a significant problem for the demand and supply of tourism sectors (Brown et al., 2008; Thapa et al., 2013). For instance, wildfires are an annual concern in Florida, affecting residents and visitors. In addition to Colorado, a tourism-dependent city, Mesa Verde National Park, a popular tourist destination, was closed because of the forest fire. Similar impacts have been seen in California, Arizona,

* Corresponding Author

(nejatiyanpour84@mail.um.ac.ir) ORCID ID 0000-0001-5539-3882
(omid.ghorbanzadeh@iarai.ac.at) ORCID ID 0000-0002-9664-8770
(Josef.Strobl@sbg.ac.at) ORCID ID 0000-0001-6234-9812
(daneshvar@um.ac.ir) ORCID ID 0000-0003-3063-3418
(h.amirnezhad@sanru.ac.ir) ORCID ID 0000-0002-4307-1146
(sabouhi@um.ac.ir) ORCID ID 0000-0002-0454-0368

Cite this study

Nejatiyanpour, E., Ghorbanzadeh, O., Strobl, J., Kakhki, M. D., Amirnezhad, H., & Sabouni, M. S. (2022). Fire vulnerability of Hyrcanian forests (FVHF): A conceptual framework for an enhanced forest fire risk management in northern Iran. 4th Intercontinental Geoinformation Days (IGD), 286-289, Tabriz, Iran

Nevada, New Mexico, Texas, Washington, and Utah (Thapa et al., 2013).

Also, In Europe, the economic losses of forest fires in the 2000-2017 period are over EUR 54 billion, around EUR 3 billion. For example, the Tuscan Region (Central Italy) spends around 12 million euros on forest fire prevention and control every year (Vicarò & Caniani, 2019). The economic effect on Greece, Spain, France, Italy, and Portugal may increase to over EUR 5 billion per year by 2070-2100 due to rapid economic growth and increased greenhouse gas emissions (Rego et al., 2018).

Therefore, the socio-economic impacts of forest fires should be evaluated as an essential part of the fire risk assessment, forest fire policy development, and management practices planning and implementation (Morton et al., 2003). And the climate, environmental, and ecological factors aren't the only factors to consider for prevention and mitigation efforts in wildfire-prone areas (de Diego et al., 2019). Despite the importance of socio-economic factors on forest fire vulnerability for budget optimization and decision-making, few studies explicitly examined socio-economic factors mixed with environmental factors.

Furthermore, a lot of research has been conducted to determine socio-economic vulnerability. The IPCC's concept and framework of vulnerability were often used as the basis for their evaluations, where vulnerability is defined by exposure, sensitivity to perturbations or external pressures, and the capacity to adjust or adapt (Adger, 2006; Sharma & Ravindranath, 2019) (see Figure 1).

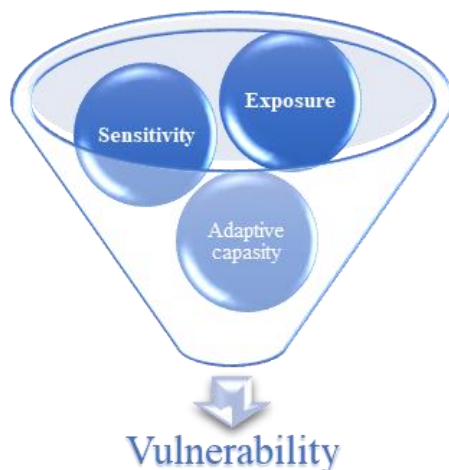


Figure 1. The concept of vulnerability

Where, exposure is the nature and the degree to which a system is pressured by environmental or sociopolitical factors. Sensitivity is how a system is modified or impacted by perturbations. Adaptive capacity is the ability of a system to evolve in order to accept environmental threats or policy changes, as well as to increase the range of variability with which it can adapt (Adger, 2006). This vulnerability concept has been used in the vulnerability to heat-related phenomena (Grigorescu et al., 2021). In contrast, this framework of vulnerability in forest fire vulnerability is less addressed.

The novelty of our study is developing a comprehensive Forest Fire Vulnerability Index (FVI) based on three main components of vulnerability and creating the Forest Fire Exposure Index (FEI), Forest Fire Sensitivity Index (FSI), and Forest Fire Adaptive Capacity Index (FACI) considering three categories; social, economic, and environmental factors, as well as producing the final forest fire vulnerability map.

2. Method

2.1. Study area

The Hyrcanian Forests World Heritage property stretch 850 km along the southern coast of the Caspian Sea and covers around 7% of remnant Hyrcanian forests in Iran (Figure 2). These ancient forests are important refugia and the world's only remaining temperate deciduous broadleaved forests Ramezani et al., 2008).

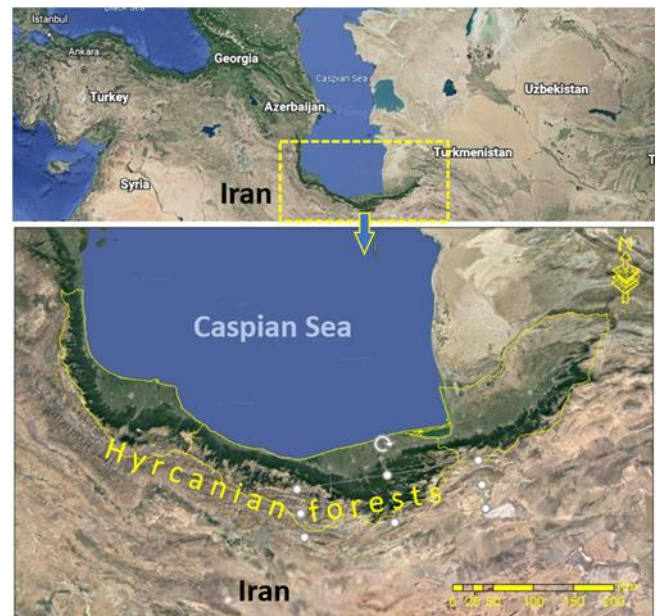


Figure 2. The Hyrcanian Forests in Iran

In the northern part of Iran, most forest fires happen on the ground surface and mainly damage young trees (Jahdi et al., 2014). As a result, regeneration is seriously impacted, and forest fires are among the most common causes of deforestation and desertification in Iran (Ghorbanzadeh et al., 2019). Although forest fires frequently happen in the Hyrcanian forests of Iran (Ghorbanzadeh et al., 2019) and have caused enormous economic and ecological losses (Adab et al., 2021). There is not a comprehensive study about fire forest vulnerability considering socio-economic and environmental factors. It is appropriate and necessary to analyze the forest fire vulnerability of the Hyrcanian forest.

2.2. Research methods

Using an empirical approach, the current study assesses socio-economic and environmental forest fire vulnerability. The indicators are chosen and ranked based on their relevance to forest fires, expert judgment, and database availability and accuracy. We consider the

various characteristics of vulnerability components to index construction. For instance, wildfires are caused by a combination of social and economic factors with natural factors (de Diego et al., 2021). Accordingly, these factors must be considered in indexing forest fire exposure. Furthermore, economic and environmental factors increase the vulnerability to the impacts of hazards (de Diego et al., 2019). Therefore, sensitivity and adaptive capacity, two other vulnerability components, are the characteristic determined by these factors (see Figure 3).

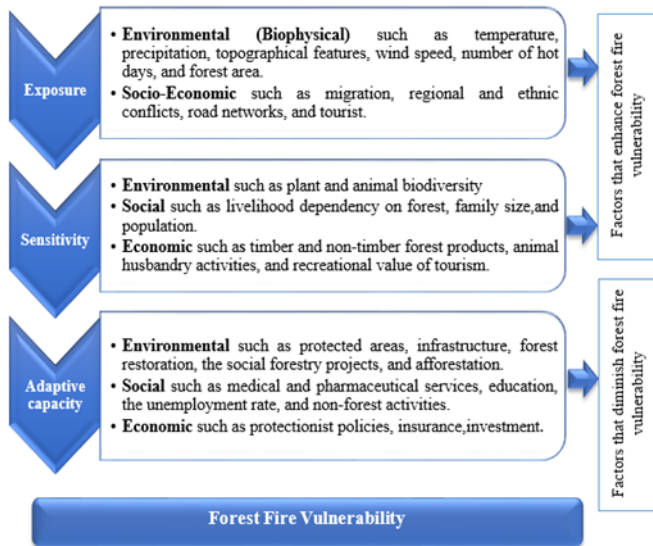


Figure 3. Framework for assessing the forest fire vulnerability

The current methodology may be applied to any region damaged by forest fires. The statistical data used in the current research, remote sensing data, geographic information systems (GIS), and the statistical data available at the Forests, Range & Watershed Management Organization (FRWO). The FVI was developed over a multi-stage sequential process that involved:

2.2.1. Selection of indicators

The indicators have been considered to investigate the various components of forest fire vulnerability. For the current study, the selected indicators are based on the previous studies approaching the general issues of natural hazards vulnerability (Grigorescu et al., 2021;) or fire forest vulnerability studies (Sadowska et al., 2021) in particular. The validation of indicators can be made using the expert judgment approach.

2.2.2. Data normalization

Because the variables of the statistical indicators are generated using various measuring units, this is an essential process.

2.2.3. Integrating the indexes into a single index

Develop a comprehensive forest fire vulnerability index by combining the Forest Fire Exposure Index (FEI),

Forest Fire Sensitivity Index (FSI), and Forest Fire Adaptive Capacity Index (FACI).

$$FVI = f(FEI, FSI, FACI)$$

2.2.4. Forest fire vulnerability mapping

Machine learning (ML) approaches can use for mapping the forest fire vulnerability of the Hyrcanian forest. Machine learning approaches have been applied to analyze natural disasters during the last two decades (Ghorbanzadeh et al., 2019).

3. Results

The spatial prediction of forest fire vulnerability for Heyrcanian can be made using state of the art ML approaches by applying the relevant conditioning factors, and the fire inventory data set. The resulting forest fire vulnerability maps measure the probability of a wildfire occurrence. Also, considering economic analysis as an integral part of proactive fire forests management leads to better-informed decisions and selecting the most effective options in a particular circumstance. Moreover, forest fire risk mapping is used for identifying locations in which a probability of loss is determined from assessments of socio-economic forest fire vulnerability.

4. Discussion

The development of an integral vulnerability index is defective without considering economic factors. We introduce a novel framework for fire forest vulnerability based on three groups of factors (socio-economic and environmental) by considering exposure, sensitivity, and adaptive capacity as vulnerability components. The results of our study by assessments of socio-economic forest fire vulnerability can help policymakers with forest fire management and lead to making better-informed decisions and selecting the most effective options in a particular circumstance. Additionally, the final forest fire vulnerability map can be used to identify areas with a high probability of loss and require prevention planning.

5. Conclusion

The current methodology for developing the FVI based on three main components of vulnerability and considering social, economic, and environmental factors is transferrable to other regions where localizing the input data may be applied to any region damaged by wildfire.

Acknowledgement

The authors are grateful for the support of the University of Salzburg, and the Institute of Advanced Research in Artificial Intelligence (IARAI) GmbH, Vienna, Austria.

References

- Adab, H., Kanniah, K. D., & Solaimani, K. (2021). Remote sensing-based operational modeling of fuel ignitability in Hyrcanian mixed forest, Iran. *Natural Hazards*, 108(1), 253–283. <https://doi.org/10.1007/s11069-021-04678-w>
- Adger, W. N. (2006). Vulnerability. *Global Environmental Change*, 16(3), 268–281. <https://doi.org/10.1016/j.gloenvcha.2006.02.006>
- Brown, R. N. K., Rosenberger, R. S., Kline, J. D., Hall, T. E., & Needham, M. D. (2008). Visitor preferences for managing wilderness recreation after wildfire. *Journal of Forestry*, 106(1).
- de Diego, J., Rúa, A., & Fernández, M. (2019). Designing a Model to Display the Relation between Social Vulnerability and Anthropogenic Risk of Wildfires in Galicia, Spain. *Urban Science*, 3(1). <https://doi.org/10.3390/urbansci3010032>
- de Diego, J., Rúa, A., & Fernández, M. (2021). Vulnerability variables and their effect on wildfires in galicia (Spain). a panel data analysis. *Land*, 10(10). <https://doi.org/10.3390/land10101004>
- Fagarazzi, C., Fratini, R., Montanino, M., Viccaro, M., Cozzi, M., Romano, S., & Riccioli, F. (2021). The economic value of fire damages in Tuscan agroforestry areas. *IForest*, 14(1), 41–47. <https://doi.org/10.3832/ifor3607-013>
- Ghorbanzadeh, O., Blaschke, T., Gholamnia, K., & Aryal, J. (2019). Forest fire susceptibility and risk mapping using social/infrastructural vulnerability and environmental variables. *Fire*, 2(3). <https://doi.org/10.3390/fire2030050>
- Gonzalez-Caban, A. (2007). Wildland Fire Management Policy and Fire Management Economic Efficiency in the USDA Forest Service. IV International Wildland Fire Conference, May.
- Grigorescu, I., Mocanu, I., Mitrică, B., Dumitrașcu, M., Dumitrică, C., & Dragotă, C. S. (2021). Socio-economic and environmental vulnerability to heat-related phenomena in Bucharest metropolitan area. *Environmental Research*, 192. <https://doi.org/10.1016/j.envres.2020.110268>
- Jahdi, R., Darvishsefat, A. A., Etemad, V., & Mostafavi, M. A. (2014). Wind effect on wildfire and simulation of its spread (Case study: Siahkal forest in northern Iran). *Journal of Agricultural Science and Technology*, 16(5).
- Mavsar, R., González-Cabán, A., & Farrera, V. (2010). The importance of economics in fire management analysis (J. Sande Silva, F. Rego, P. Fernandez, & E. Rigolot, Eds.). European Forest Institute.
- Morton, D. C., Roessing, M. E., Camp, A. E., & Tyrrell, M. L. (2003). Assessing the Environmental, Social, and Economic Impacts of Wildfire. www.yale.edu/gisf
- Peter Hirschberger, 4con forestconsulting, www.forestconsulting.de. (2016). 2017 STUDY FORESTS ABLAZE Causes and effects of global forest fires. www.forestconsulting.de
- Piralilou, S. T., Einali, G., Ghorbanzadeh, O., Nachappa, T. G., Gholamnia, K., Blaschke, T., & Ghamisi, P. (2022). A Google Earth Engine Approach for Wildfire Susceptibility Prediction Fusion with Remote Sensing Data of Different Spatial Resolutions. *Remote Sensing*, 14(3). <https://doi.org/10.3390/rs14030672>
- Ramezani, E., Marvie Mohadjer, M. R., Knapp, H. D., Ahmadi, H., & Joosten, H. (2008). The late-Holocene vegetation history of the Central Caspian (Hyrcanian) forests of northern Iran. *Holocene*, 18(2). <https://doi.org/10.1177/0959683607086768>
- Rego, F. M. C. C., Manuel Moreno, J., Vallejo Calzada, V. R., & Xanthopoulos, G. (2018). FOREST FIRES — Sparking firesmart policies in the EU. European Commission. <https://doi.org/10.2777/248004>
- Sadowska, B., Grzegorz, Z., & Stępnicka, N. (2021). Forest fires and losses caused by fires – an economic approach. *WSEAS Transactions on Environment and Development*, 17, 181–191. <https://doi.org/10.37394/232015.2021.17.18>
- Thapa, B., Cahyanto, I., Holland, S. M., & Absher, J. D. (2013). Wildfires and tourist behaviors in Florida. *Tourism Management*, 36. <https://doi.org/10.1016/j.tourman.2012.10.011>
- Viccaro, M., & Caniani, D. (2019). Forest, Agriculture, and Environmental Protection as Path to Sustainable Development. In *Natural Resources Research* (Vol. 28). <https://doi.org/10.1007/s11053-019-09497-2>



4th Intercontinental Geoinformation Days

igd.mersin.edu.tr



A correlation study for determination risk area of dengue fever and dengue hemorrhagic fever: a case study of Sisaket province, Thailand

Nutchanon Chantapoh *¹

¹ Wuhan University, The State Key Laboratory of Information Engineering in Surveying, Mapping and Remote Sensing (LIESMARS), Wuhan, Hubei, China

Keywords

GIS
Dengue fever
Correlation

Abstract

This study has purpose on analyzing dengue fever and dengue hemorrhagic fever (DF/DHF) risk zone area in Sisaket province, Thailand, by using the subdistrict-level (Tumbon) data in sick ratio, average temperature, maximum temperature, minimum temperature, relative humidity, precipitation, population density, and housing density. The meteorological data are acquired from POWER, NASA. The data is stored in points, gridding by 30 minutes of latitude and longitude, going through the inverse distance weighting tool to interpolate the meteorological data into each Tumbon. The physical socio data are from government authority, are population from each Tumbon by monthly and housing amount from each Tumbon by yearly. Correlation analysis is used to find the correlation between sick ratio and other variables to find the risk area in the study area. Hot spots analysis (Getis ord-Gi*) is used to find the clustering area of sick ratio among each Tumbon. Results are classified into cluster maps and risk zone maps, each by yearly and monthly.

1. Introduction

Thailand had first case of DF/DHF in 1949 and a widespread epidemic in 1958 in Bangkok and Thonburi area. Since 1958, the trend of infection increases and has many forms such as every other year, 2 years then stop for 1 or every 2 years. Most of patients are 0-14 years old, with most fatal symptoms in 5-9 years old. DF/DHF cases could be found along the year, yet the highest months are in rainy season (May-August) (Insects, 2019) The effects of DF/DHF could lead to radical complications. Some patients are suffered from failure of circulatory system, shocking from leaking of plasma. Without correct medical treatment, the patient might be death in 12-24 hours. GIS helps increasing the efficiency of preventive process and cover the correct areas, deescalating the infection and death rates. The benefits from applying GIS and statistical analysis to study about the diseases can be presented to relevant agencies such as provincial public health center and hospitals.

2. Method

The patient's data from public health agency of Sisaket province, Thailand. from 2010 – 2019 The data stored in spreadsheet with headers consisting of age, gender, DF or DHF, defined date, Amphoe (district), Tumbon (subdistrict), and result of treatment (recover/dead). The data is acquired from Sisaket's public health office, ministry of public health. Population and housing data is acquired from department of provincial administration (DOPA), Ministry of Interior. Meteorological data (temperature, relative humidity, precipitation) is acquired from prediction of worldwide energy resources project (POWER), National Aeronautics and Space Administration (NASA). The used tools are ArcMap 10.5 (Hotspots Analysis (Getis-Ord Gi*), Inverse Distance Weight (IDW), Zonal Statistics as Table), JASP 0.15 (Pearson's correlation analysis), and Microsoft Excel.

* Corresponding Author

*(neononny@gmail.com) ORCID ID 0000-0002-1113-769X

Cite this study

Chantapoh, N. (2022). A correlation study for determination risk area of dengue fever and dengue hemorrhagic fever: a case study of Sisaket province, Thailand. 4th Intercontinental Geoinformation Days (IGD), 290-293, Tabriz, Iran

2.1. DF/DHF in Sisaket, 2010 – 2019.

The DF/DHF data is classified into 2 forms for separate results: yearly correlation, monthly correlation. Yearly data is the summarized number of DF/DHF incidence cases through each year in the province, and monthly data is summarized number of the disease's incidence cases through each month from studied years.

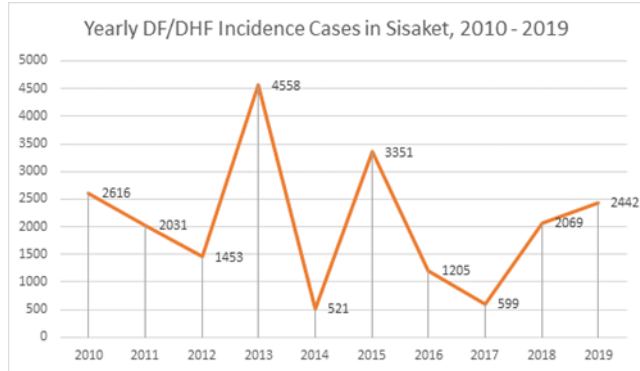


Figure 1. Yearly DF/DHF Incidence Cases in Sisaket, 2010 – 2019

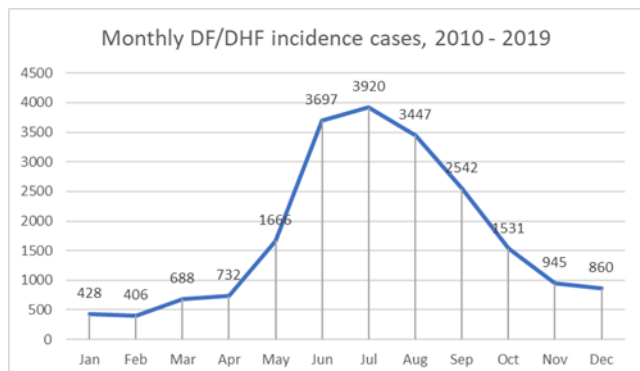


Figure 2. Monthly DF/DHF Incidence Cases in Sisaket, 2010 – 2019

2.2. Correlation Analysis

Correlation (Pearson's) tells if variables are positively related (they move in the same direction) or negatively correlated (they move in opposing directions).

$$r = \frac{n(\sum xy) - (\sum x)(\sum y)}{\sqrt{(n\sum x^2 - (\sum x)^2)(n\sum y^2 - (\sum y)^2)}}$$

r = r value (how much the data correlated, 1 is the highest)

x = variable 1 value (variables)

y = variable 2 value (sick ratio)

Insert variables: sick ratio, average temperature, maximum temperature (average), minimum temperature (average), relative humidity (average), precipitation amount (total/average), housing density.

2.2.1. Rating of variables' values

Rating by define the effect of each variable, 1 is for the lowest effect and 4 is for the highest effect. Find the mean value of entire data (\bar{x}) and its Standard Deviation (S.D.).

Table 1. Variables' values rating definition

Rating	Observed Value
4	More than $\bar{x} + 1$ S.D.
3	Between \bar{x} and less than $\bar{x} + 1$ S.D.
2	Less than \bar{x} but more than $\bar{x} - 1$ S.D.
1	Less than $\bar{x} - 1$ S.D.

3. Results

Analyze every variable by weighting and rating, the more affected factors will be defined with more score.

Weighting by adjust relation value (r value) out from negative value. Author used the lowest r value (in positive numeric) multiply by 2 and add to all

r value. Then, is to adjust the summarized into 1 by ratio. Spatially analyze risk area by multiply weight with rate, carried out the risk score for each Tumbon. Define class intervals by dividing the data range between maximum and minimum data with desired amount of class.

$$\text{Class Interval} = \frac{\text{Data}_{\max} - \text{Data}_{\min}}{\text{Amount of class}}$$

Table 2. Pearson's yearly correlation

Variable	r value	p value	n
Population	-0.015	0.503	2060
Avg. Temp.	0.006	0.795	
Max Temp.	0.169	< .001	
Min Temp	0.131	< .001	
Humidity	-0.229	< .001	
Precipitation	-0.11	< .001	
Housing	0.022	0.321	

Table 3. Pearson's monthly correlation

Variable	r value	p value	n
Population	-0.015	0.45	2472
Avg. Temp.	-0.088	< .001	
Max Temp.	-0.416	< .001	
Min Temp.	0.515	< .001	
Humidity	0.561	< .001	
Precipitation	0.658	< .001	

Results are fully displayed in risk zone maps by years 2010 – 2019 and by months from studied years. The example figures (figure 3 and figure 4) show the comparison between the years and months with the highest sick ratio with the lowest.

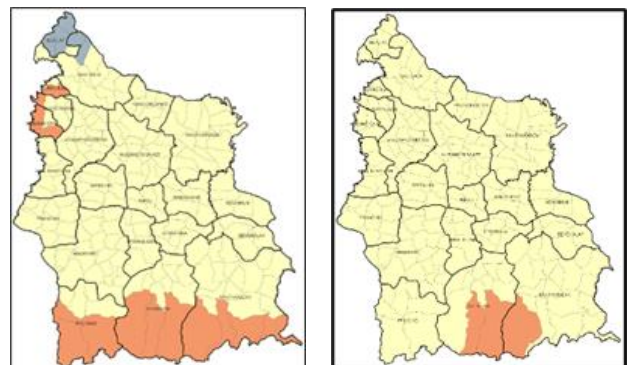


Figure 3. (From left to right) Risk zone maps of 2013, 2014

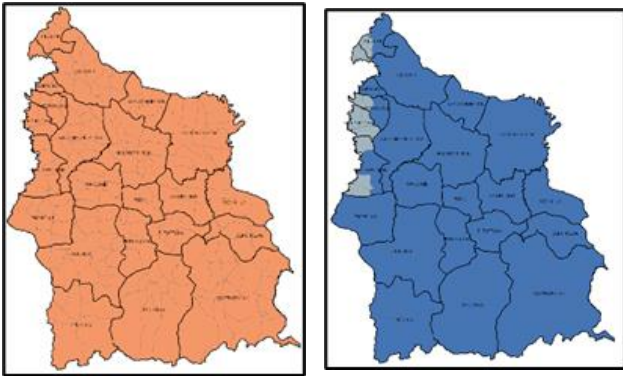


Figure 4. (From left to right) Risk zone maps of July, January

Table 4. Correlation between yearly sick ratio and risk score

Year	Sick Ratio	Average Risk Score	r score	p value
2010	179.82	2.6210	0.213	0.554
2011	139.86	1.7005		
2012	99.63	2.7474		
2013	311.76	2.5663		
2014	35.56	2.4568		
2015	228.15	2.6981		
2016	81.95	2.6843		
2017	40.69	2.1679		
2018	140.46	2.1174		
2019	165.8	3.3073		

Table 5. Correlation between monthly sick ratio and risk score

Month	Sick Ratio	Average Risk Score	r score	p value
Jan	28.2	1.5508	0.799	0.002
Feb	27.98	1.5076		
Mar	46.97	2.1720		
Apr	50.14	2.4219		
May	112.64	3.3879		
Jun	252.43	3.1727		
Jul	266.21	3.0612		
Aug	231.39	3.2425		
Sep	168.43	3.2425		
Oct	100.39	2.1813		
Nov	61.29	2.1204		
Dec	53.96	1.3356		

4. Discussion

The study of correlation and estimate risk area of DF/DHF by gathering data from agencies, has purpose for find relationship between factors and produce risk zone maps of Sisaket province. The studied data is 10-year long (2010 – 2019), is the DF/DHF incidence cases, had defined the factor that might cause the diseases. There are 6 variables involve in the study which are population density, average temperature, average maximum temperature, average minimum temperature, precipitation amount, and housing density (in monthly analysis used average precipitation instead of total amount and have no monthly housing density). For Tambon (subdistrict) level, the meteorological data might not have wide range and much difference. The estimation from geoinformatics tools is not exactly

accurate, unless the data are physically acquired from local area.

For statistical analysis results, yearly analyzing gave average maximum and minimum temperature 16.9% and 13.1% significantly positive correlate ($p < 0.001$), as well as average relative humidity and precipitation 22.9% and 11% significantly negative correlate. Meanwhile, monthly analyzing gives average temperature and maximum temperature significantly negative correlate with 8.8% and 41.6%, while average minimum temperature, relative humidity and precipitation are significantly positive correlate with 51.5%, 56.1%, and 65.8%. ($p < 0.001$). The results obviously show that monthly study provide stronger statistical correlations more than annually study. Moreover, the average risk scores show that the monthly study also provide more correlation than yearly study (79.9% and 21.3%, monthly and yearly).

5. Conclusion

The yearly correlation results in positive with maximum and minimum temperature and negative with relative humidity and precipitation, which all factor's trends are rising each year. Positive correlation r values are 16.9% and 13.1% and negative correlation r values are 22.9% and 11%. This phenomenon could lead to decrease of DF/DHF sick rate.

The monthly correlation show that maximum temperature and minimum temperature are respectively negative and positive correlated. This could lead to find the suitable temperature range for DF/DHF incidence. Moreover, the relative humidity and precipitation are both strongly positive correlated, summarizing that seasonal meteorological data are suited for study the correlation with the diseases. The most affected variables are precipitation, relative humidity, minimum temperature, and maximum temperature (negative correlated) respectively. These factors are more than 40% correlated with the sick ratio.

The monthly risk zone maps (which provide significant correlation with sick ratio) show that through the year, DF/DHF are riskier in the southern part of the studied area, Sisaket province. PHU SING, KHUN HAN, and KANTHARALAK Amphoes are the 3 Amphoes located in the south of the province, northern to the Thai-Cambodian border with a vast area of mountain forest. The study of correlation in monthly summarization provides more correlative results than yearly study. The office of provincial public health should consider in providing more density measurements in prevention and healthcare facilities.

Acknowledgement

I would like to express my appreciation to Dr. Phattraporn Soyong, professor of Burapha University and Prof. SHU Hong, professor at Wuhan university, Mr. Thanaphat Thanaratkiattikun and Dr. Pramet Kaewmesri from Geo-Informatics and Space Technology Development Agency (GISTDA), Mr. Pichet Peudkhuntod, and Ms. Kanyarat Lhaosatiekit from Sisaket public health office, Dr. Wittawin Chantapoh, Ms. Varittha

Soposuk, Royal Thai survey department (RTSD), and Sirindhorn Center of Geoinformatics (SCGI) master program batch 3 colleagues for all assistance given to me.

References

- Atiwath Waraputh. (2010). Factors Associated with Prevention and Control Behavior Toward Dengue Hemorrhagic Fever Among People Srisaket Province. (Master of Public Health Promotion). Ubon Ratchathani Rajabhat University
- Ausawadee Thawara, Apiwat Tawatsin, Jakkrawarn Sirisopa, & Phayu Phakdeenuan. (2016). Mosquitoes. Ministry of Public Health
- Budsara Thepawattanasuk. (2013). Dengue Fever and Dengue Hemorrhagic Fever in Chaoprayayomraj Hospital. Journal of Bamrasnaradura Infectious Diseases Institute, 7.
- Bureau of Communicable Diseases Led by Insects. (2019). Dengue Fever Situation Report. Department of Disease Control, : Ministry of Public Health,
- Jiratiwan Kruasilp. (2006). Geographic Information System for Determining Dengue Fever Risk Areas in Changwat Nakhon Ratchasima. (Master of Arts Program in Geography). Chulalongkorn University,
- Keerati Ponpetch. (2008). Geographic Information System for Prevention and Control Planning of Dengue Haemorrhagic Fever in Phetchaburi Province. (Master of Science). Silpakorn University, Graduate School.
- Moustafa A. Hegazi, Marwan A. Bakarman, Turki S. Alahmadi, Nadeem S. Butt, Ahmed M. Alqahtani, Badr S. Aljedaani, & Abdulrahman H. Almajnuni. (2020). Risk Factors and Predictors of Severe Dengue in Saudi Population in Jeddah, Western Saudi Arabia: A Retrospective Study. The American Society of Tropical Medicine and Hygiene.
- Muhammad Shahzad Sarfraz, Nitin K Tripathi, Taravudh Tipdecho, Thawisak Thongbu, Pornsuk Kerdthong, & Souris, M. (2012). Analyzing the spatio-temporal relationship between dengue vector larval density and land-use using factor analysis and spatial ring mapping. Bio Med Central.
- Natharin Dechasiripong. (2014). Mathematical Model for Analysis of Dengue Fever Spreading Risk Areas Based on Climatic Factors. (Doctor of Philosophy in Social Development and Environmental Management). National Institute of Development Administration,
- Prangthip Buafueang. (2013). A study of the application of Geographic Information System (GIS) for studying the spread of Dengue Haemorrhagic Fever (DHF) outbreak within Tamai District, Chanthaburi. (Master of Science (Environmental Management). National Institute of Development Administration,
- Teeranai Srithamarong. (2016). Crime Risk Area Assesment Based Geo-Spatial Statistics. (Master of Science Program in Environmental Science Thesis). Silpakorn University, Graduate School.



4th Intercontinental Geoinformation Days

igd.mersin.edu.tr



Chi-square automatic interaction detection (CHAID) algorithm for flood susceptibility assessment in Sardabroud watershed, Iran

Alireza Habibi ¹, Mahmoud Reza Delavar ^{*2}, Mohammad Sadegh Sadeghian ³, Borzo Nazari ⁴

¹University of Tehran, College of Engineering, School of Surveying and Geospatial Engineering, Department of GIS, Tehran, Iran

²University of Tehran, College of Engineering, School of Surveying and Geospatial Engineering, Center of Excellence in Geomatics Engineering in Disaster Management, Tehran, Iran

³Islamic Azad University, Department of Civil Engineering, Central Tehran Branch, Tehran, Iran

⁴University of Tehran, College of Engineering, School of Surveying and Geospatial Engineering, Department of GIS, Tehran, Iran

Keywords

GIS
Artificial intelligence
Machine Learning
Assessment
Natural hazard

Abstract

Flood, as a natural phenomenon, is the most common natural hazard that causes significant damage in the world. It is difficult to predict and identify flood zones due to variable weather conditions and various influencing factors. However, the identification and detection of early flood zones using machine learning techniques is used for smart flood management. In this study, Chi-square automatic interaction detection (CHAID) machine learning model for flood susceptibility map in Sardabroud watershed in north of Iran has been evaluated. For this purpose, a spatial database including 205 present and past flood locations with 8 conditional factors including elevation, slope, landuse, normalized difference vegetation index (NDVI), distance to river, topographic wetness index (TWI), lithology and rainfall are considered. After calculating variance inflation factors (VIF), all of the flood factors were considered for the modeling process. VIF technique uses to quantify multi-collinearity. Receiver operating characteristic (ROC), area under curve (AUC) and accuracy (ACC) metrics were used to evaluate and compare the predictability of the model. The results show that the CHAID model reaches an AUC of 0.939. This model has been proven as an efficient model for detecting flood prone areas in this watershed.

1. Introduction

Flood is known as one of the most frequent and destructive natural disasters in the world among other natural disasters such as earthquake and droughts due to causing great damage to human life and property and lives (Du et al. 2013).

The reasons for urban floods are the weakness of drainage systems and water infiltration into the ground during stormy rains and unhealthy urban growth (Darabi et al. 2019). Monsoon is one of the reasons why southeast Asian countries are most affected by floods and most of their related events (Loo et al. 2015). Iran has experienced a number of floods, especially in the northern parts of the country. For example, Noshahr in 2012, Behshahr in 2013 and Sari in 2015 have suffered from flash floods (Khosravi et al. 2016).

Therefore, optimal, efficient and proper methods should be used to reduce flood damage and losses. In the

recent years, the use of artificial intelligence (AI) methods such as machine learning (Ahmadlou et al. 2021; Khosravi et al. 2020; Shahabi et al. 2021; Arora et al. 2021) has been increased.

Nghia et al. (2020) have used the CHAID algorithm to model flash floods in the Luc Yen area of Yen Bai Province in Vietnam, using 10 conditional factors including soil type, land cover, lithology, river density, rainfall, elevation, topographic wetness index (TWI), slope, aspect, and curvature. (Tehrany et al. 2013) have also used this algorithm to model the Kelantan River Basin in northeastern Malaysia by selecting 10 flood factors. However, flood modelings using CHAID decision tree algorithm does not seem to be widely reported in the literature.

The purpose of this study is the flood modeling of Sardabroud watershed in northern Iran using CHAID

* Corresponding Author

(habibi.alireza@ut.ac.ir) ORCID ID 0000-0002-7134-149X
*(mdelavar@ut.ac.ir) ORCID ID 0000-0002-9654-6491
(m.sadeghian29@yahoo.com) ORCID ID 0000-0002-3406-9044
(borzoo.nazari@ut.ac.ir) ORCID ID 0000-0003-4064-2617

Cite this study

Habibi, A., Delavar, M. R., Sadeghian, M. S., & Nazari, B. (2022). Chi-square automatic interaction detection (CHAID) algorithm for flood susceptibility assessment in Sardabroud watershed, Iran. 4th Intercontinental Geoinformation Days (IGD), 294-297, Tabriz, Iran

algorithm to produce a flood risk map and undertake its evaluation.

2. Study area

Sardabroud watershed with an area about 460 Km² is a narrow basins originates from the snowy heights of Takht-e-Solimansar at a elevation of 4600 meters. Sardabroud watershed is located in the west of Mazandaran province, Iran. The elevation of the watershed ranges from 4800 to -31 meters and the slope ranges from 0 to 78 degrees (Figure 1). The Sardabroud river flows through several mountains including Takht-e-Soleiman and Alam Kooch, to the sea (Figure 1). This watershed is one of the tourist attractions places in Kelardasht with high average annual rainfall.

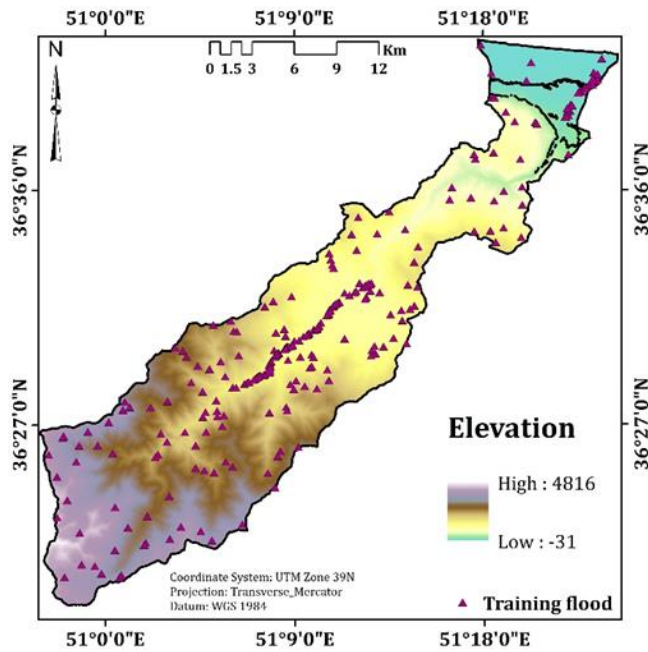


Figure 1. Study area

3. Method

In this study, several influencing factors including elevation, slope, rainfall, landuse, lithology, TWI, distance to river and NDVI have been extracted and collected for flood risk modeling using machine learning.

The CHAID algorithm process is in descending order from top to bottom, dividing large branches into smaller branches, which continue to be grouped according to specific factors. The CHAID is one of the classification decision tree techniques used in regression problems (Althuwaynee et al. 2014). CHAID algorithm has a number of titles such as automatic interaction detection, classification and regression tree (CART) and artificial neural network (ANN). CHAID algorithm uses chi-square statistics as a criterion for data separation and performs dodge separation (Eqs. 1,2, and 3) (Yeon et al. 2010).

$$\chi^2 = \sum_{j=1}^J \sum_{i=1}^I \frac{(n_{ij} - m_{ij})^2}{m_{ij}} \quad (1)$$

$$n_{ij} = \sum_{n \in D} f_{nI} (x_n = i \cap y_n = j) \quad (2)$$

$$m_{ij} = \frac{n_i \cdot n_j}{n_{ij}} \quad (3)$$

where n_{ij} = the observed cells frequency,

m_{ij} = cell frequency for $y_n = j$ and $x_n = i$.

VIF is a powerful statistical technique that detects a strong linear relationship between more than two factors in a multiple regression model (Hong et al. 2020). Accuracy value (ACC) needs to be determined for models accuracy that is calculated based on False Positive (FP), True Negative (TN), False Negative (FN) and True Positive (TP) (FP = non-flood pixels that are incorrectly known as flood pixels, TN = flood pixels that are correctly known as non-flood, FN = non-flood pixels that are incorrectly known as non-flood pixels and TP = flood pixels that are correctly known as flood pixels) (Shahabi et al. 2020).

Therefore, this algorithm has been used for flood risk modeling in this study. The research methodology proposed in this paper is presented in Figure 2. The produced map shows the probability of flooding.

4. Results

The results of calculating VIF (Table 1) for the 8 factors considered for flood modeling, shows that landuse has the lowest and elevation has the highest VIF. Therefore, none of the factors had VIF > 10. Therefore, all of the factors are considered for the modeling process.

Then, out of the total flood pixels, 70% of the data have been used for model training and 30% of the data employed for the model testing process. The AUC values for the testing process of the model are 0.939 (Figure 4).

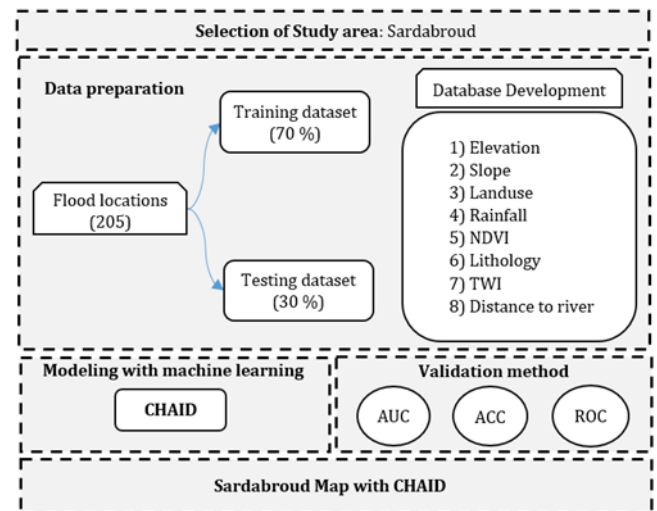


Figure 2. Research methodology

Therefore, according to the flood modeling of this watershed with CHAID algorithm, the value of AUC has been obtained as 0.939. The Accuracy value of the CHAID model for the training and testing process are 0.964 and 0.882, respectively (Table 2). The map has been produced in ArcGIS 10.3 software and illustrated in Figure 3.

Table 1. multi-collinearity analysis

Factors	VIF
Elevation	5.38
Slope	1.89
Rainfall	1.67
Distance to river	1.32
Landuse	1.03
NDVI	3.67
Lithology	1.30
TWI	1.49

Table 2. model performances

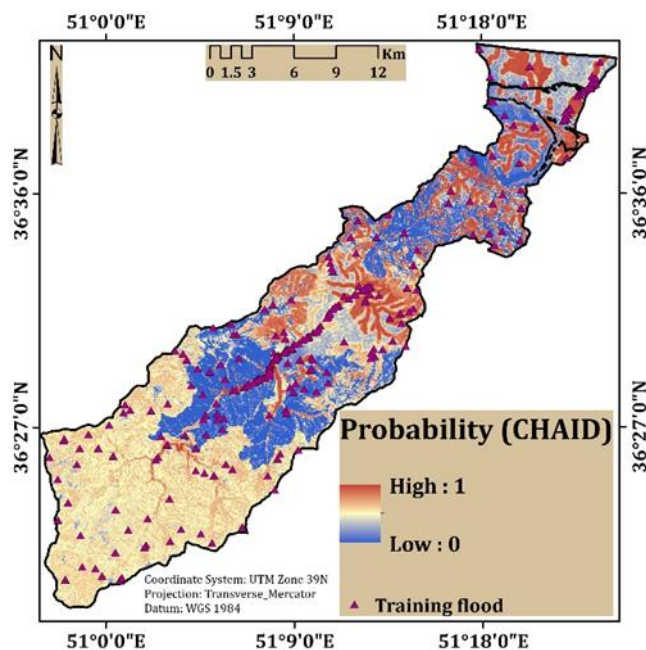
Metrics/Model	AUC	ACC
CHAID (training)	0.961	0.964
CHAID (testing)	0.939	0.882

5. Discussion

In this research, a decision tree-based machine learning model (CHAID) has been used to model flood risk in Sardabroud watershed, Iran. Elevation, slope, landuse, NDVI, TWI, rainfall, lithology and distance to river factors were used for the modeling process.

After performing multi-collinearity analysis using VIF methods, the value of VIF factors changes in a range from 1.03 to 5.38, with the highest and lowest values are related to elevation and landuse. Therefore, because VIF values are lower than 10, there is no correlation between the factors.

Therefore, the 8 factors considered for the modeling process were used. According to Figure 3, it is clear that the risk of flood in the north and middle parts of the watershed are more than other areas.

**Figure 3.** Flood susceptibility mapping

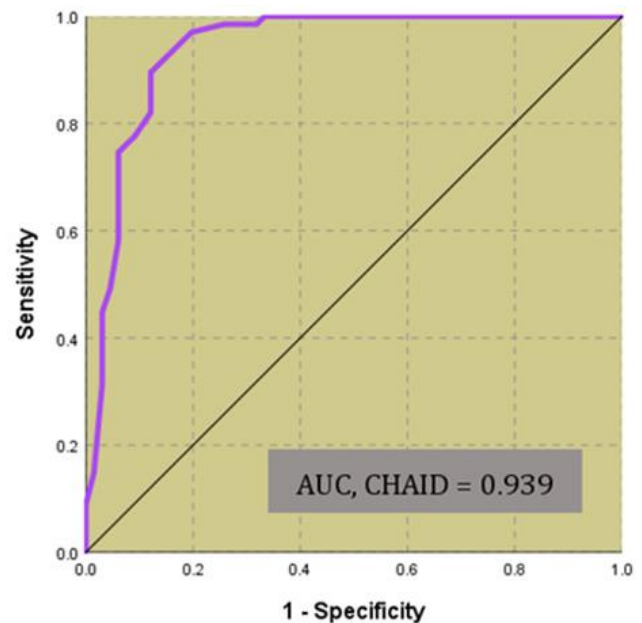
6. Conclusion

The aim of this study was to consider the factors affecting flood risk and to identify the flood susceptible zones in Sardabroud watershed, Iran.

The CHAID employed model is important for future smart flood disaster management decisions because it provides the basic information for controlling and managing flood risk.

Due to the flood damage to urban and agricultural areas, future research needs to focus on selecting and adopting effective flood parameters in the area such as population density and literacy and their relationship with economic processes and other factors affecting floods.

The method adapted in this research can be extended to larger watersheds that are at flood risk, and the accuracy of the models can be compared and evaluated with other basic machine learning models such as support vector machine (SVM) and K-nearest neighbor (KNN) methods.

**Figure 4.** Plot of the ROC curve

References

- Ahmadlou, M., Al-Fugara, A., Al-Shabeeb, A. R., Arora, A., Al-Adamat, R., Pham, Q. B., & Sajedi, H. (2021). Flood susceptibility mapping and assessment using a novel deep learning model combining multilayer perceptron and autoencoder neural networks. *Journal of Flood Risk Management*, 14(1). <https://doi.org/10.1111/jfr3.12683>
- Althuwaynee, O. F., Pradhan, B., & Ahmad, N. (2014). Landslide susceptibility mapping using decision-tree based Chi-squared automatic interaction detection (CHAID) and Logistic regression (LR) integration. 20, 012032. <https://doi.org/10.1088/17551315/20/1/012032>
- Arora, A., Arabameri, A., Pandey, M., Siddiqui, M. A., Shukla, U. K., Bui, D. T., & Bhardwaj, A. (2021). Optimization of state-of-the-art fuzzy-metaheuristic ANFIS-based machine learning models for flood susceptibility prediction mapping in the Middle Ganga Plain, India. *Science of The Total Environment*,

- 750, 141565.
<https://doi.org/10.1016/j.scitotenv.2020.141565>
- Darabi, H., Choubin, B., Rahmati, O., Torabi Haghighi, A., Pradhan, B., & Kløve, B. (2019). Urban flood risk mapping using the GARP and QUEST models: A comparative study of machine learning techniques. *Journal of Hydrology*, 569, 142–154. <https://doi.org/10.1016/j.jhydrol.2018.12.002>
- Du, J., Fang, J., Xu, W., & Shi, P. (2013). Analysis of dry/wet conditions using the standardized precipitation index and its potential usefulness for drought/flood monitoring in Hunan Province, China. *Stochastic Environmental Research and Risk Assessment*, 27(2), 377–387. <https://doi.org/10.1007/s00477-012-0589-6>
- Hong, H., Liu, J., & Zhu, A.-X. (2020). Modeling landslide susceptibility using LogitBoost alternating decision trees and forest by penalizing attributes with the bagging ensemble. *Science of The Total Environment*, 718, 137231. <https://doi.org/10.1016/j.scitotenv.2020.137231>
- Khosravi, K., Nohani, E., Maroufinia, E., & Pourghasemi, H. R. (2016). A GIS-based flood susceptibility assessment and its mapping in Iran: A comparison between frequency ratio and weights-of-evidence bivariate statistical models with multi-criteria decision-making technique. *Natural Hazards*, 83(2), 947–987. <https://doi.org/10.1007/s11069-016-2357-2>
- Khosravi, K., Panahi, M., Golkarian, A., Keesstra, S. D., Saco, P. M., Bui, D. T., & Lee, S. (2020). Convolutional neural network approach for spatial prediction of flood hazard at national scale of Iran. *Journal of Hydrology*, 591, 125552. <https://doi.org/10.1016/j.jhydrol.2020.125552>
- Loo, Y. Y., Billa, L., & Singh, A. (2015). Effect of climate change on seasonal monsoon in Asia and its impact on the variability of monsoon rainfall in Southeast Asia. *Geoscience Frontiers*, 6(6), 817–823. <https://doi.org/10.1016/j.gsf.2014.02.009>
- Nghia, N., Yariyan, P., Amiri, M., Tran, A., Pham, T. D., Phuong, D., & Bui, D. (2020). A New Modeling Approach for Spatial Prediction of Flash Flood with Biogeography Optimized CHAID Tree Ensemble and Remote Sensing Data. *Remote Sensing*, 12, 1373. <https://doi.org/10.3390/rs12091373>
- Shahabi, H., Shirzadi, A., Ghaderi, K., Omidvar, E., Al-Ansari, N., Clague, J. J., & Ahmad, A. (2020). Flood Detection and Susceptibility Mapping Using Sentinel-1 Remote Sensing Data and a Machine Learning Approach: Hybrid Intelligence of Bagging Ensemble Based on K-Nearest Neighbor Classifier. *Remote Sensing*, 12(2), 266. <https://doi.org/10.3390/rs12020266>
- Shahabi, H., Shirzadi, A., Ronoud, S., Asadi, S., Pham, B. T., Mansouripour, F., & Bui, D. T. (2021). Flash flood susceptibility mapping using a novel deep learning model based on deep belief network, back propagation and genetic algorithm. *Geoscience Frontiers*, 12(3), 101100. <https://doi.org/10.1016/j.gsf.2020.10.007>
- Tehrany, M. S., Pradhan, B., & Jebur, M. N. (2013). Spatial prediction of flood susceptible areas using rule based decision tree (DT) and a novel ensemble bivariate and multivariate statistical models in GIS. *Journal of Hydrology*, 504, 69–79. <https://doi.org/10.1016/j.jhydrol.2013.09.034>
- Yeon, Y.-K., Han, J.-G., & Ryu, K. H. (2010). Landslide susceptibility mapping in Injae, Korea, using a decision tree. *Engineering Geology*, 116(3), 274–283. <https://doi.org/10.1016/j.enggeo.2010.09.009>



4th Intercontinental Geoinformation Days

igd.mersin.edu.tr



Wind farm suitability analysis using Geographic Information System with Best-Worst Method in Amhara region of Ethiopia

Zelalem Ayalke ^{*1}, Aziz Şişman ²

¹Ondokuz Mayıs University, Institute of Graduate Studies, Department of Geomatics Engineering, Samsun, Türkiye

²Ondokuz Mayıs University, Faculty of Engineering, Department Geomatics Engineering, Samsun, Türkiye

Keywords

Wind farm
Geographic information system
Best-Worst Method

Abstract

The analysis of suitability for wind farms is important not only for finding a suitable wind potential site for energy production but also for a sustainable land use planning, environmental management and protection. The objective of this study was to identify a suitable locations for wind farms using the Geographic Information System (GIS) with Best-Worst Method (BWM). Eight criteria were used, and BWM was implemented to calculate the criteria weights. The wind speed was chosen as the most important criterion for locating wind farms, followed by slope, Power grid lines, land cover, aspect, airports, main roads, and protected areas. The suitability map of the wind farm was presented using Weighted Overlay analysis in a GIS environment. The findings indicate that the eastern and western parts of the Amhara region have good potential for generating renewable energy from the wind. The result is presented with a scale of 0 to 5 to represent the degree of suitability such as unsuitable, very low, low, moderate, high, and very high potential for wind farms.

1. Introduction

The development of renewable energy in the world is increasing as a result of population growth and industrialization (Adams, Klobodu, & Apio, 2018; DLA PIPER, 2021).

Ethiopia is one of the fastest-growing countries in the eastern part of Africa, and its' energy demand is increasing at an alarming rate due to the fast-growing economy and flourishing infrastructures. Despite the fact that Ethiopia has an enormous amount of renewable energy resources such as solar, hydro, wind, and geothermal, only a few amounts of its total hydropower potential is now utilized. As a result, traditional fuels (charcoal, fuel wood, dung cakes, and agricultural residues) account for the majority of energy consumption in the rural parts of Ethiopia, which brings significant health and environmental risks (Tiruye et al., 2021). It has a renewable energy potential of up to 45,000 MW from hydropower, 10,000 MW from wind, 5000 MW from geothermal, and an average of 5.26 kWh per square meter per day from solar energy that has yet to be completely exploited (Asress, Simonovic, Komarov, & Stupar, 2013).

Exploiting renewable energy alternatives boosts energy supply by shifting away from the usage of fossil fuels to fill the gap in electricity consumption in rural and urban areas. Renewable energy sources such as wind and solar produce little to no global warming emissions, reducing the use of fossil fuels and their adverse environmental effects. As a result, it is a viable option for generating electricity. Wind turbines and farms, have a variety of environmental and societal implications that must be properly investigated and evaluated (Kotb, Elkadeem, Elmorshedy, & Dán, 2020; Nasery, Matci, & Avdan, 2021).

A Combination of Geographic Information System (GIS) and Multi-criteria Decision Making (MCDM) can help as a decision support tool to identify the most suitable places for wind. MCDM such as Best-Worst Method (BWM) approaches attempt to evaluate several criteria simultaneously and provide an optimal solution (Ecer, 2021; Tercan, 2021).

The objective of the study is to identify a suitable locations for the wind farms using GIS with BWM in the Amhara region of Ethiopia.

* Corresponding Author

^{*}(19211596@stu.omu.edu.tr) ORCID ID 0000 – 0003 – 4223 – 0683
(asisman@omu.edu.tr) ORCID ID 0000-0001-6936-5209

Cite this study

Ayalke, Z., Şişman, A. (2022). Wind farm suitability analysis using Geographic Information System with Best-Worst Method in Amhara region of Ethiopia. 4th Intercontinental Geoinformation Days (IGD), 298-302, Tabriz, Iran

2. Method

In this study, the data such as wind speed, DEM, Land cover, administrative boundary, power grid line and protected areas were downloaded from different sources as indicated in Table 1.

Table 1. Data and sources

Data	Sources
Wind speed	https://globalwindatlas
Digital Elevation Model (DEM)	https://earthexplorer.usgs.gov /
Land cover	https://livingatlas.arcgis.com/landcover/
Administrative boundaries	https://ethiopia.africageoport.al.com/
Power grid lines	https://energydata.info/
Protected Areas	https://data.apps.fao.org/

The database was constructed and the data downloaded from different sources were organized and managed in the GIS environment. Extraction of all the parametrical data within the intended area of interest, buffering, resampling, rasterization, surface analysis, reclassification at a given scale, and weighted overlay analysis were done to identify suitable wind farms location. In this study, the general workflow is illustrated in Figure 1.

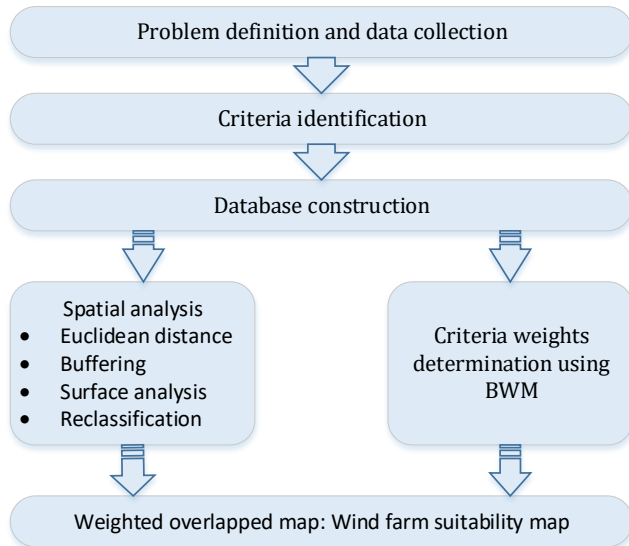


Figure 1. General workflow of the study

2.1. Location of the study area

The study was conducted in the Amhara region in the northern part of Ethiopia Figure 2. The region is dominated by a chain of mountains, hills, and valleys ranging in elevation from 505 to 4529 meters above MSL (Abera & Abegaz, 2020) and has more than 6.8 m/s wind speed; Such geographical characteristics are suitable places for energy development from the wind.

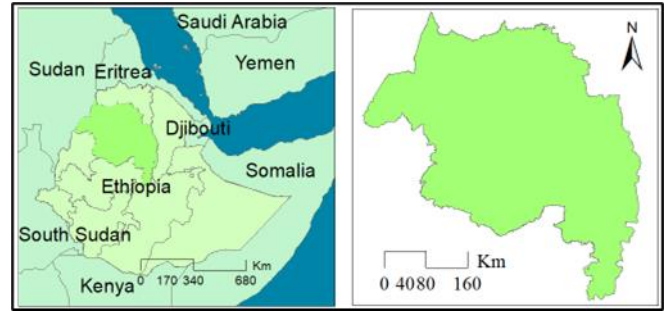


Figure 2. Location of the study area

2.2. Criteria Determination

The criteria for wind farm suitability analysis were determined based on recent literature (Ayodele, Ogunjuyigbe, Odigie, & Munda, 2018; Nasery et al., 2021; Pamucar, Gigovic, Bajic, & Janošević, 2017; Szurek, Blachowski, & Nowacka, 2014; Tercan, 2021; Xu et al., 2020; Zalhaf et al., 2022) and considering opinions of experts who dealt with similar problems. Based on literature and experts opinions eight criteria were determined and categorized as unsuitable, very low, low, moderate, high and very high as described in Table 2.

Vector and raster datasets were clipped and masked with the area of interest respectively. Multi-buffer and Euclidean distance were used for proximity analysis. Based on the scale mentioned for each criterion in Table 2, the criteria were reclassified and criteria reclassified maps were produced. The reclassified maps of the criteria are shown in Figure 3.

2.3. Determination of weight of the Criteria

Many criteria affect the location of a suitable wind farms. However, each has a different weight that has significant to determine a suitable location for the wind farm. In this study, BWM has been used to determine the weights of criteria. In multi-criteria decision-making (MCDM) problems, BWM is one of the most successful approaches for determining the weights of criteria (Rezaei, 2016). The expert first determines the best (e.g., most desirable, most important) and worst (e.g., least desirable, least important) criteria, then compares the best criterion to the other criteria, and the other criteria to the worst criterion. The weights of the criteria can be computed using equation (1).

Min ξ^L such that

$$\begin{aligned} |W_B - a_{Bj}W_j| &\leq \xi^L, \text{ for all } j \\ |W_j - a_{jW}W_W| &\leq \xi^L, \text{ for all } j \\ \sum_j W_j &= 1 \end{aligned} \quad (1)$$

$$W_j \geq 0, \text{ for all } j$$

Where,

a_{Bj} : preference for the best criterion over criterion j

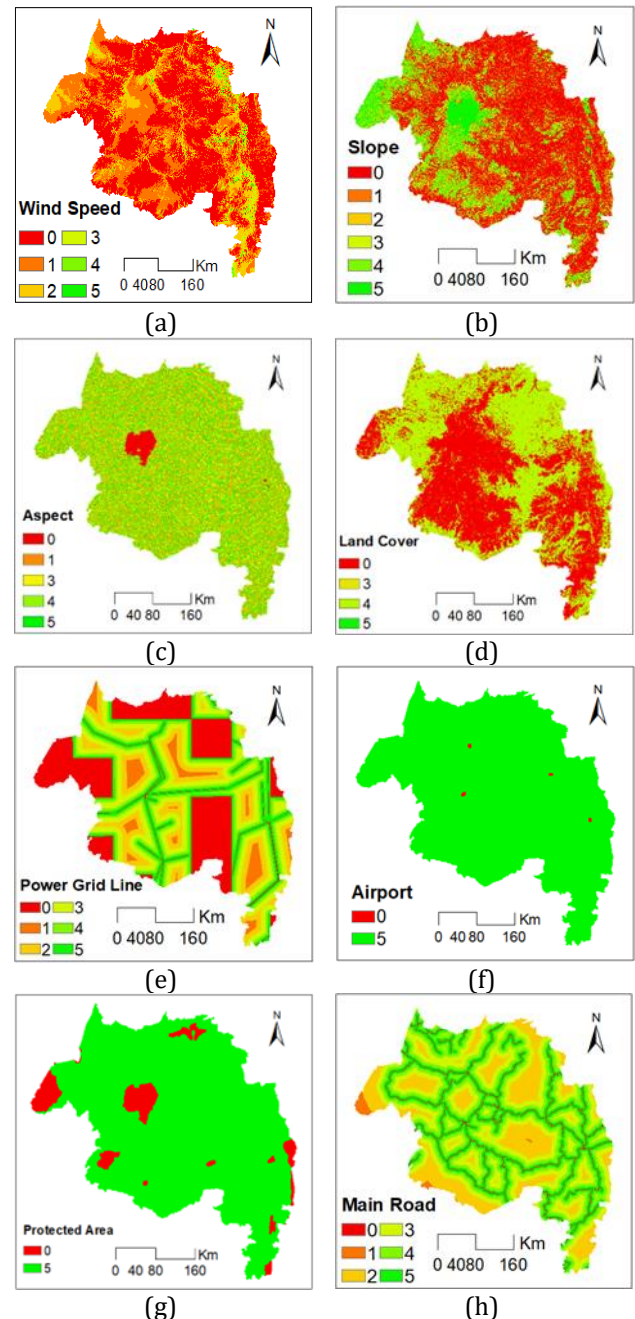
a_{jW} : preference for criterion j over the worst criterion

Table 2. Selected criteria and description

Criterion	Description
Wind speed	One of the most important criteria for wind farming. The higher the wind speed the higher the wind power. Suitability categories; <3m/s (unsuitable), 3-4m/s (very low), 4-5m/s (low), 5-6m/s (moderate), 6-7m/s (high) and >7m/s (very high).
Slope	Wind farm construction, maintenance and installation are affected by the high slope. The higher the slope the higher cost of construction, and maintenance of wind farms. Suitability categories; >15% (Unsuitable), 12-15% (very low), 9-12% (low), 6-9% (moderate), 3-6% (high) and 0-3% (very high).
Aspect	Slope orientation relative to the direction of the wind is an important criterion when it comes to making full use of the wind potential. Suitability categories; low (E,SE), moderate (N,NE,S,SW), and very high (W,NW,FLAT).
Landcover	Land cover is one of the critical factors for wind farm suitability analysis. Suitability categories; Water, crops, built-up area, cloud cover, and Trees as unsuitable, Flooded vegetation as moderate, Rangeland as high, and Bare ground as very high.
Power grid lines	Wind farms closed to power grid lines reduce the construction of new power grid lines. However, it has a negative effect on human health due to the electromagnetic field generated by power transmission lines. Suitability categories; <0.5km (unsuitable), 60-90km (very low), 30-60 (low), 10-30km (moderate), 5-10km (high) and 0.5-5km (very high).
Airports	Wind farm closed to airports affects aviation routes, communication system and navigations, which leads to collisions. suitability categories; <3km (unsuitable), 50-100km (very low), 20-50km (low), 10-20km (moderate), 5-10km (high), and 3-5 (very high).
Protected areas	Wind turbine noise and rotating blades influence animals' and birds' habitats. Suitability categories; <2000 (unsuitable) and >2000 (very suitable).
Main roads	Wind farms distance from the main roads has a positive and negative effect. Wind farms closed to the main roads reduce transportation cost during construction, and reduce the cost of construction and maintenance of new roads. Whereas the wind farm is closed to the main roads, the roads negatively affect road transportation because of loud noises. Categories; <3km (unsuitable), 50-100km (very low), 20-50km (low), 10-20 (moderate), 5-10km (high), and 3-5km (very high).

The weights and consistency of the criteria were computed using the BWM-Solver tool of Excel. The consistency ratio of decision-making ranges between 0 and 1; completely consistent and completely inconsistent respectively. In this study, the value for high consistency is expected to be less than or equal to 0.41. The consistency ratio of four experts while computing the

weights of criteria was 0.047, 0.081, 0.146, and 0.066; which indicate the consistency ratio within the prescribed acceptance limit. During the implementation of BWM, the Best criterion was wind for all experts. However, the worst criterion was different; expert 1 selects the main roads, expert 2 and 3 select the protected areas, and expert 4 selects the airports as worst criteria. Based on the average weight of the criteria wind speed and protected areas were the best and the worst criteria respectively. Calculated weights of criteria by four experts as shown in Table 2.

**Figure 3.** Criteria reclassified maps; (a) wind speed (b) slope (c) Aspect (d) land cover (e) power grid lines (f) airports (g) protected areas and (h) main roads

3. Result and Discussion

In this study, the wind speed was identified as the most important criteria for locating wind farms followed by slope, power grid lines, land cover, aspect, airports,

main roads, and protected areas. The wind farm suitability map was produced based on eight criteria using a weight overlay analysis. Figure 4 shows the wind farm suitability map produced using GIS with BWM.

Table 2 Determined weight of criteria

Criterion	Exp.1	Exp.2	Exp.3	Exp.4	Average
Wind speed	0.314	0.340	0.389	0.332	0.344
Slope	0.180	0.141	0.041	0.199	0.140
Aspect	0.120	0.105	0.059	0.133	0.104
Land cover	0.120	0.105	0.107	0.100	0.108
Power grid lines	0.090	0.105	0.178	0.080	0.113
Airports	0.090	0.105	0.107	0.033	0.084
Protection area	0.052	0.037	0.059	0.057	0.051
Main roads	0.033	0.060	0.059	0.066	0.055
Total	1.000	1.000	1.000	1.000	1.000

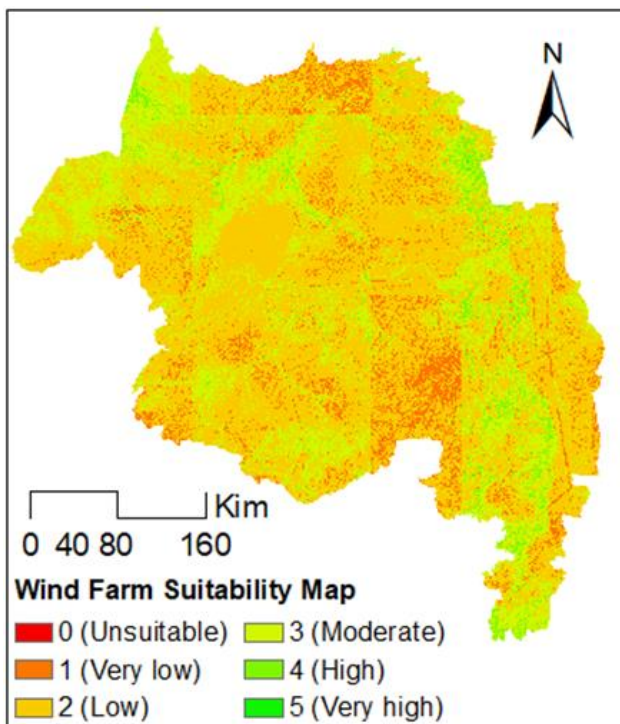


Figure 4. Wind farm suitability map

The generated wind farm suitability map using weighted overlay analysis is represented in the same value range (0 to 5) as the input reclassified criteria maps. The larger the values the more suitable the area for the location of the wind farm. The value for the criteria attributes which was considered as a constraint was 0.

In the result, the most suitable locations have been identified and presented on a suitability map. Areas that have pixel value equal to 5 (very high), 4 (high), 3 (moderate), 2 (low), 1 (very low), and 0 (unsuitable). The suitable area for the wind farms is located in the eastern and western parts of the Amhara region.

4. Conclusion

The GIS-based wind farm suitability analysis model with BWM was developed and used to analyze the

suitability of wind farm locations in the Amhara region by taking into account multiple criteria. The suitability analysis was based on eight criteria; wind speed, proximity to power grid lines, slope, aspect, land cover, protected areas, airports, and proximity to main roads. Experts' opinions were used to determine the weight of the criteria. The study shows that BWM can be used in combination with GIS to determine the best location for wind farm development. In addition, the result of wind farm suitability analysis can be helpful for decision-makers during sustainable land use planning, environmental management and protection.

References

- Abera, E. A., & Abegaz, W. B. (2020). Seasonal and Annual Rainfall Trend Detection in Eastern Amhara, Ethiopia. *J Climatol Weather Forecast*, 8, 264. doi:10.35248/2332-2594.2020.8.264
- Adams, S., Klobodu, E. K. M., & Apio, A. (2018). Renewable and non-renewable energy, regime type and economic growth. *Renewable Energy*, 125, 755–767. doi:10.1016/j.renene.2018.02.135
- Asress, M. B., Simonovic, A., Komarov, D., & Stupar, S. (2013). Wind energy resource development in Ethiopia as an alternative energy future beyond the dominant hydropower. *Renewable and Sustainable Energy Reviews*, 23, 366–378. doi:10.1016/j.rser.2013.02.047
- Ayodele, T. R., Ogunjuyigbe, A. S. O., Odigie, O., & Munda, J. L. (2018). A multi-criteria GIS based model for wind farm site selection using interval type-2 fuzzy analytic hierarchy process: The case study of Nigeria. *Applied Energy*, 228(July), 1853–1869. doi:10.1016/j.apenergy.2018.07.051
- DLA PIPER. (2021). Africa Energy Futures: Horizon 2030 report, (December), 1–61.
- Ecer, F. (2021). Sustainability assessment of existing onshore wind plants in the context of triple bottom line: a best-worst method (BWM) based MCDM framework. *Environmental Science and Pollution Research*, 28(16), 19677–19693. doi:10.1007/s11356-020-11940-4
- Kotb, K. M., Elkadeem, M. R., Elmorshedy, M. F., & Dán, A. (2020). Coordinated power management and optimized techno-enviro-economic design of an autonomous hybrid renewable microgrid: A case study in Egypt. *Energy Conversion and Management*, 221(July), 113185. doi:10.1016/j.enconman.2020.113185
- Nasery, S., Matci, D. K., & Avdan, U. (2021). GIS-based wind farm suitability assessment using fuzzy AHP multi-criteria approach: the case of Herat, Afghanistan. *Arabian Journal of Geosciences*, 14(12). doi:10.1007/s12517-021-07478-5
- Pamucar, D., Gigovic, L., Bajic, Z., & Janosevic, M. (2017). Location selection for wind farms using GIS multi-criteria hybrid model: An approach based on fuzzy and rough numbers. *Sustainability (Switzerland)*, 9(8). doi:10.3390/su9081315
- Rezaei, J. (2016). Best-worst multi-criteria decision-making method: Some properties and a linear model.

- Omega (United Kingdom)*, 64, 126–130. doi:10.1016/j.omega.2015.12.001
- Szurek, M., Blachowski, J., & Nowacka, A. (2014). GIS-Based method for wind farm location multi-criteria analysis. *Mining Science*, 21, 65–81. doi:10.5277/ms142106
- Tercan, E. (2021). Land suitability assessment for wind farms through best-worst method and GIS in Balıkesir province of Turkey. *Sustainable Energy Technologies and Assessments*, 47(July), 101491. doi:10.1016/j.seta.2021.101491
- Tiruye, G. A., Besha, A. T., Mekonnen, Y. S., Benti, N. E., Gebreslase, G. A., & Tufa, R. A. (2021). Opportunities and challenges of renewable energy production in ethiopia. *Sustainability (Switzerland)*, 13(18), 1–25. doi:10.3390/su131810381
- Xu, Y., Li, Y., Zheng, L., Cui, L., Li, S., Li, W., & Cai, Y. (2020). Site selection of wind farms using GIS and multi-criteria decision making method in Wafangdian, China. *Energy*, 207. doi:10.1016/j.energy.2020.118222
- Zalhaf, A. S., Elboshy, B., Kotb, K. M., Han, Y., Almaliki, A. H., Aly, R. M. H., & Elkadeem, M. R. (2022). A high-resolution wind farms suitability mapping using gis and fuzzy ahp approach: A national-level case study in Sudan. *Sustainability (Switzerland)*, 14(1), 1–21. doi:10.3390/su14010358

4th Intercontinental Geoinformation Days

igd.mersin.edu.tr



Low latitude ionosphere responses to solar wind forcing from GNSS data in March 2001

Chukwuma Moses Anoruo^{*1} , Francisca Nneke Okeke¹ , Kingsley Chukwudi Okpala¹ , Andres Calabia² ¹University of Nigeria Nsukka, Faculty of Physical Sciences, Department of Physics and Astronomy, Enugu, Nigeria²Nanjing University of Information Science Technology, School of Remote Sensing and Geomatics Engineering, China**Keywords**

Low latitude ionosphere
Solar wind forcing
Geomagnetic storm
Relative TEC

Abstract

We employ Global Navigation Satellite Systems (GNSS) data to investigate the low latitude ionosphere variations over the African sector (Magnetic Latitude: 0.17°) during active and quiet magnetospheric conditions during solar maximum in March 2001. The relative Total Electron Content (rTEC) index is employed to detect the variations over the threshold of $|rTEC| \geq \pm 30\%$. We observe increases in the solar wind speed, the interplanetary magnetic field (IMF), and the geomagnetic SYM-H index during the abrupt changes detected in the ionosphere. On 9 March 2001, an anomalous rTEC started at 5 h UT due to a short period of southward IMF B_z orientation. At 8 h UT, a minimum SYM-H of -139 nT was recorded under solar wind speed of 712 km/s, causing an rTEC disturbance. Results show that solar wind forcing during the prompt electric field drives positive storm-enhanced density and observed during early morning hours.

1. Introduction

The exact understanding of the ionosphere variability and its coupled variables and processes are very important for applications such as Global Navigation Satellite Systems (GNSS) navigation, positioning, and timing, radio communications, and Earth observation with remote sensing techniques (Calabia et al. 2021). Electrodynamics coupling between the magnetosphere and the high latitude ionosphere has significant impact on the low latitude ionosphere during geomagnetic storms (Sharma et al. 2020).

This phenomenon is attributed to F-region thermospheric equatorward winds, which result from momentum force and joule heating of the upper atmosphere (Richmond and Roble, 1979). In addition, thermospheric winds enhance total electron content and can change the global distribution of atmospheric chemistry (Ansari et al., 2019).

During geomagnetic storms, the low latitude electrodynamics are characterized by the disturbance dynamo electric field (DDEF) driving long-lasting effects on plasma distribution (Araki, 1985), and by the prompt penetration electric field (PPEF) that drives variations of shorter durations (Yamazaki and Kosch, 2015). The

coupling between solar wind and the magnetosphere mainly occurs in the magnetic reconnection, and it results in ionospheric disturbances. However, the relationship between solar wind characteristics and the intensities of different geomagnetic storms is difficult to understand (Ji et al. 2010; Wang et al. 2003).

Here, we present the low latitude ionosphere responses to solar wind forcing during active and quiet geomagnetic conditions under the solar maximum period of March, 2001. We employ GNSS data and space weather indices to elucidate the possible interrelations between parameters; these are briefly introduced in section 2. In section 3 our results are provided, and section 4 summarizes our conclusions.

2. Method

We employ GNSS data from the ground-based GPS station of UNAVCO to study the ADIS station at the low latitude of the African continent. Specifically, the ADIS station is located in Ethiopia at a geographical latitude of 9.035° and longitude of 38.766°; the geomagnetic latitude (MLAT) is 0.17°. The data is available at the UNAVCO website (<https://data.unavco.org>) in RINEX format, where the slant total electron content (sTEC) is provided at 30s resolution. Here we convert sTEC to

*** Corresponding Author**

^{*}(anoruchukwuma@gmail.com) ORCID ID 0000-0003-3800-6080
(francisca.okeke@unn.edu.ng) ORCID ID xxxx-xxxx-xxxx-xxxx
(kingsley.okpala@unn.edu.ng) ORCID ID xxxx-xxxx-xxxx-xxxx
(andres@calabia.com) ORCID ID xxxx-xxxx-xxxx-xxxx

Cite this study

Anoruo, C. M., Okeke, F. N., Okpala, K. C., & Calabia A. (2022). Low latitude ionosphere responses to solar wind forcing from GNSS data in March 2001. 4th Intercontinental Geoinformation Days (IGD), 303-305, Tabriz, Iran

vertical TEC (vTEC) using the thin shell model of Seemala and Valladares (2011). Then, rTEC obtained with the following formula:

$$rTEC = (TEC_{storm} - TEC_{quiet}) / TEC_{quiet} \quad (1)$$

The rTEC index is essential to exclude regular diurnal, seasonal, and solar-cycle effects (Pancheva et al. 2016). Daytime ionization is usually associated with positive storms, and usually precede the equatorial plasma fountain that is strengthened by the eastward prompt penetration of electric field (PPEF).

In order to study the geomagnetic activity, we employ SYM-H and ASY-H obtained from Service International des Indices Géomagnétiques (http://isgi.unistra.fr/oi_data_download.php). We also employ the solar wind velocity, the interplanetary magnetic field (IMF) Bz component, the IEF, the planetary Kp index, and the AE index. These indices are available at the OMNI website (<https://omniweb.gsfc.nasa.gov>).

3. Results

Figure 1 shows the space weather indices under quiet magnetospheric conditions on 26 March 2001. Figure 2 shows the space weather indices during storm conditions on 9 March 2001. The axes in both figures are arranged with the similar ranges in the y-axes. In figure 2, we observe rTEC enhancements are observed from 0 h to 2 h UT which lasted approximately 3 h. At 3 h UT, rTEC show strong decrease, which is coincident with the IMF Bz > 0 and the eastward orientation of Ey.

The minimum SYM-H reaches at 8 h UT with -139 nT, and the rTEC is 10%. The rTEC started to increase from 5 h UT reaching 30% limit at 10 h UT. At 12 h UT, the solar wind velocity shows a maximum of 741 km/s and the SYM-H is -115 nT. Then, from 16-17 h UT, another clear positive anomaly is seen.

These positive fluctuations result from combined effects of thermospheric winds and electric fields observed during the time 19 h UT. At 8 h UT, rTEC reaches the -30% limit, showing a clear negative storm. This abrupt effect may be associated with changes in thermospheric composition.

TEC anomalies observed through the deviation of quiet from geomagnetic storm time causes magnetic field disturbances and likely occurred during solar wind shockwaves that interact with Earth's magnetosphere.

The behavior of the ionosphere during the storm is determined by several electrodynamics and chemical actions and affected by solar wind forcing through magnetosphere-ionosphere coupling.

4. Discussion

The effect of IEF as motional electric field causes magnetospheric disturbance in the form of PPEF. This appears after electric fields are being inserted by solar wind forcing to the magnetosphere. The PPEF has eastward (westward) polarity during dayside/nightside and causes plasma enhancements/depletions.

We identified the horizontal disturbance of magnetic activity with Kp and the AE indices. Enhanced currents seem to flow below and within the auroral oval.

The rTEC values clearly show and detect the anomalies above selected threshold (30%). The solar wind forcing along with the other variables are clearly drivers of TEC anomalies.

The PPEF during IMF Bz < 0 strengthens ionospheric zonal electric fields and weakens during Bz > 0.

PPEF as a phenomenon of electric fields transmissions to the motion of particles in the magnetosphere, the auroral electrojet (AE) and neutral atmosphere motions by DDEF has remained the equatorial ionosphere electrodynamic coupling with the high latitude ionosphere during geomagnetic storms.

The short-term changes in the Earth's magnetic field are largely imposed by solar wind and can have direct response. It is likely seen that electric currents in space dominate in storms and serve as one major factor for vertical electrodynamics drift that influences the growth rate of Rayleigh-Taylor Instability observed mainly during morning hours in this present analysis.

The main results of this study showed that small variations in magnetic field due to the forcing of solar wind are able to modify the dynamics of the low latitude ionosphere.

5. Conclusion

We have investigated ionospheric TEC anomalies during the storm of 9 March 2001 using the rTEC index and space weather indices. We employ relative TEC to study solar wind forcing to the low latitude ionosphere during both storm and quiet conditions. Our findings are summarized as follows:

- The rTEC anomaly was observed early morning hours and that corresponds to the eastward PPEF that indicates dayside plasma uplift.
- rTEC enhancements and depletions are difficult to separate from the effect of PPEF and DDEF and need further investigation.
- Solar wind forcing indicated major driver of TEC during both storm and quiet conditions.
- At 8 h UT a minimum SYM-H of -139 nT was recorded under solar wind speed of 712 km/s, causing an rTEC disturbance.

The relations between solar wind and its interaction with different variables under different geomagnetic storms require further investigation to observe the effects in the ionosphere.

Acknowledgement

Authors are grateful to UNAVCO, OMNI-web, and Service International des Indices Géomagnétiques for provision of data.

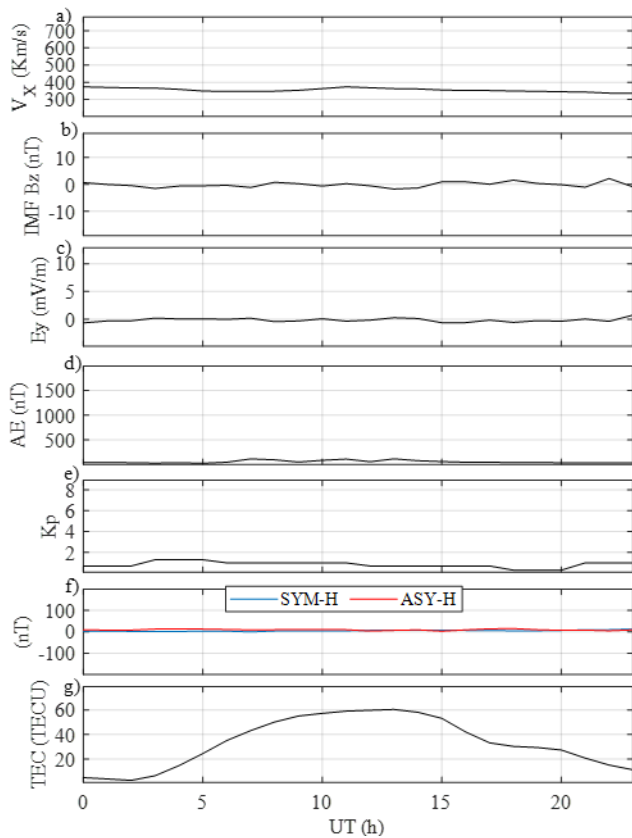


Figure 1. Space weather indices (a-f) and TEC (g) under magnetospheric quiet conditions (26 March 2001). Ranges in y-axes are set to be compared with Figure 2.

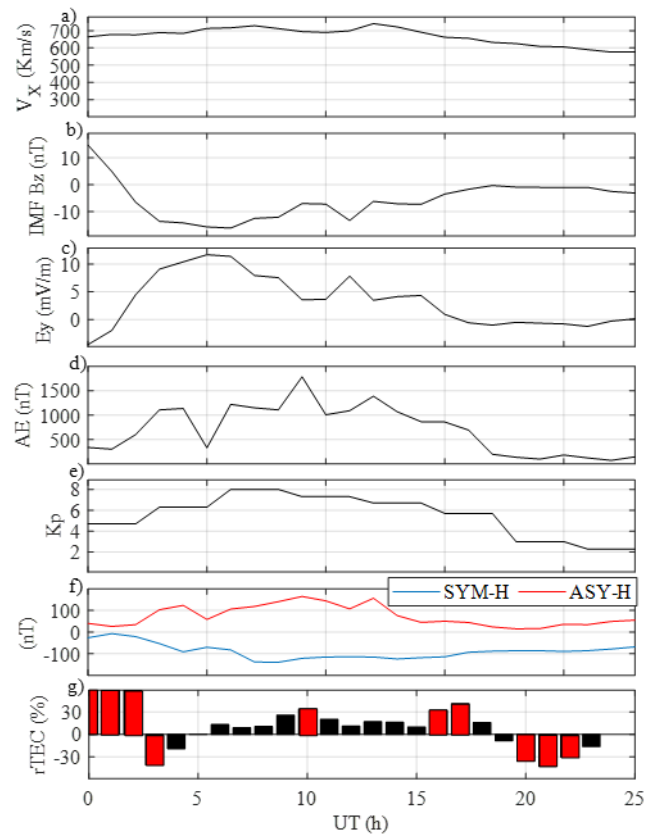


Figure 2. Space weather indices (a-f) and rTEC (g) under magnetospheric storm conditions (9 March 2001). Ranges in y-axes are set to be compared with Figure 1.

References

- Ansari, K., Park, K. D., Panda, S. K. (2019). Empirical Orthogonal Function analysis and modeling of ionospheric TEC over South Korean region. *Acta Astronaut.* 161, 313–324.
- Araki, T., Allen, J.H., Araki, Y. (1985). Extension of a polar ionospheric current to the nightside equator. *Planet. Space Sci.* 33(1), 11–16.
- Calabia, A, C Anoruo, S Munawar, C Amory-Mazaudier, Y Yasyukevich, C Owolabi, and S Jin (2021), Low-Latitude Ionospheric Responses and Coupling to the February 2014 Multiphase Geomagnetic Storm from GNSS, Magnetometers, and Space Weather Data. *Atmosphere*, 13, 518. Doi:10.3390/atmos13040518.
- Ji E.-Y., Moon Y. J., Kim K. H. & Lee D. H. (2010). Statistical comparison of interplanetary conditions causing intense geomagnetic storms ($Dst \leq -100$ nT). *Journal of Geophysical Research (Space Physics)* 115 A10232.
- Pancheva, D., Mukhtarov, P., Andonov, B. (2016). Global Structure of Ionospheric TEC Anomalies Driven by

- Geomagnetic Storms, *Journal of Atmospheric and Solar-Terrestrial Physics*, 145, 170–185, <https://doi.org/10.1016/j.jastp.2016.04.015>.
- Richmond, A.D., Roble, R.G. (1979). Dynamic effects of aurora-generated gravity waves on the mid-latitude ionosphere. *J. Atmos. Terr. Phys.* 41(7–8), 841–852.
- Seemala, G. K., & Valladares, C. E. (2011). Statistics of total electron content depletions observed over the South American continent for the year 2008. *Radio Science*, 46, RS5019. doi:10.1029/2011RS004722.
- Sharma, S. K., Singh, A. K., Panda, S. K. et al. (2020). The effect of geomagnetic storms on the total electron content over the low latitude Saudi Arab region: a focus on St. Patrick's Day storm. *Astrophys Space Sci* 365, 35. <https://doi.org/10.1007/s10509-020-3747-1>.
- Yamazaki, Y., Kosch, M. J. (2015). The equatorial electrojet during geomagnetic storms and substorms. *J. Geophys. Res. Space Phys.* 120(3), 2276–2287.



4th Intercontinental Geoinformation Days

igd.mersin.edu.tr



Using the Firefly algorithm for geoid determination

Ulku Kirici Yildirim^{*1}, Yasemin Sisman¹

¹Ondokuz Mayıs University, Engineering Faculty, Department of Geomatics Engineering, Samsun, Türkiye

Keywords

Geoid determination
Least absolute value method
Metaheuristic algorithm
Firefly algorithm

Abstract

The geoid is a mathematically complex surface. For years' geoid determination has been the topic of geomatics engineering. There are many methods for Geoid Determination, such as Polynomial Interpolation, kriging interpolation, and The Least Square Collocation etc. Outlier measurement have a corruptive effect on parameter estimation. There are two methods that are frequently used for the determination of outlier measurement, in geomatics engineering. These are The Least Square Method and The Least Absolute Value Method. These methods have advantages and disadvantages over each other. Also nowadays, very complex problems can be solved with methods such as the rapidly developing Artificial Intelligence and Machine Learning Technologies with Metaheuristics Algorithm for obtaining a close to optimum solution. There are many metaheuristic algorithms developed and used nowadays. One of them is the Firefly Algorithm. In this study, the usability of the firefly algorithm was tested to determine the outlier measurement in the geoid determination process.

1. Introduction

In applied sciences, the parameter estimation is made using adjustment procedure, because the measurements number is more than the of unknown's number. in order to increase the accuracy and precision obtained from measurements and the results of measurements. The objective of adjustment are to find out the most suitable and highest probability value of the unknowns and unknown functions without leaving out any measurement from measurement groups (Wang, 1992). Geoid determination also has an important place in Geomatics applications. In geodetic applications, elevation is measured with reference to the surface of a geoid as orthometric height. Ellipsoidal height is measured with GPS. Hence, GNSS-derived ellipsoidal heights must be transformed into orthometric heights. There is a mathematical relationship between these heights (Heiskanen, 1967).

Metaheuristic algorithms have become popular in finding the best in recent years and are still used in many optimization problems (Canayaz, 2015). Its use in Geomatics studies has just begun.

In this study, point cloud data consisting of 333 points concerning to Samsun province in Turkey was used.

Point cloud data was processed using the Cloud Compare program. The surface model of the point cloud was created using a 2nd degree polynomial. Outlier measurements were determined using The Least Absolute Value Method (LAV) and Firefly Algorithm (FA) method.

2. Method

2.1. Geoid determination and outlier measurement

The geoid is a complex surface and formed by the combination of the points have got zero potential value. The geoid determination is the most important problem in the earth. Because the geoid does not represent a regular shape. Local geoid determination studies aim was to determine a local geoid using the geoid determination methods for example Polynomial Interpolation Method (Akar, Konakoğlu, & Akar, 2022).

The polynomial technique is based on the determination of polynomial surface. The surface used to determine the geoid is generally expressed in high degree polynomials with two variables (Kirici & Sisman, 2017). The orthogonal polynomials can be represented as as follow;

* Corresponding Author

(ulku.kirici@omu.edu.tr) ORCID ID 0000 – 0002 – 3569 – 4482
(yysisman@omu.edu.tr) ORCID ID 0000 – 0002 – 6600 – 0623

Cite this study

Yıldırım, U. K., & Şişman, Y. (2022). Using the Firefly algorithm for geoid determination. 4th Intercontinental Geoinformation Days (IGD), 306-309, Tabriz, Iran

$$N(x, y) = \sum_{i=0}^m \sum_{j=0}^k a_{ij} x^i y^j$$

Polynomial equation can be written for 2nd order polynomial is as follow;

$$N = a_{00} + a_{10}x + a_{01}y + a_{20}x^2 + a_{11}xy + a_{02}y^2$$

If the number of measures is greater than the unknown number in a problem, adjustment calculation is made for a univocal solution (Montgomery, Peck, & Vining, 2021). Adjustment is a means of obtaining unique values for the unknown parameters to be determined when there are more observations than actually needed; statistical properties may be determined as by products (Ogundare, 2018). A few methods have been developed to adjustment calculation. Although, the least square adjustment is known methods, the LAV method is one of the oldest robust methods.

2.1.1. The least absolute value method

The Least Absolute Value Method (LAV) developed by Laplace. To determine the unknown parameters in the adjustment measurement, a solution is made according to an objective function. LAV method solves with $\|pv\| = [P|v|] = \min$ objective function (Sisman, Sisman, & Bektas, 2013)

In this method direct solution is not possible. The solution can be found as trial and error or linear programming problem. New unknowns are as follows for linear programming (Sisman, 2010).

$$\begin{bmatrix} A & -A & -I & I \end{bmatrix} \begin{bmatrix} X^+ \\ X^- \\ V^+ \\ V^- \end{bmatrix} = [L]$$

$$f = b^T X = [P|V|] = P^T V = P^T [V^+ \quad V^-] = \min$$

The detail of LAV can be found in (Dielman, 2005)

2.2. Metaheuristic algorithm

Metaheuristic algorithms appear as comprehensive algorithms that are above heuristics and decide which method to use in solving problems. Metaheuristics have developed dramatically. (Osman & Kelly, 1997). In order for Metaheuristic algorithms to be usable, they must meet certain criteria. At the beginning of these criteria are the closeness of the solutions they found to the optimum value and the time they spent in obtaining these solutions. The fact that the algorithms are coded in a way that can be understood by everyone and provides ease of analysis is also an important factor in the selection of algorithms (Canayaz, 2015). There are many different metaheuristic algorithms in the literature. These are; Firefly Algorithm, Genetic Algorithm (Banzhaf, Nordin, Keller, & Francone, 1998), Shuffled Frog Leaping Algorithm (Eusuff, Lansey, & Pasha, 2006), Particle

Swarm optimization (Lazinic, 2009), Ant Colony Optimization (Maniezzo, Gambardella, & Luigi, 2004) etc.

2.2.1. Firefly algorithm

Firefly Algorithm (FA) was developed by Xin She Yang (Yang, 2010b). This algorithm was based on the flashing patterns and behavior of fireflies. This method generally has three rules.

- Fireflies are unisex so that one firefly will be attracted to other fireflies regardless of their sex.
- The attractiveness is proportional to the brightness, and they both decrease as their distance increases. Thus, for any two flashing fireflies, the less bright one will move towards the brighter one. If there is no brighter one than a particular firefly, it will move randomly.
- The brightness of a firefly is determined by the landscape of the objective function (Yang & He, 2013).

In the FA, there are two important issues: the variation of light intensity and formulation of the attractiveness. For simplicity, we can always assume that the attractiveness of a firefly is determined by its brightness or light intensity which in turn is associated with the encoded objective function. In the simplest case for maximum optimization problems, the brightness I of a firefly at a particular location x can be chosen as $I(x)/f(x)$. However, the attractiveness $_$ is relative, it should be seen in the eyes of the beholder or judged by the other fireflies. Thus, it should vary with the distance r_{ij} between firefly i and firefly j . As light intensity decreases with the distance from its source, and light is also absorbed in the media, so we should allow the attractiveness to vary with the degree of absorption (Yang, 2010a).

The light intensity $I(r)$ varies with distance r monotonically and exponentially (Farahani, Abshouri, Nasiri, & Meybodi, 2011). That is;

$$I = I_0 e^{-\gamma r}$$

As firefly attractiveness is proportional to the light intensity seen by adjacent fireflies, we can now define the attractiveness by β of a firefly.

$$\beta = \beta_0 e^{-\gamma r^2}$$

γ = light absorption coefficient

r_{ij} = distance between two fireflies

$$r_{ij} = |x_i - x_j|$$

The movement of the i^{th} firefly towards the j^{th} firefly, which is more attractive (Değertekin, Lamberti, & Ülker, 2015);

$$x^{i+1} = x^i + \beta_0 e^{-\gamma r^2} (x^j - x^i) + \alpha(\text{rand} - 0.5)$$

Here, α is random selection parameter, rand is random number.

2.3. Case study

In this study, a point cloud that contains 333 points, is used as a data set. The distribution of points with known x, y and h values is shown in Figure 1.

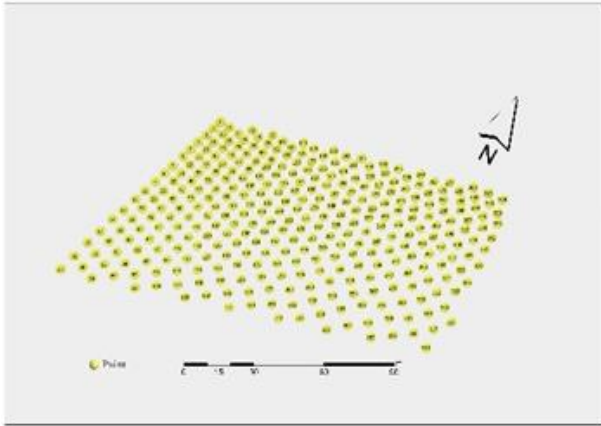


Figure 1. Data set distribution

At first, by using point cloud, surface model was created with 2nd degree polynomial equation according to LAV, which is one of the classical testing methods, then the outlier measurements were determined on this surface. After these steps, the Firefly algorithm, which is one of the metaheuristics algorithms, is applied to the same data set, and outlier measurements were determined with this method.

3. Results

LAV method determines 69 of 333 points as an outlier. This means that the 69 points do not belong to the surface and the surface belongs to 264 points. Figure 2 shows the distribution of the outliers which are found by the LAV method.

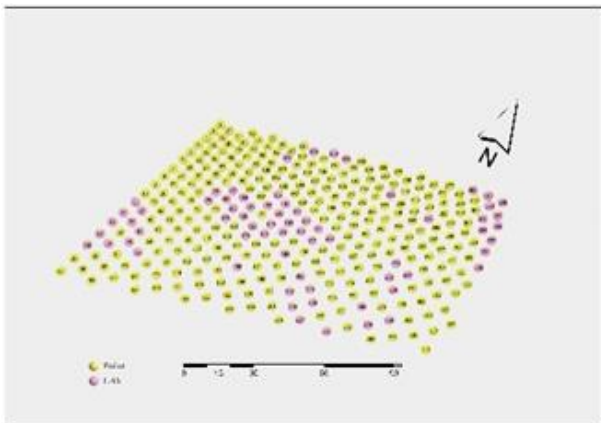


Figure 2. Outlier points of the LAV Method

Firefly Algorithm was applied to the data set and 50 of 333 points were determined as an outlier with this method. According to the firefly, the surface consists of 283 compatible points (Figure 3).

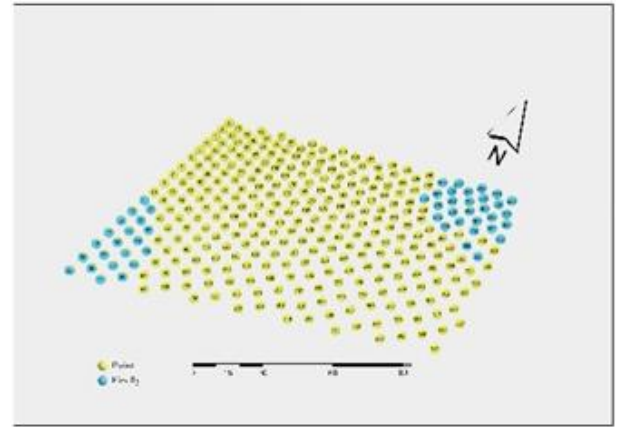


Figure 3. Outlier points of the Firefly Method

4. Discussion

As a result of LAV, 69 points were determined as an outlier while in the firefly algorithm 50 points were determined. When the points found in common by both methods are observed, it is seen that 21 points are common. Common points found by the two methods are shown in Figure 4.

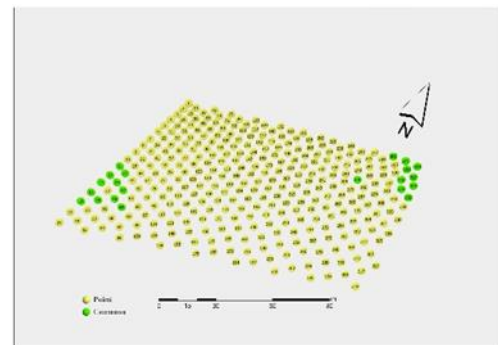


Figure 4. Common points

5. Conclusion

When the intersection points are examined, it is seen that they cover each other at the rate of 42%. The fact that the metaheuristic approaches, which is a modern method, gives consistent results with the results obtained with classical methods, reveals the usability of these methods in the field of geomatics engineering. Metaheuristic algorithms have limited use in geomatics fields, they are not widely used in geoid determination yet. In this study, the usability of the firefly algorithm in geoid determination was tested. In future work, this application can be improved by expanding the study area or by comparing the results with different methods.

Thesis should be written as Master's Thesis or Doctoral Thesis in the reference list.

References

- Akar, A., Konakoğlu, B., & Akar, Ö. (2022). Prediction of geoid undulations: Random forest versus classic interpolation techniques. *Concurrency and Computation: Practice and Experience*, e7004.
- Banzhaf, W., Nordin, P., Keller, R. E., & Francone, F. D. (1998). *Genetic programming: an introduction: on the automatic evolution of computer programs and its applications*: Morgan Kaufmann Publishers Inc.
- Canayaz, M. (2015). Cırcır böceği algoritması: Yeni bir meta-sezgisel yaklaşım ve uygulamaları.
- Değertekin, S. Ö., Lamberti, L., & Ülker, M. (2015). Uzay kafes yapıların ateş böceği algoritması yöntemiyle optimizasyonu.
- Dielman, T. E. (2005). Least absolute value regression: recent contributions. *Journal of statistical computation and simulation*, 75(4), 263-286.
- Eusuff, M., Lansey, K., & Pasha, F. (2006). Shuffled frog-leaping algorithm: a memetic meta-heuristic for discrete optimization. *Engineering optimization*, 38(2), 129-154.
- Farahani, S. M., Abshouri, A. A., Nasiri, B., & Meybodi, M. (2011). A Gaussian firefly algorithm. *International Journal of Machine Learning and Computing*, 1(5), 448.
- Heiskanen, W. A. (1967). Physical geodesy. *Determination of the Geoid from Ground Anomalies*, 8, 325-330.
- Kirici, U., & Sisman, Y. (2017). The Comparison of the Adjustment Methods in Geoid Determination Method. *FIG Working Week, Helsinki, Finland*.
- Lazinica, A. (2009). *Particle swarm optimization*: BoD-Books on Demand.
- Maniezzo, V., Gambardella, L. M., & Luigi, F. d. (2004). Ant colony optimization. In *New optimization techniques in engineering* (pp. 101-121): Springer.
- Montgomery, D. C., Peck, E. A., & Vining, G. G. (2021). *Introduction to linear regression analysis*: John Wiley & Sons.
- Ogundare, J. O. (2018). *Understanding least squares estimation and geomatics data analysis*: John Wiley & Sons.
- Osman, I. H., & Kelly, J. P. (1997). Meta-heuristics theory and applications. *Journal of the Operational Research Society*, 48(6), 657-657.
- Sisman, Y. (2010). Outlier measurement analysis with the robust estimation. *Scientific Research and Essays*, 5(7), 668-678.
- Sisman, Y., Sisman, A., & Bektas, S. (2013). Koordinat dönüşümünde deney tasarımı yaklaşımı. *Harita Teknolojileri Elektronik Dergisi*, 5(1), 37-46.
- Wang, Y. (1992). A rigorous photogrammetric adjustment algorithm based on co-angularity condition. *International Archives of Photogrammetry and Remote Sensing*, 29(B5), 195-202.
- Yang, X.-S. (2010a). Firefly algorithm, stochastic test functions and design optimisation. *International Journal of Bio-inspired computation*, 2(2), 78-84.
- Yang, X.-S. (2010b). *Nature-inspired metaheuristic algorithms*: Luniver press.
- Yang, X.-S., & He, X. (2013). Firefly algorithm: recent advances and applications. *International journal of swarm intelligence*, 1(1), 36-50.



4th Intercontinental Geoinformation Days

igd.mersin.edu.tr



Combining GIS and AHP models for landfill site selection in Niğde, Turkey

Cemil Gezgin *¹

¹Aksaray University, Engineering Faculty, Geomatics Engineering Department, Aksaray, Türkiye

Keywords

GIS
AHP
Landfill
Site selection

Abstract

Nowadays, the quick development of technology and the increase in migration from rural areas to urban areas have transformed cities into populous living places. With the increasing population, urbanization ratio and changing consumption habits, natural environment and energy problems are expanding in cities. These problems that arise in the cities not only negatively affect the economic and social life, but also affect the welfare of the people living in the city and bring many problems for local governments. With the unplanned urbanization and the environmental problems, solid waste landfill sites have started to stay within the settlement areas. GIS and MCDM have become an effective and important tool in solving environmental and spatial problems as well as in many other problems. With the integration of GIS and MCDM, suitable site selections can be made in terms of economic and environmental aspects. For this purpose, in this study; Solid waste landfill site selection study was carried out for Niğde province by using Analytical Hierarchy Method (AHP) and Geographic Information Systems (GIS). In this context, 9 evaluation criteria such as elevation, slope, geology/lithology, land use, proximity to roads, distance to settlements, protected areas, rivers and water surfaces were used to determine potential solid waste landfill areas.

1. Introduction

Undesirable materials that consist in all fields of life and arise as a result of human and other activities, which cannot be completely removed, but can be disposed of in the best possible way with various methods and efforts, are defined as solid waste (İşildar, 2018). The increase in human population and related human activities in developing countries has expedited urbanization (Sumathi et al. 2008). As a result of increasing population, migration from rural areas to cities, changes in consumption patterns, economic growth, increase in income, urbanization and industrialization, solid waste production and its diversity have increased and the negative effects of this rapidly increasing waste on the environment have turned into a problem that cannot be neglected (Aydın, 2007, Ngoc and Schnitzer, 2009; Güler and Yomralıoğlu, 2017).

Urban solid waste management, which is an environmental issue, is a sensitive area in the world countries and can be described as the try to dispose of wastes with the optimum method that does not damage the environment, aid by the local community that straightly under effect of the solid waste program in the

region (Güler, 2016; İşildar, 2018). Inappropriate solid waste management can cause significant health and environmental issues. Therefore, in order to avoid such issues, solid waste disposal methods and environmental effects should be handled sensitively in the solid waste management (Karagiannidis and Moissiopolous, 1997; Pires et al. 2010; Şener et al. 2010; Bilgilioglu et al. 2022).

Solid waste management system is a complex and multidisciplinary problem that thoroughly examines technical, social and economic factors in terms of recycling and sustainability. Site selection studies for a solid waste landfill is a complicated process that requires the processing of large amounts of spatial data. While determining the site selection criteria; In general, restrictive parameters such as land cover, geological formation, administrative borders, surface waters, highway are used (Sadek et al. 2006; Şengün et al. 2018; Ciritçi and Türk, 2019). The integration of rapidly developing Geographic Information System (GIS) and MCDM models is a suitable method in studies that require appropriate site selection and similar spatial analysis. The GIS-based MCDM approach provides important contributions to decision makers in making

* Corresponding Author

*(cemilgezgin.jfm@gmail.com) ORCID ID 0000-0002-5951-0107

Cite this study

Gezgin, C. (2022). Combining GIS and AHP models for landfill site selection in Niğde, Turkey. 4th Intercontinental Geoinformation Days (IGD), 310-313, Tabriz, Iran

appropriate site selection decisions, in terms of better understanding the problem, identifying the risks to be encountered and interpreting the results (Chen et al. 2001; Bilgilioglu, 2022).

Within this scope of study; using the Geographical Information Systems (GIS) and Analytical Hierarchy Method (AHP), which is one of the and multi-criteria decision making (MCDM) methods, the appropriate location for the solid waste disposal site and the suitability of the existing solid waste storage area were investigated in Niğde province. For this purpose, 9 criteria were used in the determination of potential solid waste disposal sites, including elevation, slope, geology/lithology, land use, proximity to roads, distance from settlements, protection areas, rivers and water surfaces.

2. Method

MCDM is a tool that consent to determine the best choice between the criteria that are evaluated more than one and simultaneously. The purpose of using MCDM methods is to make the decision-making mechanism easy and fast in situations where the number of options and criteria is high (Huang et al. 2011; Rezaeisabzevar et al. 2020). With the progression of Geographic Information Systems (GIS), different MCDM methods have found application in solving spatial problems. These methods offer a broad field of applications like, land suitability mapping, site selection studies, planning in urban and regional scale. (Uyan and Yalpir, 2016).

Among the many MCDM methods used, which model selection will be most appropriate and which model is the most suitable for the decision maker depends on the issue to be solved (Uyan, 2011). AHP is an effective approach to decision making and is definitely the most widely used MCDM method. (Dehe and Bamford, 2015). AHP, used as a decision analysis tool, is a mathematical method evolved by Saaty in 1970s as a model to analyze complex decision problems with multiple criteria (Saaty, 1980). In this study, in order to determine the most suitable location for the solid waste disposal site, the evaluation criteria were weighted using the Analytical Hierarchy Process (AHP) technique, which is one of the MCDM techniques and is frequently used in the literature.

2.1. Study area

Niğde is located in the southeast of Turkey's Central Anatolia Region and its altitude is 1,229 m above sea level. Niğde province, whose neighboring provinces are Aksaray, Kayseri, Nevşehir and Konya, is separated from the province of Mersin by the Bolkar Mountains in the south, and from the province of Adana by the natural borders formed by the Aladaglar in the southeast and east (Figure 1; Soydan 2021).

Thermal resources, archaeological sites, rich historical texture, natural beauties, mountain and winter tourism opportunities are important factors that make the city a tourism center. Niğde Province has a population of 363,725 in 2021 and has an area of approximately 7312 km². Central Anatolia's typical

continental climate is also seen in Niğde province (SERM 2020).

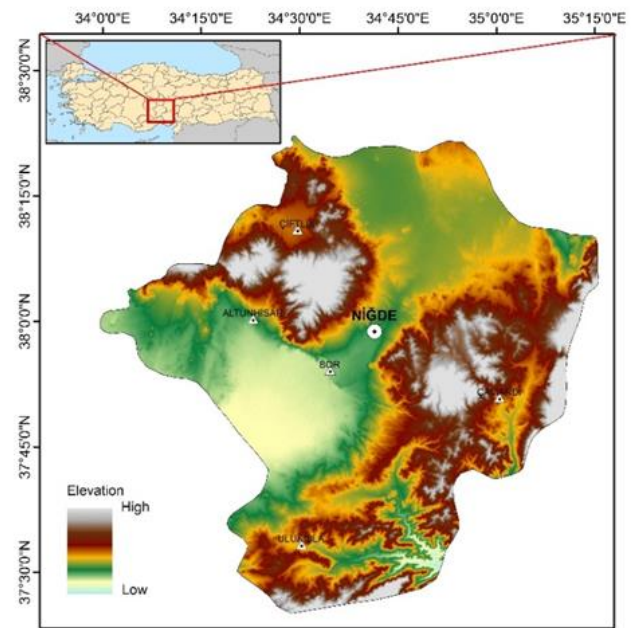


Figure 1. Study area

3. Results and Discussion

Comparison matrix for all criteria was created and the values obtained by calculating the importance levels of the criteria using AHP are given in Table 1. The pairwise comparison matrix was obtained using the opinions of experts in the field and previous literature studies. Since the Consistency Ratios (CT) obtained in the comparison matrices created in the AHP (0.0437) were below the desired value (0.10), the comparisons were considered to be consistent. All the data used in the evaluation were converted to the UTM 36-3 projection coordinate system and the pixel size was taken as 20 m in the study.

Table 1. Criteria weights

Criteria	Weight
Elevation	0.051
Slope	0.162
Lithology	0.130
Land use	0.074
Proximity to roads	0.091
Distance from settlements	0.114
Distance from protection areas	0.032
Distance from rivers	0.158
Distance from water surfaces	0.188

The criteria weights given in Table 1 show the importance of these criteria at the suitable site selection process. In this context, it has been determined that the criteria of Distance from water surfaces, rivers and slope are more important in the selection of landfill site selection, while the criteria of Distance from protection areas, elevation and lands use are less important.

The maps of each normalized criteria are given in Figure 2. In Figure 2, the areas shown in red represent very low suitable areas for the solid landfill disposal site,

while the areas shown in dark blue indicate very high suitable areas.

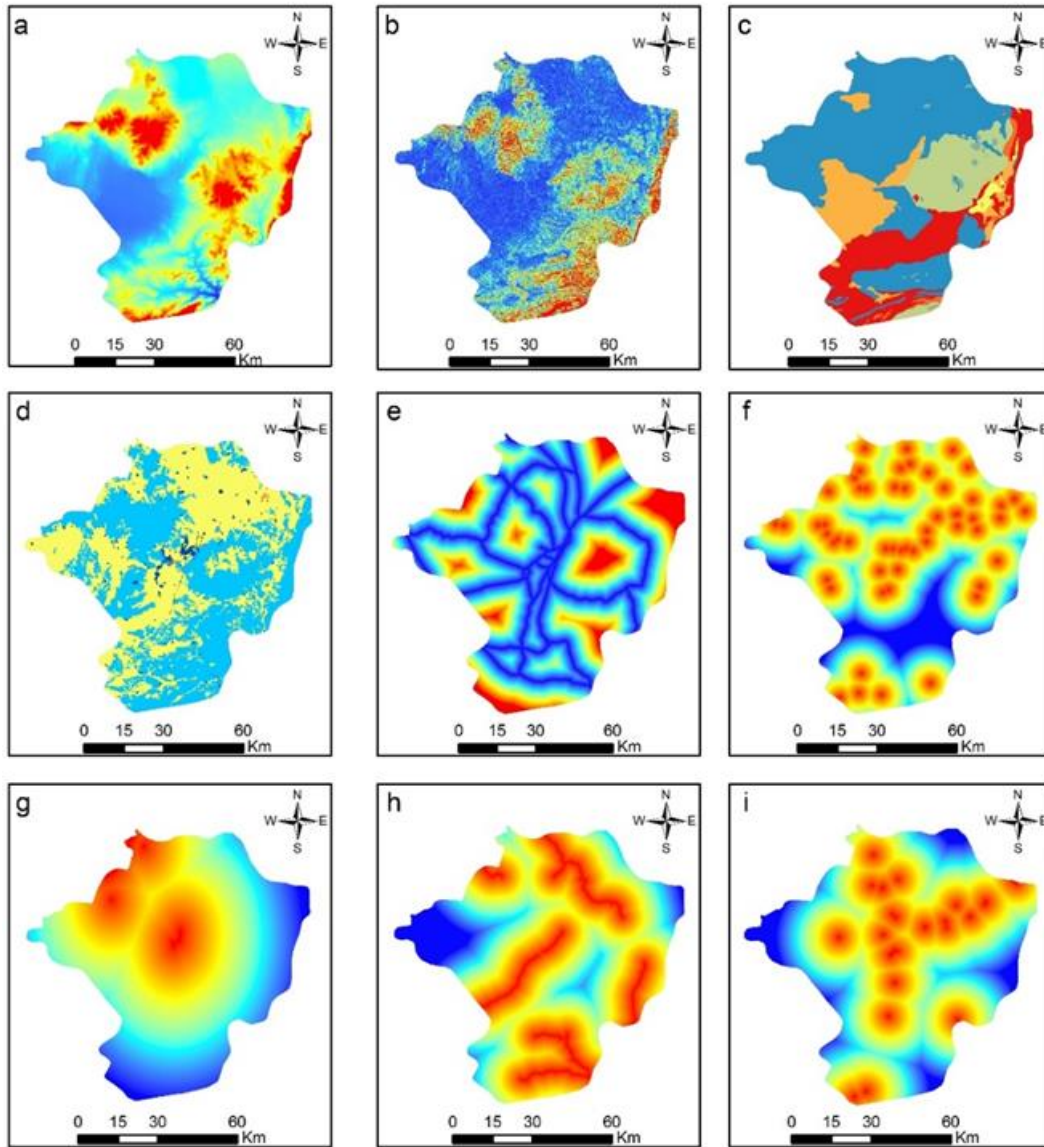


Figure 2. Evaluation criteria; a) Elevation b) Slope c) Lithology d) Land use e) Proximity to roads f) Distance from settlements g) Distance from protection areas h) Distance from rivers i) Distance from water surfaces

According to the analysis result, the study area; classified into 5 classes as very low suitable, low suitable, moderate suitable, high suitable and very high suitable and are shown in Figure 3. It is seen that central districts such as Altunhisar and Çamardı are more suitable areas for the construction of solid waste landfill sites compared to other regions. In addition to this, the existing solid waste storage facility in Niğde is located in a region that is considered very low suitable and low suitable according to the findings obtained from this study. This facility, which started its operations in 2013, is located in an area very close to the city with the expansion of Niğde province over the years. The study conducted by Ertunç et al. (2019), it is determined that the existing solid waste landfill site can affect the urban area negatively. Therefore, when the findings obtained from this study are compared with other similar studies (Öcal, 2010;

Ertunç et al. 2019) carried out in the region, it is seen that the results are similar to each other.

4. Conclusion

In this study, site selection analyzes were carried out by combining GIS and AHP methods to obtain potential solid waste landfill sites in Niğde city. For this purpose, nine criteria were selected for the site selection study and after determining the weights of these criteria with the aid of AHP method, a suitability map was created. When the produced suitability map is examined, it has been determined that the city center of Niğde and existing solid waste facility is located in very low suitable area and the districts of Altunhisar and Çamardı are more suitable areas for the new facility to be constructed.

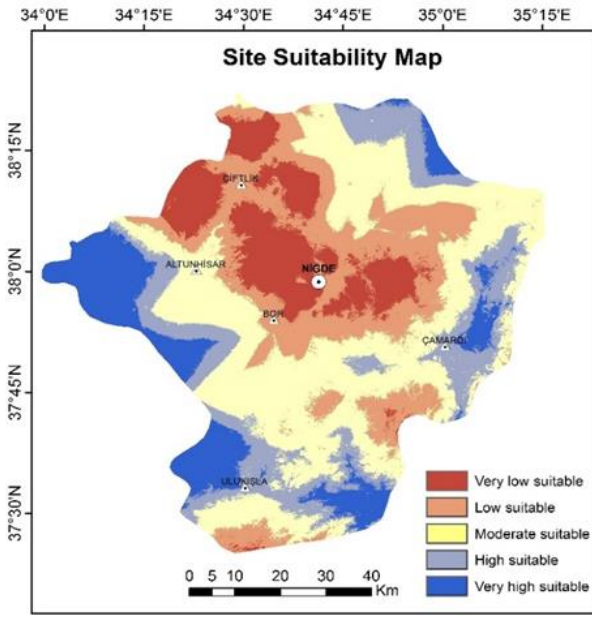


Figure 3. Solid waste landfill site suitability map of Niğde city

References

- Aydın, N. (2007). Katı atık yönetiminde optimal planlama için bulanık doğrusal programlama yaklaşımı, MS thesis, Yıldız Technical University, İstanbul.
- Bilgilioglu, S. S. (2022). Coğrafi Bilgi Sistemleri ve Bulanık Analitik Hiyerarşi Süreci ile Elektrikli Araç Şarj İstasyonu Yer Seçimi. Afyon Kocatepe Üniversitesi Fen Ve Mühendislik Bilimleri Dergisi, 22(1), 165-174.
- Bilgilioglu, S. S., Gezgın, C., Orhan, O., & Karakus, P. (2022). A GIS-based multi-criteria decision-making method for the selection of potential municipal solid waste disposal sites in Mersin, Turkey. Environmental Science and Pollution Research, 1-17.
- Chen, K., Blong, R., & Jacobson, C. (2001). MCE-RISK: integrating multicriteria evaluation and GIS for risk decision-making in natural hazards. Environmental Modelling & Software, 16(4), 387-397.
- Ciritci, D., & Türk, T. (2019). Alternatif katı atık depolama alanlarının analitik hiyerarşi süreci ve coğrafi bilgi sistemleri ile otomatik olarak belirlenmesi: Sivas ili örneği. Jeodezi ve Jeoinformasyon Dergisi, 6(1), 61-74.
- Dehe, B., & Bamford, D. (2015). Development, test and comparison of two Multiple Criteria Decision Analysis (MCDA) models: A case of healthcare infrastructure location. Expert Systems with Applications, 42(19), 6717-6727.
- Ertunç, E., Bozdağ, A., & Gökçek, Ö. B. (2019). Investigation of The Solid Waste Landfill Site selection Using The Geographic Information System In The City Of Niğde. Konya Mühendislik Bilimleri Dergisi, 7(4), 822-838.
- Güler, D., & Yomralıoğlu, T. (2017). Coğrafi bilgi sistemleri ve analitik hiyerarşi yöntemi ile düzenli deponi yer seçimi: İstanbul ili örneği. Afyon Kocatepe Üniversitesi Fen ve Mühendislik Bilimleri Dergisi, 17(4), 262-269.
- Güler, D. (2016). Analitik Hiyerarşi Yöntemi Ve Coğrafi Bilgi Sistemleri İle Alternatif Katı Atık Düzenli depolama Alanı Yer Seçimi: İstanbul İli Örneği. DR. Thesis, Istanbul Technical University, Istanbul.
- Huang, I. B., Keisler, J., & Linkov, I. (2011). Multi-criteria decision analysis in environmental sciences: ten years of applications and trends. Sci. Total Environ. 409, 3578-3594.
- İşildar, A. (2018). Çok kriterli karar verme yöntemleriyle katı atık bertaraf yöntemi seçimi. MS thesis, Pamukkale Üniversitesi, Pamukkale (in Turkish).
- Karagiannidis, A., & Moissiopolous, N. (1997). Application of electre III for the integrated management of municipal waste in the Greater Athens Area, European Journal of Operational Research, 97, 439- 449.
- Ngoc, U. N., & Schnitzer, H. (2009). Sustainable solutions for solid waste management in Southeast Asian countries. Waste Management, 29, 1982-1995.
- Öcal, T. (2010). Günümüz şehirleşme sürecinde evsel katı atık sorununa bir örnek: Niğde Şehri . Türk Coğrafya Dergisi, 55, 35-43.
- Pires, A., Martinho, G., & Chang, N. B. (2011). Solid waste management in European countries: A review of systems analysis techniques. Journal of environmental management, 92(4), 1033-1050.
- Rezaeisabzevar, Y., Bazargan, A., & Zohourian, B. (2020). Landfill site selection using multi criteria decision making: Influential factors for comparing locations. Journal of Environmental Sciences, 93, 170-184.
- Saaty, T. L. (1980). The analytic hierarchy process. McGraw-Hill, New York.
- Sadek, S., Fadel, M. E., & Freiha, F. (2006). A Multi-Criteria Modular and Flexible decision aid tool for Landfill Siting using GIS. 21st International Conference on Solid Waste Technology and Management, Philadelphia, USA. 26 - 28 Mar 2006.
- Şener, Ş., Şener, E., Nas, B., & Karagözel, R. (2010). Combining AHP with GIS for landfill site selection: a case study in the Lake Beyşehir catchment area (Konya, Turkey). Waste management, 30(11), 2037-2046.
- Şengün, M. T., Siler, M., & Engin, F. (2018). Katı Atık Depolama Alanlarının Yer Seçiminde CBS'nin Kullanımı: Malatya Örneği. Zeitschrift für die Welt der Türken/Journal of World of Turks, 10(1), 159-180.
- SERM (2020) State of environment report of Niğde province. Republic of Turkey, Ministry of Environment and Urbanization
- Soydan, O. (2021). Solar power plants site selection for sustainable ecological development in Niğde, Turkey. SN Applied Sciences, 3(1), 1-18.
- Sumathi, V. R., Natesan, U., & Chinmoy, S. (2008). GIS based approach for optimized siting of municipal solid waste landfill. Waste Management, 28, 2146-2160.
- Uyan, M., & Yalpir, Ş. (2016). Çok kriterli karar verme modeli ve CBS entegrasyonu ile tıbbi atık sterilizasyon tesislerinin yer seçimi. Afyon Kocatepe Üniversitesi Fen ve Mühendislik Bilimleri Dergisi, 16(3), 642-654.
- Uyan, M. (2011). Arazi Düzenlemesi Çalışmalarında Mekansal Karar Destek Sistemleri Kurulumu ve Uygulaması. DR thesis, Selçuk University, Konya, Turkey.



4th Intercontinental Geoinformation Days

igd.mersin.edu.tr



Exploring the effect of Steiner points on the simplification algorithms

Amir Gholami¹, Abolfazl Ghanbari ^{*1}, Neda Kaffash Charandabi ²

¹ University of Tabriz, Planning & Environmental Sciences, Remote Sensing and Geographical Information System (GIS), Tabriz, Iran

² University of Tabriz, Marand Technical College, Geomatics Engineering, Tabriz, Iran

Keywords

Least Squares
Douglas Poker
Simplification
Steiner points
Trajectory data

Abstract

With the increasing volume of spatial data generated by a variety of spatial data recording tools such as smartphones, the importance of geometric simplification approaches has become more and more over time. The goal of geometric simplification is to achieve more summarized and less complex features. It provides an algorithm that results in terms of geometric properties such as area, perimeter, and angles being more similar to the primary feature. Algorithms with lower accuracy select consecutive subsets of primary points. As a result, some points of the geometric shape are completely ignored. While the results of methods such as least squares (LS) are more accurate in geometric simplification. Also, most geometric simplification algorithms of linear features focus on points in their processes and ignore the edges. Therefore, in this study, to improve the accuracy of geometric simplification accuracy, the effect of Steiner points on Douglas Poker (DP), LS, and a combination of them (DP-LS) was investigated. For this purpose, the trajectory recorded in Einali Mountain of Tabriz was used. The results showed that the use of Steiner points on average led to an improvement of 3.46% angle changes, 914941 m² area difference, 2.66% curvature similarity, and 0.36% node reduction in DP-LS and LS methods.

1. Introduction

With the advancement of technology and the equipping of smartphones with microchips of the Global Positioning System (GPS), huge volumes of data begin to be generated (Laurila et al., 2012). Many users use them in various applications such as finding places, events, restaurants and shops, and so on. The popularity of these devices has led to an increasing amount of trajectory data (Muckell et al., 2011), which can be used to determine the mobility of people, traffic network zoning, traffic detection, social anxiety, extracting interesting and scenic places for the tourism industry (Williams & Kemp, 2020). In addition, it is used in updating the roads and obtaining the boundaries of different areas and buildings (Shu et al., 2020).

Trajectory data is so large in the initial state that, according to the research findings, if trajectory constituents are collected at 10-second intervals, one gigabyte of storage capacity is needed to store more than 4,000 objects in a given day without data compression

(Meratnia & Rolf, 2004). By increasing the volume of data storage, the transfer of this information becomes very costly and reduces user satisfaction and reduce their use.

Different methods of data simplification are used to reduce data volume and thus increase the speed of processing (Sun et al., 2016). One type of simplification method that can be applied to trajectories data, is a geometric simplification, which is usually applied to the geometric properties of linear and polygonal features (Ying et al., 2003). Linear and polygonal features are a set of nodes that are connected to each other by the edges that enable each connection between the two nodes, respectively.

During the process of geometric simplification of these features, the number of nodes decreases and therefore the volume of data is reduced, which can be in two main ways, including selecting nodes from the primary nodes of the features or producing nodes with coordinates different from the original shapes (Renjian et al., 2009).

* Corresponding Author

(amirp5576@gmail.com) ORCID ID 0000 - 0001 - 7749 - 3534
*(a_ghanbari@tabrizu.ac.ir) ORCID ID 0000 - 0001 - 6225 - 0433
(n_kaffash@tabrizu.ac.ir) ORCID ID 0000-0002-6281-9009

Cite this study

Gholami, A., Ghanbari, A., & Charandabi, N. K. (2022). Exploring the effect of Steiner points on the simplification algorithms. 4th Intercontinental Geoinformation Days (IGD), 314-318, Tabriz, Iran

Different methods are used to reduce the volume of data with different accuracy. Accuracy refers to the degree of proximity of the simplified feature to the main feature in the real world, which can be examined from various perspectives such as geometric similarity, semantic, and spatial relationships (Wang et al., 2015).

It is important that most geometric simplification algorithms try to select a subset of the primary nodes (Song & Miao, 2016) so the final geometry of the algorithm output does not have any effect from the deleted nodes. However, a number of algorithms, implemented mainly on the basis of least squares (LS), examined the effect of all primary nodes on the final geometry of the simplified feature. Thus, more accurate estimates of the original geometry of the features have been obtained (Tong et al., 2015). However, it can be seen that these algorithms in the processing are mostly focused on nodes whereas edges are also a major part of the features.

Therefore, in this study, in addition to nodes, edges were also considered and this was done with the help of Steiner points. Steiner points are known as points that are not part of the primary feature. These points could be added to solving a geometric optimization problem, to create a better solution. For example, Steiner points have been used to construct triangulations with better angles and total line length. In the context of feature simplification, the offered Steiner points can allow for less displacement than popular algorithms that do not have Steiner points (Kronenfeld et al., 2020).

In this study, the least squares (LS), Douglas Poker (DP), and the least squares and Douglas Poker (DP-LS) algorithms were compared and the effect of Steiner points on the simplification process was evaluated.

LS method is the most well-known regression analysis technique. It is utilized to solve problems in which the quantity of observations is more than the quantity of unknowns. One of the most important applications of the least squares process is fitting lines and curves to points, so it was used in this study to fit a line to each of the features' segments (Ghilani & Wolf, 2006).

The main goal of DP method is to select and maintain a few mainline points. In other words, the deleted points are completely ignored in DP and have no effect on the simplified features (Douglas & Peucker, 1973).

The DP-LS simplification method is based on DP and line-fitting algorithm, and the area and length of the feature lines are kept constant before and after feature simplification by using LS method. In this model, first, the nodes are selected by DP, then the points between them (unselected points) are not deleted. Rather, lines with the LS are fitted to these points. By doing this, the effect of the arcs is more than the DP method in the simplified features. According to the geometry features of these lines, three condition equations are calculated including area, length, end-vertexes identical, and fixed-point condition equation. The results of the research show that the DP-LS model is feasible to ensure the data quality in the simplification process (Xiaohua & Gusheng, 2004).

To implement the idea of this research, the trajectories recorded in the Einali Mountain (in north of Tabriz, Iran), which were long and complex trajectories.

2. Method

To evaluate the proposed model of this research, two trajectories were selected from the Einali Mountain, Tabriz, East Azarbaijan Province, Iran (Figure 1). The reason for choosing this region was the long and complex trajectories of this area.

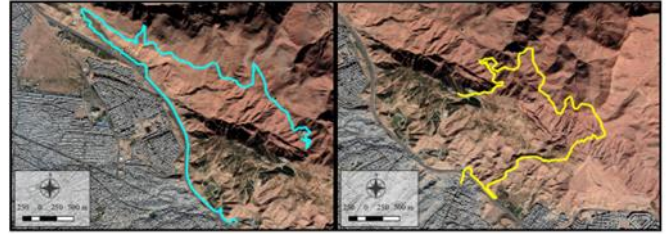


Figure 1. The study area of research, trajectory 1 (right) and trajectory 2 (left)

To investigate the effect of Steiner points on the linear features simplification, DP, DP-LS, and LS algorithms were applied to two different trajectories with three different thresholds of 1, 10, and 50 meters each. Each of the models was implemented once in the presence of Steiner points and again without them. Finally, 18 different models are obtained for each trajectory. The following describes how to create Steiner points on linear effects.

First, duplicate nodes must be removed from the trajectory. This will remove the zero edges. Steiner points are created on the edges of the trajectory at intervals of half the size of the shortest edge (L_{min}). Therefore, it can be ensured that there is at least one Steiner point on each edge. If the edge length (L_i) is not divisible by $L_{min} / 2$, then the distance of the Steiner points (D_s) for that edge is calculated according to Equations (1), (2).

$$n = \left\lceil \frac{2 \times L_i}{L_{min}} \right\rceil \quad (1)$$

$$D_s = \frac{L_i}{n} \quad (2)$$

According to this approach, creating Steiner points is a kind of preprocessing to perform the geometric simplification of linear effects, because the algorithms themselves remain unchanged and only the inputs change. In this study, the results are evaluated using five different indicators. These indicators are described below.

1. Area difference (I_1): By connecting the start and end of linear features, a polygon is obtained whose area can be calculated. The absolute value of the area difference of a linear feature, before (A_0) and after simplification (A), is used as the area difference index. The lower the value of this index, the better the simplification.

2. Reduction percentage of vertices number (I_2): Simplification of Polyline geometry is done with the aim of reducing the number of vertices and thus reducing the storage volume, and the higher the percentage of vertex reduction, the better the simplification is considered.

3. Percentage of average curvature similarity (I_3): The value of average curvature is obtained by dividing the sum of the feature geometry angles by the sum of the lengths of all its edges. The percentage similarity of the mean curvature is calculated according to Equations (3).

$$I_3 = 100 \times |MC - MC_0| / MC_0 \quad (3)$$

The mean curvature of the primary feature (MC_0) and simplified feature (MC) are obtained by dividing the sum of the angles by the sum of the lengths of their edges.

4. Percentage of changes in angles (I_4): This index is equal to the ratio of the sum of the angles of the simplified feature (Ang) to the sum of the angles of the primary feature (Ang_0) multiplied by 100. The higher the value of this index, the better the simplification.

5. Median Housdroff distance similarity (I_5): In this index, the minimum distance of each point of the primary polyline from the simplified polyline (D_{p-p_0}) and vice versa (D_{p_0-p}) is calculated. The smaller the distance, the better the simplification.

These five indicators and simplification algorithms DP, DP-LS, and LS, as well as the function required to create Steiner points, were implemented in the Python programming environment using the QGIS software API. In the next section, the implementation results are presented.

3. Results

After applying DP, DP-LS, and LS algorithms, simplified trajectory outputs were generated for different models. For example, trajectory 1 output with a threshold of 10 meters and trajectory 2 output with a threshold of 50 meters are shown in Figure 2 and Figure 3, respectively.

The similarity of all simplified shapes is that the distance of any point from them to the original feature is not more than the specified threshold. Therefore, by considering the threshold for all three algorithms equally, their performance can be evaluated by indicators. The evaluation results based on the five mentioned indicators are shown in Table 1.

According to Table 1, the values of the five evaluation indicators for the DP algorithm did not change before and after the use of Steiner points. Therefore, it can be concluded that the use of Steiner points has no effect on the performance of the DP algorithm. As mentioned, the DP algorithm only uses distance to simplification. In each iteration, it selects and holds the point farthest from the line connecting the other two points. For each edge, the start or end point is always selected and the Steiner points between them are eliminated. In the DP method, the summarized nodes are always a subset of the primary nodes, so the I_5 index for this method will always be zero.

Since the DP-LS method uses the DP method at the start of the operation, the reduction percentage of its points is similar to the DP method, according to Table 1. Therefore, whether or not Steiner points are used, combining LS with DP has no effect on improving results in terms of reducing the number of points. But according to other evaluation indicators, the use of Steiner points

has improved the performance of the DP-LS algorithm. LS algorithm implemented based on least squares. The results show that the use of Steiner points in simplification with LS algorithm, in most cases, has improved the performance of this algorithm. This result can be inferred based on all 5 implemented indicators.

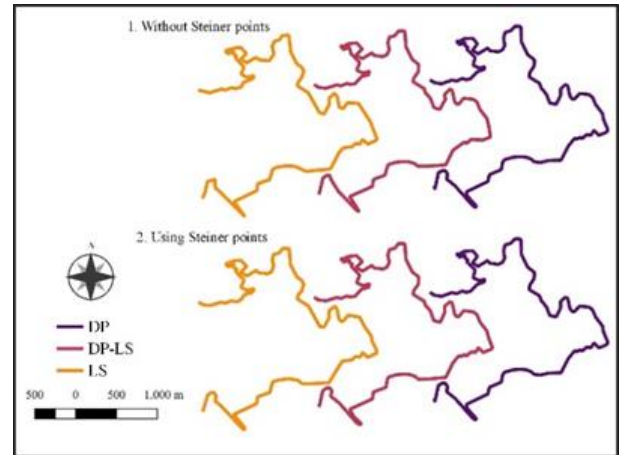


Figure 2. DP, DP-LS, and LS results for trajectory 1

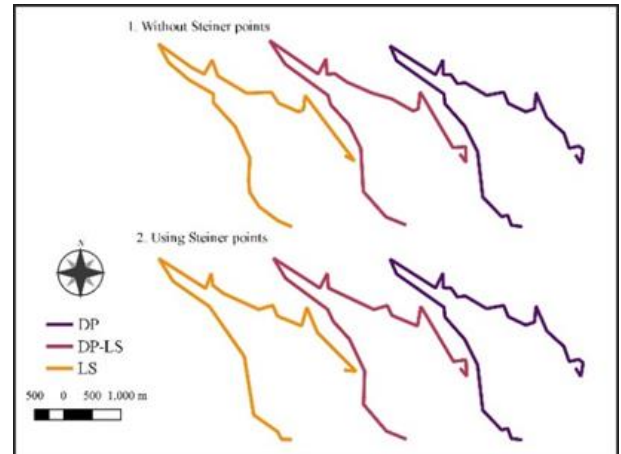


Figure 3. DP, DP-LS, and LS results for trajectory 2

Each Polyline consists of a set of points and edges. Edge lengths are ignored when fitting-based algorithms are used. Because only the points in the fitting process are used and the length of the edges is not affected. According to the results, creating Steiner points can be a good way to apply the effect of edges on the fit of the line. Thus, the longer the edge, the more points Steiner will have along it. This will affect the line fit and the output edge of the algorithm.

4. Conclusion

In this study, the effect of Steiner points on the geometric simplification of linear features was investigated. For this purpose, three algorithms DP, DP-LS, and LS with different tolerances of 1, 10, and 50 meters were applied on two different trajectories. In each model, the influence of Steiner points was evaluated by five different indicators. Based on these results, Steiner points have no effect on DP simplification.

Steiner points also have no effect on the results obtained by the DP-LS method in terms of reducing the

number of points. But the LS method has improved the simplification process about 0.72%.

The use of Steiner points based on the indices of area difference, average curvature similarity percentage, similarity percentage of changes in angles, and middle Hassdorf distance, for the DP-LS method has improved 1829830 square meters, 4.05%, 4.09%, and 5 meters,

respectively. The same improvement was 53.22 m², 1.26%, 2.82%, and 0.04 m for the LS method, respectively.

In future studies, it is suggested that other methods such as the weighted least squares (taking into account the weight in proportion to the length of the edges) be used and compared.

Table 1. The results of indicators for trajectory 1 and 2 in different model

Trajectory	Algorithm	Steiner Points	Threshold	I ₁	I ₂	I ₃	I ₄	I ₅
1	DP	No	1	1603676	68.00	54.72	54.27	0.00
1	DP	Yes	1	1603676	68.00	54.72	54.27	0.00
1	DPLS	No	1	1536	68.00	53.36	52.71	0.01
1	DPLS	Yes	1	141	68.00	61.92	61.60	0.01
1	LS	No	1	213	71.61	69.59	69.40	0.05
1	LS	Yes	1	164	71.81	73.56	73.00	0.02
1	DP	No	10	3769018	93.45	24.99	24.31	0.00
1	DP	Yes	10	3769018	93.45	24.99	24.31	0.00
1	DPLS	No	10	2708556	93.45	24.16	23.27	0.13
1	DPLS	Yes	10	2410490	93.45	27.44	27.10	0.11
1	LS	No	10	3161	93.65	27.82	27.00	0.15
1	LS	Yes	10	3113	94.12	28.40	28.10	0.15
1	DP	No	50	21945175	97.53	12.67	11.55	0.00
1	DP	Yes	50	21945175	97.53	12.67	11.55	0.00
1	DPLS	No	50	59911014	97.53	14.81	13.96	0.42
1	DPLS	Yes	50	53258062	97.53	14.94	14.11	0.18
1	LS	No	50	12822	98.00	15.57	14.30	0.17
1	LS	Yes	50	12773	98.20	16.89	14.30	0.08
2	DP	No	1	272269	73.23	48.57	30.61	0.00
2	DP	Yes	1	272269	73.23	48.57	30.61	0.00
2	DPLS	No	1	440	73.23	49.59	48.20	0.02
2	DPLS	Yes	1	396	73.23	59.83	55.55	0.02
2	LS	No	1	490	75.89	65.79	65.67	0.04
2	LS	Yes	1	432	78.29	65.83	65.67	0.04
2	DP	No	10	2956864	93.65	26.60	9.38	0.00
2	DP	Yes	10	2956864	93.65	26.60	9.38	0.00
2	DPLS	No	10	4525456	93.65	30.67	21.62	0.10
2	DPLS	Yes	10	1507018	93.65	32.29	25.96	0.08
2	LS	No	10	2794	94.62	31.22	49.21	0.14
2	LS	Yes	10	2736	95.40	32.36	59.59	0.08
2	DP	No	50	17134916	97.99	10.46	10.36	0.00
2	DP	Yes	50	17134916	97.99	10.46	10.36	0.00
2	DPLS	No	50	6056549	97.99	11.09	14.51	0.19
2	DPLS	Yes	50	5048459	97.99	11.54	14.51	0.17
2	LS	No	50	44751	98.38	15.46	30.22	0.11
2	LS	Yes	50	44693	98.64	15.98	32.05	0.03

References

- Douglas, D. H., & Peucker, T. K. (1973). Algorithms for the reduction of the number of points required to represent a digitized line or its caricature. *Cartographica: the international journal for geographic information and geovisualization*, 10(2), 112-122.
- Ghilani, Ch. D., & Wolf, P. R. (2006). *Adjustment Computations: Spatial Data Analysis*, Wiley, Fourth Edition.
- Kronenfeld, B. J., Stanislawski, L. V., Buttenfield, B. P., & Brockmeyer, T. (2020). Simplification of polylines by segment collapse: Minimizing areal displacement while preserving

area. *International Journal of Cartography*, 6(1), 22-46.

- Laurila J K, Gatica-Perez D, Aad I, Bornet O, Do T M T, Dousse O, ... & Miettinen, M. (2012). The mobile data challenge: Big data for mobile computing research (No. CONF).
- Meratnia N & Rolf A (2004) Spatiotemporal compression techniques for moving point objects. In *International Conference on Extending Database Technology* (pp. 765-782). Springer, Berlin, Heidelberg.
- Muckell, J., Hwang, J. H., Patil, V., Lawson, C. T., Ping, F., & Ravi, S. S. (2011). SQUISH: an online approach for GPS trajectory compression. In *Proceedings of the 2nd international*

- conference on computing for geospatial research & applications, pp. 1-8.
- Renjian, Z. H. A. I., Fang, W., Li, Z., & Lei, G. (2009). Line simplification based on geographic-feature constraint. ICC, Santiago.
- Shu, J., Wang, S., Jia, X., Zhang, W., Xie, R., & Huang, H. (2020). Efficient Lane-Level Map Building via Vehicle-Based Crowdsourcing. *IEEE Transactions on Intelligent Transportation Systems*.
- Song, J., & Miao, R. (2016). A novel evaluation approach for line simplification algorithms towards vector map visualization. *ISPRS International Journal of Geo-Information*, 5(12), 223.
- Sun, P., Xia, S., Yuan, G., & Li, D. (2016). An overview of moving object trajectory compression algorithms. *Mathematical Problems in Engineering*.
- Tong, X., Jin, Y., Li, L., & Ai, T. (2015). Area-preservation Simplification of Polygonal Boundaries by the Use of the Structured Total Least Squares Method with Constraints. *Transactions in GIS*, 19(5), 780-799.
- Wang, Y., Lv, H., Chen, X., & Du, Q. (2015). A PSO-neural network-based feature matching approach in data integration. In *Cartography-Maps connecting the world* (pp. 189-219). Springer, Cham.
- Williams, R., & Kemp, V. (2020). Principles for designing and delivering psychosocial and mental healthcare. *BMJ Mil Health*, 166(2), 105-110.
- Xiaohua, T., & Gusheng, X. (2004). A new least squares method based line generalization in GIS. In *IGARSS 2004. 2004 IEEE International Geoscience and Remote Sensing Symposium* (Vol. 5, pp. 2912-2915). IEEE.



4th Intercontinental Geoinformation Days

igd.mersin.edu.tr



Evaluation of geochemical analyzes in complex geological structures in GIS environment: Maden (Elazığ) district

Mehmet Ali Ertürk¹ , Cihan Yalçın²

¹Firat University, Department of Geological Engineering, Elazığ, Türkiye

²Ministry of Industry and Technology, World Bank Project Implementation Unit, Ankara, Türkiye

Keywords

Geochemical analysis
GIS
Maden Complex
Thematic maps
Turkey

Abstract

Geochemical analysis results are one of the most significant indicators that reveal the characteristics of the geological structures in a region. In particular, the differences in the composition of complex geological structures can be evident in field and Geographic Information Systems (GIS) studies. Turkey includes a character consisting of quite complex features with its geological structure. The Maden (Elazığ) complex has also attracted the attention of many researchers with its complex structure. Thematic maps are created to make the geological interpretations in this region cleaner and the field data more predictable. These maps also allow the correlation of major oxides and trace elements. In this study, the geochemical data obtained in the Maden Complex were analyzed in the QGIS program. The geochemistry of the region has been made more understandable and interpreted with heat maps. The diversification of thematic maps, which gives a new perspective to geochemical data, will provide more support to geological studies.

1. Introduction

The Southeast Anatolian Orogenic Belt (SAOB) constitutes the eastern part of the Taurus Orogenic Belt, which is one of the most critical tectonic belts in Turkey, located between the Arabian platform and Anatolian micro-plate (Şengör and Yılmaz 1981; Ertürk et al. 2018, 2022; Sar et al. 2019) This belt is a complicated part of the Alpine-Himalayan Mountain range with numerous distinct characteristics. This region has a complex geodynamic history, with northward subduction and closure of the Tethyan Ocean branch and the collision of various continental blocks. The Southeast Anatolian Orogenic Belt has been studied by many researchers in three belts from south to north (Yılmaz 1993; Yılmaz et al., 1993; Yılmaz 2019). (1) During the period from Precambrian to Early Miocene, the "Arabian Platform" consists of a thick autochthonous sedimentary sequence accumulated in the marine environment together with the base volcanic rocks (2) The "Zone of Imbrication", which occurs in the north of the Arabian Platform, which forms a reverse fault zone developed in the Late Cretaceous-Early Miocene interval, about 5-10 km in width (3) The uppermost central tectonic unit, which

includes the Middle Eocene Maden Complex, is the "Nap Zone". These zones are separated from each other by thrust faults. The study area is located north of the Bitlis-Zagros suture zone. It covers the most widespread and the best-observed regions of the Maden Complex, which have an important place in understanding the geodynamic evolution of the region.

Geochemical inputs are applied to clarify many geological problems. One of the powerful practices of these data is statistical and spatial approaches. As it is recognized, many geological studies have been supported by remote sensing and geographic information systems in recent years. These studies are carried out with advanced programs in a computer environment with technology development. Now, many GIS programs are used, and an open source coded QGIS program was used in this study.

The Maden Complex is an extraordinarily significant structure for the geology of Turkey. Major oxide and trace element analyzes were carried out of the samples compiled from the field in this region, which has many complex geological characteristics. The geochemical distribution of this complex region and the relationship between the elements can become more visible with

* Corresponding Author

(erturkmae@gmail.com) ORCID ID 0000-0003-1197-9202
*(cihan.yalcin@sanayi.gov.tr) ORCID ID 0000-0002-0510-2992

Cite this study

Ertürk, M. A., & Yalçın, C. (2022). Evaluation of geochemical analyzes in complex geological structures in GIS environment: Maden (Elazığ) district. 4th Intercontinental Geoinformation Days (IGD), 319-322, Tabriz, Iran

thematic maps in the GIS environment. Heat maps of some of the analysis results of the sample points were created, and discussions on the geological structure were prepared.

2. Method

The samples collected from the field study are detected via XRF and ICP-MS methods. The major oxides and trace element analysis detected by Ertürk et al. (2018) was digitized in the GIS environment, and sample points were located. Afterwards, heat maps dwelling on major oxide and trace elements were made.

2.1. Geological Background

The Maden Complex is situated in the Bitlis-Zagros Suture Zone, including the Zone of Imbricate and Nappe Zone. In the study are the Upper Cretaceous Guleman Ophiolite and the Maastrichtian Lower Eocene Hazar Group thrust over the Maden Complex. The Guleman Ophiolite crops widely in the east and southeast of Hazar Lake and presents its most typical outcrops around the Alacakaya-Maden districts. Regarding the formation of the Guleman ophiolites, many researchers have stated that the Guleman Ophiolites are products of the Neotethys oceanic crust that began to open from the Upper Triassic between the Pütürge Metamorphites and the Keban-Malatya massifs (Michard et al. 1984; Yazgan and Chessex 1991; Beyarslan and Bingöl 1991; Turan et al. 1995). The Guleman ophiolites emplaced on the continental crust towards the south with the closure of this ocean in the Late Cretaceous. Rizeli et al. (2016) accept that the Guleman Ophiolite was formed in the fore-arc basin at the beginning of the northward subduction of the southern branch of Neo-Tethys. According to Kaya (2004), the Hazar group consists of a red-brown basal conglomerate at the bottom, and grey, green and light brown coloured sandstone, siltstone, mudstone, shale, marl and limestone towards the top. For the formation of the unit, researchers such as Özkan (1982), Perinçek and Özkaya (1981), and Aktaş and Robertson (1984) stated that the environment initially presented terrestrial conditions. The units at the base of the Hazar group represent this terrestrial environment and are laterally associated with the Simaki Formation. They stated that the deposition basin gradually deepened with block faults, and the formation was deposited under marine conditions. In contrast, the uppermost Gehroz Formation was pelagic limestones deposited in the shelf environment.

The Maden Complex cropped out over extensive regions in the Eastern Taurus. The Maden Complex also contains basalts, basaltic andesite, andesite, dacite, diabase and pyroclastic rocks, which are intercalated and lateral-vertical transitive with all these sedimentary successions (Fig 1). The brecciation is widespread due to tectonism. Also, the region observes intensive alterations depending on the thrusts and imbrications. Basalts largely crop out in the study area. Basalts are generally greenish, brownish and bearded in colour, massive, ellipsoidal-shaped pillow lavas, and broken pillow basalts. Basalts are intercalated mainly with red cherts

and mudstones. Basaltic andesites and andesites are in grey colours compared to basalts, and it is challenging to distinguish macroscopically from basalts. However, it is possible to make this distinction according to petrographical and geochemical features. The dacites are macroscopically lighter, grey, whitish, and darker than the mafic volcanics and are fine-grained volcanic rocks. The diabbases often cut the basalts. The diabbases greenish coloured are medium grained and vary in thickness. The study area represents pyroclastic rocks represented by agglomerate, lapillistone, and tuff. The agglomerates are composed of bombs with a grain size of more than 64 mm, and a cement material welds the volcanic parts. The lapillistones have a basic and andesitic composition. The tuffs are fine grain. Ertürk et al. (2018) reported that the middle Eocene Maden magmatism developed in a post-collisional environment by asthenospheric upwelling owing to convective removal of the lithosphere during an extensional collapse. Yalçın et al. (2020) stated that Cu anomalies in Maden Complex are around Hasenekevleri (Maden-Elazığ) and said that Cu mineralization is in vein type within diabbases.

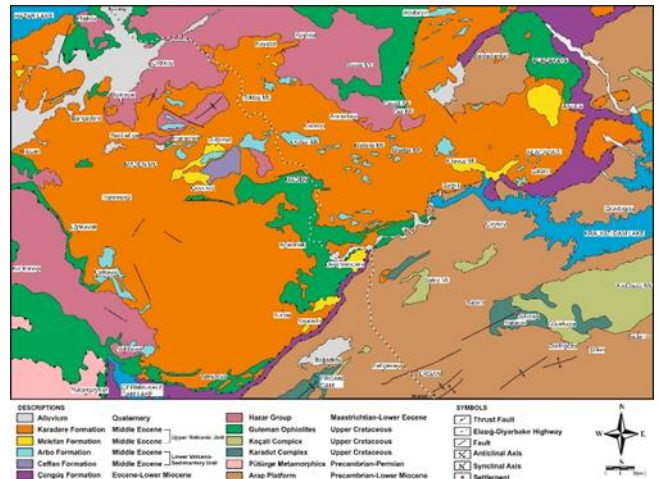


Figure 1. Geological map of the study area (modified from MTA, 2011).

3. Results

3.1. GIS application

Many samples were taken from the field in the petrographic and petrological study by Ertürk et al. (2018). Geochemical analyzes of these samples were carried out and used in many clarifications. In this study, a heat map was prepared in the QGIS program to compare and review the attribute information of the sample points. In Figure 2, it is seen that the major oxide values commonly show a similar distribution in many samples. SiO₂ is an essential component of minerals that make up many rocks. Other oxides (Fig 2) take place in the structure of silicate minerals together with SiO₂. The SiO₂ distribution also summarizes whether the rocks are acidic or basic. Higher values represent acidic rocks, while lower values represent basic and ultrabasic rocks. Except for the northeast of the study area, most basic and near-basic rock groups are observed (Fig 2).

The distribution of some trace elements is given in Figure 3. While Cr, Ga and V have a roughly similar

distribution, Cu, W and Rb have different patterns. These differences are due to lithology, mineralogy and geochemical differences. With these studies, the existence of structures with different characteristics should be correlated with field data. Therefore, the information that will be a guide will lead to more meaningful interpretations. Moreover, it is exceedingly challenging to make lithological discrimination in the Maden Complex, where rocks of many different characters are observed closely. For this reason, it is significant to evaluate the data obtained in the field in the GIS environment.

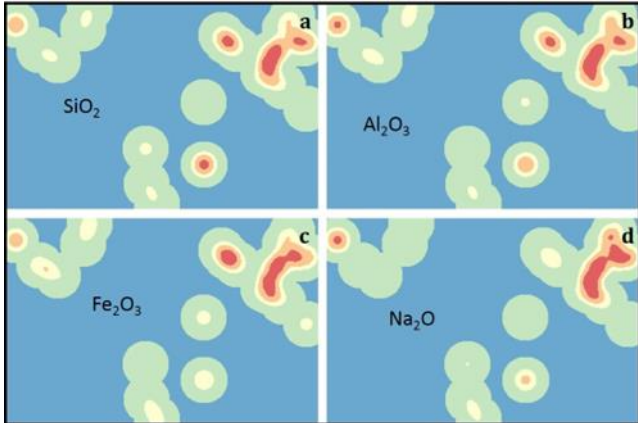


Figure 2. Heat map of the study area via major oxide contents

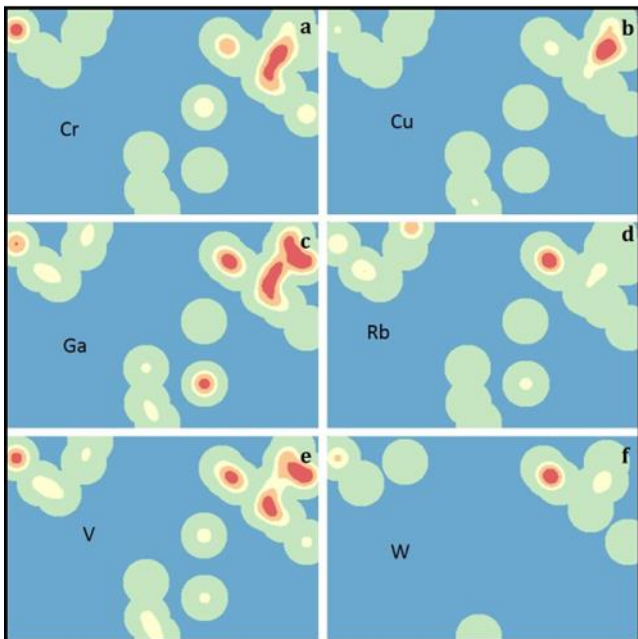


Figure 3. Heat map of the study area via trace element contents.

4. Discussion and Conclusion

GIS-based modelling has been proposed in addition to geology-geochemistry studies (Brown et al. 2003; Partington 2008). This modelling provides the geostatistical approach to the geological structures. For example, Atakoğlu and Yalçın (2021) explained the statistical properties of Sutlegen (Antalya) bauxite according to their geochemical content and set up thematic maps with the Krigging interpolation method.

Mapping minerals, elements or oxides based on multi-source geoscience data (geology, geochemistry, and remote sensing) and computer technology is an effective technique that merges information and data-driven production (Bonham-Carter 1994; Zhao 2002; Wang et al. 2016). For this reason, the data of the study conducted by Ertürk et al. (2018) in the Maden (Elazığ) district were re-evaluated in the QGIS environment. In the evaluations prepared, GIS-based thematic maps correctly exhibit the relationship of the geochemical contents of the study area correctly.

References

- Aktaş, G., & Robertson, H. F. (1984). The Maden Complex, SE Turkey: evolution of a Neotethyan active margin. In: Dixon, J.E., Robertson, A.H.F. (Eds.), *The Geological Evolution of the Eastern Mediterranean*. The Geological Society by Blackwell Scientific Publication, Oxford, London, Edinburgh, Boston, Palo Alto, Melbourne, pp. 375–401.
- Atakoğlu, O. Ö., & Yalçın, M. G. (2021). Geochemical characterization of the Sutlegen bauxite deposit, SW Antalya. *Mining of Mineral Deposits*, 15(3), 108–121. <https://doi.org/10.33271/mining15.03.108>.
- Beyarslan, M., & Bingöl, A. F. (1991). Petrographical Features of the Ispendere Ophiolite Kale-Malatya, Türkiye, *Yerbilimleri*, 19, 59–68.
- Bonham-Carter, G. F. (1994). *Geographic information systems for geoscientists: modelling with GIS*. Pergamon Press, Oxford, p. 398.
- Brown, W., Groves, D. I., & Gedeon, T. (2003). Use of fuzzy membership input layers to combine subjective geological knowledge and empirical data in a neural network method for mineral-potential mapping. *Natural Resources Research* 12, 183–200.
- Ertürk, M. A., Beyarslan, M., Chung, S-L., & Lin, T-H. (2018). Eocene magmatism (Maden Complex) in the Southeast Anatolian Orogenic Belt: Magma genesis and tectonic implications. *Geosci. Frontiers* 9, 1829–1847. <https://doi.org/10.1016/j.gsf.2017.09.008>.
- Kaya, A. (2004). Gezin (Maden-Elazığ) Çevresinin Jeolojisi, Pamukkale Üniversitesi Mühendislik Bilimleri Dergisi, 10, 1, 41–50.
- Michard, A., Whitechurch, H., Ricou, L. E., Montigny, R., & Yazgan, E. (1984). Tauric subduction (Malatya-Elazığ Provinces) and its bearing on tectonics of the Tethyan realm in Turkey, in *The Geological Evolution of The Eastern Mediterranean*, Geological Society of London, Special Publication, Eds. Dixon, J. E., Robertson, A. H. F., 17, 361–374.
- MTA (2011). 1/100.000 ölçekli Türkiye Jeoloji Haritası, Maden Tetkik ve Arama Genel Müdürlüğü, Ankara.
- Özkan, Y. Z. (1982). Guleman (Elazığ) Ofiyoliti'nin jeolojisi ve petrolojisi, *Yerbilimleri*, İstanbul, 3(1/2), 295–311.
- Partington, G. (2008). Prospectivity analysis in action: the Auzex Resources Ltd (AZX) story as applied to granite related mineral systems in Eastern Australia and New Zealand. *Australian Earth Sciences Convention*, Perth, July 20–24, p. 195.

- Perinçek, D., & Özkaya, İ. (1981). Arabistan levhası kuzey kenarının tektonik evrimi, *Yerbilimleri*, 8, 91-101.
- Rizeli M E, Beyarslan M, Wang K-L & Bingöl, A. F. (2016). Mineral chemistry and petrology of mantle peridotites from the Guleman ophiolite (SE Anatolia, Turkey): Evidence of a forearc setting. *J. Afr. Earth Science* 123, 392-402. <https://doi.org/10.1016/j.jafrearsci.2016.08.013>
- Sar, A., Ertürk, M. A., & Rizeli, M. E. (2019). Genesis of Late Cretaceous intra-oceanic arc intrusions in the Pertek area of Tunceli Province, eastern Turkey, and implications for the geodynamic evolution of the southern Neo-Tethys: Results of zircon U-Pb geochronology and geochemical and Sr-Nd isotopic analyses. *Lithos*, 350-351, 105263. <https://doi.org/10.1016/j.lithos.2019.105263>.
- Şengör, A. M. C., & Yılmaz, Y. (1981). Tethyan evolution of Turkey: A plate tectonic approach. *Tectonophysics*, 75, 181-241. [https://doi.org/10.1016/0040-1951\(81\)90275-4](https://doi.org/10.1016/0040-1951(81)90275-4)
- Turan, M., Aksoy, E., & Bingöl, A. F. (1995). Doğu Torosların Jeodinamik Evriminin Elazığ Civarındaki Özellikleri. *Fırat Üniversitesi, Fen ve Mühendislik Bilimleri Dergisi*, 7/2, 177-200.
- Wang, G. W., Du, W., & Carranza, J. M. (2016). Remote sensing and GIS prospectivity mapping for magmatic-hydrothermal base and precious-metal deposits in the Honghai district, China. *J. Afr. Earth Sci.* xxx, 1e19.
- Yalçın, C., Kumral, M., Kaya, M., & Karaman, M. (2020). Hasenekevleri (Maden-Elazığ) güneyindeki diyabazlarda gelişen hidrotermal cu cevherleşmesinin jeolojisi ve alterasyon jeokimyası, *Bitlis Eren Üniversitesi Fen Bilimleri Dergisi*, 9(3), 1282-1296. <https://doi.org/10.17798/bitlisfen.630452>, 2020.
- Yazgan, E., & Chessex, R. (1991). Geology and tectonic evolution of the southeastern Taurides in the region of Malatya. *Turk Assoc Petrol Geol* 3(1), 1-42.
- Yılmaz, Y. (1993). New evidence and model on the evolution of the southeast Anatolian orogen. *Geol. Soc. Am. Bulletin* 105, 251-271. [https://doi.org/10.1130/0016-7606\(1993\)105<0251:NEAMOT>2.3.CO;2](https://doi.org/10.1130/0016-7606(1993)105<0251:NEAMOT>2.3.CO;2)
- Yılmaz, Y. (2019). Southeast Anatolian Orogenic Belt revisited (geology and evolution). *Can. J. Earth Science* 56, 1163-1180. <https://doi.org/10.1139/cjes-2018-0170>
- Zhang, Z. H., & Zhang, B. T. (1991). Studies of U-bearing granites and associated uranium ore deposits in south China (in Chinese with English abstract), Beijing: Atomic Energy Publishing House, 70-105.
- Zhao, P. D. (2002). Three Component quantitative resource prediction and assessments: theory and practice of digital mineral prospecting. *Earth Sci. J. China Univ. Geosci.* 27 (5), 482e490 (in Chinese).

4th Intercontinental Geoinformation Days

igd.mersin.edu.tr



Landslide susceptibility assessment of the high range areas in Thiruvananthapuram district (Southwest India) using the MCDA-AHP model and geospatial techniques

Suchithra Jayakumar Anchima¹, Ajayakumar Gokul², Nelson Harshith¹, Romulus Costache^{3,4,5}, Rajendran Sobha Ajin^{*2,6}

¹Department of Civil Engineering, Marian Engineering College, Kazhakuttom, Thiruvananthapuram, Kerala, India

²Kerala State Emergency Operations Centre (KSEOC), Kerala State Disaster Management Authority (KSDMA), Thiruvananthapuram, India

³National Institute of Hydrology and Water Management, Bucharest, Romania

⁴Transilvania University of Brasov, Department of Civil Engineering, Brasov, Romania

⁵Danube Delta National Institute for Research & Development, Tulcea, Romania

⁶Resilience Development Initiative (RDI), Bandung, Indonesia

Keywords

AHP
GIS
Landslides
ROC
Susceptibility

Abstract

Landslides are one of the most frequent hazards occurring in the mountainous terrain of the Western Ghats. The purpose of this study is to use the analytical hierarchy process approach to identify landslide-susceptible zones in the Western Ghats region of Thiruvananthapuram district. A total of 11 conditioning factors were evaluated in the susceptibility modelling. A landslide susceptibility map was created using satellite data and geographic information systems (GIS), and the study area was segmented into five susceptible zones using the natural breaks method. The AHP method of landslide susceptibility modelling identified 14.76% of the area as a very high-susceptible zone. The receiver operating characteristic (ROC) technique was used to validate the created landslide susceptibility map. The landslide susceptibility map produced using the AHP model is confirmed as having excellent and outstanding prediction capability for the training and validation datasets, based on the area under the ROC curve (AUC) value. When it comes to implementing landslide mitigation techniques, decision-makers and land-use planners will find the map quite valuable.

1. Introduction

Landslides are one of the most common and frequent natural hazards in India's Western Ghats, resulting in significant property loss and casualties (Akshaya et al. 2021). As a result, a susceptibility map with enhanced prediction capabilities is required for the execution of appropriate mitigation measures (Thomas et al. 2021).

The purpose of this study is to use the MCDA-AHP model to determine the susceptibility of the Western Ghats region of Thiruvananthapuram district. The study area has a history of disastrous landslide disasters, the most catastrophic of which was the Amboori landslide disaster, which occurred on November 9, 2001 and killed 39 people (Kuriakose et al. 2009). Slope angle, land use/land cover (LULC), lithology, soil texture, road buffer, lineament buffer, normalized difference road landslide index (NDRLI), normalized burnt ratio (NBR),

modified normalized difference water index (MNDWI), normalized difference built-up index (NDBI), and advanced vegetation index (AVI) were among the 11 conditioning factors used in the modelling.

2. Method

2.1. Study area

The study area encompasses 647.12 km² and is located between 8°25' and 8°52' N latitudes and 77°0' and 77°18' E longitudes (Fig. 1). The elevation varies between 21 and 1828 m, with the highest values along the eastern boundary. This area encompasses nine villages in the Thiruvananthapuram district, namely Amboori, Keezharoor, Mannoorkara, Ottasekharamangalam, Peringamala, Thennoor, Vazhichal, Vellarada, and Vithura.

* Corresponding Author

(anchutvm97@gmail.com) ORCID ID 0000-0001-7022-0752
(megokula@gmail.com) ORCID ID 0000-0003-4741-6460
(harshith@marian.ac.in) ORCID ID 0000-0002-0523-6608
(romuluscostache2000@yahoo.com) ORCID ID 0000-0002-6876-8572
(ajinares@ieee.org) ORCID ID 0000-0003-3073-4390

Cite this study

Anchima, S. J., Gokul, A., Harshith, N., Costache, R., Ajin, R. S. (2022). Landslide susceptibility assessment of the high range areas in Thiruvananthapuram district (Southwest India) using the MCDA-AHP model and geospatial techniques. 4th Intercontinental Geoinformation Days (IGD), 323-326, Tabriz, Iran

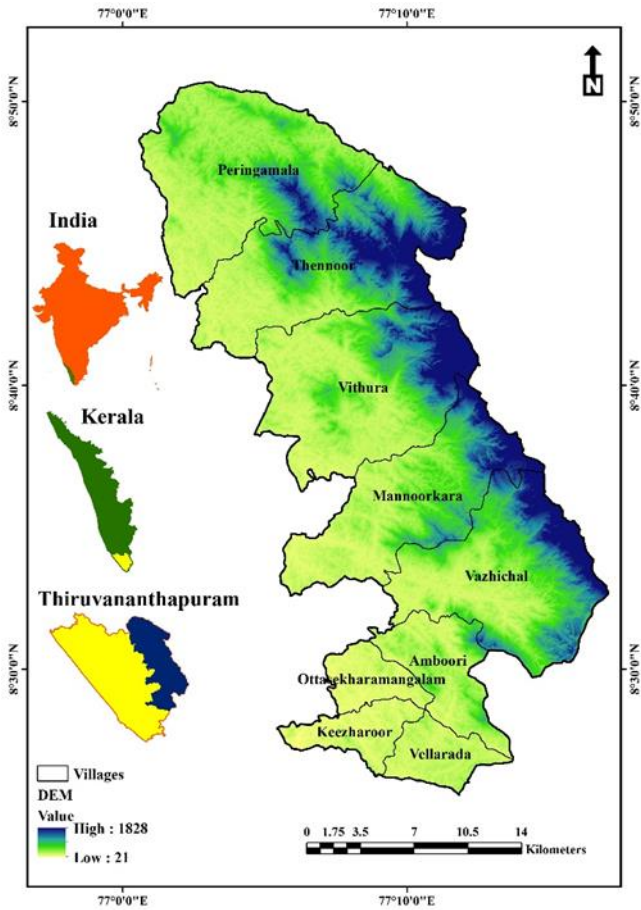


Figure 1. Location of the study area

2.2. Conditioning factors

The slope was computed from the ASTER GDEM using the ArcGIS 10.8 spatial analyst (surface) tools. The LULC types were extracted from the Landsat 8 OLI satellite images using the ERDAS Imagine 9.2 software. Various LULC types were classified using the maximum likelihood classification method (Thomas et al. 2021). The lithology was extracted from the lithology map published by the Geological Survey of India (GSI) using ArcGIS tools. The soil data was extracted from the soil map published by the National Bureau of Soil Science and Land Use Planning (NBSS&LUP) using ArcGIS tools. The road networks were extracted from the Survey of India topographic maps and updated using Google Earth Pro data, and the buffer distance of 100 m was derived using spatial analyst tools. The lineaments were derived from the Bhukosh portal (<https://bhukosh.gsi.gov.in/Bhukosh/Public>) of GSI, and the buffer distance of 100 m was derived using spatial analyst tools. NDRLI, NBR, MNDWI, NDBI, and AVI were calculated from the Landsat 8 OLI image using ArcGIS raster calculator tools. NDRLI, NBR, MNDWI, NDBI, and AVI were computed using Eq. 1 (Zhao et al. 2018), Eq. 2 (Delcourt et al. 2021, Roy et al. 2006), Eq. 3 (Xu 2006), Eq. 4 (Zha et al. 2003), and Eq. 5 (Bera et al. 2020), respectively. The thematic layers of the continuous factors and output map were classified using the natural breaks (Thomas et al. 2021) method.

$$\text{NDRLI} = \frac{(\text{SWIR1} - \text{Blue})}{(\text{SWIR1} + \text{Blue})} \quad (1)$$

$$\text{NBR} = \frac{(\text{NIR} - \text{SWIR})}{(\text{NIR} + \text{SWIR})} \quad (2)$$

$$\text{MNDWI} = \frac{(\text{Green} - \text{MIR})}{(\text{Green} + \text{MIR})} \quad (3)$$

$$\text{WRI} = \frac{(\text{SWIR1} - \text{NIR})}{(\text{SWIR1} + \text{NIR})} \quad (4)$$

$$\text{AVI} = [\text{NIR} + 1(1 - \text{Red}) \times (\text{NIR} - \text{Red})]^{1/3} \quad (5)$$

where SWIR, Blue, NIR, Green, MIR and Red stand for spectral reflectance in short wave infrared, blue, near-infrared, green, mid infrared and red bands, respectively.

2.3. AHP modelling

The AHP method for multi-criteria decision analysis was developed by Thomas L. Saaty (Saaty 1980). This approach is used to organize complex problems into a hierarchy and determine the best solution (Qazi and Abushammala 2020). The AHP method's ability to detect pairwise rating inconsistency is another noteworthy feature (Mondal and Maiti 2013). The most significant steps in AHP modelling are to generate a matrix for pairwise comparisons and to compute the eigen vector, weighting coefficient (Table 1), and consistency ratio (Table 2) (as in Akshaya et al. 2021; Thomas et al. 2021).

2.4. Validation of the susceptibility map

ROC curve method (Thomas et al. 2021) was used to validate the susceptibility map. SPSS software was used to compute the AUC value. The validation was performed using landslide incidence data from the National Remote Sensing Centre and GSI. The total number of landslides, 100, was split into training datasets (70%) and validation datasets (30%).

3. Results

According to the AHP modelling, the key causal factors include LULC, NDRLI, road buffer, slope angle, and soil. Moderate slopes, gravelly clay and loamy soil, agricultural land, higher NDRLI values, and more road cuttings characterize the high and very-high susceptible zones. The susceptibility map developed using the MCDA-AHP method has AUC scores of 0.896 (training dataset) and 0.931 (validation dataset), confirming that the results have excellent and outstanding prediction capabilities for these datasets (Fig. 2). The high and very-highly susceptible zones together constitute 47.5% of the study area, according to the map developed using the AHP approach. The landslide susceptibility map is depicted in Figure 3.

Table 1. Pairwise comparison matrix

	Slp.	LULC	NDRLI	RB	Litho.	Soil	NBR	MNDWI	NDBI	LB	AVI	Vp	Cp
Slp.	1	2	3	4	5	6	7	8	9	10	11	3.202	0.187
LULC	1/2	1	2	3	4	5	6	7	8	9	10	2.462	0.144
NDRLI	1/3	1/2	1	2	3	4	5	6	7	8	9	1.848	0.108
RB	1/4	1/3	1/2	1	2	3	4	5	6	7	8	1.413	0.082
Litho.	1/5	1/4	1/3	1/2	1	2	3	4	5	6	7	1.271	0.074
Soil	1/6	1/5	1/4	1/3	1/2	1	2	3	4	5	6	1.244	0.073
NBR	1/7	1/6	1/5	1/4	1/3	1/2	1	2	3	4	5	1.221	0.071
MNDWI	1/8	1/7	1/6	1/5	1/4	1/3	1/2	1	2	3	4	1.194	0.070
NDBI	1/9	1/8	1/7	1/6	1/5	1/4	1/3	1/2	1	2	3	1.158	0.067
LB	1/10	1/9	1/8	1/7	1/6	1/5	1/4	1/3	1/2	1	2	1.105	0.064
AVI	1/11	1/10	1/9	1/8	1/7	1/6	1/5	1/4	1/3	1/2	1	1.038	0.060
Σ	3.02	4.93	7.83	11.72	16.59	22.45	29.28	37.08	45.83	55.50	66.00	17.16	1.00

where Slp. = slope, RB = road buffer, Litho. = lithology, and LB = lineament buffer

Table 2. Normalized matrix

	Σ rank	[C]	[D] = [A]*[C]	[E] = [D]/[C]	λ_{max}	CI	CR
Slp.	3.03	0.275	3.368	12.236			
LULC	2.23	0.202	2.506	12.386			
NDRLI	1.63	0.149	1.737	11.689			
RB	1.20	0.109	1.332	12.173			
Litho.	0.89	0.080	0.957	11.897			
Soil	0.65	0.059	0.683	11.594			
NBR	0.47	0.043	0.486	11.324	11.648	0.065	0.045 (4.47%)
MNDWI	0.34	0.031	0.345	11.143			
NDBI	0.25	0.022	0.248	11.096			
LB	0.18	0.016	0.183	11.198			
AVI	0.14	0.012	0.141	11.388			
Σ	11.00	1.00		128.124			

4. Conclusion

Moderate slopes, gravelly clay and loamy soil, agricultural land, greater NDRLI values, and more road cuttings are found in the high and very-highly susceptible zones. The AUC values proved that the created map and AHP approach are effective in demarcating landslide susceptibility and can be used in locations with similar physiographic settings. The map is very useful for land-use planners to determine which villages are most susceptible to landslides. The susceptibility map can be used by decision-makers to detect landslide-prone roads and settlements. This will allow them to take the appropriate mitigation measures to protect people, infrastructure, and property; save money on relief and building efforts; and stop development activities in these areas.

References

- Akshaya, M., Danumah, J. H., Saha, S., Ajin, R. S., & Kuriakose, S. L. (2021). Landslide susceptibility zonation of the Western Ghats region in Thiruvananthapuram district (Kerala) using geospatial tools: A comparison of the AHP and Fuzzy-AHP methods. *Safety in Extreme Environments*, 3, 181-202. <https://doi.org/10.1007/s42797-021-00042-0>
- Bera, B., Saha, S., & Bhattacharjee, S. (2020). Estimation of forest canopy cover and forest fragmentation mapping using Landsat satellite data of Silabati river basin (India). *KN - Journal of Cartography and Geographic Information*, 70, 181-197. <https://doi.org/10.1007/s42489-020-00060-1>
- Delcourt, C. J. F., Combee, A., Izbicki, B., Mack, M. C., Maximov, T., Petrov, R., Rogers, B. M., Scholten, R. C., Shestakova, T. A., van Wees, D., & Veraverbeke, S. (2021). Evaluating the differenced normalized burn ratio for assessing fire severity using Sentinel-2

- imagery in Northeast Siberian Larch Forests. *Remote Sensing*, 13(12).
<https://doi.org/10.3390/rs13122311>
- Kuriakose, S. L., Sankar, G., & Muraleedharan, C. (2009). History of landslide susceptibility and a chorology of landslide-prone areas in the Western Ghats of Kerala, India. *Environmental Geology*, 57, 1553-1568.
<https://doi.org/10.1007/s00254-008-1431-9>
- Mondal, S., & Maiti, R. (2013). Integrating the analytical hierarchy process (AHP) and the frequency ratio (FR) model in landslide susceptibility mapping of Shivkhola watershed, Darjeeling Himalaya. *International Journal of Disaster Risk Science*, 4, 200-212.
<https://doi.org/10.1007/s13753-013-0021-y>
- Qazi, W. A., & Abushammala, M. F. M. (2020). Chapter 10 - Multi-criteria decision analysis of waste-to-energy technologies. In: Ren J (ed), *Waste-to-Energy*, Academic Press, pp 265-316.
<https://doi.org/10.1016/B978-0-12-816394-8.00010-0>
- Roy, D. P., Boschetti, L., & Trigg, S. N. (2006). Remote sensing of fire severity: assessing the performance of the normalized burn ratio. *IEEE Geoscience and Remote Sensing Letters*, 3(1), 112-116.
<https://doi.org/10.1109/LGRS.2005.858485>
- Saaty, T. L. (1980). *The analytic hierarchy process: planning, priority setting, resource allocation* (Decision making series). McGraw Hill, New York, United States of America.
- Thomas, A. V., Saha, S., Danumah, J. H., Raveendran, S., Prasad, M. K., Ajin, R. S., & Kuriakose, S. L. (2021). Landslide susceptibility zonation of Idukki district using GIS in the aftermath of 2018 Kerala floods and landslides: A comparison of AHP and frequency ratio methods. *Journal of Geovisualization and Spatial Analysis*, 5(2). <https://doi.org/10.1007/s41651-021-00090-x>
- Zha, Y., Gao, J. & Ni, S. (2003). Use of normalized difference built-up index in automatically mapping urban areas from TM imagery. *International Journal of Remote Sensing*, 24(3), 583-594.
- Zhao, Y., Huang, Y., Liu, H., Wei, Y., Lin, Q., & Lu, Y. (2018). Use of the normalized difference road landside index (NDRLI)-based method for the quick delineation of road-induced landslides. *Scientific Reports*, 8.
<https://doi.org/10.1038/s41598-018-36202-9>

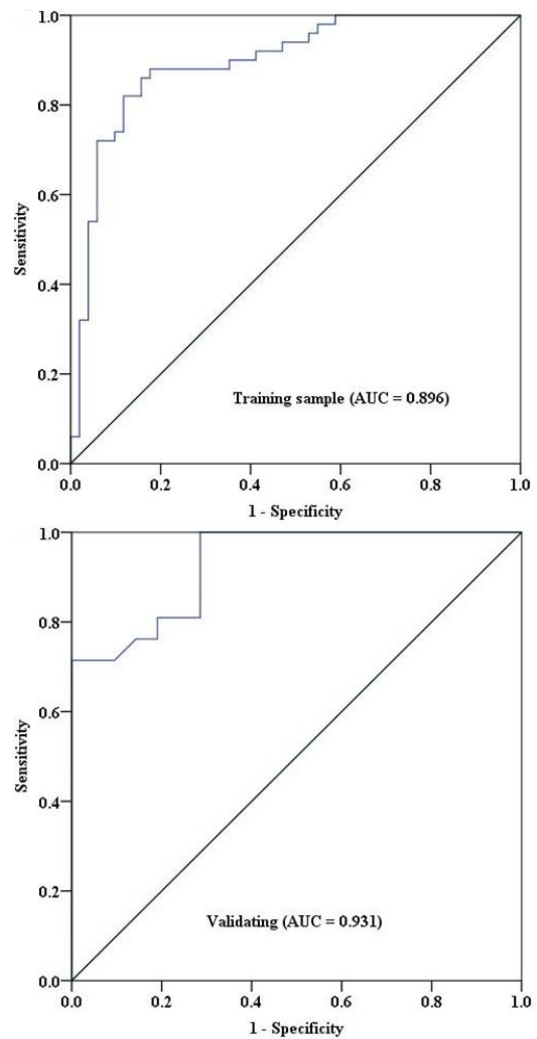


Figure 2. The ROC curves

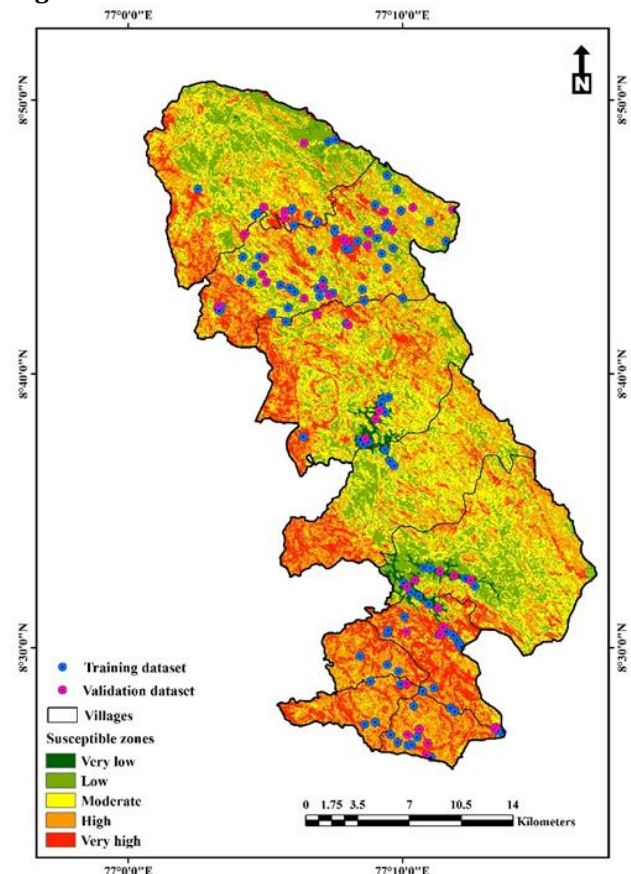


Figure 3. Landslide susceptible zones





MERSIN UNIVERSITY



4th Intercontinental Geoinformation Days (IGD) 2022

 20-21 June 2022

 09:00 – 18:00 (GMT+ 4:30)

 University of Tabriz, Iran

ISBN: 978-605-73805-7-9

<https://igd.mersin.edu.tr/>